HAL
open science

Numerical and experimental study of machining titanium-composite stacks

Jinyang Xu

To cite this version:

Jinyang Xu. Numerical and experimental study of machining titanium-composite stacks. Mechanics of materials [physics.class-ph]. Ecole nationale supérieure d'arts et métiers - ENSAM, 2016. English. NNT : 2016ENAM0022 . tel-01395481v2

HAL Id: tel-01395481

https://pastel.hal.science/tel-01395481v2

Submitted on 13 Sep 2016

HAL is a multi-disciplinary open access archive for the deposit and dissemination of scientific research documents, whether they are published or not. The documents may come from teaching and research institutions in France or abroad, or from public or private research centers.

L'archive ouverte pluridisciplinaire **HAL**, est destinée au dépôt et à la diffusion de documents scientifiques de niveau recherche, publiés ou non, émanant des établissements d'enseignement et de recherche français ou étrangers, des laboratoires publics ou privés.

2016-ENAM-0022

École doctorale n° 432 : Sciences des Métiers de l'Ingénieur

Doctorat ParisTech

T H È S E

pour obtenir le grade de docteur délivré par

l'École Nationale Supérieure d'Arts et Métiers

Spécialité " Mécanique - matériaux "

présentée et soutenue publiquement par

Jinyang XU

le 15 juillet 2016

Numerical and experimental study of machining titanium-composite stacks

Directeur de thèse : **Mohamed EL MANSORI**

Jury

M. Fabrice PIERRON, Professeur, Engineering and the Environment, University of Southampton, UK	Président
M. Steven Y. LIANG, Professeur, Georgia Institute of Technology, USA	Rapporteur
M. Hervé PELLETIER, Professeur, ICS - UPR 22 CNRS, INSA de Strasbourg, France	Rapporteur
M. Mohamed EL MANSORI, Professeur, MSMP - EA 7350, Arts et Métiers ParisTech, France	Examinateur
M. Robert PIQUET, Maître de Conférences - HDR, ICA, Université Paul Sabatier, Toulouse, France	Examinateur
M. Fahad ALMASKARI, Maître de Conférences, The Petroleum Institute, Abu Dhabi, UAE	Invité

T H È S E

Arts et Métiers ParisTech - Centre de Châlons-en-Champagne
Laboratoire Mécanique, Surfaces, Matériaux et Procédés - (MSMP - EA 7350)

Dedicated to my parents

ACKNOWLEDGMENTS

The Ph.D. work has been finalized in the Laboratory of Mechanics, Surfaces and Materials Processing (MSMP – EA 7350) of Arts et Métiers ParisTech with the financial support of the China Scholarship Council (CSC) (Contract No. 201306230091). The study experience is a valuable and glorious journey for my life. Herein I am so fortunate to know my respected supervisor and beloved colleagues, and so lucky to receive their sincere concern and kind assistance during my three-year stay in France.

First and foremost, I would like to express my sincere gratitude to my thesis director: Prof. Mohamed EL MANSORI, for his invaluable guidance and encouragement throughout my Ph.D. research. I appreciate his responsible supervision, dedicated support, and kind assistance during my stay in France. His rigorous scholarship, keen research insight, and active academic thinking have deeply encouraged me, which will inspire me to go ahead in my future research work.

I would like to thank Prof. Fabrice PIERRON from University of Southampton, UK, for accepting to be the president of my Ph.D. defense committee as well as for his insightful comments and constructive advice on my thesis. I am very grateful to Prof. Steven Y. LIANG from Georgia Institute of Technology, USA, and Prof. Hervé PELLETIER from INSA de Strasbourg, France, for accepting to be the referees and for spending their precious time and great efforts in reviewing my thesis. I am also honored to be able to invite Prof. Robert PIQUET from Université Paul Sabatier, France, and Dr. Fahad ALMASKARI from The Petroleum Institute, Abu Dhabi, UAE, to attend my Ph.D. defense, and I sincerely appreciate their valuable comments on my thesis.

I gratefully acknowledge the financial support of the China Scholarship Council (CSC), which enables me to finalize my Ph.D. study in Arts et Métiers ParisTech, France.

I would like to acknowledge and extend my appreciation to all the technicians and staffs in the MSMP laboratory of Arts et Métiers ParisTech, especially Mr. Julien VOISIN, Mr. Claude SCHMITT, Dr. Lotfi HEDJAZI, Dr. Laurence FOUILLAND-PAILLÉ and Dr. Anne HUGUET who have provided me much technical assistance throughout my Ph.D. work. Besides, I am grateful to Prof. Halim HADDADI and Dr. Sabeur MEZGHANI for providing me many helpful suggestions and constructive comments on both my research work and future job plan. Furthermore, my cordial and sincere thanks also go to all the labmates in the MSMP and my friends in France including Mohammed YOUSFI, Simon JOLIVET, Faissal CHEGDANI, Kévin SERPIN, Imane OUTMANI, Fan LI, Qing XIA, and Peng WANG with whom I have shared an enjoyable and wonderful time in France.

Last but not least, I would like to give the most heartfelt thanks to my parents for their selfless support, deep love, and endless encouragement. Their meticulous care and excellent support are the key sources of my continuous endeavor, progress, and growth in both study and life. Herein I sincerely wish them successful work, good health, and good luck.

Jinyang Xu
Arts et Métiers ParisTech - 15/07/2016

ABSTRACT

In modern aerospace industry, the use of hybrid CFRP/Ti stacks has experienced an increasing trend because of their enhanced mechanical/physical properties and flexible structural functions. The key advantages of delivering energy saving and improving system function have awarded the bi-material a promising alternative for substituting individual composite and metal applications in various industrial fields. However, due to their anisotropic mechanical behaviors and poor machinability, machining hybrid CFRP/Ti stacks in one shot time still remains the main scientific and technological challenge in modern manufacturing sectors. Particular issues may arise from the high force/temperature generation, poor surface quality, and rapid tool wear. On the current research advancement, the existing scientific work dealing with hybrid CFRP/Ti stack cutting was still performed solely via the experimental methodology, which is cost-prohibitive and time-consuming.

Compared to the previous investigations in literature, the present work aims to provide a combined numerical and experimental study on cutting comprehension of hybrid CFRP/Ti stacks. To this aim, an original FE model comprising three fundamental physical constituents was established to construct the anisotropic machinability of the bi-material system. The CFRP phase was modeled as an equivalent homogeneous material (EHM) by implementing the Hashin damage criteria to simulate the rupture and separation of the fiber/matrix system. The Ti phase was assumed isotropic with elastoplastic behavior, and Johnson-Cook criteria were utilized to replicate the local failure of the metallic phase. The CFRP/Ti interface physically described as an intermediate constituent was modeled through the concept of cohesive zone (CZ). The numerical work aims to provide preliminary inspections of the key cutting mechanisms dominating the hybrid CFRP/Ti machining in order to facilitate the post-experimental studies.

Afterward, some systematic experimental work including orthogonal cutting, combined CFRP/Ti machining, and hole drilling was carefully performed *versus* different input cutting conditions. The key responses of hybrid CFRP/Ti stack machining including chip separation process, machined surface quality, tool wear mechanism were precisely addressed via both numerical and experimental methodologies. Special foci were made on the inspections of different cutting sequences' influences on hybrid CFRP/Ti stack machining and induced bi-material interface damage formation. The combined numerical-experimental studies provide the key findings aiming to (*i*) reveal the activated mechanisms controlling the interface cutting and subsequent interface damage formation, (*ii*) clarify the influences of different cutting-sequence strategies ($^{\text{CFRP} \rightarrow \text{Ti}}_{\text{Ti} \rightarrow \text{CFRP}}$) on hybrid CFRP/Ti stack machining, (*iii*) outline the machinability classification of hybrid CFRP/Ti stacks, and (*iv*) analyze the parametric effects and tool geometry/material influences on cutting of hybrid CFRP/Ti stacks.

Contents

Chapter I **1**
1.1 Introduction 4
1.2 Material properties and characterization 5
1.2.1 FRP composite phase 5
1.2.2 Titanium alloy phase 6
1.2.3 FRP/Ti stacked assembly 7
1.3 Drilling force characterization 10
1.4 Cutting mechanisms controlling FRP/Ti drilling 13
1.4.1 FRP-phase drilling: brittle fracture dominant mechanisms 14
1.4.2 Interface drilling: interrelated and mixed cutting mechanisms 15
1.4.3 Ti-phase drilling: plastic-deformation dominant mechanisms 17
1.5 Drilling-induced damage 17
1.5.1 Hole damage produced in FRP phase 18
1.5.2 Interface damage: the weakest interfacial region 21
1.5.3 Hole damage produced in Ti phase 22
1.6 Tool wear mechanisms in FRP/Ti drilling 25
1.7 Strategies for high-quality drilling 29
1.7.1 Cutting parameters 30
1.7.2 Cutting tool 31
1.7.3 Cutting environment 35
1.8 Numerical approaches 36
1.8.1 FRP composite modeling 36
1.8.2 Ti alloy modeling 40
1.9 Concluding remarks 43

Chapter II **45**
2.1 Introduction 47
2.2 Physical behavior and basic configuration of hybrid CFRP/Ti stacks 47
2.2.1 Ti alloy phase 48
2.2.1.1 Microstructure and composition of Ti6Al4V alloy *48*
2.2.1.2 Machining behavior of Ti6Al4V alloys *49*

2.2.2 CFRP laminate phase 50
2.2.2.1 Mechanical property and behavior of CFRP laminate 50
2.2.2.2 Machining behavior of CFRP laminates 52
2.3 Geometrical features and boundary conditions of the hybrid composite model 53
2.3.1 Adopted assumptions for numerical simulations 53
2.3.2 FE model for interface cutting and interface damage formation investigation 53
2.3.3 FE model for cutting sequence and frictional response studies 56
2.3.4 Equations of motion: Abaqus/Explicit scheme 57
2.4 Material constitutive law and progressive damage criterion 58
2.4.1 Ti-phase constitutive model 59
2.4.2 CFRP-phase model 61
2.4.3 Interface constitutive model 65
2.5 Experimental validation of the OC model 68
2.6 Conclusions 71

Chapter III 73
3.1 Introduction 75
3.2 Workpiece configuration and properties 75
3.3 Cutting tool details 78
3.4 Measuring systems and experimental techniques 82
3.4.1 On-site measuring system 83
3.4.1.1 Force generation characterization 83
3.4.1.2 Chip separation process monitoring 84
3.4.2 Post-treatment analyses 84
3.4.2.1 Optical microscope and microhardness analysis 84
3.4.2.2 Surface roughness and 3D profiling 85
3.4.2.3 Hole dimensional feature measurement 88
3.4.2.4 SEM and EDS techniques 88
3.5 Experimental setup and cutting design 89
3.5.1 Orthogonal cutting and combined CFRP/Ti machining setup 89
3.5.2 Experimental setup for hole drilling 91
3.6 Conclusions 92

Chapter IV 95
4.1 Introduction 97
4.2 Key mechanism dominating interface cutting 97

4.2.1 Cutting process investigation 98
4.2.2 Mechanisms of interface damage formation 100
4.2.3 Subsurface damage study 107
4.3 Evaluation of different cutting-sequence strategies 109
4.3.1 Comparison of chip formation process 110
4.3.2 Assessment of machined surface morphology 113
4.3.3 Evaluation of induced subsurface damage 115
4.4 Parametric effects on hybrid CFRP/Ti stack machining 116
4.4.1 Cutting process inspection 116
4.4.2 Machined surface quality inspection 119
4.4.3 Parametric study on CFRP/Ti cutting responses 122
4.5 Frictional responses dominating CFRP/Ti cutting process 124
4.5.1 Frictional effects on specific cutting energy 125
4.5.2 Frictional effects on machined surface quality 129
4.5.3 Frictional effects on induced damage and surface integrity 130
4.6 Conclusions 134

Chapter V 137
5.1 Introduction 139
5.2 Chip removal process 139
5.3 Cutting process and force signal analysis 145
5.4 Parametric effects on force generation 147
5.5 Machined surface quality inspection 151
5.6 Surface roughness and microhardness 157
5.7 Tool performance and wear mode investigation 160
5.8 Conclusions 164

Chapter VI 167
6.1 Introduction 169
6.2 Drilling process and force signal characterization 170
6.3 Drilling force magnitudes and specific drilling energy 175
6.4 Analysis of chip type in drilling 180
6.5 Hole quality analysis 181
6.5.1 Surface roughness 182
6.5.2 Hole diameter and roundness error 184
6.6 Hole damage study 187

6.6.1 Hole edge morphology 187
6.6.2 Delamination damage analysis 189
6.6.3 Burr defect analysis 191
6.7 Hole wall topography and surface morphology 193
6.7.1 Hole wall topography 193
6.7.2 SEM analysis of drilled hole surface 196
6.8 Drill design implications 198
6.9 Conclusions 199

Chapter VII 203
7.1 Key conclusions 204
7.2 Future perspectives 206

Annexe A : Résumé de thèse 209

Appendix B: Publication list and scientific presentation 227

References 229

Chapter I

Literature review: the state-of-the-art advances in hybrid FRP/Ti stack machining

Nomenclature

a	Dimensional constant
A_{del}	Delamination area
A_{nom}	Nominal area of the drilled hole
b	Dimensional constant
CTF_I	Critical thrust force for metal → FRP
CTF_{II}	Critical thrust force for FRP → metal
BCC	High-temperature β phase
D	Drill diameter
D_{11}	Coefficients for the bending stiffness of FRP laminate
D_{12}	Coefficients for the bending stiffness of FRP laminate
D_{22}	Coefficients for the bending stiffness of FRP laminate
D_{66}	Coefficients for the bending stiffness of FRP laminate
D_c	Equivalent bending stiffness coefficient of FRP laminate
D_{max}	Maximum diameter of the delamination area
D_{nom}	Nominal hole diameter
D_{RAT}	Two-dimensional delamination factor
E	Elastic modulus
f	Feed rate
F_d	One-dimensional delamination factor
F_{da}	Adjusted delamination factor
FRP → Ti	Drilling strategy from FRP phase to Ti phase
FRP → Ti Ti → FRP	Drilling from FRP → Ti and/or Ti → FRP
G_{IC}	Critical energy release rate in fracture mode I
h	Dimensional constant
HCP	Low-temperature α phase
n	Spindle speed
P_{ch}	Concentrated force
q	Uniformly distributed force
R_a	Arithmetic mean roughness
R_t	Peak to valley height
R_z	Ten point mean roughness
T	Material thickness
Ti → CFRP	Drilling strategy from Ti phase to CFRP phase
t_m	Multi-tool-work interaction time
v_c	Cutting speed
WC/Co	Tungsten carbide
α	Used weight in F_{da}
α_r	Rake angle
β	Used weight in F_{da}
θ	Fiber orientation

ν	Poisson's ratio
ϕ	Drill point angle
ψ	Drill helix angle
λ	Thermal conductivity
ξ	Proportional coefficient

Abbreviation

Al	Aluminum
ALE	Arbitrary Lagrangian Eulerian
BCJ	Baummann-Chiesa-Johnson
BUE	Built-up edge
CTF	Critical thrust force
CVD	Chemical Vapor Deposition
doc	Depth of cut
EHM	Equivalent homogeneous material
FEM	Finite element method
FRP	Fiber reinforced polymer
HSS	High-speed steel
JC	Johnson-Cook
MQL	Minimum quantity lubrication
MTS	Mechanical Threshold Stress
PCD	Polycrystalline diamond
PVD	Physical Vapor Deposition
TEC	Thermal expansion coefficients
Ti	Titanium
ZA	Zerilli-Armstrong

1.1 Introduction

In modern aerospace industry, the manufacturing sectors are seeking the use of hybrid composite stacks to enhance the characteristics of new-generation structures and continuously motivate the development of mechanical assemblies favoring the energy saving [1]. Material made of multi-phases of fiber reinforced polymer (FRP) and aluminum (Al) or titanium alloy (Ti) is a typical example of hybrid composite stack configuration. The benefits of the composite-to-metal alliance arise from the ability to combine resistance and to enhance specific characteristics without significantly increasing the part weight [2]. The key advantages of delivering energy saving and improving system performance have made the material a viable candidate to override standard composites and single metal alloys in various industrial applications [3, 4]. Aircraft structures subjected to high thermo-mechanical stresses are successfully fabricated with these materials. The typical application is the use of the wing-fuselage connection of the Boeing 787 Dreamliner.

Among the available configurations of hybrid composite stacks, FRP/Ti configuration (FRP/Ti, FRP/Ti/FRP, Ti/FRP/Ti), is identified as a most popular one due to its best combination of metallurgical and physical properties including high strength-to-weight ratio, low density, excellent corrosion/erosion resistance [5-7]. In particular, the FRP/Ti stack exhibits a high strength-to-weight ratio with yield strength as high as 830 MPa and a density of roughly 4 g/cm^3 [8]. Moreover, the FRP/Ti coupling yields also many advantages over the FRP/Al coupling in several aspects such as reduced galvanic corrosion, improved specific strength, *etc*. [9, 10]. Such superior properties have made their key application focus on manufacturing the key load-bearing components of large commercial aircraft in modern aerospace industry.

With regard to its assembly, the stacked FRP and Ti phases are usually joined by mechanical fastening technique, which is the principal method currently used for aerospace structural assembly with the advantage of good reliability, easy detachability and convenient inspectability [11-14]. Since the assembly process demands a large number of holes, the good control of machining becomes extremely crucial for achieving undamaged parts. In addition, the FRP and Ti phases are often stacked together prior to being cut off in one-shot time. This minimizes the positional errors and favors tight tolerances in actual production.

Although machining FRP/Ti stack in one one-shot time is beneficial from a manufacturing standpoint [2, 8, 15, 16], the processing task still remains extremely challenging because of the large disparity in properties of involved phases. For instance, the FRP laminate shows anisotropic behavior [17, 18] and abrasive nature [19] consisting of two distinct constituents (reinforcing fiber and polymer matrix) with neatly different properties. The reinforcing fiber exhibits elastic brittle behavior and poor thermal conductivity, while the polymer matrix shows ductile behavior. As for the Ti alloy, it exhibits poor thermal conductivity, low elastic modulus, and high chemical reactivity to most used tool materials [20-22]. These characteristics typically lead to severe abrasive tool wear and tool edge chipping especially against the FRP phase [23-26]. Besides, the tool experiences serious Ti adhesion, intense flank wear and premature tool failure in Ti machining [27, 28].

Technically, the key challenges involved in hybrid FRP/Ti machining may arise from the poor conditions of the multi-tool-work interactions associated with the disparate natures of the stacked constituents. The non-compliance between the tool-metal interface, on one hand, and the tool-composite interface, on another hand, induces local interface discontinuities and, hence, affects

the cutting behavior. These discontinuities present the major obstacles to be overcome for better controlling of the cutting conditions and proper selection of the tool-work configuration, which consists of the main scientific and technological challenge. To cope with the key challenge encountered in industry, great efforts have been made in the past few decades aiming to improve the machinability of the hybrid composite stack by considering various input factors including cutting parameter, cutting tool and cutting environment. In such circumstance, pointing out a state-of-the-art advances concerning hybrid FRP/Ti machining can provide a beneficial guide for both current and future research.

This Chapter is thus dedicated to making a rigorous literature survey of the most significant achievements gained in hybrid FRP/Ti machining. The multiple aspects related to hybrid composite stack cutting have been carefully addressed based on analyses of the open literature. Several strategies and approaches devoted to high-quality machining of hybrid FRP/Ti stacks are also precisely investigated. Moreover, the numerical approaches for potential solution to hybrid FRP/Ti machining are also finally reviewed.

1.2 Material properties and characterization

1.2.1 FRP composite phase

Advanced composite laminates, such as fiber reinforced polymer (FRP) laminates have been broadly employed in structural components due to their attractive properties including high specific stiffness, high strength and high corrosion resistance. The main family of FRP laminates commonly used in industries includes CFRP (carbon fiber reinforced polymer) laminates [29], GFRP (glass fiber reinforced polymer) laminates [30], and fiber metal laminates (FMLs) [31]. Among them, the CFRP and GFRP laminates are by far the most-used constituents in a hybrid composite stack configuration in view of their high mechanical properties. The primary constituents in the FRP phase are reinforcing fibers (*e.g.*, carbon and glass) and polymer matrices (*e.g.*, thermoplastic resin and thermosetting resin). The fibers are characterized by lightweight, stiff and strong nature, which contributes to enhanced mechanical and tribological properties of the material system, while the polymer matrix binds the fibers together, providing load transfer and structural integrity. The mechanical properties of FRP laminates critically depend upon the fiber layup along the epoxy matrix. For example, the unidirectional fiber-orientation prepreg ply (UD-ply) shown in Fig.1.1(a) [32, 33] exhibits quite-different mechanical properties along/in perpendicular to the fiber direction, *i.e.*, maximum stiffness/strength along the fiber direction and minimum properties in perpendicular to the fiber direction. However, a bidirectional fiber-orientation prepreg ply (woven-ply) presented in Fig. 1.1(b) [32, 33] almost has the maximum stiffness/strength along the both directions. For multi-orientation FRP laminates, they are usually made by bonding many prepreg plies together at different fiber orientations (cross-ply) to gain enhanced properties. Fig.1.1(c) shows the scheme of one type multi-orientation FRP laminate following the quasi-isotropic stacking sequence of $[0°/45°/90°/-45°]_{6s}$ [33, 34].

The FRP laminate globally exhibits heterogeneous characteristic, anisotropic nature, and brittle behavior, which inevitably results in extremely poor machinability. Structural components made of FRP laminates are mostly manufactured in near-net-shape to gain accurate dimensional tolerance and ensure excellent assembly performance, especially in a hybrid stack configuration. The

disparate natures of the fiber-epoxy system as well as their inherent heterogeneity make the machining operation more difficult than conventional metal cutting. Drilling FRP laminate in a hybrid stack configuration exhibits a more challenging task than standard composite drilling case due to the interrelated coupling with the metal-phase cutting and serious damage in the composite-metal interface. Relevant discussion will be presented in the following subsections of this Chapter.

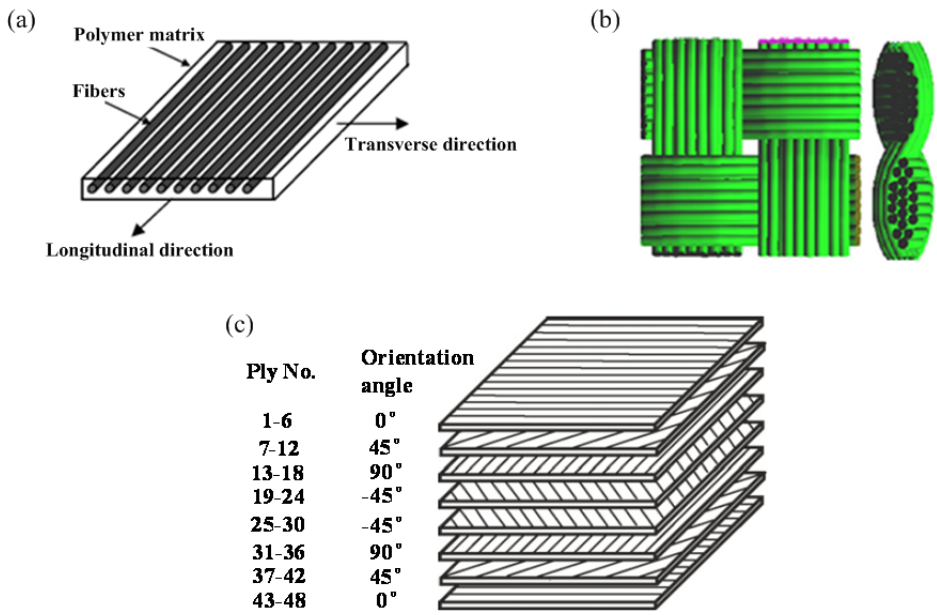

Figure 1.1. Scheme of the commonly-used FRP composite structures: (a) UD-ply laminate [32, 33], (b) woven-ply laminate [32, 33], and (c) multi-orientation laminate following quasi-isotropic stacking sequence of $[0°/45°/90°/-45°]_{6s}$ [33, 34].

1.2.2 Titanium alloy phase

Titanium alloys used in a hybrid stack configuration aim at providing high strength-to-weight ratio, high hot hardness, excellent corrosion resistance and good fatigue properties of the assembly. The superior properties of titanium phase mainly have a close relation with the presence of its metallurgical characteristics in the matrix. In the viewpoint of crystalline state, the titanium exists in two different phases referring to a low-temperature α phase (HCP) and a high-temperature β phase (BCC). The HCP structure of titanium affords a limited number of slip or shear planes while the BCC structure has more slip systems, thereby enabling more deformation locally transformed from HCP into BCC. Pure titanium typically undergoes an allotropic transformation probably at 882°C, changing from the low-temperature close-packed hexagonal α phase to the higher-temperature body-centered cubic β phase [6]. The allotropic transformation temperature is very sensitive to some certain added elements. For instance, the α stabilizers such as Al, O, N, Ga, and C elements produce an increase in the temperature while the β stabilizers such as Mo, V, Cu, Cr, Fe, Mn, Ni, ect., produce a decrease of the transformation temperature [35]. In contrast, some other neutral elements like Sn, Si, and Zr have gentle influences on the transformation temperature.

Typically, the Ti alloys can be categorized into four main groups according to its basic metallurgical characteristics: (*i*) commercially pure alloy, (*ii*) α and near α alloy, (*iii*) α - β alloy, and (*iv*) β alloy [6, 35].

- Commercially pure (unalloyed) titanium: exhibits excellent corrosion resistance and low strength properties.
- α and near α alloys: contain α stabilizers and exhibit excellent creep resistance.
- α - β alloys: comprise both α stabilizers and β stabilizers. The α - β alloys are generally structural alloys and are widely used in structures and engine components in the aerospace industry. Among them, Ti6Al4V is the most well-known one comprising about 45 % to 60 % of the total titanium production.
- β alloys: include significant quantities of β stabilizers. This type of alloys often shows high hardenability and high density.

With respect to its machinability, the titanium alloy is usually regarded as a difficult-to-cut material in current manufacturing industries, which is attributed to its inherent high strength maintained at elevated temperature and low thermal conductivity leading to high cutting temperature generation. The Ti chips are usually formed in the "serrated" nature as a result of various cycles of compression and adiabatic plastic shear phases in the chip formation process, causing high fluctuations of cutting force acting over a small tool-chip contact area (probably 1/3 of that in the case of steel) [36, 37]. Moreover, the titanium alloy also exhibits high chemical reactivity to most-used tool materials at high elevated cutting temperature. In titanium alloy drilling, special issues may arise from the high force/temperature generation, rapid tool wear and poor surface integrity. For drilling Ti phase in a hybrid composite stack configuration, the Ti drilling action obtains significant coupled influences from the composite-phase drilling making the cutting mechanisms more complicated than single Ti alloy drilling cases. Relevant discussion will be presented in the following subsections of the Chapter.

1.2.3 FRP/Ti stacked assembly

The emergence of hybrid FRP/Ti stack aims to overcome the individual limitations of each constituent involved and to obtain enhanced structural functions. The typical configurations of FRP/Ti stacks are CFRP/Ti6Al4V and GFRP/Ti6Al4V that are widely used in modern aerospace industry. The bi-material system usually offers enhanced superior properties of each stacked phase including high strength-weight ratio, higher specific strength, high corrosion resistance, *etc*., which makes them an ideal substitute for single composite or metal application and leads to an increasing demand in modern aircraft manufacturing.

Drilling is indeed one of the most important and fundamental machining operations prior to the applications of the hybrid FRP/Ti stack. However, due to the varying properties and poor machinability of the stacked constituents, drilling FRP/Ti stack with acceptable hole quality remains the most difficult and challenging task in modern manufacturing sectors. Severe hole damage, excessive interface consumption as well as rapid tool wear are the key problems encountered in drilling. Exploring the drilling behavior and improving the machinability of the FRP/Ti stacks play a crucial role in high efficiency-precision machining of the material. To this aim, great motivations have been exploited in order to address deeply the topics, and a large amount of scientific work has been undertaken within the past few decades. Table 1.1 summarizes the experimental studies that have been conducted in the open literature concerning FRP/Ti drilling topics [2, 3, 8, 15, 38-51].

Table 1.1
Experimental researches concerning hybrid FRP/Ti drilling in the open literature [2, 3, 8, 15, 38-51].

Reference	Stack configuration	Drill type	Cutting conditions	Key topics addressed
Ramulu et al. [2]	FRP (Gr/Bi)/Ti6Al4V FRP: IM-6 graphite bismaleimide composite θ = [45°/90°/-45°/0°/-45°/0°/45°/0°/-45°/90°/-45°/0°/45°/0°/45°/90°/-45°/90°/90°]$_s$ T = 7.62/3.1 mm	HSS, HSS-Co, carbide twist drills	n = 325, 660, 1115, 1750, 2750 rpm f = 0.03, 0.08, 0.13, 0.20, 0.25 mm/rev	Drilling forces, Hole production, Tool wear, Hole damage, Surface topography
Brinksmeier and Janssen [15]	AlCuMg$_2$/CFRP/Ti6Al4V θ = [45°/90°/0°/45°]$_s$ T = 10/10/10 mm	Uncoated twist drill, Step drills (uncoated, TiB$_2$, diamond) D = 16 mm, ϕ = 130° ψ = 30°	v_c = 10, 20 m/min f = 0.15 mm Cutting environment: dry and oil mist conditions	Workpiece quality, Tool wear
Park et al. [8]	CFRP/Ti6Al4V CFRP: quasi-isotropic graphite/epoxy laminate T = 7.54/6.73 mm	WC twist drills D = 9.525 mm ϕ = 135° ψ = 28°	n = 2000, 6000 rpm (CFRP) n = 800, 400 rpm (Ti) f = 0.0762 (CFRP), 0.0508 mm/rev (Ti) Cutting environment: dry and wet	Drilling forces, Tool wear, Hole quality
Park et al. [45]	CFRP/Ti6Al4V CFRP: multidirectional graphite epoxy composites T = 7.54/6.73 mm	WC, PCD drills D = 9.525 mm ϕ = 135° ψ = 28°	n = 2000, 6000 rpm (CFRP); 300, 400, 800 rpm (Ti) f = 0.0762 mm/rev (CFRP); 0.0508 mm/rev (Ti) Cutting environment: mist	Drilling forces, Tool wear
Isbilir and Ghassemieh [42]	CFRP/Ti6Al4V CFRP: T700-M21CFRP θ = [90°/-45°/0°/45°]$_{5s}$ T = 20/20 mm	TiAlN-coated drills D = 8mm ϕ = 140° ψ = 45°	n = 1400 rpm (Ti) and 4500 rpm (CFRP) f = 119 mm/min (CFRP) and 457 mm/min (Ti)	Drilling forces, Delamination, Burrs, Surface roughness, Tool wear
Kim and Ramulu [43]	FRP (Gr/Bi)/Ti6Al4V FRP: IM-6 graphite bismaleimide composite θ = [45°/90°/-45°/0°/-45°/0°/45°/0°/-45°/90°/-45°/0°/45°/0°45°/90°/-45°//90°/90°]$_s$ T = 7.62/3.1 mm	HSS-Co, split-Point, carbide drills	n = 660, 1115, 1750 rpm f = 0.08, 0.13, 0.20, 0.25 mm/rev	Drilling process optimization, Hole quality, tool wear

Brinksmeier et al. [3]	$AlCuMg_2$/CFRP/Ti6Al4V CFRP: multiphase of unidirectional prepregs T = 10/10/10 mm	Twist drill, step drill D = 16mm	v_c = 40 m/min v_f = 5 mm/min Cutting environment: minimum quantity lubrication (MQL)	Thermal and mechanical loads, Surface microstructure and damage
Shyha et al. [49]	Ti6Al4V/CFRP/Al-7050 $\theta = [45°/0°/135°/90°/45°/0°]_s$ T = 10/10/10 mm	Uncoated, CVD diamond-coated, C7-coated drills D = 6.35mm ϕ = 130° ψ = 30°	20 m/min ≤ v_c ≤ 120 m/min f = 0.05,0.10,0.15 mm/rev Cutting environment: wet, spray mist condition	Hole size, Hole surface roughness, Hole edge quality, Microhardness of metal, Chip formation
Ghassemieh [41]	CFRP/Ti6Al4V CFRP: M21E CFRP	C7-coated carbide drills D = 6mm	n = 1400 and 4500 rpm f = 119 and 457 mm/min	Drilling forces, Tool wear, Surface roughness
Beal et al. [38]	CFRP/Ti6Al4V CFRP: quasi-isotropic graphite/epoxy laminate T = 7.54/6.73 mm	WC drills D = 9.525mm ϕ = 135° ψ = 28°	n = 400, 800 rpm (Ti) n = 2000, 6000 rpm (CFRP) f = 0.0508 mm/rev (Ti) and 0.0762 mm/rev (CFRP) Cutting environment: wet lubrication condition	Drilling forces, Tool wear, Hole quality, Surface roughness
Park et al. [46]	CFRP/Ti6Al4V CFRP: quasi-isotropic graphite/epoxy laminate T = 7.54/6.73 mm	WC, BAM-coated drills	n = 2000, 6000 rpm (CFRP); 400, 800 rpm (Ti) f = 0.051 mm/rev	Tool wear, Tool performance
Fujiwara et al. [40]	CFRP/Ti6Al4V CFRP: composed of 1 ply GFRP and 10 ply CFRP T = 3/9.5 mm and 3/10.5 mm	TiAlN, TiSiN and TiAlCr/TiSi-coated drills D = 6 mm	v_c = 18.8 m/min f = 0.2 mm/rev Cutting environment: dry and mist-water cooling	Drilling forces, Tool wear, Hole quality
Tashiro et al. [50]	CFRP/Ti6Al4V CFRP: composed of 1 ply GFRP and 10 ply CFRP T = 3/9.5 mm	TiAlN, TiAlCr/TiSi coated drills D = 6mm	v_c = 9.4, 18.8 m/min f = 0.1, 0.2 mm/rev Cutting environment: dry and water-mist-cooling	Cutting forces, Tool wear, Hole quality, Cutting environment comparison
SenthilKumar et al. [48]	CFRP/Ti6Al4V	Solid WC twist drills (with different tool point angles) ϕ = 130° ψ = 30°	n = 612 and 1826 rpm f = 0.05 mm/rev	Tool wear, Chip formation, Effects of drill point angle on tool wear
Poutord et al. [47]	CFRP/Ti6Al4V T = 20.7/25.5 mm	K20 uncoated drill D = 12mm	n = 2652 rpm (CFRP); 265 rpm (Ti)	Drilling forces, Tool wear

		ϕ = 140° ψ = 30°	f = 0.05 mm/rev (CFRP); 0.2 mm/rev (Ti)	
Kuo et al. [44]	Ti6Al4V/CFRP/Al-7050 θ = [45°/0°/135°/90°/45°/0°]$_{3s}$ T = 10/10/10 mm	DLC diamond drill, CVD diamond drill D = 6.38 mm ϕ = 140° ψ = 30°	v_c = 30 m/min (Ti); v_c = 120 m/min (CFRP, Al) f = 0.08, 0.15 mm/rev	Thrust force, Torque, Tool wear, Hole accuracy, Burr formation
Carvajal et al. [39]	CFRP/Ti; CFRP/Al; CFRP/CFRP	Not specified	Variable cutting conditions including drilling machine, nature of materials, feed rate, spindle speed, *etc*.	Effects of different input factors on hole diameter
Wang et al. [51]	CFRP/Ti6Al4V, Ti6Al4V, CFRP θ = [(0°/45°/90°/-45°)$_4$ (0°/90°/0°/90°)]$_s$ T = 7.54/6.73 mm	Uncoated, AlTiN, nanocomposite coated drills D = 9.525 mm ϕ = 135° ψ = 25°	n = 6000 rpm, f = 0.0762 mm/rev (CFRP, CFRP/Ti); n = 500 rpm, f = 0.0508 mm/rev (Ti, CFRP/Ti)	Drilling forces, Tool wear mechanisms in CFRP-only, Ti-only and CFRP/Ti drilling

1.3 Drilling force characterization

Force generation represents the key cutting physics in FRP/Ti drilling, which indicates the mechanical energy consumption of multi-tool-work interactions governing the chip removal process. The force generation primarily has a close relation with the inherent properties of each stacked constituent as well as their disparate modes of chip formation. From the aspect of force analysis, the force generation induced in drilling is commonly decomposed into two components, *i.e.*, thrust force and the torque, which signify the tribological behaviors between tool-chip interaction and tool-machined surface interaction, respectively. Severe force fluctuations in both thrust and torque components are often encountered when drilling hybrid FRP/Ti stacks. The force-magnitude discrepancy mainly arises from the fiber orientation's effects on the FRP-phase drilling, the variable chip separation mode in interface drilling and the serrated chip formation in Ti-phase drilling. The changeable chip formation modes occurring on tool rake face would be the key factor significantly affecting the torque-force component in the stack drilling. The thrust force component, however, signifies the interactions between tool flank face and the machined hole wall surface. In addition, the disparate properties arising from the composite-metal phases also cause the drilling-force signal to exhibit certain stage characteristics. Fig.1.2 shows the thrust force and torque signals varied with cutting depth when drilling FRP (Gr/Bi)/Ti stack by using standard HSS drill under the fixed cutting conditions of n = 660 rpm and f = 0.2 mm/rev [2]. It is observed that three major regions referring to the FRP, interface and Ti drilling zones in thrust and torque profiles are noticeable. Furthermore, the entire hybrid FRP/Ti drilling action can also be distinguished by seven minor regions.

- Region 1 defines the period when the chisel edge firstly penetrates into the FRP phase. Both thrust and torque force components increase gradually from zero.

- Region 2 implies that the cutting lips are gradually involved in the FRP-phase drilling. The cutting-force signals increase gradually with tool advancement.
- Region 3 entails the period of full engagement of the drill lips through the FRP-phase. The thrust force and torque nearly keep constant in this region drilling.
- Region 4 denotes the period of drill bit involved in the FRP/Ti interface drilling. The tool-work interaction transfers from the absolute tool-FRP interaction, gradually to multi-tool-work interaction and finally to absolute tool-Ti interaction, resulting in the significant increase of the drilling forces.
- Region 5 indicates that the cutting lips have gradually cut into the Ti phase and continuous force elevation has been obtained. The maximum thrust force is achieved at the end of this region drilling.
- Region 6 represents that the cutting lips have totally cut into the Ti phase.
- Region 7 signifies the period that the chisel edges have gradually penetrated out of the Ti phase. The thrust force component is found to decrease gradually to zero. However, torque component above zero is expected at the end of the process due to tool friction, depending on the elastic springback effect of the composite material.

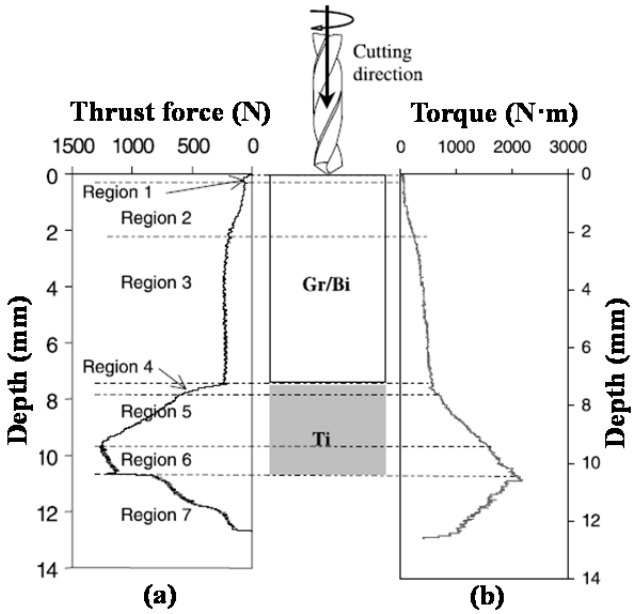

Figure 1.2. Drilling-force *versus* cutting depth when drilling hybrid FRP (Gr/Bi)/Ti stacks by using standard HSS drill. (Material: Gr/Bi FRP/Ti6Al4V, θ = [45°/90°/-45°/0°/-45°/0°/45°/0°/-45°/90°/-45°/0°/45°/0°/45°/90°/-45°/90°/90°]$_s$, cutting parameters: n = 660 rpm and f = 0.2 mm/rev) [2].

Moreover, the force generation in FRP/Ti drilling exhibits strong sensitivity to the input variables. Special variables commonly addressed are drilling parameters (spindle speed and feed rate), drilled hole number (tool wear), *etc*. Ramulu et al. [2] studied the influence of drilling parameters on the force generation when drilling FRP (Gr/Bi)/Ti stacks, as depicted in Fig. 1.3. Results showed that the feed rate played a pivotal role in affecting the thrust force magnitudes for both HSS and carbide drills. Generally, a slight increase of feed rate often gave rise to a significant elevation of the thrust force, irrespective of the tool material. This is because higher feed rate typically signifies larger

uncut chip thickness to be removed and denotes more cutting energy to be consumed, *i.e.*, the drill bit is required to cut off more chip volume per revolution and overcome much higher cutting resistance. As a result, the thrust force was elevated dramatically. In contrast, the relation between spindle speed and thrust force was inconspicuous. In addition, the spindle speed was observed to have minor effects on the thrust force generation in all regions except region 7 when using HSS and carbide drills as depicted in Fig. 1.3(b) and Fig. 1.3(d). Furthermore, in other literature [41, 42], the spindle speed was confirmed to exhibit positive effects on the drilling forces (thrust and torque components) for FRP-phase drilling while have negative effects on the drilling forces (thrust and torque components) for Ti-phase drilling. The phenomenon can be attributed to the hardening and softening effects of increased high temperature on the work materials caused by the elevated spindle speed, respectively.

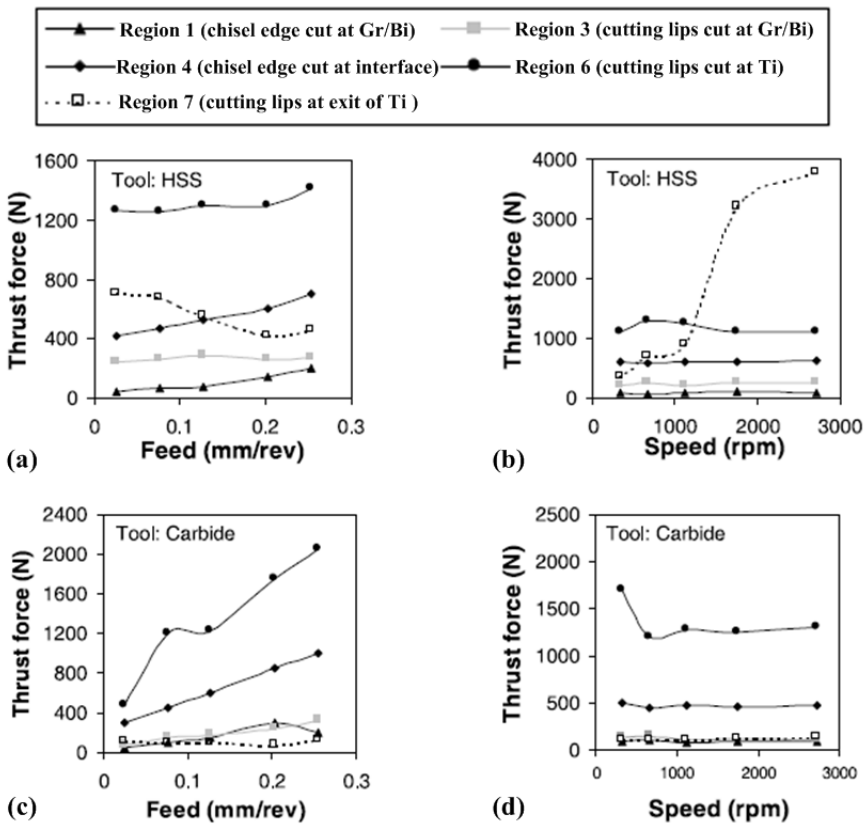

Figure 1.3. Thrust force *versus* feed rate and spindle speed when drilling hybrid FRP/Ti stacks: (a) n = 660 rpm - HSS drill, (b) f = 0.0732 mm/rev - HSS drill, (c) n = 660 rpm - carbide drill, (d) f = 0.0732 mm/rev - carbide drill work. (Material: Gr/Bi FRP/Ti6Al4V, θ = [45°/90°/-45°/0°/-45°/0°/45°/0°/-45°/90°/-45°/0°/45°/0°/45°/90°/-45°/90°/90°]$_s$, T = 7.62/3.1 mm) [2].

In most open literature, drilled hole number (tool wear) was identified as another key factor significantly influencing the drilling force generation. Fig.1.4 shows the experimental results gained by Park et al. [45] when drilling CFRP/Ti6Al4V with WC and PCD drills. It is apparent that the thrust force and torque produced in CFRP-phase and Ti-phase drilling are linearly proportional to the drilled hole number, irrespective of the used tool materials. The phenomenon can be explained by the fact that when a large number of holes have been drilled, the tool will suffer excessive and expanded tool wear. As a result, the tool undergoes high tool-work friction coefficient when drilling further uncut chip material, resulting in high cutting energy consumption and subsequent high-force

generation. The identical findings were also confirmed by Beal et al. [38], Fujiwara et al. [40], Tashiro et al. [50] and Wang et al. [51].

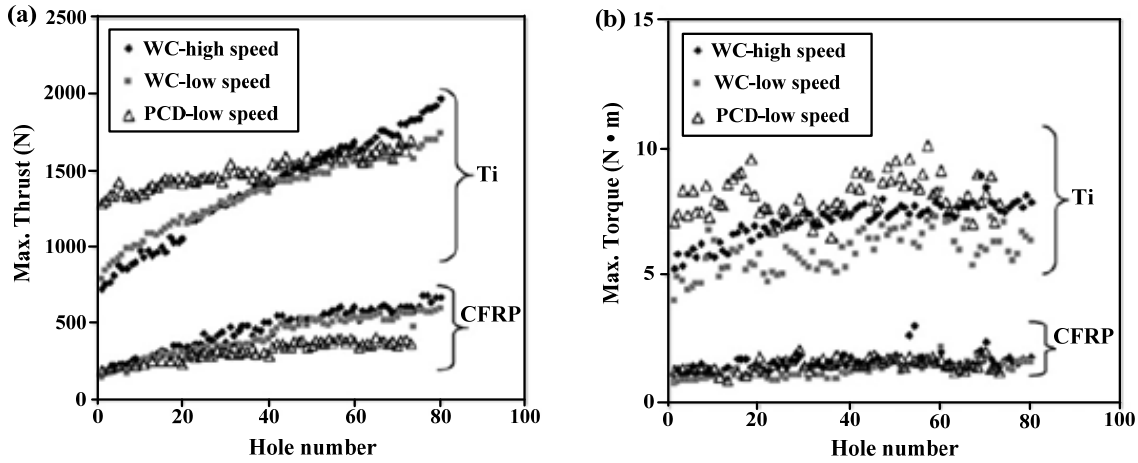

Figure 1.4. Effects of drilled hole number on (a) thrust force and (b) torque when drilling hybrid FRP/Ti stacks by using WC and PCD drills. (Material: multidirectional graphite epoxy composites/Ti6Al4V, T = 7.54/6.73 mm; cutting tools: WC and PCD with ϕ = 135°, ψ = 28°; cutting parameters: WC - high speed: *n* (CFRP) = 6000 rpm, *n* (Ti) = 800 rpm; WC-low speed: *n* (CFRP) = 2000 rpm, *n* (Ti) = 400rpm; PCD-low speed: *n* (CFRP) = 2000 rpm, *n* (Ti) = 300 rpm; *f* (CFRP) = 0.0762 mm/rev, *n* (Ti) = 0.0508 mm/rev; cutting environment: mist coolant) [45].

1.4 Cutting mechanisms controlling FRP/Ti drilling

Drilling hybrid FRP/Ti stacks exhibits behavior quite different from drilling standard composites and single metal alloys due to the multi-tool-work interaction domains. The disparate natures of each constituent make the chip formation modes more coupled and interrelated governing the bi-material machining. The interrelated mechanism dominating the material removal process plays a pivotal role in affecting the machining responses and physical phenomena. Revealing the mechanisms controlling FRP/Ti drilling can provide a beneficial guide for cutting-parameter optimization, hole-quality control and tool selection.

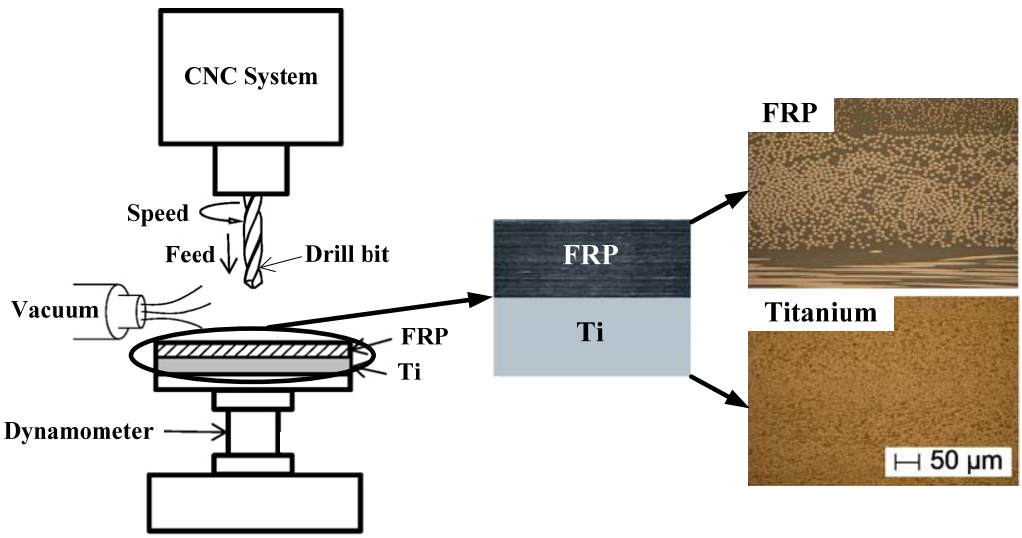

Figure 1. 5. Schematization of the FRP → Ti cutting sequence used in vertical drilling of hybrid FRP/Ti stacks [10, 45].

In FRP/Ti drilling, two different cutting-sequence strategies referring to Ti → FRP and FRP →

Ti commonly exist from the aspect of tool-entry and tool-exit throughout the material removal process. The reasonable cutting sequence would rest the FRP material on top of the Ti alloy and cut from the FRP phase first especially from the viewpoint of vertical drilling configuration as illustrated schematically in Fig. 1.5 [10, 45]. This is because in this cutting sequence the Ti alloy can act the role of supporting plate in preventing laminate deflection and limiting the workpiece dynamics during the drilling operation. Therefore, it can result in the low extent delamination damage and improved tool life. The beneficial role of FRP → Ti sequence was also proven by several relevant work [2, 42, 45]. Fig.1.6 presents a comparison of the exit CFRP surface damage generated in drilling single CFRP laminate without Ti phase and in drilling CFRP/Ti stacks [42]. It was apparent that the CFRP → Ti drilling sequence promoted less fiber pullout (probably near-net shape) than the single CFRP drilling case. Therefore, based on the proposed drilling sequence (FRP → Ti), the FRP/Ti drilling mechanisms are then discussed from FRP-phase drilling, to interface drilling and finally to Ti-phase drilling, respectively.

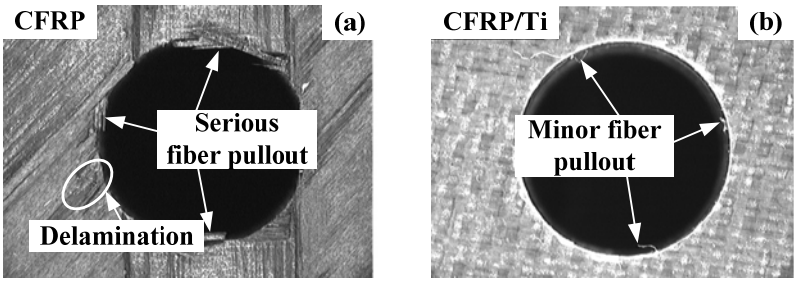

Figure 1.6. CFRP surface damage at the exit side after drilling the 1st hole: (a) drilling of standard CFRP laminates after making the 1st hole and (b) drilling of hybrid CFRP/Ti stacks (CFRP → Ti cutting sequence). (Material: CFRP (T700-M21, $\theta = [90°/-45°/0°/45°]_{5s}$, T = 20 mm) / Ti6Al4V(T = 20 mm); cutting tool: AlTiN twist drill; cutting parameters: n = 4500 rpm, f = 457 mm/min) [42].

1.4.1 FRP-phase drilling: brittle fracture dominant mechanisms

In FRP-phase drilling, the cutting mechanisms differ significantly from conventional metal cutting cases due to the brittleness and heterogeneity of the fiber/matrix system. The mechanisms governing the FRP-phase drilling should be responsible for the specific chip formation mode and chip type.

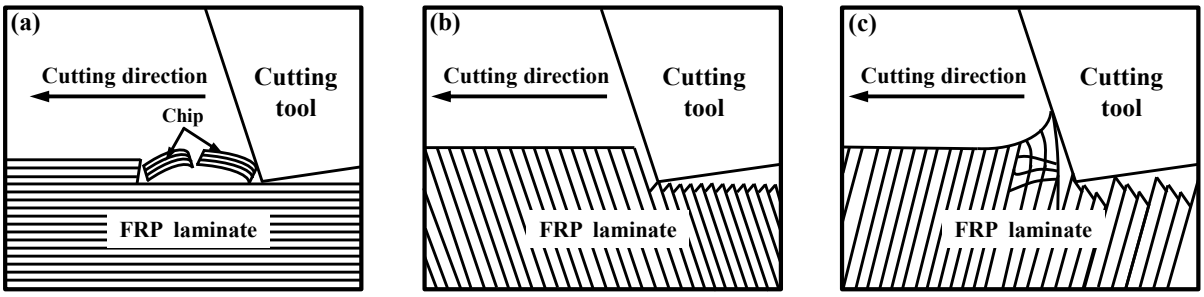

Figure 1.7. Schematization of the chip formation mechanisms in FRP laminate cutting: (a) layered peeling fracture, (b) extrusion shear fracture, and (c) bending shear fracture [52].

When drilling FRP phase, material removal occurs through a series of successive ruptures aided by diverse nature and uneven load shearing between matrix and fibers. Such chip formation is motivated by brittle fracture due to crack initiation and propagation in the primary shear zone after

the chip is partly formed as shown in Fig. 1.7 [52]. Since brittle fracture operates as the dominant cutting mode controlling the material removal process, the resected "discontinuous" chips are often produced in the form of "powdery" dust. However, the chip type produced in drilling greatly depends on the properties and fiber volume fraction of fiber/matrix system. In some cases, the "continuous" chip formation as like metal cutting can also be generated. The experimental findings obtained by Hocheng and Puw [53] indicated that when drilling carbon/epoxy the main chip-type were absolutely "discontinues" form but for carbon/acrylonitrile butadiene styrene (ABS) drilling, the predominant chip type would be "continuous" one. The activated mechanisms controlling the chip characteristics could be expalined by the fact that the material removal of the former was governed by brittle fracture while the latter was ruled by predominant plastic deformation due to the ABS's capacity of large elongation under cutting loads. In addition, when increasing fiber volume fraction, the majority of the composite materials are removed by a series of fracture due to the non-uniform plastic deformation that promotes the formation of "discontinuous" chip type. Moreover, the chip type is also influenced by input cutting parameters like feed rate. Results gained by Kim et al. [54] showed that when low-feed drilling (f = 0.02 mm/rev) of PEEK thermoplastic composites, the resected chips were typically "continuous" and curling for a wide range of speeds due to high overall toughness of the thermoplastic matrix. In contrast, when higher feed rate was employed (f = 0.25 mm/rev), the generated chips were basically "discontinuous". However, the key mechanism dominating the feed-rate effects on the chip-type transition from "continuous" to "discontinuous" was not clarified in the authors' research. Anyway, the mechanisms controlling the chip separation can be identified as the key contributor to the produced chip type. The chip-separation mechanism dominating the FRP-phase drilling, however, is critically dependent on tool rake angle (γ), *i.e.*, the angle between fiber orientation (θ) and cutting direction. However, these factors are not reviewed here individually, since the key objective of this Chapter is to survey the mechanism issues on hybrid composite stack drilling. Readers are recommanded to refer to the mentioned literature [55-63]. It should be stressed here that in drilling, the changeable fiber breaking type *versus* θ, on one hand, is a key contributor to severe hole-wall damage like delamination, fiber pullout, micro cracking, matrix degradation, *etc*. On the other hand, it makes the distribution of some local defects like fiber pullout, delamination, spalling, *etc*., exhibit regional symmetrical characteristic. These findings were also confirmed by some pertinent research work [17, 61, 64, 65].

1.4.2 Interface drilling: interrelated and mixed cutting mechanisms

In FRP/Ti drilling, the bi-material interface machining commonly involves multiple aspects of mechanical/physical consumptions and experiences mixed cutting behaviors governing the material removal process. The drilling mechanisms dominating the interface cutting are generally the interaction of both composite-leading mode and metal-leading mode. The interrelated chip separation modes make the region more vulnerable to various damage formation and defect generation.

As the drill bit penetrates into the FRP/Ti interface (as shown in Fig. 1.8), discontinuous tool-work interactions consisting of tool-FRP coupling and tool-Ti coupling take place and dominate the tool active cutting zones, causing the tool to be involved in a multi-tool-work

interaction machining. Cutting mechanism governing this region drilling comprises multiple aspects of physical and mechanical phenomena in the cutting zones and mixed cutting behaviors in the material removal process. The non-compliance among the tool-work interfaces inevitably gives rise to a particular harsh cutting condition and more interrelated cutting behavior dominating the drilling operation. The cutting edge segments as depicted in Fig. 1.8 will then experience a mixed material removal process of fiber fracture and metal elastic-plastic deformation simultaneously throughout the multi-tool-work interaction time.

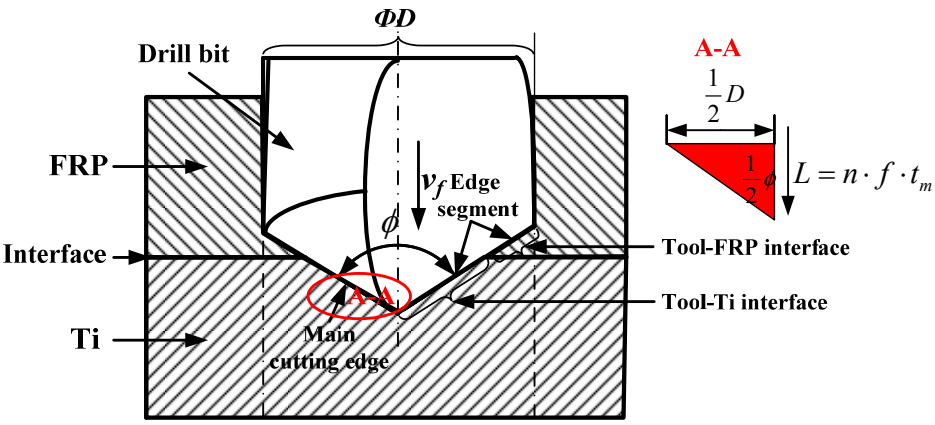

Figure 1.8. Schematization of the drill bit involved in the FRP/Ti interface drilling.

The multi-tool-work interaction time (t_m) governing the interface drilling, as illustrated in Fig.1.8, is critically dependent on the used drill diameter (D), drill point angle (ϕ), spindle speed (n) and feed rate (f), and can be expressed as follows.

$$t_m = \frac{D}{2nf}\cot\frac{\phi}{2} \tag{1.1}$$

During the interface drilling period, the main cutting edges, on one hand, undergo discontinuous and disparate thermal effects and mechanical loads from the multiple tool-work interfaces, which may result in significant weakening of tool material and serious tool blunting. On the other hand, they experience an interface transition during the material removal process, *i.e.*, transforming from absolute tool-FRP interaction to multi-tool-work interaction and finally to absolute tool-Ti interaction. As a result, the cutter will suffer intense force fluctuation and load vibration, and hence will result in the instability of the tool-work system during the stack drilling. These phenomena can be identified as a main trigger to the hole damage formation concerning the FRP/Ti interface. In addition, since the tool-FRP coupling and tool-Ti coupling exhibit disparate tribological behaviors, the drill in such condition will suffer mixed wear patterns during the interface cutting. The combined wear modes will significantly accelerate the tool wear and greatly shorten the tool life.

To alleviate the detrimental effects arising from interface drilling, reducing the multi-tool-work interaction time would be a direct solution. As shown in Eq.(1.1), it can be inferred in theory that reducing drill diameter (D) as well as increasing point angle (ϕ), spindle speed (n) or feed rate (f) can lead to the reduction of interface cutting time, and hence can promote desirable drilling results. In general, the interface drilling can be regarded as the most difficult cutting stage as compared to the FRP-phase drilling and Ti-phase drilling. However, to the authors' best knowledge, the underlying physical/mechanical behavior governing the multi-interaction area drilling and also the

parametric effects on interface drilling are still not well understood. Relevant in-depth researches focused on the issues are rarely found. The lack of experimental studies on the aforementioned issues can be attributed to the challenge and difficulty in inspecting the multiple and sophisticated tool-work interactions in actual drilling cases. In the future, special attempts should be made to address deeply the issues.

1.4.3 Ti-phase drilling: plastic-deformation dominant mechanisms

When the drill edges thoroughly cut into the Ti phase, the multi-tool-work interaction coupling governing the cutting zones is absolutely transformed into the tool-Ti interaction. The metal elastic-plastic deformation then dominates the Ti-tool interaction area. The shearing actions from the thermal-mechanical coupling effects generate "continuous" chips that flow on the tool rake face. Under such fixed cutting condition, the drilling process is assumed to reach a steady state for which the cutting force, drilling temperature, and surface integrity could be predicted to an acceptable accuracy. However, since the Ti phase has poor thermal conductivity and strong chemical affinity to used tool materials, the drilling action may cause serious hole damage and catastrophic tool failure [27, 45]. On one hand, the smaller contact area between tool-chip interfaces in Ti alloy drilling often results in stress concentration at the tool edge where the maximum cutting stresses are reached. In addition, the poor thermal conductivity of Ti alloy often results in inefficient heat dissipation and causes intense heat accumulation on tool substrate, which will lead to the severe thermal damage of the tool cutting surface. On the other hand, the hot and continuous chips produced in Ti drilling also considerably impair the FRP hole and deteriorate the hole quality during their evacuation from the bottom layer.

The unfavorable chip transportation always causes catastrophic abrasion and erosion as well as high hole-diameter tolerance in the FRP phase. Such results observed by Brinksmeier and Janssen [15] showed that the scratching effect of Ti chips on the CFRP hole could cause a high-depth erosion of approximately 300 μm by using conventional twist drill in multi-phase $AlCuMg_2$/CFRP/Ti6Al4V stack drilling. To alleviate the chip-evacuation effects, some researchers [2, 43] asserted that it was not suggested to employ cutting parameters consisting of low spindle speed and low feed rate in hybrid composite stack drilling since these parameters favored the formation of "continuous" Ti chips, which would result in a large extent of subsurface damage in the polymeric holes.

Therefore, considering the distinct cutting mechanisms for each phase drilling, it is recommended to make a compromise selection in tool geometry and cutting parameters that often lead to high drilling forces, poor hole quality and severe tool wear in hybrid composite stack drilling [43, 66, 67]. Since the Ti phase usually causes the biggest problems, it has been reported that the process parameter selection in drilling FRP/Ti stacks should match that of the more difficult-to-drill workpiece Ti alloy rather than that of the easier-to-drill material FRP [68].

1.5 Drilling-induced damage

Drilling-induced damage is often characterized by the extent of geometric defects, thermal injuries and physical damage. Since the hybrid composite stack comprises both FRP and Ti phases, the machined holes always have not only the unique defects of composite material (*e.g.*, matrix

cratering, delamination, fiber pullout, thermal alteration) but also the hole imperfections of metallic alloy (*e.g.*, hole size error, roundness error, position error, burrs). The composite-metallic damage usually results in the poor assembly tolerance and long-term performance deterioration of the machined structural components [69]. A list of the commonly addressed drilling damage in FRP/Ti cutting is summarized in Table 1.2. Fig. 1.9 [16, 43] shows the schematic diagram of the drilling-induced hole damage distribution in FRP/Ti stack.

Table 1.2
Commonly induced hole damage types when drilling hybrid FRP/Ti stacks.

Phase type	Drilling-induced damage
FRP phase	Matrix cratering, delamination, fuzzing, micro crack, fiber/matrix debonding, spalling, fiber pullout, fiber breaking, resin loss, surface cavities, thermal alteration, *etc*.
FRP/Ti interface	Discoloration ring, damage ring, delamination, *etc*.
Ti phase	Hole size error, roundness error, position error, surface drag, burr, cracking, feed marks, tearing surface, debris of microchips, surface plucking, deformed grains, surface cavities, *etc*.

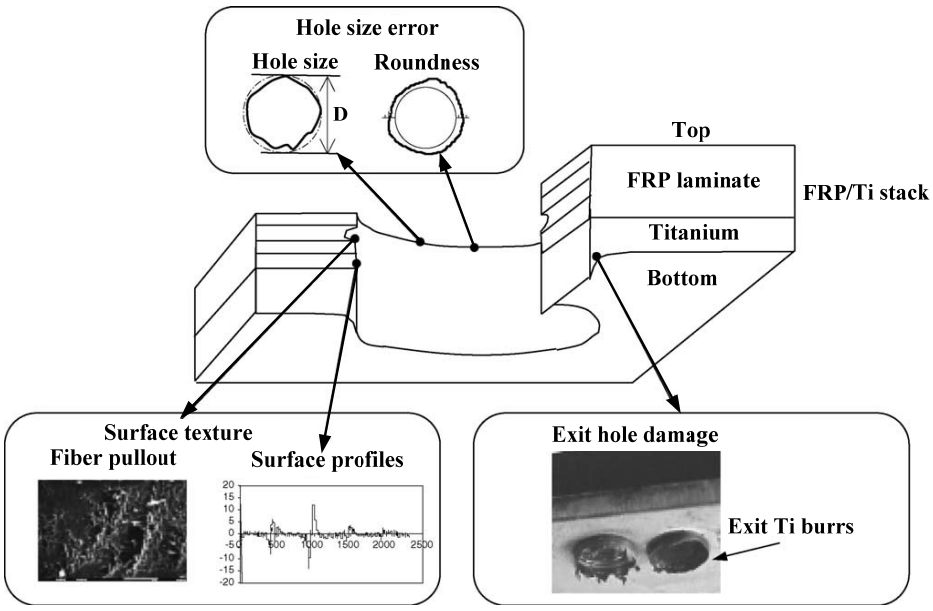

Figure 1.9. Schematization of the hole damage distribution in hybrid FRP/Ti stack drilling [16, 43].

1.5.1 Hole damage produced in FRP phase

In FRP phase drilling, damage formation commonly occurs through a series process of fiber fracture, matrix cracking and inter-laminar debonding, *etc*. Owing to the heterogeneity and anisotropy of the fiber/matrix system, severe hole damage is often promoted in drilling. Generally, the drilling-induced damage of FRP phase can be classified into four categories: geometric defects, temperature-related damage, delamination at drill-entry and drill-exit [70]. The tool geometry related damage is associated to the angle between fiber direction and the cutting edge. The temperature-induced damage including micro crack, resin loss, and matrix degradation is commonly produced by the thermal effects of drilling heat on the hole wall surface. In contrast, the damage due to delamination is usually a matter of greatest concern as it affects surface finish and work strength significantly leading to a large number of part rejections. The delamination depends on not

only fiber/matrix natures but also their adjacent properties [71, 72]. It should be stressed that in single FRP drilling, two mechanisms responsible for delamination may take place at the entry and exit of the drilled hole periphery, which are well-known as "peel-up delamination" and "push-out delamination", respectively. However, in FRP/Ti stack drilling, especially under FRP → Ti drilling sequence, the peel-up delamination may become a dominant one while the push-out delamination is less likely to happen due to the beneficial effect of bottom-supporting Ti phase on preventing the deflection and deformation of the upper composite phase. Qi et al. [73] further revealed that the bottom-supporting metal thickness also has significant effects on the push-out delamination formation, especially when the metal thickness exceeds a so-called critical value (a specified thickness threshold for the free-delamination occurrence), no push-out delamination takes place. For peel-up delamination, as the drill bit cuts into the FRP phase, the cutting edges of the drill abrade the laminate. In such case, a concentrated peeling force will be formed through the slope of the drill flutes and then will separate the plies from the uncut portions beneath the tool forming a delamination zone around the hole entry periphery, as illustrated in Fig. 1.10.

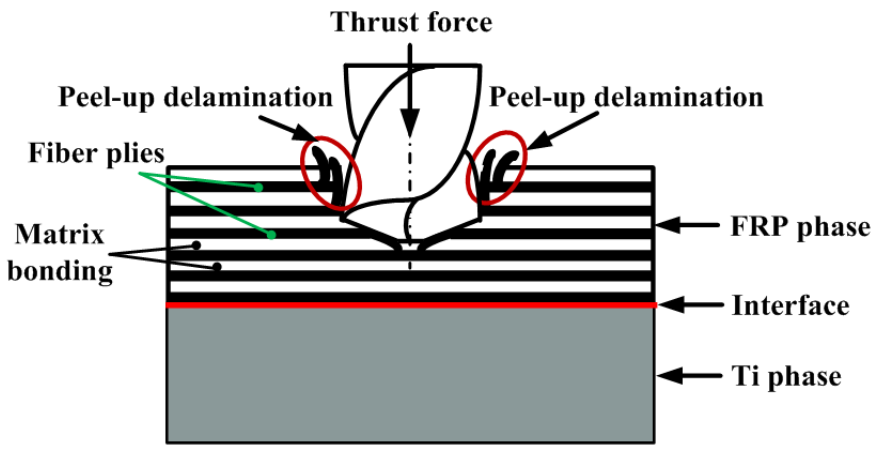

Figure 1.10. Scheme of the peel-up delamination in drilling hybrid FRP/Ti stacks (FRP → Ti cutting sequence).

Since the delamination belongs to an irreparable damage and an inter-ply failure, it is recognized as a most critical factor that severely impairs the performance of the machined components and accounts for probably 60 % of the part rejections in the aerospace industry [33, 53, 70, 74-76]. In general, it is believed by many researchers [73, 77-79] that there exists a critical thrust force (CTF) in composite drilling or composite/metal drilling, below which no delamination takes place. And for detailed information about CTF readers are recommended to refer to the aforementioned literature. In order to predict the CTF in FRP/metal stack drilling, Qi et al. [73] established the analytical models based on linear elastic fracture mechanics, classical bending plate theory and the classical lamination theory. In their models, the CTF (P) responsible for the push-out delamination was simplified and modeled as a resultant force of a concentrated one (P_{ch}) at the chisel edge and a uniformly distributed one q at the cutting lips, which could be expressed as $P_{ch} = \xi \times P$, where ξ represented a proportional coefficient varied in the range of 50 % - 70 % depending on the tool geometrical parameter and the cutting variables [80]. Both CTF models in two drilling sequences, *i.e.*, drilling from FRP → metal and drilling from metal → FRP, were discussed in their research, which are illustrated in Fig. 1.11 and summarized in Table 1.3, respectively. The results showed that the CTF obtained from the theoretical models yielded an acceptable agreement with the

experimental measurements. When drilling from FRP → metal, the CTF yielded a higher value than that operated in metal → FRP drilling sequence, which indicated that the FRP → metal drilling sequence would be more beneficial for free-delamination drilling of hybrid FRP/metal stack than its counterpart one. Furthermore, the authors also pointed out that when the metal thickness exceeded the critical thickness, no delamination damage would take place in the case of FRP → metal drilling sequence, regardless of the process parameters. However, the established models were restrained to solely predicting the CTF of conventional twist drill in drilling hybrid FRP/metal composite and ignored some internal factors like the effects of composite layup and plate shape on push-out delamination.

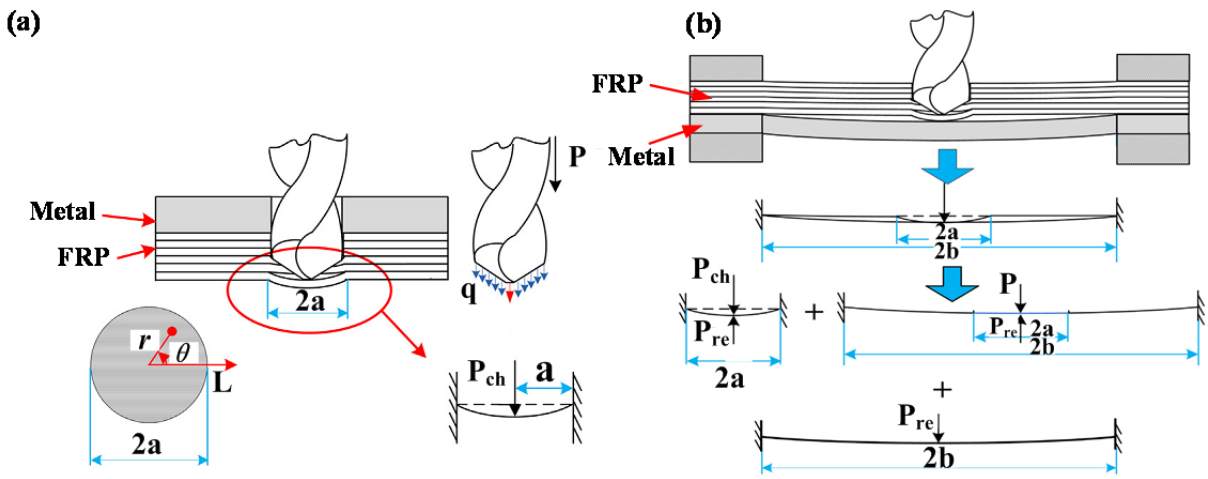

Figure 1.11. Delamination analysis for different cutting-sequence strategies applied in hybrid FRP/metal drilling: (a) metal → FRP cutting sequence and (b) FRP → metal cutting sequence [73].

Table 1.3
Analytical models for predicting CTF under different cutting-sequence strategies when drilling hybrid FRP/metal composite [73].

Drilling sequence	Scheme of delamination	Analytical model of critical thrust force (CTF)
Metal → FRP cutting sequence	Fig.1.11(a)	$CTF_I = P_I = \frac{2\sqrt{3}\pi}{\xi}\sqrt{G_{IC}\left(3D_{11}+2D_{12}+3D_{22}+4D_{66}\right)}$ $D_c = \frac{1}{3}\left(3D_{11}+2D_{12}+3D_{22}+4D_{66}\right)$
FRP → metal cutting sequence	Fig.1.11(b)	$CTF_{II} = P_{II} = \frac{2\sqrt{3}\pi}{\xi - K}\sqrt{G_{IC}\left(3D_{11}+2D_{12}+3D_{22}+4D_{66}\right)}$ $K = \frac{\frac{\xi a^2}{D} + \frac{2a^2\ln\frac{a}{b} + \left(b^2-a^2\right)}{D_c}}{\frac{9\left(1-\nu^2\right)b^2}{2Eh^3} + \frac{a^2}{b} + \frac{2a^2\ln\frac{a}{b} + \left(b^2-a^2\right)}{D_c}}$

Note: CTF_I, CTF_{II} – critical thrust forces for metal → FRP and FRP → metal drilling, respectively; G_{IC} - the critical energy release rate in mode I; ξ-proportional coefficient; D_{11}, D_{12}, D_{22}, D_{66} - coefficients stand for the bending stiffness of the uncut FRP laminate; D_c - the equivalent bending stiffness coefficient of the FRP laminate; ν - Poisson's ratio; E - elastic modulus; a, b, h - dimensional constants as shown in Fig.1.11.

In addition, the delamination visualization and assessment in hybrid FRP/Ti drilling also remain a difficult and challenging task because of its internal and external nature. At present, the most used non-destruction methods for characterizing the size, shape, and location of delamination are optical microscopy, ultrasonic C-Scan and X-ray computerized tomography [75, 78, 79, 81-85]. In addition, the extent of the delamination damage is often evaluated by using one-dimensional delamination factor (F_d) [17, 23, 79], two-dimensional delamination factor (D_{RAT} or D_F) [24, 86, 87] or adjusted delamination factor (F_{da}) [88] as listed in Table 1.4. The main differences among the three criteria rely on fact that the one-dimensional delamination factor represents the simplest way to measure the extent of delamination damage in actual production while the two-dimensional and adjusted delamination factors can accurately assess the real extent of delamination damage since they minimize the influences of a few fibers peeled up or pushed down on the delamination measurement.

Table 1.4
Delamination factors used for damage evaluation when drilling FRP laminates [17, 23, 24, 79, 86-88].

Type of delamination factor	Equation expression	Remarks	Authors
One-dimensional F_d	$F_d = \frac{D_{\max}}{D_{nom}}$	D_{max} -maximum diameter of the delamination area; D_{nom} - nominal diameter of the drilled hole	Xu et al. [17], Chen [23], Tsao and Hocheng [79]
Two-dimensional D_{RAT} or D_F	$D_{RAT} = \frac{A_{del}}{A_{nom}}$ $D_F = \left\lvert \frac{A_{del} - A_{nom}}{A_{nom}} \right\rvert \times 100\%$	A_{del} - delamination area; A_{nom} - nominal area of the drilled hole	Faraz et al. [24], Davim and Reis [86], Mehta et al. [87]
Adjusted F_{da}	$F_{da} = \alpha \frac{D_{\max}}{D_{nom}} + \beta \frac{A_{del}}{A_{nom}}$	α, β - the used weights in F_{da}	Davim et al. [88]

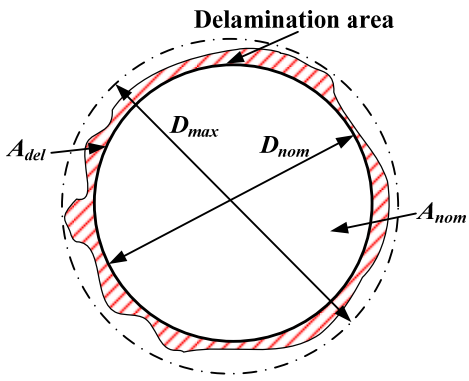

1.5.2 Interface damage: the weakest interfacial region

In FRP/Ti drilling, the interface linking the composite phase and metal phase boundaries would be the weakest region vulnerable to severe damage formation due to the particular harsh and varying cutting conditions governing the cutting zones as discussed in subsection 1.4.2. Since the FRP phase and Ti phase exhibit disparate mechanical/physical properties, it induces local interface discontinuities and non-compliance among the tool-work interfaces, which significantly affects the tool cutting behavior. When the cutting tool reaches the interface region, the tool tips and cutting

edges suffer severe shocks and vibrations due to the changeable chip separation modes from tool-FRP interaction to tool-Ti interaction and *vice versa*. Such physical phenomenon makes the drilling operation much easier to promote damage formation. Generally, the interface damage was reported in the form of discoloration ring, damage ring, fiber pullout and delamination as shown in Fig.1.12 [2]. The mentioned interface damage was often irreparable and fatal, which would promote crack initiation and fatigue fracture during the stack's assembly process.

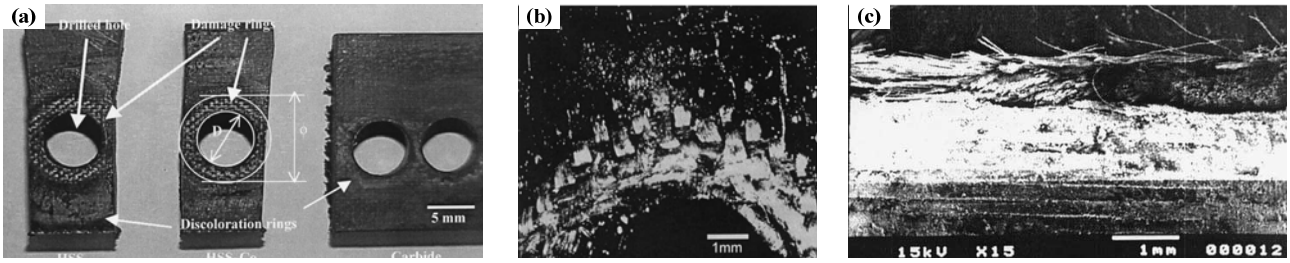

Figure 1.12. (a) Damage region at the composite/Ti interface, (b) the top view of the damage region, and (c) the side view of the damage region of (b). (Material: Gr/Bi FRP/Ti6Al4V, θ = [45°/90°/-45°/0°/-45°/0°/45°/0° 45°/90°/-45°/0°/45°/0°/45°/90°/-45°/90°/90°]$_s$, T = 7.62/3.1 mm; (a): cutting tool: HSS, HSS-Co and carbide drills, cutting parameters: n = 1750 rpm, f = 0.08 mm/rev; (b) and (c): cutting tool: HSS-Co drill, cutting parameters: n = 2720 rpm, f = 0.08 mm/rev) [2].

Concerning the interface damage formation, several scholars [2, 8] have revealed that the cutting heat and chip evacuation are the pivotal factors contributing to the damage initiation and propagation. Specific reason can be attributed to the unique physical properties of the Ti phase. Since the Ti alloy is characterized by poor thermal conductivity ($\lambda_s \approx$ 7-7.9 W·m^{-1}°C^{-1}), the cutting heat generation in the interface cannot be dissipated effectively, which, in turn, induces a local heat concentration at the bi-material interface. The accumulated cutting heat will cause thermal softening and degradation of the FRP/Ti interface. Besides, the produced continuous Ti chips also result in severe scratches and intense abrasions on the bi-material interface, leading to the force-induced delamination. In addition, Ramulu et al. [2] pointed out that the drilled hole number (tool wear) and feed rate also influenced the interface damage. For instance, when lower feed rate was used, larger interface damage was generated due to the longer tool-work engagement resulting in more Ti heat generation accumulated on the interface region. However, apart from the feed rate and tool wear, in fact, tool geometries like drill diameter and point angle (as illustrated in subsection 1.4.2) also have crucial effects on the generated interface damage, while their effects were not studied by the authors. Moreover, the explicit theories to explain the interface damage formation and the in-depth studies on quantitatively correlating the interface damage and input parameters are still significantly lacked.

1.5.3 Hole damage produced in Ti phase

When the tool edges attack the Ti phase, the previous brittle fracture changes into elastic-plastic shearing, and thus the generated surface quality tends to be improved a bit as compared to the FRP phase drilling. However, the most significant problem in hybrid composite drilling always occurs in the metal phase due to the poor thermal conductivity of the Ti alloy that leads to the localized heat generation concentrated at the tool-chip interface. The thermal congestion inevitably results in high cutting temperature governing the tool active zones, exacerbating the interface damage, burr defect, heat-induced delamination and surface roughness. The key forms of the surface defects as reported

in the literature [28, 89-91] are surface drag, burrs, cracking, feed marks, tearing surface, debris of microchips, surface plucking, surface cavities, *etc*. These aforementioned defects usually have a close relation with the thermal-mechanical effects of drilling action and depend considerably on the cutting conditions and tool geometries. However, for the purpose of FRP/Ti assembly, the burr defect produced in Ti phase may be a key problem as compared to other surface damage since it usually leads to further disassembly, deburring and re-assembly of the stack. The burr formation induced in drilling is primarily dependent on the tool geometry and tool/work orientation (that is, whether the hole axis is orthogonal or not to the plane of the exit surface of the hole) [92].

Table 1.5
Burr type classification for hybrid FRP/Ti drilling [49, 93, 94].

	Burr type A	**Burr type B**	**Burr type C**
Burr morphology [49]	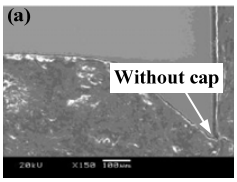	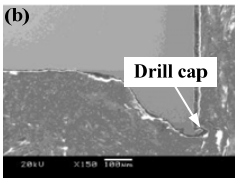	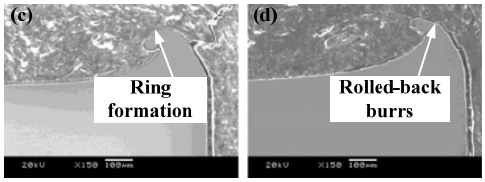
Crack location [93, 94]	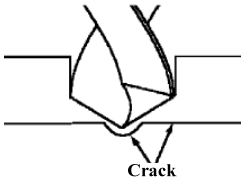	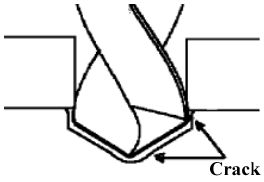	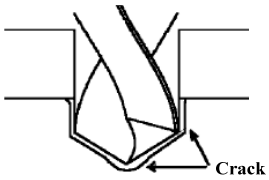

Note:
(a) and (b): hole exit; (c) and (d): hole entry. (Material: Ti6Al4V/CFRP/Al-7050, T = 10/10/10 mm, θ = $[45°/0°/135°/90°/45°/0°]_s$; cutting condition for (a, d): C7 coated drill, D = 6.35 mm, n = 20/40 m/min, f = 0.1 mm/rev, dry cutting); for (b, c): uncoated drill, D = 6.35 mm, n = 20/40 m/min, f = 0.05 mm/rev, wet cutting [49]).

Moreover, the drilling-induced burrs in Ti cutting are often classified into three types, namely type A, type B and type C according to the location of the initiated crack, as illustrated in Table 1.5. It was defined by authors Ko and Lee [93], Ko et al. [94] and Dornfeld et al. [89] that (*i*) burr type A is formed with a very small size or a negative shape due to the brittleness of the material; (*ii*) burr type B is produced as a result of some degree of plastic deformation and is characterized by a uniform drill cap; and (*iii*) burr type C typically has a severe rolled-back shape and large "ring formation" due to the crack initiated from the drill point of the cutting edges.

The results obtained by Shyha et al. [49] when drilling of Ti6Al4V/CFRP/Al-7050 stacks showed that in general, the Ti burrs with and without caps (Type A and Type B) were produced at the hole exit, while rolled-back burrs (Type C) were prevalent at hole entry, as illustrated in Table 1.5. The burrs produced in exit side of Ti phase usually cause serious problem for further assembly of the stack. To minimize or prevent the burr formation, it is critical to choose the proper cutting parameters, superior tool material as well as the efficient use of cutting fluid in the drilling cases. Kim and Ramulu [16] studied the effects of cutting parameters on the exit burr height by using carbide tools in drilling autoclaved and induction heated PIXA-M thermoplastic composite/Ti stacks. It was found that the exit burrs were highly dependent on the spindle speed and feed rate. When high feed and low spindle speed were employed, commonly lower burr height was produced, which was probably due to the low frictional heat generation at low spindle speed and reduced tool

engagement time caused by high feed rate, as shown in Fig. 1.13 (a) and Fig. 1.13 (b). However, when polycrystalline diamond (PCD) tools were utilized in drilling the same stacks, the exit damage such as titanium foil cap formation and titanium foil tearing no longer took place [95]. In addition, Shyha et al. [49] conducted a comparative study on assessing both entry and exit burr height where different drill bits and cutting environments were used in Ti6Al4V/CFRP/Al-7050 stack drilling, as presented in Fig. 1.13 (c). It was apparent that the use of fresh tools (at the first drilling) yielded better performance than the worn tools (after drilling a great number of holes) in terms of burr height. Besides, the use of cutting fluid such as wet cutting and spray mist also could reduce the burr height due to its beneficial effects on heat dissipation and thermal effect alleviation.

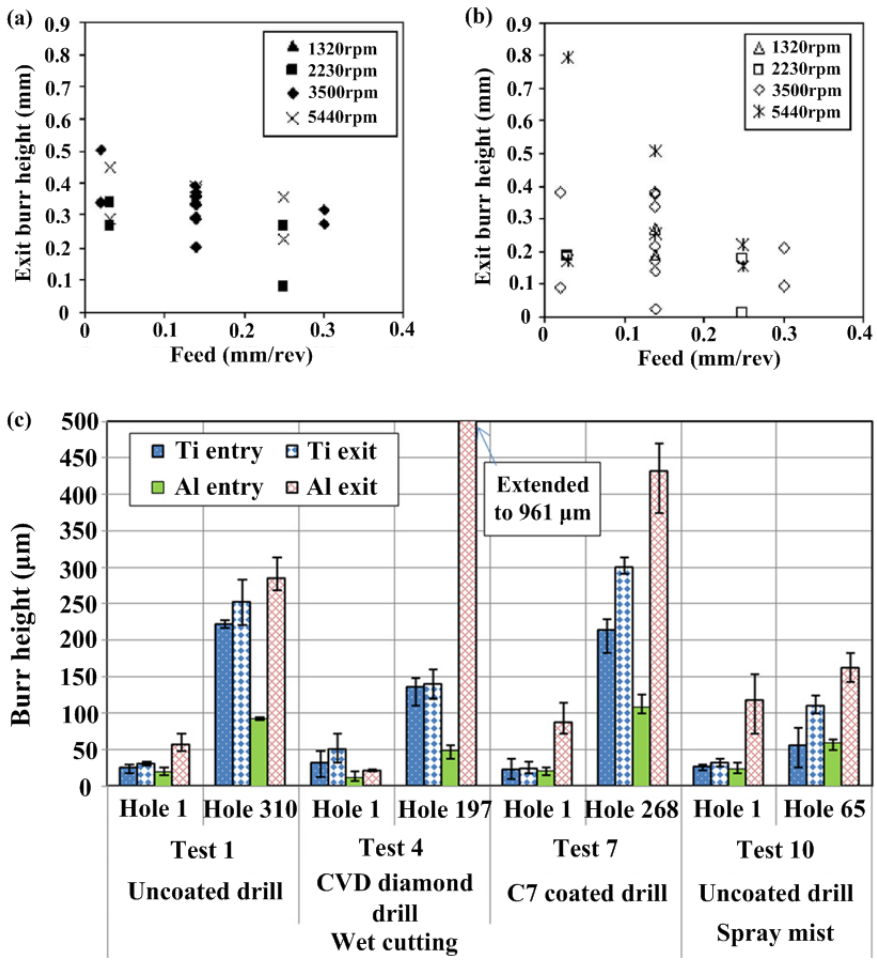

Figure 1.13. Exit burr height in function of spindle speed and feed rate when drilling thermoplastic composite/Ti stacks: (a) autoclaved stack, and (b) induction heated stack. (Material: PIXA-M thermoplastic PMC/Ti, θ = $[0°/90°/0°/0°/0°/0°/90°/0°]_s$; cutting tool: C2 grade solid carbide drill) [16]. (c) Burr height results for hole entry and hole exit with different cutting tools and cutting environments. (Material: Ti6Al4V/CFRP/Al-7050, T = 10/10/10 mm, θ = $[45°/0°/135°/90°/45°/0°]_s$; Tests 1 and 4: D = 6.35 mm, n = 20/40 m/min, f = 0.05 mm/rev; Test 7: D = 6.35 mm, n = 20/40 m/min, f = 0.10 mm/rev; Test 10: D = 6.35 mm, n = 20/40 m/min, f = 0.15 mm/rev) [49].

Apart from the aforementioned defects, the geometric imperfection such as roundness error, irregular hole diameter and surface roughness is also a critical concerns for hybrdi FRP/Ti drilling since tight dimensional and geometric tolerances (*e.g.*, arithmetic mean roughness (R_a) ≤ 3.2 µm for FRP phase and R_a ≤ 1.6 µm for Ti phase) are commonly required for better component assembly in real production. The drilled hole quality including roundness accuracy and dimensional accuracy is greatly influenced by delamination, tool wear, and cutting temperature. Since FRP and Ti phases exhibit different thermal expansion coefficients (TEC), it makes the drilling operation more difficult

to produce accurate hole diameter. In drilling, the machined holes may expand or shrink, greatly dependent on the used cutting environment. In particular, the holes produced in dry cutting condition are basically oversized due to the thermal expansion of matrix from increased cutting temperature and the unfavorable Ti chip evacuation. Besides, the results gained by Park et al. [8] also showed that the increased tool instability due to tool wear could be another key factor contributing to the formation of oversized holes. In contrast, when wet cutting or flood coolant was employed, the generated holes of each stacked phase may be undersized due to the effective heat dissipation of the cutting fluid. Such findings were also confirmed by Shyha et al. [49] when drilling Ti6Al4V/CFRP/Al7050 stacks. With regard to the hole surface roughness, the heterogeneity of FRP phase arising from the distinct natures of the fiber/matrix system usually causes the machined FRP surface to be much rougher than the drilled titanium hole surface.

In sum, despite the occurrence of various types of damage in FRP/Ti drilling, delamination induced in FRP phase and burrs produced in Ti phase are always among the most serious ones. These two types of damage often severely deteriorate the structural integrity of the machined components and result in high disassembly and rejections. Previous studies have shown that proper selection of input variables (*e.g.*, drilling parameters, cutting tool and cutting environment) would be a reasonable solution for minimizing the problems associated with drilling. The relevant illustrations will be presented in the following subsection 1.7.

1.6 Tool wear mechanisms in FRP/Ti drilling

Tool wear in FRP/Ti drilling involves a series of interrelated tribological/physical consumption during the convective chip flow governing the multi-tool-work interaction. Compared to standard FRP and single Ti alloy drilling in which separated wear mode (composite-leading wear pattern or metal-leading wear pattern) operates, the mechanisms in hybrid composite stack drilling are usually a mixture of them but are more complex, coupled and interrelated. The tool wear in FRP/Ti drilling signifies the tribological property and physical behavior at the multi-tool-work interfacial coupling. And it is a very sensitive variable greatly dependent upon (*i*) the physical/mechanical properties of workpiece and tool material, (*ii*) the sliding velocity among the convective master face and slave face and (*iii*) the specifically utilized cutting conditions. The rapid tool wear encountered in FRP/Ti drilling can be identified as a key problem in the bi-material machining. Rapid tool wear and catastrophic tool failure always account for the short tool life, poor hole quality, low cutting efficiency, and high machining cost.

Table 1.6
Wear mechanisms *versus* tool type when drilling hybrid FRP/Ti stacks.

Reference	Work material - cutting conditions	Tool type	Wear morphology	Wear mechanism
Park et al. [45]	Work material : multidirectional graphite epoxy composites/Ti6Al4V, T = 7.54/6.73 mm; Cutting parameters: (a) and (b) n = 2000 rpm (CFRP), 400 rpm (Ti); f = 0.0762 mm/rev (CFRP), 0.0508 mm/rev; (a)	WC drill (ϕ = 135° and ψ = 28°, after making 60 holes)	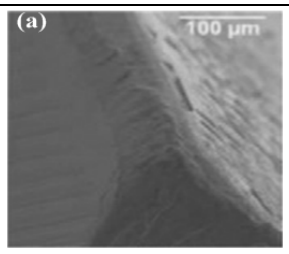	Edge rounding wear; Abrasive wear

	and (b) n = 2000 rpm (CFRP), 400 rpm (Ti); f = 0.0762 mm/rev (CFRP), 0.0508 mm/rev (Ti); (c) and (d): n = 2000 rpm (CFRP), 300 rpm (Ti); f = 0.0762 mm/rev (CFRP), 0.0508 mm/rev (Ti); cutting environment: mist coolant)	WC drill (ϕ = 135° and ψ = 28°, after making 80 holes)	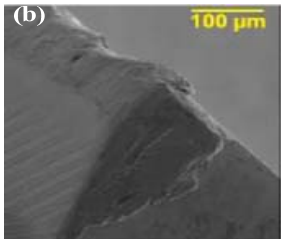	Ti adhesion; Flank wear
		PCD drill (ϕ = 135° and ψ = 28°, after making 20 holes)	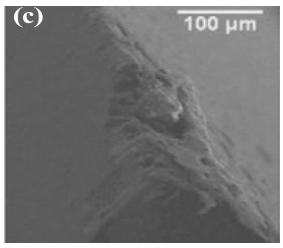	Edge rounding wear; Micro chipping
		PCD drill (ϕ = 135° and ψ = 28°, after making 60 holes)	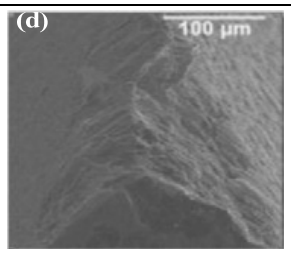	Abrasive wear; Micro fracture
Ghassemieh [41]	Work material: M21ECFRP/Ti6Al4V; Cutting parameters: n = 4500 (CFRP) /1400 rpm (Ti), f = 457.2 (CFRP)/119 mm/min (Ti).	C7-coated drill (D = 6mm)	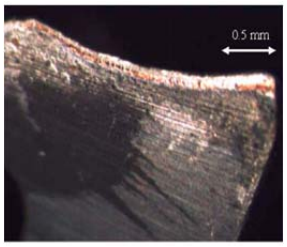	Abrasive wear
		C7-coated drill (D = 6mm)	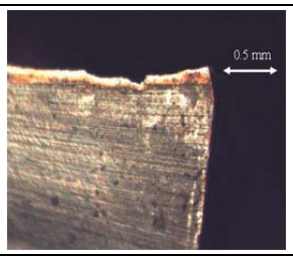	Micro chipping
Isbilir and Ghassemieh [42]	Work material : T700-M21 CFRP/Ti6Al4V, θ = $[90/-45/0/45]_{5s}$,T = 20/20 mm; Cutting parameters: n = 4500 (CFRP)/1400 rpm (Ti), f = 457 (CFRP)/119 mm/min (Ti).	TiAlN-coated drill (D = 8mm, ϕ = 140° and ψ = 45°)	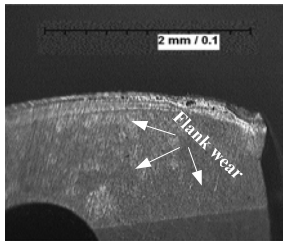	Flank wear
			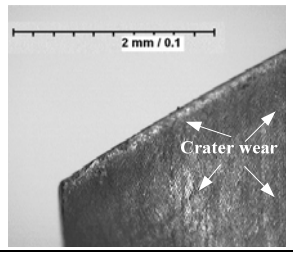	Crater wear

			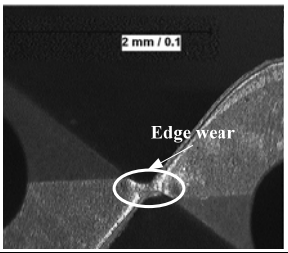	Edge wear
			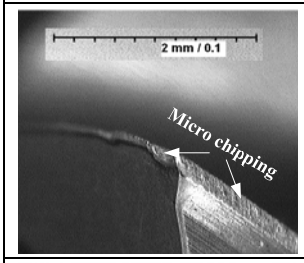	Micro chipping
			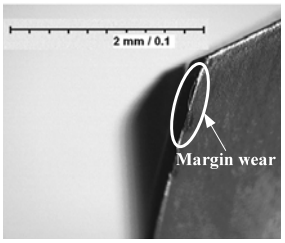	Margin wear

The geometrical changes induced on the tool active zone due to the detrimental effects from tool wear play a critical role in altering the effectiveness of tool edges on generating surface finish with required tolerance. The occurrence of tool wear inevitably leads to various undesirable results, *e.g.*, high force generation, localized heat accumulation and excessive power consumption. Generally, the final wear patterns exerted on tool material in FRP/Ti drilling primarily involve a series of interrelated wear phenomena induced by each-phase cutting. Therefore, it is particularly difficult to clarify how much of the tool wear can be attributed to individual-phase cutting. Most of the commonly-addressed tool wear modes in FRP/Ti drilling are revealed from a global way. Under specific cutting conditions, the wear mechanism in FRP/Ti drilling may be variable, greatly dependent on the properties of the used tool material. Beal et al. [38] investigated the wear mechanisms of WC drills in CFRP/Ti cutting. It was found that the WC tool suffered severe abrasion and edge deterioration in CFRP-phase drilling while underwent excessive flank wear, adhesion wear and abrasive wear in Ti-phase drilling. Poutord et al. [47] studied the local wear of K20 type uncoated drill when dry drilling of hybrid CFRP/Ti6Al4V stacks. Results confirmed that the K20 uncoated drill underwent serious Ti adhesion and edge rounding wear concerning its main cutting edges. Park et al. [45] conducted the fundamental inspections on tool wear when drilling CFRP/Ti6Al4V stack with tungsten carbide (WC) and polycrystalline diamond (PCD) drills. Abrasion, edge rounding, flank wear and adhesion wear were all detected in the stack drilling as presented in Table 1.6. For WC drills, the flank wear was primarily elongated by the Ti-phase drilling while the edge rounding was mainly caused by the abrasiveness of the hard carbon fibers in CFRP-phase drilling. Besides, in CFRP-phase drilling, the absence of built-up edge (BUE) made the main cutting edges more vulnerable to become rounded and dulled when subjected to the severe abrasive-loads of carbon fibers. Ti adhesion was observed to dominate the wear mode of WC drills by covering the entire cutting edges. The PCD drills suffered relatively less Ti chip adhesion and exhibited higher wear resistance due to their superior properties. However, the PCD drills also

experienced micro-chipping or micro-fracture at the cutting edges due to their intrinsic brittleness as shown in Table 1.6. Ghassemieh [41] studied the tool wear of C7-coated carbide drills when drilling CFRP/Ti stacks. Results confirmed that the primary wear patterns in CFRP drilling were abrasive wear, while the predominant tool failures occurring in Ti-phase drilling were micro chipping and edge fracture as depicted in Table 1.6. Owing to the adverse effects of edge chipping and coating peeling on the cutting edges, the cutter was soon deprived of the protection from the coating material and failed quickly in its rapid wear stage. Isbilir and Ghassemieh [42] carried out a comparative study of tool life when drilling hybrid CFRP/Ti stacks by using AlTiN-coated carbide drills. It was concluded that the edge wear, crater wear and abrasive wear were the main wear modes governing CFRP drilling, while for Ti drilling, the key wear mechanisms were flank wear, crater wear but no adhesion wear due to the use of coolant in drilling. This was because the coolant could effectively decrease the high cutting temperature on the tool-chip interface and remove away the resected Ti chips on tool rake face, which minimized the Ti chip adhesion. Besides, the occurrence of micro chipping also further exacerbated the friction between tool-chip interface, and deprived the tool substrate of coating protection, thus causing the final tool failure. Table 1.6 summarizes the observed wear morphologies of used AlTiN coated carbide drills after drilling hybrid CFRP/Ti6Al4V stacks.

Furthermore, Wang et al. [51] pointed out that the overall tool wear modes involved in CFRP/Ti drilling were the combination of the edge rounding wear from drilling CFRP phase and the flank wear from drilling Ti phase when using uncoated, AlTiN coated and nanocomposite coated drills. Moreover, the authors also highlighted that the profound interactions of each phase drilling might favor the improvement of the tool life in CFRP/Ti drilling as compared to single Ti drilling case. The main reason was due to the fact that the severe edge chipping was eliminated by the effects of carbon fibers in CFRP phase on brushing off the Ti adhesion and smoothing the cutting edges, which substantially increased the tool life.

Although different tool materials may exhibit disparate wear behaviors when drilling hybrid FRP/Ti stacks, several similarities can also be drawn. The predominant wear modes referring to abrasive wear, edge rounding, flank wear and adhesion wear are commonly confirmed by most of the existing researches concerning hybrid FRP/Ti drilling [38, 41, 42, 44-47, 50]. Table 1.7 then summarizes the key wear modes encountered in drilling FRP/Ti stacks with a particular reference to the used cutting conditions.

Table 1.7
Summary of the wear modes governing the hybrid FRP/Ti stack drilling for various drill bits and cutting conditions.

No.	Reference	Drilling condition	Tool wear mechanisms	
1	Park et al. [45]	CFRP/Ti6Al4V (T = 7.54/6.73 mm) *n* (CFRP): 2000, 6000 rpm; *n* (Ti): 300, 400, 800 rpm *f* (CFRP): 0.0762 mm/rev; *f* (Ti): 0.0508 mm/rev a.Tungsten carbide (WC/Co) drill b.Polycrystalline diamond (PCD) drill D = 9.525 mm Coolant: cutting fluid, flow rate at 16 mL/min	WC drill	a. Abrasive wear b. Edge rounding wear c. Severe Ti adhesion d. Flank wear
			PCD drill	a. Abrasive wear b. Edge rounding wear c. Micro chipping d. Micro fracture

2	Isbilir and Ghassemieh [42]	CFRP/Ti6Al4V(T = 20/20 mm) *n* (CFRP): 4500 rpm; *n* (Ti): 1400 rpm *f* (CFRP): 457 mm/min; *f* (Ti): 119 mm/min AlTiN-coated twist drill D = 8 mm	TiAlN-coated twist drill	a. Edge rounding wear b. Crater wear c. Abrasive wear d. Flank wear e. Micro chipping
3	Ghassemieh [41]	CFRP/Ti6Al4V *n* (CFRP): 4500 rpm; *n* (Ti): 1400 rpm *f* (CFRP): 457.2 mm/min; *f* (Ti): 119 mm/min C7-coated carbide drill D = 6 mm	C7-coated carbide drill	a. Abrasive wear b. Edge chipping c. Tool fracture
4	Beal et al. [38]	CFRP/Ti6Al4V (T = 7.54/6.73 mm) *n* (CFRP): 6000 rpm; *n* (Ti): 800 rpm *f* (CFRP): 0.0762 mm/rev; *f* (Ti): 0.0508 mm/rev a.Tungsten carbide (WC/Co) drill D = 9.525 mm Coolant: cutting fluid, flow rate at 16 mL/min	WC drill	a. Abrasive wear b. Flank wear c. Ti adhesion
5	Park et al. [46]	CFRP/Ti6Al4V(T = 7.54/6.73 mm) *n* (CFRP): 2000 rpm; *n* (Ti): 400 rpm *f* (CFRP, Ti): 0.051 mm/rev a. Standard twist drill (Uncoated WC) b. Standard twist drill (BAM-coated WC)	WC twist drill	a. Abrasion wear b. Titanium adhesion c. Flank wear
			BAM-coated drill	a. Flank wear b. Edge wear c. Coating peeling
6	Tashiro et al. [50]	CFRP/Ti6Al4V (T = 3/9.5 mm) v_c (CFRP,Ti): 18.8 m/min *f* (CFRP,Ti): 0.1 mm/rev a.TiAlN-coated drill b. TiAlCr/TiSi coated drill D = 6 mm	TiAlN-coated drill	a. Abrasive wear b. Flank wear
			TiAlCr/TiSi-coated drill	a. Abrasive wear b. Flank wear
7	Poutord et al. [47]	CFRP/Ti6Al4V (T = 20.7/25.5 mm) *n* (CFRP): 2652 rpm; *n* (Ti): 265 rpm *f* (CFRP): 0.05 mm/rev; *f* (Ti): 0.2 mm/rev a. K20 uncoated drill D = 12 mm Dry cutting condition	K20 drill	a. Edge rounding wear b. Flank wear c. Ti adhesion
8	Kuo et al. [44]	Ti6Al4V/CFRP/Al-7050 v_c (Ti): 30 m/min; v_c (CFRP, Al): 120 m/min *f* (Ti, CFRP, Al): 0.08, 0.15 mm/rev a. DLC diamond drill b. CVD diamond drill D = 6.38 mm	DLC diamond drill	a. Abrasion b. Adhesion c. Brittle fracture d. Micro chipping
			CVD diamond drill	a. Abrasion b. Adhesion c. Macro fracture

1.7 Strategies for high-quality drilling

The current research focus on hybrid FRP/Ti drilling is composed of the search for efficient processing techniques capable of producing high quality and excellent surface integrity. To this aim, high-quality drilling of hybrid FRP/Ti stacks becomes a key pursuit in modern manufacturing community. Owing to the disparate natures of FRP and Ti phases, the criteria for high-quality drilling vary with each stacked constituent. For FRP phase, the criteria require lowest delamination and fiber breaking, minimum hole shrinkage and low surface roughness [96] while for Ti phase the

criteria are the elimination of burrs and producing excellent surface finish. The effective and direct approaches for high-quality drilling of FRP/Ti stacks typically have a close relation with the cutting parameters, cutting tool and cutting environment. It is assumed that approximately 60 % of the rejections of FRP phase produced in the aerospace industry are caused by the use of improper cutting parameters, non-optimal cutting tool and unfavorable cutting environment [97-99]. Since high-quality drilling is an extremely complex and comprehensive manufacturing operation, greatly dependent on many input variables, the following subsection is dedicated to making a summary of commonly-used approaches to high-quality drilling FRP/Ti stacks with respect to cutting parameters, cutting tool and cutting environment.

1.7.1 Cutting parameters

Cutting parameters including cutting speed (v_c) (or spindle speed (n)) and feed rate (f) locally have significant influences on the cutting responses generated in FRP/Ti drilling. Proper selection of cutting parameters would be beneficial for high-quality drilling of the bi-material system. The parametric effects on drilling FRP/Ti stacks have been studied by many researchers [2, 16, 41-43, 95] as depicted in Fig. 1.14. Table 1.8 presents the summarized cutting conditions used in the referred literature. As shown in Fig. 1.14 (a), most of the investigations revealed that the effect of cutting speed on thrust force generation was insignificant when drilling hybrid FRP/Ti stacks. In contrast, the feed rate exhibited remarkable effects on the thrust force and subsurface damage in such manner that a slight increase of feed rate resulted in dramatically increased thrust force and deceased exit burr defect as illustrated in Fig. 1.14 (b) and Fig. 1.14 (c). The reasons could be explained by the fact that when feed rate increased, on one hand, the drill was required to cut off more material volume per revolution and overcome higher cutting resistance in drilling, which resulted in a dramatically increased thrust force. On the other hand, the increased feed rate led to the short engagement time between the tool-work interactions. The reduced tool-work engagement time would lead to less heat generation in the Ti layer drilling and hence reduce the exit Ti burr formation [2, 16, 43, 95].

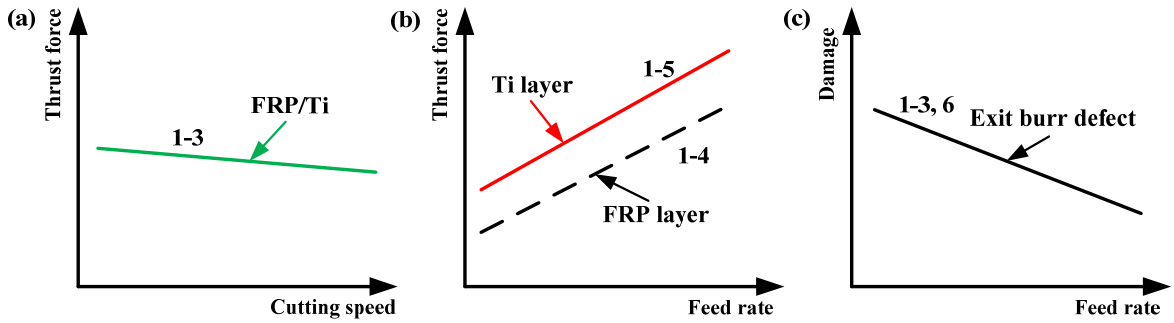

Figure 1.14. Effects of the cutting parameters on thrust force and hole damage when drilling hybrid FRP/Ti stacks [2, 16, 41-43, 95].

Table 1.8
Work-tool materials and cutting parameters used for drilling hybrid FRP/Ti stacks in Fig.1.14.

No.	Reference	Work material	Tool material	Cutting parameters
1	Ramulu et al. [2]	IM6-Gr/Bi-Ti6Al4V	HSS, HSS-Co, Carbide (C2 grade)	n : 325,660,1115,1750, 2750 rpm; f : 0.03,0.08,0.13,0.12, 0.25 mm/rev.
2	Kim and Ramulu	PIXA-M composite/Ti	Carbide (C2 grade)	n : 1320, 2230, 3500, 5440 rpm;

	[16]			*f* : 0.02,0.03,0.14,0.25,0.3 mm/rev.
3	Kim et al. [95]	IM6-Gr/Bi-Ti6Al4V	Polycrystalline diamond (PCD) drill	*n* : 325,660,1115,1750, 2750 rpm; *f* : 0.03,0.08,0.13,0.12, 0.25 mm/rev.
4	Isbilir and Ghassemieh [42]	CFRP (M21 T700GC) /Ti6Al4V	TiAlN-coated twist drill	CFRP : *n* : 4500rpm, *f*: 457 mm/min;; Ti : *n* : 4500rpm, *f*: 457 mm/min.
5	Ghassemieh [41]	CFRP(M21E)/Ti6Al4V	C7-coated carbide drill	CFRP : *n* : 3000, 4500, 6000, 9000 rpm, *f*: 355.6, 457.2, 584.2, 685.8 mm/min; Ti : *n* : 1000, 1400, 1800 rpm, *f* : 95, 119, 142, 171 mm/min; CFRP/Ti : *n* :1400,4500 rpm, *f* : 119, 457.2 mm/min.
6	Kim and Ramulu [43]	IM6-Gr/Bi-Ti6Al4V	HSS, HSS-Co, Carbide (C2 grade) drills	*n* : 660, 1115, 1750 rpm; *f* : 0.08, 0.13, 0.20, 0.25 mm/rev.

In addition, Ghassemieh [41] and Isbilir and Ghassemieh [42] reported that the measured thrust force and torque were elevated with the increased cutting speed for CFRP phase but decreased when cutting speed was elevated for Ti phase. Isbilir and Ghassemieh [42] further pointed out that the thrust force and torque produced in Ti-phase drilling were usually higher than those generated in CFRP-phase drilling as shown schematically in Fig. 1.14 b. Besides, the induced delamination and surface roughness typically increased with the elevated feed rate in both CFRP phase drilling and Ti phase drilling. Furthermore, some other scholars [50, 100-102] pointed out that the drilling conditions including high cutting speed and low feed rate usually decreased the thrust force and minimized the delamination extent in FRP-phase. In spite of this, Yang and Liu [35] stressed that the use of high cutting speed would inevitably increase the tool flank wear on drill bits, resulting in rapid tool wear rate for Ti alloy drilling. Kim and Ramulu [43], Kim and Ramulu [103] asserted that the optimal cutting conditions for achieving high-quality machined holes should be a combination of low feed and low speed when using carbide drills, while high feed and low speed are suitable for HSS-Co drills when drilling hybrid composite stacks. In general, relatively high cutting speed (150 - 200 m/min) with low feed rate (0.01 - 0.05 mm/rev) is recommended for drilling composite phase in order to minimize delamination [104, 105], while low cutting speed (10 - 30 m/min) with positive feed rate (0.05 - 0.1 mm/rev) is recommended for Ti alloy machining [2, 27].

To achieve high-quality drilling results, the selection of optimal cutting parameters should be a direct solution. However, due to the dissimilar machinability behaviors of the stacked constituents, the ideal solution for FRP phase is not the most efficient for Ti phase and *vice versa*. This leads to a compromise selection of the cutting parameters that often give rise to high drilling forces, poor hole quality, and severe tool wear in hybrid composite stack drilling [43, 66, 67]. Since the Ti-phase drilling always causes the biggest problems, the cutting parameter selection in drilling FRP/Ti stacks should match that of the difficult-to-cut Ti phase. In some cases, the cutting conditions consisting of low cutting speed and moderate feed rate may facilitate the FRP/Ti drilling and can provide excellent hole surface finish for both FRP and Ti phases [38].

1.7.2 Cutting tool

Cutting tools with superior thermo-physical properties often ensure excellent tool-work configuration for hybrid composite stack drilling. Superior tools are usually required to provide

desirable improvement of the tribological characteristics and behaviors among the tool-FRP interface and tool-Ti interface in order to combat tool wear during stack drilling. However, sometimes it is difficult to choose an ideal tool solution for meeting the stringent requirements of the FRP/Ti drilling operation since each phase cutting commonly exhibits disparate wear behaviors. As for FRP-phase drilling, the cutting tool suffers severe edge rounding wear and intense flank wear attributed to the abrasive nature of reinforcing fibers [106, 107]. Abrasion, fracture and chipping due to thermal and mechanical loads are confirmed to be the major wear mechanisms under most of cutting conditions by previous research work [106, 108-110]. In addition, since the FRP chips show inability of heat dissipation, they always cause accumulated heat on the tool tip that might cause tip chipping by thermal effects. For Ti-phase drilling, the produced chips can easily weld to the drill cutting edges due to their strong chemical affinity, thus forming BUE, which leads to severe adhesion wear of the tool. Besides, the cutter also suffers severe thermal damage and heat impact due to the poor thermal conductivity of titanium alloy, which consequently causes edge chipping and tool fracture. Therefore, for FRP/Ti stack drilling, cutting tools with (*i*) high hardness, (*ii*) high toughness, (*iii*) high wear resistance, (*iv*) good chemical inertness, and (*v*) high thermal conductivity are strongly preferred. Up to now, tool materials in a wide range including high-speed steel, carbide tools, coated tools, and super hard materials made up of PCBN and PCD have been employed in FRP/Ti cutting as shown in Fig. 1.15 [111]. For commonly-used carbide tools, cutters with low cobalt content are recommended for hybrid composite stack drilling due to their increased tool hardness and expanded abrasion resistance. For coated tools, previous researches showed that some of them with specific properties demonstrated more prominent ability to generate better surface finish and to yield longer tool life as compared to uncoated tools when cutting hybrid composite stacks [41, 42, 46, 50].

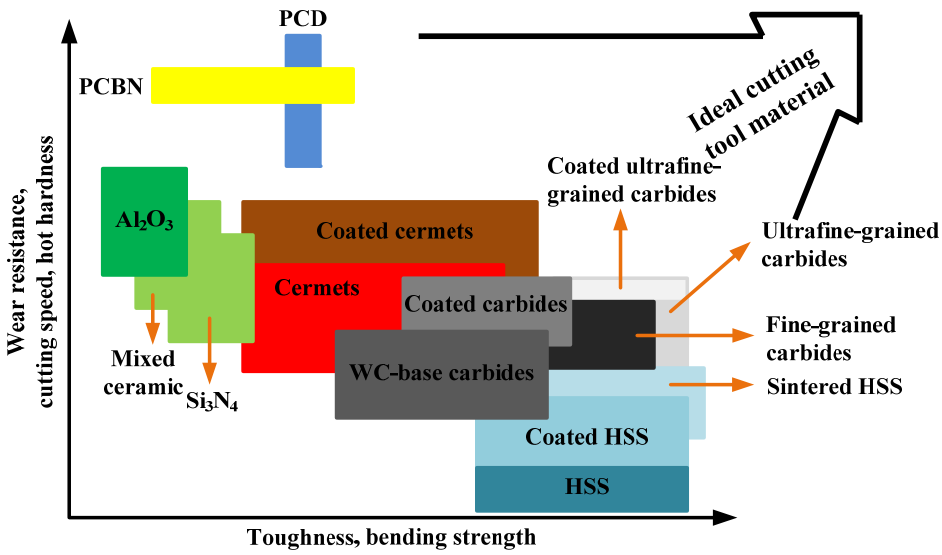

Figure 1.15. Cutting performance of different tool materials used in hybrid FRP/Ti stack drilling [111].

Coated drills differing in coating type (CBN, diamond, single-layer, multi-layer, *etc.*), deposition mode (CVD, PVD, *etc.*) are often preferred choices in actual hybrid composite stack drilling due to their superior properties and moderate tool cost. Their excellent mechanical/chemical properties (hot hardness, oxidation resistance, chemical stability, *etc.*) commonly provide superior tool-work configuration to shield the tool substrate from destructive influences during machining. However, in

fact, the suitability level of coated tools in hybrid composite stack drilling highly depends on the extent of their improvement on the tribological properties of both tool-FRP and tool-Ti interactions. As such, only some of the coated tools show excellent suitability for FRP/Ti stack drilling, part of them may exhibit inherent limitation and shortcoming. Fujiwara et al. [112] evaluated different coated tools in drilling CFRP/Ti6Al4V stacks by using TiAlN-coated, TiSiN-coated, and TiAlCr/TiSi-coated carbide drills. Results confirmed that the TiAlCr/TiSi coating outperformed TiAlN and TiSiN due to its superior wear resistance and the ability to reduce chip adhesion in the material removal process. For commonly-used Ti [C, N], TiN, Al_2O_3 coatings, they would be inappropriate solutions for FRP/Ti drilling due to their poor thermal conductivity, which would form thermal barrier against energy dissipation in FRP-phase cutting resulting in adverse effects on their wear resistance [113, 114]. The polycrystalline diamond (PCD) tool was mainly reported to have superior cutting performance when cutting single FRP composites due to its high wear resistance and thermal conductivity [115, 116]. When used in FRP/Ti stack drilling, the PCD material can also alleviate the serious Ti adhesion and exhibit excellent wear resistance despite the occurrence of micro-chipping due to its brittleness characteristic [45].

In addition, drill bits with special geometries are also qualified to perform high-quality drilling of hybrid composite stacks. The drill geometries are determined by a set of variables including characteristic angle (*e.g.*, point and helix angles), edge geometry (*e.g.*, chamfer, honed, and round edges), tool shape (twist shape, helical shape, *etc*.), *etc*. The excellent performances of special drill bits principally have a close relation with the mentioned geometrical variables, which results in minimal hole damage and minor tool wear in drilling action. Xu et al. [19] and An et al. [117] compared the tool performances of one standard twist drill and one special drill (namely “dagger drill”) in drilling of high-strength T800S/250F CFRP phase. It was found that the dagger drill generated better surface finish, *i.e.*, less burr defect and smaller delamination damage than the standard twist drill due to its smaller point angle and helix angle. Grilo et al. [118] studied the effects of different structural drill bits (SPUR drill, R950 drill and R415 drill) on the delamination damage when drilling CFRP laminates. It was concluded that the SPUR drill produced the best hole quality, generated the lowest delamination on entry and exit sides of the CFRP laminates. Wika et al. [99] conducted several drilling trials of CFRP/Ti stacks by using four different drill bits varying in flute number and helix angle. Results showed that the two-flute drill bit with higher helix angle generated smallest cutting force and lowest cutting temperature as compared to other used drills due to its large flute volume for chip evacuation and heat dissipation. SenthilKumar et al. [48] examined the effects of point angle on tool performance when drilling CFRP/Ti stacks by using 118° and 130° point angle drills. It was concluded that the drills with higher point angle (130°) outperformed those with lower point angle (118°) from the evaluation of tool wear and chip evacuation. Brinksmeier and Janssen [15] and Brinksmeier et al. [3] evaluated the comparative tool performance of step drill and orbit drill with conventional twist drill when drilling of $AlCuMg_2$/CFRP/Ti6Al4V stacks, respectively. It was revealed that the surface quality generated by step drill or orbit drill was better than that generated by conventional drill as well as lower cutting temperature and lower feed forces in all stacked phases. Furthermore, Garrick [119] argued that the drill bit manufactured with a special K-land as commonly used in Ti alloy cutting, could also strength the cutting edges and hence make the tool viable for power-feed drilling hybrid CFRP/Ti stacks. In the author’s experiments, the veined PCD drills modified with K-land design yielded increased tool life and

improved hole quality as compared to the conventional geometrical PCD drills. Recently, Kuo et al. [44] made a comparative evaluation of two different geometric diamond-coated drills (one diamond-like carbon (DLC) drill with conventional point and helix angles of 140° and 30°, respectively, and another chemical vapor deposited (CVD) drill with a 120°×180° two-stage point design accompanied by a helix angle of 30°) when cutting Ti6Al4V/CFRP/Al-7050 stacks with a particular focus on cutting forces, tool wear, hole accuracy and burr formation. The experimental findings confirmed that the CVD drill significantly outperformed the DLC diamond drill in terms of either cutting forces or hole accuracy. The reason was due to the fact that the CVD has sharper primary point angle that lowered thrust force and a secondary angle of 180° that shortened the cutting lips and hence reduced torque. In addition, the two-stage point design of CVD drill also provided improved 'self-centering' capability, thereby reducing tool deflection or run-out and guaranteeing excellent hole accuracy. Besides, drill bits designed with small chisel edge width as shown in Fig. 1.16, can also promote the lowest force generation and minimal delamination damage in FRP-phase drilling [104]. The key function of the special geometrical tools in FRP/Ti drilling primarily aims to provide beneficial effects on alleviating the hole damage (especially the delamination damage) generated in FRP-phase drilling. Successful use of special geometric tools like step drill, brad point drill, slot drill and straight-flute drill, was achieved to improve the machined hole quality when drilling FRP composites by previous research work [77, 109, 111, 120-129].

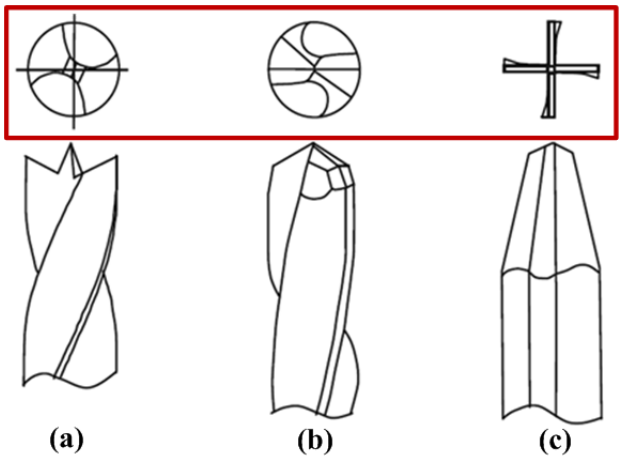

Figure 1. 16. Different drill bits with small chisel edge width:
(a) candle stick drill, (b) multifaceted drill and (c) straight flute drill [104].

Overall, the ideal cutting tool for high-quality drilling of FRP/Ti stacks should be a good match of proper tool material and optimal tool geometry. From the aspect of tool material, drill bits with high wear resistance, high hardness, and high thermal conductivity will be a primary choice. With regard to tool geometry, despite the fact that various researches have been done for hybrid composite stack drilling in the past few decades, most of the work was still performed by simple comparison of special and conventional tools in terms of one or multiple aspects of drilling responses. The tool geometry design was mostly based on the empirical experience rather than the reasonable theoretical criteria. No explicit theoretical explanation was proposed to reveal the intrinsic mechanisms governing the tool geometry optimization or improvement. The detailed theoretical standards and criteria for tool geometry design of hybrid FRP/Ti stack drilling are urgently needed to be established in the future.

1.7.3 Cutting environment

For FRP/Ti drilling, a proper selection of cutting environment would be another feasible approach for facilitating the high-quality machining. The use of cutting fluid in hybrid FRP/Ti drilling can globally attain the following benefits: (*i*) reducing the tool-chip frictional coefficient, (*ii*) lubricating the tool-chip interface, (*iii*) dissipating the cutting heat especially generated in Ti-phase drilling, and (*iv*) removing away the chip adhesion on tool surface. For composite phase, the effects of cutting fluid primarily focus on (*i*) preventing "dust" like chip clogging on drill flutes, (*ii*) reducing force generation and cutting temperature on tool-chip interface, and (*iii*) improving the machined surface quality of the FRP phase. Several researches have proven that the use of cutting fluids in hybrid composite stack drilling could greatly improve the machined hole quality and expand the tool life as compared to dry cutting environment. Brinksmeier and Janssen [15] compared the minimum quantity lubrication (MQL) and dry cutting environment when drilling $AlCuMg_2$/CFRP/Ti6Al4V stacks. It was found that the MQL significantly reduced the chip adhesion on hole surface and generated better hole quality (especially tight diameter tolerance) than dry cutting condition. Besides, the use of MQL also prevented the BUE formation on tool faces and hence alleviated the tool wear rate. Fujiwara et al. [40] asserted that the drill bit used under water-mist-cooling process could also yield longer tool life than under dry cutting condition when drilling CFRP/Ti6Al4V stacks. The use of water mist effectively decreased the force generation, reduced the chip adhesion and promoted tight hole diameter in contrast with the dry cutting condition.

The beneficial effects of cutting fluid on drilling action are critically dependent on its delivery type (*e.g.*, flooding, spraying, dripping, misting, brushing), especially on its access level to the tool-chip active zone. Shyha et al. [49] conducted several drilling trials of Ti6Al4V/CFRP/Al-7050 stacks by employing three different fluid-delivering methods referring to flood coolant (through spindle spray), wet cutting and spray mist. Results showed that both flood coolant and wet cutting produced undersized holes with the deviation of 14 μm and the maximum error of -20 μm, respectively. In contrast, the spray mist environment gave rise to significantly oversized holes with the tolerances increased from 80 μm at the first hole to 120 μm when the drill was totally worn out. The use of high pressure through spindle made flood coolant generate the best roundness and lowest surface roughness due to the improved lubricant/coolant access to the tool-chip interface. Therefore, in order to maximize the benefits of cutting fluid, through-spindle coolant system (aka through-tool coolant system) should be recommended in FRP/Ti drilling since it can deliver fluid through spindle and tool passages directly to the cutting zones.

However, the use of cutting fluid inevitably results in severe damage to the environmental and work environmental sustainability due to the substantial content of chemical additives, which are more or less toxic to human health. To solve the problem, near-dry cutting has drawn due attention in ecologically machining of hybrid FRP/Ti stacks. This is because the near-dry cutting preserves the environment with combined impacts of ecological and economic. For instance, MQL drilling considered as a near-dry cutting is assumed as a promising necessity for hybrid composite stack machining. The MQL technique involves the usage of a small amount of biodegradable oil droplet dispensed to the tool-chip interfaces by compressed air flow, which can greatly reduce cutting temperature, improve surface quality and expand tool life [7, 20, 21]. Since the small quantity of

used biodegradable oil is less waste polluted, decomposable and non-toxic, the MQL solution can be successfully used to fulfill the demands of environmental and work environmental sustainability when machining hybrid FRP/Ti stacks. Brinksmeier and Janssen [15] employed the MQL machining method in drilling Ti/CFRP/Al stacks aiming at realizing economical drilling of multi-layer materials. Different cutting fluids and supply strategies were utilized in drilling. The use of MQL with internal supply produced the tightest diameter tolerances as compared to the conventional dry cutting condition. Serious BUE adhesion and tool flank wear were clearly reduced once MQL was applied. The MQL technique exhibited a suitable solution for realizing high-quality production of the stacked composite material.

Although very limited open literature [15, 40, 49] is reported to employ cutting fluid in hybrid FRP/Ti stack drilling, the use of cutting fluid indeed has demonstrated excellent prospects to improve the machinability of the material. For proper selection of cutting fluid, a comprehensive consideration of both manufacturing process (*e.g.*, fluid type, delivery type, machining cost,) and human/environmental impacts should be seriously taken. With regard to near-dry cutting, in some cases, even though it is confirmed to be beneficial for hybrid composite stack drilling from an ecological and economic viewpoint, proper steps are still required to be taken in order to make this technology more environmentally friendly and cost efficient.

1.8 Numerical approaches

Advances in numerical techniques have given researchers and engineers a promising tool to develop reliable numerical models for predicting various manufacturing processes. The numerical approach offers an attractive alternative route to achieving in-depth studies of the complex mechanisms governing the chip removal process. In spite of the developed numerical techniques, to date, modeling FRP/Ti machining is still very challenging as it's a 3D dynamic process with multi-tool-work interaction domains. Currently, most of the FE approaches available in the open literature focus on the individual FRP composite and individual Ti alloy cutting modeling. The relevant research work regarding the coupled FRP/Ti machining is still scarcely reported. For precisely simulating the hybrid composite stack cutting, the accurate FRP and Ti phase models are critically demanded. On this basis, the following subsections aim to provide a brief literature survey on the topics of individual FRP composite and Ti alloy cutting modeling in order to offer a beneficial guideline for simulating hybrid FRP/Ti machining.

1.8.1 FRP composite modeling

Finite element method (FEM) has drawn due attention in FRP cutting modeling in order to reveal the implicit mechanisms encountered in actual cutting operations within the past few decades. Tremendous research work has been performed in the composite model establishment aiming to provide a better understanding of the activated chip separation mode, force generation, induced subsurface damage, *etc*.

To describe the mechanical and physical behaviors of the fiber/matrix system, typically three types of FE models are widely employed in FRP cutting modeling, namely, (a) macro-mechanical model [55, 130, 131], (b) micro-mechanical model [132, 133] and (c) macro-micro mechanical

model [134, 135].

In macro-mechanical model, the FRP composite is generally simulated as a so-called equivalent homogeneous material (EHM) with equivalent anisotropic properties [55, 136, 137], which greatly reduces the complexity in establishing two-phase microstructure and decreases the computation cost during the numerical calculation. Following its simplification characteristics, a large number of scientific researches have been conducted by using this modeling approach. Arola and Ramulu [55] adopted the macro-mechanical models for simulating the chip formation when cutting glass/epoxy composites. A 2D quasi-static plane stress analysis incorporating both maximum stress and Tsai-Hill failure criteria was utilized. The model was reported to capture accurately the estimations of cutting force while the thrust force predictions failed to comply with the experimental results. Ramesh et al. [136] analyzed the stress distribution and chip failure modes governing the FRP machining by using an anisotropic plastic theory. The maximum stress levels were found to occur near the tool tip for 0° fiber orientation, while for other fiber orientations, the maximum stresses were identified below the tool tip. In addition, Mahdi and Zhang [137] established a quasi-static 2D macro-mechanical model by using the Tsai-Hill criteria for orthogonal cutting modeling of fiber reinforced composites. The variation of cutting force *versus* fiber orientation was precisely studied. The Tsai-Hill criteria were found to yield reasonable cutting predictions compared with the experimental measurements. Moreover, several researchers also intend to use the macro-mechanical model to inspect the cutting-induced damage of machined FRP composites. Bhatnagar et al. [138] adopted the EHM finite elements to assess the extent of subsurface damage occurring below the trim plane when machining GFRP. A special focus was made on clarifying the influence of the depth of cut on the final damage extent promoted in the specimens. The Tsai-Hill contour beneath the trim plane was used as an indicator for evaluating the depth of internal damage induced by cutting. By comparing to the experimental measurements, the model was found to succeed in predicting the damage trends during cutting. However, the damage generated beyond 60° fiber orientation still remained under-predicted. The discrepancies between the predicted and measured values were mainly caused by the lack of modeling the interfacial properties of fiber/matrix system. Moreover, Rao et al. [139] proposed a 3D macro-mechanical model for investigating the cutting behavior of unidirectional CFRP composites. Both numerical and experimental inspections were performed for a wide range of fiber orientations, depths of cut, and tool rake angles. It was reported that the predicted cutting force and chip formation mechanism matched well with the experimental observations. Further, Santiuste et al. [130] presented a macro-mechanical model to study the chip formation and subsurface damage by implementing Hashin damage criterion. The cutting behaviors of both CFRP and GFRP laminates with different fiber orientations (15°, 30°, 45°, 60°, 75° and 90°) were precisely studied with a particular focus on the cutting-force estimation, crack initiation and damage evolution prediction. Results showed that the predicted force generation *versus* fiber orientation yielded a consistent variation trend with the experimental results gained by Bhatnagar et al. [138] as shown in Fig.1.17. In their models, the GFRP was simulated as a ductile material by suffering a widely extended damage zone beneath the tool tip, while the CFRP was modeld as a brittle material under machining operations due to the predominant catastrophic failure in chip separation with minor or no damage progression. It was found that the CFRP cutting produced less subsurface damage as compared to that of GFRP machining due to the different levels of energy needed to complete the chip breakage, as depicted in Fig.1.18. In addition, the fiber orientation was

also found to have significant effects on both CFRP and GFRP chip separation and subsurface damage formation. Specifically, an increase of fiber orientation usually led to an elevated crushing damage beneath the machined surface.

With respect to micro-mechanical models, the reinforcing fibers, epoxy matrix, as well as the fiber/matrix interface of the FRP composites, are modeled separately in order to accurately replicate the local cutting behaviors in micro scales. The current researches of micro-mechanical models in FRP cutting simulation primarily focus on the force generation prediction, local damage estimation, and chip formation inspection. Nayak et al. [140] performed a comparative analysis of the micro-mechanical and macro-mechanical FE models in orthogonal cutting of UD-GFRPs. The micro-mechanical model was developed by two-phase material system consisting of disparate physical entities, *i.e.*, a single fiber and surrounding matrix. It was found that the two-phase micro-mechanical model based on a specific fiber/matrix separation criterion provided consistent cutting force and thrust force predictions with the experimental findings. In contrast, the macro-mechanical model based on the Tsai-Hill failure criteria was found to only accurately predict the cutting force generation while failed to capture the thrust force.

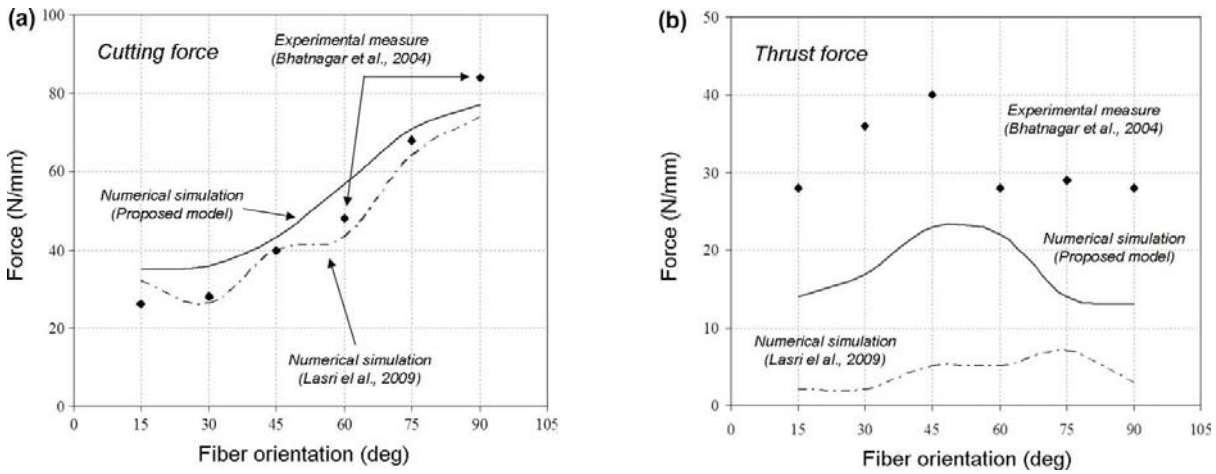

Figure 1.17. Force generation in function of fiber orientation when cutting GFPR laminates: (a) cutting force and (b) thrust force [130, 138, 141].

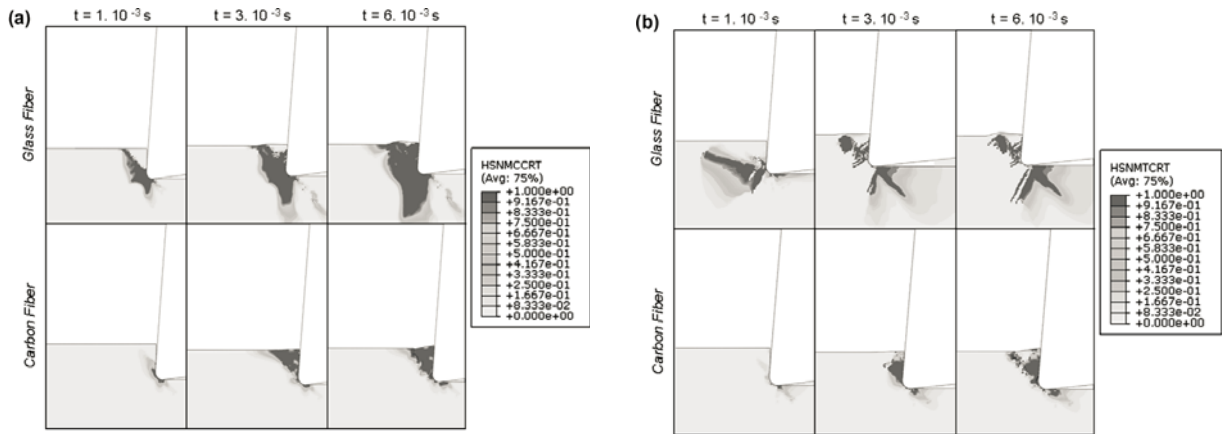

Figure 1.18. Evolution of the matrix damage: (a) crushing and (b) cracking during the chip formation: comparison between CFRP and GFRP with 45° fiber orientation [130].

Further, to inspect the micro-scale chip formation and subsurface damage involved in FRP cutting, Calzada et al. [133] developed a dynamic micro-mechanical model by modeling the fiber,

matrix and fiber/matrix interface separately when simulating the CFRP cutting process. The interface was modeled as a third phase using traditional continuum elements by implementing two different damage criteria accounting for the normal and tangential failure of the elements during the chip removal process. From the simulation observations, the micro-mechanical approach yielded sufficient capabilities of replicating the internal fiber fracture and subsurface damage *versus* different fiber orientations as presented in Fig.1.19. The simulated results yielded a good agreement with the experimental findings. Moreover, the FE results also confirmed that the rounded tool tended to induce bending-dominant failure while the sharp tool seemed to generate crushing-dominant failure as shown in Fig.1.20. The micro-mechanical model showed a good alternative for process optimization of fiber orientation and tool geometry when cutting CFRP composites.

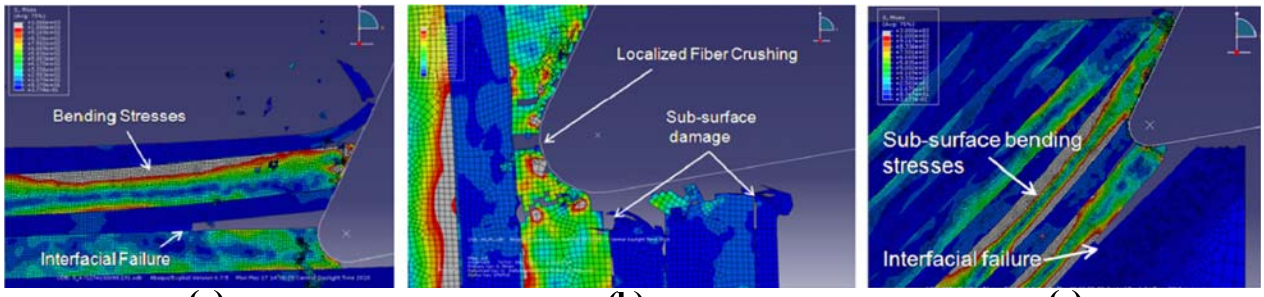

(a) **(b)** **(c)**

Figure 1.19. Micro-mechanical models for simulating different failure mechanisms *versus* fiber orientation (θ) when cutting CFRP laminates: (a) $\theta = 0°$ fiber orientation, (b) $\theta = 90°$fiber orientationand (c) $\theta = 135°$ fiber orientation [133].

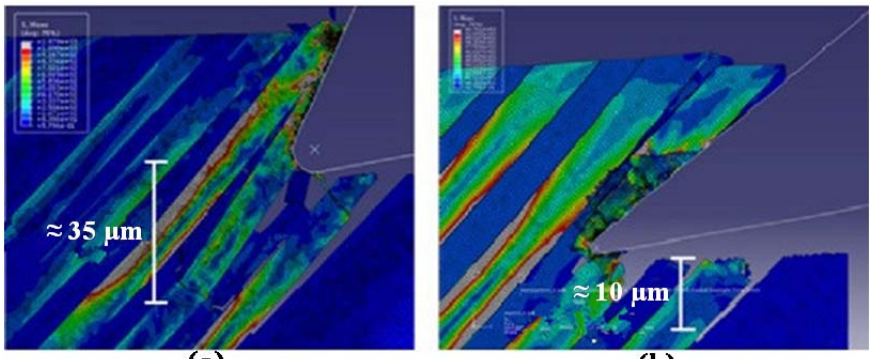

(a) **(b)**

Figure 1.20. Effect of tool geometry on subsurface damage when cutting CFRP laminates: (a) rounded tool shape and (b) sharp tool shape [133].

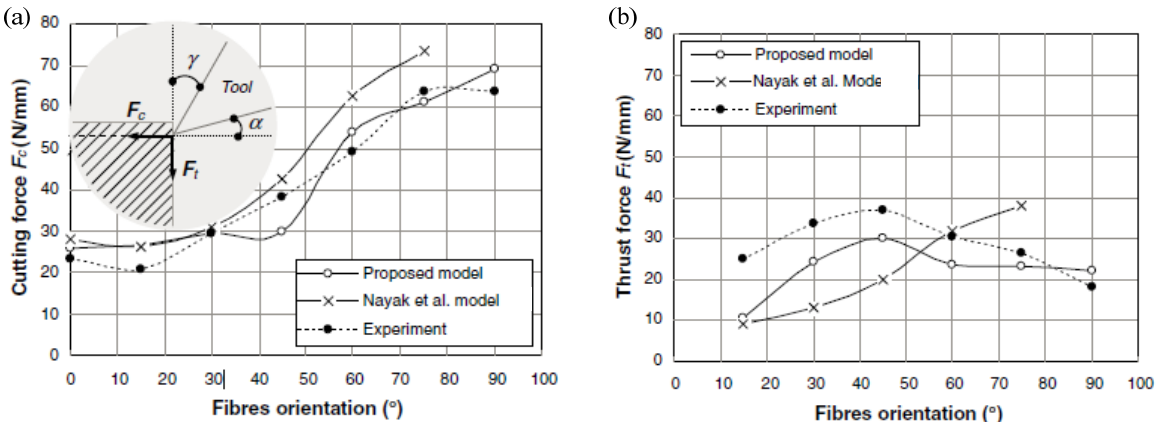

Figure 1.21. Measured and predicted force generation for machining GFRP lamintes with reference to the simulation and experimental results gained by Nayak et al. [140]: (a) cutting force and (b) thrust force [134].

Since the micro-mechanical model requires high computation time and the macro-mechanical model shows less capability of predicting the composite cutting responses, there is a need to propose a new model combining both efficiency and accuracy of the micro and macro mechanical models. In such circumstance, the micro-macro mechanical model considering both the micro and macro scales of modeling was developed. In the new model, the micro-mechanical constituent is used in the vicinity of the tool-work interaction where the fiber and matrix are modeled separately, while the macro-mechanical model is implemented far away from the tool-chip active zones in which the FRP composite is model as an equivalent homogeneous material (EHM). Mkaddem et al. [134] developed a micro-macro model for machining simulation of GFRP laminates accompanied by several comparisons with the experimental results gained in the existing literature. The proposed micro-macro model yielded a more accurate cutting force prediction than that of the model developed by Nayak et al. [140] as shown in Fig. 1.21 (a). The mean error to the experimental results as recorded by Mkaddem et al. [134] was about 6 %, while the mean error for the model proposed by Nayak et al. [140] reached approximately 17 %. In addition, the predicted thrust force values also agreed well with the experimental observation as shown in Fig.1.21 (b).

Globally, the previous studies on cutting modeling of standard composite materials have gained sufficient advancements. The numerical work in either macro-scale modeling or micro-scale modeling has obtained great achievements. However, for researches on cutting modeling of the newly emerged hybrid composite stacks (*e.g.*, CFRP/Ti), they were still rarely reported, which should deserve significant investigations.

1.8.2 Ti alloy modeling

Titanium alloys are extensively used for serving as a key constituent in hybrid composite stacks, which acts a crucial role in enhancing the mechanical/physical properties of the multi-material assembly. However, the titanium alloy is usually characterized as an extremely difficult-to-cut material. One of the key causes may arise from its low thermal conductivity that gives rise to (*i*) high temperature and high pressure localized at the tool-chip interface, (*ii*) severe plastic instability localized in adiabatic shear bands, and (*iii*) excessive tool wear by thermal fatigue and diffusion. The other cause is due to its high chemical reactivity with most-used tool materials and its low elastic modulus. Conventional experimental methods have provided sufficient capabilities of mechanism prediction in titanium alloy cutting but are often time consuming and very costly. In contrast, the numerical approach should be a promising alternative that enables good predictions of Ti machining mechanisms with low cost and high efficiency.

In FEM, titanium alloys are commonly considered as a homogeneous elastic-plastic material. Tremendous research work has been performed in the past few decades with a particular focus on the chip formation prediction and cutting force estimation. The sawtooth chip is usually a key representative chip characteristic in titanium machining even at a relatively low cutting speed. The chip segmentation is an important factor that significantly affects the machining process (*e.g.*, cutting force, cutting temperature and machined surface quality), which, in turn, causes due attention in the simulation researches. To accurately capture the sawtooth chip formation in titanium machining, a large number of material laws have been developed including Johnson-Cook (JC) material model [142, 143], Zerilli-Armstrong (ZA) model [144], Mechanical Threshold Stress

(MTS) [145], Baummann-Chiesa-Johnson (BCJ) model [146], Obikawa-Usui model [147], Rhim-Oh [148] model, *etc*., coupled with a fracture criterion such as the JC damage law [149-152], deformation energy-based criterion [153, 154], ductile fracture criterion [147] to describe the metal material flow and chip separation when subjected to high stress, high strain and high strain rate conditions. The mentioned constitutive laws commonly yield reliable descriptions of the thermoplastic instability governing the chip removal process and the crack initiation/propagation inside the primary shear zone when cutting modeling of titanium alloys.

Xi et al. [155] adopted the JC material law based on the updated Lagrangian formulation to simulate thermally turning operation of Ti6Al4V alloy. The element deletion algorithm based on equivalent plastic displacement was implemented to produce the chip separation. The predicted chip morphology showed a strong correlation with the experimental observation, as depicted in Fig.1.22.

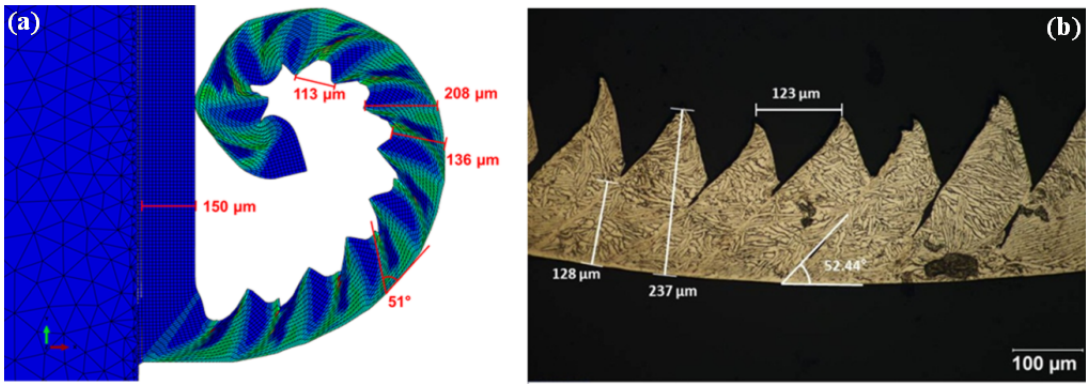

Figure 1.22. Comparison between (a) simulated and (b) experimental chip formation when machining Ti6Al4V alloys (the contour shown in the simulation results is the equivalent plastic strain) [155].

Chen et al. [156] implemented the JC material law with an energy-based ductile fracture criterion for modeling the high-speed machining of Ti6Al4V alloys. To accurately model the serrated chip morphology, the damage evolution was developed based on a constant density of failure energy for each case studied. The failure energy was refined to correlate with the element characteristic length. The simulated results in terms of cutting force and chip morphology yielded good agreements with the experimental findings [157], as shown in Fig.1.23, which confirmed the credibility of the ductile failure criterion for HSM of Ti alloys.

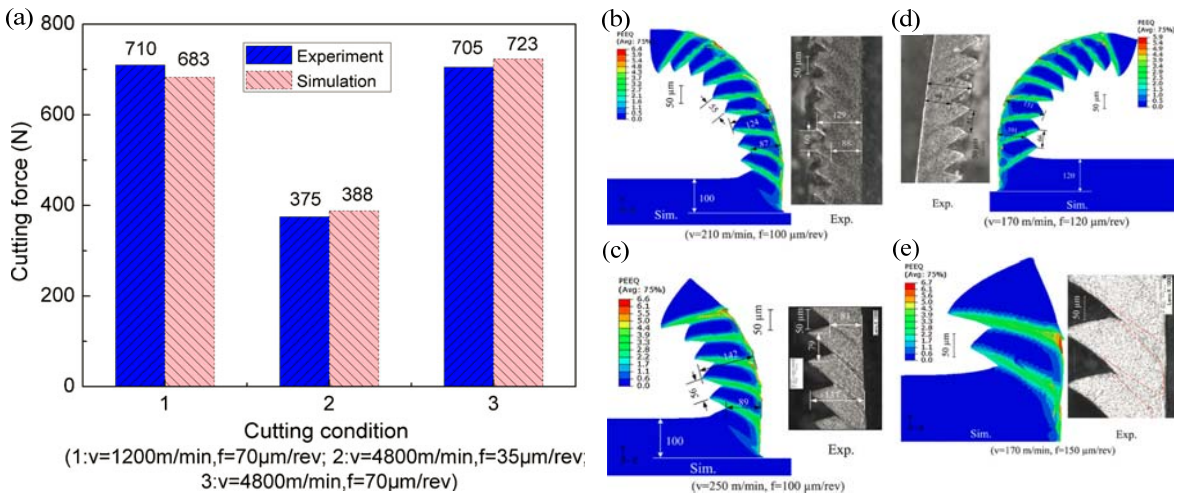

Figure 1.23. Predicted and experimental results when machining Ti6Al4V alloys: (a) cutting force [156, 157] and (b) - (e) chip morphology [156].

In addition, since the conventional JC law ignores the strain softening effects, it leads to making some necessary modifications of the original constitutive law in order to achieve more accurate predictions of Ti machining responses. Calamaz et al. [158] introduced a new material constitutive law, namely, TANH (Hyperbolic TANgent) law, into a 2D numerical simulation of serrated chip formation when machining Ti6Al4V alloys. The new model was modified based on the conventional JC law and was added by new terms to model the strain softening at elevated strains and temperatures. The model was found to enhance the segmentation phenomenon governing the chip removal process due to the introducing of strain softening effects. The numerical results based on the TANH law yielded a better agreement with the experimental findings in terms of chip morphology than that of the conventional JC law. As shown in Fig.1.24, under the cutting speed of 60 m/min, the JC law produced a continuous chip where the deformation was low and uniform (Fig.1.24 (a)), exhibiting quite differences from the experimental chip (Fig.1.24 (c)). In contrast, the numerical results gained by the TANH law produced a consistent serrated chip morphology that matched well with the experimental one.

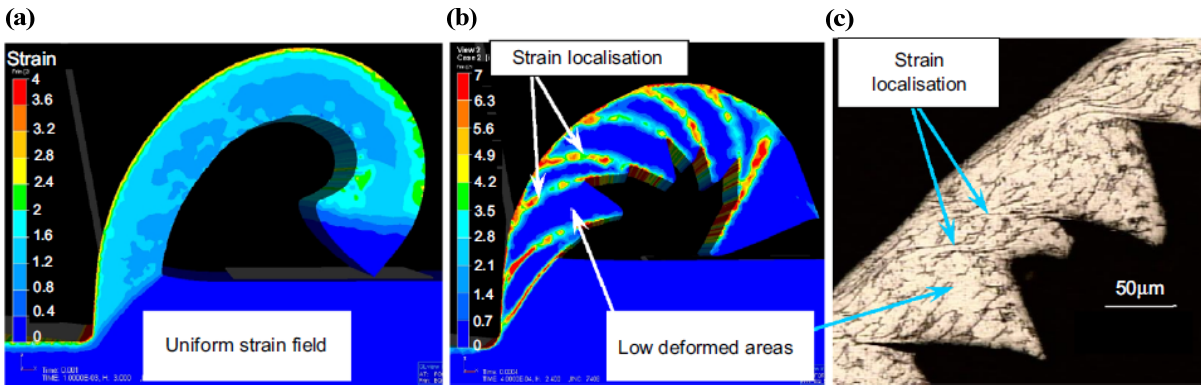

Figure 1.24. Chip morphology comparison between different implemented constitutive laws and experimental observations when machining Ti6Al4V alloys under the cutting speed of 60 m/min and feed (depth of cut) of 0.1 mm: (a) Johnson-Cook (JC) law, (b) TANH law, and (c) experimental result [158].

Furthermore, based on the previous research work conducted by Calamaz et al. [158], Sima and Özel [159] developed a new modified material law based on the conventional JC model through a comprehensive introduction of the flow softening, strain hardening and thermal softening effects and also their coupled interactions. The flow softening parameters were validated on a set of experimental data in terms of cutting forces and chip morphology. The FE simulation results revealed sufficient capabilities of modeling the chip formation process for adiabatic shearing in Ti6Al4V machining. More recently, Liu et al. [160] presented an enhanced constitutive material model based on the Zerilli-Armstrong (Z-A) law for simulating the deformation of Ti6Al4V alloys at high strains and strain rates in machining. The new model was incorporated a failure function that captured the additional loss in material strength due to void and crack formation in the shear bands at high strains and high strain rates. The enhanced constitutive model yielded consistent results with the experimental findings obtained by Cotterell and Byrne [161].

In sum, the scientific researches dealing with titanium alloy cutting modeling have gained fruitful advancements in the past few decades. The proper material law development as well as the pertinent FE technology offers excellent inspection and reliable prediction of various cutting phenomena induced in Ti alloy machining, *e.g.*, chip formation mechanics, force generation, and cutting temperature. The insightful results should ensure successful metallic phase cutting modeling in a hybrid composite stack configuration.

1.9 Concluding remarks

Through the rigorous literature review, it was outlined that tremendous advancements have been achieved concerning hybrid FRP/Ti machining and thus have led to a better understanding of the cutting physics in machining. To improve the machinability of hybrid FRP/Ti stacks, great efforts have been made primarily focusing on the experimental investigations. Based on the comprehensive analyses of the referred literature, some key conclusions on the current state-of-the-art advances and several prospects on future work can be drawn as follows.

- The disparate natures of hybrid FRP/Ti stacks have inevitably resulted in the local interface discontinuities and non-compliance tool-work interaction governing the hybrid stack machining. The interface discontinuities make the cutting condition much harsher and cutting mechanism more complex controlling the material removal process. The brittle fracture governing the FRP chip formation and the variable fiber breaking types *versus* fiber orientation are the key sources contributing to the hole damage formation in the drilling action. The hot and sharp-edge Ti chips produced in the bottom Ti phase drilling always cause severe abrasion and erosion on the machined FRP holes. In addition, compared to the pure FRP-phase and Ti-phase machining, the interface cutting could be considered as a most challenging operation due to the multi-tool-work interaction and the severe transfer of mechanical/physical response dominating the chip removal process. At present, the in-depth cutting behavior governing FRP/Ti interface machining is still understudied and future work is expected to address deeply the issue.
- The drilling-induced damage of hybrid FRP/Ti stacks comprises both polymeric imperfection and metallic defect. Among them, the interface damage is usually the most serious one. The delamination damage and burr defects are regarded as the main problems in actual production since these two types of damage often lead to poor assembly tolerance and high rejections of the machined components.
- Tool wear mechanisms controlling FRP/Ti stack drilling are usually the coupling and interaction of both composite-leading and metal-leading wear modes. Despite the wear discrepancies among different drill materials, abrasive wear, edge rounding wear, flank wear and adhesion wear are typically the predominant wear patterns governing the tool wear progression from a global perspective.
- Potential solutions to high-quality drilling of FRP/Ti stack were discussed in detail *versus* cutting parameters, cutting tools and cutting environment. The high-quality drilling, however, is a comprehensive and interactive manufacturing operation, dependent on many internal-external factors like tool material/geometry, drilling parameter, cutting environment as well as the workpiece properties and the used machine tool. To achieve high-quality results, profound expertise and rich experience based on the mentioned issues are required to propose a superior tool-external-factor configuration for hybrid FRP/Ti machining.
- With respect to the numerical studies, the majority of the previous work was primarily performed on the cutting modeling of standard composite (*e.g.*, CFRP or GFRP) or single metal phase (*e.g.*, Ti alloy). To date, nearly rare research work on dealing with hybrid

composite stack cutting modeling has been reported in the open literature. Nevertheless, the accumulated knowledge and expertise should provide sufficient help for future work on numerical simulation of hybrid FRP/Ti machining.

Furthermore, despite the fact that various well-performed studies have covered a variety aspects of hybrid FRP/Ti stack machining, there still exist several blind research areas that should deserve due investigations in the pertinent research fields. The relevant research topics lack of studies are summarized as follows.

- In the current research state, nearly all the existing literature work dealing with hybrid FRP/Ti machining was performed solely via the experimental method, which is very costly and time consuming. In contrast, the numerical approach in reality should be an alternative tool that can significantly help to optimize the mechanism investigations when cutting this multi-phase material. However, the relevant researches concerning the numerical modeling and FE analyses of hybrid FRP/Ti cutting have been scarcely reported. In the future, great efforts should be devoted to this promising research direction. And a combined research of both numerical simulation and experimentation is also critically demanded to ensure an improved FRP/Ti cutting understanding.
- Besides, the interface cutting as pointed out in this review chapter usually plays a key role in affecting the finally induced damage formation of the FRP/Ti interface region. However, relevant researches concerning this topic are rarely reported in the open literature. Moreover, most of the scholars ignored to inspect the influences of different cutting-sequence strategies ($\begin{smallmatrix}\text{FRP} \rightarrow \text{Ti}\\ \text{Ti} \rightarrow \text{FRP}\end{smallmatrix}$) on hybrid FRP/Ti machining process. The key differences between the two mentioned cutting-sequence strategies ($\begin{smallmatrix}\text{FRP} \rightarrow \text{Ti}\\ \text{Ti} \rightarrow \text{FRP}\end{smallmatrix}$) and also their influences on FRP/Ti machining responses are still not well studied.
- Eventually, it is well-known that the multi-tool-work interaction is the key root of various mechanical/physical phenomena induced in the FRP/Ti chip removal process. Many methods capable of improving the frictional behavior of the multi-tool-work interaction (*e.g.*, the use of optimal cutting parameters, superior cutting tools and favorable cutting environments) have been confirmed to improve significantly the machinability of the composite-to-metal alliance as widely-reported in the open literature. However, the activated mechanisms dominating the influences of the multi-tool-work interaction on hybrid FRP/Ti machining are still lack of studies.

The relevant research limitations as criticized above are thereby the key objectives of present Ph.D. work. To address precisely the aforementioned issues, the combined numerical and experimental studies were performed aiming to achieve an enhanced CFRP/Ti cutting comprehension.

Chapter II

FE models for cutting modeling of hybrid CFRP/Ti stacks

Nomenclature

CFRP → Ti	Cutting-sequence strategy from CFRP phase to Ti phase
CFRP → Ti Ti → CFRP	Cutting from CFRP → Ti and/or Ti → CFRP
f	Feed rate
F_c	Cutting force
F_t	Thrust force
Ti → CFRP	Cutting-sequence strategy from Ti phase to CFRP phase
v_c	Cutting speed
α	Tool rake angle
γ	Tool clearance angle
μ	Multi-tool-work frictional coefficient
θ	Fiber orientation

Abbreviation

CZ	Cohesive zone
EHM	Equivalent homogeneous material
JC	Johnson-Cook
OCC	Orthogonal cutting configuration

2.1 Introduction

Through the rigorous literature survey of Chapter I, it is outlined that the current research focus of hybrid CFRP/Ti stack machining is performed solely via the conventional experimental methodology. Researches dedicated to the numerical modeling of hybrid CFRP/Ti stack machining are limitedly found and scarcely reported. Compared to the great interests of numerical studies of standard composite machining and single Ti-alloy machining, relatively rare scientific work exists on dealing with hybrid CFRP/Ti cutting modeling. The key challenges as reported by Vijayaraghavan and Dornfeld [14] may arise from the complexity of establishing reliable constituents, accurately describing the disparate natures of the composite-to-metal system as well as the complicated modeling of interface behavior.

In addition, despite the fact that various experimental studies have provided a better understanding of the cutting mechanisms governing the hybrid CFRP/Ti machining, several physical mysteries are still remaining unknown as discussed in Chapter I. Specifically, the implicit cutting phenomena dominating the hybrid CFRP/Ti machining can be globally summarized as follows: (*i*) the key mechanisms controlling the interface cutting and interface damage formation, (*ii*) the influences of different cutting-sequence strategies ($^{\text{CFRP}\rightarrow\text{Ti}}_{\text{Ti}\rightarrow\text{CFRP}}$) on hybrid CFRP/Ti machining, and (*iii*) the parametric effects and frictional responses governing the CFRP/Ti cutting operation. Moreover, the conventionally-used experimental method is often cost-prohibitive, time-consuming and even difficult to inspect some key dynamic mechanisms dominating the interface damage formation. In contrast, numerical approach indeed, should be a promising method offering the new possibilities to overcome the several technical limitations arising from experimentation with high efficiency and low cost.

Based on these incentives, the Chapter II is thus dedicated to developing an original FE model for modeling the cutting physics of hybrid CFRP/Ti stacks. To complete the establishing work of the numerical models, the physical behavior and basic configuration of the CFRP/Ti composite are firstly investigated. By considering the actual machining characteristics, several phenomenological assumptions are adopted to rationalize the setup of the proposed orthogonal cutting configuration (OCC) of hybrid CFRP/Ti stacks. Afterward, the geometrical features, physical details of tool-work interactions and boundary conditions (BC) of the developed FE models are presented correspondingly. Furthermore, the implemented constitutive laws and damage criteria for the construction of the CFRP/Ti cutting behavior are illustrated subsequently with respect to each stacked phase. Finally, prior to the post applications, the hybrid CFRP/Ti cutting model is also validated rigorously with the experimental results extracted from the open literature to ensure its sufficient computational credibility.

2.2 Physical behavior and basic configuration of hybrid CFRP/Ti stacks

As elaborated in Chapter I, the hybrid composite stack globally exhibits anisotropic machinability and heterogeneous behavior. The most-used hybrid composite stack is configured by laminated CFRP composite and Ti6Al4V alloy. The presence of the laminated composite is usually a key factor that results in the significantly anisotropic machinability of the sandwich related to its composite fiber orientation (θ). Fig.2.1 shows a typical configuration of hybrid CFRP/Ti stack and its structural application in one aircraft component.

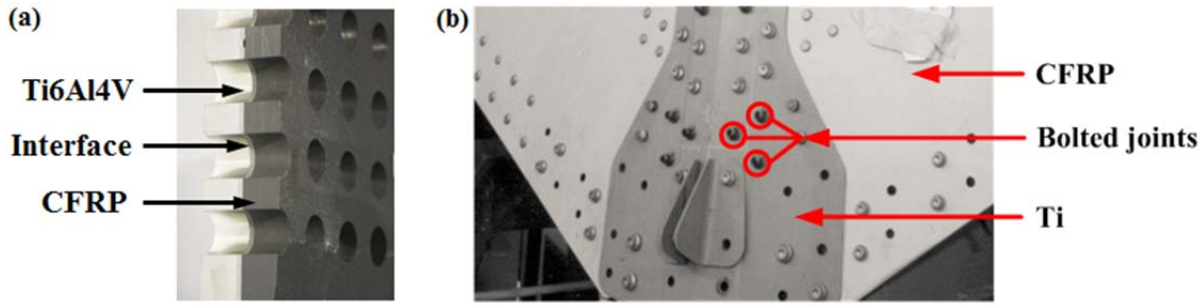

Figure 2.1. (a) Typical hybrid CFRP/Ti configuration and (b) its structural application in an aircraft component (Source: Boeing homepage: http://www.boeing.com/commercial/aeromagazine/articles).

Regarding the manufacturing process of hybrid CFRP/Ti stacks, at present, the most-used production is drilling, which involves the cutting action from one phase to another phase during the entire chip removal process. Since modeling of drilling is a complicated task due to the 3D dynamic process with multiple interacting material domains, it can be abstracted as a composition of several orthogonal cutting operations with respect to several phenomenological assumptions [14]. As shown in Fig.2.2, the drilling action can be simplified as orthogonal cutting configuration (OCC) when the following assumptions: (*i*) the simplification of the complex drill tool geometry, (*ii*) the ignorance of the rotational spindle speed, (*iii*) the ignorance of the chip evacuation's effects on the machined work surface, *etc*., are considered. Despite the simplification of some details of the multi-tool-work geometrical features involved in the real production, the OCC still takes into account the elementary features of the real cutting and the most essential variables for numerical simulation. Moreover, it also represents the most convenient way to reveal the fundamental cutting mechanisms dominating the real CFRP/Ti machining by taking into account the specification of different cutting-sequence strategies ($^{\text{CFRP}\rightarrow\text{Ti}}_{\text{Ti}\rightarrow\text{CFRP}}$).

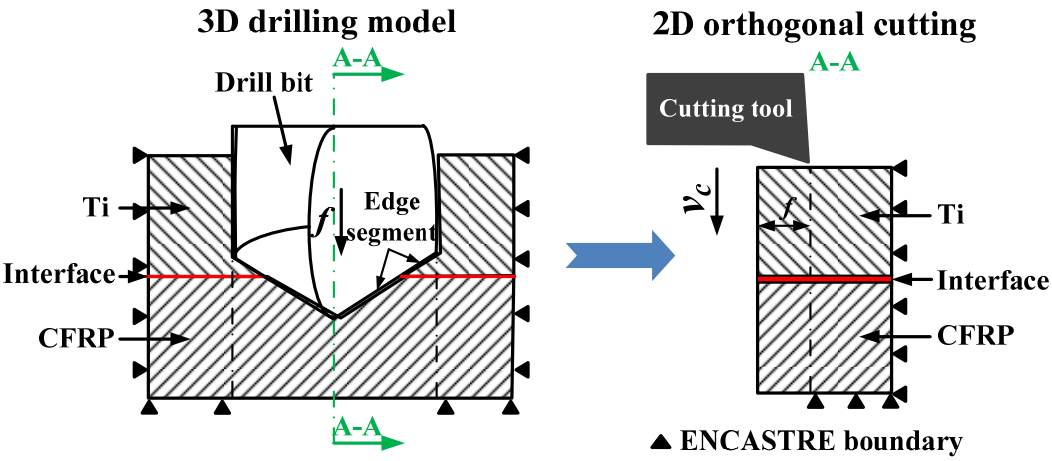

Figure 2.2. 3D drilling action and its simplified 2D OCC for hybrid CFRP/Ti stack machining.

2.2.1 Ti alloy phase

2.2.1.1 Microstructure and composition of Ti6Al4V alloy

Ti6Al4V alloy is a most-used alpha-beta (α+β) titanium alloy that has been extensively employed in aerospace and biomedical applications due to its high strength-to-weight ratio and outstanding corrosion resistance. The basic chemical composition of the alpha-beta alloy (Ti6Al4V)

is listed in Table 2.1. The Ti6Al4V alloy commonly has a duplex microstructure, with roughly 60 % of primary α nodules α_p phase and 40 % of lamellar colonies of second α and β phases, $\alpha_s + \beta$ as depicted in Fig.2.3 [162]. According to Castany et al. [162], the nodules and lamellar colonies usually have the same size. Lamellar colonies consist of secondary α plates α_s with an average thickness of about 500 nm separated by thin β plates (see in Fig. 2.3). The α plates between two α_s plates are sometimes discontinuous and have a few tens of nanometers thickness as shown at the points A and B of Fig. 2.3 (b). Small β phases (about 100 nm size) are sometimes presented at the grain boundaries between the nodules and the lamellar colonies.

Table 2.1
Chemical composition of Ti6Al4V alloy.

	C	Fe	N	O	Al	V	Ti
Content (*wt.*%)	< 0.08	< 0.25	< 0.05	0.2	5.5 - 6.76	3.5 - 4.5	**Balance**

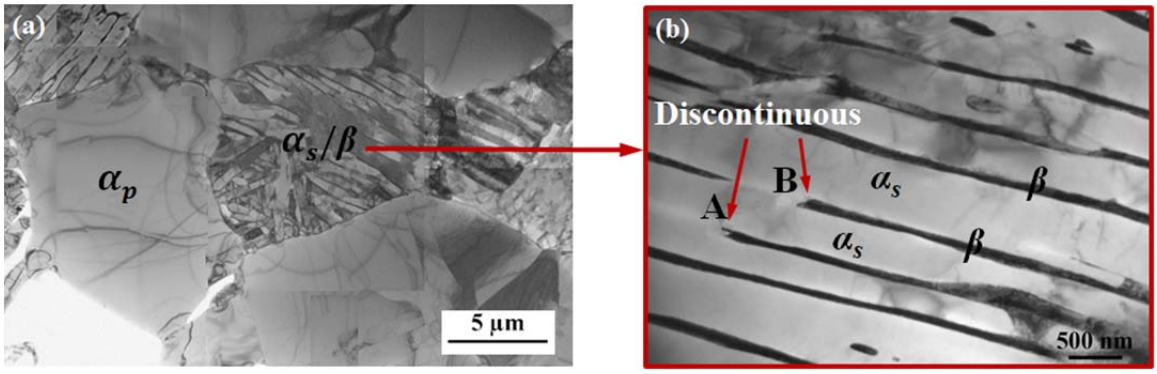

Figure 2.3. Microstructure of Ti6Al4V alloy with primary α_p phase and lamellar colonies $\alpha_s + \beta$ [162].

2.2.1.2 Machining behavior of Ti6Al4V alloys

Similar to most metallic materials, the Ti6Al4V alloy totally exhibits isotropic and homogeneous behavior. However, the machinability of this alloy is extremely poor due to its inherent properties like low thermal conductivity and high chemical reactivity to most-used tool materials. In machining, the chip separation process of Ti6Al4V alloys is primarily governed by the elastic-plastic deformation mode. High flow strain/stress rate and cutting temperature will be generated and intensified inside the shear zones of the uncut chip layer, resulting in the crack initiation, subsequent propagation and final chip separation. The resected chip morphologies of Ti6Al4V alloy are always characterized by “continuous” or “serrated” shapes, which can be transformed from one type to another, greatly dependent on the utilized cutting parameters, tool material/geometry and cutting environment. Since the chip removal process involves a series of interrelated thermo-mechanical influences, to model such complicated physical phenomena, a material constitutive model that can accurately capture the constitutive behavior of the Ti alloy under the high strain/strain rate/temperature conditions is critically demanded. In such case, the commonly-used Johnson-Cook (JC) constitutive model that considers carefully the mentioned thermo-mechanical influences arising from material plastic deformation in cutting was adopted as a feasible solution to the Ti phase modeling in the current research work.

2.2.2 CFRP laminate phase

2.2.2.1 Mechanical property and behavior of CFRP laminate

CFRP laminates have been widely employed in various industrial sectors since 1950s due to their superior mechanical properties and flexible structural functions. The CFRP composite is usually fabricated by high strength carbon fibers embedded in a polymer matrix. The fibers, which have very small diameters and are generally considered continuous, provide the key strength and stiffness of the composite substrate, while the matrix, which has comparatively poor mechanical properties, separates and disperses the fibers. The primary function of the matrix aims to bind the fibers together and transfer loads to the fibers through shear stresses that are developed at the fiber/matrix interface. Concerning the layup of the CFRP laminates, typically three types of setups exist, *i.e.*, unidirectional prepreg ply (UD-ply), woven ply and multi-orientation ply as discussed previously in subsection 1.2.1 of Chapter I. Fig. 2.4 shows the scheme of the UD-ply and multi-orientation configurations of CFRP laminates where (1, 2, 3) represents the material coordinate system of the composite material [163]. Owing to the disparate natures of the fiber and matrix phases, the key properties of CFRP laminates depend significantly on many factors (fiber/matrix type, fiber volume fraction, *etc.*), especially the fiber orientation (θ). As such, the composite exhibits anisotropy and heterogeneity related to the used fiber orientation (θ).

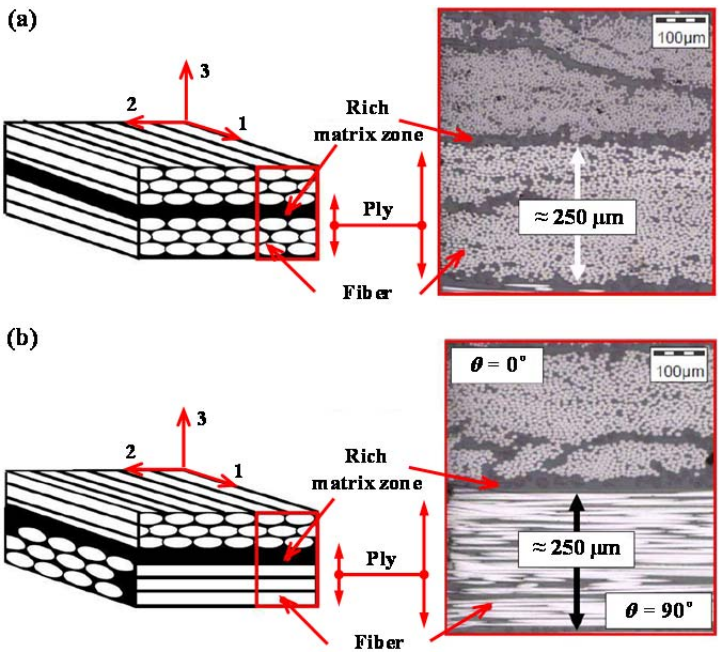

Figure 2.4. Scheme of (a) unidirectional (UD) CFRP laminate and (b) multi-orientation CFRP laminate [163].

Specifically, for the unidirectional (UD) CFRP laminate, the linear elasticity can be easily defined by giving the properties associated with the three material's principal directions: the moduli of elasticity E_1, E_2, E_3; the shear moduli G_{12}, G_{13}, G_{23}; and the Poisson's ratios υ_{12}, υ_{13}, υ_{23}. Note that the subscripts (1, 2, 3) here indicate the fiber direction, transverse direction and through-thickness direction, respectively. Moreover, under the orthogonal configuration, *i.e.*, the coordinate system (1, 2, 3) is consistent with the fiber direction, transverse direction and through-thickness direction,

respectively, the mechanical behavior of the CFRP laminate can be defined as the following strain-stress relationship [164].

$$\{\sigma\} = [G]\{\varepsilon\} \tag{2.1a}$$

$$\begin{Bmatrix} \sigma_{11} \\ \sigma_{22} \\ \sigma_{33} \\ \sigma_{12} \\ \sigma_{13} \\ \sigma_{23} \end{Bmatrix} = \begin{bmatrix} G_{1111} & G_{1122} & G_{1133} & 0 & 0 & 0 \\ G_{1122} & G_{2222} & G_{2233} & 0 & 0 & 0 \\ G_{1133} & G_{2233} & G_{3333} & 0 & 0 & 0 \\ 0 & 0 & 0 & G_{1212} & 0 & 0 \\ 0 & 0 & 0 & 0 & G_{1313} & 0 \\ 0 & 0 & 0 & 0 & 0 & G_{2323} \end{bmatrix} \begin{Bmatrix} \varepsilon_{11} \\ \varepsilon_{22} \\ \varepsilon_{33} \\ \varepsilon_{12} \\ \varepsilon_{13} \\ \varepsilon_{23} \end{Bmatrix} \tag{2.1b}$$

where $\{\sigma\}$ is the stress vector; $[G]$ is the stiffness matrix; $\{\varepsilon\}$ is the strain vector; E_1, E_2, E_3 are moduli of elasticity; G_{12}, G_{13}, G_{23} are shear moduli. For the orthogonal configuration, the G_{ijkl} components of Eq. (2.1b) can be given as follows, where v is Poisson's ratio.

$$\begin{cases} G_{kkkk(k=1,2,3)} = E_k \left(1 - v_{ij} v_{ji}\right)_{(i \neq j \neq k)} \psi \\ G_{kkll(k=1,2;\, l=2,3;\, k<l)} = E_k \left(v_{lk} + v_{ik} v_{lk}\right)_{(i \neq j \neq k)} \psi \\ G_{klkl(k=1,2;\, l=2,3;\, k<l)} = G_{kl} \end{cases} \tag{2.2}$$

where $\psi = 1/\left(1 - v_{12}v_{21} - v_{23}v_{32} - v_{31}v_{13} - 2v_{21}v_{32}v_{13}\right)$ is a constant parameter.

Furthermore, considering a 2D plane-stress simulation condition where $\sigma_{33} = \sigma_{13} = \sigma_{23} = 0$, then it can be inferred that $\varepsilon_{13} = \varepsilon_{23} = 0$ and $\varepsilon_{33} = [(\upsilon_{31} + \upsilon_{21}\upsilon_{32})\, E_{11}\varepsilon_{11} + (\upsilon_{32}+\upsilon_{12}\upsilon_{31})\, E_{22}\varepsilon_{22}] / [(\upsilon_{12}\upsilon_{21} - 1)\, E_{33}]$. Besides, for the orthogonal configuration of the fiber/matrix system, the following equivalent relations can also be obtained: $E_{33} = E_{22}$, and $(\upsilon_{13} / E_{11}) = (\upsilon_{23} / E_{22}) = (\upsilon_{31} / E_{22}) = (\upsilon_{32} / E_{22})$. Then the stiffness matrix can be simplified as a 3 × 3 order matrix and the strain-stress behavior of the CFRP laminate can be expressed as follows.

$$\begin{Bmatrix} \sigma_{11} \\ \sigma_{22} \\ \sigma_{12} \end{Bmatrix} = \begin{bmatrix} \dfrac{E_{11}}{1 - \dfrac{E_{22}}{E_{11}} v_{12}^2} & \dfrac{v_{12}E_{22}}{1 - \dfrac{E_{22}}{E_{11}} v_{12}^2} & 0 \\ \dfrac{v_{12}E_{22}}{1 - \dfrac{E_{22}}{E_{11}} v_{12}^2} & \dfrac{E_{22}}{1 - \dfrac{E_{22}}{E_{11}} v_{12}^2} & 0 \\ 0 & 0 & G_{12} \end{bmatrix} \begin{Bmatrix} \varepsilon_{11} \\ \varepsilon_{22} \\ \varepsilon_{12} \end{Bmatrix} \tag{2.3}$$

In addition, for an arbitrary global coordinate system (X, Y, Z), *i.e.*, the fiber direction is not consistent with the X-axis direction and approximately there exists an intersection angle (θ) between them, then a matrix transformation of the strain-stress relation under orthogonal configuration should be required as summarized below.

$$\begin{Bmatrix} \sigma_{XX} \\ \sigma_{YY} \\ \sigma_{XY} \end{Bmatrix} = [T_1] \begin{Bmatrix} \sigma_{11} \\ \sigma_{22} \\ \sigma_{12} \end{Bmatrix} \tag{2.4}$$

$$\begin{Bmatrix} \varepsilon_{XX} \\ \varepsilon_{YY} \\ \varepsilon_{XY} \end{Bmatrix} = [T_2] \begin{Bmatrix} \varepsilon_{11} \\ \varepsilon_{22} \\ \varepsilon_{12} \end{Bmatrix} \tag{2.5}$$

where (σ_{XX}, σ_{YY}, σ_{ZZ}) and (ε_{XX}, ε_{YY}, ε_{ZZ}) indicate the stress components and strain components in the (X, Y, Z) coordinate system; $[T_1]$ and $[T_2]$ are the matrix transformations and can be defined as follows. Note that θ is the intersection angle between the fiber orientation and the X-axis direction, which can be considered as the fiber orientation.

$$[T_1] = \begin{bmatrix} \cos^2\theta & \sin^2\theta & -2\sin\theta\cos\theta \\ \sin^2\theta & \cos^2\theta & 2\sin\theta\cos\theta \\ \sin\theta\cos\theta & -\sin\theta\cos\theta & \cos^2\theta - \sin^2\theta \end{bmatrix} \tag{2.6}$$

$$[T_2] = \begin{bmatrix} \cos^2\theta & \sin^2\theta & -\sin\theta\cos\theta \\ \sin^2\theta & \cos^2\theta & \sin\theta\cos\theta \\ 2\sin\theta\cos\theta & -2\sin\theta\cos\theta & \cos^2\theta - \sin^2\theta \end{bmatrix} \tag{2.7}$$

2.2.2.2 Machining behavior of CFRP laminates

In CFRP laminate machining, the chip separation process commonly involves a series of successive fracture aided by diverse nature and uneven load sharing between the matrix and fibers. Owing to the distinct properties of the reinforcing fiber and polymer matrix, basically four types of failure modes govern the material breakage operation, *i.e.*, fiber-tensile failure, fiber-compression failure, matrix-tensile failure and matrix-compression failure. The CFRP chip is usually resected in the form of “discontinuous” or “dust” morphology due to the predominant brittle-fracture material removal mode.

For cutting modeling of CFRP laminates, three methodologies have been reported in the open literature, *i.e.*, the micro-mechanical method, macro-mechanical method and micro-macro mechanical method. The key differences among the mentioned methods can be reflected in the material structure level of the fiber/matrix system. For micro-mechanical model, the numerical scale is set around 1 - 20 μm which takes into account the microstructural details of the fiber phase, fiber/matrix interface and matrix phase. The macro-mechanical method, however, ignores the microstructural details of the fiber/matrix composition and assumes the laminate as an equivalent homogeneous material (EHM) by considering also its equivalent anisotropy related to the fiber orientation (θ). The micro-macro mechanical method proposed by Mkaddem et al. [134] aims to obtain the combined benefits of the two scale methods by considering both the microstructural configuration and macro effects of the composite material.

In current numerical modeling, the micro-mechanical and micro-macro mechanical methods are inappropriate for present cases since the key concern of current research focus on the entire behavior of stacked composites with large material scale involved. As such, the macro-mechanical method was adopted for the current modeling of the CFRP-phase machining. In addition, the damage criteria taking into account both the brittle fracture mechanism and the rupture of the respective fiber and matrix phases are also significantly required for CFRP cutting modeling, which

will be illustrated in subsection 2.4.2.

2.3 Geometrical features and boundary conditions of the hybrid composite model

The hybrid composite stack made of CFRP/Ti6Al4V was adopted as the studied work material in current numerical modeling. Such hybrid composite stack configuration is a most-used setup in real production of aerospace industry and thus exhibits high research value. In current numerical modeling, the commercial FEA software Abaqus^{TM} (Version 6.11, Dassault Simulia, Paris, France), a Lagrangian explicit code, was employed to simulate the orthogonal cutting process of hybrid CFRP/Ti stacks. The key objectives are to numerically investigate (*i*) the key mechanisms and physical phenomena controlling interface cutting and interface damage formation, (*ii*) the influences of different cutting-sequence strategies ($^{\text{CFRP} \rightarrow \text{Ti}}_{\text{Ti} \rightarrow \text{CFRP}}$) on hybrid CFRP/Ti machining, and (*iii*) the parametric effects and frictional responses dominating the bi-material cutting. To this aim, two setups of numerical models differing in tool geometries were established following the below common characteristics.

- Each numerical model incorporates four basic physical constituents, *i.e.*, tool part, Ti part, interface and CFRP part.
- Each model has the identical material constitutive models, physical behavior and boundary conditions (BC).

2.3.1 Adopted assumptions for numerical simulations

For orthogonal cutting modeling of hybrid CFRP/Ti stacks, the following assumptions are adopted as summarized below.

- ⇨ The cutting tool was considered as a rigid body without any deformation during the cutting process.
- ⇨ The mechanical properties of the Ti alloy were assumed to be temperature-dependent.
- ⇨ Since the temperature of the CFRP cutting has a minor influence on the chip removal process, the mechanical properties of the CFRP laminate were considered to be temperature-independent, and constant values were utilized. Besides, the failure model of the CFRP phase was assumed to be independent upon temperature.
- ⇨ Finally, for frictional response studies, the frictional coefficients of tool-Ti interaction and tool-CFRP interaction were assumed to be the same in order for an easy FE analysis.

2.3.2 FE model for interface cutting and interface damage formation investigation

To investigate the fundamental mechanisms governing the interface cutting and subsequent damage formation, the FE model consisting of four basic phases, *i.e.*, the tool part, Ti part, interface part and CFRP part was developed into the Abaqus/Explicit code (Version 6.11). The basic

geometries of the tool-workpiece couple and boundary conditions are illustrated schematically in Fig.2.5. The established OC model has a geometrical dimension of 2 mm ×1 mm ($L \times H$) for the hybrid CFRP/Ti stack workpiece. A sufficient cutting length of approximately 1 mm was defined for both CFRP phase and Ti phase in order to achieve the steady chip separation process during the hybrid CFRP/Ti stack machining. The fiber orientation (θ) of the CFRP phase was defined based on the material coordinate system (1, 2) where 1 signifies the fiber direction, 2 indicates the transverse direction, as shown schematically in Fig.2.5 [4, 165].

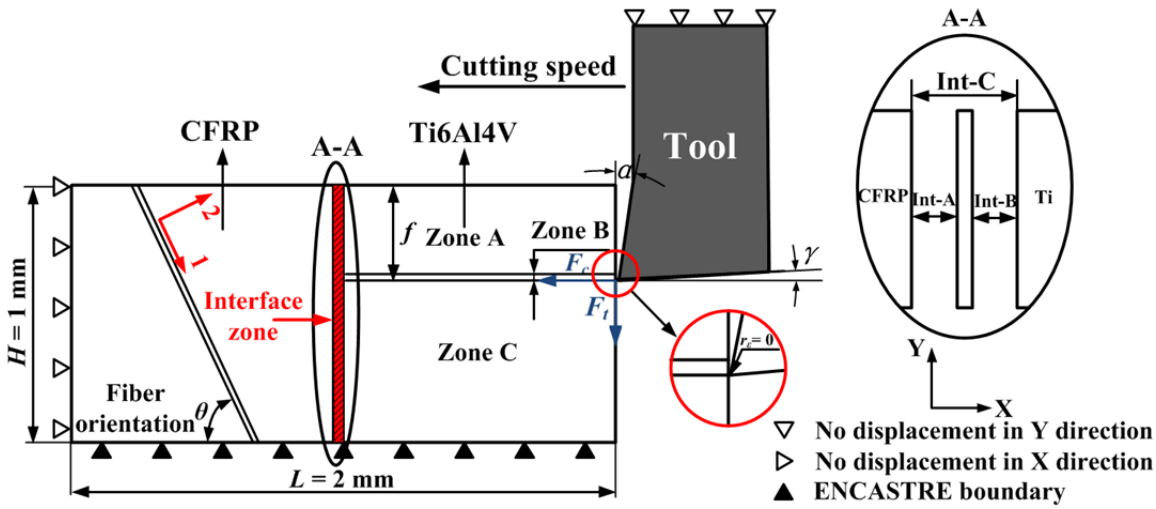

Figure 2.5. Schematic illustration of the established OC model (α = 12° and γ = 7°): (1, 2) represents the material coordinate system where 1 → fiber direction, 2 → transverse direction, F_c indicates the cutting force and F_t signifies the thrust force [4, 165].

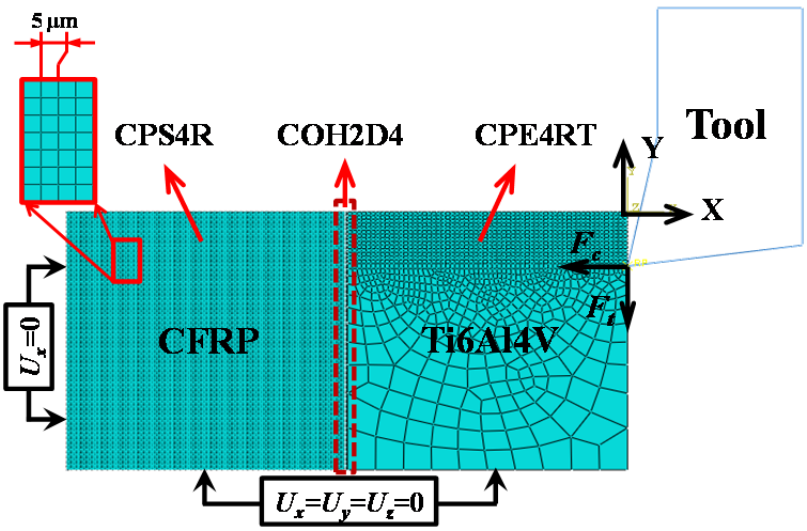

Figure 2.6. Mesh generation of the proposed hybrid composite model for hybrid CFRP/Ti stack machining (U_x = 0 denotes the constraint on the X direction, U_x = U_y = U_z = 0 signifies the constraint on all directions, F_c indicates the cutting force and F_t signifies the thrust force).

The cutting tool was modeled as a rigid body and was imposed by a cutting velocity on its reference node toward the horizontal direction (*i.e.*, negative X-axis) to finalize the complete cutting simulation. The tool edge primarily produces two force components, *i.e.*, cutting force (F_c) and thrust force (F_t) controlling the chip removal process as shown in Fig.2.5. Moreover, the tool was configured by defined geometries of rake angle (α) of 12° and clearance angle (γ) of 7° as depicted in Fig.2.5. It should be noted that a positive rake angle was used in the present model for interface

cutting investigation. This setup aims to minimize the severe element distortion occurring during the CFRP/Ti interface cutting and thus to ensure a better numerical inspection and FE analysis. The center of the tool tip was placed exactly at the feed-rate distance from the upper surface. Fixed displacements were applied on both bottom and left edges of the stack model. Additionally, the bottom edge of the OC model was restrained in all directions (ENCASTRE) while the left edge was constrained to move along the horizontal direction (X direction), as shown in Fig.2.5.

The mesh generation of the established hybrid composite stack model is depicted in Fig.2.6. For Ti phase, it was modeled as a fully isotropic and homogeneous material. A four-node plane-strain thermally coupled quadrilateral element type CPE4RT, which has better convergence properties was utilized for a coupled temperature-displacement analysis and enhanced hourglass control was selected for the whole set of the Ti elements. Besides, the entire Ti phase was separated into three physical zones in order to achieve better contact management: (*i*) Zones A → denotes the separated chip layer; (*ii*) Zone B → signifies the predefined separation path; and (*iii*) Zone C → represents the machined Ti surface, where mesh generation exhibited different characteristics. Both Zones A and B were defined by very fine mesh density, whereas Zone C was constructed by coarse mesh element density far away from the vicinity of the tool-work contact region. The surface-to-surface contact algorithm was used to model the interaction between the cutting tool, Zone A and Zone B. The kinematic contact algorithm was assigned to the contact pairs in order to avoid element penetration. Friction in the orthogonal cutting commonly occurs at the contact surfaces of tool and workpiece, rake face and chip surface. The frictional shearing stress is the average of shearing stress at tool-chip interface. In the present work, the Coulomb's friction law was utilized to describe the contact behavior.

Concerning the CFRP phase, the composite in reality consists of two distinct phases (reinforcing fiber and polymer matrix) and globally exhibits anisotropic properties. However, for simulations in a macro-mechanical model, the CFRP laminate is commonly assumed as an equivalent homogeneous material (EHM) by most numerical study cases [55, 134, 136, 137, 141, 166]. In the present model, the EHM assumption was adopted. The CFRP phase was modeled as an EHM by using four-node plane-stress linearly interpolated elements (CPS4R) with reduced integration and automatic hourglass control. It should be noted that a plane strain analysis, which is used typically for metal cutting, was not appropriate for machining CFRP laminates due to the extent of out of plane material displacement observed while cutting experiments [63, 167, 168]**.** To achieve the balance between the simulation accuracy and time efficiency, the mesh density of the composite phase was set around 5 µm by referring to some relevant research work [141, 166]. The interaction between CFRP phase and tool was ruled through the algorithm surface-node-surface contact available in the Abaqus/Explicit code (Version 6.11).

To link the Ti phase and CFRP phase together, an interface layer was introduced in the FE model and was simulated as a quick transition zone by using cohesive elements. It should be stressed that the use of interface layer here serves as a technical control for the "Ti-to-CFRP" contact management during simulation. A triangular traction-separation cohesive formulation with linear softening was used to represent its mechanical responses. The assembly of the interface layer with both Ti phase and CFRP phase was carried out by setting a constraint type joining (tie constraint). Furthermore, two contact pairs (Int-A and Int-B) with the specification of penalty contact algorithm and rough friction formulation were established among the interface zone, Ti phase and CFRP phase

as shown in Fig.2.5, which made the interface zone as a slave surface. Moreover, an additional contact pair referring to the Int-C (as shown in Fig.2.5) was also assigned between the Ti phase and CFRP phase to avoid them to penetrate into each other when the cohesive elements were eroded.

2.3.3 FE model for cutting sequence and frictional response studies

In hybrid CFRP/Ti stack machining, typically two different cutting-sequence strategies, *i.e.*, (*i*) cutting from Ti → CFRP and (*ii*) cutting from CFRP → Ti, exist from the aspect of tool-entry and tool-exit throughout the entire chip removal process. To inspect the cutting sequence's influences on the hybrid composite stack machining, two kinds of OC models with respect to the two mentioned different cutting sequences ($^{\text{CFRP}\,\rightarrow\,\text{Ti}}_{\text{Ti}\,\rightarrow\,\text{CFRP}}$) were established as depicted in Fig.2.7 [169, 170]. As elaborated before, the present OC models also consist of four fundamental constituents and have the same boundary conditions. Moreover, the characteristics of the mesh generation and the definitions of tool-work interactions in current models were also made the same as like the previous model in subsection 2.3.1. The key difference between current and previous FE models can be reflected in the use of 0° rake angle for the tool part. This is because the use of 0° tool rake angle aims to meet with the subsequent experimental validations of the orthogonal cutting process.

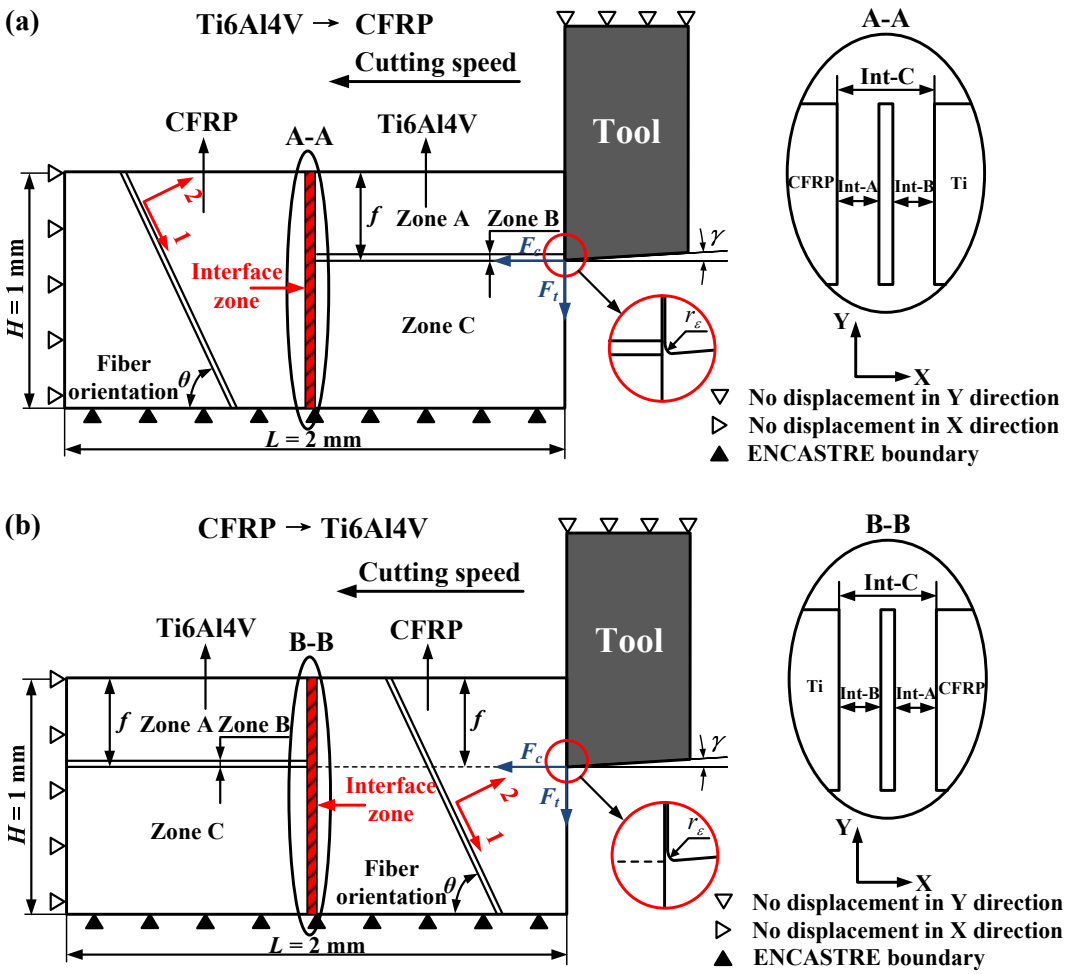

Figure 2.7. Schematic illustration of the established OC models for hybrid CFRP/Ti stack machining ($\alpha = 0°$, $\gamma = 7°$ and $r_\varepsilon = 2$ µm): (a) Ti → CFRP cutting sequence and (b) CFRP → Ti cutting sequence ((1, 2) represents the material coordinate system where 1 → fiber direction, 2 → transverse direction, F_c indicates the cutting force and F_t signifies the thrust force) [169, 170].

With respect to the frictional behavior of the multi-tool-work interaction, it plays a pivotal role in affecting the various physical phenomena promoted in the hybrid composite stack machining, and thus determines the surface integrity of the machined part. However, the friction characteristics dominating the tool-chip/work interface are difficult to determine since it is influenced by many factors such as cutting speed, contact pressure, and temperature. Extensive studies have been performed on the mechanics of interaction along the tool-chip/work interface, and several models have revealed that there exist two distinct regions of sticking and sliding governing the tool-chip/work interface. In the current simulation, the most-used Zorev's model [171] that considers the mentioned two distinct friction regions was adopted. This model, also termed as an extended Coulomb friction model, was used here to simulate the multi-tool-work interaction and was given as follows.

$$\begin{cases} Sticking\ region: \tau = \overline{\tau}_{\max}\ ;\ when\ \tau \geq \overline{\tau}_{\max} \\ Sliding\ region: \tau_{crit} = \mu\sigma;\ when\ \tau < \overline{\tau}_{\max} \end{cases} \tag{2.8}$$

where τ_{crit} is defined as the critical shear stress, at which sliding of the surfaces starts as a fraction of the contact pressure, σ, between the surfaces ($\tau_{crit} = \mu\sigma$). The shear stress limit is typically introduced in the cases when the contact pressure stress may become very large causing the Coulomb theory to provide a critical shear stress at the interface that exceeds the yield stress in the material beneath the contact surface. An upper bound estimate for $\overline{\tau}_{\max}$ is $\sigma_y / \sqrt{3}$, in which σ_y is the von Mises yield stress of the material adjacent to the surface.

Concerning the frictional response studies, the friction coefficient of the multi-tool-work interaction (μ) was considered as a key input variable for numerical computation. Different μ values were implemented into the Abaqus/Explicit code (Version 6.11) in order to inspect the key frictional responses dominating hybrid CFRP/Ti stack machining.

2.3.4 Equations of motion: Abaqus/Explicit scheme

To study the dynamic physical phenomena promoted in the hybrid CFRP/Ti stack machining, the explicit scheme integrated in the commercial Abaqus™ software that has better computational convergence was adopted throughout the entire FE analysis. The Abaqus/Explicit procedure was formulated based on the implementation of an explicit integration rule together with the use of diagonal element mass matrices. The equation of motion for the body was integrated using an explicit central difference integration rule as illustrated as follows:

$$\left.\begin{aligned} u^{(i+1)} &= u^{(i)} + \Delta t^{(i+1)} \dot{u}^{(i+1)} \\ \dot{u}^{(i+1/2)} &= \dot{u}^{(i-1/2)} + \frac{1}{2}\left(\Delta t^{(i+1)} + \Delta t^{(i)}\right) \ddot{\boldsymbol{u}}^{(i)} \end{aligned}\right\} \tag{2.9}$$

where u is the displacement vector; $\dot{u}$ represents the velocity; $\ddot{u}$ denotes the acceleration; and the superscripts including i, i-1/2, i+1/2 refer to the increment number and middle-increment number. The central difference integration operator is explicit in that the kinematic state may be advanced using known values of $\dot{u}^{(i-1/2)}$ and $\dot{u}^{(i)}$ from the previous increment. The explicit integration rule provides high computation efficiency due to the use of diagonal element mass matrices because the accelerations at the beginning of the increment may be computed as follows [172].

$$\ddot{\boldsymbol{u}}^{(i)} = \boldsymbol{M}^{-1} \cdot \left(\boldsymbol{F}^{(i)} - \boldsymbol{I}^{(i)} \right) \tag{2.10}$$

where $\boldsymbol{M}$ represents the "Lumped" mass matrix; $\boldsymbol{F}$ denotes the applied load vector; $\boldsymbol{I}$ refers to the internal force vector. The explicit procedure integrates through time by using many small time increments for assuring convergence.

To attain the calculation convergence, the explicit integration operator is assumed to be conditionally stable, so the time increment (Δt) must satisfy:

$$\Delta t \leq \frac{2}{\omega_{\max}} \tag{2.11}$$

where $\omega_{\max}$ is the maximum element eigenvalue. A conservative estimation of the stable time increment is calculated by the value for all the elements. The above stability limit can be written as follows:

$$\Delta t = \min\left(\frac{L_e}{c_d} \right) \tag{2.12}$$

in which, L_e is the mesh characteristic element dimension, and c_d is the current effective, dilatational wave speed in the considered material.

2.4 Material constitutive law and progressive damage criterion

The simulated hybrid CFRP/Ti stack was composed of one Ti6Al4V alloy for the metallic phase, one unidirectional (UD) carbon/epoxy T300/914 laminate for the CFRP phase accompanied with a third interface layer as discussed in subsection 2.3. The basic mechanical/physical properties of the hybrid CFRP/Ti stack are summarized in Table 2.2. Detailed material behaviors and implemented damage criteria for each physical constituent are illustrated in the following subsections.

Table 2.2
Material properties of the simulated hybrid CFRP/Ti stack [131, 159, 173-178].

Workpiece material					
Ti6Al4V alloy [159, 173]		**T300/914 CFRP** [131, 174, 175]		**Interface** [176-178]	
Density (ρ)	4430 kg/m^3	Longitudinal modulus (E_1)	136.6 GPa	υ	0.33
Young's modulus (E)	$E = 0.7412 \cdot T + 113.375$ [GPa]	Transverse modulus (E_2)	9.6 GPa	K_{nn}	2.0 GPa
Poisson's ratio (υ)	0.342	In-plane shear modulus (G_{12})	5.2 GPa	$K_{ss} = K_{tt}$	1.5 GPa
Thermal expansion coefficient (α_T)	$\alpha_T = 2\times10^{-9} \times T + 9\times10^{-6}$ [°C^{-1}]	Major Poisson's ratio (υ_{12})	0.29	t_n^f	60 MPa
Melting temperature (T_m)	1680 °C	Longitudinal tensile strength (X_T)	1500 MPa	$t_s^f = t_t^f$	80 MPa
Room temperature (T_r)	25 °C	Longitudinal compressive strength (X_C)	900 MPa	G_n^C	0.78 N/mm
Thermal	$\lambda = 7.039\, e^{0.0011 \cdot T}$	Transverse tensile	27 MPa	$G_s^C = G_t^C$	1.36

conductivity (λ)	[W/(m·°C)]	strength (Y_T)			N/mm
Specific heat (c_p)	$c_p = 2.24\, e^{0.0007 \cdot T} \times 10^6 / \rho$ [J/(kg·°C)]	Transverse compressive strength (Y_C)	200 MPa	—	
—		In-plane shear strength (S_{12})	80 MPa		
		Longitudinal shear strength (S_L)	80 Mpa		
		Transverse shear strength (S_T)	60 MPa		

2.4.1 Ti-phase constitutive model

The material behavior of Ti6Al4V phase was assumed to be isotropic and elastic-plastic with thermal softening by using the isotropic plasticity model available in the Abaqus/Explicit code (Version 6.11). The material properties for the Ti phase (Ti6Al4V alloy) can be found in Table 2.2 [159, 173]. The Young's modulus (E), thermal expansion coefficient (α_T), thermal conductivity (λ) and specific heat (c_p) are considered to be temperature-dependent in order to represent accurately the property variation of the titanium phase *versus* thermal influence during the cutting process.

In FE modeling, accurate material flow stress models are highly required to capture the constitutive behavior of work material under high strain/strain rate/temperature conditions encountered in machining. The constitutive model proposed by Johnson-Cook (JC) [142, 143] was applied in this investigation, which offers a satisfactory description of the ductile material behavior by considering large strains, high strain rates and temperature-dependent visco-plasticity encountered in machining. The JC material model also takes into account the effects of strain hardening, strain rate sensitivity and thermal softening behavior as illustrated in Eq. (2.13).

$$\bar{\sigma} = \underbrace{\left(A + B\bar{\varepsilon}^{n}\right)}_{\text{Strain hardening}} \underbrace{\left(1 + C \ln \frac{\dot{\bar{\varepsilon}}}{\dot{\bar{\varepsilon}}_0}\right)}_{\text{Strain rate sensitivity}} \underbrace{\left[1 - \left(\frac{T - T_r}{T_m - T_r}\right)^{m}\right]}_{\text{Thermal softening behavior}} \tag{2.13}$$

where $\bar{\sigma}$ denotes the equivalent flow stress; $\bar{\varepsilon}$ is the equivalent plastic strain; $\dot{\bar{\varepsilon}}$ is the equivalent plastic strain rate; $\dot{\bar{\varepsilon}}_0$ is the reference equivalent plastic strain rate; T is the workpiece temperature; T_m is the material melting temperature; T_r is the room temperature. A, B, C, m and n are material constants, which are usually determined by fitting the strain-stress curves obtained by split-Hopkinson bar. In this simulation, the JC material constants are selected from the literature of Lesuer [179] and Xi et al. [155] as shown in Table 2.3.

Table 2.3
Input parameters for JC constitutive model and JC damage law [155, 179].

JC constitutive model	***A* (MPa)**	***B* (MPa)**	***C***	***n***	***m***
	1098	1092	0.014	0.93	1.1
JC damage law	D_1	D_2	D_3	D_4	D_5
	-0.09	0.25	-0.5	0.014	3.87

In order to simulate the chip separation process, an energy-based ductile failure criterion was applied in the FE computation. The failure damage criteria consist of two-stage laws, *i.e.*, the failure initiation law and failure evolution law, to describe the failure responses of ductile material as shown in Fig.2.8 [172]. The failure formation includes two steps as described as follows.

Step 1: Damage initiation. The JC failure model was used as a damage initiation criterion, which contains five failure parameters that need to be determined (D_1 - D_5) as presented in Eq. (2.14). In JC failure model, damage initiation is assumed to happen when a scalar damage parameter (ω) reaches 1. The ω parameter is defined based on a cumulative law as described in Eq. (2.15).

$$\bar{\varepsilon}_i = \left[D_1 + D_2 \exp\left(D_3 \frac{P}{\bar{\sigma}} \right) \right] \left(1 + D_4 \ln \frac{\dot{\bar{\varepsilon}}}{\dot{\bar{\varepsilon}}_0} \right) \left[1 + D_5 \left(\frac{T - T_r}{T_m - T_r} \right) \right] \tag{2.14}$$

$$\omega = \sum \frac{\Delta \bar{\varepsilon}}{\bar{\varepsilon}_i} \tag{2.15}$$

where $\bar{\varepsilon}_i$ is the equivalent plastic strain at damage initiation; P is the hydrostatic pressure; $P/\bar{\sigma}$ is the stress triaxiality; D_1 - D_5 are JC damage parameters; ω is the scalar damage parameter and $\Delta\bar{\varepsilon}$ is the equivalent plastic strain increment. The parameters summarized in Table 2.3 [155, 179] were adopted for D_1 - D_5 in the cutting simulation.

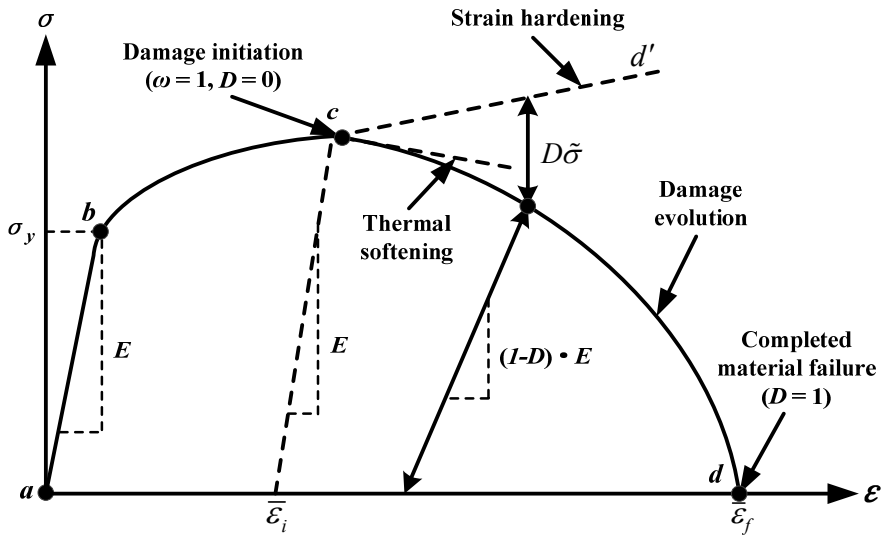

Figure 2.8. Typical uniaxial strain-stress response of ductile material failure process [172].

Step 2: Damage evolution. When the ductile material damage is initiated, the strain-stress relationship no longer accurately represents the real material behavior. On this basis, the Hillerborg's fracture energy proposal [180] was used to reduce mesh dependency by creating a displacement-stress response after damage initiation. Hillerborg defines the energy required to open a unit area of crack (G_f) as a material parameter, and the fracture energy is represented as follows:

$$G_f = \int_{\bar{\varepsilon}_i}^{\bar{\varepsilon}_f} L \sigma_y d\bar{\varepsilon} = \int_0^{\bar{u}_f} \sigma_y d\bar{u} \tag{2.16}$$

where $\bar{\varepsilon}_i$ is the equivalent plastic strain at damage initiation; $\bar{\varepsilon}_f$ is the equivalent plastic strain at failure; L denotes the characteristic length; σ_y signifies the yield stress; $\bar{\varepsilon}$ is the equivalent plastic strain; $\bar{u}_f$ is the equivalent plastic displacement at failure and $\bar{u}$ is the equivalent plastic displacement.

The FE model applied the planar quadrilateral continuum element (CPE4RT), and then characteristic length (L) was defined as a half typical length of a line across a second order element. As the direction in which fracture occurs was not known in advance, so the definition of characteristic length was used.

A linear damage parameter (D_l) was used for joint layer according to the following equation:

$$D_l = \frac{L\bar{\varepsilon}}{\bar{u}_f} = \frac{\bar{u}}{\bar{u}_f} \tag{2.17}$$

where the equivalent plastic displacement at failure ($\bar{u}_f$) was computed as follows:

$$\bar{u}_f = \frac{2G_f}{\sigma_y} \tag{2.18}$$

In contrast, an exponential damage parameter (D_e) was used for chip layer according to the following equation:

$$D_e = 1 - \exp\left(-\int_0^{\bar{u}} \frac{\bar{\sigma}}{G_f} d\bar{u}\right) \tag{2.19}$$

At any given time during the FE calculation, the equivalent flow stress in the material is given by the following equation:

$$\bar{\sigma} = (1 - D)\tilde{\sigma} \tag{2.20}$$

where $\tilde{\sigma}$ denotes the effective (or undamaged) equivalent flow stress computed in the current increment and D represents the damage parameter (D_l or D_e).

In this study, G_f is provided as an input parameter and theoretically is a function of Poisson's ratio (υ), Young's modulus (E) and fracture toughness (K_C) as shown in Eq.(2.21). Considering the different fracture mechanics [181] occurring in the chip-separation process, two different values of fracture energies were utilized as input data in the Abaqus/Explicit code (Version 6.11): $(G_f)_I$ for the joint layer (Zone B) and $(G_f)_{II}$ for the chip layer (Zone A). The $(G_f)_I$ denotes the fracture energy of mode I which is a tensile mode (opening mode normal to the plane of the fracture) whereas $(G_f)_{II}$ signifies the fracture energy of mode II which is a shearing one (sliding mode acting parallel to the plane of the fracture). The relevant values for the facture-energy calculation according to the two modes are summarized in Table 2.4 [182].

$$\left(G_f\right)_{I,II} = \left(\frac{1-\upsilon^2}{E}\right)\left(K_C^2\right)_{I,II} \tag{2.21}$$

Table 2.4
Fracture toughness properties of Ti6Al4V alloy [182].

E	υ	K_{IC}	K_{IIC}
113 GPa	0.342	75 $MPa\sqrt{m}$	74.6 $MPa\sqrt{m}$

2.4.2 CFRP-phase model

For CFRP phase, the simulated material was a unidirectional (UD) carbon/epoxy T300/914

laminate and its mechanical/physical properties are summarized in Table 2.2 [131, 174, 175]. The CFRP laminate was assumed as an EHM by considering also its anisotropic behavior related to the fiber orientation (θ). The definition of the composite fiber orientation (θ) was made based on the introduction of the material coordinate system (1, 2) into the CFRP phase as shown schematically in Figs.2.5 and 2.7, respectively, where the 1-direction indicates the forward fiber direction and 2-direction denotes the transverse direction (perpendicular to the fiber direction).

The cutting behavior of CFRP laminates has been confirmed by many experimental studies [52, 60, 183, 184] to be dominated by brittle-fracture mechanisms of the fiber/matrix system following four fundamental types of failure modes, *i.e.*, fiber-tensile failure, fiber-compression failure, matrix-tensile failure and matrix-compression failure. Table 2.5 then shows the schematization of the four fundamental types of fiber/matrix failure in a 2D configuration. For the relative fiber failure, *i.e.*, fiber-tensile damage and fiber-compression damage, the predominant factor is longitudinal stress (σ_{11}) as depicted in Table 2.5. The damage tip usually takes place in the perpendicular to fiber direction and then suffers a quick propagation through the entire fiber cross section, resulting in the final cracking/crushing damage. With respect to the matrix-tensile and matrix-compression failure, they are primarily caused by the coupled effects of the transverse stress (σ_{22}) and the in-plane shear stress (σ_{12}) according to the theory proposed by Hashin [185]. The relative matrix damage often takes place in terms of severe tearing/crushing of the substrate accompanied by certain extent of interface debonding as illustrated in Table 2.5.

A "discontinuous" shape of chips is always noted with respect to different cutting conditions in the material machining. To replicate the rupture of the fiber/matrix system, the most-used Hashin damage criteria [185, 186] that consider the mentioned four types of failure were thereby adopted in the numerical simulation. The basic expressions of the Hashin damage criteria are illustrated in Table 2.6, where σ_{11} signifies the stress in the fiber direction, σ_{22} denotes the stress in the transverse direction, and σ_{12} represents the in-plane shear stress. In addition, for detailed illustration regarding the Hashin damage criteria, readers are recommended to refer to the work done by Hashin et al. [185, 186].

Table 2.5
Schematic illustration of the fiber/matrix failure modes for the CFRP laminate machining in a 2D configuration.

Damage mode of fiber/matrix failure	Before damage	After damage
Fiber-tensile failure	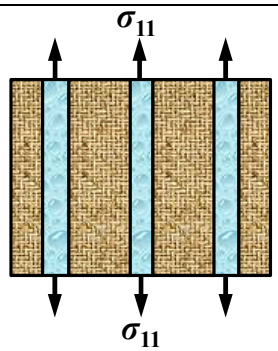	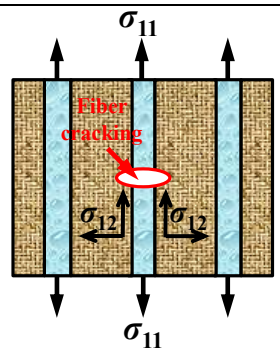

Fiber-compression failure	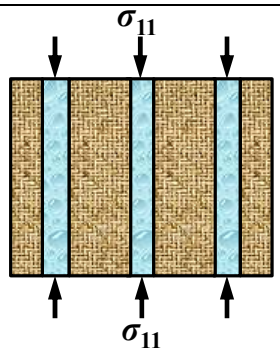	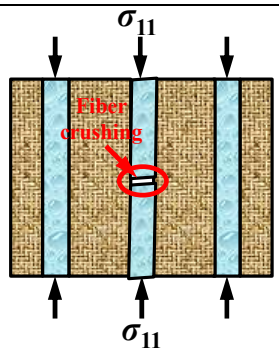
Marix-tensile failure	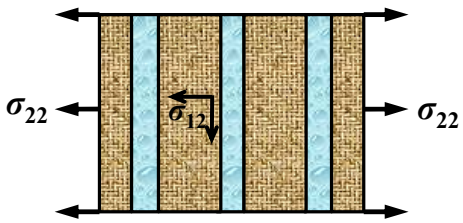	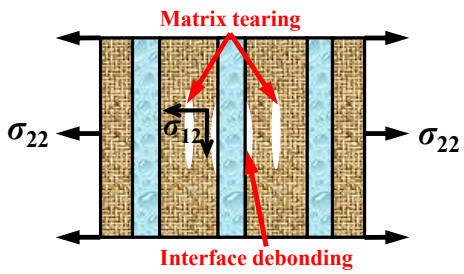
Matrix-compression failure	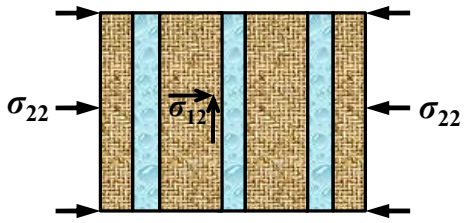	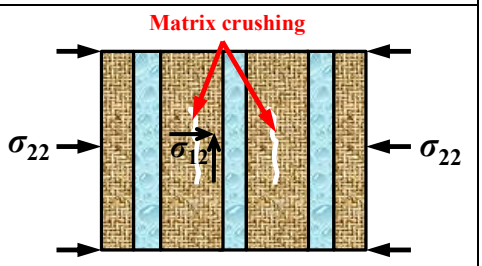

Table 2.6
General formulation of Hashin damage criteria for CFRP machining [186].

Failure mode	Failure criteria	Associated defined variable	Reduced material properties
Fiber-tensile failure ($\sigma_{11} \geq 0$)	$D_{ft}^2 = \left(\frac{\sigma_{11}}{X_T}\right)^2 + \left(\frac{\sigma_{12}}{S_L}\right)^2$	HSNFTCRT	$E_1, E_2, G_{12}, \upsilon_{12} \rightarrow 0$
Fiber-compression failure ($\sigma_{11} < 0$)	$D_{fc}^2 = \left(\frac{\sigma_{11}}{X_C}\right)^2$	HSNFCCRT	$E_1, E_2, G_{12}, \upsilon_{12} \rightarrow 0$
Matrix-tensile failure ($\sigma_{22} \geq 0$)	$D_{mt}^2 = \left(\frac{\sigma_{22}}{Y_T}\right)^2 + \left(\frac{\sigma_{12}}{S_L}\right)^2$	HSNMTCRT	$E_2, G_{12} \rightarrow 0$
Matrix-compression failure ($\sigma_{22} < 0$)	$D_{mc}^2 = \left(\frac{\sigma_{22}}{2S_T}\right)^2 + \left[\left(\frac{Y_C}{2S_T}\right)^2 - 1\right]\frac{\sigma_{22}}{Y_C} + \left(\frac{\sigma_{12}}{S_L}\right)^2$	HSNMCCRT	$E_2, G_{12} \rightarrow 0$
	Note: σ_{11} indicates the stress in fiber direction, σ_{22} signifies the stress in the transverse direction, and σ_{12} denotes the in-plane shear stress.		

During the CFRP-phase cutting modeling, the element erosion of the composite layer is conducted through the concept of stiffness degradation [141, 166], *i.e.*, when one type of the fiber/matrix failure occurs, the relevant material properties will be degraded automatically according to the satisfied failure mode, as shown in Table 2.6. In the present analysis, the material

property degradation depends on four associated defined variables, as listed below: (*i*) the first variable noted HSNFTCRT represents the fiber-tensile failure mode; (*ii*) the second HSNFCCRT represents the fiber-compression failure mode; (*iii*) the third HSNMTCRT represents the matrix-tensile failure mode; (*iv*) the fourth HSNMCCRT represents the matrix-compression failure mode. When any of the mentioned failure modes reaches the unity, the relevant material properties (E_1, E_2, G_{12} or υ_{12}) will be degraded into zero as shown in the last right column of Table 2.6. For detailed implementation of the stiffness degradation scheme, a column stiffness matrix [Ψ_1, Ψ_2, Ψ_3, Ψ_4] was firstly introduced and could be defined as follows.

$$\Psi_1 = \frac{E_1}{E_1^0}, \Psi_2 = \frac{E_2}{E_2^0}, \Psi_3 = \frac{G_{12}}{G_{12}^0}, \Psi_4 = \frac{\upsilon_{12}}{\upsilon_{12}^0} \tag{2.22}$$

where (E_1^0, E_2^0, G_{12}^0, υ_{12}^0) indicate the initial values of the material stiffness parameters (before degradation), and (E_1, E_2, G_{12}, υ_{12}) signify the actual values of the material stiffness parameters (after degradation).

As such, it can be assumed that before CFRP phase cutting (*i.e.*, the cutting tool doesn't attack the fresh composite material), the material stiffness matrix should have the following initial values: [Ψ_1, Ψ_2, Ψ_3, Ψ_4] = [1, 1, 1, 1]. Besides, with the cutting progression of the CFRP composite, especially when one type of the aforementioned failure modes is initiated, the value of Ψ_i (i = 1, 2, 3 or 4) will be degraded correspondingly depending on which type of the failure criterion is satisfied. In addition, the relation between the introduced material stiffness matrix and the implemented Hashin damage criteria can be summarized as follows.

- All the Ψ_i (i = 1, 2, 3 and 4) parameters will be degraded gradually when either the fiber-tensile failure or the fiber-compression failure takes place, *i.e.*, HSNFTCRT = 1 or HSNFCCRT = 1.
- The parameters Ψ_2 and Ψ_3 will be degraded accordingly while the Ψ_1 and Ψ_4 parameters remain 1 when the matrix-tensile failure or the matrix-compression failure occurs, *i.e.*, HSNMTCRT = 1 or HSNMCCRT = 1.

With respect to the implementation of the progressive damage algorithm, the updated stress-strain relation after the fiber/matrix failure occurrence can be expressed as follows.

$$\dot{\sigma} = [G]\dot{\varepsilon} \tag{2.23}$$

where $$[G] = \frac{1}{1 - \frac{\Psi_2 E_2^0}{\Psi_1 E_1^0}\Psi_4^2\left(\upsilon_{12}^0\right)^2}\begin{bmatrix} \Psi_1 E_1^0 & \Psi_2\Psi_4 E_2^0 \upsilon_{12}^0 & 0 \\ \Psi_2\Psi_4 E_2^0 \upsilon_{12}^0 & \Psi_2 E_2^0 & 0 \\ 0 & 0 & \left[1 - \frac{\Psi_2 E_2^0}{\Psi_1 E_1^0}\Psi_4^2\left(\upsilon_{12}^0\right)^2\right]\Psi_3 G_{12}^0 \end{bmatrix} = f\left(\{\sigma\}\right).$$

To solve the nonlinear differential equation, the explicit scheme of Euler integration (with an iterative incremental loading) was adopted during the FE calculation.

$$\{\sigma\}_n = \{\sigma\}_{n-1} + \Delta\{\sigma\}_n \tag{2.24}$$

where $\Delta\{\sigma\}_n$ = $\{\Delta\sigma_{11}, \Delta\sigma_{22}, \Delta\sigma_{12}\}_n$ represent the corresponding stress increments of the composite material after each increment of the tool movement.

To update the nth increment accompanied with the cutting tool's advancement, the following equation was utilized: $\Delta\{\sigma\}_n = [G]_{n-1}\Delta\{\varepsilon\}_n$. Note that the effective stiffness matrix $[G]_{n-1}$ was evaluated by using the state parameters from the beginning of the increment $\{\Psi_i\}_{n-1} = f(\{\sigma\}_{n-1})$ as discussed above. During the FE computation, the material properties at each integration point were computed for each given load. The failure modes were then evaluated and if any failure criterion reached the unity, the relevant local properties would be automatically reduced to zero according to the implemented stiffness degradation scheme. The degradation of both longitudinal and shear moduli was ruled by the fiber failure modes while the degradation of transverse and shear moduli was governed by the matrix failure modes. The procedure was repeated several times until the occurrence of the complete CFRP chip separation. Moreover, Fig.2.9 also shows the global flow chart for the progressive damage algorithm for CFRP-phase machining.

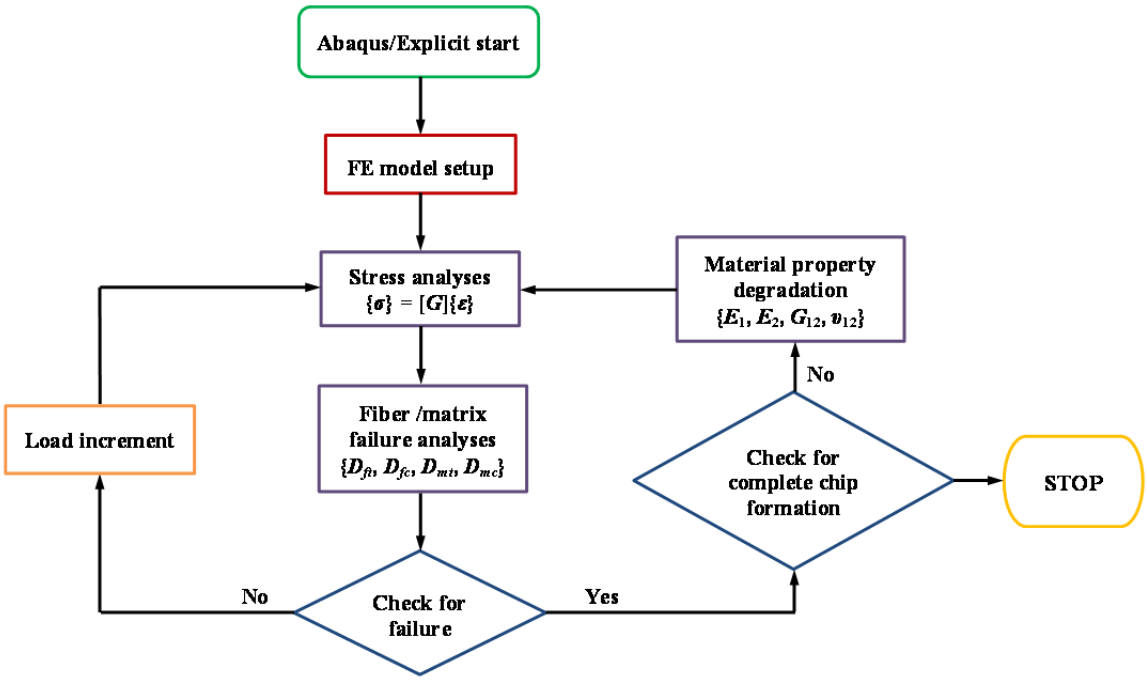

Figure 2.9. Global flow chart for the progressive damage algorithm for CFRP-phase machining.

2.4.3 Interface constitutive model

The interface model used here aims to serve as a technical control for the "Ti-to-CFRP" contact management and to facilitate the characterization of interface damage formation during the cutting simulation. It should be noted that in real CFRP/Ti configurations, some of them don't exist such adhesive layer and each stacked layer is only combined together during machining. The interface layer liking the metallic phase and composite phase was modeled as a cohesive zone by using cohesive interaction allowing interfacial-damage propagation between the two joint phases as a fracture mechanics phenomenon. The cohesive zone commonly takes into account the coupled effects of different modes of linear crack mechanics and hence makes it possible to predict the phenomena of delamination initiation that widely occur at the interface of two joint phases. In the current simulation, a very small thickness of approximately 5 µm was utilized for the interface zone aiming to minimize its influence on some other machining responses such as CFRP/Ti chip separation modes, force generation, *etc*. In the cohesive zone, typically three types of traction

stresses exist, *i.e.*, the normal traction stress (σ_n), the shear traction stresses (σ_s and σ_t) in two directions (s and t directions). The mechanical behavior ($\sigma = f(\delta)$) of the cohesive zone is commonly assumed to be governed by traction-separation linear elastic law and linear softening law, as depicted in Fig.2.10. Note that the enclosed areas by the linear $\{\sigma_n, \sigma_s, \sigma_t\}$ curves and the $\{\delta_n, \delta_s, \delta_t\}$ axes are always defined as the critical released rate energies $\{G_n^C, G_s^C, G_t^C\}$ in the normal and two shear directions, respectively.

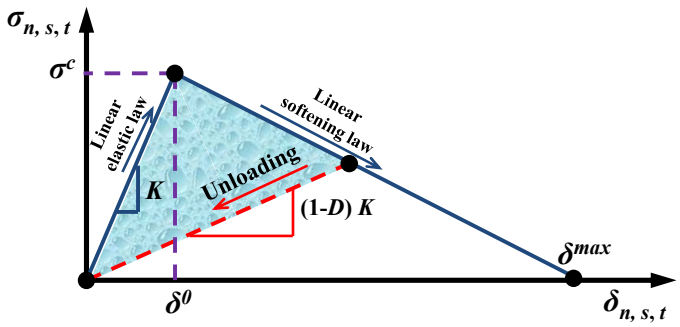

Figure 2.10. Scheme of the mechanical responses of the cohesive zone in function of $\sigma = f(\delta)$ relation.

$$\begin{cases} G_n^C = \int_0^{\delta_n^{\max}} \sigma_n(\delta)\, d\delta_n \\ G_s^C = \int_0^{\delta_s^{\max}} \sigma_s(\delta)\, d\delta_s \\ G_t^C = \int_0^{\delta_t^{\max}} \sigma_t(\delta)\, d\delta_t \end{cases} \tag{2.25}$$

Besides, supposing that the thickness of the cohesive zone is T_c, then the according three traction strains (ε_n, ε_s, ε_t) can be defined as follows.

$$\varepsilon_n = \frac{\delta_n}{T_c},\ \varepsilon_s = \frac{\delta_s}{T_c},\ \varepsilon_t = \frac{\delta_t}{T_c} \tag{2.26}$$

when $\delta < \delta^0$, the cohesive interaction exhibits linear elastic behavior, and the $\sigma = f(\varepsilon)$ relation can be expressed as follows.

$$\sigma = \begin{Bmatrix} \sigma_n \\ \sigma_s \\ \sigma_t \end{Bmatrix} = \begin{bmatrix} K_{nn} & 0 & 0 \\ 0 & K_{ss} & 0 \\ 0 & 0 & K_{tt} \end{bmatrix} \begin{Bmatrix} \varepsilon_n \\ \varepsilon_s \\ \varepsilon_t \end{Bmatrix} \tag{2.27}$$

where K_{nn}, K_{ss} and K_{tt} are stiffnesses in the normal and in the two shear directions.

In addition, when $\delta^0 \le \delta \le \delta^{\max}$, the cohesive interaction will be dominated by the linear softening law and the following $\sigma = f(\varepsilon)$ relation can be obtained.

$$\sigma = \begin{Bmatrix} \sigma_n \\ \sigma_s \\ \sigma_t \end{Bmatrix} = \begin{bmatrix} (1-D)K_{nn} & 0 & 0 \\ 0 & (1-D)K_{ss} & 0 \\ 0 & 0 & (1-D)K_{tt} \end{bmatrix} \begin{Bmatrix} \varepsilon_n \\ \varepsilon_s \\ \varepsilon_t \end{Bmatrix} \tag{2.28}$$

where D signifies the damage parameter. When $D = 0$, it indicates that the cohesive zone doesn't experience the yield process, while $D = 1$ denotes that the cohesive layer has been totally damaged and has lost its load-carrying capability.

Moreover, as shown in Fig. 2.10, for the status of traction displacement (δ) larger than $\delta^{\max}$ (*i.e.*, $\delta > \delta^{\max}$), it can imply the delamination occurrence of the cohesive zone. Specifically, the

fundamental mechanics governing the cohesive interaction can be illustrated schematically in Fig. 2.11, where the mechanical responses of the cohesive zone are reflected under different deformation modes [187]. As shown in this figure, cohesive element in No.1 point indicates that the material element exists in the linear elastic zone; the No.2 point represents the yield point of the cohesive layer and also the initiation of the interface delamination; the No.3 point denotes that the material element has entered into the linear softening zone; the No.4 point signifies the beginning of the full damage occurrence and the No.5 point implies that the material has been totally damaged.

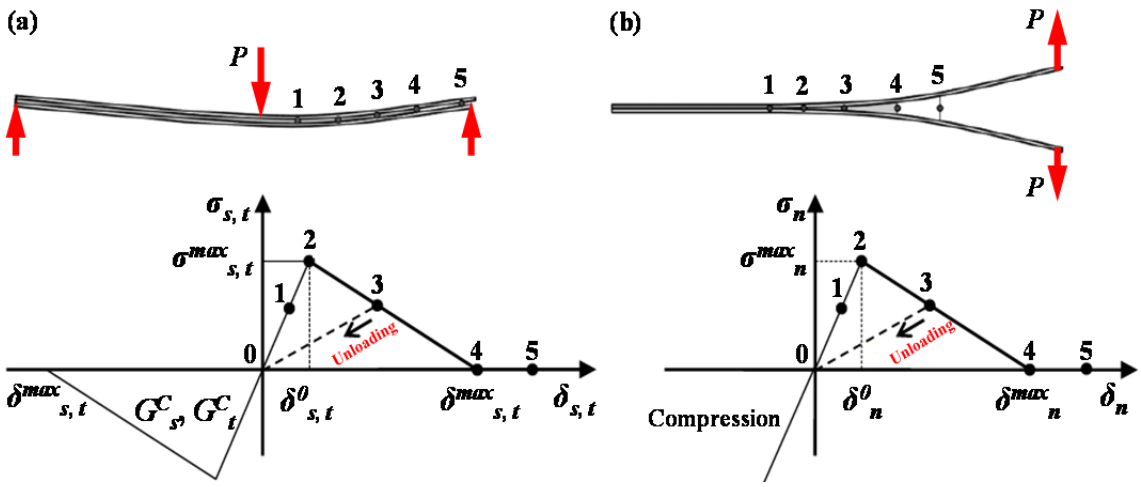

Figure 2.11. Scheme of the mechanical responses of the cohesive zone under different fracture modes [187]: (a) fracture mode II and mode III, (b) fracture mode I.

In addition, since the interface delamination is not caused by one single crack mode, to accurately simulate the delamination phenomenon, it is essential to consider the crack criteria under the conditions of mixed fracture modes. To this aim, the surface-based traction-separation law together with linear softening criterion was firstly adopted to reproduce the mechanical responses of the cohesive interaction. The failure initiation law required to motivate damage among the interface layer is based on the quadratic stress criterion [188, 189] as illustrated by the following equation.

$$\left(\frac{\sigma_n}{t_n^f}\right)^2+\left(\frac{\sigma_s}{t_s^f}\right)^2+\left(\frac{\sigma_t}{t_t^f}\right)^2=1 \tag{2.29}$$

where σ_n, σ_s and σ_t represent the normal traction stress, shear traction stresses in two directions, respectively; t_n^f, t_s^f and t_t^f denote the peak normal failure strength and peak shear failure strengths in two directions, respectively.

Once the damage onset was satisfied, the Benzeggagh-Kenane (BK) damage criteria [190] and potential law [191] were utilized to simulate the damage evolution dominating the cohesive interaction, as presented in Eq. (2.30) and Eq. (2.31). The BK criteria are based on the energy dissipated due to failure considering the traction-separation responses characterized in terms of released rate energies in the normal and two shear directions (G_n, G_s and G_t).

$$G_n^C+\left(G_s^C-G_n^C\right)\left(\frac{G_s+G_t}{G_n+G_s+G_t}\right)^\eta=G^C \tag{2.30}$$

$$\left(\frac{G_n}{G_n^C}\right)^\beta+\left(\frac{G_s}{G_s^C}\right)^\beta+\left(\frac{G_t}{G_t^C}\right)^\beta=1 \tag{2.31}$$

where G_n, G_s and G_t are the released rate energies in the normal and two shear directions, respectively; G_n^C, G_s^C and G_t^C are the critical values of released rate energies; η and β are the parameters of the laws.

Besides, the used traction-separation law is specified by means of the stiffnesses in the normal and in the two shear directions (K_{nn}, K_{ss} and K_{tt}), the interface resistance in each direction (t_n^f, t_s^f and t_t^f) and the damage evolution through the critical released rate energies (G_n^C, G_s^C and G_t^C). The input parameters for interface zone were adopted rigorously based on the comprehensive selection of relevant research work [176-178], as listed in Table 2.2.

2.5 Experimental validation of the OC model

Owing to the significant lack of the experimental studies concerning orthogonal cutting of hybrid CFRP/Ti stacks in the open literature, the stack model was validated separately in terms of each phase verification with the experimental results extracted from the literature. Moreover, since the CFRP/Ti interface was considered as a quick transition zone and a very small thickness was defined, its influence on some other machining responses (*e.g.*, CFRP/Ti chip formation mode, force generation, cutting strain/stress) could be ignored. Besides, the input parameters for the interface zone were also selected carefully from the existing literature, in which it had been already validated and proven good suitability for multi-material modeling. Therefore, the validation work was performed solely concerning the Ti-phase verification and CFRP-phase verification by referring to the open literature. Each model was improved and refined carefully until it was capable of replicating consistent results with the experimental observations. For validation purpose, all the numerical simulations were run under the same cutting conditions as used in the literature. Fig.2.12 presents a global flow chart for the validation work of hybrid CFRP/Ti cutting model.

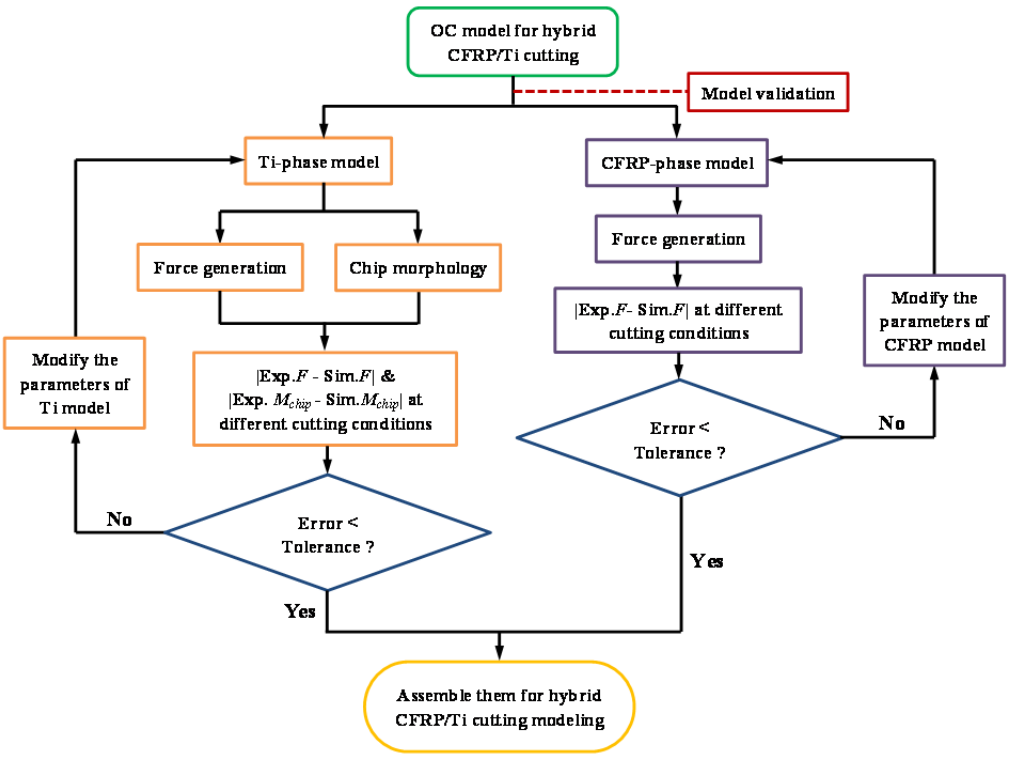

Figure 2.12. Global flow chart for the validation work of hybrid CFRP/Ti stack cutting model.

The Ti-phase model was validated rigorously by means of force generation and chip morphology with experimental data from the literature [160, 161, 192], which were the commonly-used metrics for validations of metal cutting modeling. Fig. 2.13 and Table 2.7 show the comparison between the simulated and experimentally measured force magnitudes [160, 161], and the calculated average errors among them, respectively. Note that the force magnitudes (in N/mm) were normalized as the ratio between the average level of force generation and the workpiece thickness. It was apparent that the simulated force generation yielded a strong agreement with the experimental measurements for various cutting speeds and feed rates as depicted in Fig. 2.13. Globally, the average errors between the simulated and experimental results were controlled below 10 % as summarized in Table 2.7. Furthermore, the comparisons between the simulated and experimental chip morphologies were also performed as shown in Fig.2.14. The serrated chip morphology was validated by three parameters, *i.e.*, valley, peak, and pitch, as compared with the experimental results from the literature [192]. As shown in Table 2.8, the dimensions of the simulated chip morphologies matched well with the experimental ones with the maximum predicted error of 25.7 %. The above validations confirmed the credibility of the established Ti phase model.

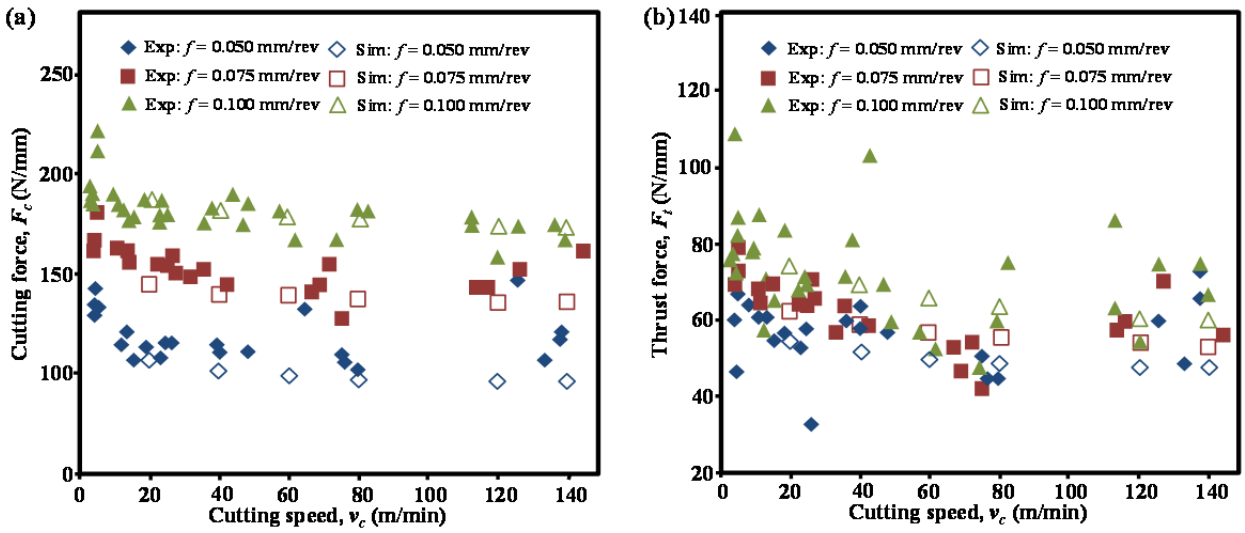

Figure 2.13. Comparison of the simulated (Sim.) and experimental (Exp.) force generation [160, 161] in Ti-phase cutting modeling for different cutting speeds at feeds of 0.05, 0.075 and 0.100 mm/rev: (a) F_c - cutting force; (b) F_t - thrust force.

Table 2.7
Average error between the simulated and experimental force generation [160, 161] in Fig.2.13.

Test condition	Average error for F_c (%)	Average error for F_t (%)
f = 0.050 mm/rev	-9.31	-8.32
f = 0.075 mm/rev	-6.86	-2.15
f = 0.100 mm/rev	+1.73	+1.36

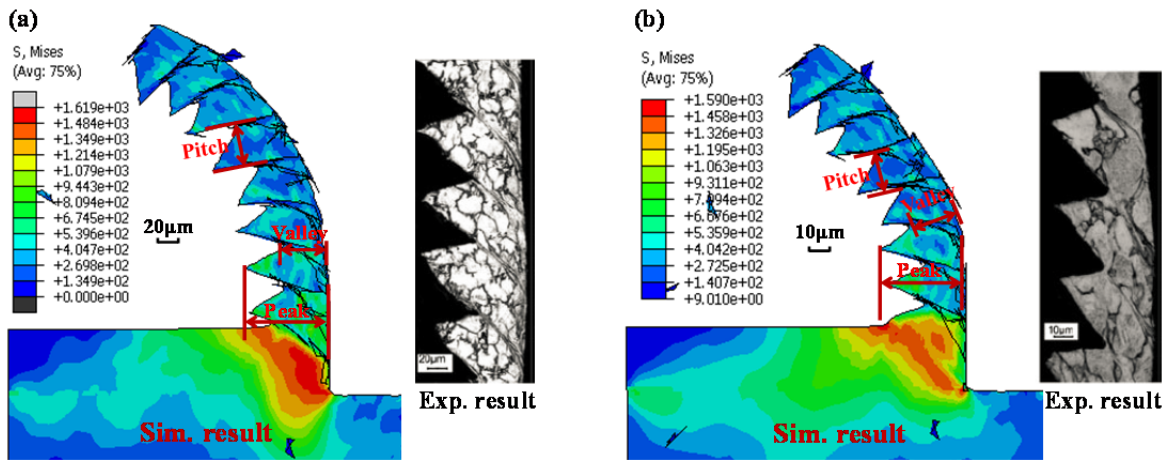

Figure 2.14. Comparison of the simulated and experimental chip morphologies [192] in Ti-phase cutting modeling (Sim: simulated, Exp: experimental): (a) test condition 1 (v_c = 1200 m/min, f = 70 µm/rev) and (b) test condition 2 (v_c = 4800 m/min, f = 35 µm/rev).

Table 2.8
Comparison between the simulated and experimental chip geometries in Fig. 2.14.

Scheme of the Ti chip geometry	Test condition	Method	Pitch L_c (µm)	Peak h_1 (µm)	Valley h_2 (µm)
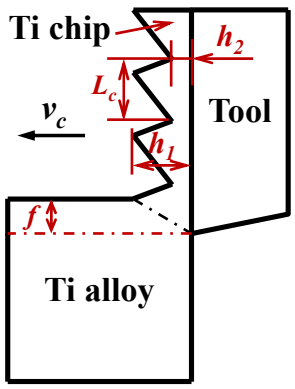	v_c = 1200 m/min, f = 70 µm/rev	Simulation	52.3 ± 6	95.6 ± 4	47.2 ± 3
		Experimentation [192]	68.2	105.7	50.3
		Error (%)	23.3	9.6	6.2
	v_c = 4800 m/min, f = 35 µm/rev	Simulation	27.2 ± 4	41.7 ± 6	25.4 ± 5
		Experimentation [192]	36.6	45.6	23.6
		Error (%)	25.7	8.6	-7.6

Note: L_c, h_1 and h_2 denote the lengths of chip pitch, chip peak and chip valley, respectively.

Moreover, for CFRP-phase model, it was validated through the simplest manner of force generation (cutting force and thrust force) comparison, which was the most-used criterion for the validations of composite cutting modeling. Fig. 2.15 presents the comparative results of the predicted and experimentally measured forces *versus* fiber orientation (θ). It was noticeable that the estimated force magnitudes of both cutting force and thrust force yielded strong correlations and consistent variation trends with the experimental results gained by Iliescu et al. [175]. In addition, the predicted chip morphologies in θ = 0° and 45° also agreed well with the experimental results from the literature [175], which confirmed the sufficient credibility of the established CFRP-phase cutting model. After the experimental validation, each constitutive model was assembled to perform the hybrid CFRP/Ti stack cutting modeling.

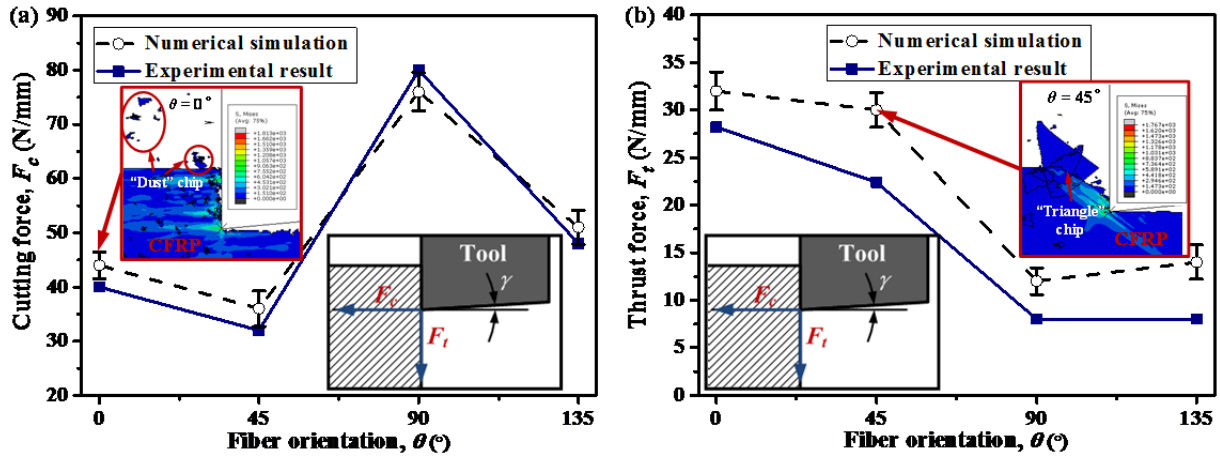

Figure 2.15. Comparison of the simulated and experimental force generation [175] in CFRP-phase cutting modeling: (a) cutting force (F_c) and (b) thrust force (F_t) (cutting condition: v_c = 6 m/min, f = 0.2 mm, α = 0°).

2.6 Conclusions

This Chapter offers the physical description of the established FE models for cutting modeling of hybrid CFRP/Ti stacks. To inspect the fundamental mechanisms controlling the bi-material machining, the simplified orthogonal cutting configuration (OCC) was adopted. The established OC model comprises four basic phases, *i.e.,* tool phase, Ti phase, interface phase and CFRP phase. Different constitutive laws and failure criteria were implemented into the Abaqus/Explicit code (Version 6.11) to construct the entire machining behavior of the hybrid composite stacks. According to the pertinent illustrations, the constitutive details of the developed numerical models can be summarized as follows.

- The Ti-alloy phase is assumed isotropic with elastoplasticity behavior during the cutting process. The Johnson-Cook criteria and Hillerborg's fracture energy based approach are utilized to replicate the local failure of the metallic phase.
- The CFRP phase is modeled as an equivalent homogeneous material (EHM) by considering also the anisotropic behavior related to its fiber orientation (θ). Hashin damage criteria considering four basic types of fiber/matrix failure are adopted to replicate the rupture of the composite layer and the subsequent chip separation.
- The CFRP/Ti interface physically described as an intermediate constituent is modeled using the concept of cohesive zone (CZ). The material separation within the CZ is controlled by traction-separation criteria. The interface used in the hybrid composite model aims to serve as a technical control for the "Ti-to-CFRP" contact management, and a very small thickness (approximately 5 µm) is defined for the interface zone in order to minimize its influence on some other CFRP/Ti machining responses.
- Two setups of OC models for hybrid CFRP/Ti cutting modeling are established. The proposed FE models also take into account the influences of different cutting-sequence strategies ($^{\text{CFRP}\rightarrow\text{Ti}}_{\text{Ti}\rightarrow\text{CFRP}}$) for the numerical simulation.

Chapter III

Experimental details and cutting design

Nomenclature

CFRP → Ti Ti → CFRP	Cutting from CFRP → Ti and/or Ti → CFRP
f	Feed rate
F_c	Cutting force
F_t	Thrust force
R_a	Arithmetic mean roughness
R_q	Root mean squared roughness
R_z	Ten point mean roughness
R_p	Maximum peak height
R_v	Maximum valley depth
v_c	Cutting speed
WC/Co	Tungsten carbide
α	Tool rake angle
γ	Tool clearance angle
μ	Multi-tool-work frictional coefficient
θ	Fiber orientation

Abbreviation

CVD	Chemical Vapor Deposition
EDS	Energy Dispersive Spectrometer
MTCVD	Medium Temperature Chemical Vapor Deposition
OC	Orthogonal cutting
OCC	Orthogonal cutting configuration
OM	Optical microscope
PCD	Polycrystalline diamond
PVD	Physical Vapor Deposition
SEM	Scanning Electron Microscope

3.1 Introduction

The Chapter III aims to elaborate the details of the experimental arrangement as well as the involved experimental techniques and measuring systems applied throughout the entire Ph.D. research. Note that the experimental studies primarily invovle three types of hybrid CFRP/Ti stack manufacturing, *i.e.*, orthogonal cutting (considering different cutting-sequence strategies ($^{\text{CFRP}\rightarrow\text{Ti}}_{\text{Ti}\rightarrow\text{CFRP}}$)), combined CFRP/Ti machining and hole drilling, with two key objectives to (*i*) facilitate the previous numerical studies and (*ii*) provide an enhanced CFRP/Ti cutting comprehension in a more realistic way. The main structure of this chapter was organized as follows.

- Workpiece material and properties: this subsection offers the information regarding the geometrical dimensions, workpiece configuration and mechanical properties of the used CFRP/Ti specimens.
- Cutting tool details: this subsection provides the details of the tool shape, material composition, geometrical dimension and angles for two sets of cutting tools specified for orthogonal cutting (OC), combined CFRP/Ti cutting and hole drilling.
- Measuring systems and experimental techniques: this subsection aims to illustrate the used machine tools, the adopted on-site measuring systems and the post-treatment analysis instruments involved in the experimental studies of hybrid CFRP/Ti stack cutting.
- Cutting test design: this subsection presents the details of the experimental arrangements for orthogonal cutting, combined bi-material machining, and hole drilling. A special focus is made on the illustration of the experimental setup for each cutting test with respect to the adopted cutting variables (cutting speed (v_c), feed rate (f), spindle speed (n), *etc.*).

3.2 Workpiece configuration and properties

During the experimental studies, each stacked composite workpiece comprises one annealed Ti6Al4V alloy (355HV) and one T300/914 CFRP laminate. Three configurations of hybrid CFRP/Ti specimens provided by VN Composites Company in France were adopted for the investigations of orthogonal cutting, combined CFRP/Ti machining and drilling operation. Fig.3.1 depicts the overall micrographs of one type of the hybrid CFRP/Ti configurations utilized in experimentation with respect to their individual microstructures. It can be seen that the initial microstructure of the Ti6Al4V alloy (Fig. 3.1(b)) consists of white α grain phase with average grain size around 10 µm (ranging from 5 µm to 20 µm) surrounded by the inclusions of black β grains. For the CFRP laminate, the distinct two-phase microstructures are clearly visible in Fig.3.1(c), where the white round/oval phase with an average diameter of probably 7 µm represents the carbon fiber and the surrounding phase denotes the resin matrix.

For orthogonal cutting and combined CFRP/Ti machining, the stacked composite laminate is fabricated by unidirectional (UD) carbon/epoxy T300/914 prepreg (60 % fiber volume fraction) with a fiber orientation of θ = 0°, 45° or 90° by using hand lay-up technique and sheet molding compound.

For drilling trials, each hybrid composite stack is composed of one Ti6Al4V alloy sheet and one

multi-orientation T300/914 CFRP laminate (60 % fiber volume fraction) subjected to the following stacking sequence of $[45°/-45°/0°/90°]_s$. Each stacked material has 4 mm thickness and the entire CFRP/Ti specimen has the total dimensions of 254 mm (length) × 34.5 mm (width) × 8 mm (thickness).

The basic dimensions, geometries and configurations of the used CFRP/Ti specimens are summarized in Table 3.1. It should be noted that during the orthogonal cutting of the multi-phase materials, different cutting-sequence strategies (*i.e.*, cutting from Ti → CFRP and CFRP → Ti) were applied on the top and bottom surfaces of the workpiece types 1, 2 and 3, respectively, as depicted in Table 3.1. For the combined CFRP/Ti machining, the total thickness of the workpiece types 4, 5 and 6 was set around 4 mm by considering the effective cutting length (7.4 mm) of the used polycrystalline diamond (PCD) tipped inserts. Besides, Table 3.2 also shows the basic mechanical/physical properties of the used hybrid CFRP/Ti specimens.

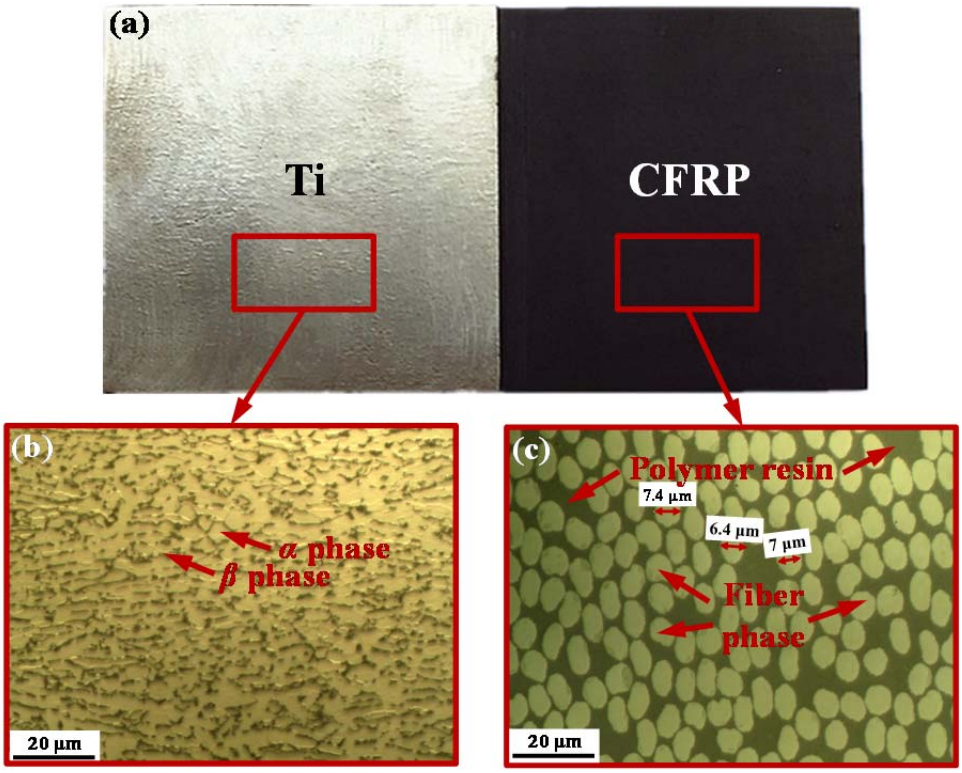

Figure 3.1. (a) Global photograph showing one typical representation of the used hybrid CFRP/Ti6Al4V specimens, (b) optical microstructure of the Ti6Al4V phase, and (c) optical microstructure of the CFRP phase ($\theta = 0°$).

Table 3.1
Basic dimension and configuration of the used hybrid CFRP/Ti6Al4V specimen.

Workpiece type	CFRP type	Ti alloy type	θ	Dimension ($L \times H \times D$)
Types 1-3	T300/914	Ti6Al4V	0°, 45°, 90°	90 mm × 45 mm × 4 mm

	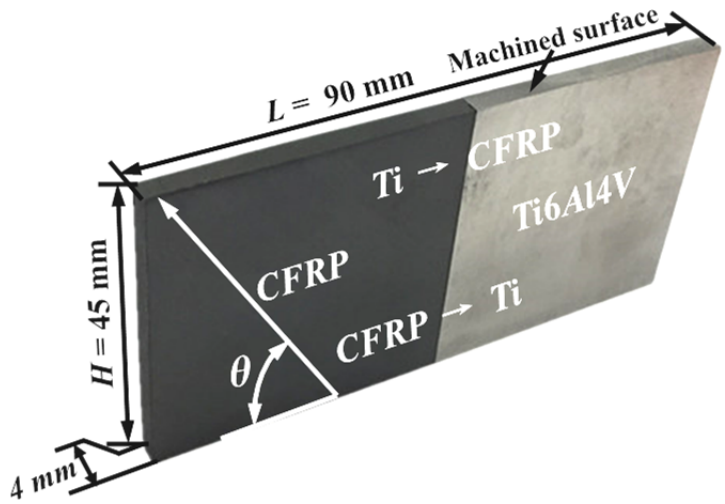			
Types 4-6	T300/914	Ti6Al4V	0°, 45°, 90°	90 mm × 45 mm × 4 mm
	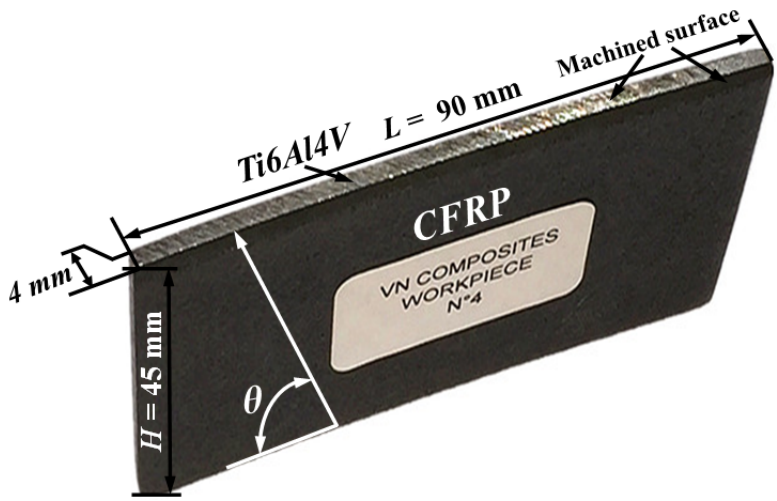			
Type 7	T300/914	Ti6Al4V	$[45°/-45°/0°/90°]_s$	254 mm × 34.5 mm × 8 mm
	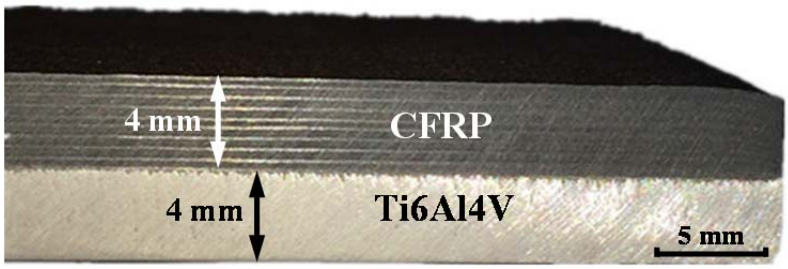			

Table 3.2
Basic mechanical/physical properties of the used hybrid CFRP/Ti6Al4V specimen.

Workpiece material			
Ti6Al4V alloy		**T300/914 CFRP**	
Tensile strength (σ_b)	900-1160 Mpa	Tensile strength (σ_b)	1860 MPa
Elongation (δ)	8 %	Tensile modulus (σ_b)	135 GPa

Density (ρ)	4430 kg/m^3	Tensile strain	1.3 %
Young's modulus (E)	113 GPa	Compressive strength	1470 Mpa
Poisson's ratio (υ)	0.342	Flexural strength	1810 MPa
Thermal expansion coefficient (α_T)	9.1×10^{-6} °C^{-1}	Flexural modulus	125 GPa
Thermal conductivity (λ)	7.0 W/(m·°C)	ILSS	10 kgf/mm^2
—		Fiber volume fraction	60 %

3.3 Cutting tool details

To finalize the experimental investigations, two setups of ISO-specified cutting tools, *i.e.*, cutting inserts and drill bits, provided by Sandvik Coromant were utilized. For orthogonal cutting trials, the superior polycrystalline diamond (PCD) tipped inserts (ISO reference: TCMW16T304FLP CD10) was adopted. The PCD material was welded to a tungsten carbide (WC/Co) made tool substrate, as shown in the detailed illustration of Table 3.3. The CD 10 grade, according to the information provided by Sandvik Coromant, comprises fine to medium-fine PCD grain crystals with an average diameter of 7 μm, which exhibits high suitability for semi-finishing and finishing non-ferrous and non-metallic materials. The basic mechanical/physical properties of the tipped PCD materail are shown in Table 3.4. Besides, the PCD cutting zone is usually ground with a very small cutting radius (probably 5 μm) and a quite flat surface to ensure a sharp cutting edge for the industrial manufacturing operations. Fig.3.2 shows the optical photograph and SEM observation of the PCD tipped cutting zone.

Moreover, the PCD commonly represents one of the hardest materials and shows high wear resistance and low friction characteristics, which has been confirmed to be capable of alleviating significantly the serious abrasive wear and adhesion wear resulting from hybrid CFRP/Ti stack machining by the existing literature [45]. In addition, the PCD tipped insert has an effective cutting length of 7.4 mm with defined geometries of rake angle (α = 0°) and clearance angle (γ = 7°). The detailed geometrical parameters and overall morphology of the PCD tool are summarized in Table 3.3. Furthermore, additional four types of coated inserts with the identical geometric dimensions but different coating grades were utilized for the combined CFRP/Ti machining. These four inserts have the same tool geometrical angles (rake angle of α = 0° and clearance angle of γ = 7°) and are all made up of the tungsten carbide (WC/Co) substrate. For better experimental classification and comparison, the four types of inserts were designated as tools A, B, C and D throughout the entire experimental studies and analyses. Note that tools A, B, C and D are all MTCVD (Medium Temperature Chemical Vapor Deposition) coated inserts with the identical multi-layer coating composition (TiN+Al_2O_3+TiCN) but different coating grades. For tools A and C, they are fabricated by gradient and fine coating grades, respectively, while for tools B and D, they are both manufactured by medium coarse coating grade.

With respect to the mechanical/physical properties of the coating composition, the titanium-based coatings (TiN and TiCN) commonly provide excellent wear resistance, thermal stability, and low friction coefficient, which can significantly alleviate the severe flank wear, micro-chipping failure and thermal-induced damage of the cutting edges. In contrast, the key advantages of the aluminum oxide (Al_2O_3) primarily aim to offer maximum thermal and chemical

protection during the material removal process. Table 3.5 also summarizes their comparative properties in terms of their potential cutting performances in real manufacturing operations.

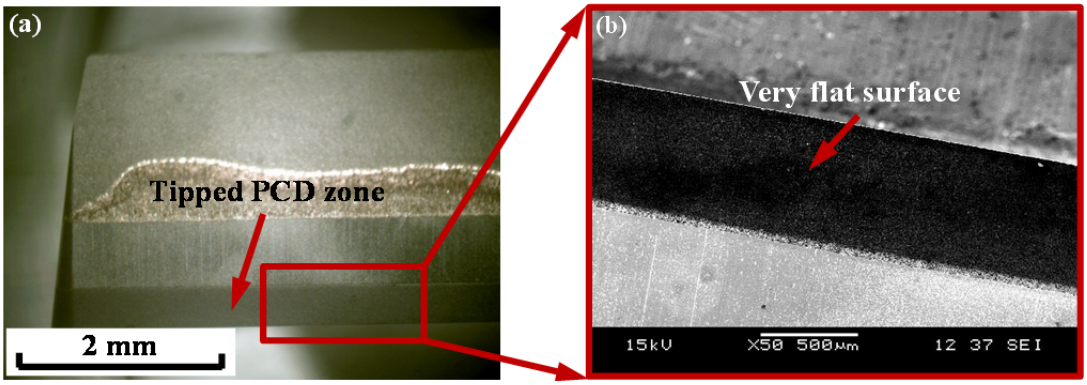

Figure 3.2. (a) Optical photograph and (b) SEM observation of the PCD tipped cutting zone.

Table 3.3
Details of the used PCD tipped insert for orthogonal cutting trials.

Cutting tool						
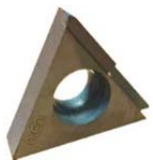	Tool material composition					
	ISO reference	Tipped material	Diamond grade	Welded Substrate		
	TCMW16T304FLP CD10	PCD	Medium-coarse	WC/Co		
	Geometrical dimension (mm)					
	Rake angle	Clearance angle	*iC*	*S*	r_ε	*L*
	0°	7°	9.525	3.96875	0.3969	16.4978
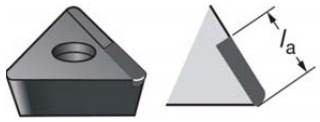	Effective cutting length (l_a)		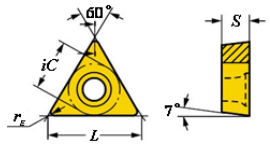			
	7.4 mm					

Table 3.4
Mechanical/physical properties of the tipped PCD material.

Average grain size	Hardness (knoops)	Density	Thermal conductivity at 20 °C
7 µm	50.0 GPa	4120 kg/m^3	540 W/(m·°C)

Table 3.5
Summary of the comparative properties and cutting performances of the used coating composition.

Coating composition		TiN	TiCN	Al_2O_3
Mechanical properties	Hardness (Vickers)	2300	3000	1440
	Oxidation temperature	550 °C	400°C	1750°C
	Friction coefficient	~0.65	~0.45	~2.66
	Thickness	2 - 4 µm	2 - 4 µm	2 - 4 µm
	Arithmetic mean	0.20	0.17	0.30

	roughness (R_a)			
Manufacturing benefits		☐ **TiN:** excellent wear resistance, thermal stability, and low friction coefficient. ☐ **TiCN:**. good adhesion, excellent toughness, superior wear resistance and built-up (BUE) resistance. ☐ **Al_2O_3:** superior thermal and chemical stability.		
Industrial application		☐ **TiN:** general purpose for machining ferrous materials including drilling, reaming, counterboring and milling of chip classes 20 to 140 materials. ☐ **TiCN:** excellent for cutting of cast irons, high silicon, aluminum alloys, copper, and all abrasive materials. ☐ **Al_2O_3:** suitable for machining many useful alloys, superalloys, and metallic compounds.		

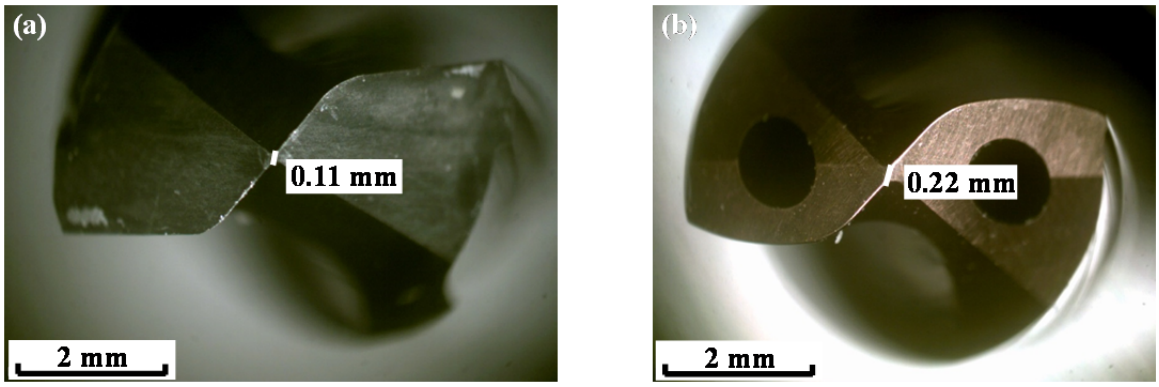

Figure 3.3. Micrographs showing the drill-tip zones for the used drill bits (× 30): (a) drill A (uncoated solid carbide drill bit) and (b) drill B (PVD TiAlN-coated drill bit).

For drilling trials, two types of standard twist drills (ISO references: 452.1-0635-044A0-CM H10F and R846-0635-50-A1A 1220) with the identical cutting diameter of 6.35 mm, provided by Sandvik Coromant, France, were adopted for the hole making as shown in Table 3.6 and Table 3.7, respectively. The first drill bit designated by drill A is an uncoated solid carbide tool with two main cutting edges, a short 0.11 mm-length chisel edge, a small helix angle of 20° and a point angle of 135°. In contrast, the second drill bit designated by drill B is a PVD TiAlN-coated carbide twist drill manufactured with two flutes, a long 0.22 mm-length chisel edge and a large helix angle of 27.2° and a point angle of 140°. The TiAlN coating commonly can provide superior wear resistance and stable high hardness to cope with the high force/temperature conditions developed in the challenging multi-material drilling process. In addition, Fig. 3.3 also shows the micrographs of the drill-tip zones of the employed two different drill bits. It is noticeable that the drill A is characterized by 2-facet feature without internal lubrication hole. By contrast, the drill B has 4-facet characteristics and two internal lubrication holes that can facilitate the application of through-tool lubrication. For better monitoring the wear progress of the used cutting tools governing the hybrid CFRP/Ti stack machining, the initial statuses of the fresh tool cutting surfaces are recorded as summarized in Table 3.8. Note that the optical micrographs of the tool cutting surfaces were performed by using a Nikon toolmaker's SMZ-2T microscope with 30 magnification and 1 µm resolution while the SEM observations of the tool edge morphologies were captured by using a

JSM-5510LV SEM system manufactured by JEOL company with the following specifications: magnification of ×18 to ×300, 000; modes of operation: HV (high vacuum) and LV (low vacuum) and accelerating voltage: 0.5 to 30 kV.

Table 3.6
Details of the used uncoated drill (drill A) for hybrid CFRP/Ti stack drilling.

Drill A						
	Tool material composition					
	ISO reference	Substrate	Grade			
	452.1-0635-044A0-CM H10F	Solid tungsten carbide	K20			
	Geometrical dimension (mm)					
	Diameter (D_c)	Point angle	Helix angle	l_2	l_4	l_6
	6.35 mm	135°	20°	102.784mm	41.272 mm	50.8 mm
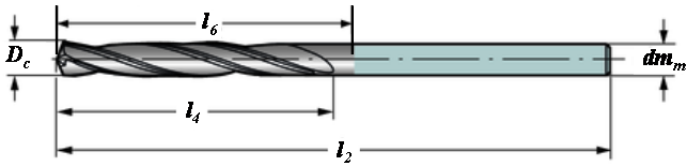						

Table 3.7
Details of the used PVD coated drill (drill B) for hybrid CFRP/Ti stack drilling.

Drill B						
	Tool material composition					
	ISO reference	Coating type	Coating material	Coating grade	Substrate	
	R846-0635-50-A1A 1220	PVD	TiAlN	Medium-coarse	Solid carbide	
	Geometrical dimension (mm)					
	Diameter (D_c)	Point angle	Helix angle	l_2	l_4	l_6
	6.35 mm	140°	27.2°	91 mm	32.9 mm	53 mm
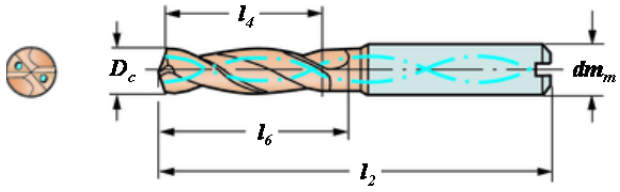						

Table 3.8
The initial statuses of the fresh tool surface morphologies before hybrid CFRP/Ti stack machining.

Tool reference	**Optical micrograph (× 30)**	**SEM of tool rake face**	**SEM of tool flank face**
PCD	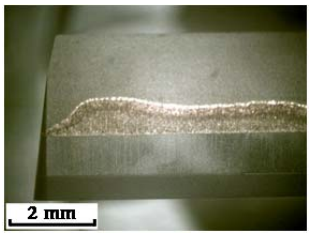	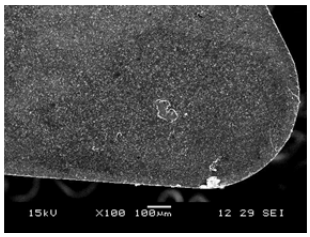	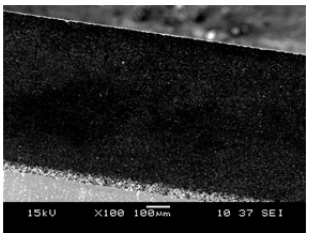

Tool A		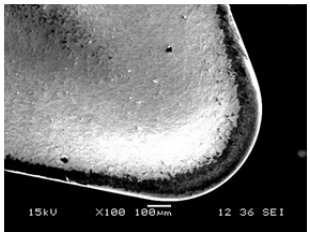	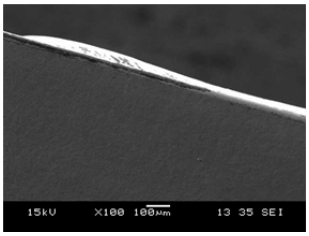
Tool B	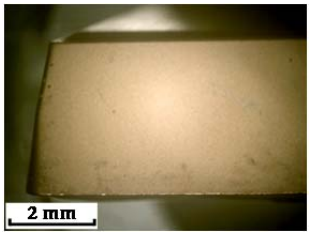	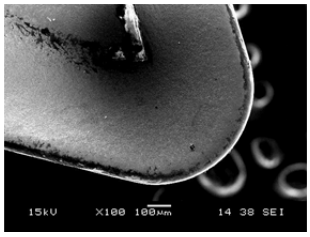	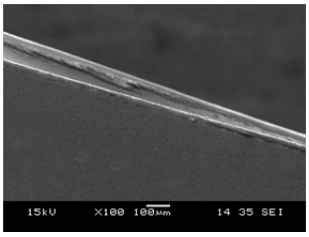
Tool C	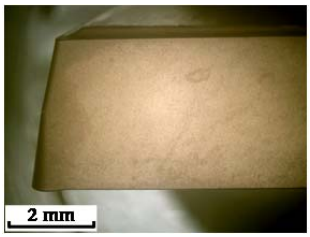	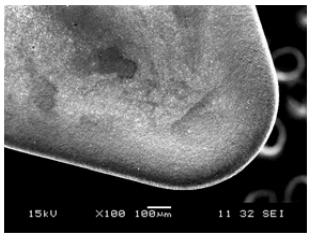	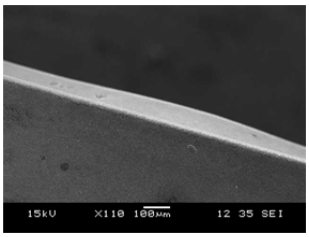
Tool D		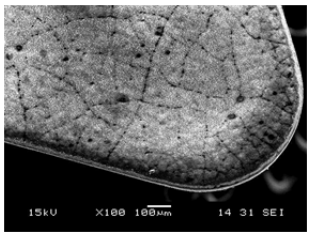	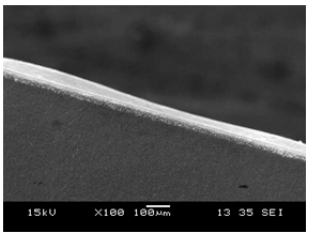
Drill A	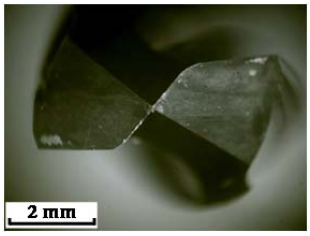	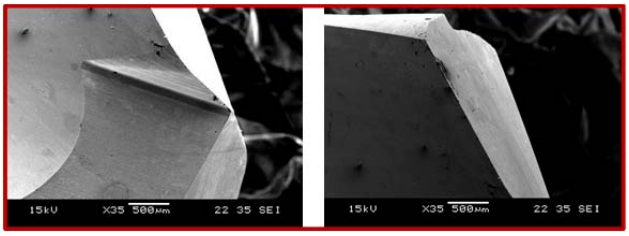	
Drill B	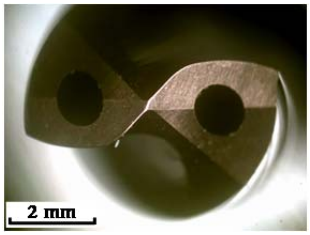	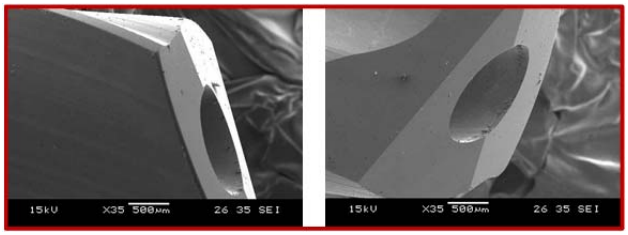	

3.4 Measuring systems and experimental techniques

As elaborated in subsection 3.1, the experimental work of hybrid CFRP/Ti stack machining includes both on-site measurements and post-treatment analyses. The on-site measurements aim to measure the force generation signatures and capture the dynamic chip separation process dominating the hybrid CFRP/Ti stack machining. By contrast, the post-treatment analyses aim to

investigate the machined workpiece quality, cutting-induced subsurface damage, worn-out tool surface morphology, resected chip type, *etc*. To this aim, a variety of measuring systems and experimental techniques have been adopted and utilized during the experimental analyses. The following subsections then illustrate the detailed procedures regarding the on-site and post-treatment analyses when machining hybrid CFRP/Ti stacks.

3.4.1 On-site measuring system

3.4.1.1 Force generation characterization

For each cutting configuration of hybrid CFRP/Ti stack machining (orthogonal cutting, combined CFRP/Ti machining and drilling), the force generation in each cutting trial was recorded and measured by using a piezoelectric Kistler dynamometer (type 9255B for orthogonal cutting and combined CFRP/Ti machining, and type 9271A for hole drilling), connected to a multichannel charge amplifier (type 5017B1310 for orthogonal cutting and combined bi-material cutting, and type 5019A130 for hole drilling) and a data acquisition board that converts the recorded signals from the sensors inside the dynamometer to voltage signals. The LabVIEW Signal Express software (National Instruments, USA) was utilized to collect the recorded voltage signals at an acquisition frequency of 1 kHz. Fig.3.4 shows the schematization of the force measurement setup when orthogonal cutting of hybrid CFRP/Ti stacks. It should be noted that in Fig.3.4, the specimen was put inside a fixture and then was clamped through the fastening connections of the front-rear steel plates. The entire fixture was firmly mounted on the Kistler dynamometer for capturing the generated force signal. After the force signal acquisition, two force components respectively exerted along/perpendicular to the cutting-speed direction (*i.e.*, F_c (cutting force), F_t (thrust force) for orthogonal cutting and combined CFRP/Ti cutting; T (torque) and F_t (thrust force) for drilling) were calculated as the average values of the steady-varied force signal generated in the CFRP/Ti machining. For orthogonal cutting and hole drilling, the force generation in CFRP phase cutting and Ti phase cutting was calculated individually while for combined CFRP/Ti machining, the force generation was only measured as the combined CFRP/Ti phase cutting. Besides, each force calculation was repeated three times under the identical conditions so as to get reliable results.

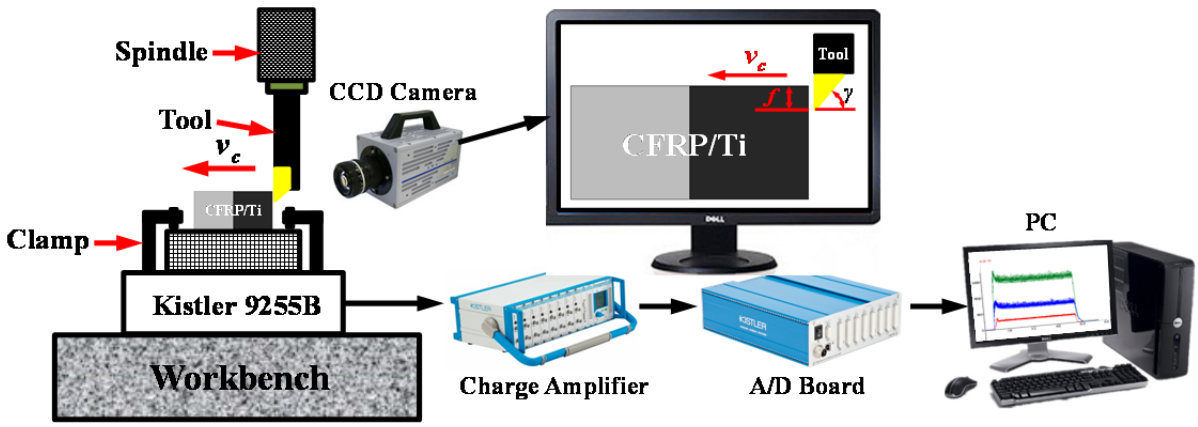

Figure 3.4. Scheme of the force measurement system when orthogonal cutting of hybrid CFRP/Ti stacks.

3.4.1.2 Chip separation process monitoring

To inspect the dynamic cutting mechanisms controlling hybrid CFRP/Ti stack machining, the CFRP/Ti chip separation process under the orthogonal cutting configuration (OCC) was captured by using a high-speed camera. The charged coupled device (CCD) camera (FASTCAM SA5 model) was utilized to record the optical frames at an acquisition rate of 20,000 fps. In addition, the high-speed video capture was performed with a special focus on the interface region cutting when the tool edges cut from one phase to another phase and *vice versa*. Moreover, the dynamic chip separation processes under different cutting-sequence strategies ($^{\text{CFRP} \rightarrow \text{Ti}}_{\text{Ti} \rightarrow \text{CFRP}}$) and different cutting parameters (θ, v_c, and f) were also recorded to facilitate an enhanced cutting mechanism comprehension.

3.4.2 Post-treatment analyses

The post-treatment analyses dominating the entire experimental work include the studies of the machined CFRP/Ti surface quality (subsurface damage extent, workpiece morphology, surface integrity, hole geometrical feature, *etc*.), the inspections of the tool wear (tool worn surface morphology, tool wear mechanism and tool failure mode), the examinations of the resected chips (chip geometric morphology, chip type, *etc*.). The detailed procedures with respect to each type of analyses are discussed below.

3.4.2.1 Optical microscope and microhardness analysis

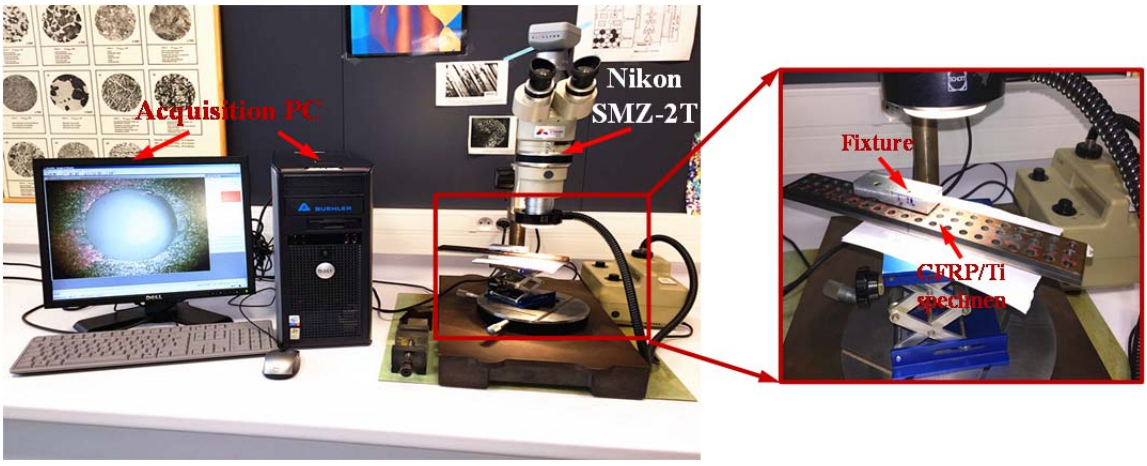

Figure 3.5. Process setup for the Nikon SMZ-2T optical microscope system.

The optical microscope (OM) studies were performed by using a telescope binocular Nikon tool maker's SMZ-2T microscope with the magnifications ranging from × 10 to × 120. The OM is equipped with a Sony SSC-DC38P camera and coupled to an image analysis software CLEMEX Vision, as shown in Fig.3.5. The key objectives are to quantitively analyze the cutting-induced subsurface damage extent (fiber/matrix damage length, Ti burr width, hole delamination extent, *etc*.), tool wear land and resected chip type. For cutting-induced subsurface damage analyses, the fiber/matrix damage length, Ti burr width and drilling-induced hole delamination were measured by using the built-in software (OmniMet Images & Measures, Buehler®, USA) linked to the Nikon

SMZ-2T microscope. For quantitively recording the wear status of the used cutting tools, the tool flank wear was measured several times through the mentioned OM examination according to the ISO Standard 3685 (1993) with average flank wear width (VB) used for carbide tools. Each measurement was repeated three times under identical conditions in order to get reliable results.

In addition, the microhardness of the machined hybrid Ti surfaces was also examined by using the 1600-5100 MicroMet Hardness Tester (Buehler®). A load of 100 *gf* over a 10 s dwell time was employed for each measurement.

3.4.2.2 Surface roughness and 3D profiling

Surface roughness is an important indicator for evaluating the machined surface finish resulting from hybrid CFRP/Ti stack cutting. Having high surface roughness values in drilled CFRP/Ti holes may lead to excessive wear and severe fatigue of the assembly, and degrade the material capability of resisting corrosion. To quantitively evaluate the real extent of the machined surface roughness, various roughness parameters have been introduced and employed in the industrial applications. Up to now, the most-used standard roughness parameters are arithmetic mean roughness (R_a), root mean squared roughness (R_q), ten point mean roughness (R_z), maximum peak height (R_p), and maximum valley depth (R_v), as summarized in Table 3.9.

Table 3.9
The general formula of the commonly-used surface roughness parameters.

Parameter	Description	General Formula
R_a	Arithmetic mean roughness	$R_a = \frac{1}{n}\sum_{i=1}^{n}\lvert y_i \rvert$
R_q	Root mean squared roughness	$R_q = \sqrt{\frac{1}{n}\sum_{i=1}^{n}\lvert y_i \rvert^2}$
R_z	Ten point mean roughness	$R_z = \frac{\sum_{i=1}^{5} y_{pi} + \sum_{i=1}^{5} y_{vi}}{5}$
R_p	Maximum peak height	$R_p = \max_i y_i$
R_v	Maximum valley depth	$R_v = \min_i y_i$
Scheme of representative roughness parameter definition	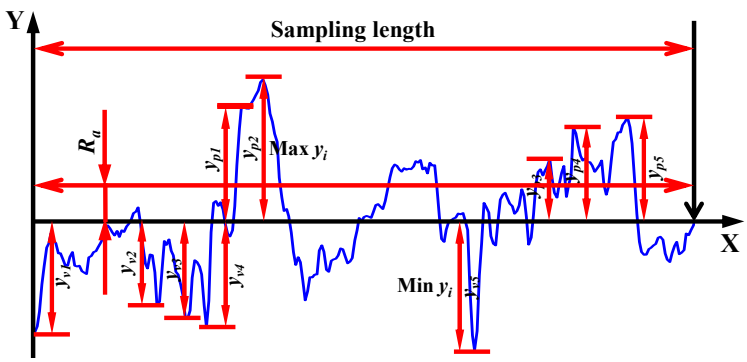	

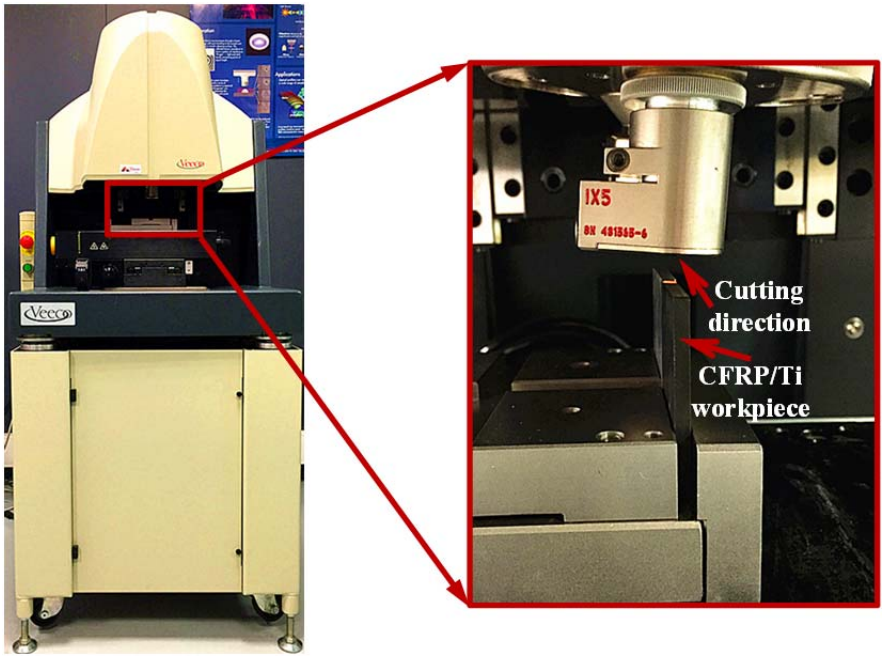

Figure 3.6. Photograph showing the used Veeco white-light interferometer profiling system.

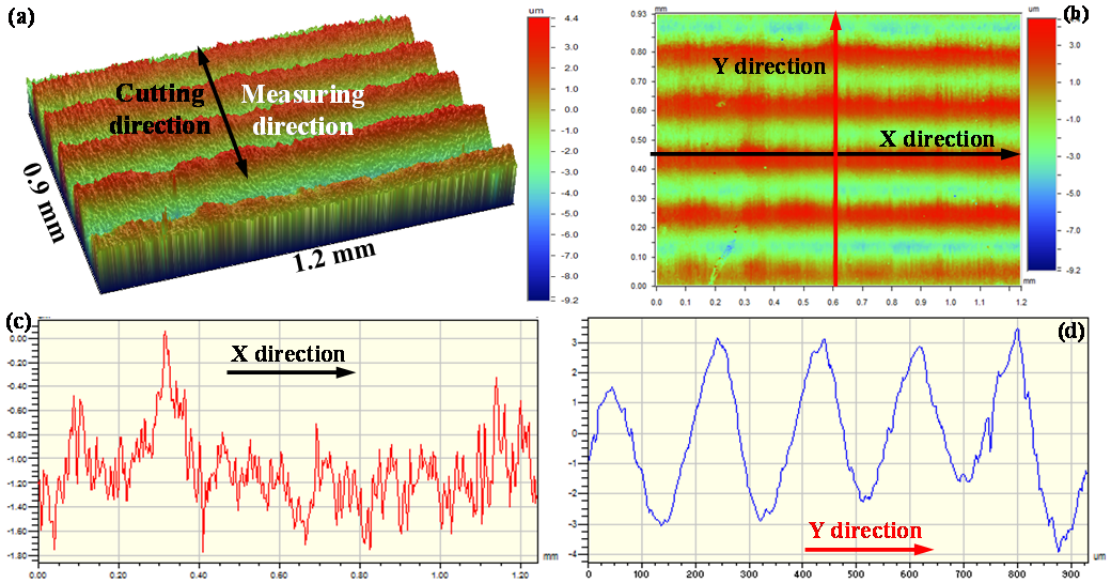

Figure 3.7. Typical representation of (a) surface roughness measuring direction, (b) 2D surface profiling, (c) and (d) surface height in a 2D configuration of one CFRP/Ti specimen.

In the present experimental studies, the most-used surface roughness parameters (R_a, R_q, and R_z) were adopted to analyze quantitively the machined CFRP/Ti surface finish. For OC trimmed CFRP/Ti specimens, the surface roughness measurement was performed by using a white-light interferometer (Wyko 3300NT) as shown in Fig. 3.6. The Veeco interferometer usually firstly replicates the real 3D topography of the machined surface with a defined scanning area of 1.2 mm × 0.93 mm. Afterward, the required roughness parameters can be calculated based on the replicated topography through the built-in Vision software. For each surface roughness calculation, the measurement was performed concerning the cutting speed direction and was repeated three times under identical conditions in order to get reliable results. A scheme of the surface roughness measuring direction and several obtained representative surface profiles from orthogonoal cutting of hybrid CFRP/Ti workpieces is shown in Fig. 3.7. Besides, the white-light interferometer was also

used to replicate the machined surface topography (*e.g.*, OC trimmed CFRP/Ti surface and drilled CFRP/Ti hole wall surface) in order to facilitate the analyses of induced surface damage formation.

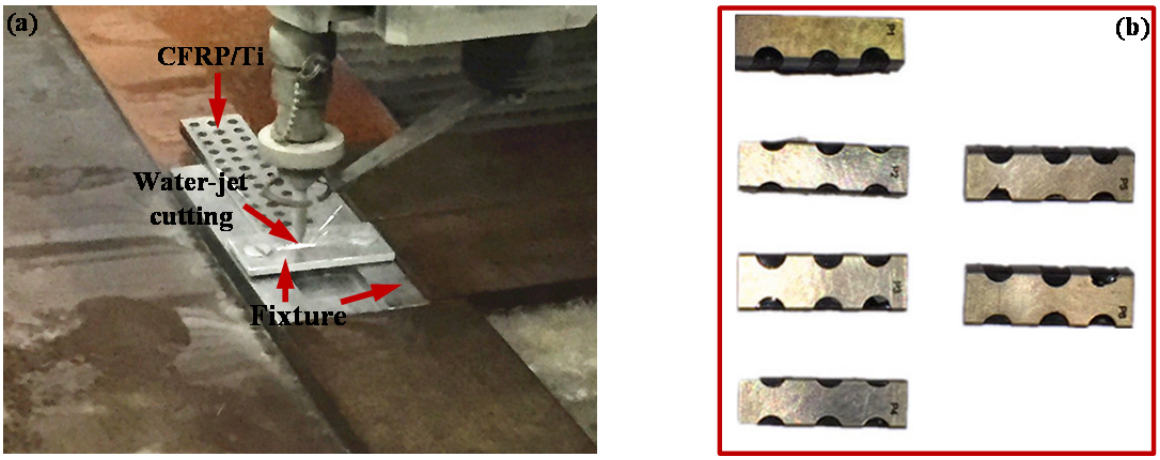

Figure 3.8. (a) On-site water-jet machining process of hybrid CFRP/Ti specimens and (b) scheme of several separated CFRP/Ti hole parts.

Further, to recorde the drilled CFRP/Ti hole topography, the machined holes were cut off into several parts through the hole center by using the water-jet machining technology. To prevent the secondary cutting-induced damage on the hole wall surfaces, resin spraying on each drilled hole was made. The water-jet cutting was performed on a Resato ACM 3015 machine tool with a constant cutting speed of 7 mm/min and a water pressure of 3,600 bars. Fig. 3.8 shows the on-site water-jet machining of one hybrid CFRP/Ti specimens and also the separated hole parts.

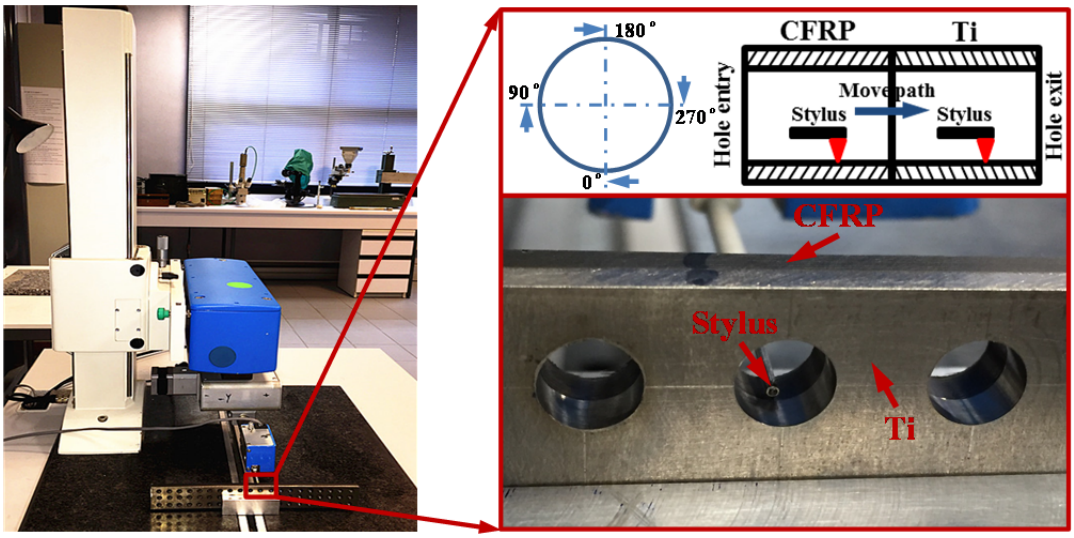

Figure 3.9. Experimental setup for the surface roughness measurement of drilled CFRP/Ti holes.

Additionally, for the drilled CFRP/Ti holes, a 2D surface Hommel Wave surface profilometer with a diamond stylus of 2 µm tip radius and a cut-off length of 0.8 mm, was also used to measure the arithmetic mean roughness (R_a). The R_a of each drilled hole was measured based on each individual material layer as shown in Fig.3.9. The built-in Surfascan software was utilized to transfer and record the collected data from the stylus to the PC. A total evaluation length of 3 mm was set in the built-in software of the surface profilometer for each hole surface of stacked layers along the drilling direction.

The CFRP/Ti samples were placed such that the drilled holes were facing the stylus on the

entrance side, and then the stylus was carefully lowered until reaching the contact with the hole wall surface. Afterward, the stylus was controlled automatically to traverse along the internal hole surface with defined evaluation length. For each measurement, the procedure was repeated four times for each hole by rotating the sample 90° along its side, and the mean value of the four measurements was calculated through the Surfascan software for each stacked layer hole.

3.4.2.3 Hole dimensional feature measurement

In hybrid CFRP/Ti stack drilling, the accurancy of hole dimensional features including hole diameter and roundness error is usually a fundamental requirement for the drilled holes in order to ensure tight assembly of the stacked composite. In this study, the hole dimensional features were examined by using the Mitutoyo BHN506 Coordinate Measuring Machine (CMM) with a steel-made ruby roll of 1 mm tip radius (type A-5000-7806). Since the two stacked phases exhibit disparate thermal expansion coefficients (TECs) and elastic moduli, the diameter (Φ) measurement was made on each individual layer. For each stacked phase, two measurements were done on the hole sides with 1 mm from hole onset and 1 mm from hole exit, which were respectively marked as Φ_o and Φ_e.

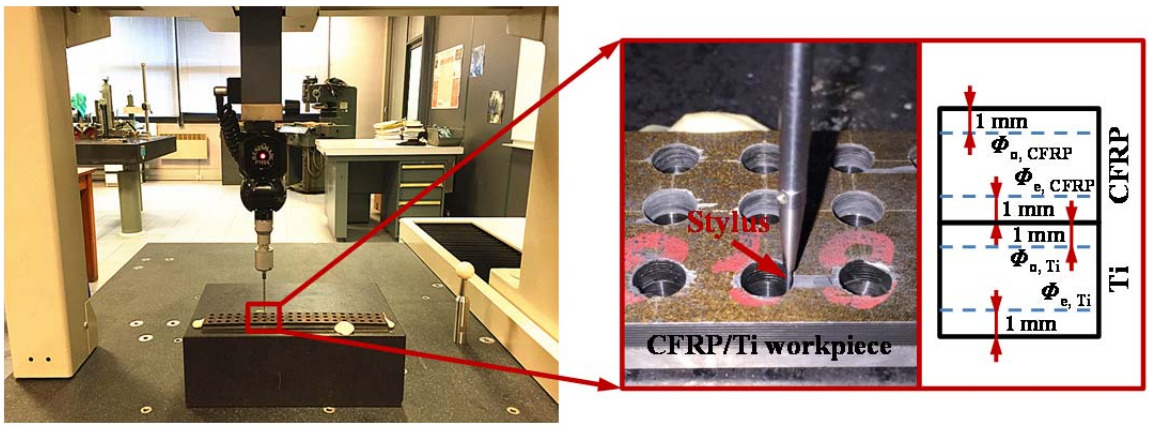

Figure 3.10. Photograph showing the process setup of hole dimensional feature measurement.

For each Φ measurement, the stylus was automatically placed on 8 points evenly distributed (with intersection radian of $\pi/4$) on the circumference of the treated hole side and then defined their corresponding coordinate positions. Afterward, a built-in software (Metrosoft Quartis R11, Wenzel, Germany) was used to transfer the collected coordinate position data from the stylus to the PC and finalize the measurement. A scheme of the hole diameter measurement is also shown in Fig.3.10.

3.4.2.4 SEM and EDS techniques

The SEM and EDS techniques applied in the present experimental studies aims to reveal the activated mechanisms controlling the CFRP/Ti subsurface damage formation, the resected chip morphology and the tool wear progression. A scanning electron microscope (SEM) - model JSM-5510LV, manufactured by JEOL company was utilized to capture the micrographs of the examined work-tool surfaces at a low vacuum mode. The basic specifications of the JSM SEM equipment are defined as follows: magnification of × 18 to × 300, 000; modes of operation: HV

(high vacuum) and LV (low vacuum) and accelerating voltage: 0.5 to 30 kV. Besides, several energy-dispersive X-ray spectroscopy (EDS) studies were also performed to facilitate the chemical element analysis of the worn tool surface and the machined work surface. The EDS analysis was carried out by using the JSM-5510LV type SEM equipped with an energy-dispersive X-ray spectrometer (EDS, JEOL (EUROPE) SAS, Paris, France) in correlation with measurements obtained with an optical profilometer. Fig. 3.11 then presents the photograph of the used SEM and EDS equipment.

Moreover, it should be noted that the key applications of the SEM and EDS analyses aim to (*i*) observe the machined CFRP/Ti surface and (*ii*) inspect the worn tool surface morphology. For workpiece surface analyses, the CFRP/Ti surface morphologies before and after cutting were both recorded in order to complete a comparative study. Besides, since the CFRP phase exhibits low conductivity (unlike the Ti alloy sample), the spraying gold treatment on the CFRP fresh/machined surfaces was also conducted in order to improve the imaging quality. With respect to the tool worn surface inspection, all the examined tool worn surfaces were cleaned by using acetone cleaning treatment prior to the SEM shooting. The SEM analyses were preformed on both tool rake and flank surfaces with a particular emphasis on the main cutting edges.

Figure 3.11. Photograph showing the used JSM-5510LV type scanning electron microscope (SEM).

3.5 Experimental setup and cutting design

To comprehensively investigate the fundamental cutting physics controlling hybrid CFRP/Ti stack machining, the orthogonal cutting, combined CFRP/Ti machining and hole drilling were all performed with respect to different cutting conditions or cutting-sequence strategies. Since the CFRP-phase cutting and Ti-phase cutting require different optimal ranges of cutting parameters due to their disparate machinability behaviors, the used cutting parameters (cutting speed (v_c) and feed rate (f)) were adopted based on a compromise parametric selection. The following subsections then illustrate the detailed procedures employed in each configuration of CFRP/Ti machining.

3.5.1 Orthogonal cutting and combined CFRP/Ti machining setup

The orthogonal cutting and combined CFRP/Ti machining were all conducted on a GSP - EL 136 Shaper machine with maximum power of 5, 222 W, maximum stroke of 650 mm and maximum

speed of 100 m/min. For orthogonal cutting operation, the workpiece types 1, 2 and 3 with respect to three fiber orientations of 0°, 45° and 90° were selected for the trimming trials as discussed in subsection 3.2. For combined CFRP/Ti machining, the workpiece types 4, 5 and 6 in terms of 0°, 45° and 90° fiber orientations were utilized. With respect to the used cutting tools, the PCD tipped insert as illustrated in subsection 3.3, was adopted for orthogonal cutting trials while tools A, B, C and D were selected for combined CFRP/Ti machining. The used tools all have the identical geometrical angles (*i.e.*, α = 0° and γ = 7°), and the detailed tool material composition can be found in subsection 3.3. In addition, the tool holder used for mounting the inserts was STFCR 2525 M 16-4 (ISO) Sandvik model.

The tests were performed under dry cutting conditions. The CFRP/Ti specimens were clamped manually inside the machine bearing, on the top of the dynamometer, between two hard steel plates. The tool cutting direction was made through the X-axis direction of the Shaper machine tool. During the edge trimming process (*i.e.*, both orthogonal cutting and combined bi-material machining), the Kistler dynamometer (type 9255B) and CCD camera (FASTCAM SA5 model) were all used to measure the force generation and record the chip separation process, respectively. Fig. 3.12 then shows the experimental setup for orthogonal cutting of hybrid CFRP/Ti stacks.

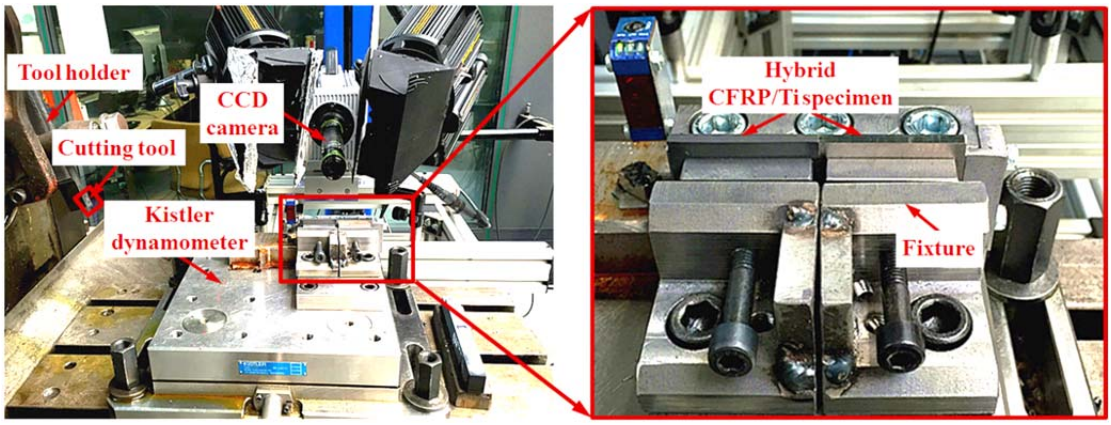

Figure 3.12. Experimental setup for orthogonal cutting of hybrid CFRP/Ti stacks.

Table 3.10
Summary of the used cutting conditions for both orthogonal cutting and combined CFRP/Ti machining.

Orthogonal cutting				
Cutting speed, v_c (m/min)	Feed rate, f (mm/rev)	Fiber orientation (θ)	Cutting sequence	Cutting tool
20, 32, 50, 80	0.05, 0.10, 0.15, 0.20	0°, 45°, 90°, 135°	CFRP → Ti Ti → CFRP	PCD

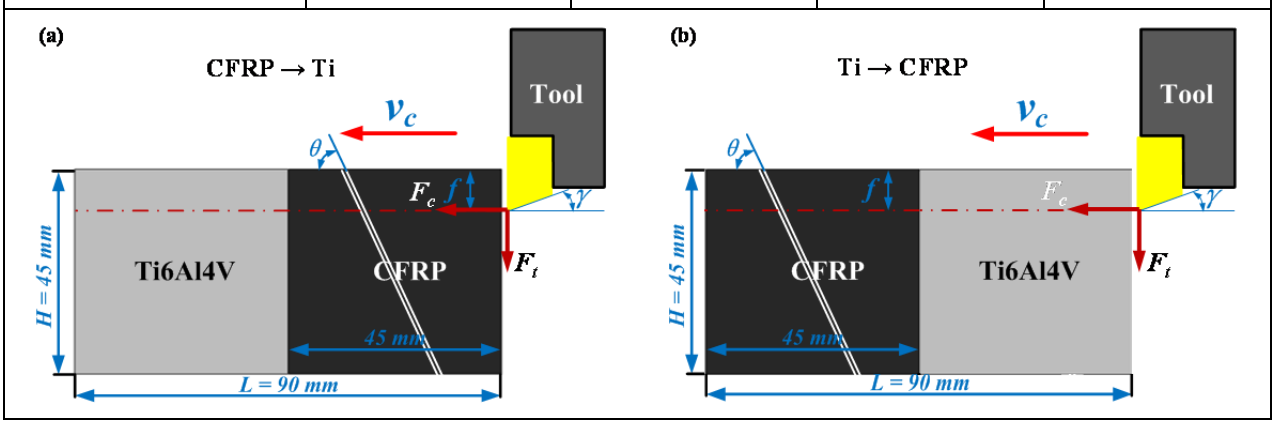

Combined CFRP/Ti machining				
Cutting speed, v_c (m/min)	Feed rate, f (mm/rev)	Fiber orientation (θ)	Cutting sequence	Cutting tool
20, 32, 50, 80	0.05, 0.10, 0.15, 0.20	0°, 45°, 90°	N/A	Tools A - D

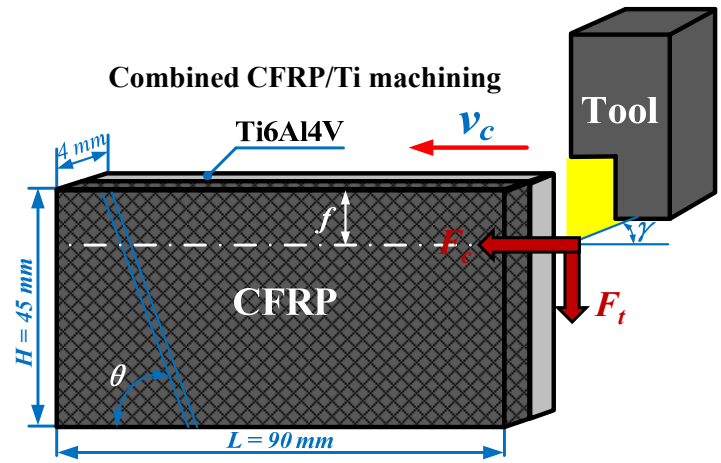

In addition, as the utilized cutting parameters usually play a significant role in affecting the cutting mechanism investigation during the defined machining configurations, a careful selection is of great importance. Since the CFRP-phase cutting and Ti-phase cutting exhibit different machinability behaviors, a compromise parametric selection was thereby adopted. Table 3.10 also shows the definition of used cutting variables and the selected parametric values for both orthogonal cutting and combined CFRP/Ti machining. Note that in the orthogonal cutting trials, the different cutting-sequence strategies ($^{\text{CFRP} \rightarrow \text{Ti}}_{\text{Ti} \rightarrow \text{CFRP}}$) were considered.

3.5.2 Experimental setup for hole drilling

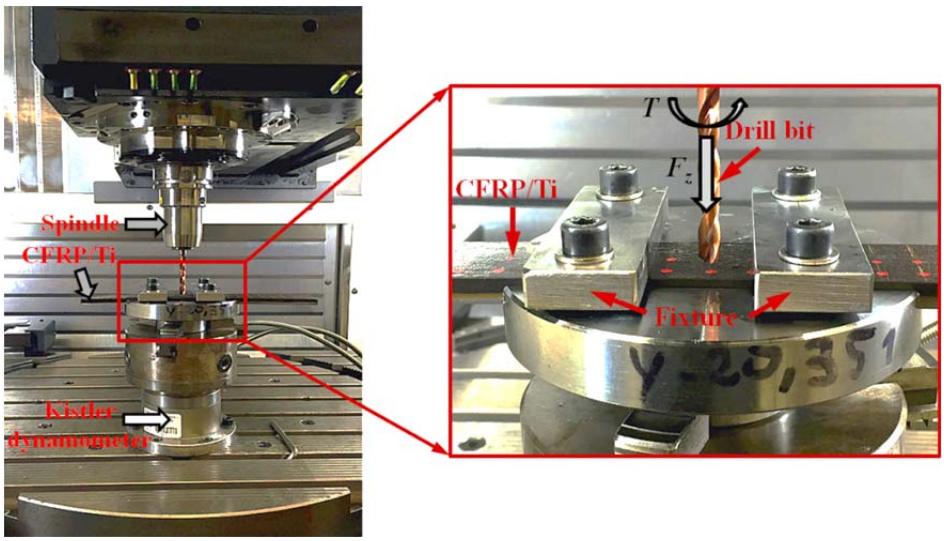

Figure 3.13. Experimental setup for drilling hybrid CFRP/Ti stacks (CFRP → Ti drilling sequence).

The drilling trials were performed on a high speed, five-axis CNC machining center DMU 60 monoBLOCK under the dry cutting conditions, as shown in Fig.3.13. The workpiece type 7 fabricated with the dimension of 254 mm × 34.5 mm × 8 mm was adopted for the drilling tests.

Both drill A and drill B as designated in subsection 3.3 were utilized to finalize the drilling operations. The detailed drill geometrical angles and their deposited coating types can be found in Table 3.6 and Table 3.7, respectively. Moreover, a piezoelectric Kistler dynamometer (type 9271A) was also employed to measure the drilling force generation. A fixture was utilized to clamp the CFRP/Ti plate from the top side during drilling. The entire fixture was then firmly mounted on the drilling dynamometer for measuring the generated thrust force and torque signals. A multichannel charge amplifier (type 5019A130) connected to a data acquisition board was used to convert the drilling signals into voltage signals. Afterward, the LabVIEW Signal Express software (National Instruments, USA) was employed to plot the recorded data and calculate the average values of the force signals. The used cutting conditions for drilling hybrid CFRP/Ti stacks are summarized in Table 3.11 with respect to the adopted cutting-sequence strategies and used drill bits.

3.6 Conclusions

This Chapter provides the description of the used measuring systems, the adopted experimental techniques, and the defined trial setup for the arrangement of hybrid CFRP/Ti stack machining. The used work-tool configuration, the employed cutting conditions as well as the detailed experimental procedures are precisely elaborated. In sum, the entire experimental investigations governing the hybrid CFRP/Ti machining primarily comprise the following three parts: (*i*) orthogonal cutting, (*ii*) combined bi-material machining and (*iii*) hole drilling. Moreover, the key objectives to be achieved during each type of cutting configurations are also summarized as follows.

- Orthogonal cutting: (*i*) records the dynamic cutting process and chip separation mode, (*ii*) clarifies the different cutting sequences' influences and parametric effects on force generation, induced subsurface damage formation, machined surface morphology, *etc*., and (*iii*) reveals the tool wear mechanisms and failure modes controlling orthogonal cutting operation.
- Combined bi-material machining: (*i*) captures the dynamic chip removal process, and (*ii*) investigates the parametric effects on force generation, machined surface morphology, *etc*.
- Drilling operation: (*i*) clarifies the tool-work interaction and machinability classification dominating hybrid CFRP/Ti stack drilling, (*ii*) inspects the different cutting sequences' influences on various hybrid CFRP/Ti drilling responses including hole diameter, hole surface roughness, hole damage extent, and (*iii*) evaluates the tool performances of different tool geometries/materials in drilling hybrid CFRP/Ti stacks.

Table 3.11
Summary of the test number and used cutting conditions for hybrid CFRP/Ti stack drilling.

Drilling trial				
Test No.	**Cutting speed, v_c (m/min)**	**Spindle speed, n (rpm)**	**Feed rate, f (mm/rev)**	**Cutting sequence and drill bit**
1 - 5	15	752	0.03, 0.06 0.09, 0.12 and 0.15	CFRP → Ti (Φ 6.35 mm) Drill A and drill B
6 - 10	30	1504		
11 - 15	45	2256		
16 - 20	60	3008		

1 - 5	15	752	0.03, 0.06 0.09, 0.12 and 0.15	Ti → CFRP (*Φ* 6.35 mm) Drill B (TiAlN coating)
6 - 10	30	1504		
11 - 15	45	2256		
16 - 20	60	3008		

Scheme of the drilled hole distribution in the hybrid CFRP/Ti specimen

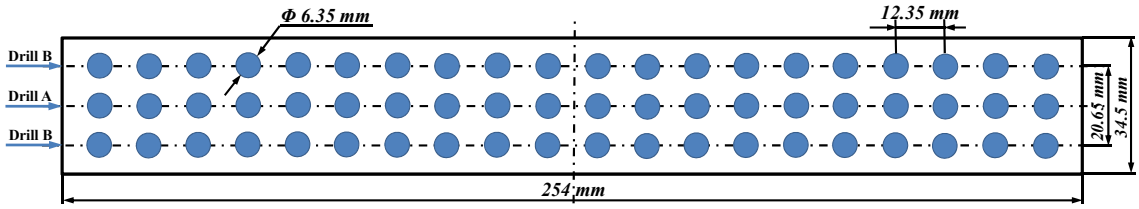

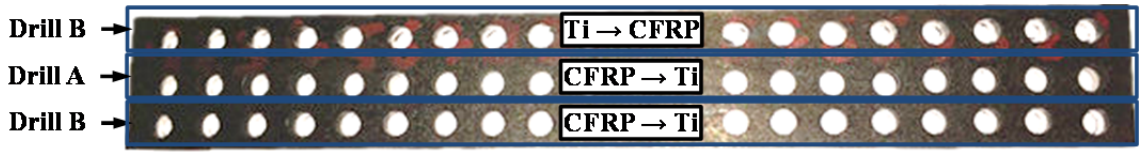

Chapter IV

Numerical results and FE analyses: fundamental mechanisms and key phenomena controlling hybrid CFRP/Ti stack machining

Nomenclature

a_c	Cutting depth
CFRP → Ti	Cutting-sequence strategy from CFPR phase to Ti phase
$\substack{\text{CFRP} \rightarrow \text{Ti} \\ \text{Ti} \rightarrow \text{CFRP}}$	Cutting from CFRP → Ti and/or Ti → CFRP
D_{CFRP}	Composite-phase damage extent
D_{del}	Interface delamination extent
f	Feed rate
F_c	Main cutting force
$F_{c,\ CFRP}$	Main cutting force of CFRP-phase cutting
$F_{c,\ Ti}$	Main cutting force of Ti-phase cutting
N	Number of sampling nodes
R_a	Arithmetic mean roughness
r_ε	Tool edge radius
Ti → CFRP	Cutting-sequence strategy from Ti phase to CFRP phase
u	Specific cutting energy
$\bar{u}$	Equivalent specific cutting energy
v_c	Cutting speed
w	Cutting width
X	Nominal machined surface height
X_i	Real machined surface height
α	Tool rake angle
γ	Tool clearance angle
θ	Fiber orientation
μ	Friction coefficient of the multi-tool-work interaction

Abbreviation

AIZ	Affected interface zone
M_{CFRP}	Machinability of pure CFRP-phase cutting
$M_{\text{CFRP/Ti}}$	Machinability of stacked CFRP/Ti composite
M_{Ti}	Machinability of pure Ti-phase cutting
OCC	Orthogonal cutting configuration

4.1 Introduction

The Chapter IV was dedicated to revealing the key mechanisms and physical phenomena controlling hybrid CFRP/Ti machining by considering various cutting conditions utilized including cutting parameters (v_c and f), fiber orientation (θ), cutting sequence strategy ($^{\text{CFRP} \rightarrow \text{Ti}}_{\text{Ti} \rightarrow \text{CFRP}}$), *etc*. As discussed in Chapter I, several physical mysteries involved in hybrid CFRP/Ti machining still remain unknown in the pertinent research fields. To improve the cutting comprehension of the bi-material system, the key objective of current work is to numerically investigate (*i*) the key mechanisms dominating interface cutting and subsequent damage formation, (*ii*) the influences of different cutting-sequence strategies on hybrid CFRP/Ti machining, (*iii*) the parametric effects on hybrid CFRP/Ti cutting operation, and (*iv*) the frictional responses governing the bi-material removal process. The key structure of the present chapter was organized as follows.

- First and foremost, the cutting mechanisms and parametric effects controlling interface machining and induced interface delamination formation were studied.
- Afterward, the influences of different cutting-sequence strategies ($^{\text{CFRP} \rightarrow \text{Ti}}_{\text{Ti} \rightarrow \text{CFRP}}$) on the various cutting responses of hybrid CFRP/Ti stacks including chip removal process, machined surface morphology, and induced damage extent were precisely investigated.
- Moreover, the effects of different input cutting parameters including cutting speed (v_c), feed rate (f), and fiber orientation (θ) on various CFRP/Ti cutting responses were inspected.
- Finally, the frictional behavior of the multi-tool-work interactions controlling hybrid CFRP/Ti machining was studied with respect to the specific cutting energy consumption, machined surface morphology, induced damage extent and surface integrity.

Besides, since the CFRP-phase cutting and Ti-phase cutting require different ranges of cutting parameters due to their dissimilar machinability behaviors [43, 45, 67], the used cutting parameters (v_c and f) were adopted based on a compromise parametric selection. During the numerical studies, several comparisons between simulated results and experimental data from the open literature were performed in order to validate the credibility of the established FE models.

4.2 Key mechanism dominating interface cutting

In hybrid CFRP/Ti stack machining, three cutting stages are usually involved, *i.e.,* Ti-phase cutting, interface cutting, and CFRP-phase cutting. Among them, the interface region (aka the "Ti-to-CFRP" contact boundary) represents the most difficult-to-cut zone as compared to the Ti-phase cutting and CFRP-phase cutting due to the existence of changeable chip-separation modes. The interface is often characterized as a physically intermediate transition zone that really exists in the CFRP/Ti cutting operation. In CFRP/Ti machining, the interface region experiences interrelated cutting behaviors controlling the chip removal process. Despite its great importance, research studies concerning the interface cutting are still significantly lacked. Several cutting phenomena still remain misunderstood including (*i*) the key mechanisms dominating the interface delamination formation, (*ii*) the parametric effects on induced interface damage extent, and (*iii*) the machinability classification of hybrid CFRP/Ti stacks, *i.e.*, which region cutting actually reflects the machinability

of pure Ti-phase cutting (M_{Ti}), stacked material cutting ($M_{CFRP/Ti}$), and pure CFRP-phase cutting (M_{CFRP}), respectively. Moreover, considering the high cost of conventional experimental studies, the numerical investigations of the key physical phenomena in interface machining were firstly presented.

4.2.1 Cutting process investigation

Machining hybrid CFRP/Ti stacks is quite different from standard-composite and single-metal cutting cases due to the multi-tool-work interaction domains. The disparate natures of each constituent make the chip separation modes more interrelated and coupled governing the bi-material interface machining [4]. The interface cutting commonly experiences changeable chip-separation modes and severe transitions of thermal/mechanical responses (*e.g.*, force generation, cutting temperature, strain/stress flow). To reveal the key phenomena controlling CFRP/Ti cutting, the evolution of force generation in function of cutting time and chip formation under fixed cutting conditions of $v_c = 40$ m/min, $f = 0.2$ mm/rev and $\theta = 0°$ is presented in Fig.4.1. The force generation in CFRP/Ti cutting was decomposed into two components, *i.e.*, the cutting-force component (F_c) and the thrust force component (F_t), which signify the tribological interactions between tool rake and chip surfaces, tool flank and machined surfaces, respectively. It is noticeable that the entire hybrid CFRP/Ti cutting operation can be distinguished by seven minor regions (regions 1-7) from the force signal variation as depicted in Fig. 4.1 (a).

- Region $a \rightarrow b$ denotes the period when the cutting tool firstly penetrates into the Ti phase. During this period, the onset of tool-Ti interaction takes place and the cutting force is predicted to increase gradually from zero.
- Region $b \rightarrow c$ signifies the steady cutting duration of Ti-phase machining. The force generation is estimated to reach a steady variation state.
- Region $c \rightarrow d$ represents the period when the cutting edges gradually cut off the Ti phase. In such duration, the cutting force is found to decrease gradually due to the exit of the tool-Ti interaction controlling the chip removal process.
- Region $d \rightarrow e$ implies the period of cutting edge involved in the CFRP/Ti interface machining. The pure tool-Ti interaction has been transformed into the multi-tool-work interaction. The quick force signal variation signifies the quick transition zone of the interface cutting.
- Region $e \rightarrow f$ indicates that the cutting edge has gradually cut into the CFRP phase. Previous multi-tool-work interaction is eventually transformed into final tool-CFRP interaction.
- Region $f \rightarrow g$ demonstrates the pure tool-CFRP interaction dominating the steady-cutting state of CFRP phase.
- Region $g \rightarrow h$ entails the period that the cutting edge gradually finalizes the CFRP phase machining. The cutting force is observed to experience an abnormal increase due to the spring-back effects of the CFRP phase.

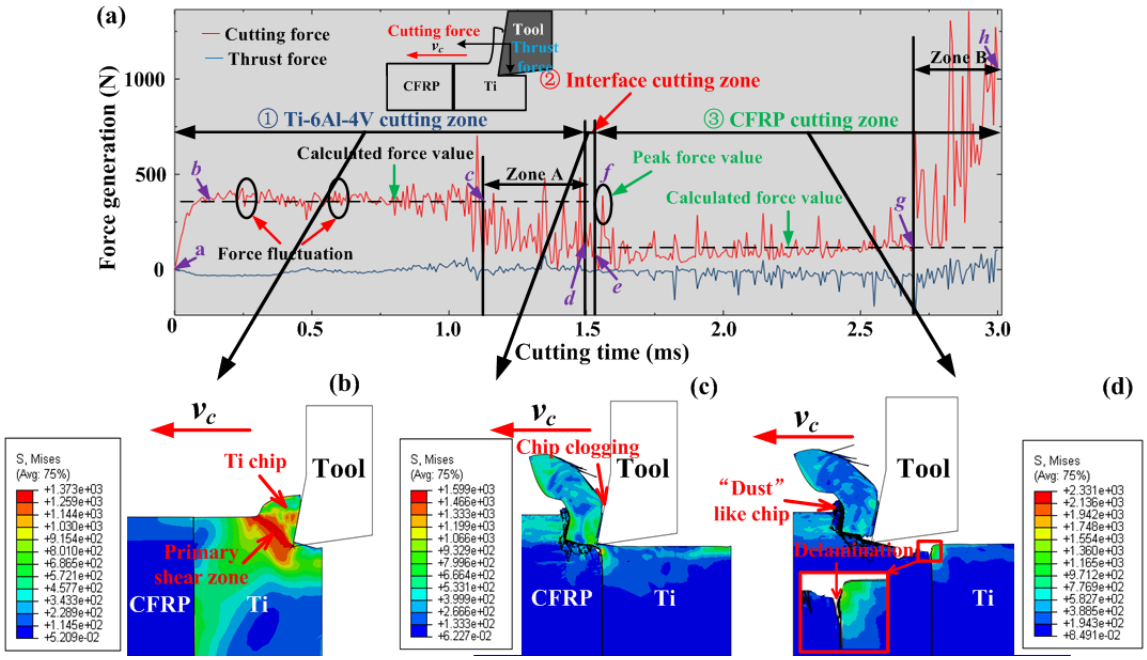

Figure 4.1. Typical representation of the force signal and chip removal process *versus* cutting time in CFRP/Ti machining: (a) force signal in terms of cutting time, (b) Ti-phase cutting, (c) interface cutting, and (d) CFRP-phase cutting (v_c = 40 m/min, f = 0.2 mm/rev and θ = 0°).

In addition, as shown in Fig.4.1 (b), when the tool edge initially cuts into the Ti phase, the material separation occurs through an elastic-plastic deformation mode that controls the tool-Ti interaction area. The shearing actions arising from the thermo-mechanical coupled effects produce "continuous" chip morphology that flows on the tool rake face. It should be noted that the Ti-chip morphology shows a strong sensitivity to the input factors including cutting parameters and tool geometries during machining. Since very low cutting speed and positive tool rake angle are used in current simulation case, the resected chip shape exhibits a more "continuous" feature rather than "serrated" appearance. Under the fixed cutting conditions, the machining operation gradually achieves a steady state for which the force generation approximately attains a stable variation condition. Besides, despite the steady cutting process reached, the high-frequency force fluctuation is also prevalent in the Ti-phase cutting as described in Fig.4.1(a). The force generation usually signifies the mechanical-energy consumption of tool-work interactions in cutting and presents a close relation with the inherent properties of studied work materials. Since the Ti alloy exhibits ductile behavior and low thermal conductivity, the chip separation typically involves serious thermo-plastic instability and shear localization in the primary cutting zone. Such phenomenon will promote a quick occurrence of crack initiation and progression dominating the active cutting zones and result in the instability of the tool-work interaction controlling the chip removal process, as reflected in the cyclic force fluctuations. In addition, when cutting time (t) approximately exceeds 1.0 ms, the cutting-force component is observed to suffer a gradual reduction. The physical phenomenon can be explained by the decreased uncut Ti chip thickness contributing to the reduction of force resistance when the tool tends to finalize the Ti-phase cutting. With the tool advancement, especially when the cutting edge cuts into the interface region, the previously resected Ti chip adheres on tool rake face and substitutes the tool edge for further chip separation. Owing to the transition from tool-Ti interaction to tool-CFRP interaction, the cutting force magnitudes undergo a quick drop throughout the interface cutting. In such circumstance, the chip

separation mode is transformed gradually from plastic deformation to brittle fracture, which inevitably results in the serious transfer of mechanical/physical loads exerted on the tool-work system. The harsh cutting conditions dominating CFRP/Ti interface cutting will be the key contributor that promotes the severe damage formation in the bi-material interface.

With further cutting progression, the tool tip completely cuts across the interface region and induces a large extent of delamination damage on the interface area as shown in the magnified view of Fig.4.1 (d). When the tool penetrates into the CFRP phase, the material removal takes place through successive ruptures aided by diverse nature and uneven load sharing among fiber/matrix systems. Since brittle fracture operates as the predominant cutting mode, the resected chip morphology is produced in the form of "discontinuous" shape (especially "dust"-like appearance), as illustrated in Fig.4.1 (d). Concerning the force generation, both cutting force and thrust force signals are predicted to undergo severe fluctuations and high-frequency variations. However, the mechanisms leading to the physical phenomena are disparate. For the cutting force variation, it is induced due to the crack initiation and evolution governing the chip separation process. By contrast, the thrust force fluctuation is mainly attributed to the intense bouncing-back effects on tool flank surface arising from the released carbon fibers in the machined CFRP surface [184].

Moreover, when cutting tool is about to finish the cutting process, a significant increase of cutting force becomes pronounced as shown in Fig.4.1 (a). The abnormal phenomenon can be explained as follows. When the tool cuts into the CFRP phase, the Ti chips adhere on tool rake face and substitute the cutting edge for further chip separation. In addition, the produced "dust"-like composite chips also cause serious clogging on ahead of Ti chips. Owing to these phenomena, the accumulated chip volume will inevitably lead to the dramatic rise of the cutting resistance, and hence the higher cutting force generation.

4.2.2 Mechanisms of interface damage formation

In CFRP/Ti cutting, the interface region usually experiences tremendous mechanical/thermal energy transfer arising from the disparate phase machining. The interrelated chip separation modes and mixed machining responses are the key characteristics of interface cutting. As such, the machinability of the interface zone plays a significant role in affecting the final subsurface damage formation of the "CFRP-to-Ti" contact boundary. In spite of its importance, nearly rare existing work has been reported to address this issue. To reveal the complicated mechanisms controlling interface machining, the chip removal process in terms of cutting time was firstly investigated under the fixed cutting conditions of $v_c = 40$ m/min, $f = 0.2$ mm/rev, and $\theta = 0°$, as presented in Table 4.1 [4].

It can be drawn that typically four stages can be drawn from the interface damage progression. As the tool edge is fully involved in the Ti-phase cutting (probably at the machining time of $t = 0.9$ ms), the produced Ti chip curles down toward the interface region above the trim plane with the facilitation of tool movement, as shown in the stage I of Table 4.1. Afterward, the affected interface region tends to bend and dump toward the joint CFRP surface accompanied by penetration into the fiber/matrix substrate. As the tool further advances, the Ti chips gradually cut into the CFRP layer and replace the machining action of the tool edge for uncut chip removal. In such case, the initial crack is motivated adjacent to the bi-material interface beneath the trim plane with the maximum-stress concentration.

The crack damage seems to extend and propagate toward the CFRP phase that deviates from the crack tip. More importantly, when cutting time reaches 1.47 ms, the crack trajectory focuses more on the tool cutting direction accompanied by quick damage evolution and progression whereas deviates far from the Ti phase boundary. Such phenomenon inevitably gives rise to the so-called "delamination" damage. Finally, when the tool tip completely cut through the interface region, both delamination lengths in cutting-speed direction (X-direction) and through-thickness direction (Y-direction) attain steady values as depicted in the stage IV of Table 4.1.

Table 4.1
Mechanisms of CFRP/Ti interface damage formation (v_c = 40 m/min, f = 0.2 mm/rev and θ = 0°) [4].

Stage I
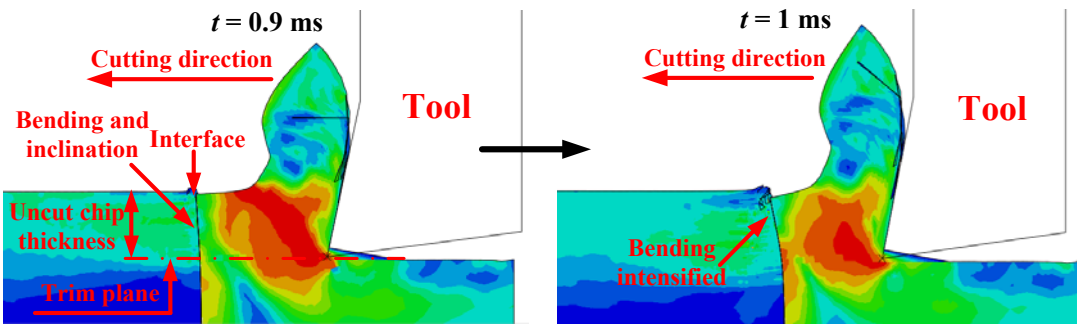
• Interface region above the trim plane (inside the uncut chip thickness) suffers severe extrusions from joint Ti chip required to be cut off. • The affected interface region tends to bend and dump toward the joint CFRP layer surface accompanied by penetrations into its substrate.
Stage II
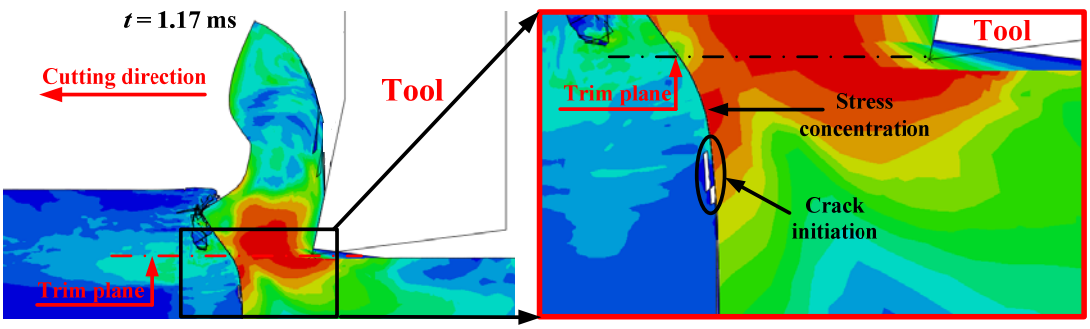
• An initial crack is motivated at the vicinity of the interface region beneath the trim plane with a maximum-stress concentration. • The crack damage seems to propagate toward the CFRP phase deviating far from the crack tip.
Stage III

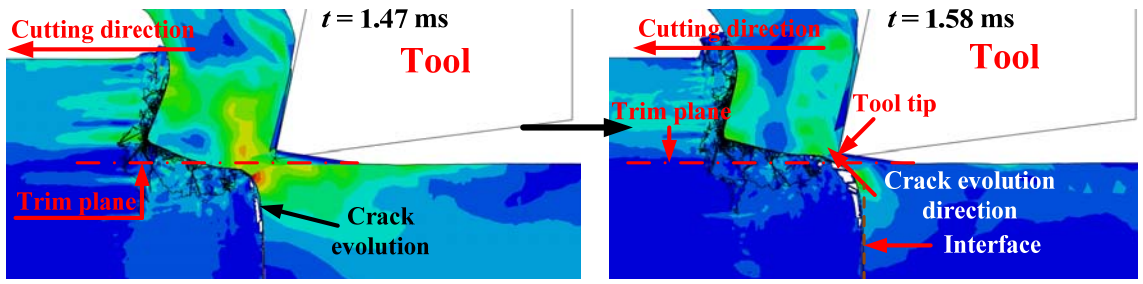

- With further tool advancement, the crack trajectory experiences a quick damage evolution toward the tool cutting direction while deviates far away from the Ti phase boundary.
- The key manifestations are severe delamination extent and increased tearing in the cutting-speed direction.

Stage IV

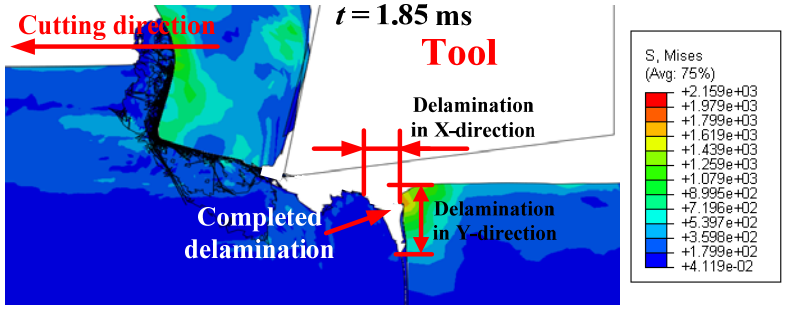

- As the tool tip completely cuts through the Ti/CFRP interface, the delamination lengths in cutting direction and through-thickness direction reach stable values.
- A "V shape"-like notch is ultimately formed along the bi-material interface region.

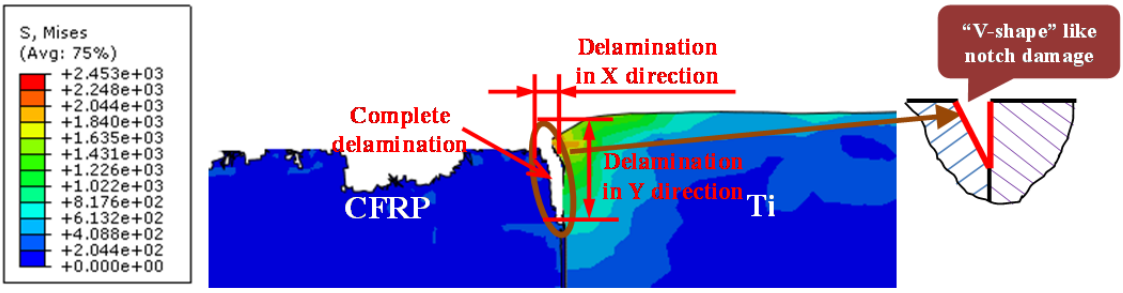

Figure 4.2. FE observation of interface damage when cutting hybrid CFRP/Ti stacks ($v_c = 40$ m/min, $f = 0.2$ mm/rev and $\theta = 0°$).

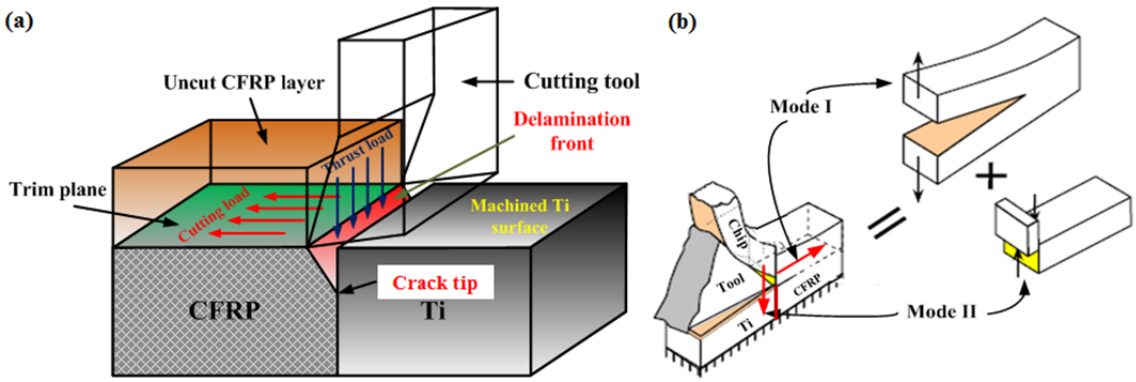

Figure 4.3. Schematization of (a) the crack path occurring in interface region when machining hybrid CFRP/Ti stacks and (b) fracture modes I and II dominating the cutting operation.

Moreover, as shown in Fig. 4.2, the key manifestation of the interface damage is a "V shape"-like notch damage on the "CFRP-to-Ti" contact boundary. A large extent of delamination damage becomes pronounced in both tool-cutting direction (X-direction) and through-thickness direction (Y-direction) as depicted in Fig.4.2. However, the key manifestation is the severe tearing in the CFRP-phase boundary deviating far from the Ti-phase boundary. The physical phenomena demonstrate that the crack trajectory should experience a quick damage evolution concerning the tool cutting direction during the machining process. The key mechanisms controlling the crack trajectory and evolution in the bi-material interface are strongly influenced by two important factors. The first is the relative fracture toughness arising from the stacked constituents of the bi-material system. It is believed that the crack path prefers to take place toward the brittler constituent characterized by lower fracture toughness since it needs less energy to open and propagate the crack damage [178, 193, 194]. In such case, the preferred crack path occurring in CFRP/Ti interface should exhibit more approximation to the CFRP-phase boundary due to its relatively lower fracture toughness as compared to its counterpart [165]. Another factor is the specific fracture mode encountered along the bi-material interface. Fig.4.3 shows the scheme of the crack path and fracture modes I and II in cutting. It can be seen that when the tool edge completely passes through the Ti-phase boundary, the load path promoted in the bi-material system is uniquely applied on the uncut CFRP and interface layers while the machined Ti-phase surface is deprived of load occupation. As such, the cutting load parallel to the tool cutting direction together with the thrust load perpendicular to the cutting direction will produce mixed damage modes (fracture modes I and II) concentrated on the interface region. Consequently, it results in a sole path evolution of crack trajectory approaching the cutting direction. This phenomenon inevitably gives rise to the so-called "delamination" damage.

To specify the dynamic process of delamination formation and also the affected interface zone (AIZ), 9 interface nodes beneath the trim plane are selected to characterize their X-direction displacement in terms of cutting time (t) as shown in Fig.4.4. Table 4.2 summarizes the depth beneath the trim plane of the selected interface nodes. The AIZ studied here is devoted to clarifying the actual cutting time that indeed influences the interface damage formation during the orthogonal cutting process.

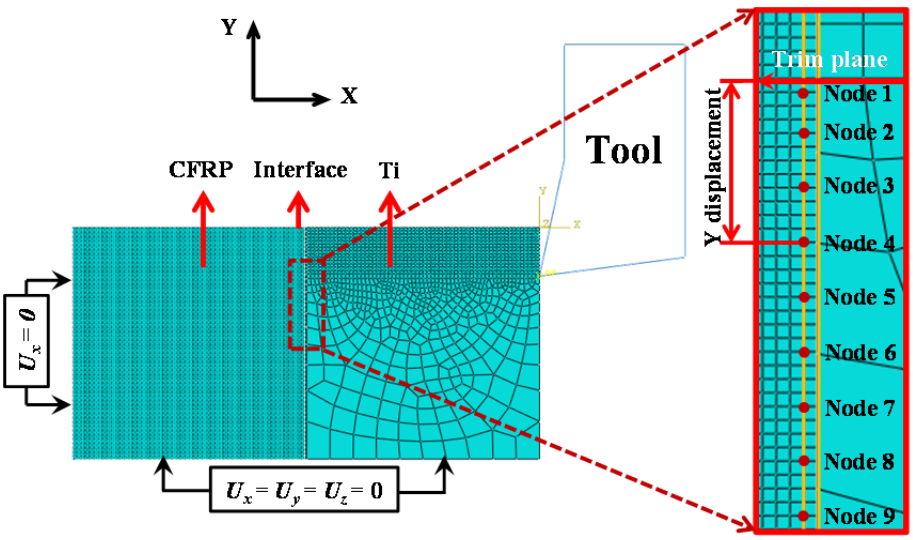

Figure 4.4. Scheme of selected interface nodes in CFRP/Ti model.

Table 4.2
Y-displacement from the trim plane of selected nodes in the interface zone.

No. of node	Depth beneath the trim plane (µm)	No. of node	Depth beneath the trim plane (µm)
1	5	2	20
3	40	4	60
5	80	6	100
7	120	8	140
9	160	—	

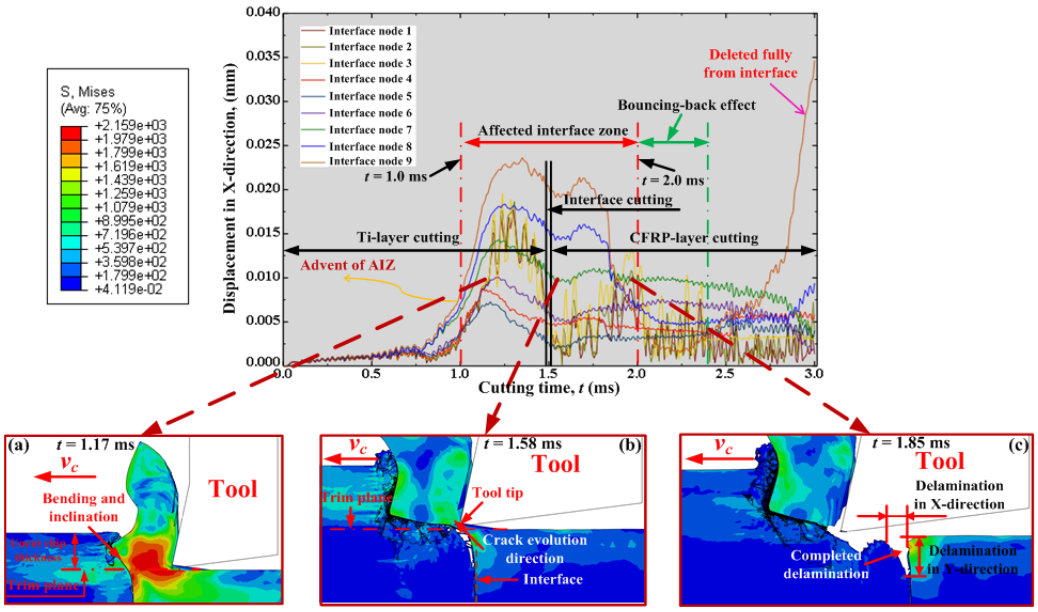

Figure 4.5. Displacement in the X-direction of selected interface nodes *versus* cutting time (t): (a) cutting process at t = 1.17 ms, (b) cutting process at t = 1.58 ms and (c) cutting process at t = 1.85 ms.

Fig.4.5 illustrates the X displacement evolution of the selected interface nodes with respect to cutting time (t) under the fixed cutting conditions of v_c = 40 m/min, f = 0.2 mm/rev and θ = 0°. It is apparent that the X displacements of selected interface nodes generally undergo three variation stages, *i.e.*, initial variation stage, rapid variation stage and steady variation stage during the total cutting duration (t = 3.0 ms). At the beginning of cutting, all the selected interface nodes are predicted to suffer a slow-rate displacement variation, which indicates that the chip removal process initially has slight/minor effects on the interface region. However, with the cutting progression, the machining operation gradually promotes significant influences on the output responses of interface region due to the fact that all the selected interface nodes begin to experience high-extent displacement fluctuations and quickly enter into the rapid variation stage. The physical phenomena are predicted to take place in the Ti-phase cutting period approximately at the cutting time of 1.0 ms. Such evidence signifies the advent of affected interface zone (AIZ) prior to the interface-cutting period as illustrated in Fig.4.5. The occurrence of AIZ commonly implies that the CFRP/Ti interface has suffered dramatic influences arising from the Ti-chip removal process. As depicted in Fig.4.5 (a), the produced Ti chip causes severe bending and inclination effects on the interface zone and also the uncut CFRP-chip layer. The pronounced displacement variation in AIZ strongly demonstrates the appearance of serious detaching and separation concerning the interface zone. In addition, the interface nodes located near the trim plane typically undergo larger X displacements as

compared to their counterparts far away from the trim plane. The reason may be caused due to the different levels of influences arising from the tool-work interactions. When cutting time approximately reaches 2.0 ms, the X displacements of selected interface nodes gradually achieve the steady variation state, indicating the diminishing trend of the cutting influences on interface region. For instance, as shown in Fig.4.5(c), the delamination lengths in X and Y directions reach their stable values. In such case, the AIZ can be defined probably at the duration of $t \in$ [1.0 ms, 2.0 ms]. As for the severe displacement fluctuation occurring in steady variation state, the reason may be induced due to the bouncing-back effects from adjacent CFRP elements still affected by the local cutting operation. At the end of the cutting process, all the selected interface nodes are about to attain the constant displacements in X direction except the interface node 1. The dramatic displacement increase of interface node 1 demonstrates that the node has been deleted completely from the interface zone.

To quantify the delamination extent occurring at the interface regime, three indicators, *i.e.*, D_X, D_Y and S_D are introduced for evaluation in this study, where D_X signifies the delamination length in tool-cutting direction (X-direction), D_Y denotes the delamination length in through-thickness direction (Y-direction) and S_D implies the delamination area of the damage zone as shown schematically in Fig.4.6. The delamination area (S_D) is defined as illustrated in Eq. (4.1).

$$S_D = 0.5 \times D_X \times D_Y \tag{4.1}$$

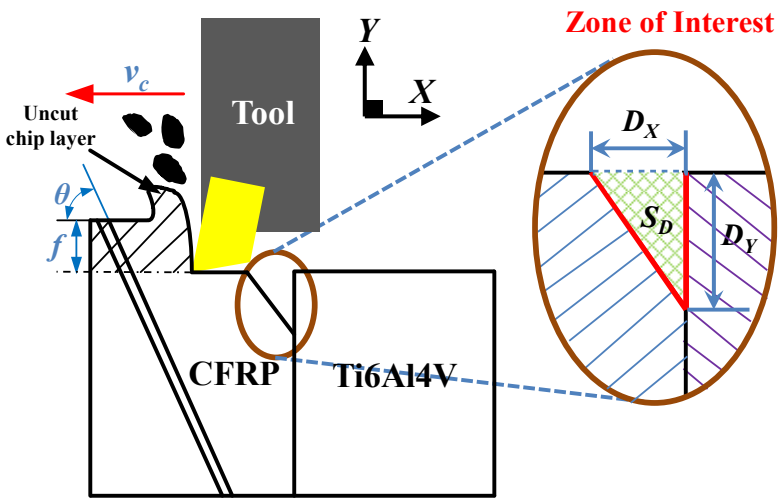

Figure 4.6. Scheme of delamination damage evaluation in CFRP/Ti cutting.

Fig.4.7 presents the evolution of interface delamination damage in terms of cutting time (t). The results confirm that all the delamination indicators (D_X, D_Y and S_D) exhibit the similar evolution trends as like the X displacements of selected interface nodes *versus* cutting time (t) in Fig.4.5. The comparison mutually demonstrates the reliability of the two numerical observations. Moreover, as depicted in Fig.4.7, from the geometrical consideration, the entire hybrid CFRP/Ti stack cutting can be divided into three stages referring to (*i*) Ti-phase cutting, (*ii*) interface cutting, and (*iii*) CFRP-phase cutting in terms of their respective cutting lengths. However, such category actually cannot reflect the real machining behavior of the bi-material system due to the ignorance of the interactive cutting influences arising from each-phase cutting. In reality, the entire CFRP/Ti cutting process can be divided into three basic zones based on the interactive influences of each phase machining.

(*i*) Pure Ti-phase cutting $t \in [0, 1.0 \text{ ms}] \rightarrow$ signifies the cutting period concerning the absolute Ti-phase machining with minimum influence affecting the CFRP/Ti interface and the CFRP zone. Such zone represents the machinability of the single Ti-alloy phase (M_{Ti}).

(*ii*) AIZ cutting $t \in [1.0, 2.0 \text{ ms}] \rightarrow$ denotes the cutting duration concerning the machining variation of the bi-material interface arising from Ti-phase cutting and CFRP-phase cutting. Moreover, the AIZ cutting zone in reality represents the real machinability of the stacked CFRP/Ti material ($M_{\text{CFRP/Ti}}$).

(*iii*) Pure CFRP-phase cutting $t \in [2.0, 3.0 \text{ ms}] \rightarrow$ implies the cutting time concerning the absolute CFRP-phase machining and reflects the machinability of the standard CFRP phase (M_{CFRP}).

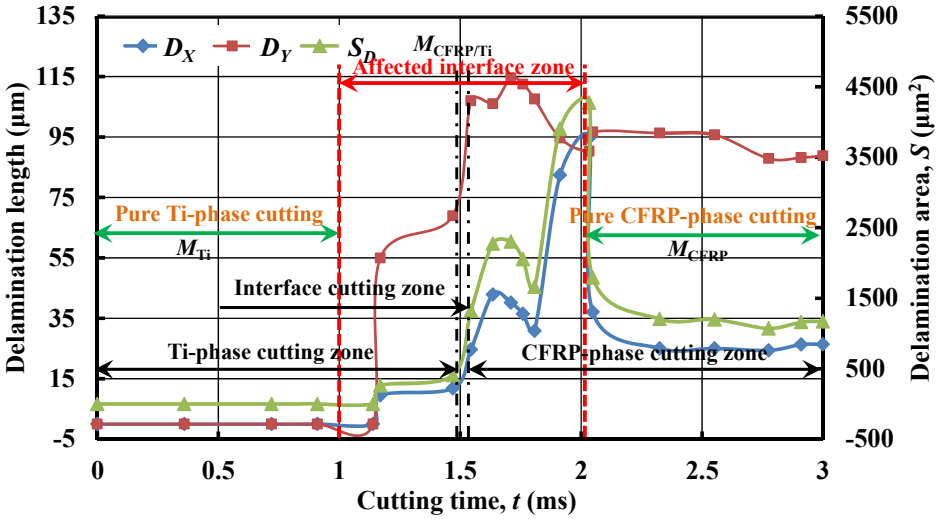

Figure 4.7. Evolution of delamination damage (D_X, D_Y and S_D) in function of cutting time (t).

During the pure Ti-phase cutting zone, all D_X, D_Y and S_D nearly remain the constant values (probably 0 values), indicating no delamination occurring in the interface zone. With the continuation of cutting process, especially when t reaches the AIZ, the three delamination indicators totally suffer a dramatic increase with elevated cutting time. Such phenomenon signifies that the delamination damage is primarly formed at the AIZ cutting period. Besides, the subsequent reduction of the delamination indicators in the AIZ may be caused due to the bouncing-back effects from adjacent CFRP elements affected by the cutting operation. Moreover, with further increased t, especially in the pure CFRP-phase cutting zone, D_X, D_Y and S_D gradually reach their steady values, which means that the post CFRP-phase cutting generates less effects on the interface delamination formation.

Moreover, to inspect the effects of input variables on the AIZ and also on the interface delamination extent, a parametric study is performed by considering various cutting speeds and feed rates. Figs.4.8 and 4.9 then present the acquired results. Note that in Fig.4.8, the symbol "**I**" indicates the cutting duration of AIZ and the interface delamination extent (D_{del}) is measured based on the D_Y length (delamination length in through-thickness direction (Y-direction)). As can be seen in Fig.4.8, both v_c and f are found to have significant effects on the AIZ cutting time. Specifically, v_c exhibits a negative impact on the AIZ cutting duration while the impact of f is positive. A parametric combination of high v_c and low f commonly results in a lowest AIZ cutting duration. Moreover, as evident in Fig.4.9, all the examined parametric variables show a pronounced influence on the interface delamination extent. The impact of v_c is found to be negative, *i.e.*, an increase of v_c results

in the reduction of D_{del}, while the impact of f is positive. The mechanisms controlling the variation phenomena can be ascribed to their specific influences on AIZ. This is because when v_c is elevated, typically a reduced cutting time of AIZ is achieved as illustrated in Fig.4.8. As such, the decreased AIZ will inevitably alleviate the damage extent of the induced interface delamination. In contrast, an increase of f usually leads to an increased AIZ (as depicted in Fig.4.8), and hence gives rise to a higher extent of interface delamination as shown in Fig.4.9(b). Therefore, through the above analyses, for minimizing the extent of interface delamination, high cutting speed and low feed rate should be strongly preferred.

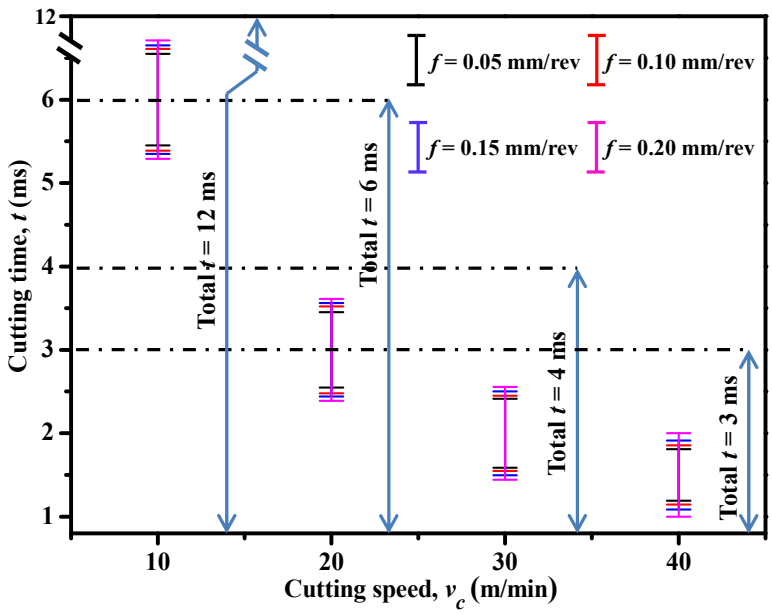

Figure 4.8. Effects of cutting speed (v_c) and feed rate (f) on cutting duration of AIZ (**Note:** "**I**" indicates the cutting duration of AIZ) ($\theta = 0°$).

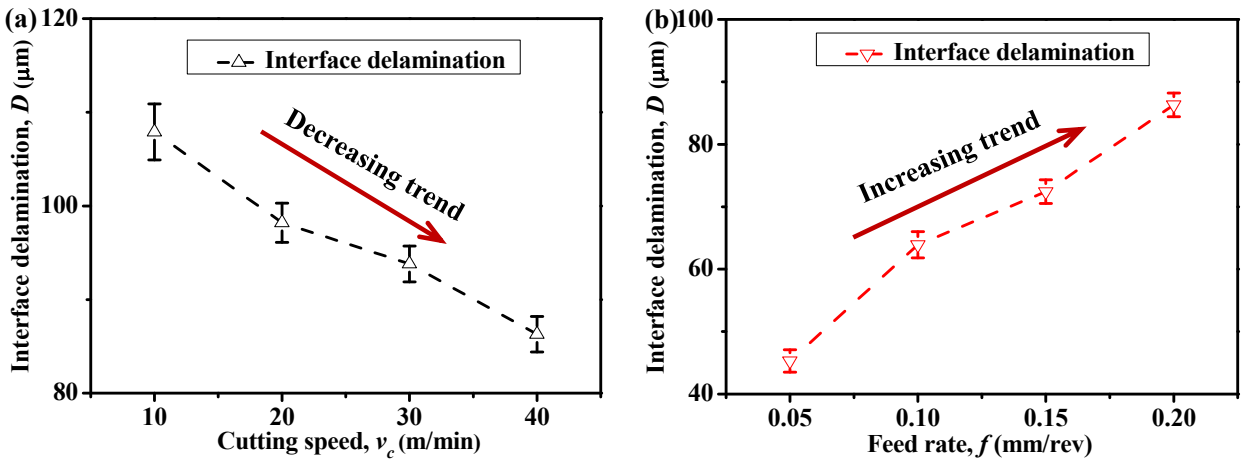

Figure 4.9. Interface delamination extent (D) in function of: (a) cutting speed (v_c) ($f = 0.2$ mm/rev and $\theta = 0°$) and (b) feed rate (f) ($v_c = 40$ m/min and $\theta = 0°$).

4.2.3 Subsurface damage study

Apart from the severe interface imperfection, the subsurface damage occurring in composite phase is also a particular concern when machining hybrid CFRP/Ti stacks. As discussed before, the composite-phase damage takes place following four types of fiber/matrix failure, *i.e.*, fiber

compression damage, fiber tensile damage, matrix compression damage and matrix tensile damage. To inspect the subsurface composite damage resulting from the CFRP/Ti cutting operation, a parametric analysis was performed. The fiber/matrix failure was measured as the largest distance from the machined CFRP surface to the deepest damaged area, as shown schematically in Fig.4.10. The fiber/matrix failure extent was predicted and studied *versus* fiber orientation (θ) under the fixed cutting conditions of v_c = 40 m/min and f = 0.2 mm/rev as depicted in Fig.4.11. It is noticeable that the fiber orientation (θ) exhibits a significant influence on the evolution of the various types of fiber/matrix damage during the chip removal process. The subsurface damage extent increases with elevated θ, especially the elevation becomes pronounced when θ beyond 60° as depicted in Fig.4.11. All the damage types tend to reach their maximum extents at θ = 90°. With further increasing fiber orientation, the subsurface damage seems to suffer a slight decrease. Such findings of the fiber orientation's effects on composite damage agree well with the observations of Arola et al. [168], Wang and Zhang [184] when cutting CFRP laminates. The mechanisms controlling the mentioned phenomena can be attributed to the change of failure modes from bending and crushing in case of θ = 0° to a fracture by compression and interfacial-shearing mode for positive fiber orientation (0° < θ ≤ 90°) [57, 60, 195], which inevitably leads to the in-depth fiber/matrix damage. For θ above 90°, chip-separation modes are transformed to be dominated by pressing, inter-laminar shearing, matrix cracking and fiber/matrix interface debonding. This evidence will result in less energy consumption for chip separation and lower cutting resistance encountered in machining. As a result, a lower extent of damage formation is promoted.

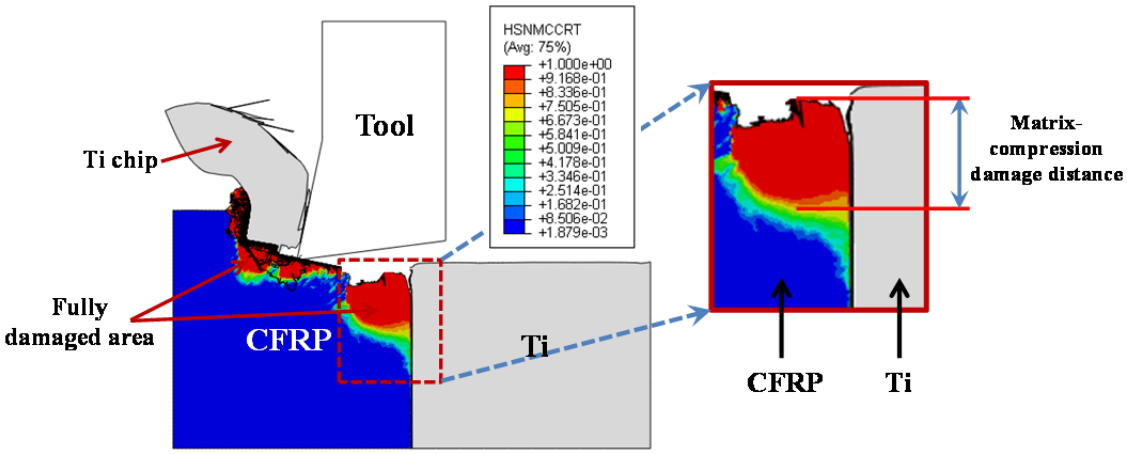

Figure 4.10. Scheme of the damage measurement in CFRP phase (**Note:** HSNMCCRT represents the matrix-compression failure mode).

In addition, Fig.4.12 also shows the parametric effects of v_c and f on the cutting-induced composite-phase damage. Note that the composite-phase damage (D_{CFRP}) was evaluated based on the type of fiber/matrix failure that causes the largest extent of damage (*e.g.*, as shown in Fig.4.11, matrix-compression damage causes the maximum damage extent). Afterward, D_{CFRP} was measured as the largest distance from the machined CFRP surface to the deepest damaged area. Each measurement was repeated three times in order to ensure the sufficient credibility of the acquired results. As shown in Fig.4.12, it is noticeable that f has a remarkable effect on the composite-phase damage in such manner that a small increase of f results in a dramatically elevated D_{CFRP}. In contrast, an increase of v_c typically leads to a direct reduction of D_{CFRP}. The phenomena imply that the use of high-speed cutting (HSC) may benefit the reduction of composite-phase damage

formation when machining hybrid CFRP/Ti stacks. Therefore, based on the above analyses, the optimum cutting parameters for composite damage minimization should consist of small fiber orientation, high cutting speed, and low feed rate when machining this bi-material system.

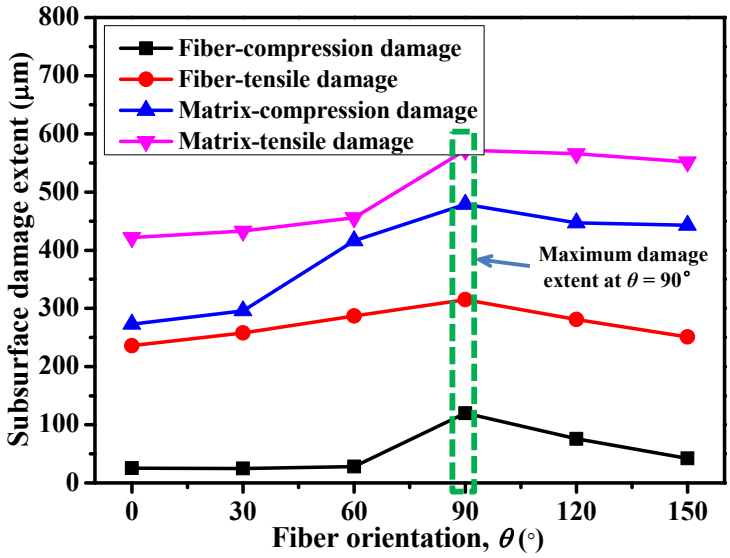

Figure 4.11. Fiber/matrix damage extent *versus* fiber orientation (θ) (v_c = 40 m/min and f = 0.2 mm/rev).

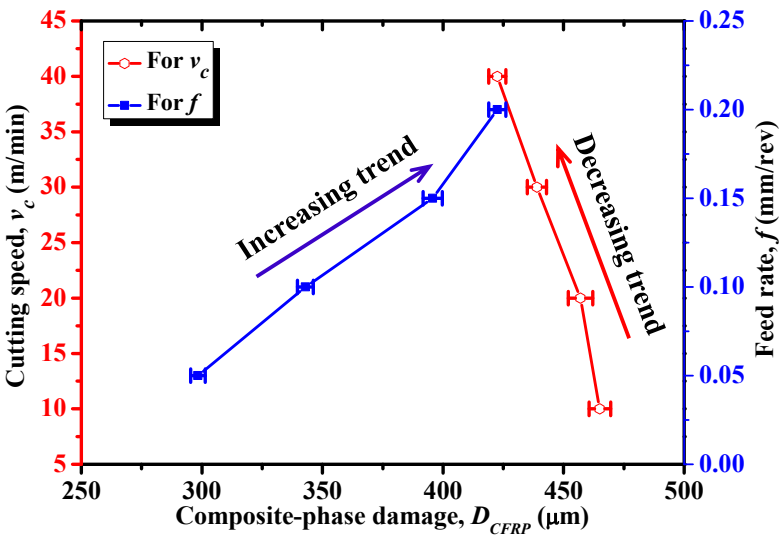

Figure 4.12. Effects of v_c (f = 0.2 mm/rev and θ = 0°) and f (v_c = 40 m/min and θ = 0°) on composite-phase damage (D_{CFRP}) (θ = 0°).

4.3 Evaluation of different cutting-sequence strategies

In hybrid CFRP/Ti machining, two different cutting-sequence strategies, *i.e.*, CFRP → Ti and Ti → CFRP, exist from the aspect of tool entry and tool exit throughout the entire chip removal process [169]. The cutting-sequence strategy indeed plays a vital role in affecting the final machining responses when cutting the bi-material system. However, such interesting phenomenon is still scarcely revealed by local existing literature. The key differences between the two different cutting-sequence strategies and also their real influences on hybrid CFRP/Ti machining are still not well studied. In such circumstance, the following subsection is dedicated to making a comparative study on the two different cutting-sequence strategies in terms of chip formation process, machined

surface morphology and induced subsurface damage. The key objective of the numerical analyses is to identify the most reasonable cutting-sequence strategy that favors the CFRP/Ti cutting.

4.3.1 Comparison of chip formation process

Machining hybrid CFRP/Ti stacks commonly involves interrelated and coupled chip separation modes due to the multi-tool-work interaction domains. The chip separation mode, however, operates as the key role in affecting the final induced cutting phenomena, *e.g.*, force generation, machined surface quality, induced damage formation. In the present contribution, a comparative study of chip formation process under different cutting-sequence strategies ($^{\text{CFRP}\rightarrow\text{Ti}}_{\text{Ti}\rightarrow\text{CFRP}}$) was performed under the cutting conditions of v_c = 40 m/min, f = 0.2 mm/rev and θ = 45°. Figs. 4.13, 4.15 and 4.16 show the chip formation process dominating the hybrid CFRP/Ti stack cutting under the cutting-sequence strategy of CFRP → Ti.

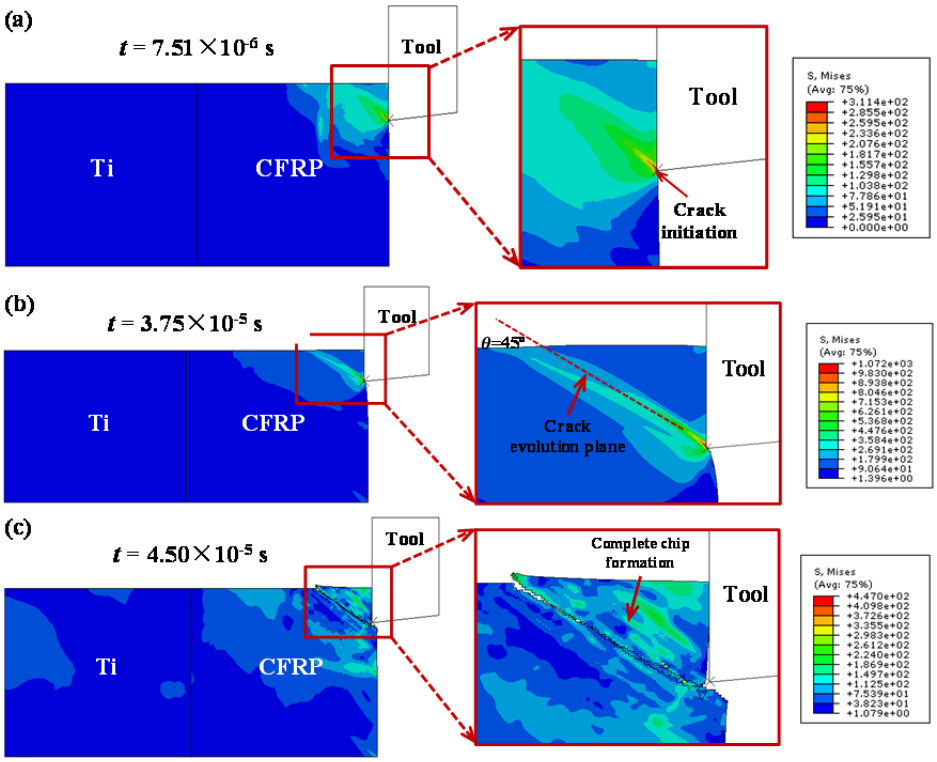

Figure 4.13. Chip formation process when cutting hybrid CFRP/Ti stacks under the CFRP → Ti cutting sequence: (a) t = 7.51 × 10^{-6} s, (b) t = 3.75 × 10^{-5} s, and (c) t = 4.50 × 10^{-5} s.

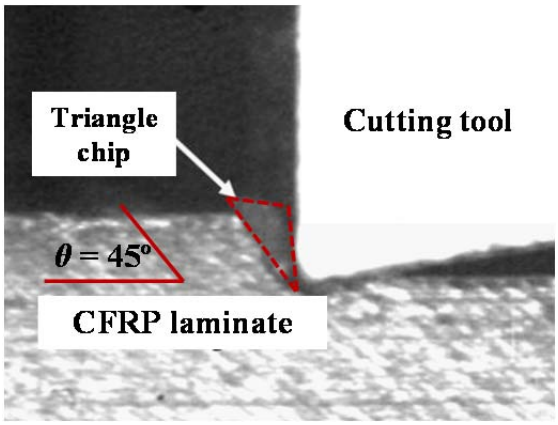

Figure 4.14. Experimental observation of the chip formation when cutting T300/914 CFRP laminates with 45° fiber orientation [175].

As shown in Fig.4.13, the chip separation of CFRP phase is mainly dominated by a primary fracture along the fiber/matrix interface toward the interior of the uncut chip thickness. When the tool initially cuts into the CFRP layer, the composite material and principally the fibers will be crushed under the tool advancement. In such circumstance, the micro crack is initiated in the vicinity of the tool tip. Afterward, the crack suffers a quick propagation in the parallel direction to the fiber orientation of $\theta = 45°$ due to the fiber/matrix debonding, as illustrated in Fig.4.13(b). With further tool advancement, the crack failure reaches the free surface of the composite phase and results in the complete chip formation characterized by a discontinuous "triangle shape" due to the predominant brittle-fracture chip-separation mode. It should be noted that the simulated CFRP chip morphology shows a consistent agreement with the experimental observation gained by Iliescu et al. [175] when cutting T300/914 CFRP laminates with 45° fiber orientation as shown in Fig. 4.14. The results further confirm the credibility of the developed CFRP numerical model.

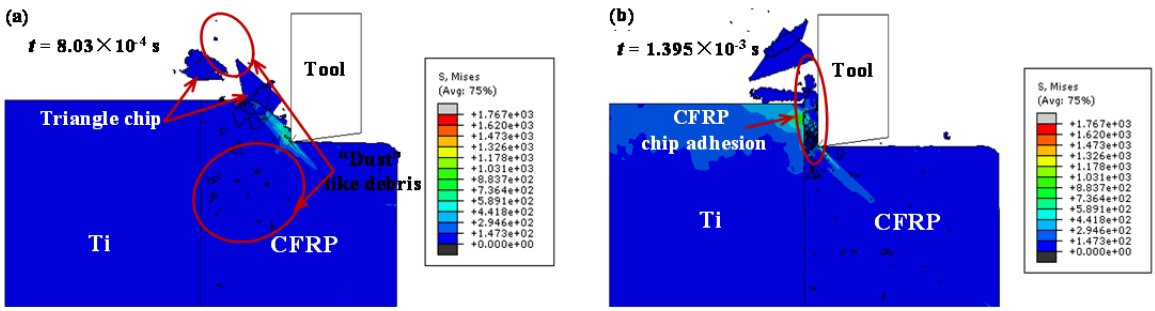

Figure 4.15. Chip formation process when cutting hybrid CFRP/Ti stacks under the CFRP → Ti cutting sequence: (a) t = 8.03 × 10^{-4} s and (b) t = 1.395 × 10^{-3} s.

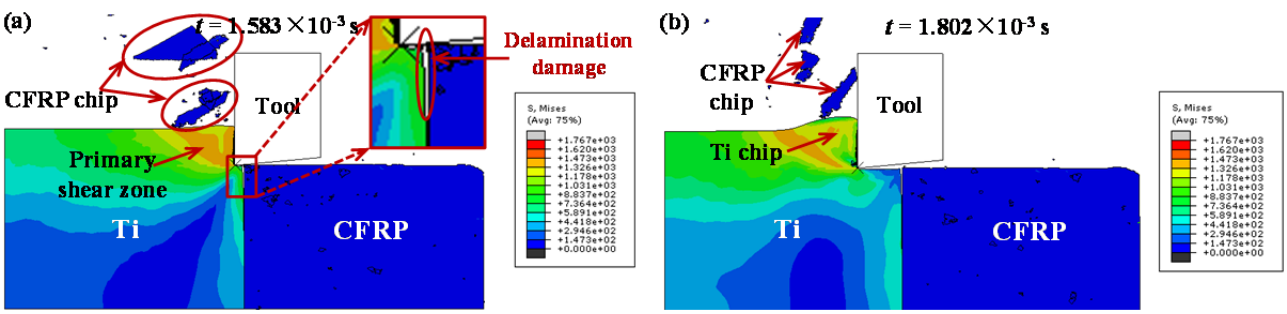

Figure 4.16. Chip formation process when cutting hybrid CFRP/Ti stacks under the CFRP → Ti cutting sequence: (a) t = 1.583 ×10^{-3} s and (b) t = 1.802 × 10^{-3} s.

With the progression of the CFRP/Ti cutting operation, successive "triangle" chips are produced governing the CFRP-phase machining as depicted in Fig.4.15(a). When the tool cutting edge approximately reaches the interface zone, the previously resected CFRP chips adhere on tool rake face and substitute the tool edges for further chip separation as shown in Fig.4.15(b). As the tool tip cuts across the interface region, delamination damage takes place along the bi-material interface as seen in the magnified view in Fig.4.16(a). When the tool edge fully cuts into the Ti phase as shown in Fig. 4.16(b), previous tool-CFRP interaction is completely transformed into the absolute tool-Ti interaction. The elastic-plastic deformation then operates as the predominant chip-separation mode for the metallic phase machining. The shearing actions arising from the mechanical/thermal effects in the primary shear zone generate "continuous" chips that flow on tool rake face. The CFRP/Ti cutting operation is assumed to reach a steady state under such circumstance.

In addition, Figs.4.17- 4.19 also show the chip separation process of CFRP/Ti machining under the

Ti → CFRP cutting sequence. As observed in Fig.4.17 (a), when tool edge firstly cuts into the Ti layer, high-stress concentration takes place in the vicinity of the tool-chip interface. The cutting stress then suffers a quick evolution toward the free surface of the uncut chip thickness through the primary shear zone with the facilitation of tool advancement as shown in Fig. 4.17 (b). The elastic-plastic behavior of the metallic phase results in the "continuous"-like chip formation. It should be highlighted that the resected Ti chip morphology under the simulated cutting conditions appears more "continuous"-like rather than "serrated"-like due to the use of extremely low cutting speed in modeling, which minimizes the segmentation frequency of the chip removal process dominating the Ti phase machining. Besides, when cutting tool probably attains the middle cutting distance of the Ti phase (approximately $t = 6.03\times10^{-4}$ s), severe damage initiation is promoted along the CFRP/Ti interface and more precisely occurring inside the CFRP phase. The physical phenomena should be induced by the cutting influences arising from the initial Ti-phase machining. This is because with the further cutting progression, the uncut Ti chip becomes much thinner and hence can easily bend into the brittle interface region and CFRP phase, which will inevitably lead to the serious damage evolution of the brittle composite phase due to its bending and inclination effects (as shown in Fig.4.18(b)). Furthermore, when the rigid tool completely cuts across the interface region, the previously-resected Ti chip adheres on tool rake face and substitutes the tool edge for further chip separation. Meanwhile, delamination damage is detected to take place concerning the "Ti-to-CFRP" contact boundary. The adhered Ti chip pushes down the uncut composite layer and results in extremely serious damage of the fiber/matrix system as seen in Fig.4.19. Consequently, the machined surface is produced particularly rough and serious cracks are visible beneath the trimmed plane.

The above numerical analyses demonstrate that the CFRP → Ti cutting sequence is more beneficial for easy chip separation of hybrid CFRP/Ti stacks than Ti → CFRP cutting sequence. Both chip adhesion phenomena are found to take place on tool rake face in machining irrespective of the used cutting-sequence strategies ($^{\text{CFRP}\,\rightarrow\,\text{Ti}}_{\text{Ti}\,\rightarrow\,\text{CFRP}}$). The key mechanisms dominating the cutting sequence's effects on hybrid composite stack machining can be explained by the different extents of influences arising from the initial-phase cutting on final-phase cutting owing to their disparate cutting behaviors.

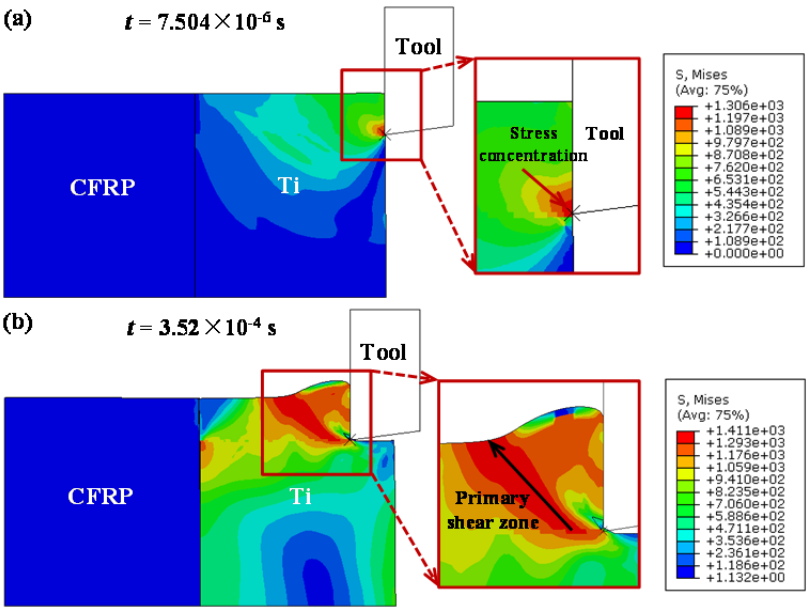

Figure 4.17. Chip formation process when cutting hybrid CFRP/Ti stacks under the Ti → CFRP cutting sequence: (a) $t = 7.504 \times 10^{-6}$ s and (b) $t = 3.52 \times 10^{-4}$ s.

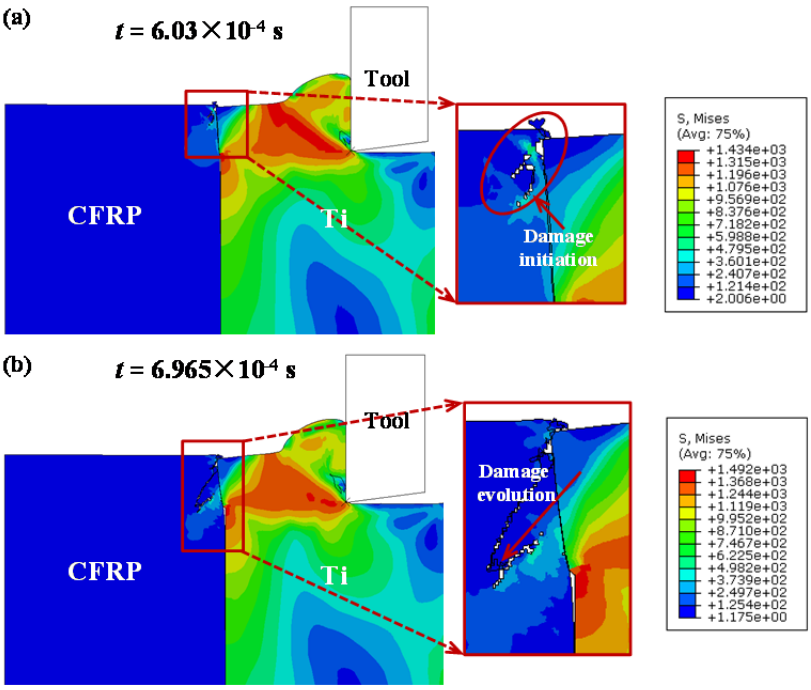

Figure 4.18. Chip formation process when cutting hybrid CFRP/Ti stacks under the Ti → CFRP cutting sequence: (a) t = 6.03 × 10^{-4} s and (b) t = 6.965 × 10^{-4} s.

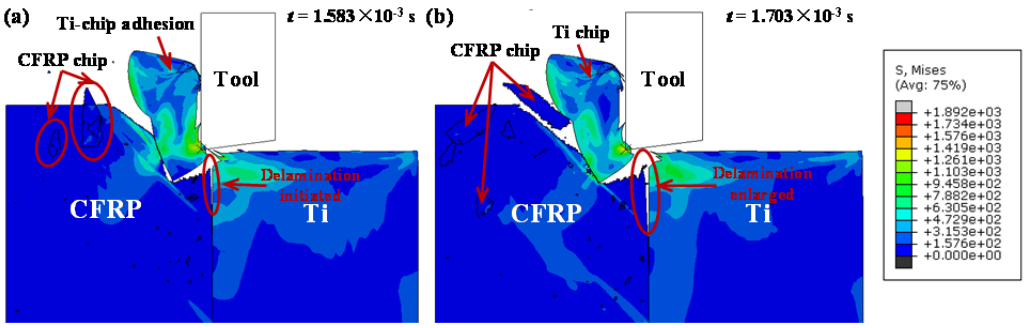

Figure 4.19. Chip formation process when cutting hybrid CFRP/Ti stacks under the Ti → CFRP cutting sequence: (a) t = 1.583 × 10^{-3} s and (b) t = 1.703 × 10^{-3} s.

4.3.2 Assessment of machined surface morphology

In hybrid CFRP/Ti stack machining, the machined surface quality plays a key role in affecting the service performance of the manufactured components and consequently the final part acceptance. Various types of physical defects or geometric imperfections are easily promoted in multi-material machining due to the discontinuity of the tool-work interactions in the chip separation process [165].

To clarify its practical influences on CFRP/Ti cutting process, a comparative inspection was made through the examination of the machined surface quality in terms of different cutting sequences ($^{\text{CFRP}\rightarrow\text{Ti}}_{\text{Ti}\rightarrow\text{CFRP}}$) under the fixed cutting conditions (v_c = 40 m/min, f = 0.2 mm/rev and θ = 45°). Figs. 4.20 and 4.21 present the comparative FE observations after the completion of the CFRP/Ti cutting process.

Through the comparison of Figs.4.20 and 4.21, it is noticeable that the CFRP → Ti cutting sequence produces much smoother surface morphology than its counterpart one. In Fig.4.20, nearly rare crack is detected beneath the machined CFRP/Ti surface in CFRP → Ti cutting sequence. By contrast, the machined surface in Ti → CFRP cutting sequence appears much rougher and extremely uneven as depicted in Fig.4.21. Serious cracks are pronounced especially concerning the machined

CFRP-phase surface. The phenomenon can be attributed to the serious Ti-chip adhesion on tool rake face that replaces the cutting edge for further chip separation and promotes severe scratching effects on the machined composite surface. And consequently severe subsurface damage is generated.

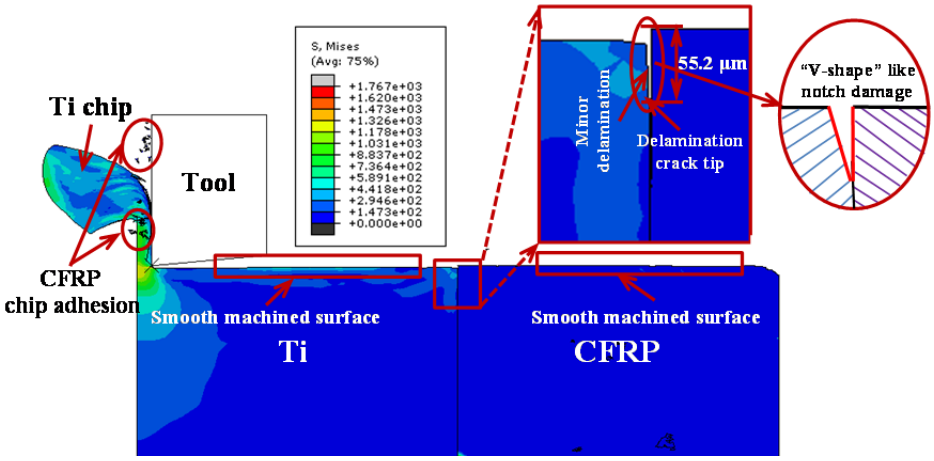

Figure 4.20. Machined surface morphology in the CFRP → Ti sequence (v_c = 40 m/min, f = 0.2 mm/rev and θ = 45°).

Moreover, with respect to the weakest interface zone, the damage mode occurring at the bi-material interface usually exists in the form of delamination imperfection ("V shape"-like notch) as discussed in subsection 4.2.2. In the current simulation, the delamination damage is all detected along the "CFRP-to-Ti" contact boundary regardless of the used cutting-sequence strategy ($^{\text{CFRP} \rightarrow \text{Ti}}_{\text{Ti} \rightarrow \text{CFRP}}$). The activated mechanisms of delamination can be attributed to the combined effects of both fracture mode I and fracture mode II exerted on the interface region [4, 165]. As shown in Figs. 4.20 and 4.21, the cutting sequence indeed exhibits a significant impact on the interface damage formation. In Ti → CFRP cutting sequence, typically a large length of delamination damage is produced on the bi-material interface. The predicted delamination length (D_{del} = 202.6 µm) is approximately 3.67 times longer than that (D_{del} = 55.2 µm) generated in CFRP → Ti cutting sequence. The reason can be explained by the fact that in CFRP → Ti cutting sequence the Ti alloy can act as the role of supporting plate in preventing CFRP laminate deflection and ensuring the stability of the tool-work interaction during the cutting operation. As a result, a lower extent of interface delamination is promoted. In contrast, when operated in Ti → CFRP cutting sequence, the CFRP phase cannot act the role of supporting plate for Ti-phase cutting due to the relative brittleness of the fiber/matrix system. Therefore, a higher extent of delamination is produced on the CFRP/Ti interface.

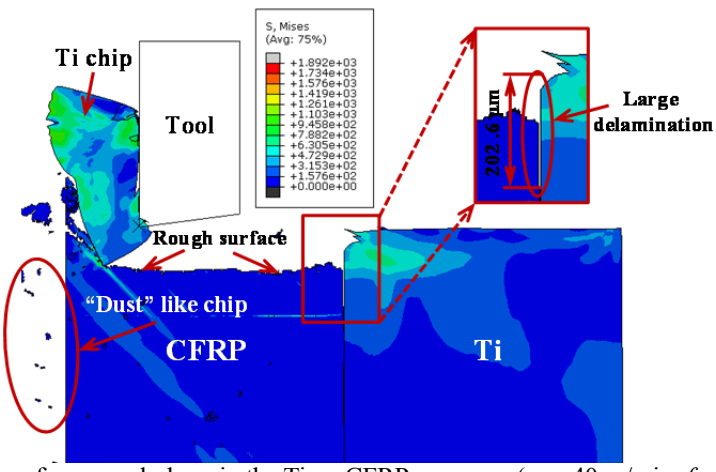

Figure 4.21. Machined surface morphology in the Ti → CFRP sequence (v_c = 40 m/min, f = 0.2 mm/rev and θ = 45°).

4.3.3 Evaluation of induced subsurface damage

As illustrated in subsections 4.3.1 and 4.3.2, severe subsurface damage can be induced by the CFRP/Ti machining operation. To quantitatively study the actual influence of cutting-sequence strategy on the induced damage extent, four different fiber orientations (θ = 0º, 45º, 90º and 135º) of the CFRP phase are tested under the cutting conditions of v_c = 40 m/min and f = 0.2 mm/rev. The damage studies are focused on the analyses of interface delamination and fiber/matrix failure promoted in the CFRP phase. For interface delamination, the extent was measured as the maximum length from the ideal machined surface to delamination crack tip as shown schematically in the magnified interface zone of Fig.4.22. Besides, the composite damage was evaluated based on the damage failure that caused the maximum damage extent of the composite phase during the CFRP/Ti cutting process. Afterward, the composite damage extent was measured as the maximum length from the machined CFRP surface to the deepest failure zone as shown schematically in Fig.4.22. Each measurement was repeated three times in order to get reliable results.

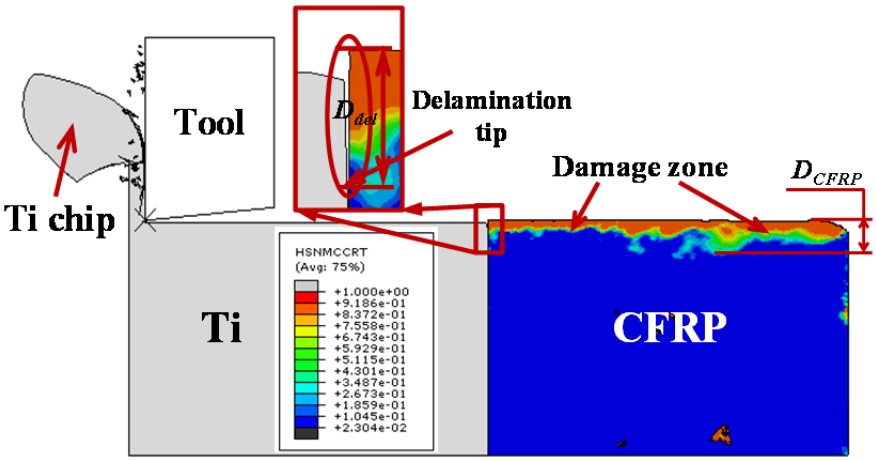

Figure 4.22. Scheme of the composite-phase damage (D_{CFRP}) measurement when cutting hybrid CFRP/Ti stacks (v_c = 40 m/min, f = 0.2 mm/rev and θ = 45°) (**Note:** HSNMCCRT indicates the Hashin matrix-compression failure).

Figs.4.23 and 4.24 present the evolution of the predicted interface delamination length and composite damage length *versus* fiber orientation (θ). It is apparent that the subsurface damage extent induced in CFRP → Ti cutting sequence exhibits much smaller value than that operated in Ti → CFRP cutting sequence. The comparison strongly confirms that the CFRP → Ti cutting sequence should be a reasonable cutting strategy for hybrid CFRP/Ti stack machining that can minimize several subsurface damage induced by cutting.

Besides, the trends of both interface delamination and composite damage *versus* θ show high similarities, regardless of the used cutting sequences ($^{\text{CFRP}\rightarrow\text{Ti}}_{\text{Ti}\rightarrow\text{CFRP}}$). When θ increases from 0º to an acute angle, the two types of subsurface damage increase gradually until they reach the maximum extents at θ = 90º, as depicted in Figs.4.23 and 4.24, respectively. Afterward, the subsurface damage experiences a slight reduction when θ becomes an obtuse angle. The key mechanisms governing the variation phenomena can be attributed to the changeable chip separation modes in CFRP-phase machining when θ varies in hybrid CFRP/Ti stack cutting. Furthermore, the observation of the maximum damage extent at θ = 90º also shows a good agreement with the experimental studies conducted by Wang and Zhang [196] when cutting UD-FRP composites.

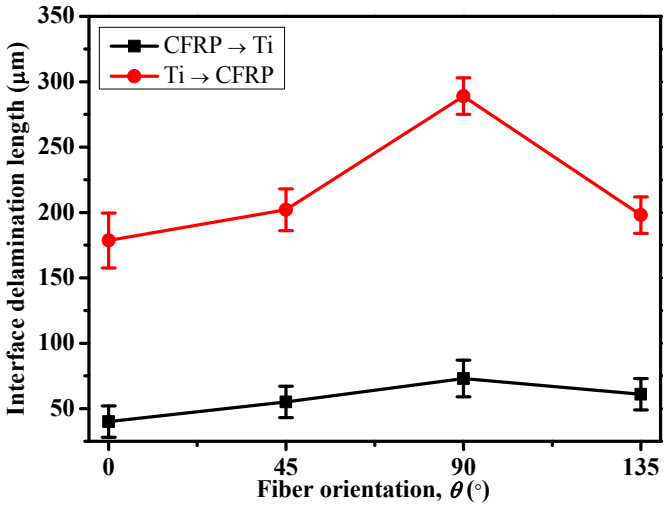

Figure 4.23. Evolution of interface delamination length in function of θ under different cutting-sequence strategies (v_c = 40 m/min and f = 0.2 mm/rev).

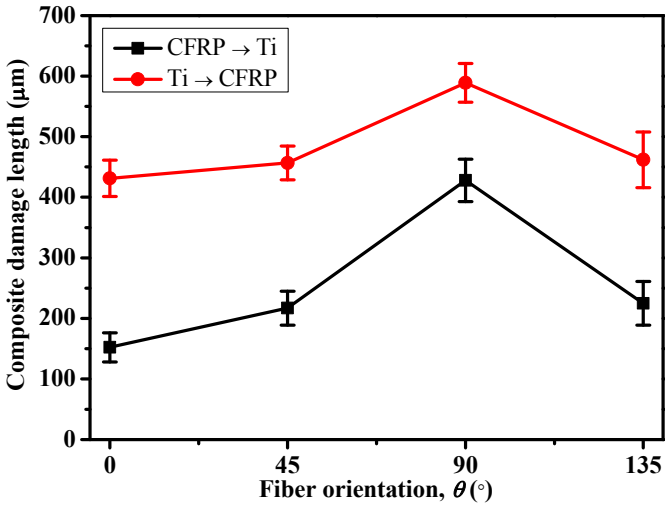

Figure 4.24. Evolution of composite damage length in function of θ under different cutting-sequence strategies (v_c = 40 m/min and f = 0.2 mm/rev).

4.4 Parametric effects on hybrid CFRP/Ti stack machining

The machining process of hybrid CFRP/Ti stacks is affected by many internal and external parametric factors, especially the fiber orientation (θ), cutting speed (v_c) and feed rate (f). To inspect the parametric effecs on CFRP/Ti machining, the fiber orientation's influence on the hybrid CFRP/Ti machining was firslty investigated in terms of chip removal process and machined surface quality. Afterward, the parametric effects of cutting parameters (v_c and f) on various machining responses were presented. It is the key objective to clarify the most influential factor that greatly affects the hybrid CFRP/Ti machining.

4.4.1 Cutting process inspection

To inspect the fiber orientation's influences on CFRP/Ti cutting operation, two different fiber orientations (θ = 0° and θ = 60°) were examined.

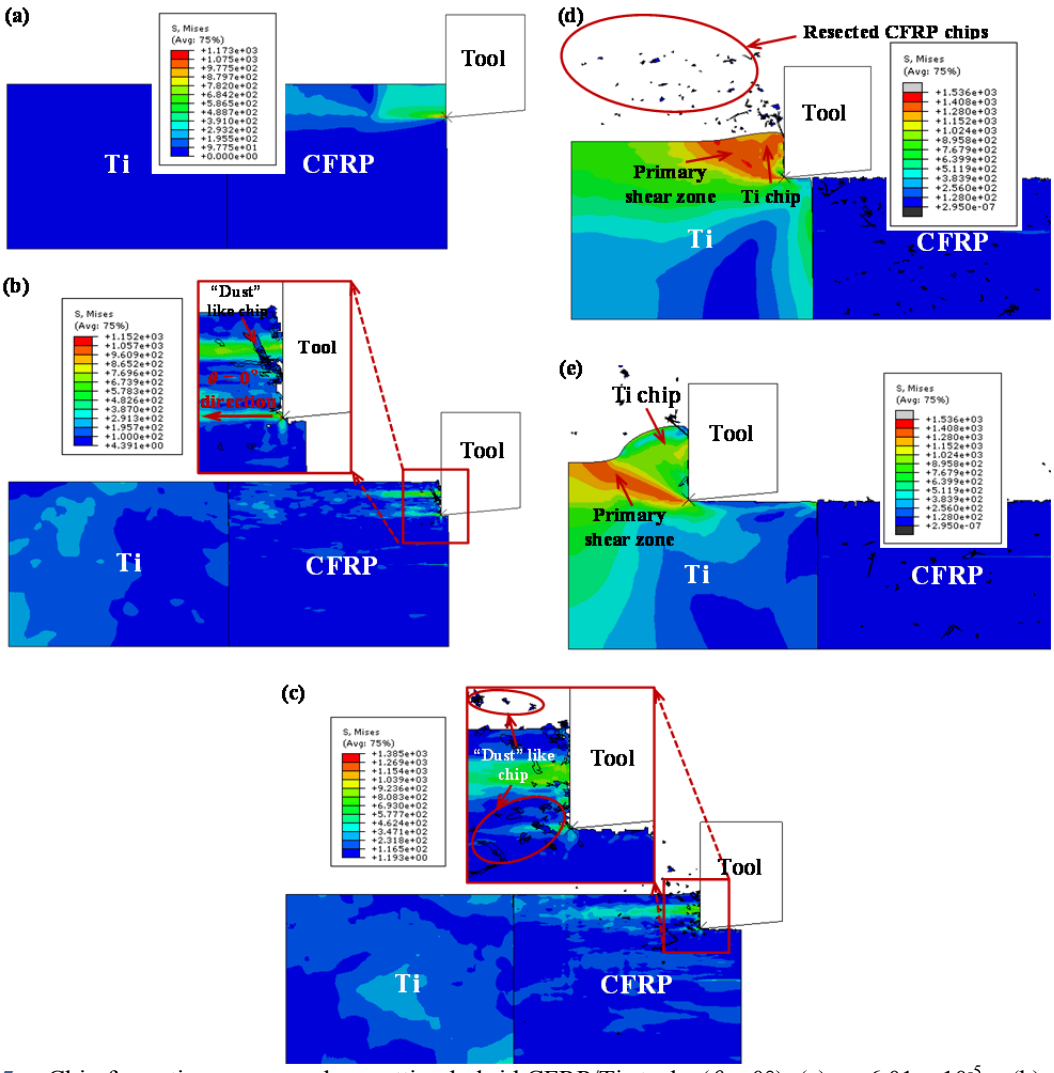

Figure 4.25. Chip formation process when cutting hybrid CFRP/Ti stacks ($\theta = 0°$): (a) $t = 6.01 \times 10^{-5}$ s, (b) $t = 2.12 \times 10^{-4}$ s, (c) $t = 7.52 \times 10^{-4}$ s, (d) $t = 6.72 \times 10^{-3}$ s, and (e) $t = 9.12 \times 10^{-3}$ s ($v_c = 10$ m/min and $f = 0.2$ mm/rev).

Figs.4.25 and 4.27 then show the chip formation process *versus* different fiber orientations (θ) under the fixed cutting conditions of $v_c = 10$ m/min and $f = 0.2$ mm/rev. As depicted in Fig.4.25, it is noticeable that when the tool edge firstly cuts into the CFRP phase, the "dust"-like chips are produced along tool rake face. The physical phenomenon is mainly caused by the predominant brittle-fracture chip-separation mode that results in "discontinuous" chip morphology. Such numerical observation also achieves a good agreement with the reality of CFRP cutting from the open literature [60, 105] as depicted in Fig.4.26. Facture/crack regime inside the uncut chip layer is observed to propagate in the parallel direction of the 0° fiber orientation. This evidence indicates that the global fiber fracture occurs through the horizontal direction. This is because in the cutting case of $\theta = 0°$, the rupture of fiber/matrix system is caused by a combination of bending load and crushing effects arising from tool advancement that generate fiber/matrix interface debonding concerning the fiber axis direction, *i.e.*, the fiber orientation's direction. When the tool tip cuts into the Ti phase, the "continuous" chip type is generated along tool rake face. It should be highlighted that under the simulated cutting conditions, the produced Ti-chip morphology appears more "continuous"-like rather than "serrated"-like due to the use of extremely low cutting speed ($v_c = 10$ m/min) which minimizes the segmentation frequency of the Ti chip removal process. In addition, the used $v_c \times f$ value (0.002 m^2/min) is also much lower than the critical value of 0.004 m^2/min for

the occurrence of Ti-chip segmentation as confirmed by several experimental researches [197, 198]. The Ti chip separation is primarily caused by the crack initiation and progression followed by the sequence of initiating from the tool tip, propagating inside the primary shear zone, and finally reaching the chip-free surface.

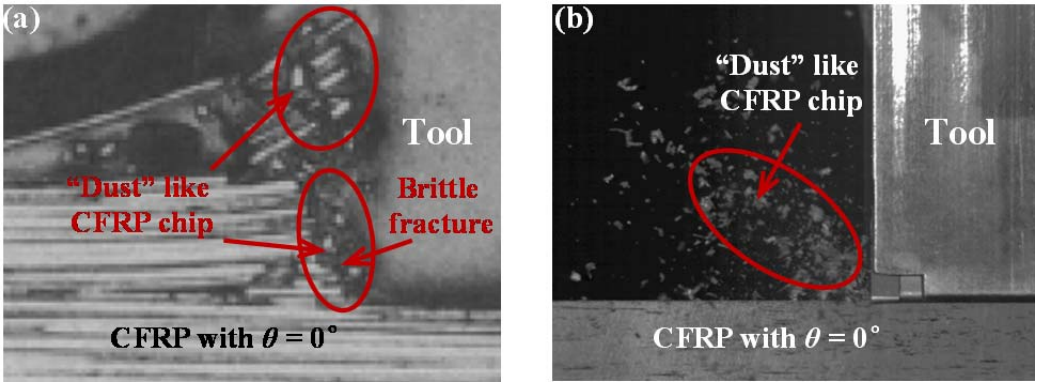

Figure 4.26. Experimental observation of the resected chip formation when orthogonal cutting of CFRP laminates with 0° fiber orientation: (a) high speed video image from Koplev et al. [60] and (b) high speed video image from Mkaddem et al. [105].

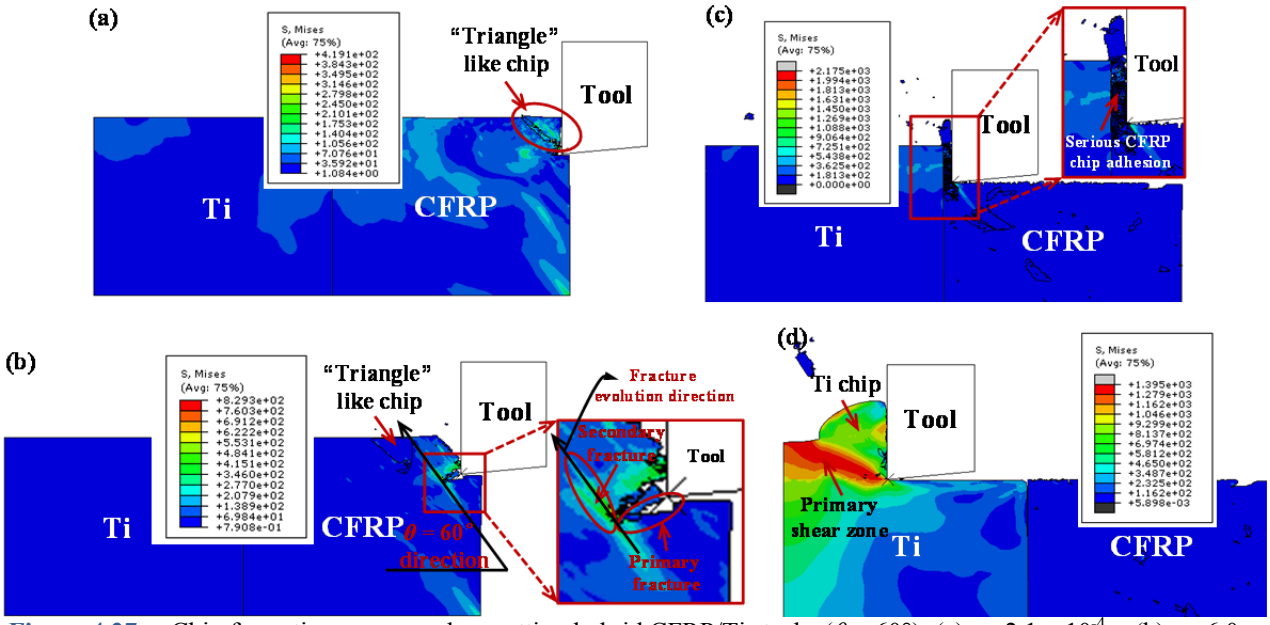

Figure 4.27. Chip formation process when cutting hybrid CFRP/Ti stacks ($\theta = 60°$): (a) $t = 2.1 \times 10^{-4}$ s, (b) $t = 6.0 \times 10^{-4}$ s, (c) $t = 5.64 \times 10^{-3}$ s, and (d) $t = 9.44 \times 10^{-3}$ s ($v_c = 10$ m/min and $f = 0.2$ mm/rev).

With respect to the cutting case of $\theta = 60°$, when the tool initially penetrates the CFRP phase, the crack/fracture initiation and propagation are also observed toward the fiber-orientation direction. However, the main difference between the cutting cases of $\theta = 60°$ and $\theta = 0°$ is that the "triangle"-like chip is produced for machining $\theta = 60°$ CFRP/Ti stacks. This is because, for acute θ cutting, the composite chip formation is induced by a succession of two main fracture mechanisms: the primary fracture and the secondary fracture. As shown in the magnified view of Fig. 4.27 (b), the primary fracture is caused by compression-induced shearing perpendicular to the fiber-orientation direction while the secondary fracture is promoted by fiber/matrix debonding concerning the fiber-orientation direction ($\theta = 60°$). When the secondary fracture reaches the composite free surface, it results in the complete chip with a "triangle" shape. The simulated results

agree well with the experimental observations of Iliescu et al. [175] and Arola and Ramulu [55] as shown in Fig. 4.28. With the tool further advancement, especially when the cutting edge reaches the interface zone, the previously resected CFRP chip is found to adhere on tool rake face as shown in Fig. 4.27 (c). As the tool fully cuts into the Ti phase (as shown in Fig.4.27 (d)), the produced Ti chip appears "continuous"-like morphology as the same observed in the cutting case of $\theta = 0°$ (as depicted in Fig. 4.25 (e)).

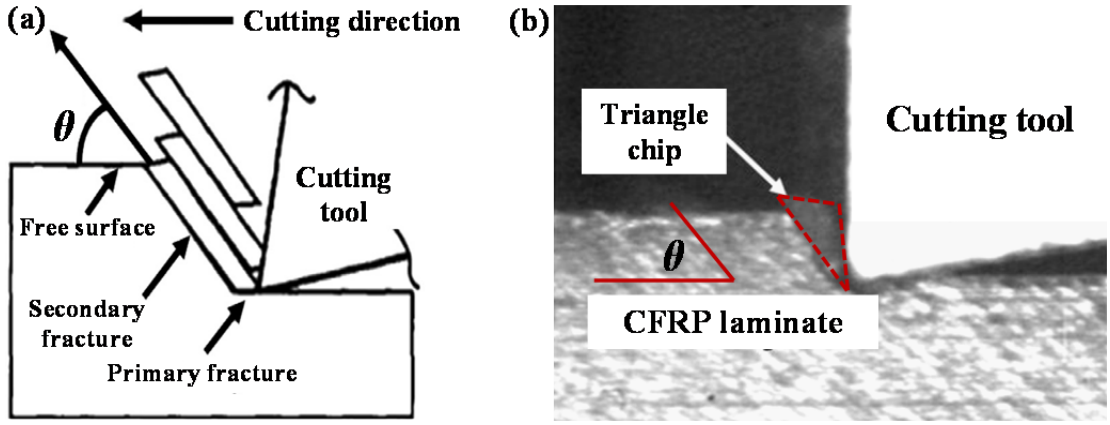

Figure 4.28. Resected chip formation in orthogonal cutting of unidirectional composite with acute θ angle: (a) schematization of experimental chip formation from the work of Arola and Ramulu [55] and (b) high speed video image from experimental work of Iliescu et al. [175].

4.4.2 Machined surface quality inspection

In hybrid CFRP/Ti stack cutting, the machined surface quality plays a key role in affecting the service performance of the material-made components, and consequently determines the final part acceptance. Since the fiber orientation often has a significant effect on the cutting behavior of CFRP/Ti stacks, to clarify its real influences on the trimmed CFRP/Ti surface quality, the different machined surface morphologies *versus* θ were studied. Figs. 4.29 - 4.32 then show the comparative results under two different fiber orientations of $\theta = 0°$ and 60°, respectively.

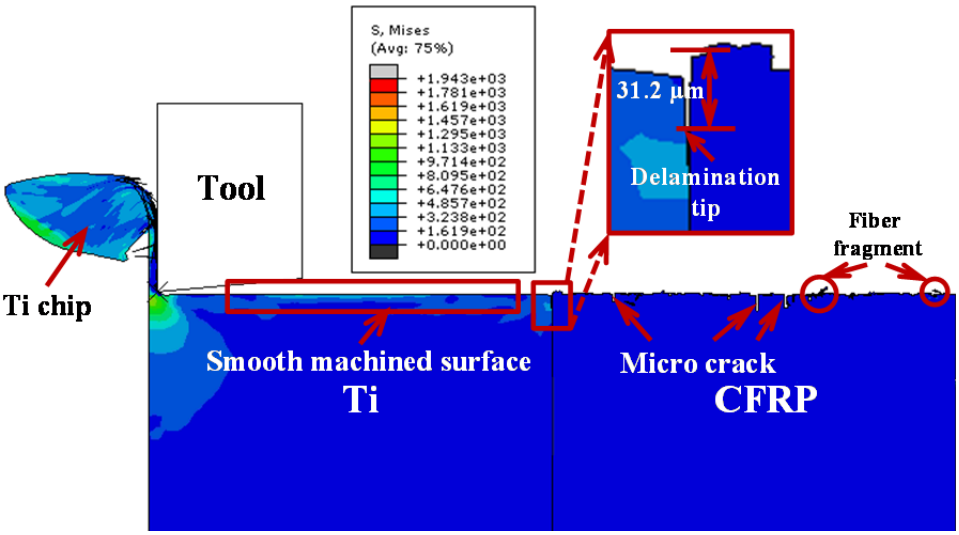

Figure 4.29. Machined surface morphology when cutting hybrid CFRP/Ti stacks under $\theta = 0°$ ($v_c = 10$ m/min and $f = 0.2$ mm/rev).

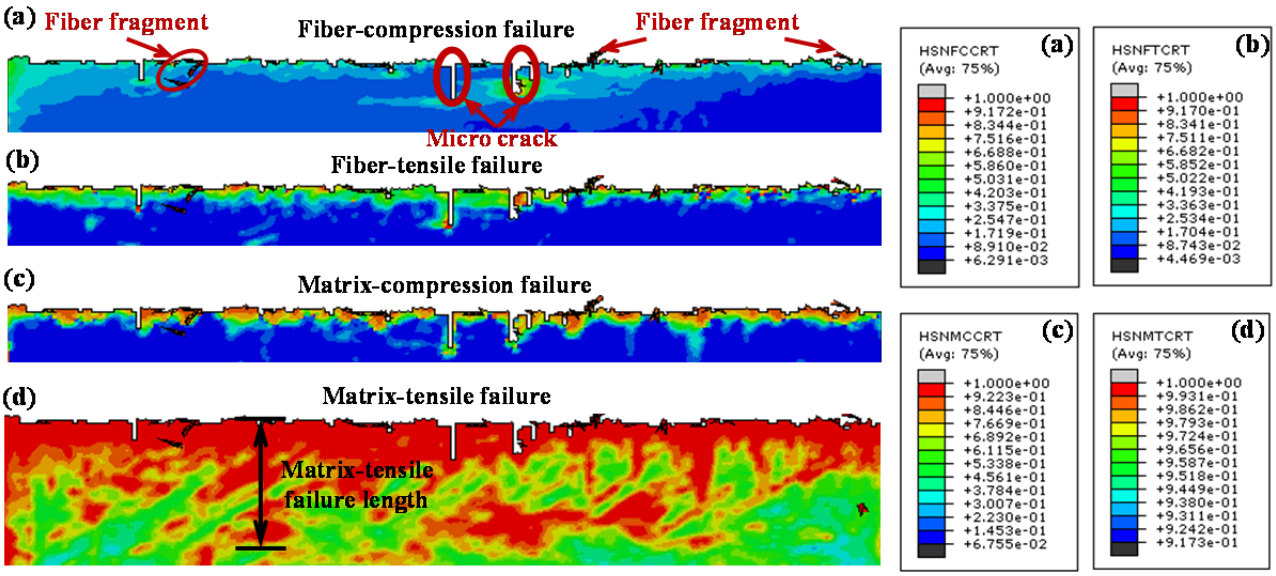

Figure 4.30. Machined CFRP surface damage under $\theta = 0°$ ($v_c = 10$ m/min and $f = 0.2$ mm/rev): (a)fiber-compression failure, (b) fiber-tensile failure, (c) matrix-compression failure, and (d) matrix-tensile failure.

As shown in Fig. 4.29 and Fig. 4.31, the machined surface of CFRP phase appears much rougher and more uneven than that of the trimmed Ti phase regardless of the used fiber orientations. Various micro crack, fiber fragment and surface damage are detected along/beneath the trimmed CFRP surface. In contrast, the machined surface in Ti phase appears very flat and smooth nearly without defects. The reason can be attributed to the predominant plastic-deformation mode controlling the chip separation process of Ti-phase machining that results in the "continuous"-like chip formation. As such, the machined surface will be generated much smoother than its counterpart one (the machined CFRP surface). Furthermore, as seen in the two examined θ configurations, delamination damage is observed to take place concerning the bi-material interface. The fiber orientation is found to have a positive impact on the interface delamination extent. As shown in Fig. 4.31, under $\theta = 60°$ condition, typically a large length of delamination damage is promoted along the CFRP/Ti interface. The predicted delamination length ($D_{del} = 80.6$ µm) is approximately 2.58 times longer than that ($D_{del} = 31.2$ µm) generated under $\theta = 0°$ condition.

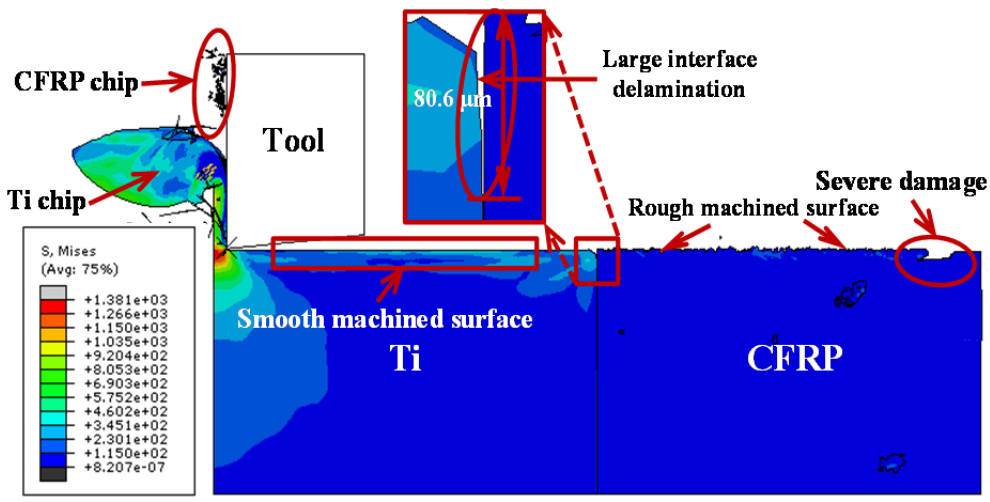

Figure 4.31. Machined surface morphology when cutting hybrid CFRP/Ti stacks under $\theta = 60°$ ($v_c = 10$ m/min and $f = 0.2$ mm/rev).

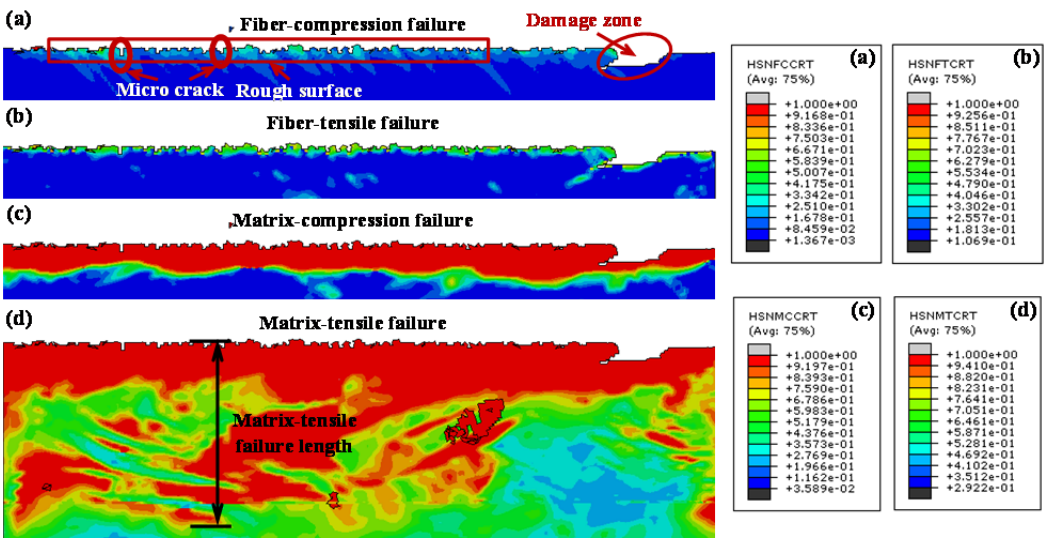

Figure 4.32. Machined CFRP surface damage under $\theta = 60°$ ($v_c = 10$ m/min and $f = 0.2$ mm/rev): (a)fiber-compression failure, (b) fiber-tensile failure, (c) matrix-compression failure, and (d) matrix-tensile failure.

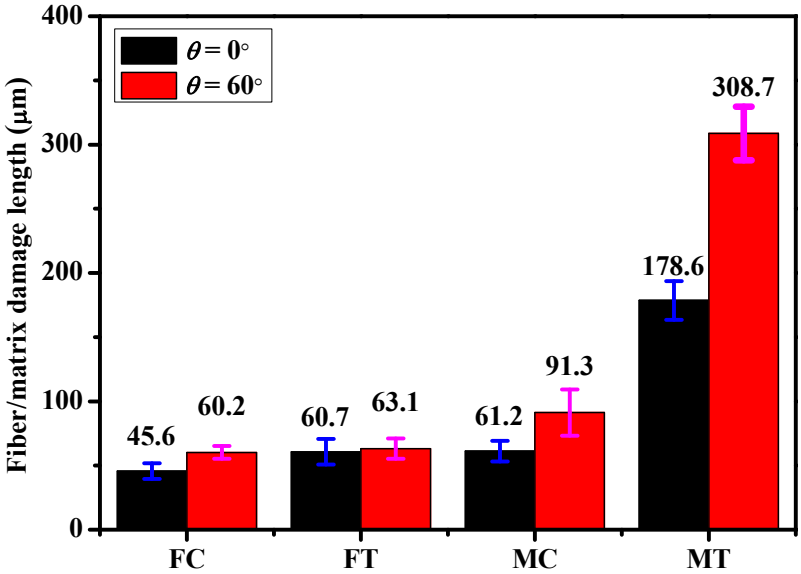

Figure 4.33. Comparative results of fiber/matrix failure induced in hybrid CFRP/Ti stack machining with two different fiber orientations of $\theta = 0°$ and $\theta = 60°$ ($v_c = 10$ m/min, $f = 0.2$ mm/rev, FC indicates the fiber-compression failure length, FT denotes the fiber-tensile failure length, MC signifies the matrix-compression failure length and MT represents the matrix-tensile failure length).

Concerning the CFRP-phase damage, the machined surface is found to comprise four types of damage including fiber-compression failure, fiber-tensile failure, matrix-compression failure and matrix-tensile failure as illustrated in Figs. 4.30 and 4.32, respectively. To objectively clarify the fiber orientation's effects on the composite-phase damage, each fiber/matrix damage extent was measured as the maximum length from the machined surface to the deepest failure zone. Fig. 4.33 then presents the comparative results between $\theta = 0°$ and $\theta = 60°$, where FC indicates the fiber-compression failure length, FT denotes the fiber-tensile failure length, MC signifies the matrix-compression failure length and MT represents the matrix-tensile failure length. The fiber orientation is found to have a remarkable influence on the composite-phase damage. As shown in Fig.4.33, an increase of θ usually results in a significant elevation of the mentioned four types of fiber/matrix failure. The reason can be explained by the change of chip separation mechanisms with respect to the fiber orientation. This is

because in the case of lower θ angle (θ = 0°), the rupture of fibers is caused by a combination of compression and tensile loads and thus generates a rupture plane parallel to the horizontal direction. As a result, a little bit small failure area is produced beneath the machined composite surface. In contrast, when machining CFRP composite with higher fiber orientation (θ = 60°), the mechanical bending will become a predominant chip-separation type and high cutting resistance will be encountered during the chip removal process. Hence, a deeper fiber/matrix damage area is promoted after the completion of machining.

4.4.3 Parametric study on CFRP/Ti cutting responses

Input cutting variables including cutting speed (v_c), feed rate (f), fiber orientation (θ), always have great influences on the machining responses of hybrid composite stacks. To objectively elaborate their relative effects on CFRP/Ti cutting, a diverse range of input variables including v_c of 20, 40, 60 m/min, f of 0.05, 0.075, 0.1 mm/rev, and θ of 0°, 30°, 60°, 90°, were tested. Note that the simulated force magnitudes (in N/mm) were normalized as the ratio between the average level of force generation and the workpiece thickness. The composite-phase damage is evaluated based on the damage failure that causes the maximum imperfection extent of the CFRP phase. For example, the maximum damage failure occurring in θ = 0° CFRP/Ti material is the matrix-tensile failure as shown in Fig. 4.33. Afterward, the composite-phase damage extent was measured as the maximum length from the machined CFRP surface to the deepest failure zone. The interface delamination extent was measured as the maximum length from the machined surface to the delamination tip as shown schematically in the magnified interface zone of Fig. 4.29. In addition, each cutting force measurement and damage length measurement were repeated three times so as to get reliable results. Figs.4.34 - 4.36 then show the variation of cutting-force generation (F_c), composite-phase damage and interface delamination *versus* cutting speed (v_c), feed rate (f) and fiber orientation (θ), respectively. The comparisons between the simulated F_c results and the experimental measurements from the open literature [161, 199] are also made as shown in Figs.4.34 and 4.35, respectively.

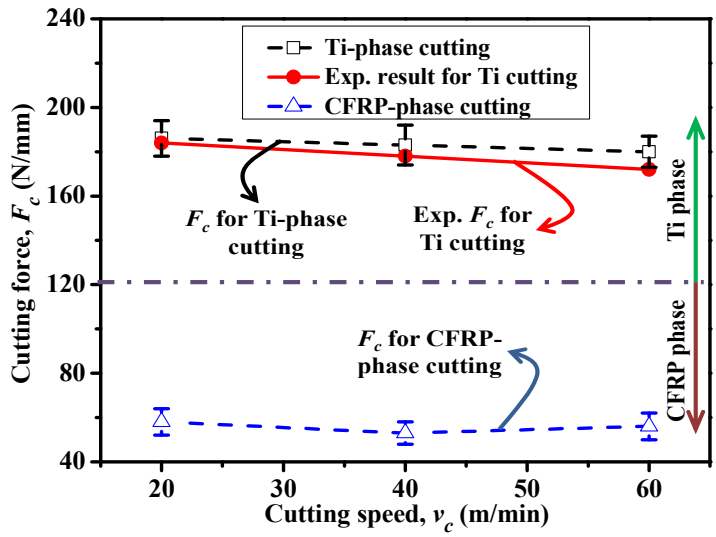

Figure 4.34. Cutting-force generation (F_c) *versus* cutting speed (v_c) when cutting hybrid CFRP/Ti stacks (f = 0.1 mm/rev and θ = 0°) (Exp. result for Ti cutting extracted from Cotterell and Byrne [161]).

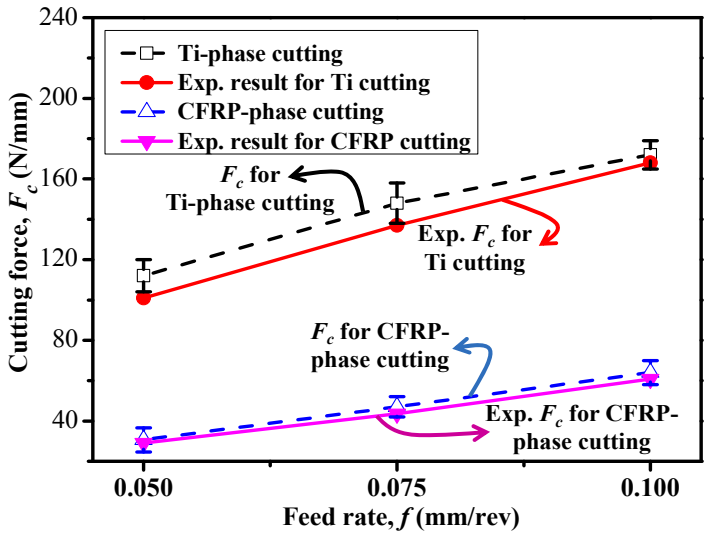

Figure 4.35. Cutting-force generation (F_c) *versus* feed rate (f) when cutting hybrid CFRP/Ti stacks (v_c = 60 m/min and θ = 0°) (Exp. result for Ti cutting extracted from Cotterell and Byrne [161] and Exp. result for CFRP cutting extracted from Iliescu et al. [199]).

As depicted in Figs. 4.34 and 4.35, it is noticeable that the cutting speed shows an insignificant effect on the CFRP/Ti cutting-force generation, especially for the CFRP-phase machining. For Ti-phase cutting, the v_c exhibits a negative impact on the F_c magnitudes, *i.e.*, an increased v_c results in a decreased F_c. The phenomenon can be explained by the fact that when v_c increases, typically high cutting temperature will be promoted on the tool-chip interface and then soften the uncut workpiece material. As such, the cutting resistance will be significantly reduced. In contrast, the feed rate is found to have remarkable influences on the cutting-force generation for both Ti-phase cutting and CFRP-phase cutting. This is because when increasing f, the tool is required to cut off more chip volume per revolution. In such circumstance, the higher cutting resistance is encountered during the material removal process and hence results in the significantly elevated F_c generation. Such findings of parametric effects on F_c generation also agree well with the experimental observations of Ghassemieh [41], Isbilir and Ghassemieh [42] when machining hybrid CFRP/Ti6Al4V stacks. Furthermore, the simulated F_c magnitudes also yield a consistent agreement with the experimental observations from the open literature [161, 199] as presented in Figs.4.34 and 4.35, respectively. These comparisons further confirm the sufficient credibility of the proposed FE model. Besides, for the simulated higher F_c magnitudes in Ti-phase cutting than the experimental ones [161], the reason can be attributed to the serious CFRP adhesion on tool rake face that contributes to the increased cutting resistance in final Ti-phase machining as discussed in subsection 4.4.1.

Concerning the induced damage when cutting hybrid CFRP/Ti stacks, the fiber orientation is observed to have a pronounced effect on the composite-phase damage and interface delamination as depicted in Fig. 4.36. The key mechanisms dominating the physical phenomena can be attributed to the changeable chip-separation modes *versus* fiber orientation (θ). This means with the increase of θ, the chip removal process for the CFRP phase will be dominated increasingly by bending/compression cutting coupled with out-of-plane shearing, which results in the difficulty in chip breakage and consequently severe damage extent. It should be noted that such findings also agreed well with the numerical prediction and experimental measurement from the open literature [168, 184] when machining CFRP composites. In Fig.4.36, the simulated increasing trend for the

fiber orientation's effects on the composite-phase damage is in good agreement with the predicted trend from Arola et al. [168].

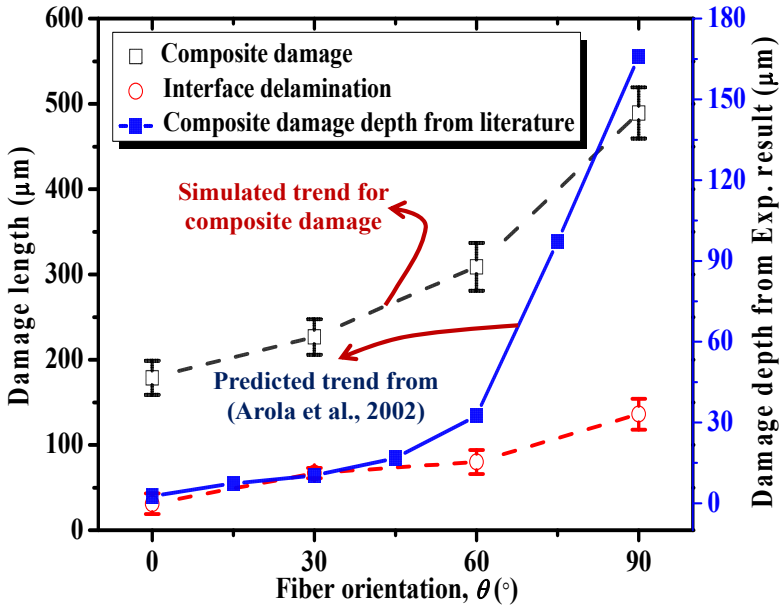

Figure 4.36. Composite-phase damage and interface delamination in function of fiber orientation (θ) when cutting hybrid CFRP/Ti stacks (v_c = 10 m/min and f = 0.2 mm/rev) (Comparative results extracted from Arola et al. [168]).

Moreover, the fiber orientation also exhibits a significant effect on the interface delamination formation in such manner that a small increase of θ typically results in a high extent of delamination damage as depicted in Fig.4.36. The reason can be explained as follows: when θ increases ($0° \leq \theta \leq 90°$), typically a higher cutting force will be generated [55, 184] when machining CFRP composites. The higher cutting force is then exerted across the bi-material interface and leads to the severe opening cracking of the interface region. As such, a larger extent of interface delamination is promoted. The above phenomena indicate that for minimizing the serious induced subsurface damage, a small θ configuration should be adopted when machining hybrid CFRP/Ti stacks.

4.5 Frictional responses dominating CFRP/Ti cutting process

In hybrid CFRP/Ti stack machining, the multi-tool-work interaction is the key root of various mechanical/physical phenomena induced in the chip removal process. Previous studies have shown that improving the frictional behavior of the multi-tool-work interaction can directly improve the machinability of the hybrid composite stack and hence can minimize the cutting energy consumption, reduce the affected subsurface damage and improve the machined surface quality. To this aim, several successful methods including the use of optimal cutting parameters [43, 103], superior tool materials [44, 45, 99] and favorable cutting environments [15, 40] have been widely employed in real production of hybrid CFRP/Ti stacks in order to achieve desirable cutting results. Despite all that, the activated mechanisms dominating the influences of the multi-tool-work interaction on hybrid CFRP/Ti stack machining are still lack of studies. On this basis, this subsection aims to clarify the mentioned issues through the numerical analyses.

Specifically, the multi-tool-work interaction can be decomposed into two fundamental couplings (i) the tool-chip coupling including tool-Ti/chip and tool-CFRP/chip interactions → controlling the

entire chip-separation mode and the material removal process of the bi-material system; and (*ii*) the tool-work coupling comprising tool-Ti/work and tool-CFRP/work interactions → dominating the various induced surface damage and the machined part quality of the stacked material. The key characteristics directly ruling the behavior of multi-tool-work interaction are the friction coefficient (μ). To inspect the fundamental frictional responses of hybrid CFRP/Ti stack cutting, the alteration of friction coefficient of the multi-tool-work interaction is adopted as a key input variable for achieving the desired pursuit. The key metrics for frictional-response studies are specific cutting energy consumption, machined surface quality and induced damage extent.

Since the CFRP-phase cutting and Ti-phase cutting require different ranges of cutting parameters due to their dissimilar machinability behaviors [43, 45, 67], the used v_c and f values were adopted based on a compromise selection, as summarized in Table 4.3.

Table 4.3
Details of the input variables for studying fricitonal repsones when cutting modeling of hybrid CFRP/Ti stacks.

Cutting speed, v_c (m/min)	10, 20, 30, 40
Feed rate, f (mm/rev)	0.05, 0.10, 0.15, 0.20
Fiber orientation, θ (°)	$\theta_i = i \cdot d_\theta$ (i = 0, 1, …, 12, d_θ = 15°)
Friction coefficient, μ	0.05, 0.10, 0.20, 0.30, 0.40

4.5.1 Frictional effects on specific cutting energy

In chip removal process, the friction coefficient governing the tool-work interface is a key root of the force generation occurring at tool rake face and flank face. In the following subsection, an indicator namely, specific cutting energy (u) [170, 200, 201], was introduced to inspect the parametric effects on the anisotropic machinability of the studied bi-material. The specific cutting energy, u (J/cm^3) signifies the machining energy consumed for the removal of unit volume of workpiece material in cutting, which can be expressed as follows:

$$u = \frac{P_c}{MMR} \tag{4.2}$$

where P_c denotes the machining power; MMR represents the material removal rate in cm^3/s unit. In addition, the P_c and MMR can be expressed as follows:

$$P_c = F_c \times v_c \tag{4.3}$$

$$MMR = v_c \times a_c \times w \tag{4.4}$$

where F_c signifies the main cutting force; v_c indicates the cutting speed; a_c and w denote the cutting depth and cutting width, respectively.

The u then can be defined by Eq.(4.5) through the mathematical derivation of substituting Eqs.(4.2), (4.3) and (4.4).

$$u = \frac{F_c}{a_c \times w} \tag{4.5}$$

The specific cutting energy (u) is an important parameter for machinability evaluation of materials, which can directly reflect the difficulty of the chip separation in actual machining. It

should be noted that in the present numerical configuration, the cutting depth (a_c) refers to the feed rate (f) while the cutting width (w) is equal to 1 mm [201].

Firstly, the cutting sequence's influences and cutting parameters' effects on the specific cutting energy consumption when machining hybrid CFRP/Ti stacks were studied. Fig. 4.37 then shows the obtained numerical results and also several comparisons with experimental results extracted from the open literature [161]. As can be seen from this figure, the predicted u values of the Ti-phase cutting show a consistent variation trend with the experimental results extracted from the literature. The cutting sequence indeed exhibits certain effects on the specific cutting energy (u) consumed in hybrid CFRP/Ti stack machining. Specifically, the stacked phase (*e.g.*, Ti phase or CFRP phase) which is machined lastly in one cutting sequence typically consums a little bit more specific cutting energy than that performed firstly in the another cutting sequence, *e.g.*, the Ti-phase machining gives rise to more u consumption in the CFRP → Ti cutting sequence than in the Ti → CFRP cutting sequence. The predominant reason, as revealed in our numerical findings, shows that in either CFRP → Ti or Ti → CFRP cutting sequences, severe resected chip adhesion arising from the firstly cutoff phase is observed on tool rake face that substitutes the main cutting edge for further chip separation and hence increases the u consumption.

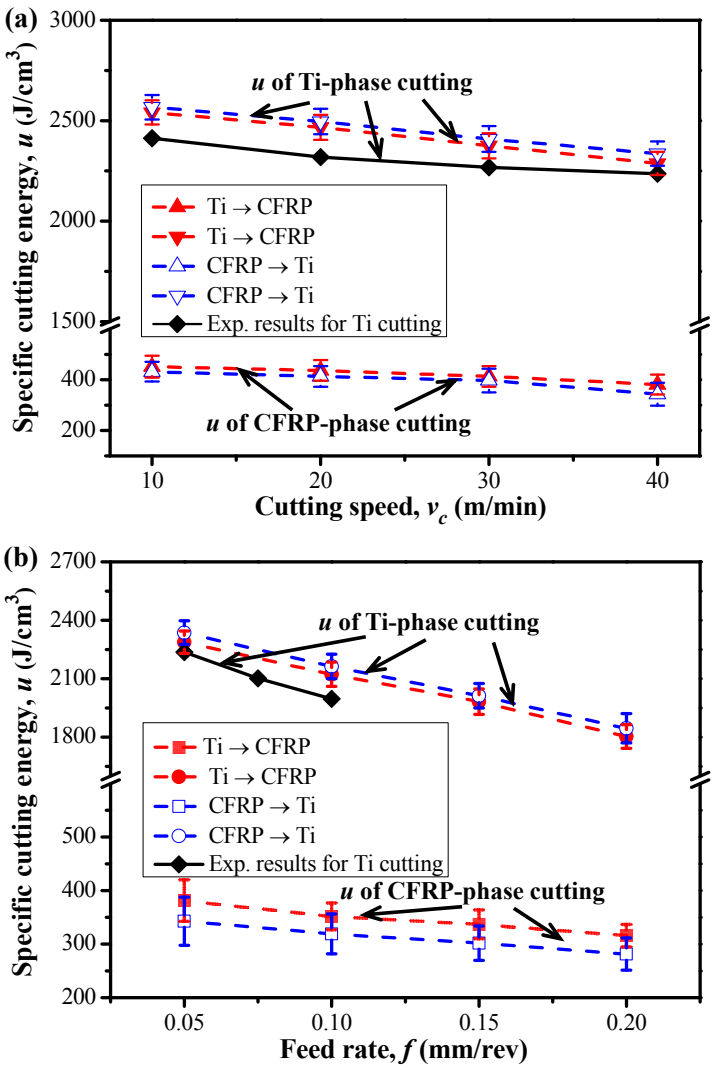

Figure 4.37. Effects of the cutting parameters and cutting-sequence strategies on the specific cutting energy (u) when machining hybrid CFRP/Ti stacks: (a) u *versus* v_c (f = 0.05 mm/rev, θ = 0° and μ = 0.3) and (b) u *versus* f (v_c = 40 m/min, θ = 0° and μ = 0.3) (Exp. result for Ti-phase cutting extracted from Cotterell and Byrne [161]).

Besides, the cutting speed is found to have a negative impact on the specific cutting energy for both Ti-phase cutting and CFRP-phase cutting, *i.e.*, an increased v_c typically leads to the apparently decreased u consumption. The phenomenon can be associated with the thermal softening effects on the work material when v_c is elevated. The evidence also confirms that the high-speed cutting (HSC) may favor the improvement of the CFRP/Ti machinability. Besides, the impact of feed rate is also predicted to be negative. Despite the fact that an elevated f normally leads to an increased cutting force generation, the energy consumed to remove one unit volume of workpiece material, however, decreases correspondingly due to the reduced cutting pressure. The specific behavior can be explained by the well-known phenomenon namely as "chip size effect" [202, 203], which states that there is a substantial reduction of the specific cutting energy with an increase of the uncut chip size. Such findings also agree well with some experimental observations in either metal alloy cutting [202, 203] or CFRP composite cutting [52, 204] from the literature. Furthermore, it can be concluded that to minimize the u consumption, a combination of high cutting speed and high feed rate should be adopted when machining hybrid CFRP/Ti stacks.

In the following study, the cutting parameters of v_c = 40 m/min and f = 0.20 mm/rev were adopted for simulation. To inspect the frictional effect of μ on the global machinability of the hybrid composite stack, the equivalent specific cutting energy ($\bar{u}$) was introduced as expressed below.

$$\bar{u} = \frac{F_{c,CFRP} + F_{c,Ti}}{2 \times a_c \times w} \tag{4.6}$$

where $F_{c,CFRP}$ and $F_{c,Ti}$ denote the main cutting forces of CFRP-phase cutting and Ti-phase cutting, respectively.

Fig. 4.38 shows the effect of μ on the equivalent specific cutting energy ($\bar{u}$) of hybrid CFRP/Ti stacks. Note that in Fig.4.38, the equivalent specific cutting energy ($\bar{u}$) is plotted in a polar map in function of fiber orientation (θ) with the range of 0 ~ 360°. For 180 ~ 360° range, it can be described by fiber orientation angle (θ) after subtracting 180°.

As depicted in Fig.4.38, the equivalent specific energy consumed during hybrid CFRP/Ti stack cutting exhibits strong anisotropy *versus* the input fiber orientation (θ), regardless of the used friction coefficient (μ). The entire $\bar{u}$ map shows a "pigeon"-like shape where the $\bar{u}$ magnitudes are smaller in the second and fourth quadrants when cutting is performed in the reverse fiber direction (θ = 90~180°/270~360°), and larger in the first and third quadrants when cutting is performed in the forward fiber direction (θ = 0~90°/180~270°). In addition, the maximum $\bar{u}$ magnitude takes place when cutting is performed in the perpendicular to fiber direction (θ = 90°/270°), which is approximately 2 times than that of the minimum value, forming the wings of the "pigeon"-shaped map as shown in Fig. 4.38 (a). In contrast, there is a slight increase of $\bar{u}$ in the positions (θ = 165°/345°) close to the horizontal axis across the second and fourth quadrants, which forms the head and tail of the "pigeon"-shaped map as depicted in Fig. 4.38 (a). The "pigeon"-like $\bar{u}$ map, in some extent, reflects the anisotropic machinability of the hybrid CFRP/Ti stacks, which depends significantly on the properties of the stacked constituents, the chip-separation modes of the each-phase cutting, and the anisotropy of the CFRP composite phase.

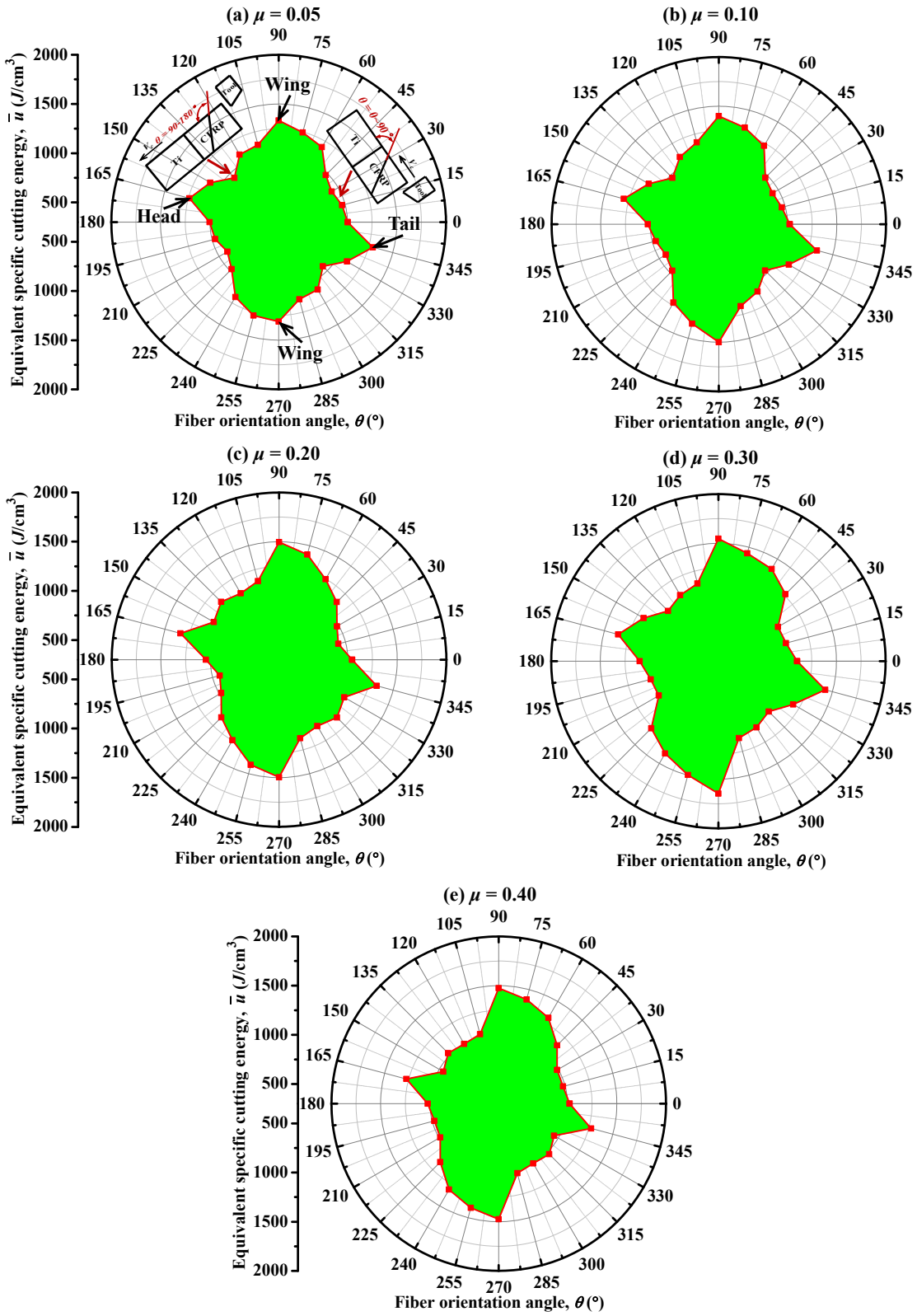

Figure 4.38. Effect of the friction coefficient (μ) on the equivalent specific cutting energy ($\overline{u}$) of hybrid CFRP/Ti stacks (v_c = 40 m/min and f = 0.20 mm/rev): (a) μ = 0.05, (b) μ = 0.10, (c) μ = 0.20, (d) μ = 0.30, and (e) μ = 0.40.

Concerning the μ's effect, it shows a significant influence on the $\overline{u}$ magnitudes of the bi-material machining. As depicted in Fig.4.38, the shape and range of the specific energy map globally suffer an amplified process with the increase of μ. At the minimum friction coefficient of μ = 0.05, the $\overline{u}$ values in various directions are the lowest, which shows the best machinability. In

addition, the "amplification" trend becomes more remarkable especially when μ increases from 0.05 to 0.30. The phenomenon signifies that in such circumstance the frictional behavior of the multi-tool-work interaction plays a vital role in affecting the machinability of the material. When μ reaches over 0.30, the "pigeon"-like area mostly remains the same, and more precisely, suffers a little bit shrinkage, as compared between Fig.4.38 (d) and Fig.4.38 (e), indicating the negative impact arising from the μ's behavior. Such abnormal phenomenon can be explained as follows. The actual μ's effects on the $\bar{u}$ consumption depend significantly on the competition between the thermal softening and cutting resistance enhancement dominating the chip removal process. This means when μ exceeds a threshold value (probably 0.30 in current case), the thermal softening due to the increased cutting temperature from elevated μ, may become a dominant factor that totally affects the chip separation process of hybrid CFRP/Ti stacks and hence will reduce the overall $\bar{u}$ consumption.

4.5.2 Frictional effects on machined surface quality

In hybrid CFRP/Ti stack machining, severe cutting-induced damage will be formed beneath the machined surface that significantly affects the machined surface quality. To clarify the μ's effects on the machined CFRP/Ti surface quality, the most-used one-dimensional arithmetic mean roughness (R_a) was introduced for the comparative studies under the reasonable CFRP → Ti cutting sequence as discussed in subsection 4.3. Note that for each machined-phase surface, nearly $N = 100$ sampling nodes were selected on the machined surface within the sample length (L = 1-mm cutting length). Each measurement was repeated three times in order to ensure the sufficient credibility of the acquired results. Fig. 4.39 then shows the schematic diagram of the R_a calculation on the machined surface. The R_a is expressed as follows.

$$R_a = \frac{\sum_{i=1}^{N} \left| X_i - \bar{X} \right|}{N} \tag{4.7}$$

where X_i denotes the real machined surface height of the i-th node; $\bar{X}$ represents the average value of the measured surface heights; N signifies the number of the selected sampling nodes.

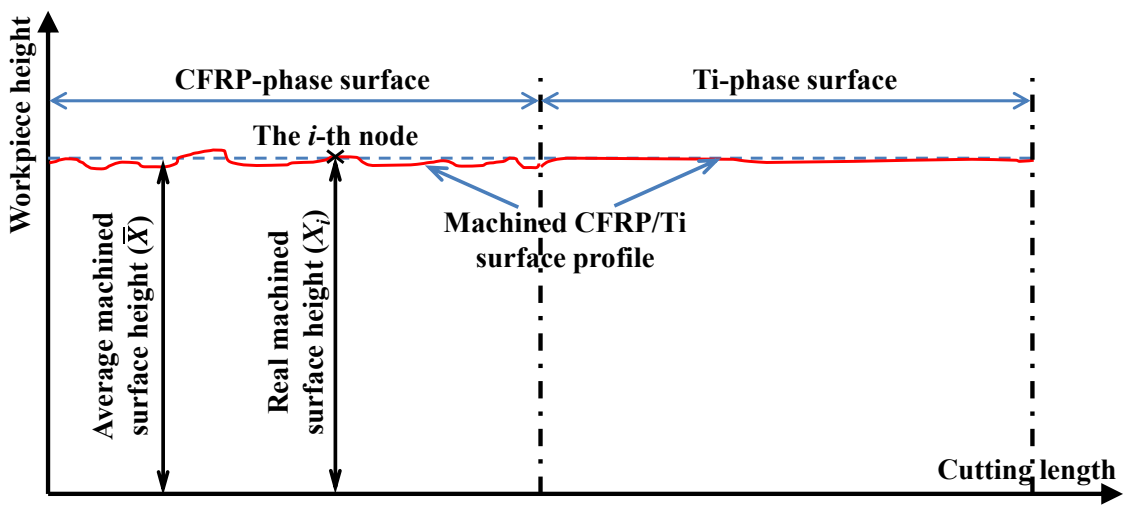

Figure 4.39. Schematic diagram showing the R_a calculation on the machined CFRP/Ti surface.

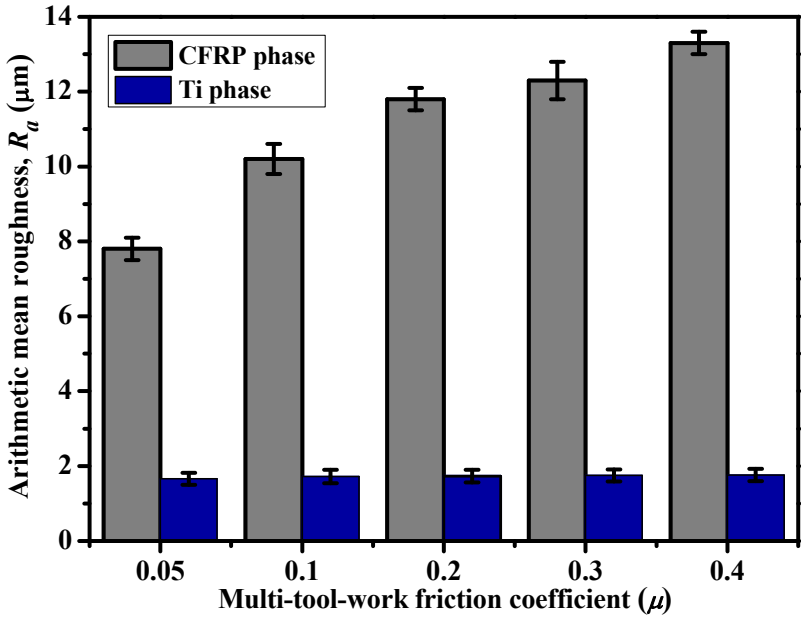

Figure 4.40. Effect of the multi-tool-work friction coefficient (μ) on the arithmetic mean roughness (R_a) when cutting hybrid CFRP/Ti stacks (v_c = 40 m/min, f = 0.2 mm/rev, θ = 0° and CFRP → Ti cutting sequence).

Fig. 4.40 shows the μ's effects on the simulated R_a of each machined surface (CFRP phase and Ti phase) when cutting hybrid CFRP/Ti stacks under the fixed cutting conditions of v_c = 40 m/min, f = 0.2 mm/rev and θ = 0°. It is apparent that the μ has a pronounced effect on the R_a of CFRP phase surface in such manner that an increase of μ commonly gives rise to an obviously elevated R_a value. The phenomenon indicates that high friction coefficient controlling the multi-tool-work interaction will deteriorate the machined surface quality. This is because when μ is elevated, high cutting resistance and high heat generation will dominate the chip removal process, which results in the poor machinability of the workpiece and consequently severe damage formation on the machined surface. As a result, the machined surface finish is destroyed greatly and leads to the high surface roughness. In contrast, the μ's effects on the R_a of the Ti-phase surface seem to be insignificant and slight. The simulated R_a values mostly remain the same in terms of the μ's variation. It should be noted that the mesh size effects have affected the R_a measurement in current simulations. For Ti phase, the mesh size was set around 10 μm, which is much higher than its commonly generated R_a-value range. In such circumstance, the R_a value is predicted to be affected slightly by the μ's effects during the simulation process. Despite all that, the generated R_a values of Ti phase surface are all lower than those of the machined CFRP surface, regardless of the implemented μ values. This is because, in Ti-phase cutting, the predominant chip-separation mode is elastic-plastic deformation that favors the generation of smooth surface finish. By contrast, the brittle-fracture chip-separation mode governing the CFRP-phase cutting usually results in severe micro-crack or micro-fracture on/beneath the machined surface that significantly deteriorates the machined surface finish and gives rise to the high R_a values.

4.5.3 Frictional effects on induced damage and surface integrity

As studied in subsection 4.3, the CFRP → Ti cutting sequence is confirmed to be a reasonable cutting strategy favoring the hybrid CFRP/Ti stack machining. Therefore, the following numerical studies are performed under this optimal cutting sequence. To inspect the effects of the

multi-tool-work friction coefficient and also the input cutting parameters on the cutting-induced damage extent, a special focus was made on the analyses of composite-phase damage, interface delamination, and the induced residual stresses, respectively. Note that since there exist four types of fiber/matrix damage in the CFRP composite machining, the composite-phase damage (D_{CFRP}) was evaluated based on the type that caused the largest extent of failure. Afterward, D_{CFRP} was measured as the largest length from the machined CFRP surface to the deepest damaged area, as shown schematically in Fig.4.22. For the interface delamination (D_{del}), it was measured as the maximum length from the nominal machined surface to the delamination crack tip as shown schematically in the magnified interface zone of Fig.4.22. The residual stresses were measured as a function of depth from the machined surface. All the simulations were performed under the indentical CFRP → Ti cutting sequence. Each measurement was repeated three times in order to ensure the sufficient credibility of the obtained results.

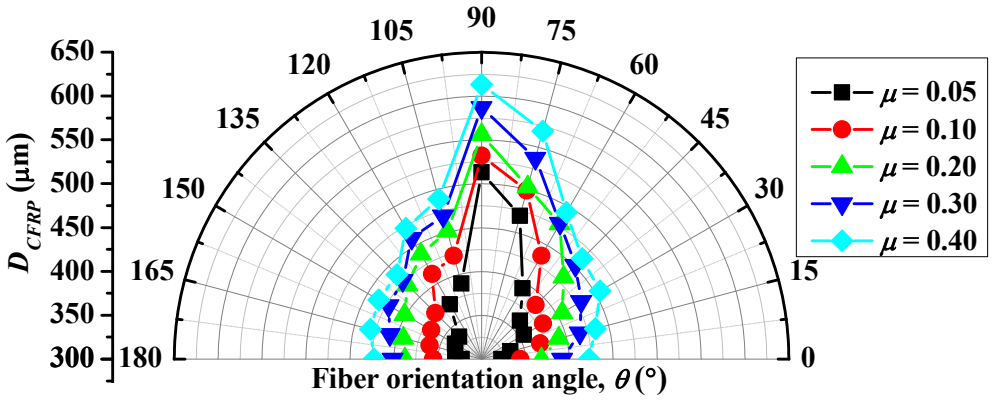

Figure 4.41. Effect of the multi-tool-work friction coefficient (μ) on the composite-phase damage extent (D_{CFRP}) (v_c = 40 m/min, f = 0.2 mm/rev and CFRP → Ti cutting sequence).

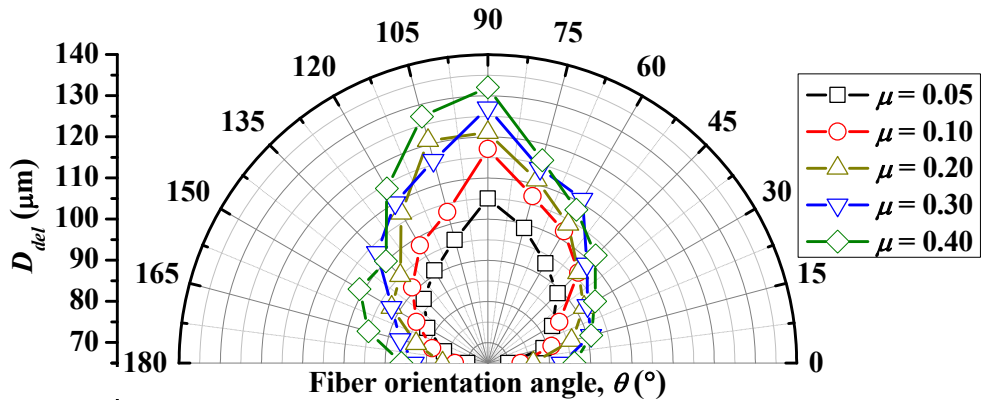

Figure 4.42. Effect of the multi-tool-work friction coefficient (μ) on the interface delamination extent (D_{del}) (v_c = 40 m/min, f = 0.2 mm/rev and CFRP → Ti cutting sequence).

Figs.4.41 and 4.42 show the influences of the multi-tool-work friction coefficient (μ) on the two types of cutting-induced damage extents (D_{CFRP} and D_{del}) under the fixed cutting conditions of v_c = 40 m/min and f = 0.20 mm/rev, respectively. It is noticeable that the μ has a pronounced effect on the extents of composite-phase damage (D_{CFRP}) and interface delamination (D_{del}). At the maximum friction coefficient of μ = 0.40, all the induced damage extents in various fiber orientations are the highest, indicating the poorest machined surface quality. The reason can be attributed to the enhanced thermal-mechanical coupled loads exerted on the machined surface when μ is elevated. The fiber orientation (θ), however, is observed to have an anisotropic effect on the D_{CFRP} and D_{del}.

Such influence shows the identical variation trend as that on equivalent specific cutting energy ($\bar{u}$), in which the minimum/maximum damage extents are produced at θ = 0°/90°, respectively. Moreover, with regard to the parametric effects (v_c and f), the cutting speed is found to globally have a negative impact on the D_{CFRP} and D_{del} extents (except the abnormal ponit of v_c = 10 m/min for D_{del}) while the impact of feed rate is totally positive, as depicted in Fig.4.43. Besides, a combination of high cutting speed and low feed rate commonly results in the minimal induced damage formation.

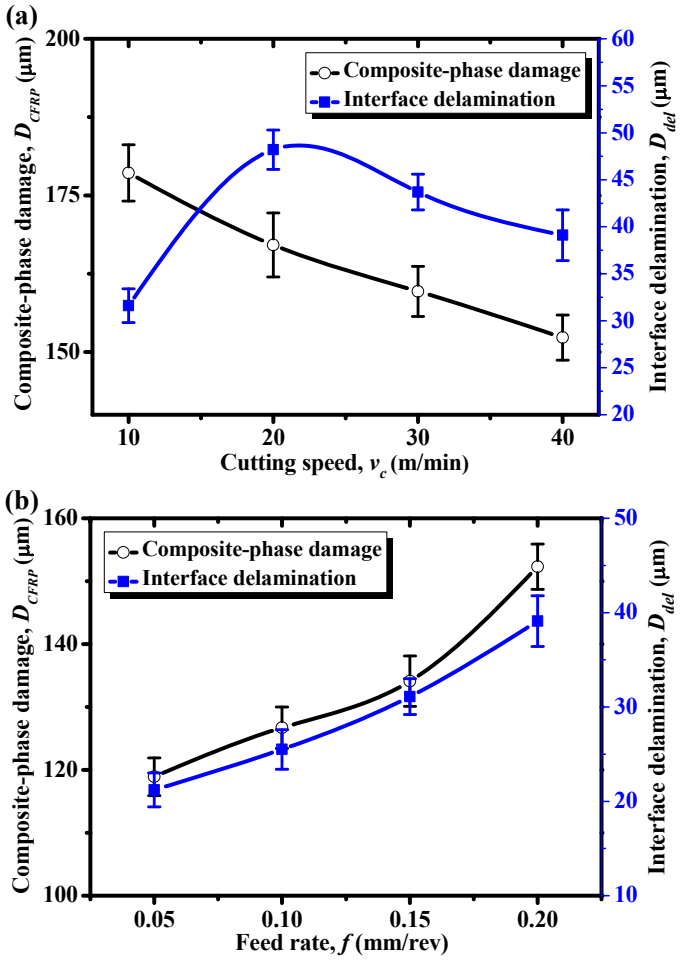

Figure 4.43. Parametric effect of (a) cutting speed (v_c) (f = 0.2 mm/rev, θ = 0° and μ = 0.3) and (b) feed rate (f) (v_c = 40 m/min, θ = 0° and μ = 0.3) on D_{CFRP} and D_{del}.

Furthermore, for the machined Ti-phase surface, the induced residual stresses which are usually considered as a key surface-integrity criterion for metallic material machining, were studied in terms of the multi-tool-work friction coefficient (μ). Note that the residual stresses were measured in the middle-length region of the machined Ti-phase (as shown schematically in the region II of the machined Ti surface in Fig.4.44(b)), where the cutting operation could be assumed to reach a steady state. In addition, for accurately estimating the real residual stress status, three unloading steps including (*i*) release of the cutting forces, (*ii*) release of clamping forces, and (*iii*) release of the workpiece to the room temperature were also implemented at the end of each cut prior to the measurement. Fig.4.44(a) presents the μ's effects on the residual stress distribution beneath the machined surface. As can be seen in this figure, the residual stresses remain on the machined surface (0 μm depth) are all predicted to be negative regardless of the used friction coefficients,

indicating the presence of compressive stresses. With the increase of depth, the compressive stresses firstly experience an enhanced process within the depth range of 0 ~ 10 μm. Afterward, all the compressive stresses are found to suffer a significant reduction *versus* the increased depth. Besides, a threshold depth (40 μm) is also detected, beyond which, the residual stresses basically reach a stable state accompanied by a very slight variation, indicating the minimal influences arising from the cutting process. Moreover, the acquired results presented in Fig.4.44(a), also clearly indicate that the μ has a significant influence on the residual stress profile beneath the machined surface. An increase of μ usually gives rise to the increased tensile stresses and decreased compressive stresses. From the viewpoint of the fatigue performance of the machined parts, the compressive stresses contribute to the fatigue life while the tensile stresses are destructive for surface integrity and thus should be strongly avoided [205]. The detrimental effects of μ on the cutting-induced residual stress imply that the multi-tool-work frictional behavior affects the residual stress distribution primarily via its thermal influence instead of its mechanical effects. That means when μ increases, a large amount of cutting heat will be generated along the tool-work interface, and subsequently is exerted on the machined Ti surface. Consequently, the highly increased cutting temperature results in the enhancement of the tensile stresses and the reduction of the compressive stresses. In such circumstance, the machined surface integrity is deteriorated greatly.

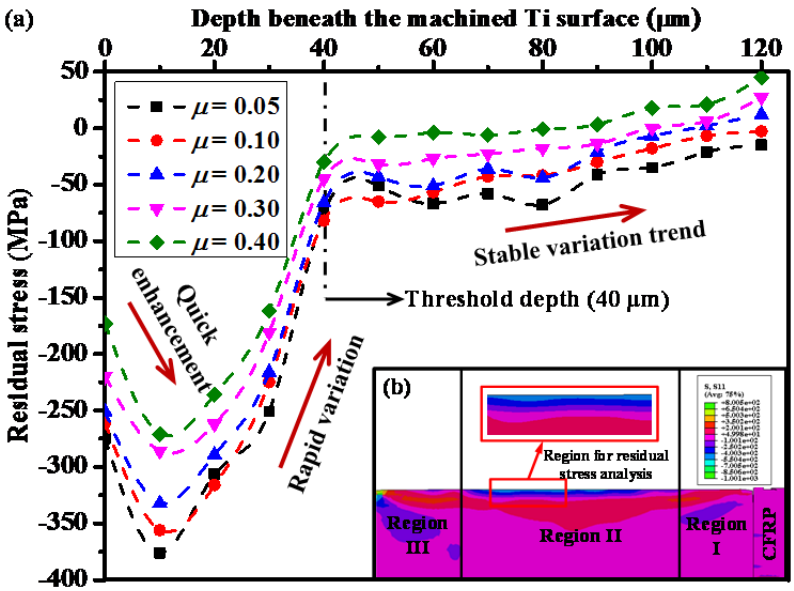

Figure 4.44. (a) Effect of the multi-tool-work friction coefficient (μ) on the residual stress profile of the machined Ti-phase surface when cutting hybrid CFRP/Ti stacks (v_c = 40 m/min, f = 0.2 mm/rev, θ = 0° and CFRP → Ti cutting sequence) and (b) scheme of the residual stress measurement in the machined Ti surface (region I → the onset of the Ti-phase cutting; region II→the steady state of the Ti-phase cutting and region III →the exit of the Ti-phase cutting).

The above analyses imply that for improving the machined surface quality, small multi-tool-work friction coefficient as well as low fiber orientation, high cutting speed and low feed rate should be preferentially selected when cutting hybrid CFRP/Ti stacks. The μ's effect on the induced residual stresses of the machined Ti-phase surface is totally detrimental, indicating that the predominant factor is thermal influence. For realizing the improvement of the multi-tool-work frictional behavior, *i.e.*, reducing μ, the application of effective cutting fluid and the use of superior tool material can be adopted in the real production of the bi-material system.

4.6 Conclusions

This Chapter has provided comprehensive FE studies of the key mechanisms and physical phenomena governing the hybrid CFRP/Ti stack machining. The proposed FE models offer reliable estimations of the various CFRP/Ti cutting responses dominating the bi-material machining by several comparisons with the experimental results from the literature. Based on the results acquired, the key conclusions can be drawn from this study.

- The disparate natures of each stacked constituent make the CFRP/Ti cutting process exhibit three distinct cutting stages, *i.e.*, Ti-phase cutting, interface cutting and CFRP-phase cutting. The chip separation modes controlling the bi-material cutting comprise both elastic-plastic deformation and brittle fracture. The changeable chip removal mechanisms typically resulted in extremely harsh conditions dominating the interface cutting. Severe force fluctuation is observed as the key characteristic governing the hybrid CFRP/Ti stack cutting. Serious chip adhesion on tool rake face is found to be the key factor contributing to the dramatic increase of cutting force generation in the post CFRP-phase machining.

- Numerical results highlight the occurrence of severe delamination damage concerning the CFRP/Ti interface. FE analyses reveal that the initiation and evolution of interface delamination primarily take place at the cutting period of AIZ. The formation of CFRP/Ti interface damage involves a series of detaching and tearing variation governing the AIZ cutting time. The key mechanisms of interface damage formation can be attributed to the coupled effects of fracture modes I and II arising from the unique mechanical loads exerted on the bi-material interface region. The key morphological characteristic of the interface delamination is a “V shape”-like notch on the “CFRP-to-Ti” contact boundary.

- Interface cutting confirms the significant role of cutting speed and feed rate in affecting the AIZ cutting duration. The input variables (v_c and f) indeed exhibit pronounced effects on the interface delamination extent via the manner of their influences on the AIZ. For minimizing the severe interface damage formation, a parametric combination of high cutting speed and low feed rate should be adopted.

- The entire CFRP/Ti cutting operation can be physically divided into three cutting zones from the viewpoint of the interrelated influences arising from each-phase machining: (*i*) pure Ti-phase cutting, (*ii*) AIZ cutting, and (*iii*) pure CFRP-phase cutting. Among them, the AIZ cutting in reality reflects the real machinability of the coupled CFRP/Ti material ($M_{\mathrm{CFRP/Ti}}$), which can be considered as the most difficult-to-cut zone due to the occurrence of interrelated cutting influences and the existence of the weakest interface zone. In such case, to fundamentally improve the machinability of the hybrid CFRP/Ti stack, a special attention should be paid to the in-depth mechanism investigation and cutting-parameter optimization of the AIZ cutting zone. In the future, more systematic studies should be performed to address precisely the aforementioned issues.

- The CFRP → Ti cutting sequence is confirmed to favor the chip breakage of the bi-material system. The chip-adhesion phenomenon operates as a key factor in affecting the cutting-sequence’s influence on hybrid composite stack machining. The CFRP → Ti cutting

sequence is more beneficial for high-quality machining of CFRP/Ti stacks than Ti → CFRP cutting sequence. For improving the machinability of hybrid CFRP/Ti stacks, the reasonable CFRP → Ti cutting sequence should be preferentially adopted in actual production to minimize the induced damage formation and guarantee better-machined surface quality.

- Parametric studies highlight the significant effect of feed rate on the cutting-force generation, and the crucial role of fiber orientation in affecting the composite-phase damage and interface delamination when cutting hybrid CFRP/Ti stacks. The impact of cutting speed on CFRP/Ti cutting force is found to be generally negative due to the softening effects of increased cutting temperature on work material when v_c is elevated. For minimizing the cutting-force generation and the severe induced damage extent, low feed rate, high cutting speed and small θ configuration should be strongly recommended when machining hybrid CFRP/Ti stacks.

- The multi-tool-work friction coefficient (μ) plays a crucial role in affecting the various frictional responses when cutting hybrid CFRP/Ti stacks primarily via its thermal and mechanical influences. However, for specific machining response, the actual μ's effect depends significantly on which factor (thermal or mechanical influence) dominates the affecting process. In such case, different mechanisms are observed in the numerical studies. For cutting energy consumption, the μ's influence primarily depends on the competition between the thermal softening and cutting-resistance enhancement governing the chip-separation process when μ is elevated. A threshold μ value is then predicted around 0.3, beyond which, the μ's impact on $\overline{u}$ consumption is negative due to the increased thermal softening over cutting-resistance enhancement when μ increases. In addition, the μ also exhibits a significantly positive impact on the induced subsurface damage formation owing to the enhanced thermal-mechanical loads exerted on the machined surface when μ is elevated. With respect to the induced residual stress of machined Ti part, the predominant factor arising from μ's influences is thermal effect that increases the tensile stresses while decreases the compressive stresses.

- The numerical studies eventually point out that improving the multi-tool-work frictional behavior, *i.e.*, reducing μ, will be a direct and beneficial solution for achieving high-quality machining of hybrid CFRP/Ti stacks. To this aim, several applications capable of reducing μ, like the use of effective cutting fluid and superior tool material, can be adopted in the real production of the sandwich material. Moreover, for improving the machined surface quality, the choice of high cutting speed, low feed rate, and small fiber orientation should be made when cutting hybrid CFRP/Ti stacks.

Chapter V

Experimental studies on orthogonal cutting mechanisms of hybrid CFRP/Ti stacks

Nomenclature

CFRP → Ti Ti → CFRP	Cutting from CFRP to Ti and/or Ti to CFRP
f	Feed rate
F_c	Cutting force
F_t	Thrust force
R_a	Arithmetic mean roughness
R_q	Root mean squared roughness
R_z	Ten point mean roughness
v_c	Cutting speed
α	Tool rake angle
γ	Tool clearance angle
θ	Fiber orientation

Abbreviation

BUE	Built-up edge
EDS	Energy Dispersive Spectrometer
OCC	Orthogonal cutting configuration
OM	Optical microscope
PCD	Polycrystalline diamond
SEM	Scanning Electron Microscope

5.1 Introduction

Orthogonal cutting is often a fundamental representation of complicated machining operations for inspecting the key cutting mechanisms dominating the material removal process. To improve the fundamental cutting comprehension of hybrid CFRP/Ti stacks, tremendous scientific work has been performed in the past few decades by various worldwide scholars, *e.g.*, Ramulu et al. [2], Brinksmeier and Janssen [15], Fujiwara et al. [40], Ghassemieh [41], Isbilir and Ghassemieh [42], Kim and Ramulu [43], Kuo et al. [44], Park et al. [45], Shyha et al. [49], Wang et al. [51]. Their key research topics focus on (*i*) experimental studies on the machinability evaluation and process optimization of hybrid CFRP/Ti stacks [2, 15, 43], (*ii*) parametric studies on the subsurface damage formation [15, 40-42, 49], and (*iii*) tool performance comparison and tool wear mechanism [44, 45, 51], *etc*. Compared to the already-performed research work, this Chapter aims to reveal the most fundamental mechanisms controlling the bi-material cutting via the orthogonal cutting method.

To this aim, the CFRP/Ti orthogonal cutting subjected to different cutting-sequence strategies ($^{\text{CFRP}\rightarrow\text{Ti}}_{\text{Ti}\rightarrow\text{CFRP}}$) was implementated so as to clarify their influences on the bi-material machinability. The key machining responses including chip removal process, force genration, machined surface morphology, surface integrity were comphrehneive studied. Meanwhile, several cutting trials of combined CFRP/Ti machining were also performed to inspect the force generation and the correspondingly tool performance. During the experimental investigations, a special attention was paid to the studies of the activated tool wear mechanisms when machining different fiber orientation configured CFRP/Ti stacks.

With respect to the used tool-work configuration, experimental setup and measuring system, please refer to the relevant illustrations in Chapter III.

5.2 Chip removal process

The characteristics of chip formation are of great importance for understanding the responses of work materials when subjected to machining operations. The chip removal process governs the machined surface quality as well as the wear behavior of the utilized cutting tools. In this work, the in-situ CCD camera was used to gather and analyze the dynamic characteristics of the chip formation when trimming CFRP/Ti stacks with PCD tipper inserts as illustrated in details in subsection 3.4.1.2. Figs. 5.1 - 5.3 show the recorded CFRP/Ti cutting images with respect to different fiber orientations (θ) and cutting sequence strategies ($^{\text{CFRP}\rightarrow\text{Ti}}_{\text{Ti}\rightarrow\text{CFRP}}$). Additionally, the scheme of the cutting mechanisms *versus* different fiber orientations of CFRP/Ti stacks is also given in Table 5.1. It can be seen that when machining 0° fiber orientation, the compressive load resulting from the tool advancement will initiate an interfacial debonding inside the fiber/matrix interface that causes the fiber layers to peel up and to slide on tool rake face (Ref. Table 5.1). Afterward, the tool advance leads the fibers to break perpendicular to their axes under buckling. In such circumstance, the real tool-chip contact length acting on tool rake face should be a little bit larger than the nominal depth of cut (*i.e.*, feed rate (f) in current case) as shown in Table 5.1. Besides, since the brittle fracture acts as a predominant chip separation mode of 0° CFRP phase, various “discontinuous” chips are generally formed (Ref. Fig.5.1(a)). The small chips produced are qualified by “powdery” nature due to a series of fractures in chip removal process as shown in Fig.5.4(a). In addition, when cutting 45°

CFRP in a hybrid composite stack, the tool advancement will cause severe compressive shear and bending actions among the uncut fibers, and initiate cracks occurring in fibers above or below the trim plane. Then, an interfacial shear appears at the end of the primary fracture and propagates in a direction toward the fiber orientation until completely releasing the chips. With the ongoing chip removal process, the 45° CFRP machining will result in a tool-chip contact length approximately equal to the nominal depth of cut as schematically illustrated in Table 5.1. Moreover, when cutting 90° CFRP/Ti stacks, the uncut fibers in the CFRP phase will suffer serious compressive loading with an out-of-plane shear that leads to the inter-laminar deformation [57]. In such case, the carbon fibers ahead of tool rake face will undergo severe splintering as soon as the tool edge come in contact with them, and severe fiber/matrix cracking takes place beneath the trim plane as depicted in Fig. 5.3(c). When the shearing stress exceeds the shearing limit of the fibers, it results in the complete chip formation. The real tool-chip contact length dominating the 90 CFRP chip separation is assumed to be much larger than the nominal depth of cut as shown in Table 5.1. Through the comparative analyses among different fiber orientations, it can be expected that the fiber orientation of the stacked CFRP phase has a great effect on tool-chip contact length on tool rake face that will consequently affect the wear behavior of the utilized tools in multilayer stack Cutting. Detailed analyses will be performed in the following subsection 5.7.

Furthermore, as exhibited in Figs. 5.1 - 5.3, when machining in CFRP → Ti cutting sequence, the tool edge initially cuts into the CFRP phase and results in the “powdery” like chip formation due to the predominant brittle fracture chip separation mode. The resected CFRP chips are basically in the form of dust (Ref. Fig. 5.4 (a)) and spread quickly into the surrounding environment with the tool advancement (*e.g.*, Fig.5.1 (a) - (c), Fig.5.2 (a) - (c) and Fig.5.3 (a) - (c)). Further, when the tool edge cuts across the interface region, a long “continuous” chip type is produced flowing along tool rake face due to the transition of chip removal mechanisms from brittle fracture to plastic deformation. In addition, through the entire CFRP → Ti cutting inspection, nearly neither severe chip/material cracking nor fracture phenomena are observed in the interface zone and CFRP phase.

By contrast, apart from the identically observed chip separation modes and resected chip types, the Ti → CFRP cutting usually promotes serious cracking damage concerning the weakest interface region, as shown in Fig.5.1 (e). The key cause is due to the serious Ti chip adhesion on tool rake face that replaces the tool edge for further CFRP chip separation and hence causes significant extrusion/scratching effects on the uncut CFRP chip layers. The observation of the problematic Ti chip adhesion in Ti → CFRP cutting also agrees well with the numerical findings in subsection 4.2 of Chapter IV. Besides, it is also observed that the problematic Ti chip adhesion occurs for all examined fiber orientations. The detrimental phenomenon, on one hand, should inevitably deteriorate the machined surface quality and contribute greatly to the elevated force generation [165, 169]. On the other hand, it will result in the built-up edge (BUE) on tool rake face and accelerate premature tool failures like micro chipping or edge fracture.

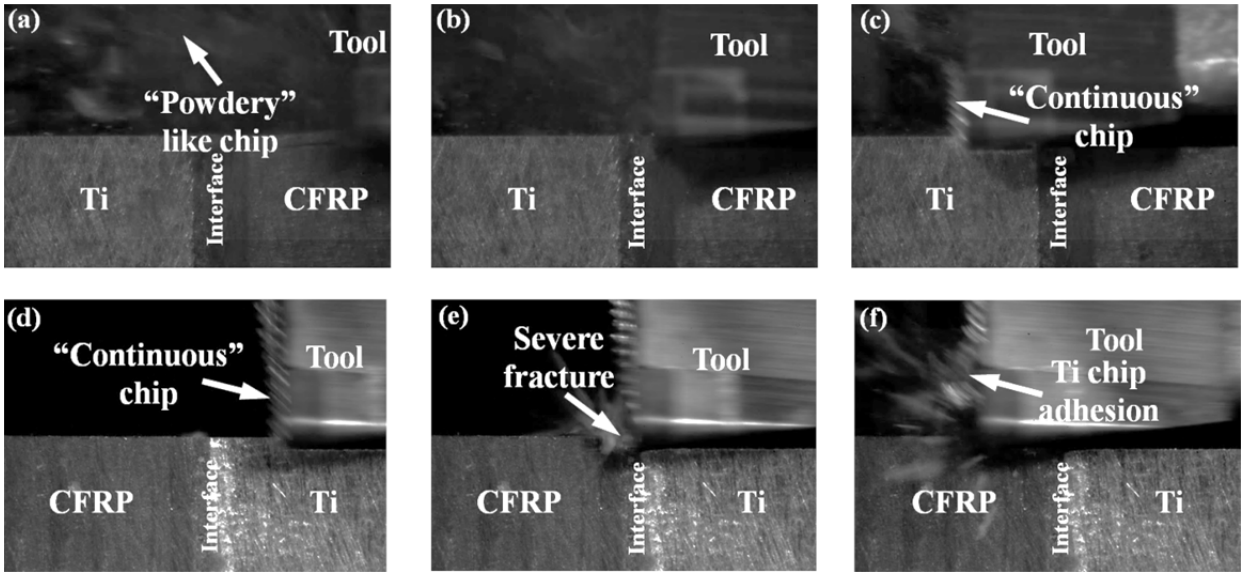

Fig.5.1. High speed camera images showing the orthogonal cutting chip separation of hybrid CFRP/Ti stacks ($\theta = 0°$, v_c =50 m/min and f = 0.20 mm/rev): (a) - (c) CFRP → Ti cutting sequence and (d) - (f) Ti → CFRP cutting sequence.

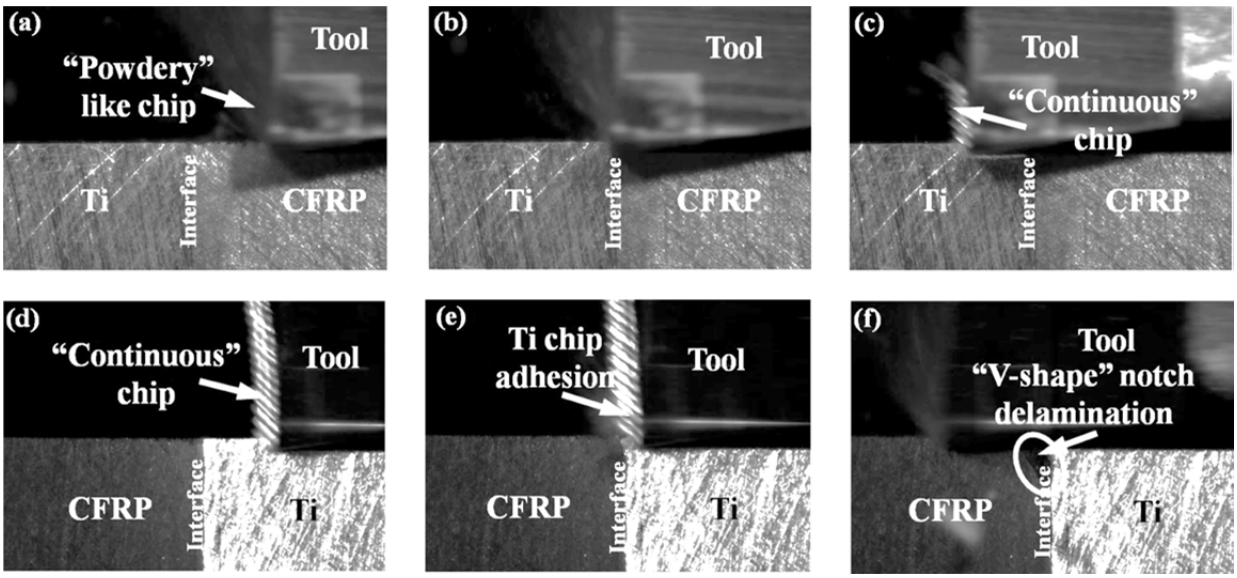

Fig.5.2. High speed camera images showing the orthogonal cutting chip separation of hybrid CFRP/Ti stacks ($\theta = 45°$, v_c =50 m/min and f = 0.20 mm/rev): (a) - (c) CFRP → Ti cutting sequence and (d) - (f) Ti → CFRP cutting sequence.

Moreover, the Ti → CFRP cutting is also found to promote severe subsurface damage concerning the interface zone and subsequent CFRP phase. As depicted in Fig.5.2 (f), when the tool edge completely cuts across the interface region, a "V shape"-like notch delamination is eventually induced, which is in agreement with the numerical observation in subsection 4.2.2 of Chapter IV. For higher fiber orientation, *e.g.*, $\theta = 90°$, the Ti chip adhesion is found to cause a high extent of fiber/matrix splintering beneath the machined CFRP surface as depicted in Fig.5.3 (f) due to its severe extrusion/scratching effects on the uncut chip materials.

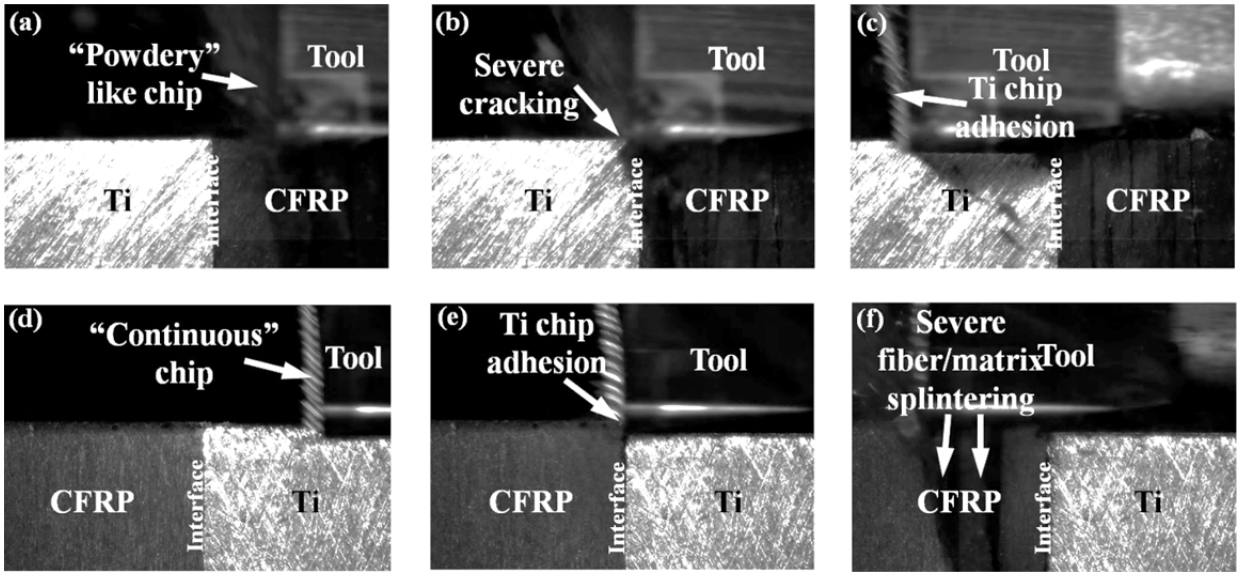

Fig.5.3. High speed camera images showing the orthogonal cutting chip separation of hybrid CFRP/Ti stacks ($\theta = 90°$, v_c =50 m/min and f = 0.20 mm/rev): (a) - (c) CFRP → Ti cutting sequence and (d) - (f) Ti → CFRP cutting sequence.

Table 5.1
Scheme of the chip separation mechanisms *versus* different fiber orientations of CFRP/Ti stacks.

Fiber orientation	Schematization	Chip removal characteristics
$\theta = 0°$	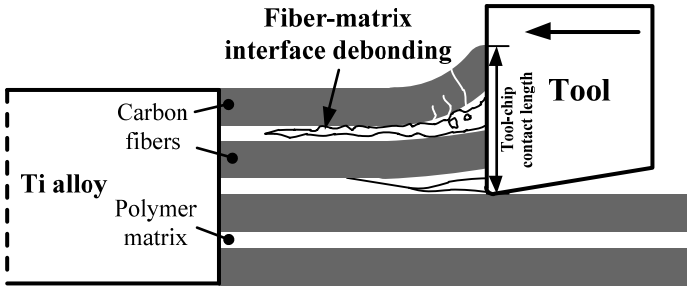	(a) Compression shear → interfacial debonding → buckling → fiber fracture (b) Tool-chip contact length is a little bit larger than the nominal depth of cut.
$\theta = 45°$	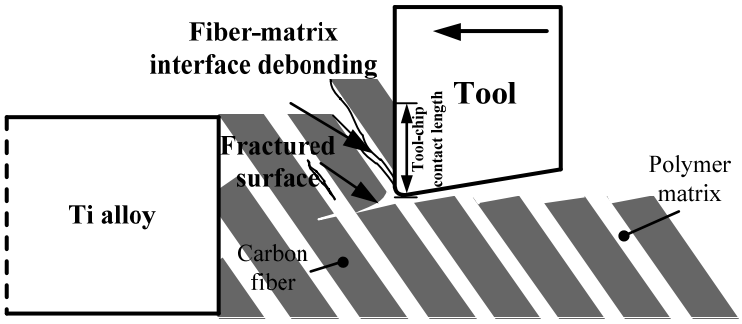	(a) Compressive shear + bending → fiber cracking → interfacial debonding → fiber fracture (b) Tool-chip contact length is approximately equal to the nominal depth of cut.
$\theta = 90°$	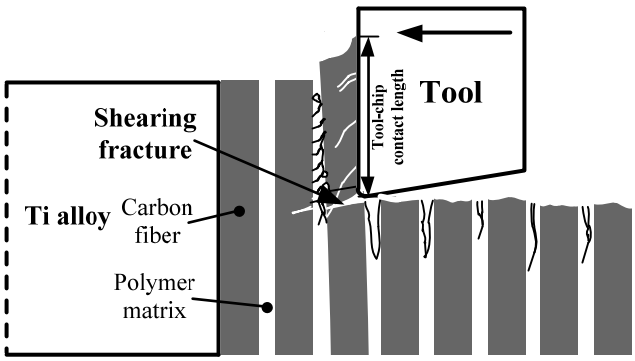	(a) Compression shear + out-of-plane shear → inter-laminar deformation → fiber fracture (b) Tool-chip contact length is much larger than the nominal depth of cut.

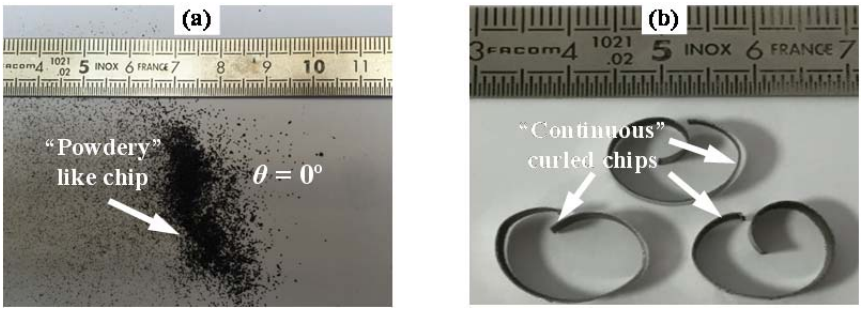

Fig.5.4. Representative chip types in cutting hybrid CFRP/Ti stacks ($\theta = 0°$, $v_c = 50$ m/min, $f = 0.20$ mm/rev and CFRP → Ti cutting sequence): (a) CFRP chip type and (b) Ti chip type.

Further, a summary of the key cutting phenomena observed in the on-site machining of CFRP/Ti stacks is provided in Table 5.2, in which a comparative inspection between two different cutting sequence strategies is presented. Through the acquired results, it can be drawn that the CFRP → Ti cutting sequence globally shows a better suitability for orthogonal cutting of hybrid CFRP/Ti stacks due to the avoided serious Ti chip adhesion. For Ti → CFRP cutting, the key problem encountered in machining is Ti chip adhesion replacing the tool cutting edge for further composite phase cutting which should causes significantly detrimental influences on the final CFRP/Ti cutting.

Table 5.2
A summary of the observed physical phenomena in the on-site orthogonal cutting of hybrid CFRP/Ti stacks.

Cutting strategy	Fiber orientation (θ)	Key phenomena observed in machining
CFRP → Ti	$\theta = 0°$	(a) Initially "powdery" like chips rapidly spread to the surrounding environment, which was harmful for the respiratory systems of machinists. (b) Subsequently "continuous" Ti chips were produced on tool rake face. (c) An amount of smoke was induced due to the high cutting heat promoted in Ti phase cutting. (d) Smooth machined interface and CFRP surface were produced.
	$\theta = 45°$	(a) Initially "powdery" like chips rapidly spread to the surrounding environment, which was harmful for the respiratory systems of machinists. (b) Subsequently "continuous" Ti chips were produced on tool rake face. (c) An amount of smoke was induced due to the high cutting heat promoted in Ti phase cutting. (d) Smooth machined interface and CFRP surface were produced.
	$\theta = 90°$	(a) Difficult CFRP chip separation was observed due to the severe fiber/matrix debonding in the CFRP laminate. (b) A number of "powdery" CFRP chips were produced. (c) Cracking damage took place inside the CFRP laminate and interface zone. (d) Subsequently "continuous" Ti chips were produced on tool rake face. (e) Poor machined CFRP surface and interface were generated.
Ti → CFRP	$\theta = 0°$	(a) Initially "continuous" Ti chips were produced accompanied by a mount of heat-induced smoke. (b) Ti chip adhered on tool rake face when the tool edge cut into the interface zone. (c) Severe cracking damage took place in the interface zone. (d) Finally "powdery" like CFRP chips were produced.
	$\theta = 45°$	(a) Initially "continuous" Ti chips were produced accompanied

		by a mount of heat-induced smoke. (b) Serious Ti chip adhesion was found on tool rake face when the tool edge cut into the interface zone. (c) "V shape" like delamination damage took place in the interface zone. (d) Finally "powdery" like CFRP chips were produced. (e) Poor machined CFRP surface and interface were generated.
	$\theta = 90°$	(a) Initially "continuous" Ti chips were produced accompanied by a mount of heat-induced smoke. (b) Serious Ti chip adhesion was found on tool rake face when the tool edge cut into the interface zone. (c) "V shape" like delamination damage took place in the interface zone. (d) Poor CFRP chip separation and difficult Ti chip evacuation were observed. (e) Severe fiber/matrix splintering took place in the CFRP laminate. (f) Extremely poor machined CFRP surface and interface were generated.

With respect to combined CFRP/Ti machining, the high-speed video images in Fig.5.5 show that when the tool edge cuts the two stacked materials together, both "continuous" and "powdery" chips are generated simultaneously ahead of tool rake face, indicating the occurrence of coupled plastic deformation and brittle fracture modes. Besides, since the two materials show disparate chip separation modes, the tool main cutting edge involved in the bi-material removal should suffer uneven stress/temperature distribution, which will inevitably cause severe cutting vibration and tool-work instability, and hence accelerate the subsequent premature tool failure.

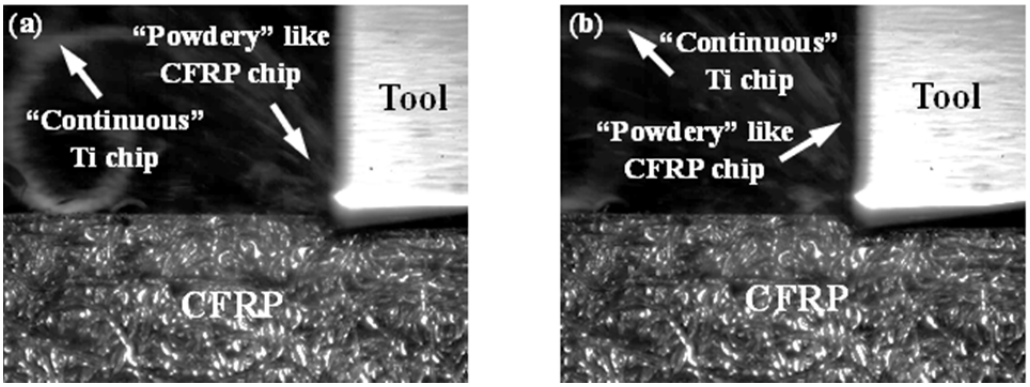

Fig.5.5. High speed camera images showing the combined CFRP/Ti chip separation process ($\theta = 0°$, $v_c = 50$ m/min and $f = 0.20$ mm/rev): (a) tool A and (b) tool B.

Through the chip removal analyses, it can be concluded that the CFRP → Ti cutting sequence globally shows better suitability for orthogonal cutting of hybrid CFRP/Ti stacks due to the avoided serious Ti chip adhesion. For Ti → CFRP cutting, the key problem encountered in machining is Ti chip adhesion which more or less causes significantly detrimental influences on the final machining responses, *e.g.,* induced subsurface damage formation and trimmed surface finish. For combined CFRP/Ti cutting, both brittle fracture and plastic deformation take place simultaneously and result in the coupled "powdery" and "continuous" chip formation. Such phenomenon will inevitably induce the instability of the tool-work interaction and initiate the premature tool failure.

5.3 Cutting process and force signal analysis

In hybrid CFRP/Ti stack machining, monitoring the force signal developed in the chip removal process is an effective method to inspect the on-site status of the tool-work interaction controlling the bi-material cutting operation. Specifically, the force generation promoted in orthogonal cutting can be decomposed into two basic components, *i.e.*, cutting force (F_c) and thrust force (F_t), which signify the tribological behaviors between the tool-chip interaction and tool-work interaction, respectively. Fig.5.6 shows the obtained force signal profiles with respect to different fiber orientations and cutting sequence strategies ($^{\text{CFRP}\rightarrow\text{Ti}}_{\text{Ti}\rightarrow\text{CFRP}}$). It is noticeable that the force profiles promoted in either $\theta = 0°$ or $\theta = 45°$ exhibit the identical variation law *versus* cutting time. Besides, the force signal generated in Ti-phase cutting is commonly much higher than that promoted in CFRP-phase cutting. The activated mechanisms should be ascribed to the specific chip separation mode of the metallic phase and its relatively higher mechanical/physical properties [4, 165, 169]. Moreover, as depicted in Fig.5.6, a sudden increase/decrease of cutting force (F_c) is observed when the tool edge cuts across the interface zone in either CFRP → Ti cutting sequence or Ti → CFRP cutting sequence. The phenomena indeed should cause severe cutting vibration of the tool-work interaction and accelerate the premature tool chipping failure for the used PCD tools. Additionally, for the identical stacked phase machining, the force profile promoted in post phase cutting commonly yields a little bit higher magnitudes as compared to that generated in the initial phase cutting, *e.g.*, the F_c of Ti-phase cutting in CFRP → Ti sequence often shows a higher force value than that obtained in Ti → CFRP cutting sequence as can be seen in Fig.5.6 (b).

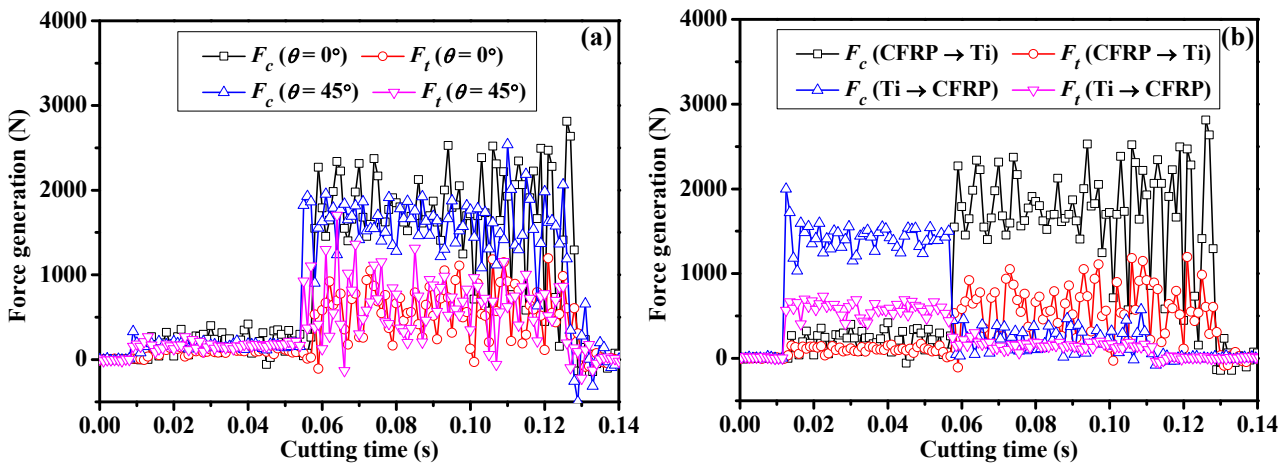

Fig.5.6. Recorded force signals *versus* cutting time when orthogonal cutting CFRP/Ti stacks: (a) force generation under different fiber orientations ($\theta = 0°$ and 45°) and (b) force generation in different cutting sequences ($^{\text{CFRP}\rightarrow\text{Ti}}_{\text{Ti}\rightarrow\text{CFRP}}$).

Since all the recorded force signals in either different fiber orientations or different cutting sequences show the similar variation law, the force profile developed in CFRP → Ti cutting sequence with $\theta = 0°$ is taken as an example for illustration of CFRP/Ti cutting process. The following Fig.5.7 then shows the obtained force signal in terms of cutting time under the fixed cutting conditions of $v_c = 50$ m/min and $f = 0.20$ mm/rev.

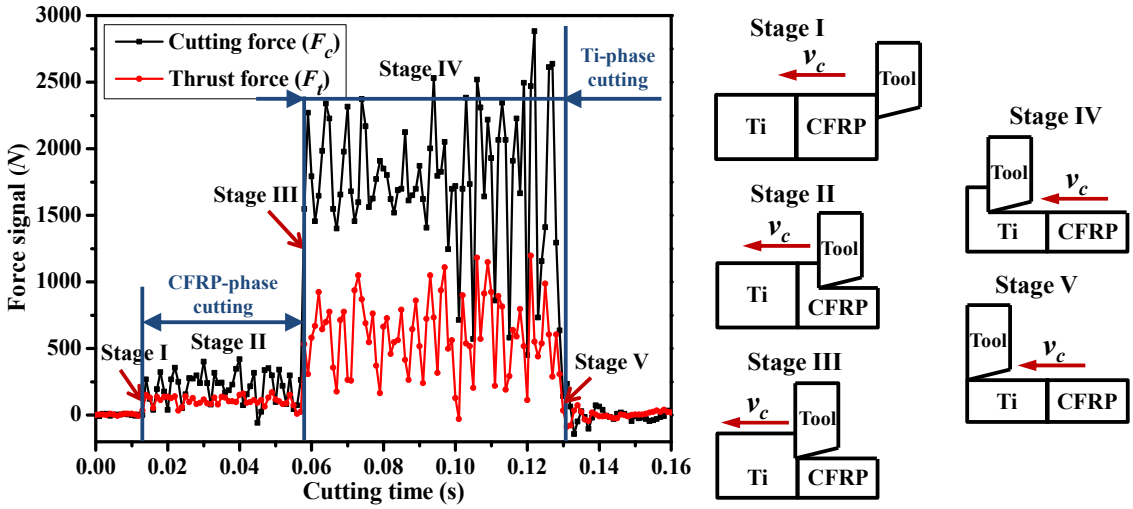

Fig.5.7. Illustration of the CFRP/Ti orthogonal cutting process by means of force signal development ($\theta = 0°$, $v_c = 50$ m/min and $f = 0.20$ mm/rev).

It is apparent that the entire force signal (F_c and F_t) can be globally distinguished into five cutting stages, in which the overall CFRP/Ti cutting process can be clearly described. As depicted in Fig. 5.7, the first stage I signifies that the tool edge firstly cuts into the CFRP phase, and both cutting force (F_c) and thrust force (F_t) increase gradually from zero. Afterward, the force signal suffers a steady variation due to the periodical chip separation process governing the composite phase machining, which can be denoted as cutting stage II. Moreover, when the tool cuts across the interface region, *i.e.*, the tool edge gradually attacks the Ti alloy phase, the force signal experiences a quickly increasing trend due to change of cutting mechanisms from brittle fracture to plastic deformation, as implied by cutting stage III. In addition, when the tool edge is completely involved in the Ti phase machining, both two force components enter into a stable variation state which signifies the cutting stage IV. Finally, when the cutting tool fulfills the CFRP/Ti machining, all the force signals gradually decrease into zero, as described by the cutting stage V in Fig.5.7.

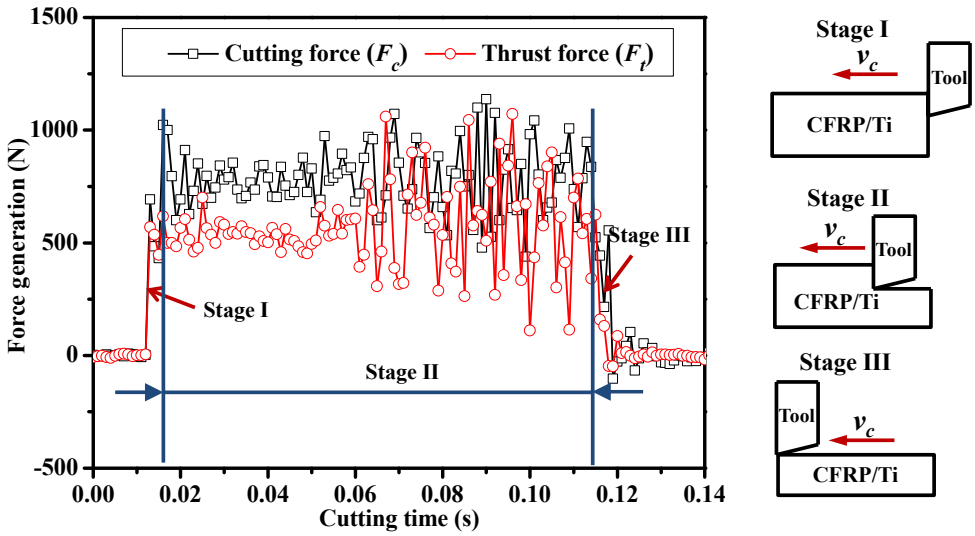

Fig.5.8. Illustration of the combined CFRP/Ti cutting process in terms of force signal development ($\theta = 0°$, $v_c = 50$ m/min and $f = 0.20$ mm/rev).

With respect to the combined CFRP/Ti machining, the cutting process involves three stages as depicted in Fig.5.8. The first stage I denotes the gradual engagement of tool-work interaction, in

which the force signal suffers a quick increasing trend. With the tool advancement, especially when the tool edge fully engages in the bi-material machining, the cutting process reaches a stable status (see stage II in Fig.5.8), where both F_c and F_t magnitudes undergo a cyclic variation process. When the tool edge gradually cuts across the hybrid CFRP/Ti stack, both F_c and F_t signals decrease quickly into zero, which signifies the final cutting stage III.

5.4 Parametric effects on force generation

In the following subsections, the force generation in orthogonal cutting of hybrid CFRP/Ti stacks was measured based on each phase machining. Each force component (cutting force (F_c) and thrust force (F_t)) was calculated based on the force signal promoted under the steady cutting process. Figs. 5.9 - 5.11 then show the obtained results with respect to different cutting conditions and cutting sequence strategies.

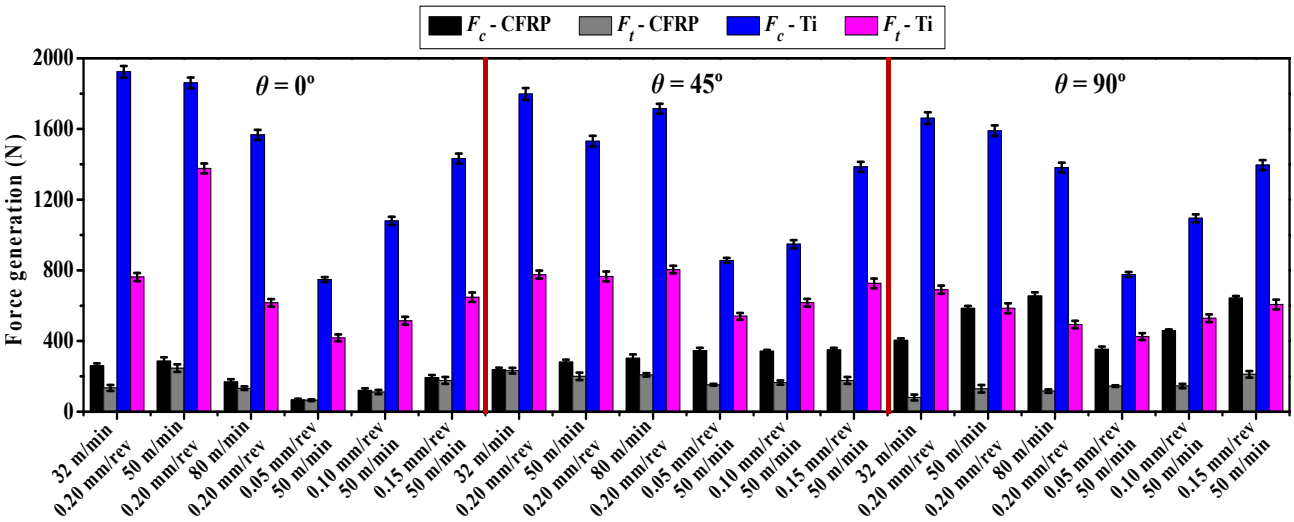

Fig.5.9. Parametric effects on force generation when orthogonal cutting of hybrid CFRP/Ti stacks in the CFRP → Ti cutting sequence.

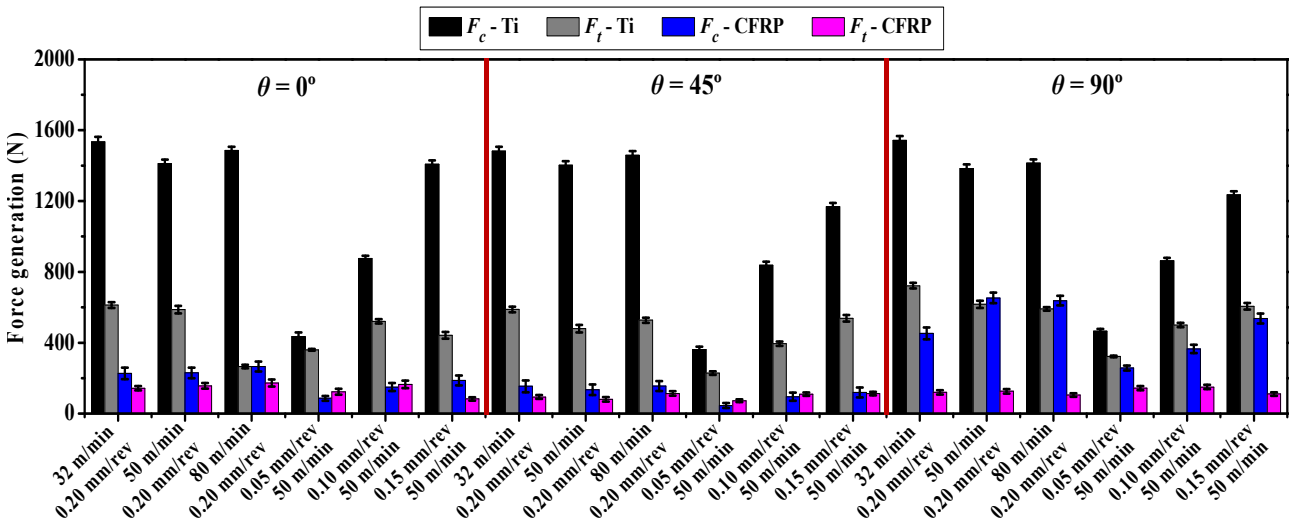

Fig.5.10. Parametric effects on force generation when orthogonal cutting of hybrid CFRP/Ti stacks in the Ti → CFRP cutting sequence.

It is noticeable that the CFRP/Ti force develoepment is closely related to the utilized cutting

parameters regardless of the used cutting sequence strategies. Globally, the cutting speed (v_c) shows an irregular impact on the force magnitudes, greatly dependent on the competition between its influence on tool wear progression and on work material softening. This means when its influence on softening workpiece stiffness becomes a predominant factor, its impact on CFRP/Ti force generation is negative, *i.e.*, an increased v_c usually decreases the force magnitudes (*e.g.*, F_c of Ti phase cutting in Fig.5.9 and F_c of CFRP/Ti cutting in Fig.5.10). On the contrary, when the cutting speed's effect on tool wear progression becomes a leading factor, the impact of cutting speed will be positive, *i.e.*, an elevated v_c will give rase to a high force generation (*e.g.*, F_c of CFRP phase cutting (θ = 45° and 90°) in Fig.5.9). By contrast, the feed rate (f) is observed to totally have a positive impact on the CFRP/Ti force development in both CFRP → Ti and Ti → CFRP cutting sequences. This is because the feed rate (f) signifies the uncut chip thickness in the present study. And when f increases, the tool edge is required to cut off more chip volume per cutting time, which will inevitably greatly increase the cutting resistance required for further chip separation and hence result in the dramatically elevated force generation.

Besides, the large cutting force (F_c) gap between the CFRP phase cutting and Ti phase cutting as illustrated in Figs.5.9 and 5.10 also indicates that there should exist a sudden force increase/decrease occurring at the CFRP/Ti interface when the tool edge cuts from one phase to another phase and *vice versa*. Such physcial phenomenon will inevitably lead to the severe cutting vibration and tool-work instability governing the chip removal process, which may exacerbate the machined surface quality and initiate the premature tool failures like micro chipping or edge fracture.

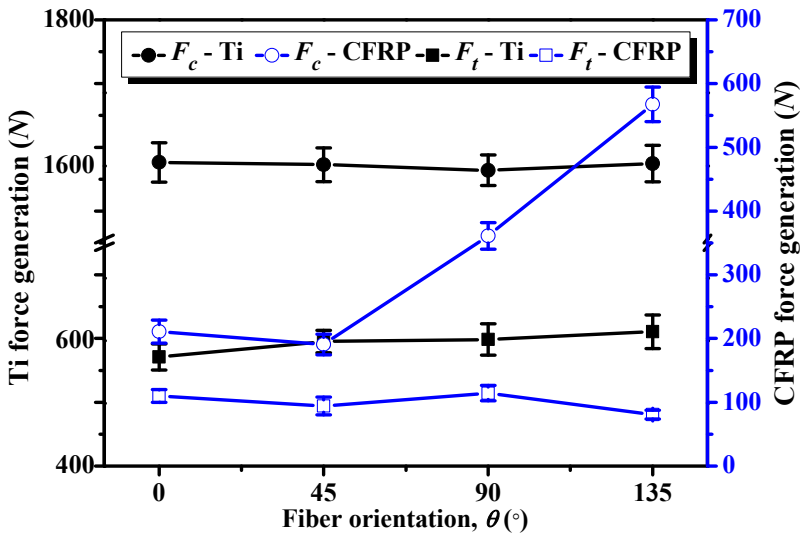

Fig.5.11. Force generation *versus* fiber orientation (θ) when cutting hybrid CFRP/Ti stacks (v_c = 50 m/min and f = 0.20 mm/rev)

Furthermore, the effects of fiber orientation (θ) on CFRP/Ti force generation in CFRP → Ti cutting sequence are also shown in Fig.5.11. It can be seen that the fiber orientation (θ) has a significant effect on the cutting force development of CFRP-phase cutting, while its influence on Ti force generation is irregular and approximately negligible. The key mechanisms dominating the θ's influences on CFRP/Ti cutting force generation can be globally attributed to the varied chip-separation modes governing the CFRP-phase cutting when θ changes. In contrast, the θ's effect on thrust force (F_t) of CFRP-phase cutting is found to be very slight. This is because the key source

of F_t often results from the bouncing-back effects of the trimmed CFRP fibers on tool flank surface, which should have less dependence on fiber orientation (θ) than that of chip separation process occurring on tool-chip interface that contributes mainly to the cutting force generation (F_c). Moreover, with respect to Ti → CFRP cutting, the similar findings are also noticed for θ's influences on CFRP/Ti force generation, which are thereby not provided here.

To evaluate the machinability of hybrid CFRP/Ti stacks, an indicator, namely specific cutting energy (u - J/cm^3), was used for the assessment, which can be defined as follows in orthogonal cutting configuration [200].

$$u = \frac{F_c}{a_c \times w} \tag{5.1}$$

where F_c represents the main cutting force in N unit; a_c and w denote the cutting depth and cutting width in mm unit, respectively.

The specific cutting energy (u) commonly signifies the cutting energy consumed to remove one unit-volume work material in machining, which is coherently determined by the mechanical properties of the studied work-tool configuration [170]. Fig. 5.12 shows the obtained u values *versus* the input cutting parameters (cutting speed (v_c) and feed rate (f)) in CFRP → Ti cutting sequence, in which, the u consumption was calculated based on each stacked phase machining (CFRP phase cutting and Ti phase cutting). As depicted in this figure, the cutting speed (v_c) is identified to have a negative impact on the u consumption except the abnormal findings for 90° CFRP cutting as shown in Fig.5.12(a). Besides, the f's effects on u are totally negative for all tested fiber orientations, in which an increased f often results in the decreased specific cutting energy consumption and improved machinability of the work material. The observed variation trends also agree well with the numerical predictions in subsection 4.5.1 of Chapter IV. Moreover, the Ti phase cutting basically consumes much u than that of CFRP phase cutting regardless of the used fiber orientations. The key cause of the phenomenon can be attributed to its relatively high mechanical/physical properties and specific chip separation mode of plastic deformation [170]. Besides, in the case of Ti → CFRP cutting, the identical observation is also found for the variation of specific cutting energy *versus* the input cutting parameters.

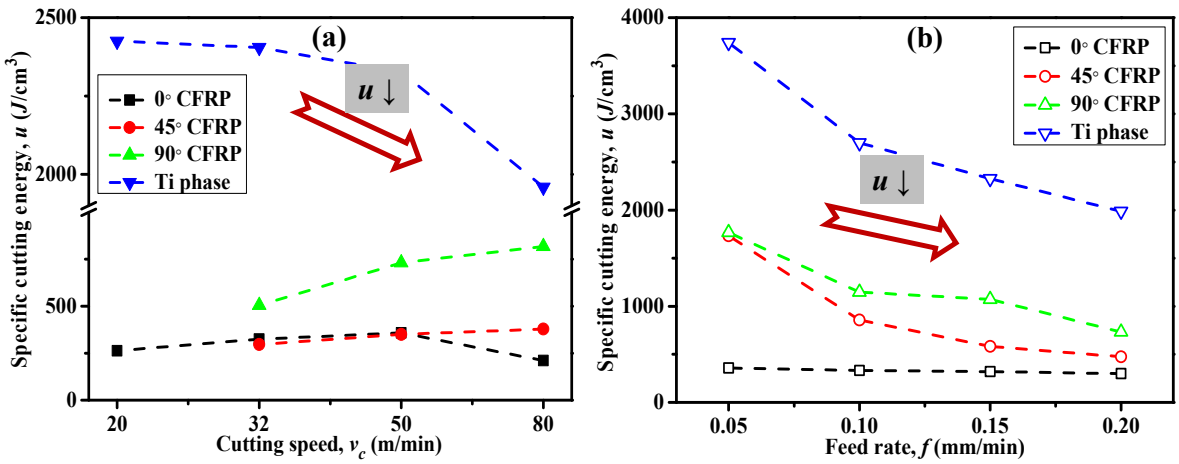

Fig.5.12. Parametric effects of (a) cutting speed (v_c) and (b) feed rate (f) on specific cutting energy consumption (u) when orthogonal cutting of hybrid CFRP/Ti stacks in the CFRP → Ti cutting sequence.

With respect to the force generation in machining combined CFRP/Ti stacks, the force

magnitudes can be considered as the sum of both CFRP-phase cutting and Ti-phase cutting due to the simultaneous machining of each stacked constituent. Figs.5.13 and 5.14 show the obtained results in terms of different cutting tools (for detailed information regarding the used tools A - D, please refer to subsection 3.3 of Chapter III) when machining the identical $\theta = 0°$ CFRP/Ti stacks.

As depicted in the two figures, the feed rate (f) is found to have a significantly positive impact on both F_c and F_t for all the used cutting tools. By contrast, the impact of cutting speed (v_c) on CFRP/Ti force generation is obscure and minor. Moreover, tools B and D are found to promote relatively high cutting forces than those of tools A and C. The reasons can be attributed to the differences in coating grade for the tested tool inserts as illustrated in subsection 3.3 of Chapter III. Since tools B and D were fabricated by medium-coarse coating grade, the actual coating's mechanical/physical properties involved in cutting should be inferior to those manufactured by fine coating grade with the same tool geometrical angles. In addition, when using tools B and D, serious Ti chip adhesion or built-up edge (BUE) is identified on tool main cutting edge. The occurrence of this phenomenon should inevitably accelerate tool flank wear and initiate premature tool failure, which, in turn, results in the higher force generation. In general, tool A is observed to show the best cutting performance with minimum force generation when machining combined CFRP/Ti stacks as compared to its counterpart ones.

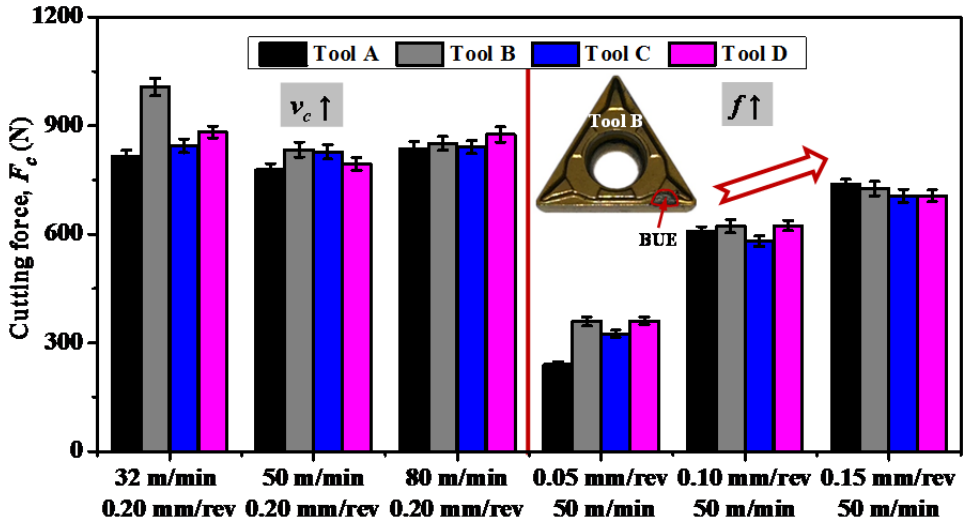

Fig.5.13. Parametric effects on cutting force (F_c) when machining combined CFRP/Ti stacks ($\theta = 0°$).

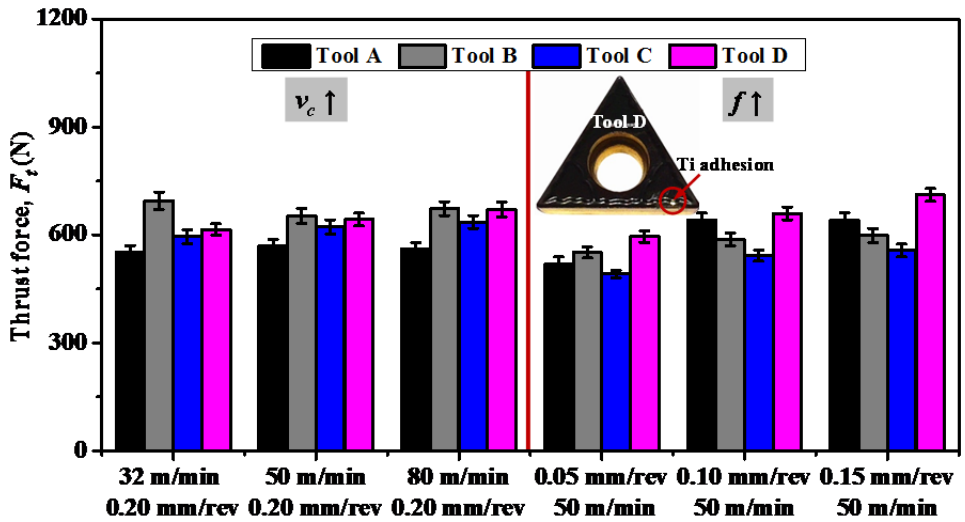

Fig.5.14. Parametric effects on thrust force (F_t) when machining combined CFRP/Ti stacks ($\theta = 0°$).

5.5 Machined surface quality inspection

Machined surface quality resulting from various machining operations is usually a critical factor that significantly affects the service performance of the manufactured components and determines the final part acceptance. Owing to the disparate machinability behaviors of the stacked composite laminate and metal alloy, machining hybrid CFRP/Ti stacks often promotes severe subsurface damage consisting of both composite-phase imperfection and metallic phase defect [1, 4]. In the present study, the machined CFRP/Ti surfaces under different fiber orientations (θ = 0°, 45°, 90° and 135°) when using CFRP → Ti cutting sequence were examined via both optical microscope (OM) and SEM inspections. Note that for each θ configured CFRP/Ti specimen, each new PCD tool was utilized in order to prevent the tool wear influences on the trimmed surface.

Fig.5.15 shows the comparative photographs of the machined CFRP/Ti surfaces with respect to different fiber orientations (θ = 0°, 45° and 90°) under the fixed cutting conditions of v_c = 50 m/min and f = 0.2 mm/rev. As shown in Fig.5.15, the machined Ti phase surface seems to be much smoother than that of the CFRP composite phase, irrespective of the used θ configurations. Besides, the CFRP/Ti specimen machined under θ = 90° configuration commonly suffers serious induced defects as depicted in Fig.5.15(c). As illustrated in the magnified view of the machined CFRP surface in Fig.5.15(d), a large extent of carbon fiber splintering is promoted along the two machined surface boundaries. The SEM observations presented in Fig.5.16 also confirm that cutting higher 90° fiber orientation induces much severer fiber/matrix damage along the machined CFRP surface boundaries, where various types of defects including fiber pullout, resin loss and fiber splintering become prevalent. The phenomena indicate that an increased fiber orientation in the hybrid CFRP/Ti stack will definitively result in serious cutting-induced damage formation. The activated mechanism can be attributed to the varying chip separation modes *versus* fiber orientation (θ), which greatly affects the machined surface morphology of the composite phase. The reason may be due to the fact that when machining a high θ configured CFRP phase (*e.g.*, θ = 90° in the current case), the chip removal process is governed by bending/compression separation coupled with serious out-of-plane shearing, which inevitably leads to the severe induced subsurface damage.

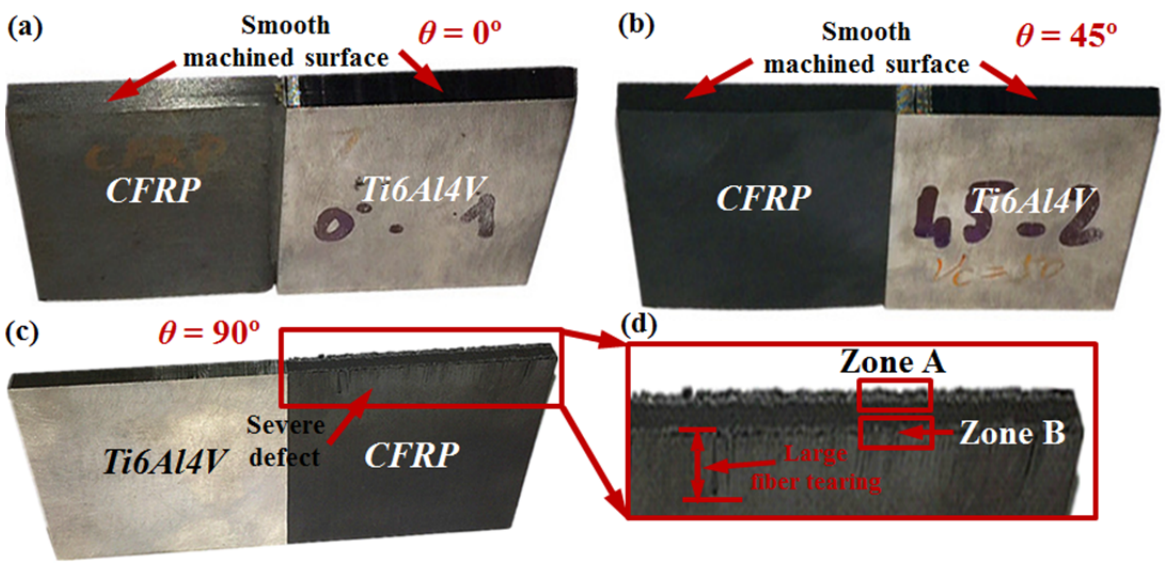

Fig.5.15. Machined CFRP/Ti surfaces *versus* θ in the CFRP → Ti cutting sequence: (a) θ = 0°, (b) θ = 45°, (c) θ = 90°, and (d) magnified view of the machined CFRP surface in Fig.5.15(c) (v_c = 50 m/min and f = 0.20 mm/rev).

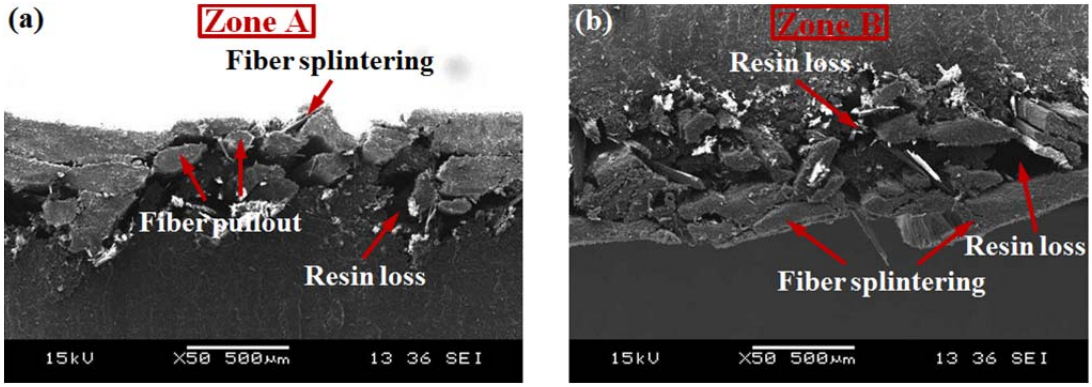

Fig.5.16. SEM micrographs showing the edge boundary zones of the machined CFRP surface: (a) zone A in Fig.5.15(d) and (b) zone B in Fig.5.15(d).

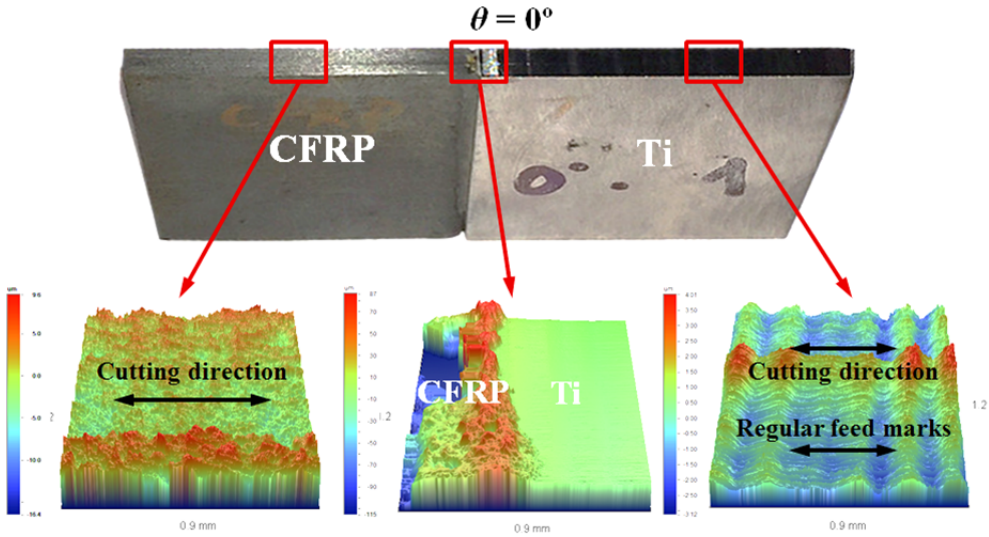

Fig. 5.17. Topographic maps for trimmed CFRP/Ti surface with 0° fiber orientation in the CFRP → Ti cutting sequence (v_c = 50 m/min and f = 0.20 mm/rev).

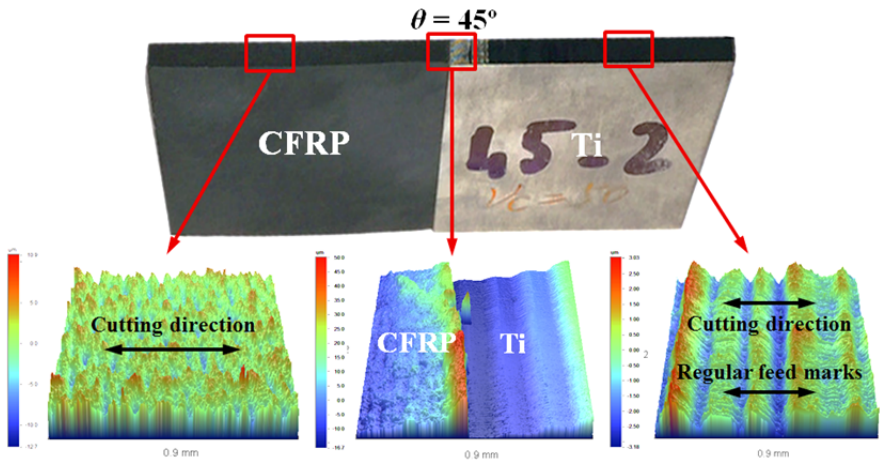

Fig. 5.18. Topographic maps for trimmed CFRP/Ti surface with 45° fiber orientation in the CFRP → Ti cutting sequence (v_c = 50 m/min and f = 0.20 mm/rev).

In addition, the 3D topographies of the trimmed CFRP/Ti surfaces with different fiber orientations in the CFRP → Ti cutting sequence are also shown in Figs.5.17 - 5.19. Note that the topographic maps for each trimmed CFRP surface and Ti surface were recorded on the middle machined surface zones, which signify the steady cutting stage of the work materials. The topographic analyses show that for machined Ti surface, the regular feed marks on the generated

surfaces are formed, which should be caused due to the varying extents of elastic-plastic deformation of the trimmed Ti surface after suffering severe ploughing or shearing actions resulting from the hard sticking and sliding of tool flank face. The interface linking the metallic phase and composite phase often suffers severe subsurface damage especially when a high fiber orientation is used. Further, the trimmed CFRP surfaces with low fiber orientation (θ = 0°) usually exhibit much flatter topographies than those with high fiber orientations (*e.g.*, θ = 45° and 90°).

Furthermore, Figs.5.20 - 5.23 also illustrate the SEM images of different CFRP/Ti surfaces after machining with PCD tools in terms of different fiber orientations under the identical cutting conditions of v_c = 50 m/min and f = 0.20 mm/rev. Note that in the mentioned four figures, every three SEM observations were performed on the machined Ti phase, interface and CFRP phase, respectively, with the same magnification of × 50.

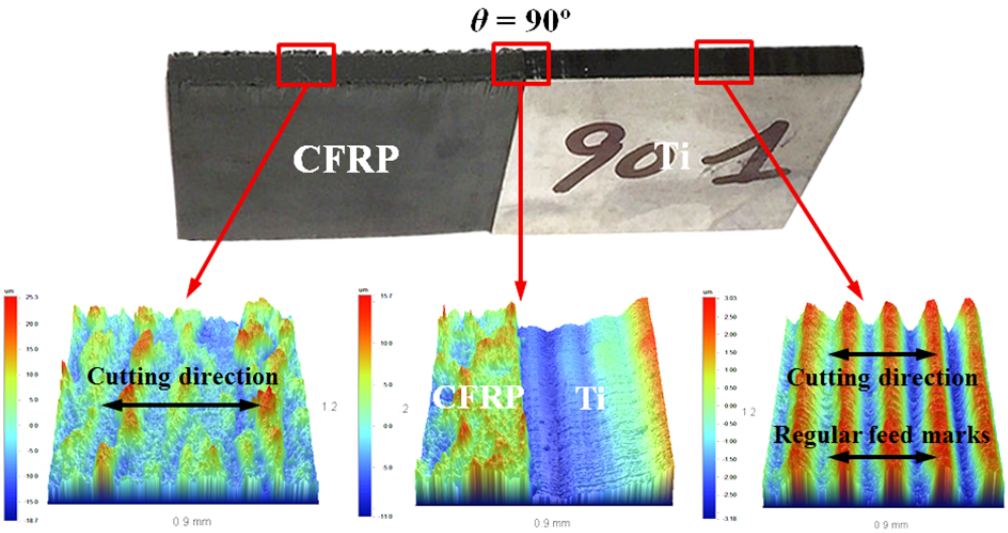

Fig. 5.19. Topographic maps for trimmed CFRP/Ti surface with 90° fiber orientation in the CFRP → Ti cutting sequence (v_c = 50 m/min and f = 0.20 mm/rev).

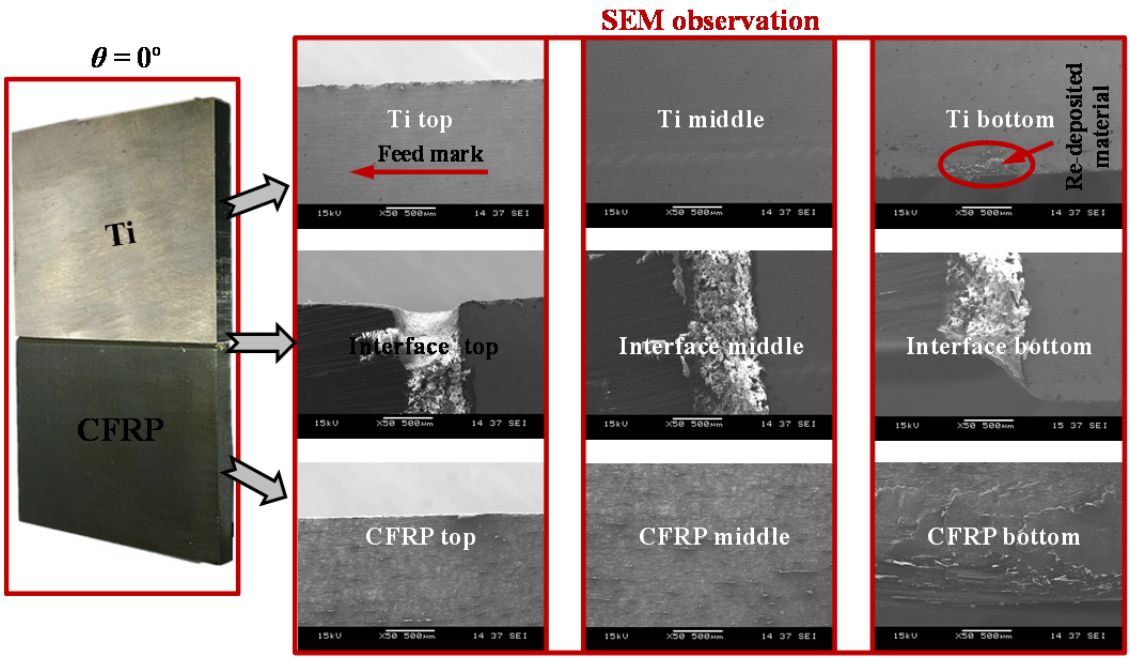

Fig.5.20. Machined CFRP/Ti surface when cutting with PCD tools under θ = 0° (v_c = 50 m/min and f = 0.20 mm/rev).

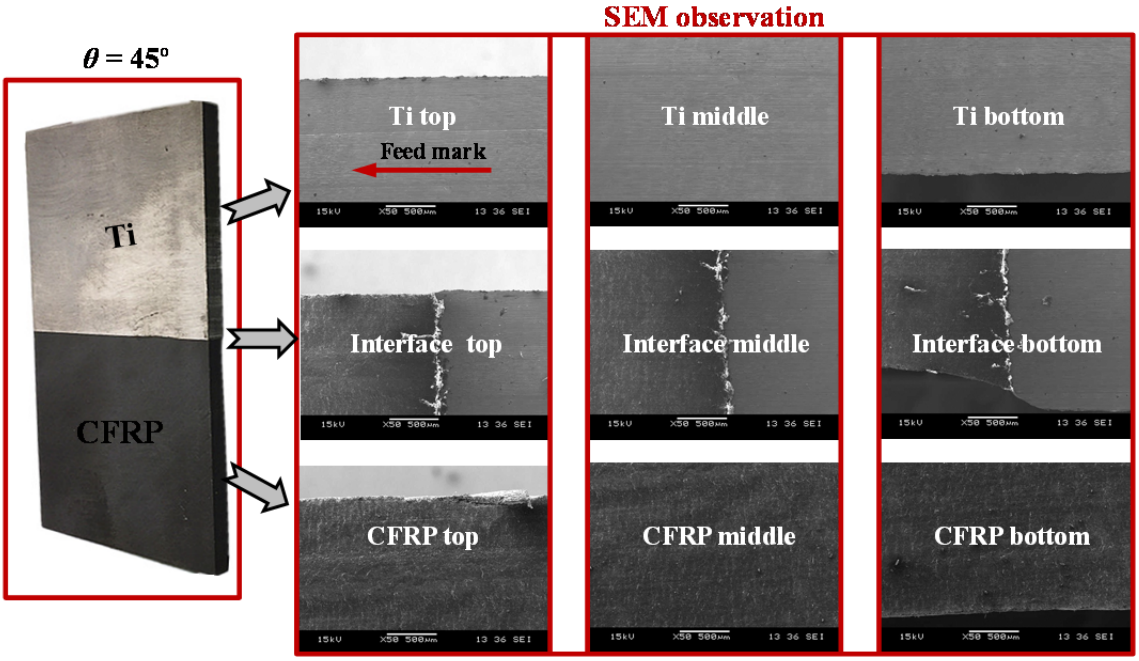

Fig.5.21. Machined CFRP/Ti surface when cutting with PCD tools under $\theta = 45°$ ($v_c = 50$ m/min and $f = 0.20$ mm/rev).

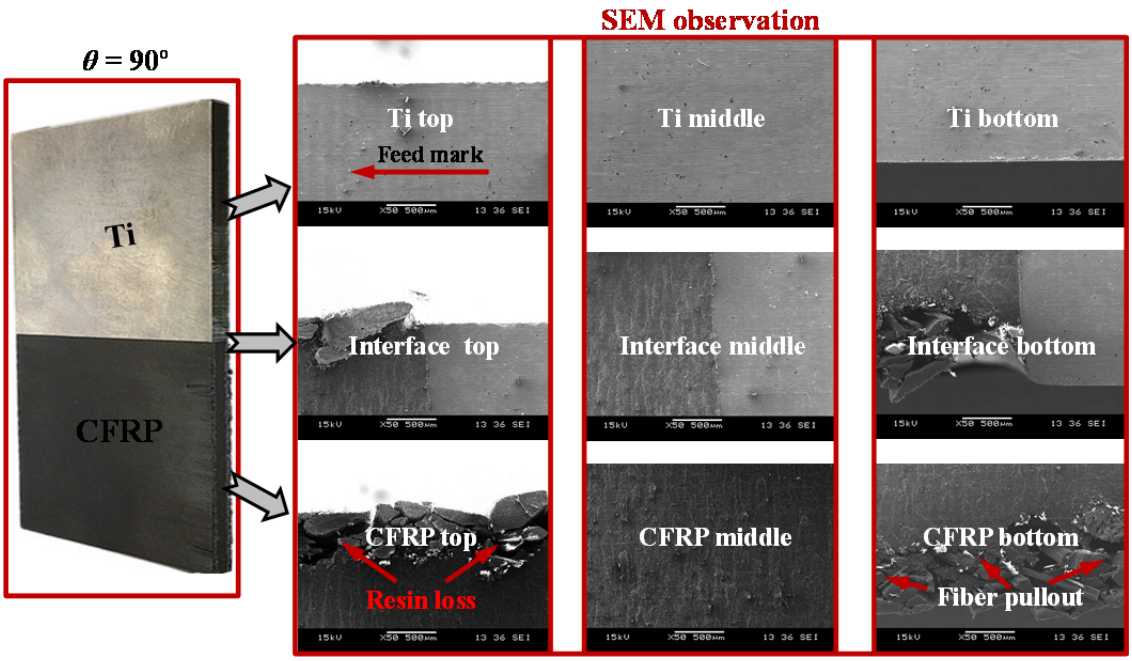

Fig.5.22. Machined CFRP/Ti surface when cutting with PCD tools under $\theta = 90°$ ($v_c = 50$ m/min and $f = 0.20$ mm/rev).

Globally, machining CFRP/Ti stacks with high fiber orientations (*e.g.*, θ = 90° and 135°) commonly promotes much poorer machined surface quality, especially for the trimmed CFRP surfaces as depicted in Figs.5.22 and 5.23. In the mentioned two figures, a larger extent of cutting-induced fiber/matrix damage is promoted along the machined CFRP surface boundaries as compared to the cases of lower fiber orientations, *e.g.*, $\theta = 0°$ and 45°, as depicted in Figs.5.20 and 5.21. The activated mechanisms controlling the varied damage formation can be attributed to the changes of CFRP chip separation modes *versus* fiber orientation (θ). Besides, the machined Ti phase surface typically seems to appear much smoother than that generated in the interface region and CFRP phase, regardless of the used θ's configurations. The primary damage forms of the trimmed Ti surface are found to be the deformation of feed mark and re-deposited chip material.

The feed marks commonly run toward the tool cutting direction, which occur probably due to the plastic flow of material during the cutting process [37, 206]. The re-deposited chip material on the Ti surface is probably caused by the highly localized temperature promoted at the cutting interface that greatly facilitates the welding/adhesion process. The interface linking both CFRP phase and Ti phase is usually machined with serious cracking damage due to the sudden force variation exerted on the "CFRP-to-Ti" contact boundary when the tool edge cuts from CFRP phase to Ti phase. Besides, the major surface imperfections observed for the machined CFRP surface are fiber pullout, resin loss and surface cavity. In addition, the CFRP fiber/matrix damage extent (D_{CFRP}) is also found to increase quickly when fiber orientation (θ) is elevated, *e.g.*, D_{CFRP} = 0.16 mm for θ = 0° and D_{CFRP} = 5.99 mm for θ = 90°.

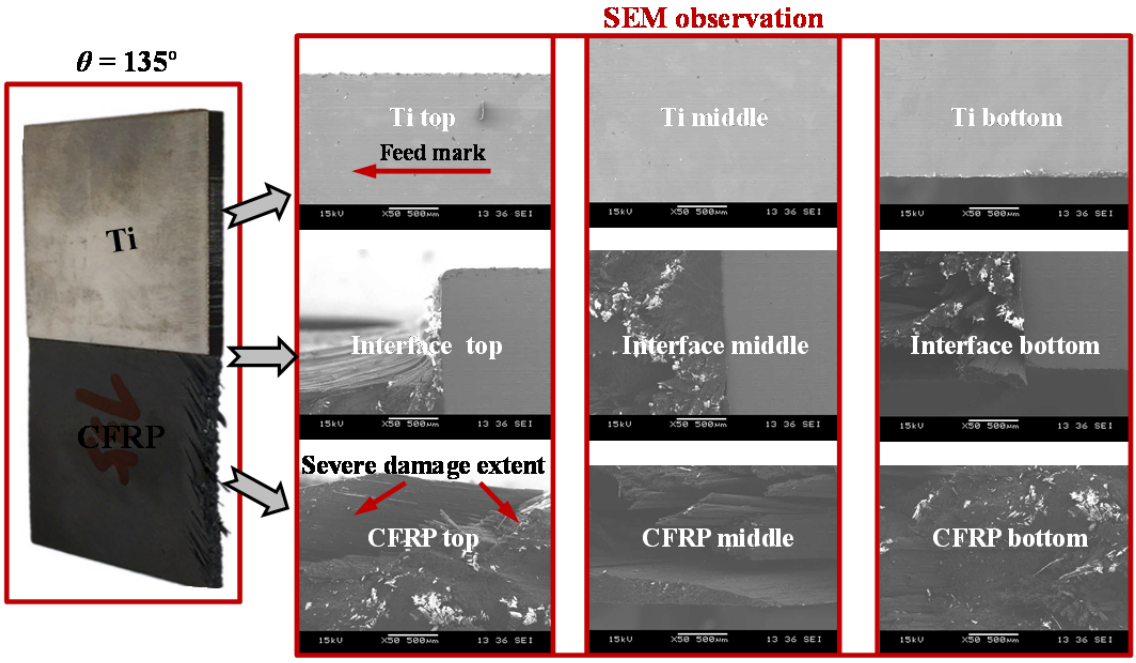

Fig.5.23. Machined CFRP/Ti surface when cutting with PCD tools under θ = 135° (v_c = 50 m/min and f = 0.20 mm/rev).

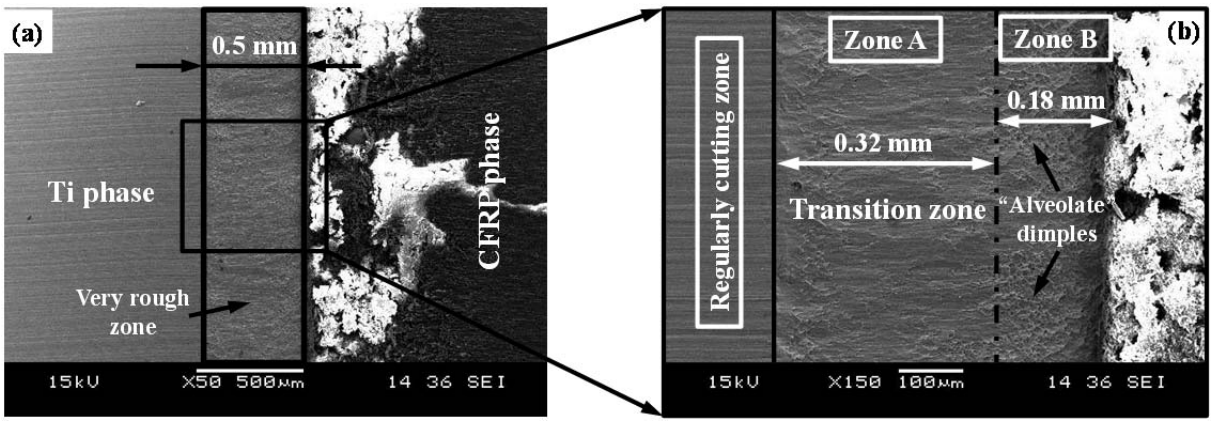

Fig.5.24. SEM images showing the machined interface zone in the Ti → CFRP cutting sequence (θ = 0°, v_c = 50 m/min and f = 0.20 mm/rev): (a) global view and (b) magnified view of the trimmed Ti surface close to the interface.

With regard to the Ti → CFRP cutting sequence, apart from the similarly observed damage modes for respectively machined Ti surface and CFRP surface, one key difference is noticed for the trimmed surface morphology near the interface region. As depicted in Fig.5.24, for θ = 0° CFRP/Ti workpiece, a very thin Ti-phase zone with quite disparate surface morphologies compared to the

regularly machined Ti surface is promoted around the interface region. The aforementioned Ti surface zone is characterized by highly rough and uneven texture with an approximately 0.5 mm width. The observed dissimilar surface morphologies of the identical Ti phase should indicate the changes of the Ti chip separation mode occurring near the interface zone. Moreover, through the magnified view of the rough zone, it is interesting to note that various small "alveolate" dimples are detected in zone B close to the interface region as shown in Fig.5.24(b). Such physical phenomena clearly confirm the occurrence of rapid ductile fracture on the thin and rough zone. Besides, it is also identified that the small dimples usually take place with a higher density close to the interface zone with a width of approximately 0.18 mm. By contrast, in zone A far from the CFRP/Ti interface, only very minor dimples are observed through the SEM analyses. The findings probably indicate the transition of Ti chip separation modes from plastic deformation to rapid ductile fracture occurring in zone A. The activated mechanisms controlling the very thin rapid ductile fracture zone can be attributed to the varying cutting behaviors of the interface zone due to the relative brittleness of the composite phase as discussed in details in subsection 4.2.2 of Chapter IV. Moreover, it can also estimate that the occurrence of rapid ductile fracture zone close to the interface will greatly increase the surface roughness of the interface region. In addition, with respect to θ = 45° and 90° CFRP/Ti specimens, the occurrence of rapid ductile fracture is not so clear as shown in Fig.5.25.

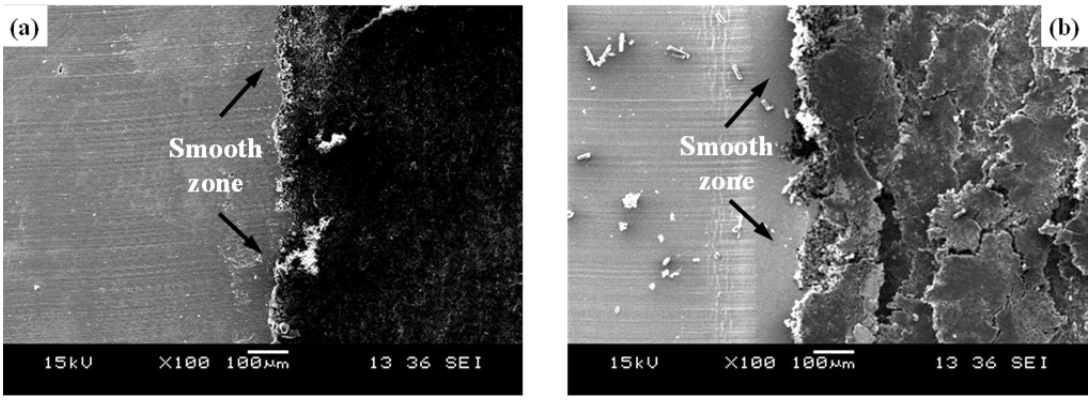

Fig.5.25. SEM images showing the machined interface zones in the Ti → CFRP cutting sequence (v_c = 50 m/min and f = 0.20 mm/rev): θ = 45° and (b) θ = 90°.

For machined surface morphology under combined CFRP/Ti cutting, the identical damage types are found to take place on both CFRP phase and Ti phase as depicted in Figs.5.26 and 5.27. However, due to the noninterference of each stacked phase cutting, the interface zone is observed to remain intact without the occurrence of severe cracking damage even when machining θ = 90° CFRP/Ti stack as shown in Fig.5.27.

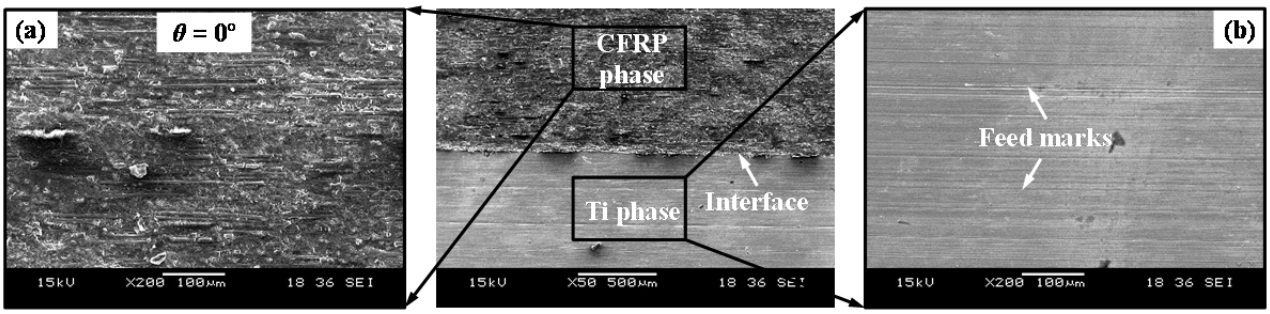

Fig.5.26. SEM images showing the machined CFRP/Ti surface in combined interface cutting operation (θ = 0°, v_c = 50 m/min and f = 0.20 mm/rev): (a) magnified view of CFRP surface and (b) magnified view of Ti surface.

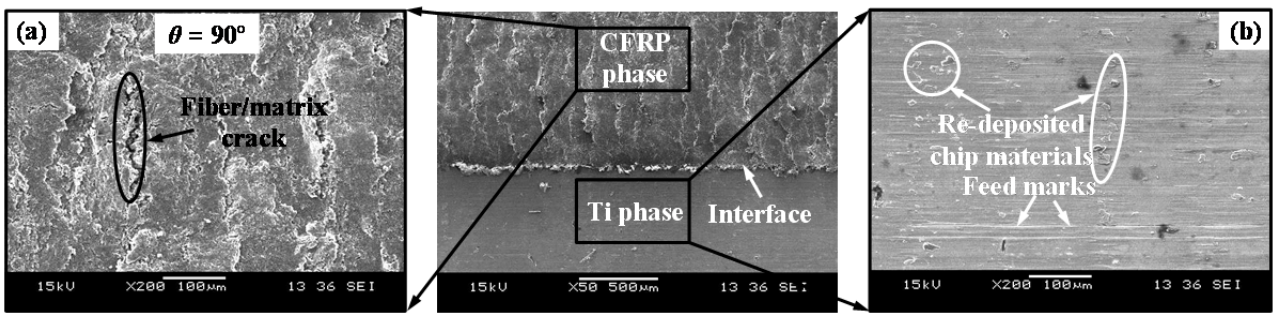

Fig.5.27. SEM images showing the machined CFRP/Ti surface in combined interface cutting operation ($\theta = 90°$, v_c = 50 m/min and f = 0.20 mm/rev): (a) magnified view of CFRP surface and (b) magnified view of Ti surface.

5.6 Surface roughness and microhardness

In this subsection, the machined surface quality including surface roughness and microhardness was examined in terms of used cutting parameters and cutting sequence strategies ($^{\text{CFRP} \rightarrow \text{Ti}}_{\text{Ti} \rightarrow \text{CFRP}}$). The most-used surface roughness parameters (R_a, R_q, and R_z) were adopted for quantitive analyses. Note that the surface roughness measurement was made on individual CFRP surface, interface and Ti surface by using a Veeco white-light interferometer (Wyko 3300NT) with a total scanned area of 0.93 mm × 3.6 mm. The detailed illustration regarding the surface roughness measurement is presented in subsection 3.4.2.2 of Chapter III. For microhardness analysis, the measurement was made only on the trimmed Ti surface by using the 1600-5100 MicroMet Hardness Tester (Buehler®) with a load of 100 *gf* and a dwell time of 10 s.

Figs. 5.28 - 5.30 show the acquired surface roughness parameters under various cutting parameters and fiber orientations. It is noticeable that the measured arithmetic mean roughness (R_a) of trimmed Ti surface exhibits much lower values as compared to that of the machined CFRP surface, which in some extent confirms the better surface finish of the Ti phase surface. Besides, the observation also agrees with the SEM and topography analyses of the trimmed CFRP/Ti surfaces. In addition, the R_a obtained in the CFRP/Ti interface region usually yields the biggest magnitudes than the individual CFRP phase and Ti phase. The phenomenon should indicate the highly uneven and rough surface profile generated in the interface zone. Moreover, for machined Ti surface, the cutting speed (v_c) is found to have a negative impact on R_a and R_q promotion, while the feed rate (f) exhibits a totally positive impact, in which an increased f gives rise to gradually elevated R_a and R_q values. By contrast, the parametric effect on machined CFRP surface roughness is obscure, and the variation law is not so noticeable as that of the Ti surface. Further, the comparative results shown in Fig.5.31 also strongly indicate the significant effects of fiber orientation (θ) on the generated surface finish. It can be seen in Fig.5.31 that when machining high θ configured CFRP/Ti stacks, the measured R_a parameter of the trimmed CFRP surface increases dramatically from the minimum value of 1.80 μm with 0° fiber orientation to the maximum value of 3.63 μm with 90° fiber orientation under the cutting conditions of v_c = 32 m/min and f = 0.20 mm/rev. The reasons can be attributed to the formation of severe subsurface damage when θ is elevated.

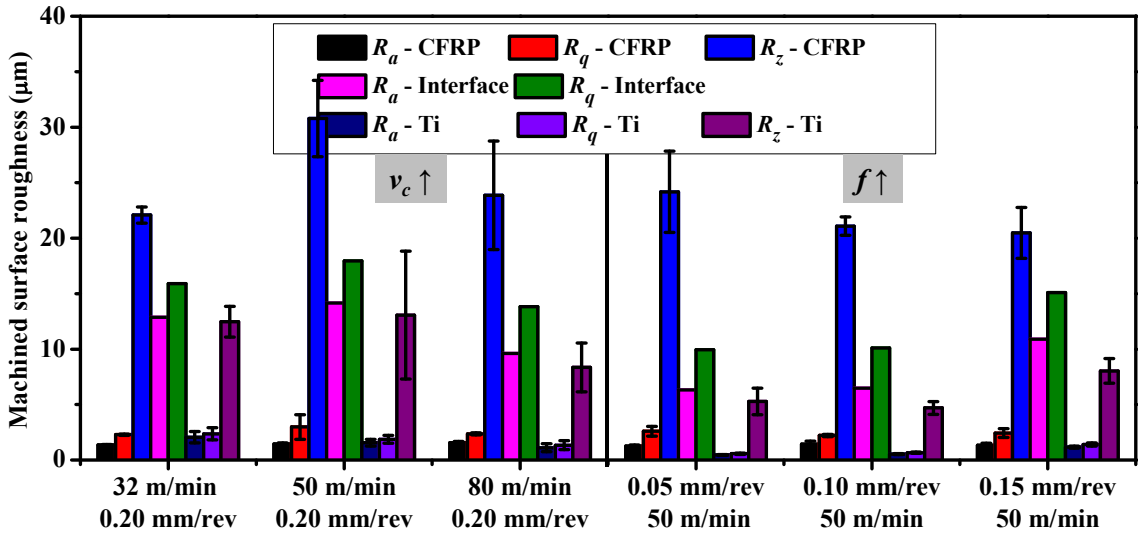

Fig. 5.28. Variation of measured surface roughness (R_a, R_q and R_z) for trimmed $\theta = 0°$ CFRP/Ti surfaces in the CFRP → Ti cutting sequence.

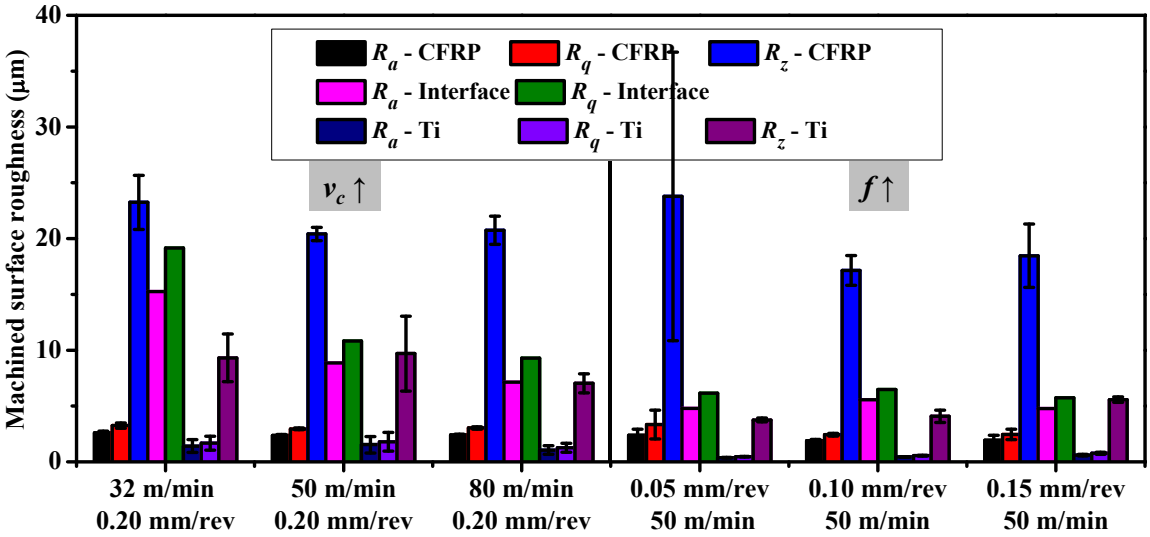

Fig. 5.29. Variation of measured surface roughness (R_a, R_q and R_z) for trimmed $\theta = 45°$ CFRP/Ti surfaces in the CFRP → Ti cutting sequence.

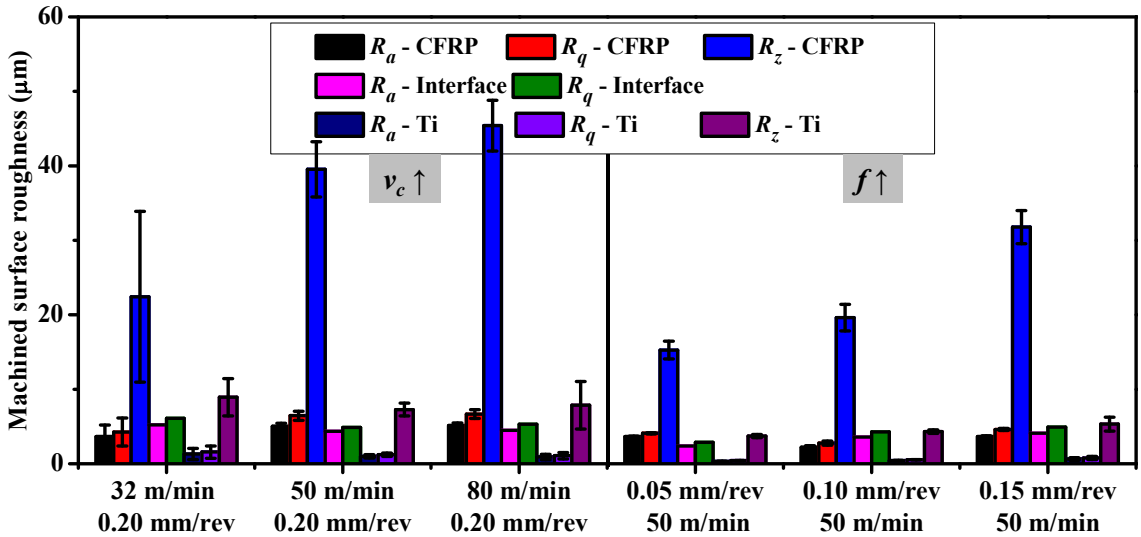

Fig.5.30. Variation of measured surface roughness (R_a, R_q and R_z) for trimmed $\theta = 90°$ CFRP/Ti surfaces in the CFRP → Ti cutting sequence.

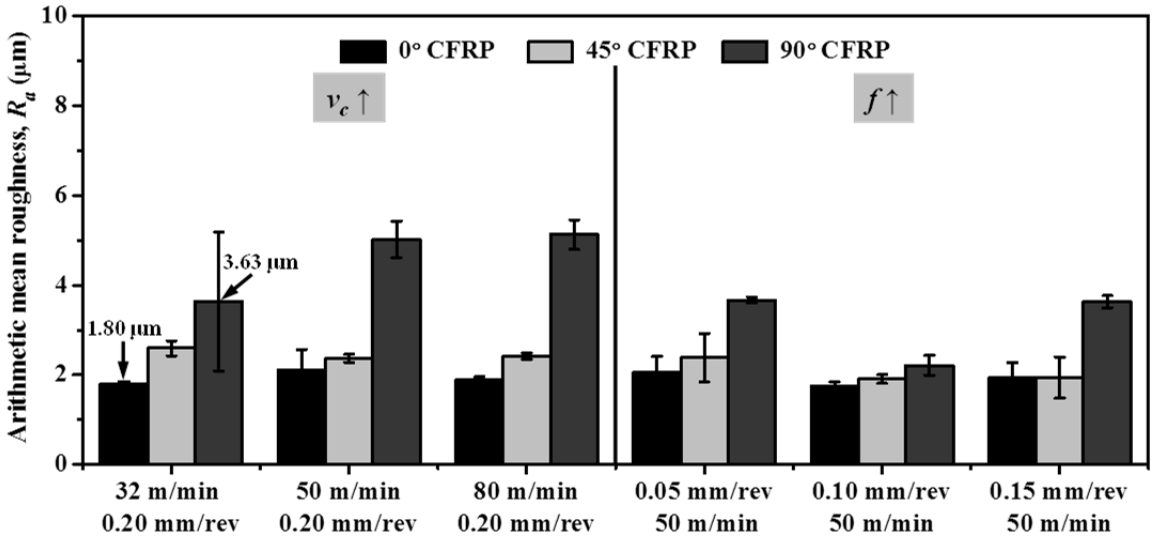

Fig.5.31. Comparative R_a values of machined CFRP surfaces with different fiber orientations (θ).

In addition, Fig.5.32 also shows the comparative R_a results obtained in two different cutting sequence strategies ($^{\text{CFRP}\rightarrow\text{Ti}}_{\text{Ti}\rightarrow\text{CFRP}}$) for $\theta = 0°$ CFRP/Ti stacks. It is apparent that the measured R_a values of the trimmed CFRP surface in the Ti → CFRP cutting sequence are much higher than those gained in CFRP → Ti cutting, irrespective of the used cutting conditions. The reasons can be attributed to the serious Ti chip adhesion on tool rake face that substitutes the tool edge for further CFRP phase cutting as illustrated in subsections 5.2. By contrast, the promoted Ti surface roughness in Ti → CFRP cutting, however, exhibits much lower value than that generated in CFRP → Ti cutting. This is because in Ti → CFRP cutting, the tool often cuts off the Ti phase firstly with fresh cutting edge and prevents the problematic CFRP chips adhesion on tool rake face. Besides, the generated interface in Ti → CFRP cutting sequence commonly shows lower surface finish (higher R_a values) as compared to that promoted in CFRP → Ti cutting as depicted in Fig.5.32. This observation also confirms the findings of the very thin rapid ductile fracture zone occurring close to the interface region which contributes to the highly rough machined surface as discussed in subsection 5.5.

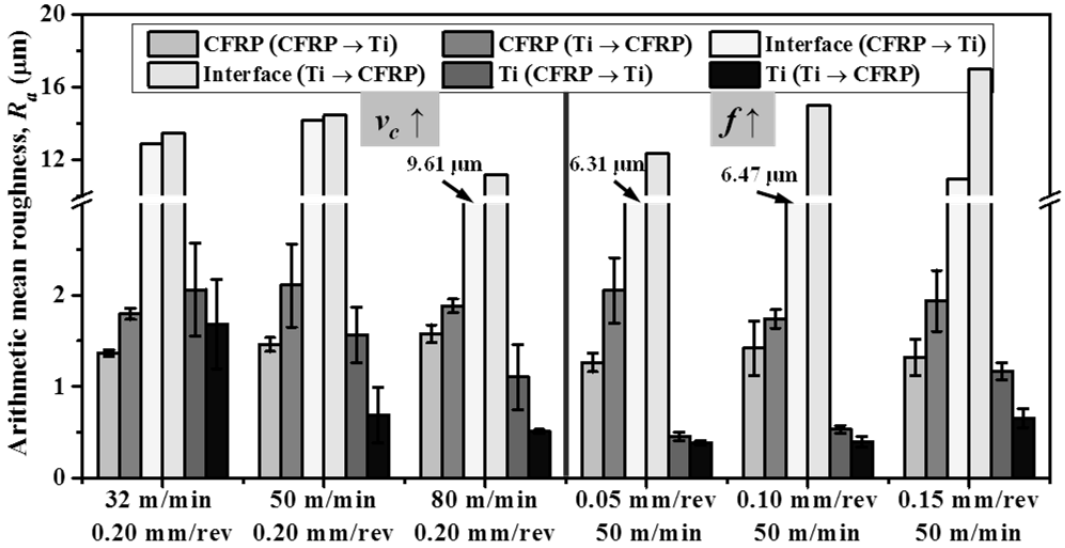

Fig.5.32. Comparative R_a values of machined CFRP/Ti surfaces ($\theta = 0°$) under different cutting sequence strategies.

Further, for investigating the surface integrity of the Ti surface, the microhardness of the

machined Ti phase in the CFRP → Ti cutting sequence was measured with regard to different cutting conditions as depicted in Fig.5.33. Both cutting speed (v_c) and feed rate (f) are found to have a negative impact on the microhardness of the trimmed metallic surfaces. When cutting is operated under low feed-rate conditions, *e.g.*, f = 0.05 mm/rev, the measured microhardness values are all higher than the bulk hardness (355 $HV_{0.10}$) of the Ti alloy regardless of the used fiber orientations (θ), which signifies the severe strain hardening of the trimmed metallic surfaces resulting from the CFRP/Ti cutting. With the increase of feed rate, the strain hardening effects decrease gradually and result in the reduced microhardness. In contrast, when cutting is operated under high speed condition, *e.g.*, v_c = 80 m/min, the machined Ti surface microhardness in θ = 0° CFRP/Ti stacks yields a much lower value of 341.9 $HV_{0.10}$ than its bulk hardness. The phenomenon clearly indicates the occurrence of thermal softening on the trimmed Ti surface when cutting speed is elevated.

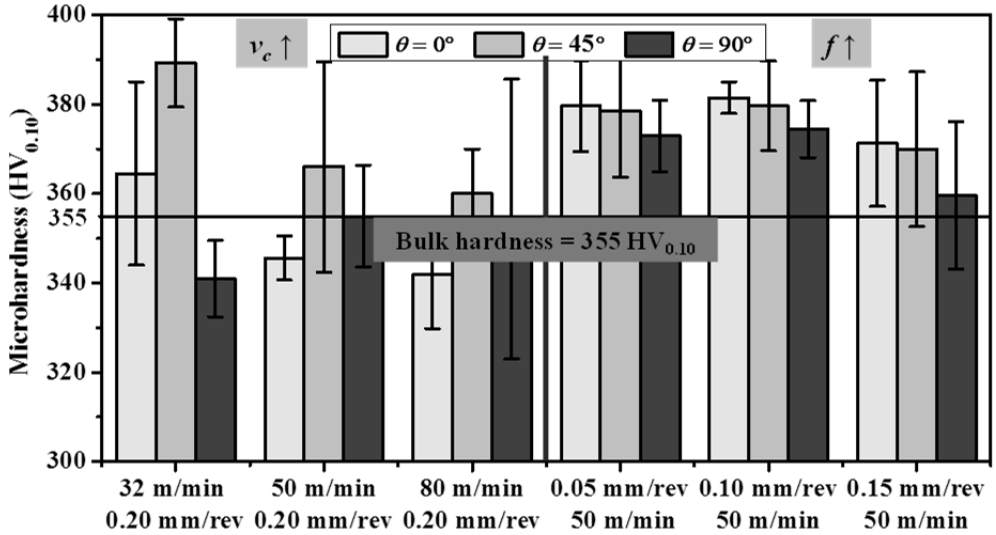

Fig.5.33. Variation of microhardness of machined Ti phase *versus* different fiber orientations (θ) and cutting conditions in the CFRP → Ti cutting sequence.

5.7 Tool performance and wear mode investigation

Tool wear is an inevitable phenomenon governing various manufacturing processes, which greatly determines the tool lifetime and the subsequently machined surface quality. Owing to the anisotropic machinability of hybrid CFRP/Ti stacks, severe tool wear progression may take place because of the coupled influences arising from both metal-leading wear mechanism and composite-leading wear mechanism. With respect to the used tool material, previous researches have confirmed the superior performance of PCD tool involved in Ti alloy machining or CFRP composite machining due to its high hardness and high wear resistance. However, the actual performance of the PCD tools when orthogonal cutting of hybrid CFRP/Ti stacks was still not revealed in the open literature. In this subsection, the fundamental tool wear modes controlling the identical PCD tipped inserts for cutting different fiber orientation configured CFRP/Ti specimens were studied through both optical microscope and SEM analyses.

Figs.5.34 and 5.35 show the tool rake and flank surfaces of the worn PCD tool after cutting θ = 0° CFRP/Ti stack. It can be seen that a large white strip zone with an approximate area of 0.42 mm × 4.53 mm takes place concerning the PCD tool rake face, which signifies the actual crater wear land and the tool-chip interaction area during the chip removal process. Besides, it is also worth

mentioning that the major contribution to the large crater wear zone should be attributed to the Ti alloy cutting since the CFRP cutting contributes very minor effects on tool crater wear formation due to the insignificant or nonexistent contribution of secondary shear zone in heat generation resulting from the brittle-fracture predominant chip separation as addressed by several research work [105, 207]. That's to say, in Ti alloy cutting, the predominant chip separation is plastic deformation characterized by "continuous" or "serrated" chip formation, which shall result in a longer tool-chip contact length. By contrast, the CFRP cutting is dominated by brittle fracture with "powdery" chip formation as discussed earlier in subsection 5.2, and hence the chip separation should contribute less to the formation of tool crater wear zone. Besides, along the main cutting edge, the catastrophic failure of edge chipping is also detected on the examined PCD tool. For the occurrence of edge chipping failure, it should be attributed to the sudden force variation resulting from the CFRP/Ti interface machining and also the inherent brittleness of the PCD material. Further, since the Ti alloy shows strong chemical affinity to most tool materials, the EDS analyses on tool zone A also identify a large number of Ti elements on tool rake face as shown in Fig. 5.34, which confirms the occurrence of adhesion wear or diffusion wear.

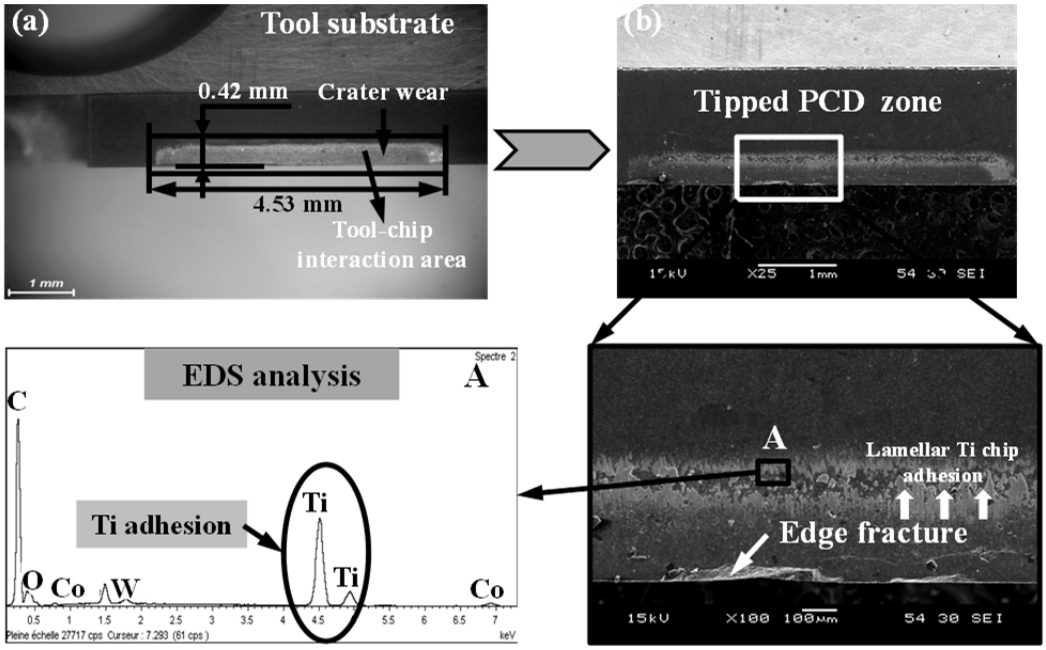

Fig.5.34. Surface morphologies on the worn rake face of the used PCD tipped insert after cutting $\theta = 0°$ CFRP/Ti stacks: (a) optical micrograph of tool rake surface and (b) SEM observation of tool crater wear zone.

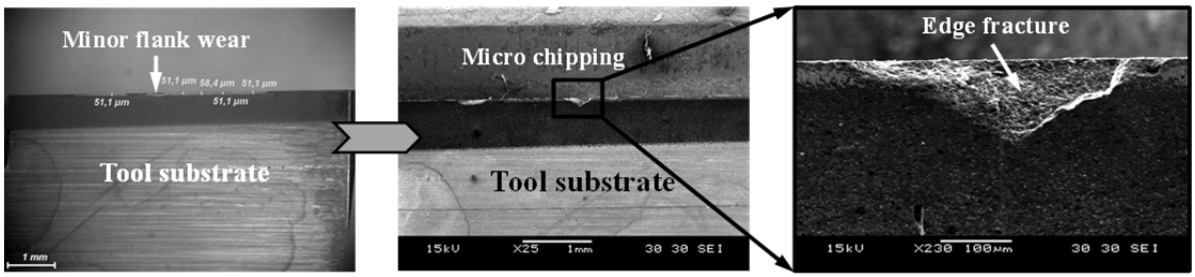

Fig. 5.35. Surface morphologies on the worn flank face of the used PCD tipped insert after cutting $\theta = 0°$ CFRP/Ti stacks.

Moreover, the optical microscope analysis on tool flank face also reveals that after the completion of orthogonal cutting tests, a very minor flank wear land is found along the main cutting

edge, which should be owing to the high wear resistance and high hardness of the PCD material. Meanwhile, the edge chipping is identified along the flank wear land though the SEM observation. The occurrence of such tool failure will greatly deteriorate the tool edge sharpness and make the tool completely lose its cutting capability.

Besides, for cutting other θ configured CFRP/Ti specimens, the similar tool wear modes and wear morphologies are also observed as depicted in Figs.5.36 and 5.37. The key difference among the observed tool wear morphologies lies on the width of the crater wear land, which in reality signifies the real contact length of the tool-chip interaction dominating the hybrid CFRP/Ti stack machining. As can be seen that when cutting 90° CFRP/Ti specimen, the width of tool crate wear land is promoted approximately 0.50 mm, while for 0° and 45° specimens they are 0.42 mm and 0.41 mm, respectively. Since the same cutting length and identical fresh PCD tool are used for each cutting test, the physical phenomena should indicate that the different fiber orientations of the stacked CFRP phase indeed have a significant influence on modifying the geometrical features of the tool active zone. As illustrated earlier in subsection 5.2, when cutting different θ configured unidirectional (UD) composites, the tool-chip contact length should vary due to the inherent fiber/matrix separation modes occurring on tool rake face. When cutting higher θ configured UD composite, *e.g.*, θ = 90°, commonly a longer tool-chip contact length is promoted. In such case, when the tool edge initially attacks the CFRP phase, the carbon fibers with different fiber orientations should induce disparate extents of crater wear width on tool fresh rake face and then modify its original geometrical features. Consequently, when the tool cuts across the subsequent Ti phase, the final tool-chip interaction length should be changed and then result in the different crater wear lengths.

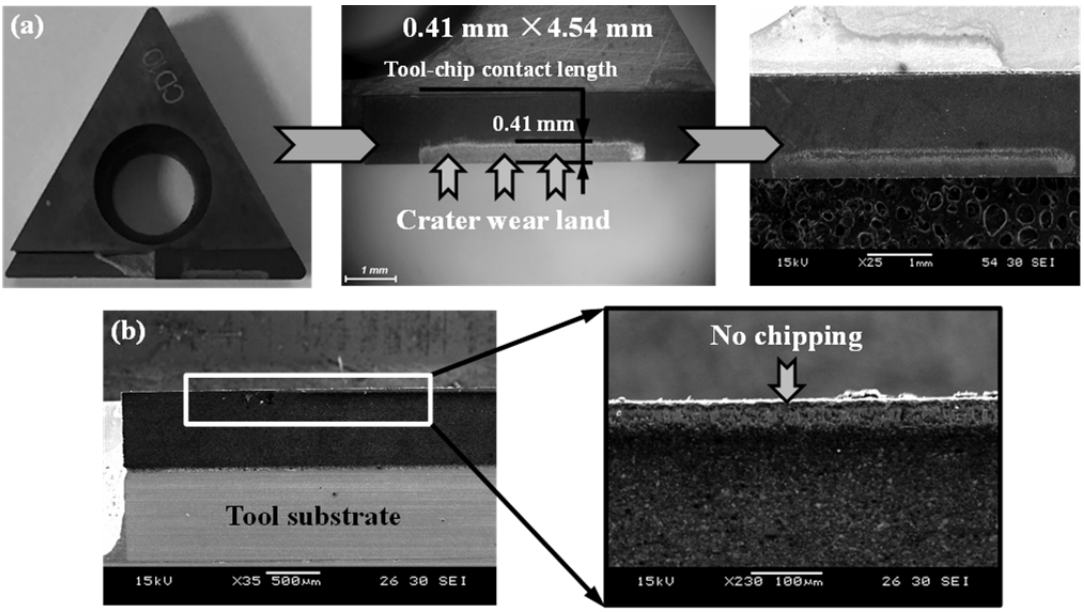

Fig.5.36. Surface morphologies of the worn PCD tipped insert after cutting θ = 45° CFRP/Ti stacks: (a) tool rake surface and (b) tool flank surface.

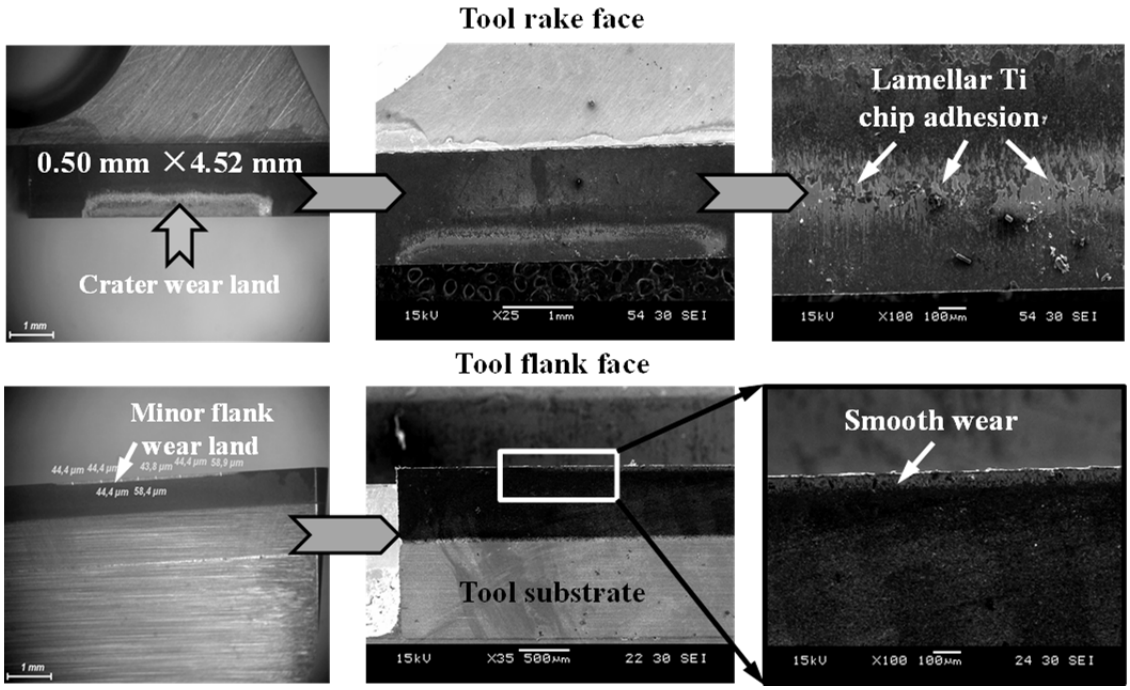

Fig.5.37. Surface morphologies of the worn PCD tipped insert after cutting θ = 90° CFRP/Ti stacks.

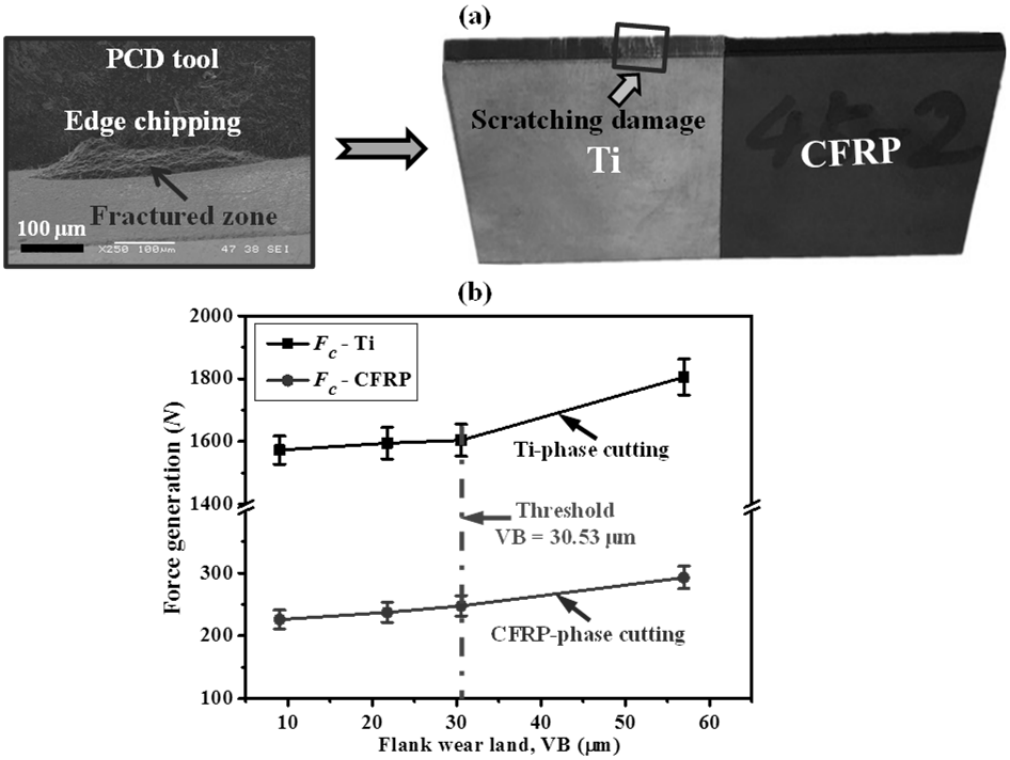

Fig.5.38. (a) Effects of tool failure on machined CFRP/Ti surface quality ($\theta = 45°$, $v_c = 32$ m/min and $f = 0.20$ mm/rev) and (b) influences of tool flank wear width (VB) on CFRP/Ti cutting force generation ($\theta = 45°$, $v_c = 32$ m/min and $f = 0.20$ mm/rev).

Finally, the influences of tool failure on the machined CFRP/Ti surface quality and the effects of tool flank wear (VB) on CFRP/Ti cutting force generation are shown in Fig.5.38. As depicted in Fig.5.38(a), it is noticeable that when tool failure (edge chipping) takes place on the main PCD cutting edge, the machined CFRP/Ti surface is deteriorated significantly. The severe scratching damage on the machined Ti surface is clearly visible as shown in the right photograph of Fig.5.38(a). The damaged area on the machined surface may be caused due to the ineffective cutting

action arising from the fractured zone of the PCD cutting edge, which causes severe scratching on the trimmed workpiece surface when it loses its fresh sharpness. Besides, the tool wear progression in terms of flank wear width (VB) is also identified to have a considerable influence on the cutting force generation when machining hybrid CFRP/Ti stacks as shown in Fig.5.38 (b). With the progression of tool wear extent, the CFRP/Ti cutting force gradually suffers a remarkable increasing trend, especially when the VB reaches a threshold value of probably 30.53 μm. The main cause should be attributed to the serious deterioration of the tool edge sharpness when the tool wear is expanded, which inevitably gives rise to the increased tool-chip friction coefficient and subsequently leads to high cutting resistance and cutting energy consumption. In sum, the effects of tool failure or tool wear on hybrid CFRP/Ti stack cutting are entirely detrimental. To guarantee excellent machined surface quality and to minimize the high force generation, a strict control of tool wear should be rigorously taken when cutting hybrid CFRP/Ti stacks.

5.8 Conclusions

In this Chapter, the fundamental cutting mechanisms of hybrid CFRP/Ti stacks when subjected to orthogonal cutting configuration have been studied. The basically available bi-material cutting configurations including different cutting sequence strategies ($^{\text{CFRP} \rightarrow \text{Ti}}_{\text{Ti} \rightarrow \text{CFRP}}$) and combined material machining were carefully performed by using superior PCD tools and various coated carbide tools, respectively. The key cutting responses including chip separation process, cutting force generation, machined surface quality, tool performance and tool wear mechanisms were precisely addressed. Based on the experimental results acquired, the following key conclusions can be drawn.

- Through the chip separation mode inspection, both brittle fracture and plastic deformation mechanisms are identified to govern the entire orthogonal cutting operations of hybrid CFRP/Ti stacks in either CFRP → Ti cutting sequence or Ti → CFRP cutting sequence. The resected CFRP and Ti chips are found to be “powdery” dust and “continuous” nature, respectively. Besides, serious Ti chip adhesion is also found in the Ti → CFRP cutting sequence, which is be a key cause of the “V shape” like delamination in the interface zone and the severe cracking damage inside the machined CFRP phase. The detected phenomenon agrees well with the numerical observations when cutting modeling of hybrid CFRP/Ti stacks under the identical cutting sequence. The combined CFRP/Ti cutting usually involves the coupled chip separation modes of brittle fracture and plastic deformation, thus resulting in the combined “powdery” and “continuous” chip formation. The phenomenon, to some extent, will inevitably induce uneven stress/temperature distribution on tool main cutting edge and result in the instability of the tool-work interaction.

- Force signal analysis shows the basic five and three cutting stages involved in orthogonal cutting of hybrid CFRP/Ti stacks and combined CFRP/Ti machining, respectively. Besides, fiber orientation (θ) is found to have a pronounced effect on the CFRP/Ti cutting force for the CFRP-phase cutting while its influence on Ti phase cutting force is negligible. Moreover, the cutting speed (v_c) is identified to have a positive impact on CFRP/Ti cutting force when low speed is used, whereas when high speed is employed, its impact is negative. By contrast, the feed rate (f) totally has a significantly positive impact on both cutting force and thrust

force when orthogonal cutting of hybrid CFRP/Ti stacks. When machining combined CFRP/Ti stacks, the similar parametric effects are observed, and tool A with gradient coating grade is found to promote the lowest force generation as compared to its counterpart ones.

- The surface quality studies highlight that the key damage promoted on the trimmed CFRP/Ti surface primarily takes place in the CFRP phase and interface region. Fiber orientation (θ) is confirmed to have a significant role in affecting the finally machined CFRP/Ti surface quality. The key damage modes of the machined Ti phase are the deformation of feed marks and re-deposited chip materials while the major imperfections occurring on the machined CFRP surface are fiber pullout, resin loss, and surface cavity. In addition, when cutting is operated from Ti to CFRP, one key difference is the occurrence of rapid ductile fracture in the trimmed interface region. For machined CFRP/Ti surface under combined interface cutting, the intact interface zone without severe cracking damage is found due to the noninterference of each stacked phase machining.
- Both feed rate (f) and fiber orientation (θ) are found to have a significantly positive impact on the finally generated surface roughness, irrespective of the used cutting sequence strategies. The Ti → CFRP cutting sequence is found to promote much higher surface roughness than CFRP → Ti cutting due to the serious Ti chip adhesion on tool rake face that substitutes the tool edge for further CFRP phase separation. By contrast, the machined Ti surface roughness under Ti → CFRP sequence is observed to yield lower magnitudes due to the fresh tool edge firstly cutting off the metallic phase. Further, the microhardness analysis also confirms the effects of thermal softening because of elevated cutting speed (v_c) and strain hardening due of decreased feed rate (f) on the trimmed Ti surface when orthogonal cutting of hybrid CFRP/Ti stacks.
- Tool performance and wear analyses reveal that the PCD tool commonly suffers serious crater wear but minor flank wear when orthogonal cutting of hybrid CFRP/Ti stacks. The former should be primarily attributed to the Ti phase cutting while the latter can be owing to its extremely high wear resistance during the chip removal process. In addition, the tool failure mode for PCD tools is identified to be edge chipping due to the sudden force variation resulting from CFRP/Ti interface cutting and also the PCD's inherent brittleness. Both tool failure and tool wear progression are confirmed to have totally detrimental influences on the machined CFRP/Ti surface quality and cutting force generation. To ensure an excellent machined surface quality, the use of freshly sharp tool and a stringent control of tool wear should be seriously taken when cutting hybrid CFRP/Ti stacks.

Chapter VI

Experimental studies on hybrid CFRP/Ti stack drilling

Nomenclature

CFRP → Ti Ti → CFRP	Drilling from CFRP → Ti and/or Ti → CFRP
CFRP → Ti	Drilling strategy from CFRP phase to Ti phase
D	Drill diameter
D_{max}	Maximum diameter of the delamination area
D_{nom}	Nominal hole diameter
E_k	Specific drilling energy
f	Feed rate
F_d	One-dimensional delamination factor
F_z	Thrust force
L	Total length of drill main cutting edge
$L_{\text{tool-CFRP}}$	Drill edge segment length of tool-CFRP interaction
$L_{\text{tool-Ti}}$	Drill edge segment length of tool-Ti interaction
M_{CFRP}	Machinability of pure CFRP-phase drilling
$M_{\text{CFRP/Ti}}$	Machinability of stacked CFRP/Ti interface drilling
M_{Ti}	Machinability of pure Ti-phase drilling
n	Spindle speed
R_a	Arithmetic mean roughness
R_q	Root mean squared roughness
R_z	Ten point mean roughness
T	Torque
Ti → CFRP	Drilling strategy from Ti phase to CFRP phase
t_m	Multi-tool-work interaction time
v_c	Cutting speed
ψ	Drill helix angle
Φ	Nominal diameter
$\Phi_{e,CFRP}$	Hole exit diameter of CFRP phase
$\Phi_{e,Ti}$	Hole exit diameter of Ti phase
$\Phi_{o,CFRP}$	Hole onset diameter of CFRP phase
$\Phi_{o,Ti}$	Hole onset diameter of Ti phase
ϕ	Drill point angle
η	Tool-work interaction ratio
η_A	Ratio of $L_{\text{tool-CFRP}}$ to L
η_B	Ratio of $L_{\text{tool-Ti}}$ to L

Abbreviation

CTF	Critical thrust force
MFD	Multifaceted drill
TEC	Thermal expansion coefficient

6.1 Introduction

As addressed in Chapter I, mechanical drilling is a frequently-used operation for high-quality finishing of hybrid CFRP/Ti stacks prior to their post fastening assembly. Owing to their anisotropic behavior and poor machinability, drilling hybrid CFRP/Ti stacks in one-shot time has brought great challenges in modern manufacturing community. With respect to the drilling process, typically two different cutting sequence strategies, *i.e.*, drilling from CFRP → Ti and from Ti → CFRP, exist from the aspect of tool entry and tool exit.

To improve the machinability of hybrid CFRP/Ti stacks, a careful selection of cutting sequence strategy is always of great importance. Through the rigorous literature survey in Chapter I, it was understood that the majority of previous research work concerning hybrid CFRP/Ti stack drilling was performed solely using the CFRP → Ti cutting sequence. It was believed by many scholars [2, 42, 43, 45] that the CFRP → Ti cutting sequence is often a reasonable strategy for minimizing the severe induced hole damage when vertical drilling of the bi-material system. Their key supporting arguments were that in such drilling sequence, a low extent of exit delamination damage can be achieved due to the supporting role of the bottom Ti alloy in preventing laminate deflection and limiting the workpiece dynamics [1, 2]. Besides, an analytical model proposed by Qi et al. [73] when drilling FRP/metal stacks also confirmed that the FRP → metal drilling sequence usually yields a higher CTF (critical thrust force) value than that obtained in metal → FRP drilling sequence, *i.e.*, the FRP → metal drilling can promote a lower delamination extent as compared to its counterpart one. However, this drilling sequence itself has several inherent disadvantages. For instance, it will inevitably result in the serious problems of Ti chip evacuation while drilling the bottom Ti phase. Since hot, long and spiral features usually characterize the drilled-out Ti chips, it will cause severe abrasion/erosion actions on the machined CFRP phase and greatly deteriorate its hole quality. Moreover, the spiral Ti chips can easily entangle themselves with the drill margins, and cause premature tool failure like micro chipping or edge fracture. By contrast, the Ti → CFRP drilling is capable of promoting efficient Ti chip transportation and quick heat dissipation due to the short chip evacuation length involved in drilling. However, this drilling sequence is likely to induce a higher extent of delamination damage of the composite phase. To date, a comparative study to highlight the different benefits between the two cutting sequences in drilling has not yet been reported in the open literature. Further, the machinability classification of hybrid CFRP/Ti stacks with respect to the feature of tool-work interaction is also not clearly addressed.

Based on these incentives, this chapter aims to contribute and clarify the following aspects: (*i*) the features of tool-work interaction and machinability classification in the CFRP/Ti drilling, (*ii*) the influences of different cutting sequences ($^{\text{CFRP}\rightarrow\text{Ti}}_{\text{Ti}\rightarrow\text{CFRP}}$) on hybrid CFRP/Ti drilling responses, and (*iii*) the effects of different tool geometrical features and tool materials on CFRP/Ti drilling performance. To this aim, the comparative drilling trials of hybrid CFRP/Ti stacks were performed by adopting different tool geometries/materials and drilling sequence strategies. The fundamental machining responses including drilling forces, machined hole quality (*e.g.*, surface roughness, hole diameter, roundness error, and hole wall morphology) and drilling-induced damage (*e.g.*, delamination extent and burr defect) were precisely addressed *versus* the utilized cutting conditions [208].

Moreover, for the used drill-work configuration and detailed procedures of the on-site force measurement and post-treatment analysis, please refer to the relevant discussions in Chapter III.

6.2 Drilling process and force signal characterization

The drilling force signals developed in function of cutting time can be utilized as an effective method to monitor the status of the on-site drill-work interaction. In hybrid CFRP/Ti drilling, the most complicated cutting stage usually takes place in the bi-material interface (aka "CFRP-to-Ti" contact boundary) due to the occurrence of the coupled composite-metal drilling process. Fig.6.1 shows the scheme of the drill tip position involved in the CFRP/Ti interface drilling under the cutting sequence of CFRP → Ti, in which the drill main cutting edge is simplified as a straight line for easy interpretation. As can be seen from this figure, when the drill tip firstly attacks the interface zone, the previous pure tool-CFRP interaction is gradually transformed into a multi-tool-work interaction.

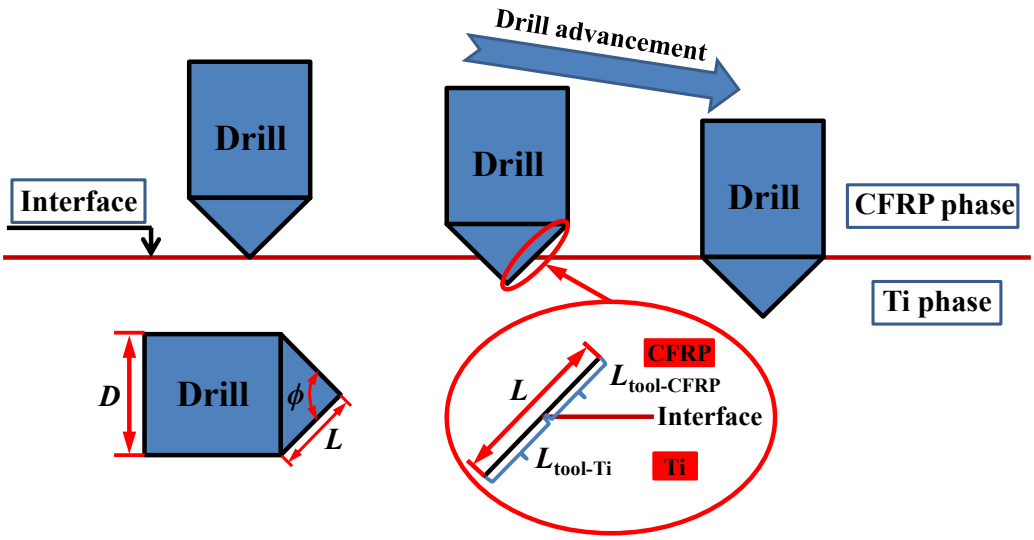

Figure 6.1. Scheme of the drill tip position involved in CFRP/Ti interface drilling (CFRP → Ti cutting sequence).

The drill main cutting edge is then separated into two key segments that are responsible for tool-CFRP interaction and tool-Ti interaction, respectively. Considering that the total length of the drill main cutting edge is L, the corresponding edge segments for tool-CFRP interaction and tool-Ti interaction can be designated as $L_{\text{tool-CFRP}}$ and $L_{\text{tool-Ti}}$, respectively. Besides, the ratios of the segments of the tool-work interactions ($L_{\text{tool-CFRP}}$ and $L_{\text{tool-Ti}}$) to the total drill main edge length (L) can be respectively defined as follows.

$$\eta_A = \frac{L_{tool-CFRP}}{L} \in [0,1] \tag{6.1}$$

$$\eta_B = \frac{L_{tool-Ti}}{L} \in [0,1] \tag{6.2}$$

where $\eta_A = 0$ and $\eta_B = 0$ indicate the inexistence of tool-CFRP and tool-Ti interactions, respectively; $\eta_A = 1$ and $\eta_B = 1$ signify the full tool-CFRP and full tool-Ti interactions, respectively.

With the ongoing drilling advancement, both η_A and η_B values change dynamically within the interval range of $\eta \in [0, 1]$, greatly dependent on the implemented drilling sequences. During the interface cutting, the combined chip separation modes including brittle fracture and elastic-plastic deformation should simultaneously take place along the main cutting edges and then result in the coupled CFRP chip and Ti chip formation. Moreover, the total cutting time (t_m) governing the interface drilling can be roughly estimated through the following equation [1].

$$t_m = \frac{D}{2nf}\cot\frac{\phi}{2} \tag{6.3}$$

where D is the used drill diameter; ϕ is drill point angle; n and f are spindle speed and feed rate, respectively. As shown in this equation, drill point angle (ϕ) has a negative impact on the interface drilling duration (t_m), *i.e.*, an increased ϕ commonly reduces the t_m duration.

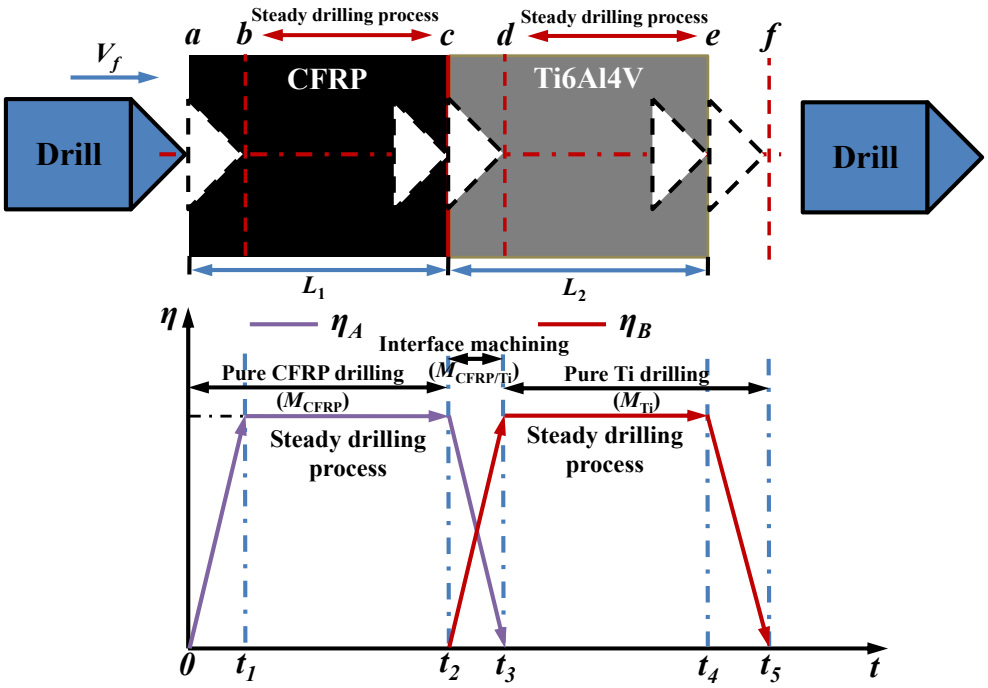

Figure 6.2. Scheme of the tool-work interaction ratio (η) *versus* cutting time (t) governing hybrid CFRP/Ti stack drilling (CFRP → Ti cutting sequence strategy).

Considering the one-shot drilling cycle of hybrid CFRP/Ti stack machining, the total drilling process can be specified in terms of tool-work interaction ratio (η) *versus* the cutting time (t) from the aspects of hole entry and hole exit, as shown schematically in Fig.6.2. Note that in Fig.6.2, L_1 and L_2 represent the individual workpiece thickness of the CFRP phase and Ti phase, respectively; t_1 - t_5 are the representative time frames of different cutting stages involved in CFRP/Ti drilling and can be defined as follows.

$$\begin{bmatrix} t_1 \\ t_2 \\ t_3 \\ t_4 \\ t_5 \end{bmatrix} = \begin{bmatrix} \frac{D}{2nf}\cot\frac{\phi}{2} \\ \frac{L_1}{nf} \\ \frac{L_1}{nf} + \frac{D}{2nf}\cot\frac{\phi}{2} \\ \frac{L_1 + L_2}{nf} \\ \frac{L_1 + L_2}{nf} + \frac{D}{2nf}\cot\frac{\phi}{2} \end{bmatrix}, \left(L_1, L_2 > \frac{D}{2}\cot\frac{\phi}{2} \right) \tag{6.4}$$

As depicted in Fig.6.2, when the drill tip initially penetrates into the CFRP phase, the η_A parameter experiences a quick elevation through the drilling duration of $t \in [0, t_1]$, which signifies

the gradual engagement of the pure tool-CFRP interaction. With the tool advancement, particularly when the drill cutting edges are fully involved in the CFRP-phase machining (stage *b* - *c*), the η_A parameter maintains the maximum value of 1 until the drill tip cuts into the interface zone. Since in such drilling status, the η_A equal to 1 indicates the full tool-CFRP interaction, the cutting stage *b* - *c* can be considered as a steady drilling process due to the full engagement of tool cutting edges in drilling. After the completion of the pure tool-CFRP interaction ($t \in [0, t_2]$), the drill edges are gradually involved in the interface cutting, in which the η_B parameter increases gradually from zero while the η_A parameter suffers a decreasing trend. The phenomena indicate the occurrence of the multi-tool-work interaction dominating the chip separation process. In such circumstance, the drill cutting edges should undergo a coupled composite-metal chip removal mode and result in the combined "powdery"-like and "continuous"-like chip formation. Since the η_A and η_B parameters vary dynamically with cutting time, the cutting edges will inevitably experience a severe transition of drilling-induced mechanical/thermal responses. For instance, the disparate machinability behaviors of the CFRP and Ti phases will induce different levels of force generation and cutting temperature, and hence result in the uneven stress/heat distribution on the drill cutting edges, which may cause the instability of the drilling process and initiate serious tool catastrophic failure. Since in such drilling stage, the main cutting edges experience a combined CFRP/Ti material removal process, the cutting duration of $t \in [t_2, t_3]$ (aka cutting stage *c* - *d*) in reality can reflect the machinability of the stacked CFRP/Ti interface drilling ($M_{\mathrm{CFRP/Ti}}$). Moreover, when the drill edges completely cut into the Ti phase, the previous multi-tool-work interaction is eventually transformed into the pure tool-Ti interaction. And elastic-plastic deformation then acts as a predominant chip separation mode. In such case, the η_B parameter keeps a constant maximum value of 1 and the drilling stage *d* - *e* ($t \in [t_3, t_4]$) can be identified as a steady cutting process as shown in Fig.6.2. Finally, when the drill tip penetrates into the exit boundary of the Ti phase, the pure tool-Ti interaction ratio (η_B parameter) decreases quickly to zero until the completion of the drilling operation. The drilling stage *d* - *f* then reflects the machinability of the individual Ti phase (M_{Ti}).

To better monitor the on-site status of the tool-work interactions dominating the hybrid CFRP/Ti stack machining, the drilling force signal in function of cutting time (*t*) was utilized as an effective method to facilitate the drilling comprehension, as shown in Fig.6.3. Note that in Fig.6.3, the comparative drilling force signals were decomposed into two main components, *i.e.*, thrust force signal (F_z) and torque signal (T), that were obtained under the identical CFRP → Ti cutting sequence. A comparative result of the force signals developed by two different drill bits (drill A and drill B) is presented. It is noticeable that the total drilling force signals can be classified into five cutting stages ($a \rightarrow b \rightarrow c \rightarrow d \rightarrow e \rightarrow f$) for all the tested drill bits and cutting parameters, which signify the different statuses of the tool-work interactions governing the drilling operation as elaborated above. In addition, the force signal profiles captured in the current study also show a similar pattern with the observations of drilling hybrid (Gr/Bi)/Ti stacks [2] and drilling CFRP/Al stacks [209]. Besides, the force profiles (F_z and T) generated in the Ti-phase drilling always yield much higher magnitudes than those of the force profiles gained in the CFRP-phase drilling, regardless of the implemented cutting conditions. The reason can be attributed to the high mechanical/physical properties of the titanium alloy and its specific chip removal mechanism, *i.e.*, elastic-plastic deformation [4, 169]. Further, when the drill edges cut across the CFRP/Ti interface region, a sudden increase of drilling forces is identified in the force profile *c* - *d* as shown in Fig.6.3,

which will result in the instability of the tool-work interaction dominating the chip removal process. Additionally, the force comparisons between drill A and drill B also show that under the identical cutting conditions, the PVD TiAlN-coated drill (drill B) promotes much higher force magnitudes than its counterpart one (drill A), especially for the thrust force component (F_z) as illustrated in Fig.6.3. The TiAlN-coated drill in reality should induce lower drilling forces as compared to the uncoated one due to the effective role of the TiAlN coating in anti-abrasion and anti-friction. However, a higher thrust force (F_z) is still obtained throughout both CFRP-phase drilling and Ti-phase drilling. Such abnormal phenomena can be explained as follows. The thrust force magnitudes developed in drilling are highly dependent on the competition between the influences of tool material composition and tool geometrical feature when fixed drilling parameters are applied. Since drill B has a longer chisel edge length of 0.22 mm which is approximately 2 times than that of drill A, the severe extrusion deformation action (aka "negative rake angle cutting") caused by the longer chisel edge length for chip removal in drill B should make a more significant contribution to the force development in contrast with drill main cutting edges. In addition, drill B also has a larger point angle and a larger helix angle than drill A. For a large point angle in drill B, it will inevitably decrease the sharpness of drill main cutting edges and increase the nominal chip layer thickness for chip separation. Besides, the larger helix angle for drill B will also increase the proportion of thrust force in the nominal force generation promoted by the drill marginal edges. Consequently, a higher thrust force (F_z) is generated by drill B when drilling CFRP/Ti stacks under the identical cutting conditions.

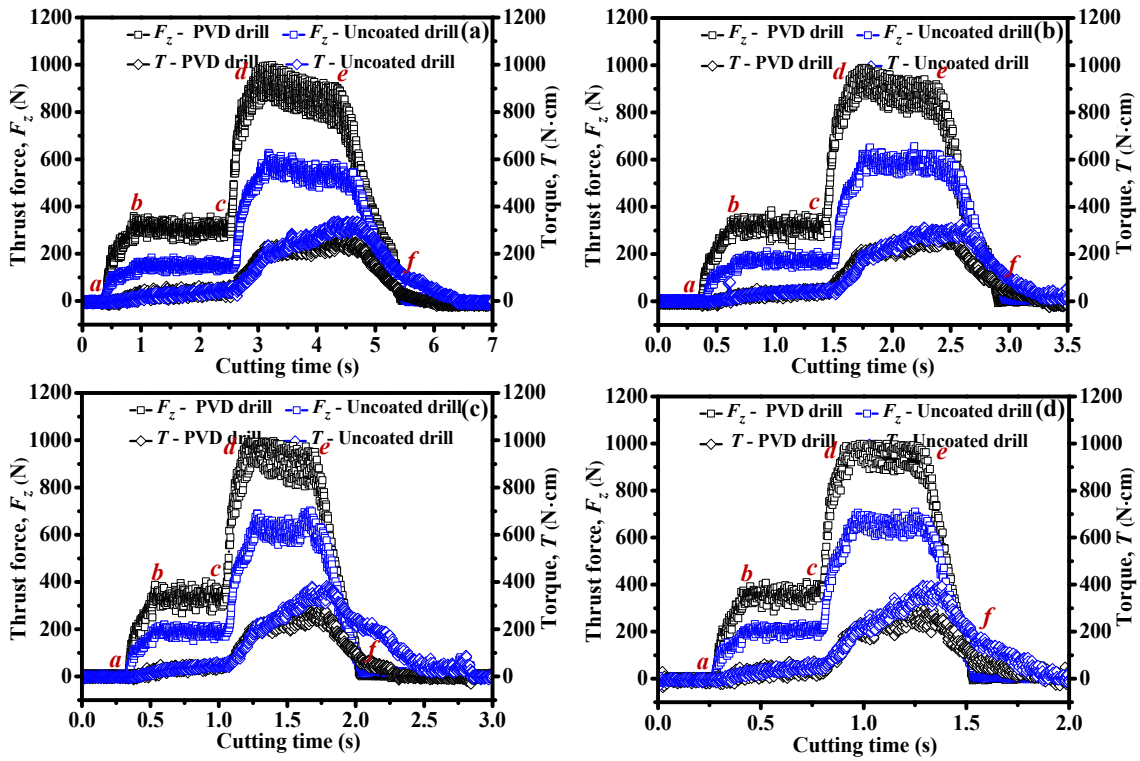

Figure 6.3. Drilling force signals *versus* cutting time (t) when drilling hybrid CFRP/Ti stacks with different tool materials under the CFRP → Ti cutting sequence: (a) v_c=15 m/min, f = 0.15 mm/rev, (b) v_c = 30 m/min, f = 0.15 mm/rev, (c) v_c = 45 m/min, f = 0.15 mm/rev, and (d) v_c = 60 m/min, f = 0.15 mm/rev.

Furthermore, the comparative drilling signals obtained in two different cutting sequence strategies ($^{\text{CFRP}\rightarrow\text{Ti}}_{\text{Ti}\rightarrow\text{CFRP}}$) by using the identical drill B are depicted in Fig.6.4. It is clear that the drilling force signals promoted in either CFRP → Ti or Ti → CFRP cutting sequences show the similar five

cutting stages as discussed earlier, but vary in an opposite direction. Specifically, the Ti → CFRP drilling is observed to generate a little bit lower force magnitudes than those promoted in the CFRP → Ti cutting sequence, particularly for the thrust force (F_z) generation. Considering that the identical fresh drill bit was used for each drilling sequence and the tool wear extent was minor, the reasonable explanation can be that the Ti chip evacuation has certain influences on the drilling force measurement. This is because when operated in Ti → CFRP cutting sequence, the spiral Ti chips can be firstly and quickly transported from the top Ti holes and hence will result in a negligible influence on the force signal measurement. In contrast, the CFRP → Ti drilling usually leads to a long-time and difficult Ti chip evacuation from the machined bottom Ti holes, which will inevitably cause severe scratching effects on the drilled CFRP hole wall surfaces and hence may affect the force measurement.

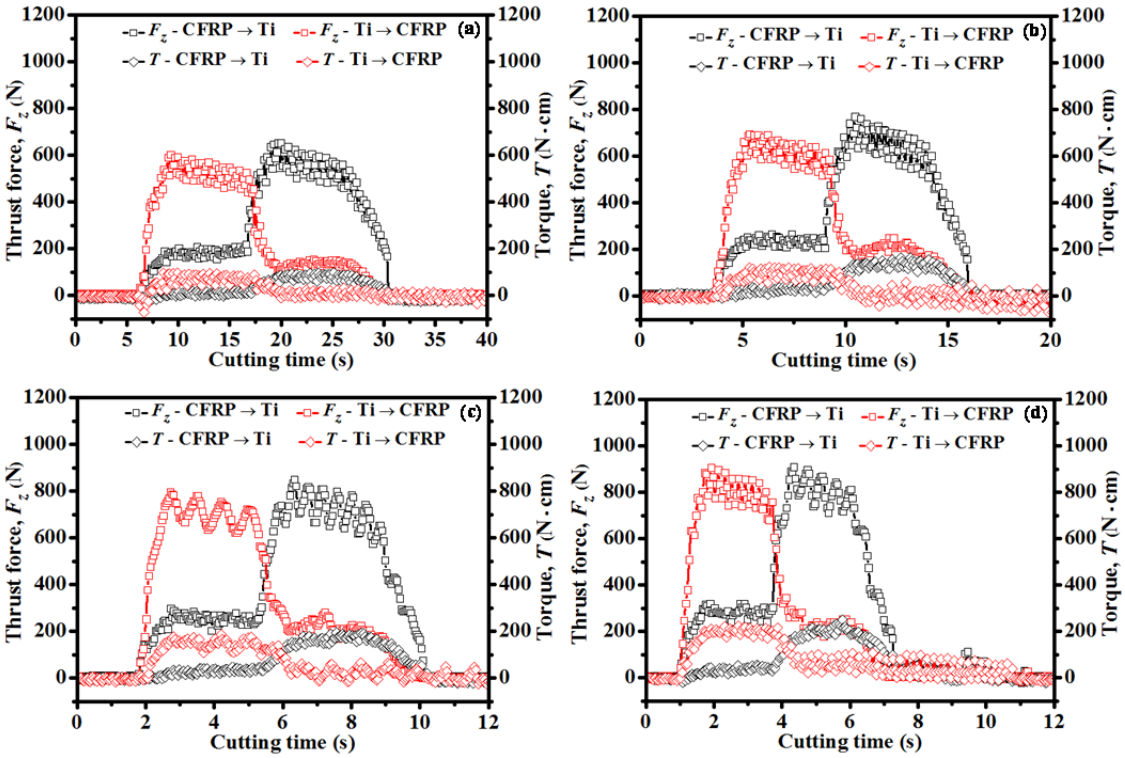

Figure 6.4. Drilling force signals *versus* cutting time (t) under two different cutting sequences ($^{\text{CFRP}\to\text{Ti}}_{\text{Ti}\to\text{CFRP}}$) with the same drill B: (a) v_c = 15 m/min, f = 0.03 mm/rev, (b) v_c = 15 m/min, f = 0.06 mm/rev, (c) v_c = 15 m/min, f = 0.09 mm/rev, and (d) v_c = 15 m/min, f = 0.12 mm/rev.

Through the above analyses, the CFRP/Ti drilling operation in both CFRP → Ti cutting sequence and Ti → CFRP cutting sequence can be classified into five basic cutting stages in terms of the status of tool-work interaction, as summarized in Table 6.1.

Table 6.1
Summary of the drilling stages and machinability classification when drilling hybrid CFRP/Ti stacks.

Cutting sequence	Drilling stage	Drilling time (t)	η parameter	Machinability classification
CFRP → Ti	Stage a - b	$t \in [0, t_1]$	$\eta_A \to 1$ $\eta_B = 0$	M_{CFRP}
	Stage b - c	$t \in [t_1, t_2]$	$\eta_A = 1$ $\eta_B = 0$	
	Stage c - d	$t \in [t_2, t_3]$	$\eta_A \to 0$ $\eta_B \to 1$	$M_{\text{CFRP/Ti}}$
	Stage d - e	$t \in [t_3, t_4]$	$\eta_A = 0$	M_{Ti}

			$\eta_B = 1$	
	Stage *e* - *f*	$t \in [t_4, t_5]$	$\eta_A = 0$ $\eta_B \rightarrow 0$	
Ti → CFRP	Stage *f* - *e*	$t \in [0, t_1]$	$\eta_B \rightarrow 1$ $\eta_A = 0$	M_{Ti}
	Stage *e* - *d*	$t \in [t_1, t_4\text{-}t_2]$	$\eta_B = 1$ $\eta_A = 0$	
	Stage *d* - *c*	$t \in [t_4\text{-}t_2, t_4\text{-}t_2\text{+}t_1]$	$\eta_B \rightarrow 0$ $\eta_A \rightarrow 1$	$M_{\mathrm{CFRP/Ti}}$
	Stage *c* - *b*	$t \in [t_4\text{-}t_2\text{+}t_1, t_4]$	$\eta_B = 0$ $\eta_A = 1$	M_{CFRP}
	Stage *b* - *a*	$t \in [t_4, t_5]$	$\eta_B = 0$ $\eta_A \rightarrow 0$	
Note: $t_1 - t_5$ expressions can be found in Eq.(6.4); M_{CFRP}, $M_{\mathrm{CFRP/Ti}}$ and M_{Ti} signify the machinability of pure CFRP-phase drilling, stacked CFRP/Ti interface drilling, and pure Ti-phase drilling, respectively.				

6.3 Drilling force magnitudes and specific drilling energy

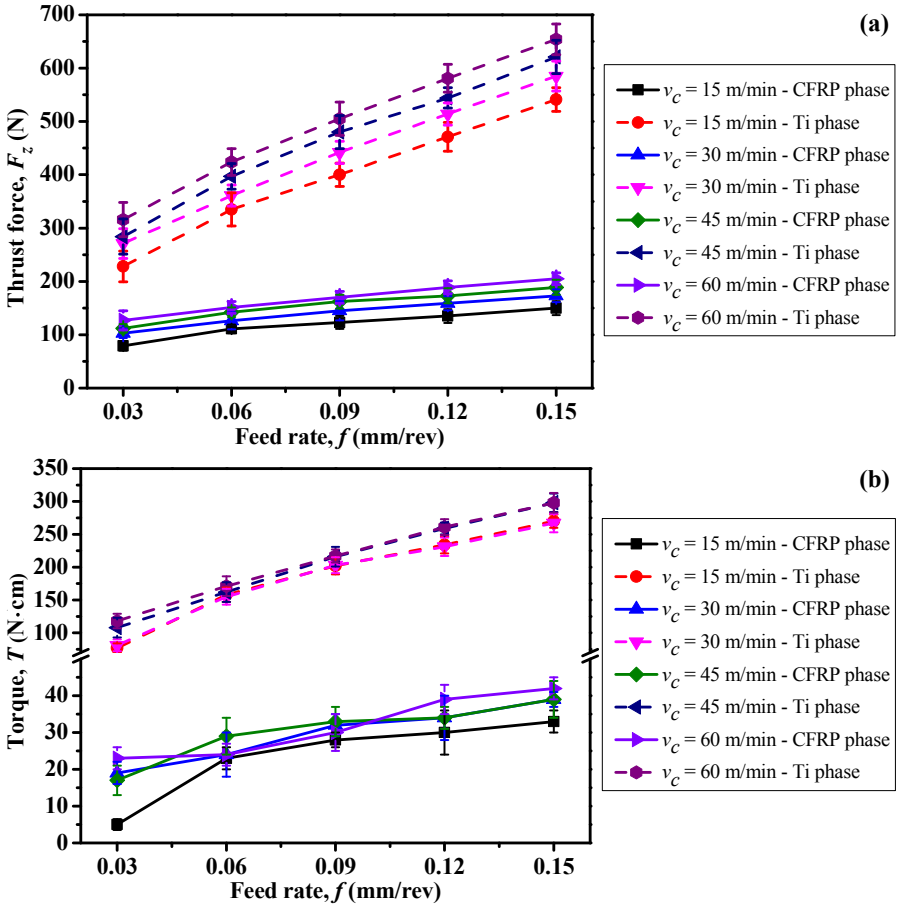

Figure 6.5. Parametric effects on drilling forces when drilling hybrid CFRP/Ti stacks with drill A in the CFRP → Ti cutting sequence: (a) thrust force (F_z) and (b) torque (T).

To clarify the parametric effects on the force generation when drilling hybrid CFRP/Ti stacks, Figs. 6.5 - 6.7 show the obtained force evolution in terms of different drill bits and cutting sequence strategies. Note that the force magnitudes presented in the aforementioned figures were measured on each phase drilling and calculated based on the mean values of the steady drilling stages ($\eta_A = 1$ or $\eta_B = 1$). As shown in these figures, the feed rate (f) is confirmed to have a significantly positive impact on the drilling force magnitudes (F_z and T) in the case of all drill bits and cutting sequence strategies. An increase of f usually gives rise to the dramatically elevated F_z and T. The observation

agrees well with the experimental results of Ramulu et al. [2], Kim and Ramulu [16] when drilling composite/titanium stacks. The reason can be due to the increase in chip cross-sectional area (*i.e.*, increased chip stiffness) as f is elevated, which will greatly increase the cutting resistance for chip breakage and hence lead to the larger drilling forces [129]. Besides, the impact of cutting speed on drilling force magnitudes is also found to be positive in either Ti phase drilling or CFRP phase drilling but less comparable to the feed rate. These findings show a good agreement with the observation of Ramulu et al. [2] when drilling composite/titanium stacks by using HSS drills. Also, for some other previous studies [16, 95], it was usually observed that the increased cutting speed (or spindle speed) commonly facilitates the reduction of thrust force and torque (particularly for drilling metal phase) when drilling hybrid composite stacks. Such different observations between present investigation and the mentioned studies [16, 95] probably indicate that in the tested cutting speed range, the increased cutting temperature with elevated v_c approximately has less significant effects on softening the work material than on tool wear progression. In addition, the experimental results also show that for minimizing the drilling forces, an optimal combination of low feed rate (f) and low cutting speed (v_c) should be adopted in drilling.

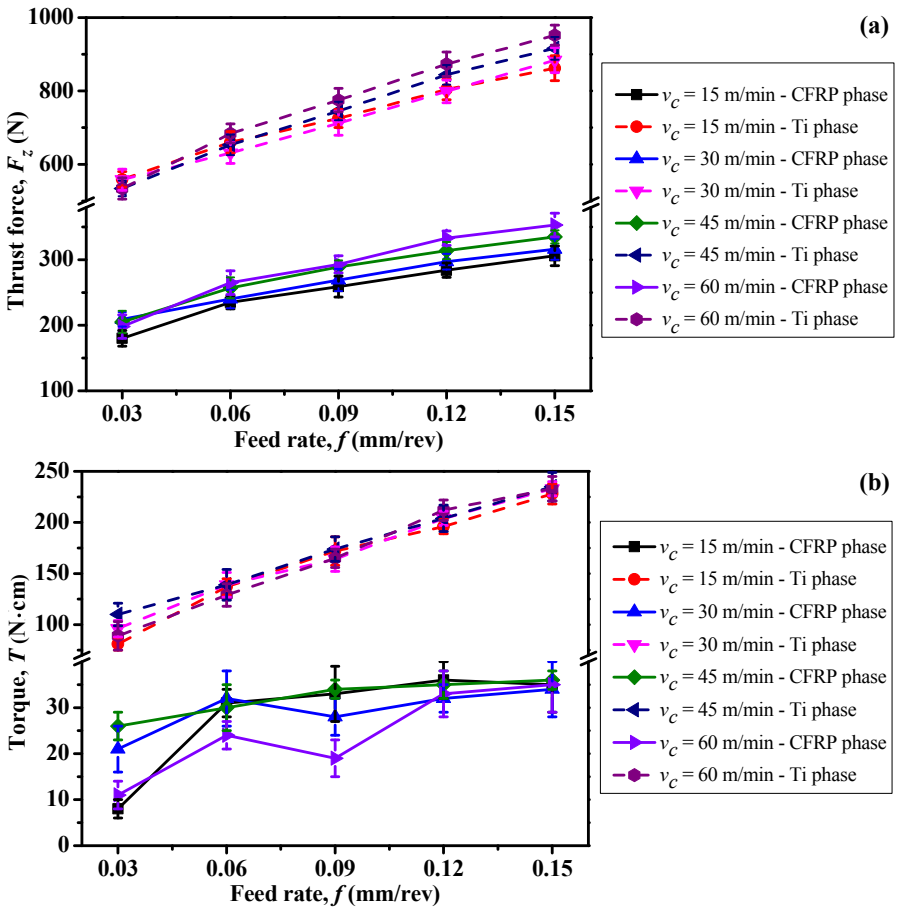

Figure 6.6. Parametric effects on drilling forces when drilling hybrid CFRP/Ti stacks with drill B in the CFRP → Ti cutting sequence: (a) thrust force (F_z) and (b) torque (T).

Further, Figs. 6.8 and 6.9 also depict the comparative F_z and T magnitudes among different drill bits and cutting sequence strategies at various feed rates. The results confirm the significantly positive impact of f on F_z and T components as discussed earlier. Additionally, the uncoated drill A is observed to promote the lowest thrust force (F_z) as compared to the TiAlN-coated drill B when operated in either CFRP → Ti or Ti → CFRP cutting sequences under the same cutting parameters.

For torque (T) component, the phenomenon is not fully noticeable, particularly for the Ti-phase drilling. Nevertheless, such findings agree well with the previous force-signal observation in subsection 6.2. This evidence further confirms the more predominant role of tool geometrical feature (*i.e.*, chisel edge length, point angle, helix angle) in affecting the drilling-force generation than the tool material composition. Finally, the Ti → CFRP cutting sequence is also found to globally generate lower force magnitudes (F_z and T) as compared to the CFRP → Ti drilling for drill B as depicted in Figs.6.8 and 6.9.

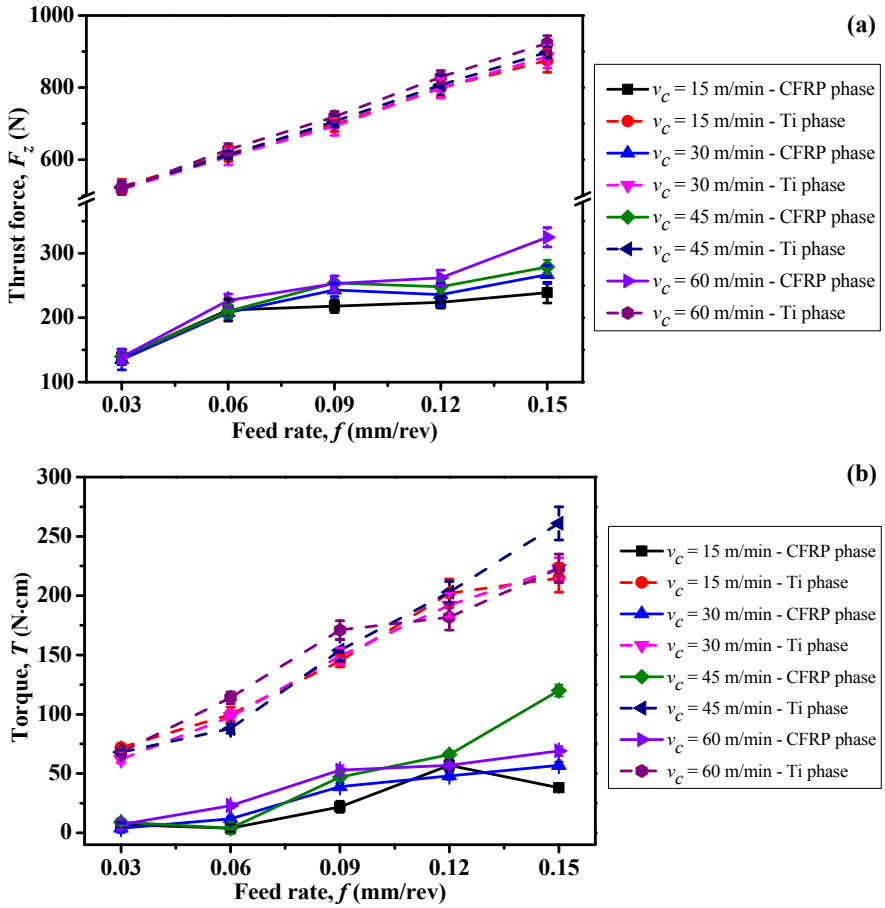

Figure 6.7. Parametric effects on drilling forces when drilling hybrid CFRP/Ti stacks with drill B in the Ti → CFRP cutting sequence: (a) thrust force (F_z) and (b) torque (T).

To evaluate the machinability of hybrid CFRP/Ti stacks, an indicator, namely, specific drilling energy (E_k - J/cm^3) [30, 210], was introduced as expressed by the following equation.

$$E_k = \frac{T \times \omega \times 1000}{MRR} \tag{6.5}$$

where T is the drilling torque in N·m; ω is the rotation speed in rad/s, and MMR is the material removal rate in mm^3/s. The specific drilling energy signifies the number of cutting energies required to remove one unit volume of chips during the drilling operation, which is highly dependent on the inherent properties of the tool-work configurations. Therefore, it can be used as an indicator to quantitatively assess the machinability of the work materials under particular cutting conditions.

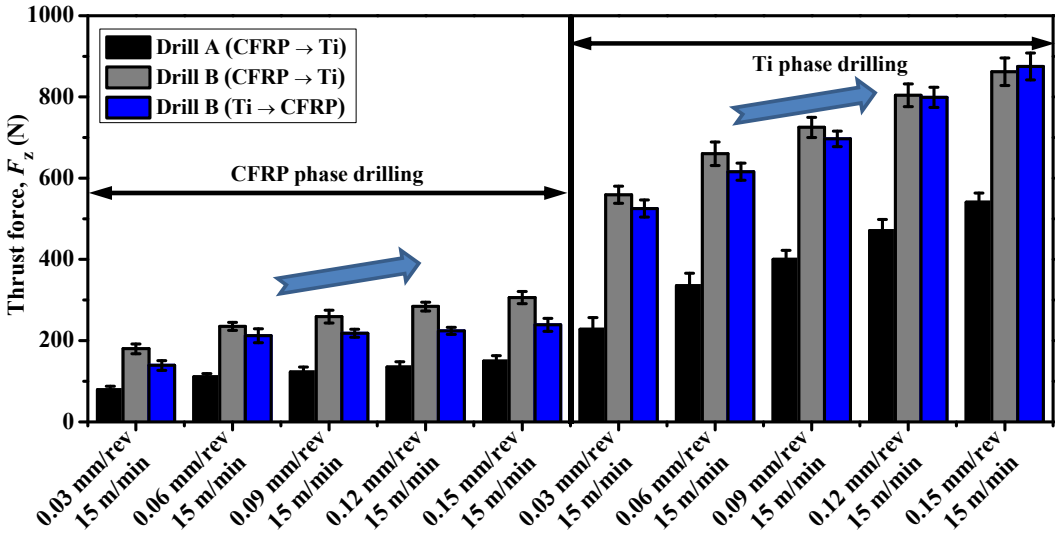

Figure 6.8. Comparative F_z among different drill bits and cutting sequence strategies at different feed rates.

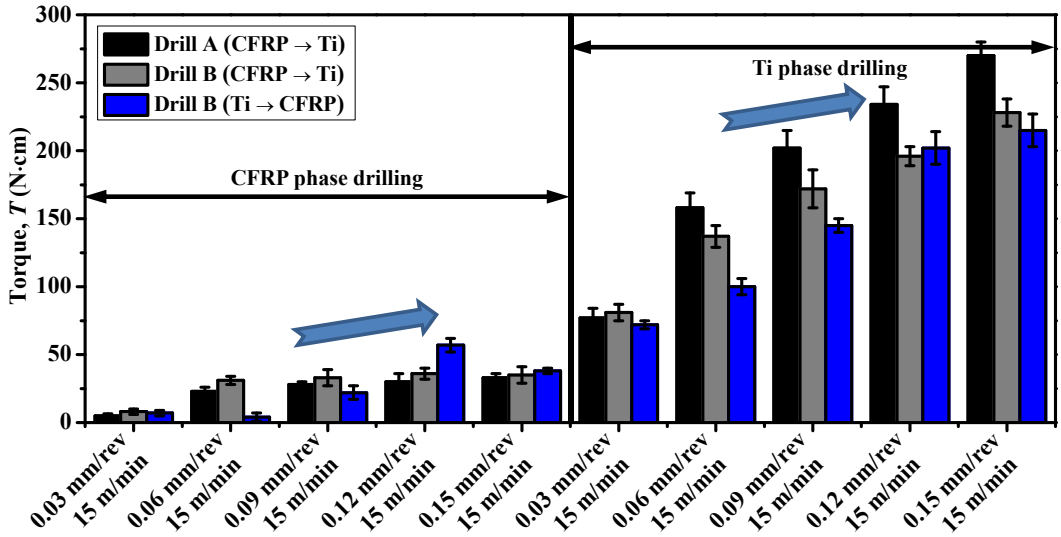

Figure 6.9. Comparative T among different drill bits and cutting sequence strategies at different feed rates.

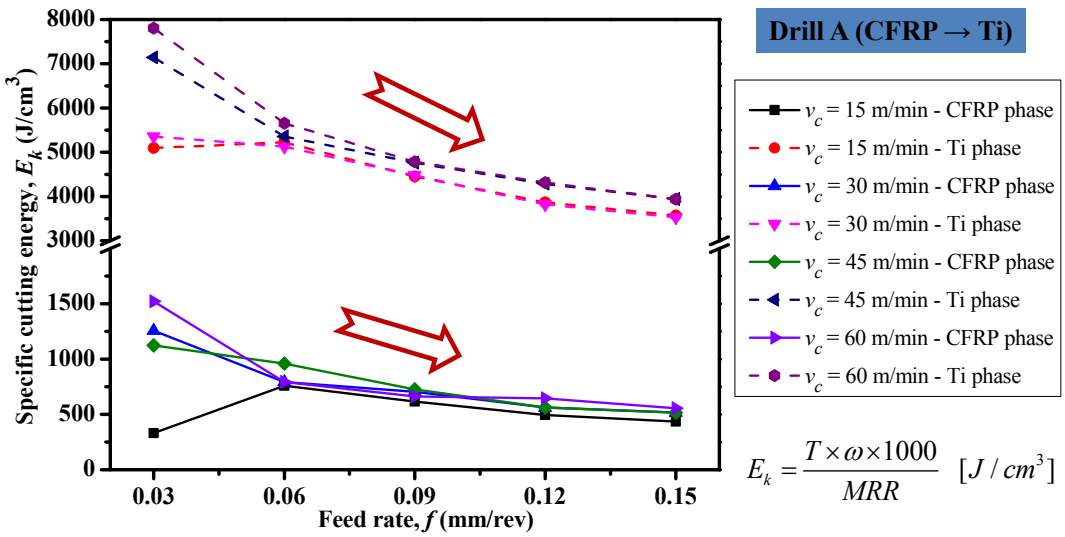

Figure 6.10. Parametric effects on specific drilling energy (E_k) when drilling CFRP/Ti with drill A in the CFRP → Ti cutting sequence strategy.

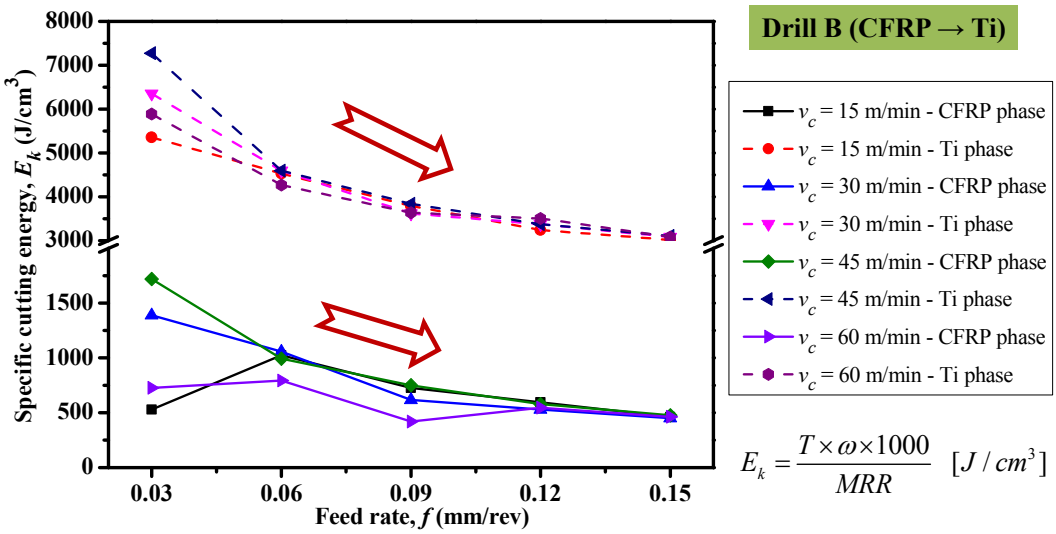

Figure 6.11. Parametric effects on specific drilling energy (E_k) when drilling CFRP/Ti with drill B in the CFRP → Ti cutting sequence strategy.

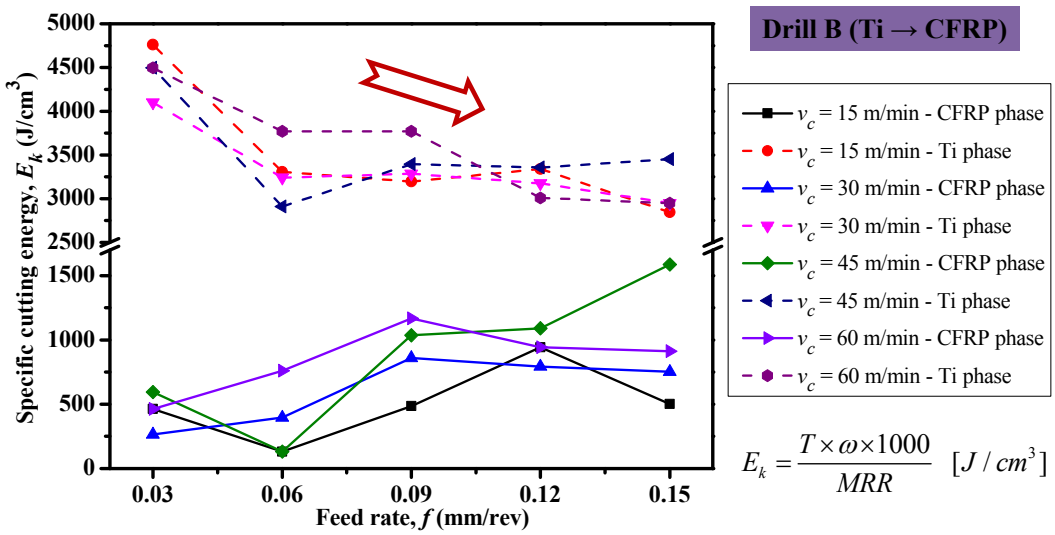

Figure 6.12. Parametric effects on specific drilling energy (E_k) when drilling CFRP/Ti with drill B in the Ti → CFRP cutting sequence strategy.

As shown in Figs. 6.10 and 6.11, the specific drilling energy (E_k) in either Ti phase drilling or CFRP phase drilling for drill A and drill B when subjected to CFRP → Ti cutting sequence is found to globally undergo a sharp decreasing trend with elevated feed rate, except that a small increasing variation occurs when operated at lowest feed rate and lowest cutting speed. For cutting speed, its impact on E_k is found to be negative but less comparable to that of feed rate. The lowest specific drilling energy consumption is observed when drilling at the highest feed rate of 0.15 mm/rev and the highest cutting speed of 60 m/min. Such findings agree well with some experimental observations in either metal alloy cutting [202, 203] or CFRP composite cutting [52, 204] from the open literature. With respect to drill B under the Ti → CFRP cutting sequence, the effect of feed rate on E_k is apparently negative, whereas the variation law of E_k *versus* cutting speed is not fully clear and probably suffers a slightly increasing trend as depicted in Fig.6.12. In addition, the Ti phase drilling consumes much more drilling energy than that of the CFRP phase drilling for all cutting trials due to its specific plastic-deformation chip separation mode and relatively high mechanical/physical properties. By comparing Figs.6.10 - 6.12, it can be observed that the

TiAlN-coated drill B operated in Ti → CFRP cutting sequence entirely promotes less E_k consumption than that of drill A and drill B under the CFRP → Ti cutting sequence. The reduced E_k values for drill B in Ti → CFRP cutting sequence usually indicate the decreased cutting energy consumption and improved machinability of the hybrid CFRP/Ti stack.

6.4 Analysis of chip type in drilling

In hybrid composite stack drilling, an excellent chip breakability of the metallic phase is often required to cut chips into segments aiming to solve the chip tangling problem on drill flutes and to minimize the detrimental effects of chip evacuation on drilled hole wall surface. As reported in literature [209], to facilitate the chip breaking in drilling, one possible solution was to increase feed rate (depth of cut). To evaluate the chip breakability in drilling hybrid CFRP/Ti stacks, a comparative investigation among different drill bits and cutting parameters was conducted. Since the CFRP chips were resected in the form of "powdery" dust that was difficult to gather, only the separated Ti chips were collected. As shown in Fig.6.13, when drilling is operated under low feed-rate conditions (*e.g.*, f = 0.03 mm/rev) with drill B, typically long and ribbon type Ti chips are produced and tangled along the drill body. It is worth mentioning that the occurrence of such phenomena, on one hand, will cause severe abrasion/erosion effects on the drilled hole surfaces and deteriorate the drilled surface finish. On the other hand, it will accelerate the incidence of premature tool failure like micro chipping or edge fracture.

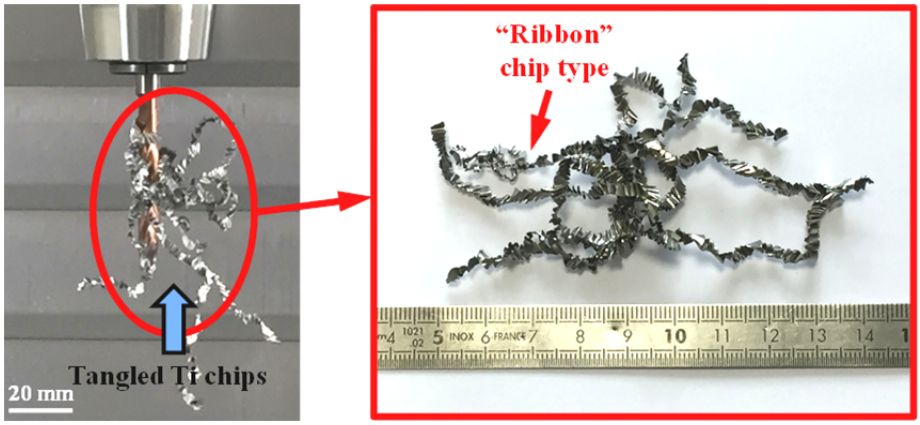

Figure 6.13. Photographs showing the tangled Ti chips on drill body and resected "ribbon" type chips after drilling with drill B in the CFRP → Ti cutting sequence (v_c = 30 m/min, f = 0.03 mm/rev).

Furthermore, Figs. 6.14 and 6.15 also show the representative Ti chips produced in drilling of CFRP/Ti stacks when using different drill bits at various feed rates and cutting speeds, respectively. It is apparent that for drill A in the CFRP → Ti cutting sequence, the resected chips are of mixed type, partly ribbon type and rest are of spiral type. In the case of drill B in the CFRP → Ti cutting sequence, both long to short spiral and ribbon chips are produced, whereas for drill B in the Ti → CFRP cutting sequence, they are primarily uniform spiral type with long ribbon features. Besides, it is again identified that with an increase in feed rate, the Ti chips are separated into small segments after drilling, indicating the improved chip breakability and easier chip evacuation. The activated mechanisms can be attributed to the increased chip cross-sectional area (improved stiffness of the chip layer) when f is elevated. The similar observations are also reported by Zitoune et al. [209] for chips of hybrid CFRP/Al stacks when using plain carbide (K20) drills and by Pawar et al. [211] for

aluminum chip formation when drilling GLARE fiber metal laminates with different geometrical carbide drills. By contrast, the effects of cutting speed on chip breakability are marginal and the Ti chips basically remain the same length and type regardless of the varied cutting speed as shown in Fig.6.15.

Drill type	**Feed rate, *f* (mm/rev)**				
	0.03	0.06	0.09	0.12	0.15
Drill A (CFRP → Ti)					
Drill B (CFRP → Ti)					
Drill B (Ti → CFRP)					

Figure 6.14. Variation of the resected Ti chip shapes *versus* feed rate (*f*) at a constant cutting speed of 15 m/min while drilling hybrid CFRP/Ti stacks.

Drill type	**Cutting speed, v_c (m/min)**			
	15	30	45	60
Drill A (CFRP → Ti)				
Drill B (CFRP → Ti)				
Drill B (Ti → CFRP)				

Figure 6.15. Variation of the resected Ti chip shapes *versus* cutting speed (v_c) at a constant feed rate of 0.03 mm/rev while drilling hybrid CFRP/Ti stacks.

6.5 Hole quality analysis

In hybrid composite stack drilling, hole quality including machined surface roughness, hole size and geometrical accuracy is often a critical concern to ensure a tight stack assembly. For machined CFRP/Ti surface, the maximum R_a values (arithmetic mean roughness) of 3.2 µm and 1.6 µm are

usually required for CFRP phase and Ti phase, respectively [1]. For drilled CFRP hole size, a diameter tolerance less than 30 µm is often demanded [15]. Previous studies [42, 43, 49] have shown that the hole quality is greatly affected by input cutting variables (cutting speed and feed rate) when drilling hybrid composite stacks. In the following subsections, a comparative investigation on drilled surface roughness, hole diameter and roundness error is performed with respect to the used cutting parameters and implemented cutting sequence strategies.

6.5.1 Surface roughness

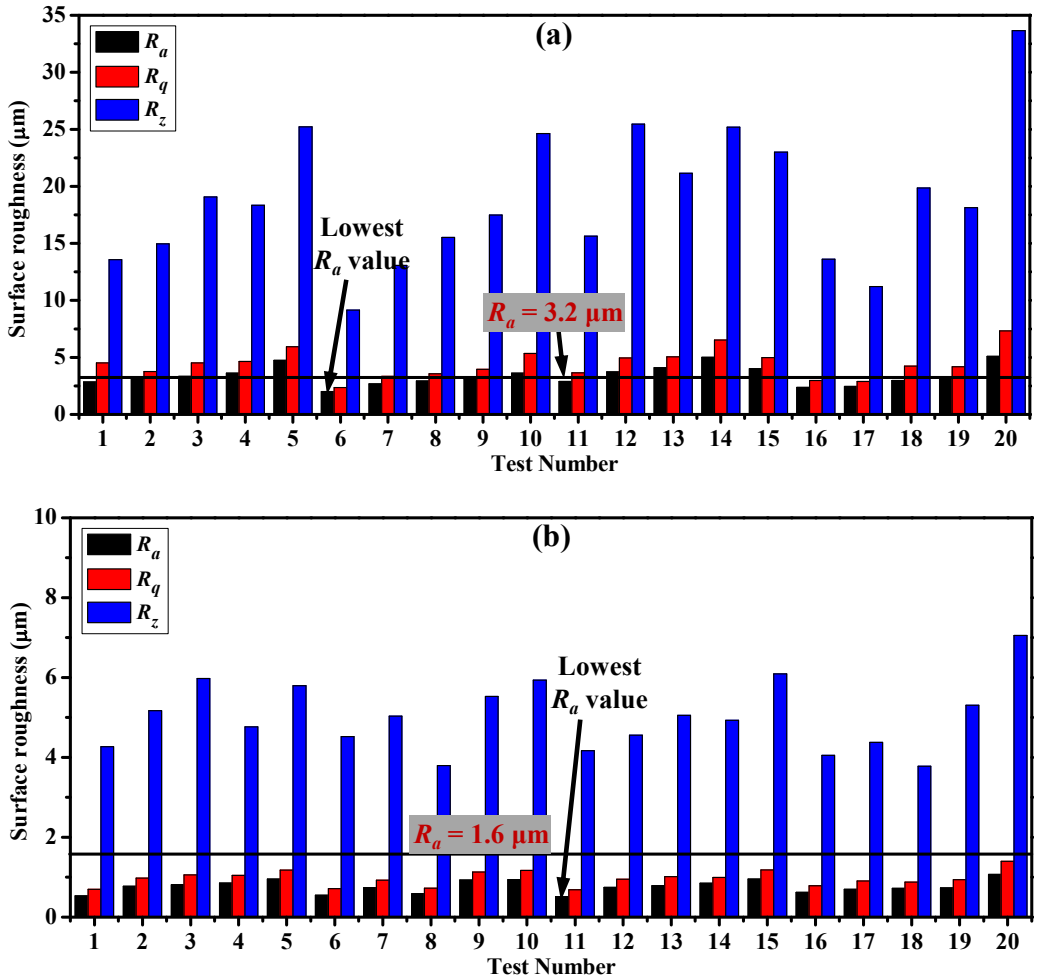

Figure 6.16. Variation of measured (R_a, R_q, R_z) parameters of drilled holes for drill A in CFRP → Ti cutting sequence: (a) CFRP phase and (b) Ti phase (Cutting conditions for test Nos. 1-20 can be found in Table 3.11 of Chapter III).

Figs. 6.16 - 6.18 show the most-used R_a, R_q, and R_z parameters *versus* the cutting speed and feed rate after drilling hybrid CFRP/Ti stacks. All the surface roughness measurements were made on the two individual materials (CFRP phase and Ti phase). As depicted in these figures, the R_a values measured in the CFRP phase for drill A and drill B in the CFRP → Ti cutting sequence are partly lower than the required R_a criterion of 3.2 µm particularly when low feed rates are applied. However, for drill B in the Ti → CFRP cutting sequence, the drilled CFRP surface finish completely meets the R_a requirement. For R_a values of the machined Ti phase, they are totally controlled below the criterion value of 1.6 µm for all examined drill bits and cutting parameters. Besides, the surface roughness values of machined Ti phase ($R_a \in$ [0.5111 µm, 1.073 µm] for drill A, $R_a \in$ [0.373 µm, 1.301 µm] for drill B) are much lower than those measured in the CFRP phase ($R_a \in$

[2.016 µm, 5.100 µm] for drill A, $R_a \in$ [1.146 µm, 4.919 µm] for drill B) when operated in the identical CFRP → Ti cutting sequence. On the contrary, for Ti → CFRP cutting sequence, the R_a values of the CFRP phase are obtained within the range of 0.4 - 2.0 µm, showing the comparable magnitudes to those of the machined Ti phase ($R_a \in$ [0.279 µm, 1.331 µm]). In addition, the measured CFRP surface roughness parameters in the Ti → CFRP cutting sequence are entirely lower than those gained in the CFRP → Ti cutting sequence with the same drill B. The phenomena indicate that the Ti → CFRP drilling favors the improvement of the drilled hole surface finish. Since for each drilling sequence, the identical fresh drill bit was used, the principal cause due to different influences of tool wear on drilled surface finish could be negligible. Therefore, one reasonable explanation should be that the Ti chip evacuation indeed has a remarkable influence on the machined CFRP surface. This is because when drilling from Ti phase to CFRP phase, the resected spiral Ti chips can be firstly transported from the top drilled Ti holes without any damage on the bottom CFRP hole surface. In contrast, when drilling from CFRP → Ti, the sharp and hot Ti chips produced in the bottom Ti phase will cause serious abrasion/erosion effects on the relatively brittle CFRP hole wall surfaces during their long-time evacuation, and hence will greatly deteriorate the CFRP hole quality and give rise to the increased surface roughness. Besides, the R_a values promoted by the TiAlN-coated drill B are slightly lower than those generated by the uncoated drill A when performed under the identical cutting conditions, mainly due to the superior mechanical/physical properties of TiAlN coating against the severe friction of the tool-chip interaction in drilling.

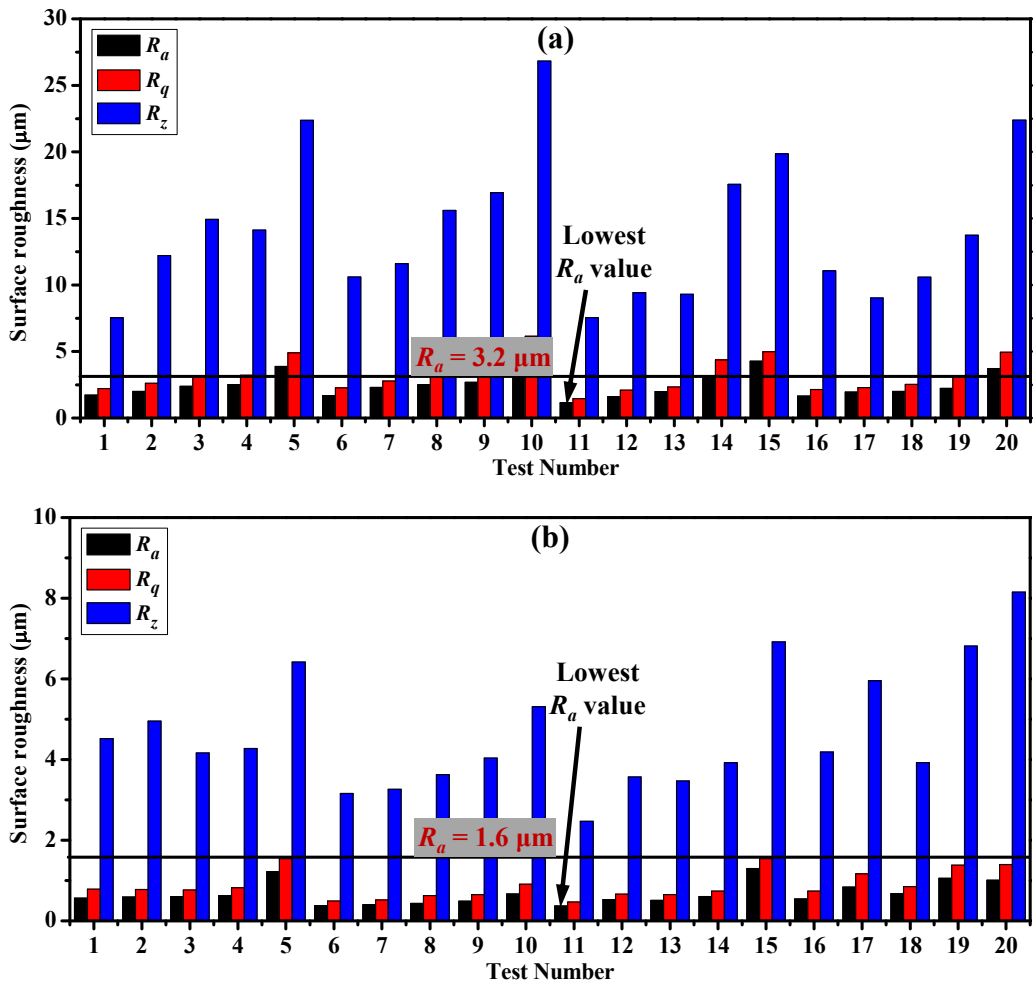

Figure 6.17. Variation of measured (R_a, R_q, R_z) parameters of drilled holes for drill B in CFRP → Ti cutting sequence: (a) CFRP phase and (b) Ti phase (Cutting conditions for test Nos. 1-20 can be found in Table 3.11 of Chapter III).

Moreover, the feed rate is confirmed to have a remarkable influence on the drilled hole surface roughness for all tested trials, where increasing f greatly increases the surface roughness parameters. For instance, the maximum values of R_a, R_q, R_z parameters are usually measured on holes drilled under highest feed-rate conditions (*e.g.*, test Nos. 5, 10, 15 and 20 as shown in Figs. 6.16 - 6.18). In contrast, the effect of cutting speed on surface roughness is obscure and insignificant. Additionally, the comparative results in Figs. 6.16 - 6.18 also show that for achieving better surface finish (*i.e.*, lower surface roughness), the Ti → CFRP cutting sequence as well as the combination of low feed rate and moderate cutting speed should be adopted when drilling hybrid CFRP/Ti stacks.

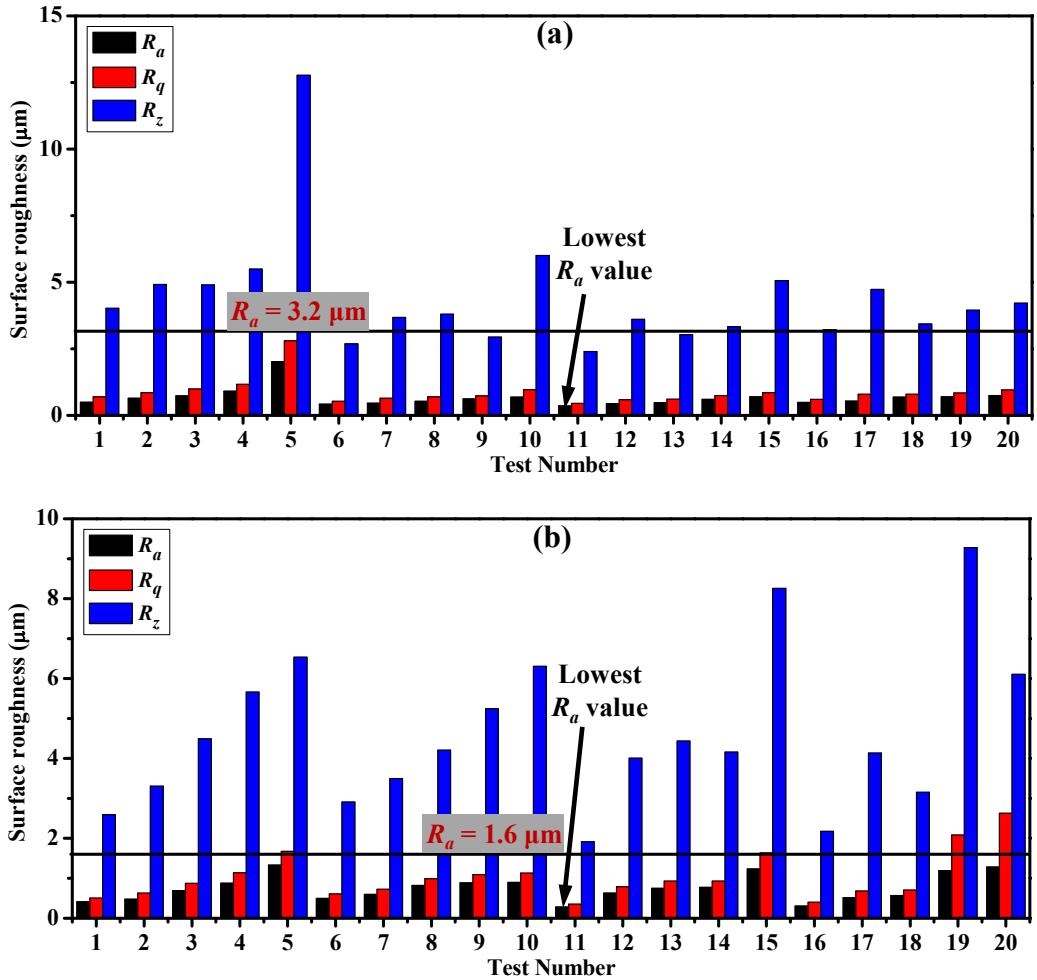

Figure 6.18. Variation of measured (R_a, R_q, R_z) parameters of drilled holes for drill B in Ti → CFRP cutting sequence: (a) CFRP phase and (b) Ti phase (Cutting conditions for test Nos. 1-20 can be found in Table 3.11 of Chapter III).

6.5.2 Hole diameter and roundness error

In hybrid CFRP/Ti stack drilling, the disparate thermal expansion coefficients between stacked composite laminate and metal alloy make it more difficult to produce consistent hole size. Therefore, the hole diameter and roundness error measurements were made on each individual layer.

Figs. 6.19 - 6.21 show the evolution of various measured hole diameters ($\Phi_{o,CFRP}$, $\Phi_{e,CFRP}$, $\Phi_{o,Ti}$ and $\Phi_{e,Ti}$) for each stacked phase *versus* the utilized cutting conditions. Firstly, it is clear that both cutting speed and feed rate have a significant influence on the drilled hole diameters. For CFRP → Ti cutting sequence (see Figs.6.19 and 6.20), the produced hole size in either CFRP phase or Ti phase is totally oversized (larger than Φ_{nom} = 6.35 mm), irrespective of the used drill bits. By

contrast, the hole diameters produced in the Ti → CFRP cutting sequence are partly oversized and partly undersized, greatly dependent on the used cutting parameters (Ref. Fig.6.21). Besides, the Ti → CFRP cutting sequence is found to promote more consistent CFRP and Ti hole diameters close to the nominal drill diameter (Φ_{nom}) of 6.35 mm than those obtained in the CFRP → Ti drilling sequence as shown in Fig.6.21. The predominant factor for the latter (hole diameters in CFRP → Ti drilling) should be attributed to the intense influences of Ti chip evacuation on the hole wall circumference. This is because when drilling is operated in the CFRP → Ti cutting sequence, the resected sharp and hot Ti chips should cause detrimental abrasions on the drilled CFRP hole wall circumferences, and hence will enlarge their original hole circles during the evacuation process. By contrast, the Ti → CFRP cutting sequence prevents the drilled CFRP holes from serious erosions of the Ti chip ejection, thus producing more consistent hole diameters.

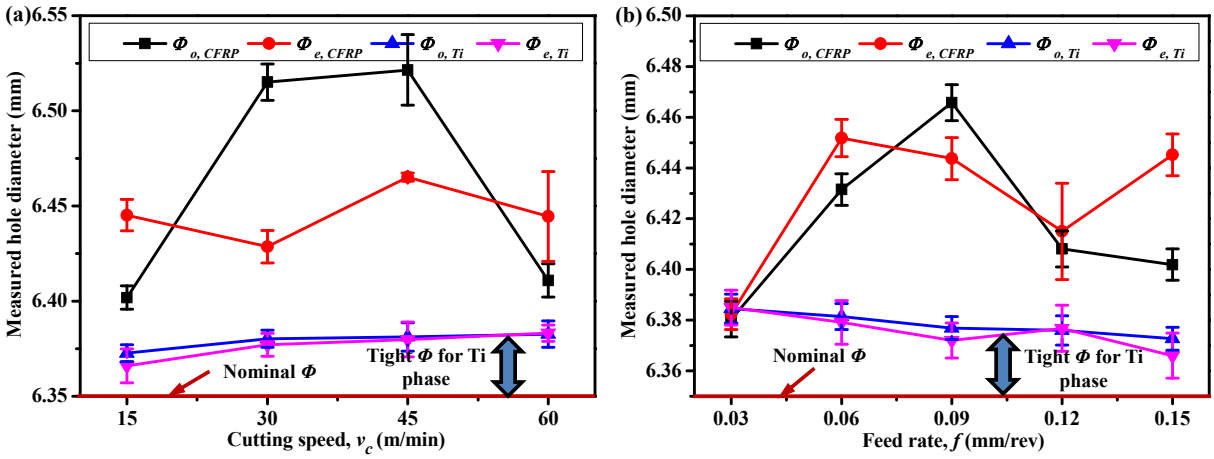

Figure 6.19. Effects of (a) cutting speed (v_c) (f = 0.15 mm/rev) and (b) feed rate (f) (v_c = 15 m/min) on drilled hole diameters for drill A in the CFRP → Ti cutting sequence.

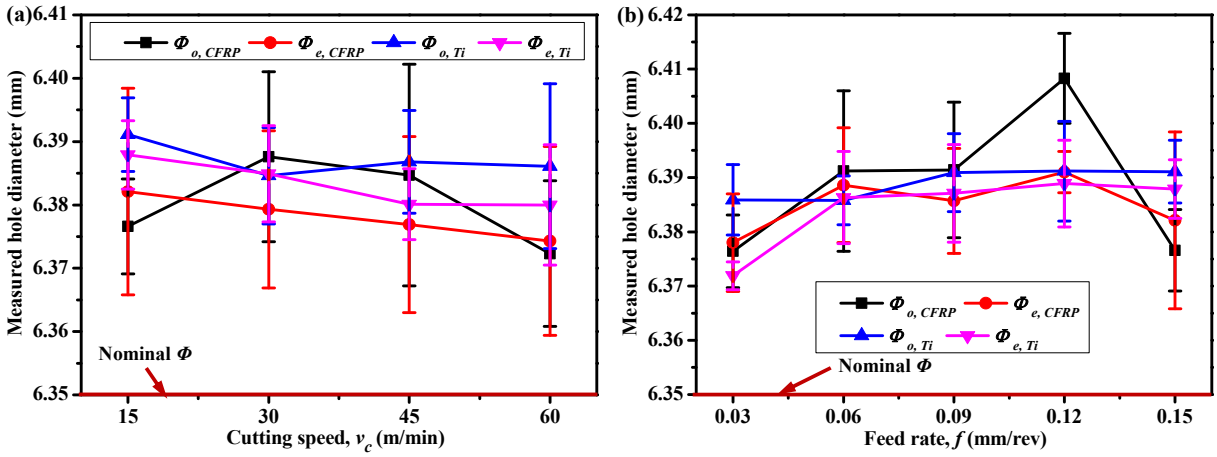

Figure 6.20. Effects of (a) cutting speed (v_c) (f = 0.15 mm/rev) and (b) feed rate (f) (v_c = 15 m/min) on drilled hole diameters for drill B in the CFRP → Ti cutting sequence.

Moreover, from the aspect of achieving consistent hole size, the TiAlN-coated drill B is found to yield a better performance than its counterpart one (uncoated drill A) under the same CFRP → Ti cutting sequence. The reason may be due to the superior behaviors of the TiAlN coating in maintaining sharp cutting edges and excellent wear resistance for either CFRP phase hole making or Ti phase hole making. As for drill A in CFRP → Ti cutting sequence, a large disparity in hole

diameters of CFRP phase and Ti phase is identified (see Fig. 6.19). The Φ_{Ti} commonly exhibits a much smaller value (much closer to Φ_{nom}) than that of Φ_{CFRP} due to the different TECs and elastic moduli of the Ti phase and CFRP phase. Besides, based on the acquired results in Figs. 6.19 - 6.21, it can be concluded that for generating tight hole diameters, the Ti → CFRP cutting sequence, low feed rate and low cutting speed should be adopted when drilling hybrid CFRP/Ti stacks.

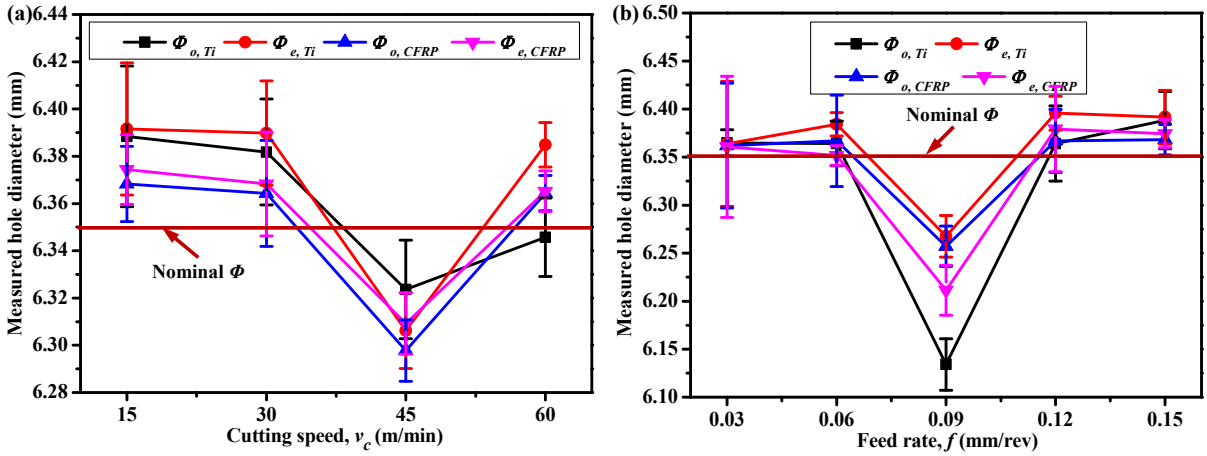

Figure 6.21. Effects of (a) cutting speed (v_c) (f = 0.15 mm/rev) and (b) feed rate (f) (v_c = 15 m/min) on hole drilled hole diameters for drill B in Ti → CFRP cutting sequence.

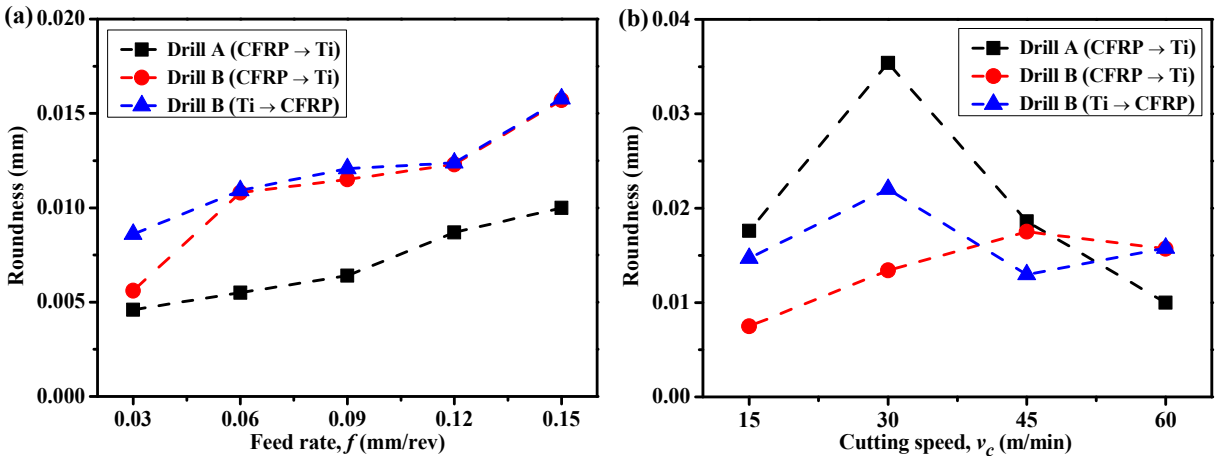

Figure 6.22. Effect of (a) feed rate (v_c = 60 m/min) and (b) cutting speed (f = 0.15 mm/rev) on hole roundness error of CFRP phase for different drill bits and cutting sequences.

Additionally, the parametric effects on hole roundness error of CFRP phase and Ti phase when using different drill bits and cutting sequences are also shown in Figs.6.22 and 6.23, respectively. The roundness error is usually a two-dimensional geometric tolerance that permits how much a feature can deviate from a perfect circle [209]. As depicted in the two figures, when low feed rate is applied (*e.g.*, f = 0.03 mm/rev), the roundness error in either CFRP hole or Ti hole is found to be around 5 - 10 μm. With the increase of feed rate, the roundness error is observed to firstly experience a quick evolution and finally reach its maximum value at f = 0.15 mm/rev. Besides, the cutting speed is found to have a great influence on the measured roundness error. However, its evolution law *versus* roundness error is not fully clear. In some cases, the cutting speed exhibits a positive impact on roundness error (*e.g.*, drill B in CFRP → Ti cutting sequence in Fig.23 (b)), whereas for other cases, it shows a totally negative impact (*e.g.*, drill B in Ti → CFRP cutting sequence in Fig.23 (b)). In summary, to minimize hole roundness error, typically a parametric

combination of low feed rate and low cutting speed should be utilized for hybrid CFRP/Ti stack drilling.

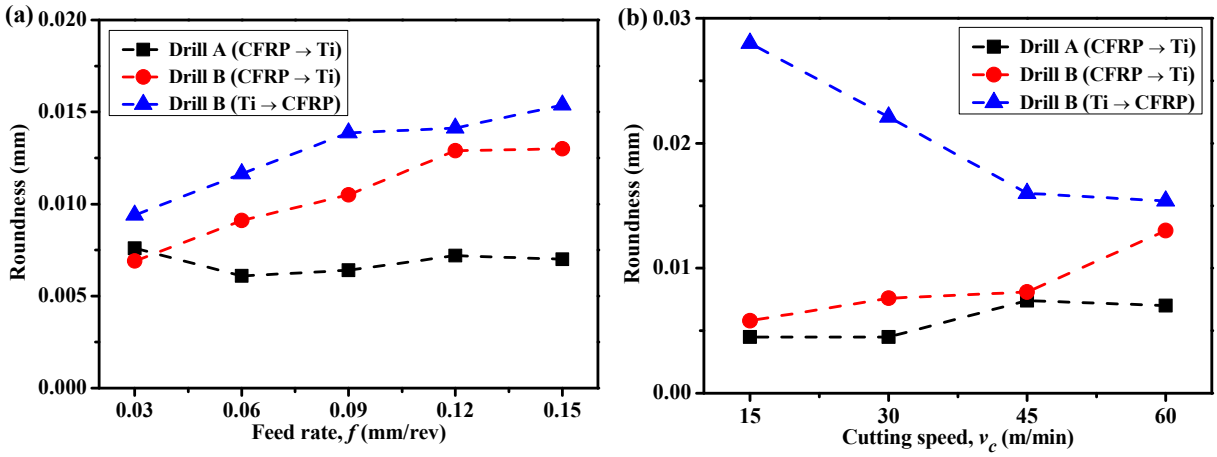

Figure 6.23. Effect of (a) feed rate (v_c = 60 m/min) and (b) cutting speed (f = 0.15 mm/rev) on roundness error of Ti phase for different drill bits and cutting sequences.

6.6 Hole damage study

When drilling hybrid CFRP/Ti stacks, the cutting-induced damage comprises both polymeric defects (*e.g.*, matrix cratering, delamination, fiber pullout, and thermal alteration) and metallic imperfections (*e.g.*, hole size error, position error, and burrs). Among them, the delamination damage promoted in CFRP phase and the burr defect produced in Ti phase are usually the key problems for the assembly of the bi-material system. To investigate the hole damage extent during hybrid CFRP/Ti stack drilling, the drilled hole edge morphology is firstly inspected. Afterward, the delamination damage and burr defect are analyzed.

6.6.1 Hole edge morphology

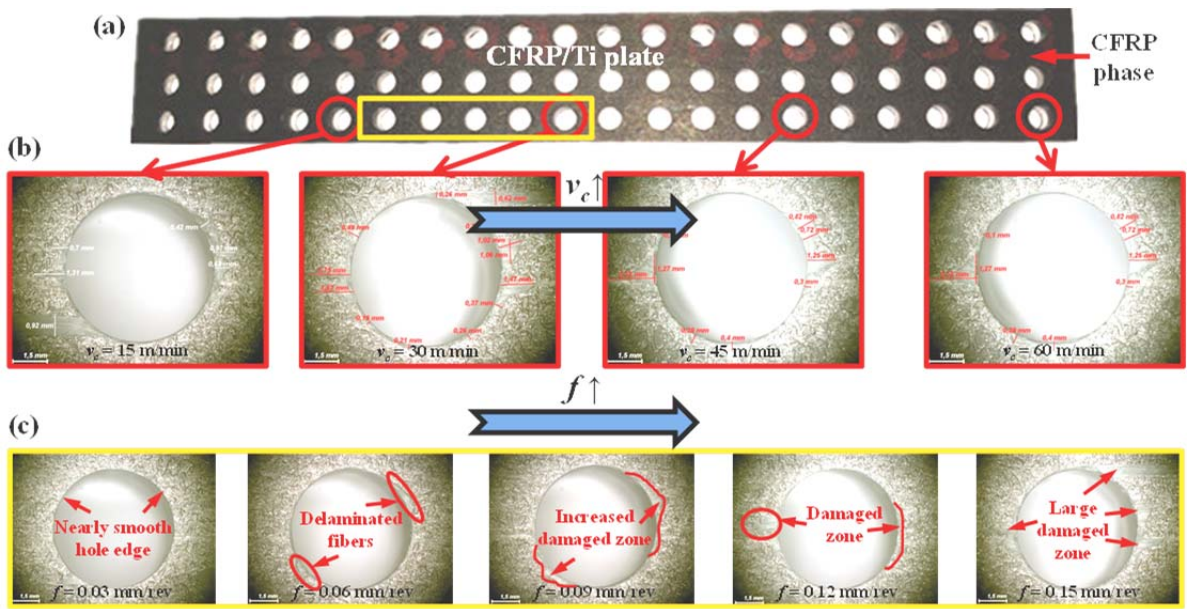

Figure 6.24. Hole edge morphologies of drilled CFRP phase *versus* cutting parameters with drill B in the CFRP → Ti cutting sequence strategy: (a) global hole distribution in the CFRP/Ti plate, (b) f = 0.15 mm/rev, and (c) v_c = 30 m/min.

Fig. 6.24 shows the recorded hole edge morphologies of CFRP phase *versus* cutting speed (v_c) and feed rate (f) when using drill B in the CFRP → Ti cutting sequence. It is noticeable that the feed rate exhibits a great influence on the machined hole edge quality. When drilling is operated at a low feed rate (f = 0.03 mm/rev), nearly a smooth hole edge is achieved as depicted in Fig. 6.24 (c). With the increase of f, a large area of damaged zone is promoted concerning the hole edge circumference, especially when f reaches its maximum value of 0.15 mm/rev. By contrast, the effect of cutting speed (v_c) on the hole edge damage extent is not so significant as shown in Fig.6.24 (b). In the following subsections 6.6.2 and 6.6.3, several quantitative analyses are conducted to clarify the actual parametric influences on the drilling-induced hole damage in terms of delamination damage and burr defect.

Drill type	**Feed rate, *f* (mm/rev)**				
	0.03	0.06	0.09	0.12	0.15
Drill A (CFRP → Ti)	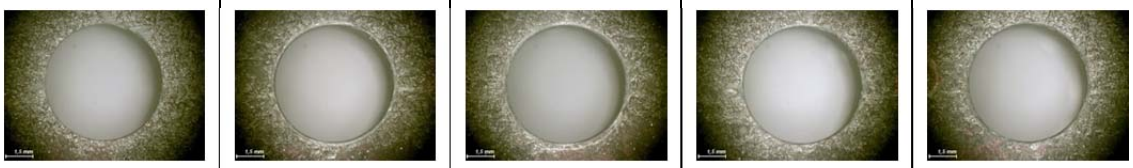				
Drill B (CFRP → Ti)					
Drill B (Ti → CFRP)					

Figure 6.25. Comparative hole edge sides of drilled CFRP phase for different drill bits and cutting sequence strategies.

Drill type	**Feed rate, *f* (mm/rev)**				
	0.03	0.06	0.09	0.12	0.15
Drill A (CFRP → Ti)	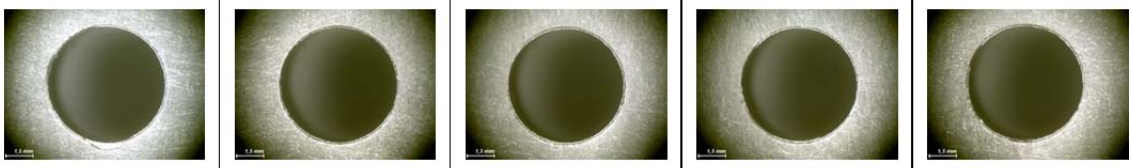				
Drill B (CFRP → Ti)	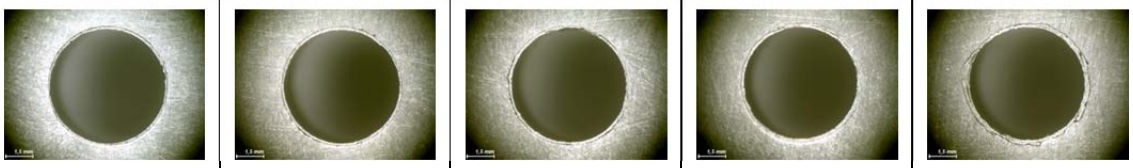				
Drill B (Ti → CFRP)	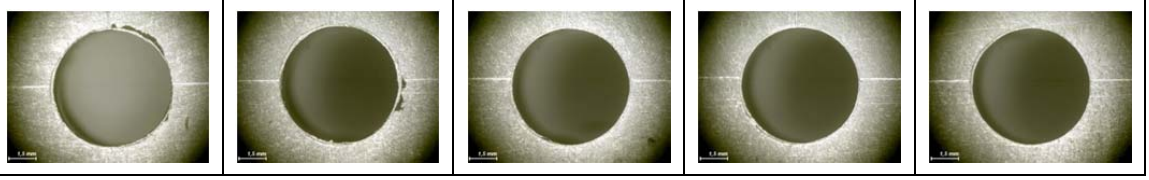				

Figure 6.26. Comparative hole edge sides of drilled Ti phase for different drill bits and cutting sequence strategies.

Moreover, Figs. 6.25 and 6.26 also present the comparative hole edge morphologies of both

CFRP phase and Ti phase after drilling with different drill bits and cutting sequences. Apart from the significantly positive impact of f on the hole edge morphology, the CFRP → Ti cutting sequence commonly promotes more accurate CFRP hole shapes and lower fiber/matrix damage as compared to the Ti → CFRP cutting sequence as depicted in Fig.6.25. The key cause can be attributed to the supporting role of the bottom Ti phase in preventing laminate deflection and limiting the workpiece dynamics when drilling from CFRP phase to Ti phase. Besides, the uncoated drill A is found to produce a little bit higher quality of hole exit edge than that of drill B under the same cutting sequence and cutting parameters. For drilled Ti hole edge, the feed rate is identified to have a remarkable effect on the induced burr formation. However, the influences of different drill bits and cutting sequences on drilled Ti hole edges are not fully apparent.

6.6.2 Delamination damage analysis

In hybrid CFRP/Ti stack drilling, the delamination inside occurring in the composite phase is often a most critical failure mode due to its irreparable nature, which accounts for a large number of part rejections in the real production. To assess its damage extent, the most-used one-dimensional delamination factor (F_d) based on the maximum diameter is adopted in this work. The F_d is defined as the ratio of the maximum diameter (D_{max}) of the delamination area to the nominal hole diameter (D_{nom}), as given by Eq.(6.6) [19, 23, 81].

$$F_d = \frac{D_{\max}}{D_{nom}} \tag{6.6}$$

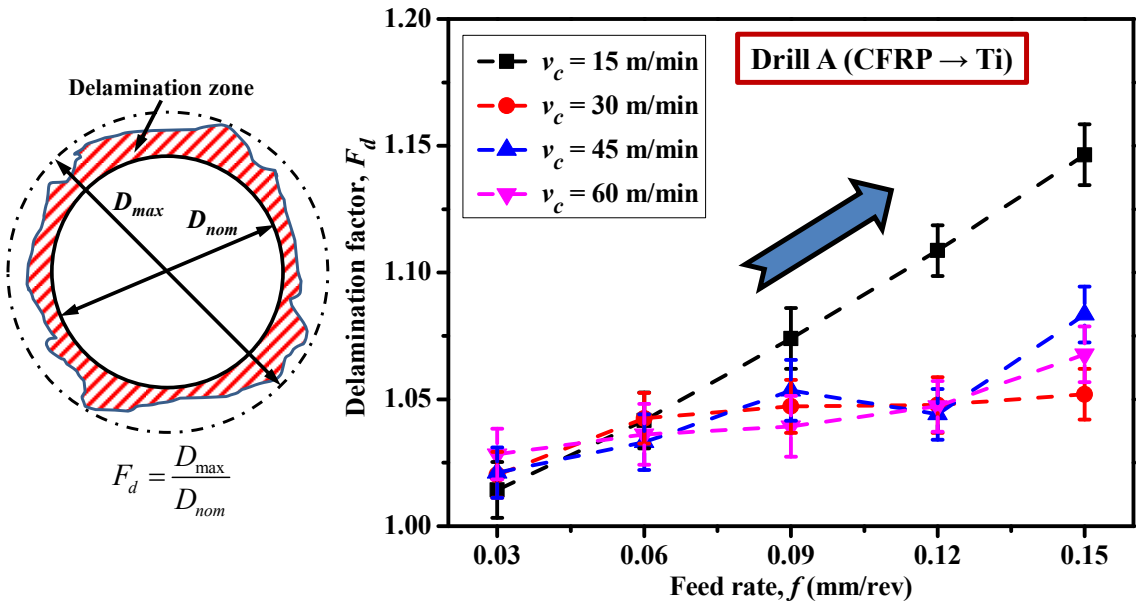

Figure 6.27. Parametric effects on delamination factor (F_d) when using drill A (CFRP → Ti cutting sequence).

Figs. 6.27 - 6.29 show the parametric effects on drilling-induced delamination extent with respect to different drill bits and cutting sequences. It is noticeable that the feed rate shows a predominant role in affecting the drilling-induced delamination in such manner that a small increase of f usually promotes greatly elevated F_d, regardless of the used drills or cutting sequences. Besides, the cutting speed (v_c) probably shows a negative impact on the evolution of F_d especially for drill A

and drill B when operated in the CFRP → Ti cutting sequence. However, for Ti → CFRP drilling, the v_c's impact on F_d is found to be generally positive (*i.e.*, an increased v_c typically gave rise to a higher delamination factor).

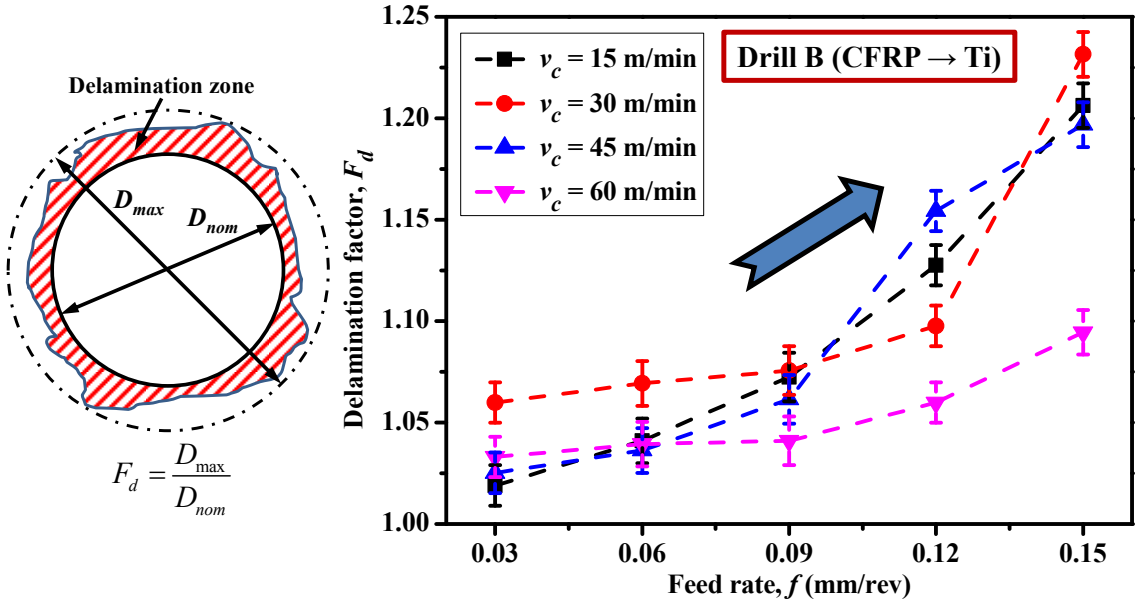

Figure 6.28. Parametric effects on delamination factor (F_d) when using drill B (CFRP → Ti cutting sequence).

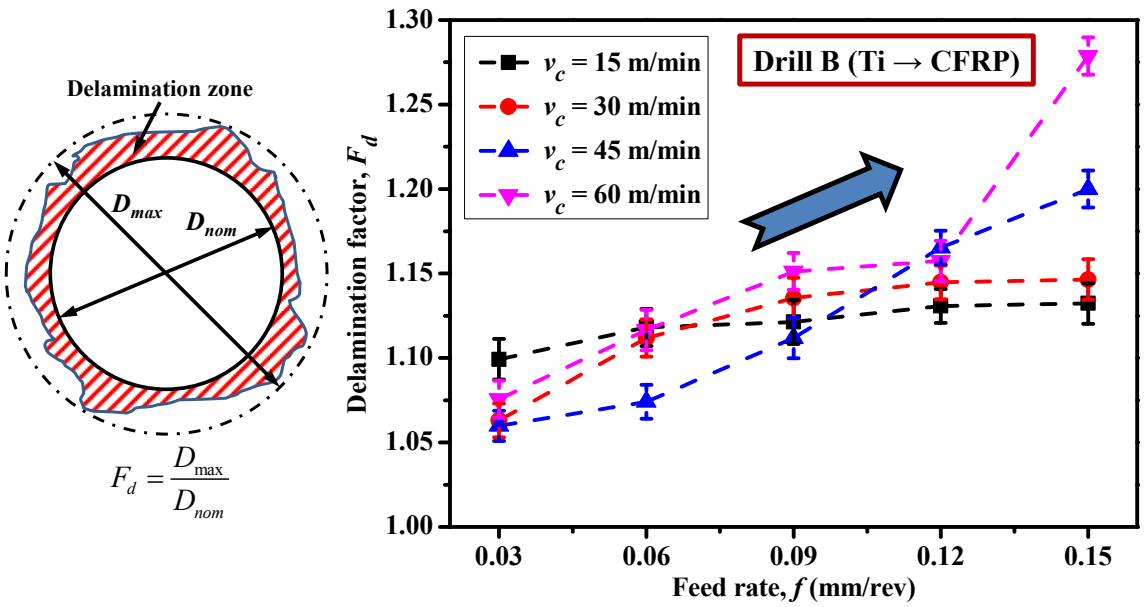

Figure 6.29. Parametric effects on delamination factor (F_d) when using drill B (Ti → CFRP cutting sequence).

Moreover, Fig.6.30 also gives the comparative F_d results when drilling hybrid CFRP/Ti stacks with respect to different drill bits and cutting sequences. The results further confirm the significantly positive impact of f on F_d. Also, it is clear that the CFRP → Ti drilling globally induces a lower delamination extent than that of Ti → CFRP drilling, except two abnormal drilling results (test No. 5: v_c = 15 m/min, f = 0.15 mm/rev and test No. 10: v_c = 30 m/min, f = 0.15 mm/rev) in Fig.6.30. The activated mechanisms as addressed earlier should be attributed to the supporting effects of the bottom Ti alloy on increasing the stiffness of the exit CFRP hole layer when drilling CFRP/Ti stacks. In addition, such findings also agree with the predictions of the analytical models

proposed by Qi et al. [73] for modeling delamination-free drilling of FRP/metal stacks. Furthermore, through the comparisons between drill A and drill B, it can be inferred that the uncoated drill A generates lower delamination extent than its counterpart one. The reason can be attributed to the availability of the superior geometrical features (*e.g.*, small chisel edge length, low point angle and helix angle) that promote lower thrust force than drill B (as discussed in subsection 6.2). As such, a lower delamination factor (F_d) is obtained. Overall, to minimize delamination damage, the CFRP → Ti drilling together with drill A should be adopted when drilling hybrid CFRP/Ti stacks.

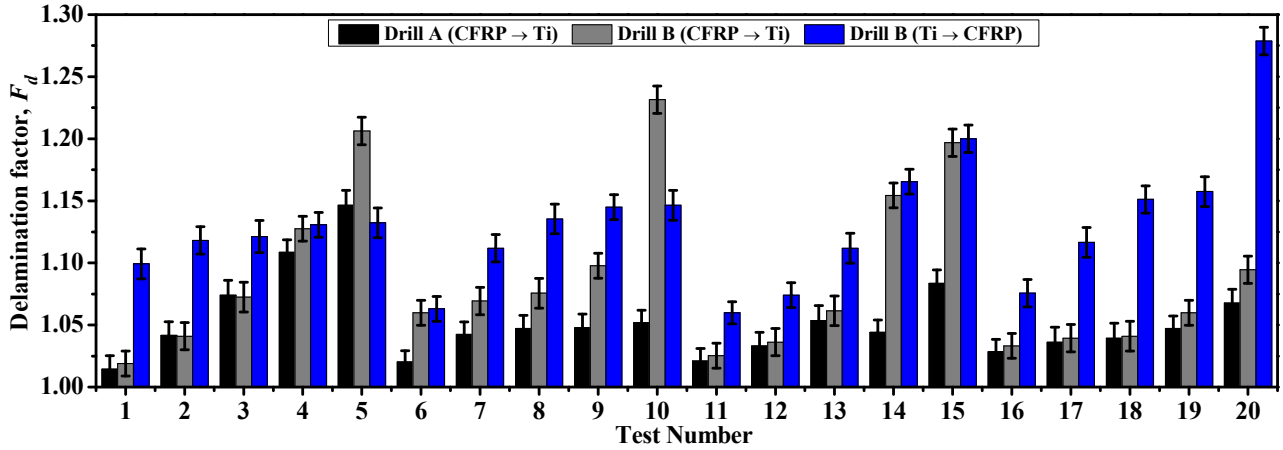

Fig.6.30. Comparative results of delamination factor (F_d) with respect to different drill bits and cutting sequence strategies (Cutting conditions for test Nos. 1-20 can be found in Table 3.11 of Chapter III).

6.6.3 Burr defect analysis

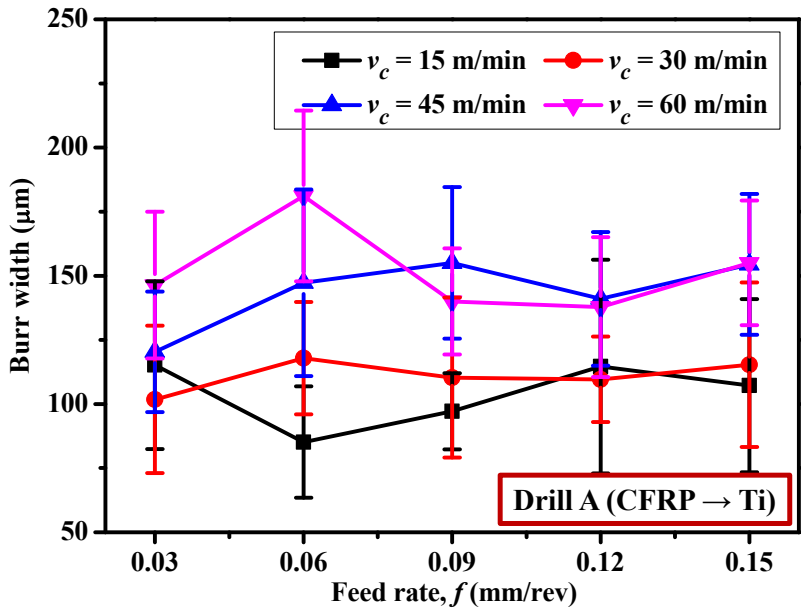

Figure 6.31. Parametric effects on burr width when using drill A (CFRP → Ti cutting sequence).

To ensure a tight CFRP/Ti assembly, the burr defect produced in the Ti phase is often a key problem as compared to other metallic surface damage since it usually leads to further disassembly, deburring and re-assembly of the stacks. The drilling-induced burr formation as reported in the literature is often highly dependent on the tool engagement time, thrust force generation and frictional heat generation [2, 43].

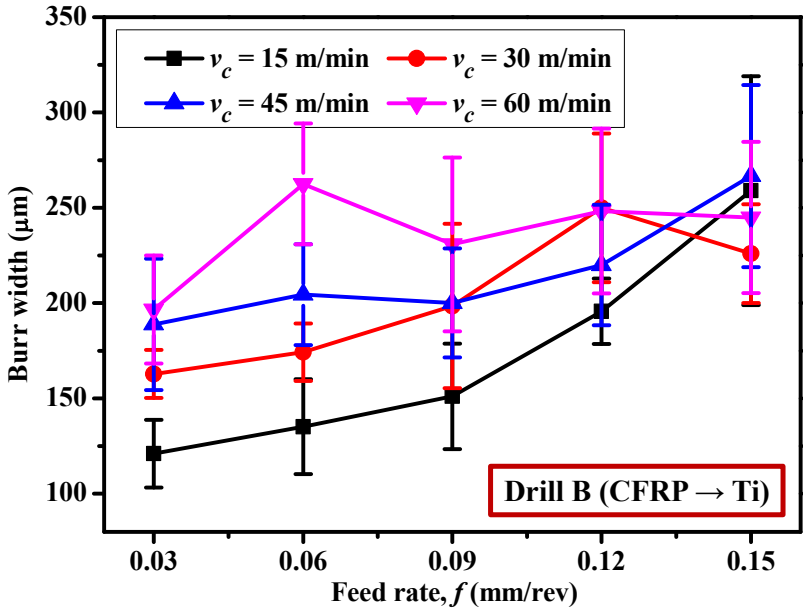

Figure 6.32. Parametric effects on burr width when using drill B (CFRP → Ti cutting sequence).

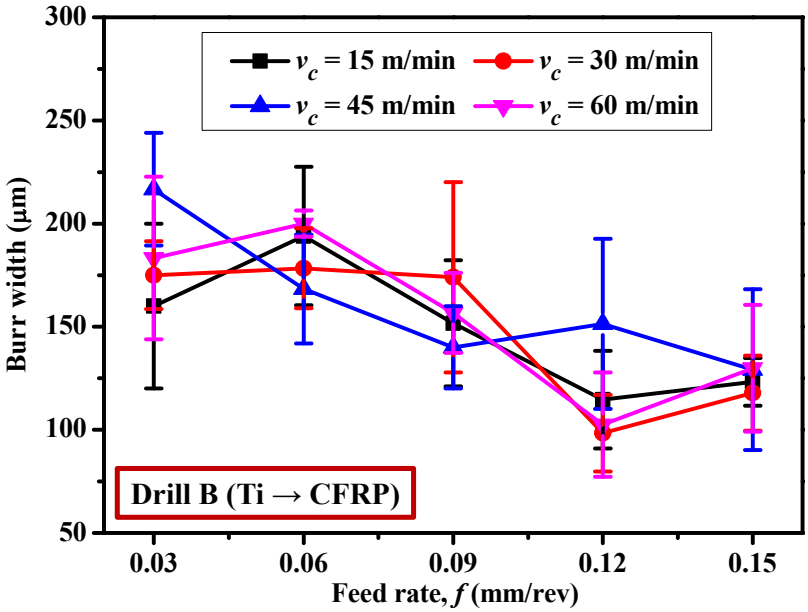

Figure 6.33. Parametric effects on burr width when using drill B (Ti → CFRP cutting sequence).

Figs.6.31 - 6.33 show the effects of cutting speed and feed rate on burr width when drilling hybrid CFRP/Ti stacks with respect to different drill bits and cutting sequences. It can be seen that the variation law of burr width promoted by drill A in CFRP → Ti cutting sequence (see Fig.6.31) *versus* feed rate (f) is not fully clear, in which the minimum and maximum burr widths are nearly similar and close to each other. By contrast, the impact of f on burr width for drill B is totally positive or negative, greatly dependent on the used cutting sequence strategies. For the observation in Fig.6.33, an increased feed rate normally decreases the induced burr width, which agrees well with the observation of Ramulu et al. [2] when drilling hybrid (Gr/Bi)/Ti stacks. Moreover, the impact of cutting speed on the induced burr extent is generally positive, *i.e.*, an increased v_c often gives rise to the elevated burr width formation. The reason can be attributed to the softening effects of the highly generated frictional heat on surrounding work material when v_c is elevated, which greatly degrades the stiffness of the exit Ti layer and makes it more difficult for cutting off.

Further, the comparative results in Fig.6.34 also reveal that the drill B operated in the CFRP → Ti cutting sequence normally promotes higher burr widths than its counterpart one, especially under high cutting-speed conditions. In contrast, the drill A globally shows the best performance, with which a lowest burr width can be obtained under the low-feed conditions. Moreover, from the aspect of minimizing burr defect formation, the Ti → CFRP drilling produces lower defect extent if high feed rates are applied as compared to the CFRP → Ti drilling.

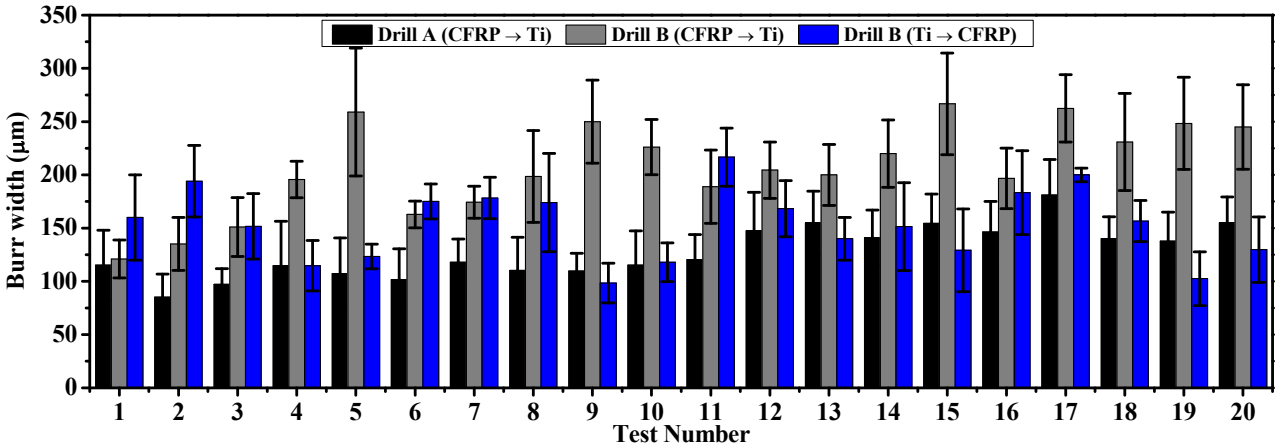

Fig.6.34. Comparative results of burr width with extent respect to different drill bits and cutting sequence strategies (Cutting conditions for test Nos. 1-20 can be found in Table 3.11 of Chapter III).

6.7 Hole wall topography and surface morphology

To examine the hole wall topography and surface morphology of drilled CFRP/Ti holes, the CFRP/Ti specimens were cut off into several parts across the hole center by using the water-jet machining technology. The detailed illustration of the sample preparation can be found in subsection 3.4.2.2 of Chapter III.

6.7.1 Hole wall topography

The hole wall topographic map of each stacked phase was recorded by using the Veeco white-light interferometer, as discussed in subsection 3.4.2.2 of Chapter III. Fig. 6.35 shows the global drilled CFRP/Ti hole topographies with respect to different drill bits under the fixed cutting conditions of $v_c = 30$ m/min and $f = 0.03$ mm/rev. Results show that the hole wall surface promoted by drill B is basically much smoother than that generated by drill A. The reason may be due to the superior wear resistance and high surface hardness of the TiAlN coating that can maintain sharp cutting edges for both CFRP-phase drilling and Ti-phase drilling. Besides, for machined Ti-phase surface, small parallel grooves induced by either drill A or drill B are observed, which can denote the feed mark signatures of drill advancement on the machined Ti hole wall surface from hole onset to hole exit. Besides, the burr defect formation is also found at exit side of the Ti phase as depicted in Fig.6.35. Moreover, for drilled CFPR hole surface, severe fiber/matrix crack is detected on areas close to the interface region when using drill A, as shown in Fig.6.35 (a). This is because the interface linking CFRP phase and Ti phase is usually the weakest zone vulnerable to serious damage formation due to the transitions of disparate chip separation modes and drilling force/heat responses. For the occurrence of the fiber/matrix crack, it can be attributed to the different properties of the fiber/matrix system and correspondingly disparate chip removal mechanisms.

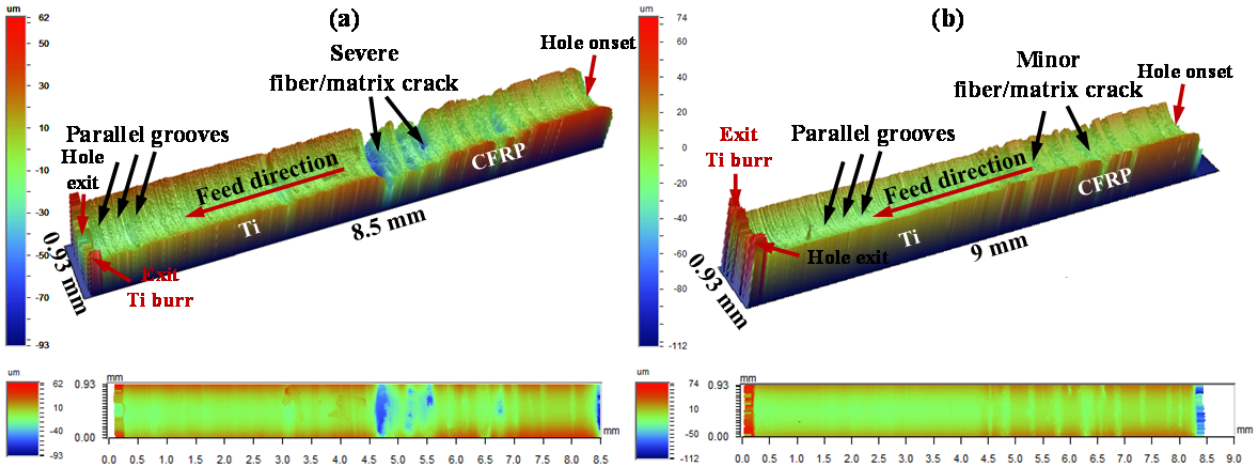

Fig.6.35. 3D topographic maps of drilled CFRP/Ti holes (v_c = 30 m/min, f = 0.03 mm/rev and CFRP → Ti cutting sequence): (a) drill A and (b) drill B.

To inspect the parametric effects and cutting-sequence's influences on the drilled hole topography, Figs. 6.36 and 6.37 show the obtained results under the constant cutting speed of 30 m/min. As shown in Fig.6.36, the drilled Ti hole surfaces generally show better surface quality than those promoted in CFRP phase drilling and interface drilling. When drilling is operated at low feed-rate conditions (*e.g.*, f = 0.03 mm/rev), serious chip adhesion (aka re-deposited chips) is observed on machined Ti hole wall surface. The findings agree well with the observation by Shyha et al. [49] when drilling hybrid Ti/CFRP/Al stacks. The key damage form occurring in the drilled CFRP hole surface is basically fiber/matrix crack while for the interface region it is delamination failure. In addition, the feed rate is found to have a remarkable influence on the induced hole wall surface topography. In the case of drill B in either CFRP → Ti or Ti → CFRP cutting sequences, the identical observations are noticed for the machined hole wall topography, which are thereby not provided here.

Feed rate, f (mm/rev)	**Drilled CFRP/Ti hole**		
	CFRP phase	Interface	Ti phase
f = 0.03	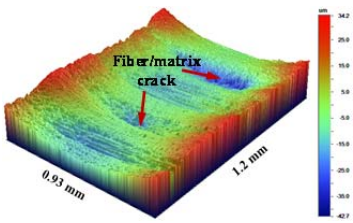	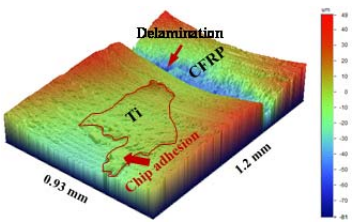	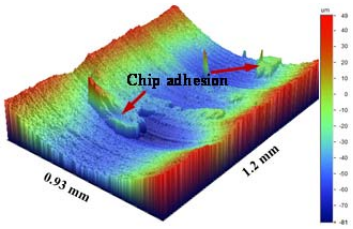
f = 0.06	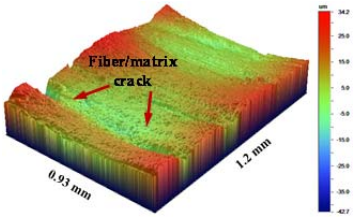	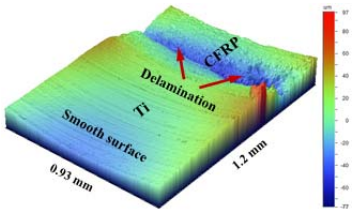	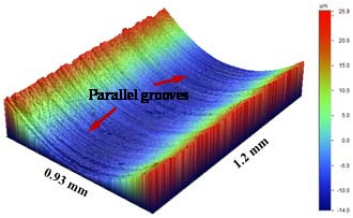

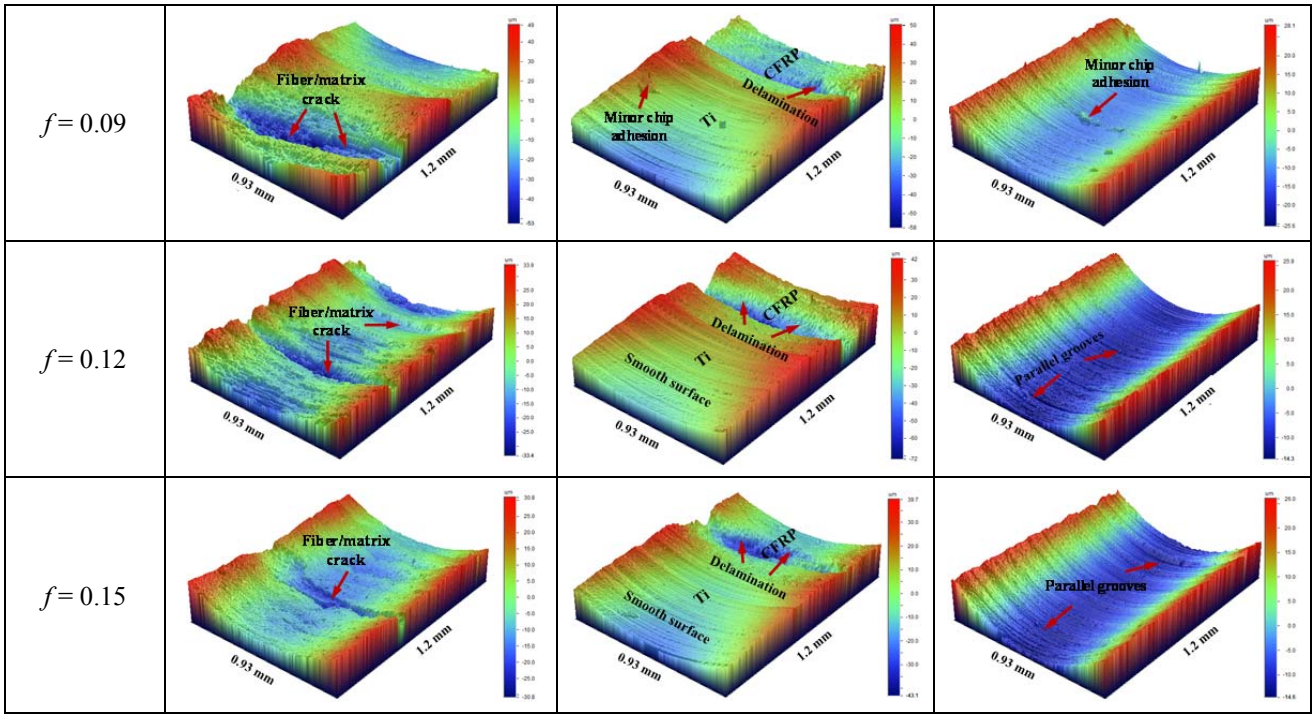

Fig.6.36. 3D topographic maps of drilled holes when using drill A under CFRP → Ti cutting sequence (v_c = 30 m/min).

Besides, the comparative results in Fig.6.37 also indicate that the CFRP/Ti holes are produced with more serious surface defect/damage formation on hole wall surfaces in CFRP → Ti drilling as compared to the Ti → CFRP cutting sequence. Owing to the detrimental scratching effects of Ti chip evacuation on the drilled CFRP holes, a large amount of fiber/matrix cracking is generated in the CFRP → Ti cutting sequence, regardless of the used drill bits as shown in Fig.6.37. In contrast, the Ti → CFRP drilling globally generates much smoother hole surface morphology in both CFRP phase and Ti phase. Since this type of cutting sequence prevents the drilled CFRP holes from the abrasion/erosion effects of Ti chip transportation, only a minor extent of fiber/matrix crack is detected on the machined CFRP surface.

Drilling sequence	**Drilled CFRP/Ti hole**		
	CFRP phase	Interface	Ti phase
Drill A (CFRP → Ti)	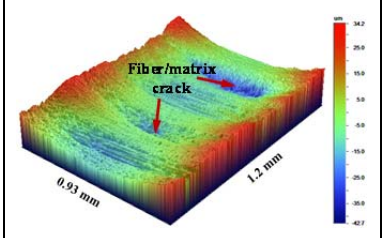	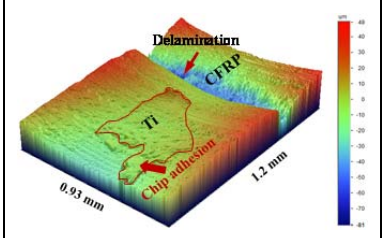	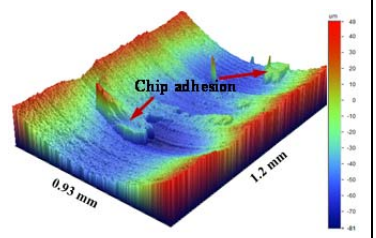
Drill B (CFRP → Ti)	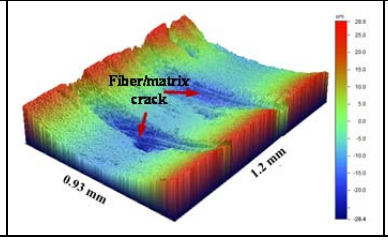	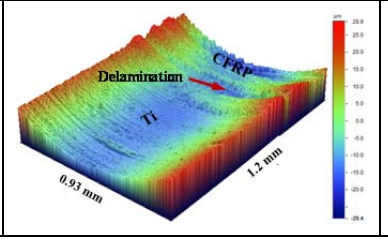	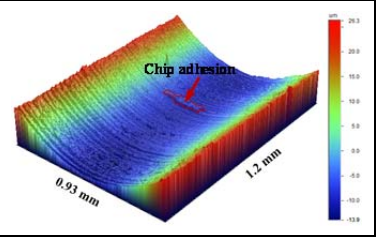

Drill B (Ti→ CFRP)	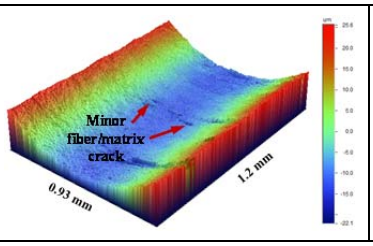	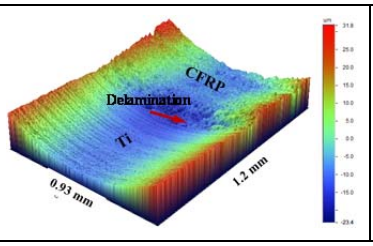	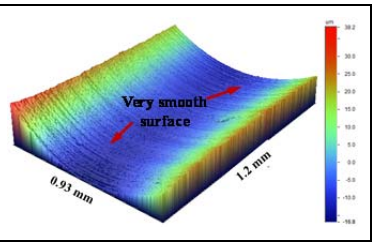

Fig.6.37. Comparative hole topographies under different cutting sequences (v_c = 30 m/min and f = 0.03 mm/rev).

6.7.2 SEM analysis of drilled hole surface

To clarify the cutting sequence's effects on the drilled hole wall surface morphology, SEM analyses are performed on each stacked phase with respect to hole entry and hole exit sides as depicted in Figs.6.38 - 6.40. Moreover, the different surface morphologies concerning the drilled interface regions are also investigated and compared in Fig.6.41.

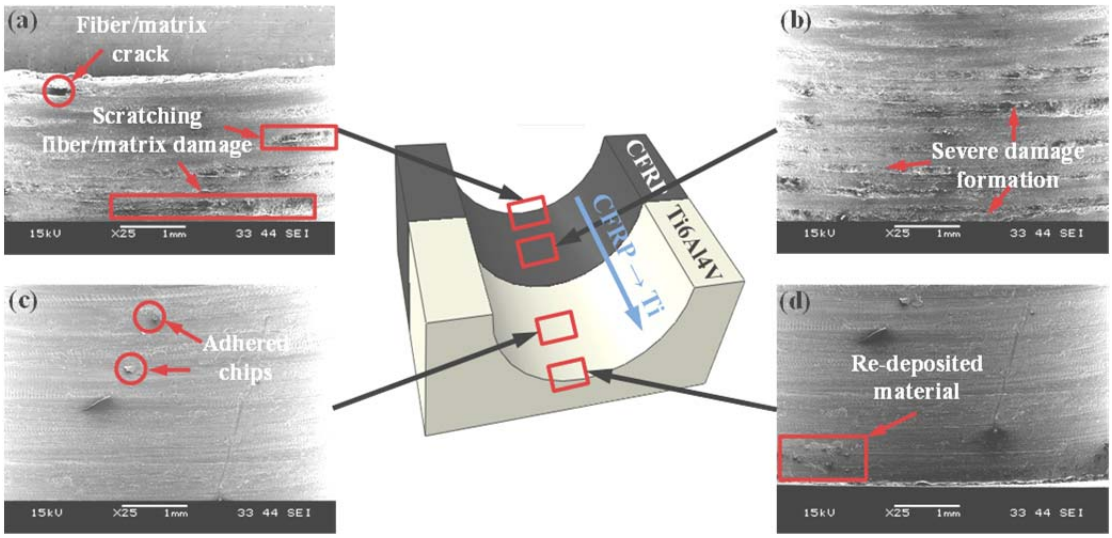

Fig.6.38. SEM images of the drilled CFRP/Ti hole wall morphologies with drill A in CFRP → Ti cutting sequence: (a) entry CFRP surface; (b) middle CFRP surface; (c) middle Ti surface and (d) exit Ti surface.

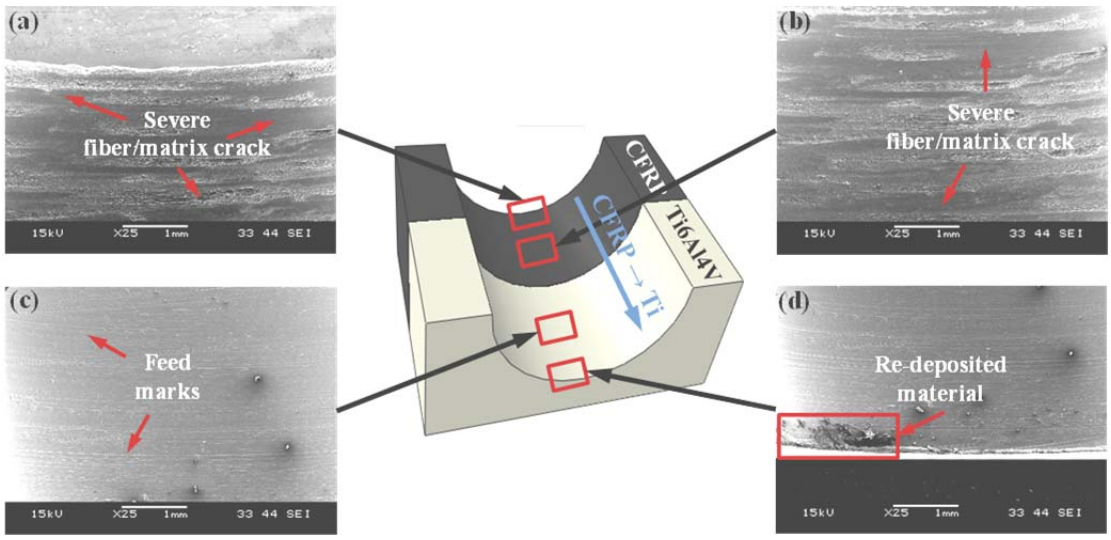

Fig.6.39. SEM images of the drilled CFRP/Ti hole wall morphologies with drill B in CFRP → Ti cutting sequence: (a) entry CFRP surface; (b) middle CFRP surface; (c) middle Ti surface and (d) exit Ti surface.

As seen from these figures, the CFRP surface promoted in CFRP → Ti sequence commonly exhibits much severer fiber/matrix splintering damage than that drilled in Ti → CFRP sequence. The reason as addressed earlier should be due to the serious scratching effects of bottom Ti chip evacuation on the brittle polymeric hole wall surfaces. In addition, the drilled CFRP surface in either CFRP → Ti or Ti → CFRP cutting sequences is much rougher than the machined Ti surface due to the predominant brittle fracture chip separation mode. The key damage forms of the drilled CFRP hole surface are found to be fiber/matrix crack, delamination and splintering, while for Ti hole surface they are re-deposited chip material and feed mark. Such findings also agree well with the 3D topography analyses as discussed in subsection 6.7.1. Besides, the PVD TiAlN-coated drill B is found to have no improvement on the drilled CFRP/Ti hole surface morphologies as compared to the uncoated drill A when performed under the identical cutting sequence. On the contrary, the machined CFRP surface generated by drill B often exhibits higher extents of fiber/matrix damage due to the higher force generation promoted by the tool.

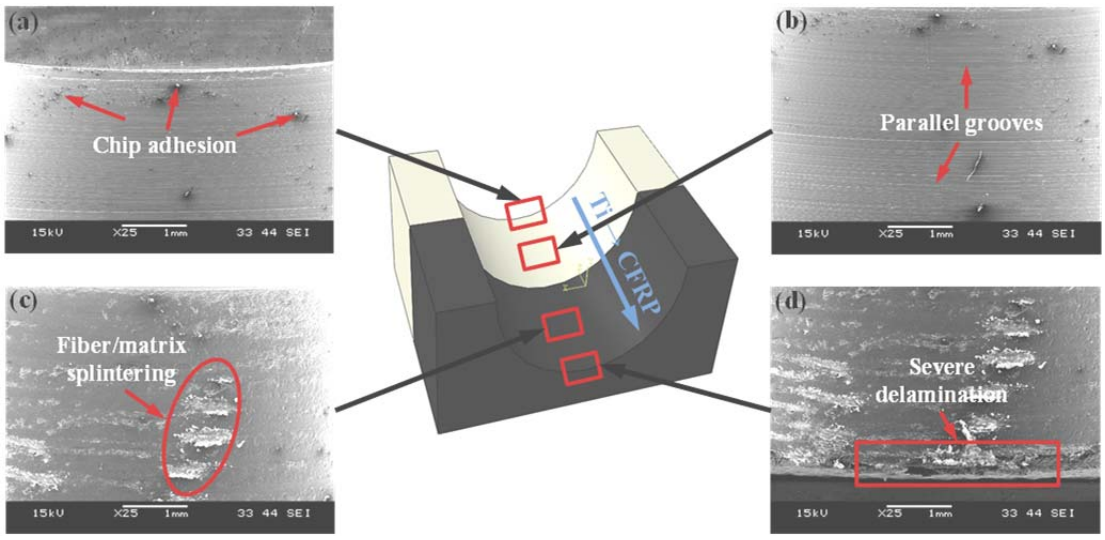

Fig.6.40. SEM images of the drilled CFRP/Ti hole wall morphologies with drill B in Ti → CFRP cutting sequence: (a) entry Ti surface; (b) middle Ti surface; (c) middle CFRP surface and (d) exit CFRP surface.

Further, with respect to the interface morphologies under different cutting sequences, the damage promoted in the interface region usually occurs in the machined CFRP phase. The CFRP → Ti drilling commonly induces severe CFRP surface damage at the interface zone due to the detrimental effects of Ti chip evacuation. By contrast, the interface damage promoted in Ti → CFRP drilling sequence is not clearly visible, which should be attributed to the avoided Ti chip evacuation.

Drill bit & cutting sequence	Drill A (CFRP → Ti)	Drill B (CFRP → Ti)	Drill B (Ti → CFRP)
Interface morphology	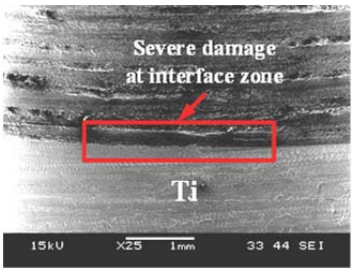	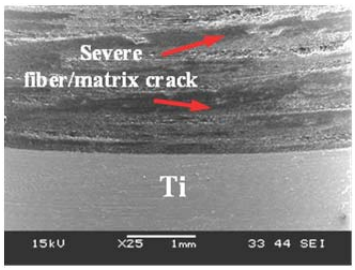	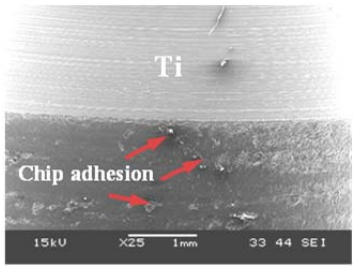

Fig. 6.41. Comparative SEM images of interface morphologies for different drill bits and cutting sequences.

6.8 Drill design implications

In manufacturing processes, tool material composition and tool geometrical feature are two important factors that greatly influence the on-site cutting-induced phenomena including force generation, heat transfer, subsurface damage, and tool wear. The functionality of drill geometrical feature affects the cutting phenomena primarily via its influences on chip separation mode. By contrast, the tool material composition mainly aims to alter tool-chip frictional coefficient and tool wear behavior. In such case, when two types of twist drills differing in geometrical feature and material composition are employed, the observed disparate tool performances should be attributed to the competition between the influences of tool geometry and tool material on drilling responses. That's to say, the drill performance depends significantly on which factor acts as a predominant role in affecting the final drilling-induced phenomena.

Regarding the used conventional twist drill, it is well known that the drill rake angle decreases toward the drill center (drill tip) and approaches large negative values in the chisel edge zone. Thus, while the outer edge produces a smooth chip, the inner does not. The material under the chisel edge is subjected to severe extrusion deformation by large displacements instead of shearing cutting. In addition, the chisel edge is also assumed to contribute approximately 50 - 60 % of the total thrust force generation (F_z). As such, the drill bit A which has a short chisel edge length should promote a lower F_z magnitude since the chisel edge acts as a vital role as shown in Fig.6.8. Besides, even though drill B has a protection of TiAlN coating, however, the coating probably induces negligible effects on reducing the tool-chip friction coefficient in order to decrease the thrust force as the coating often suffers severe peeling or micro chipping when drilling hybrid CFRP/Ti stacks. The experimental work done by Isbilir and Ghassemieh [42] has shown that when applying TiAlN coating in drilling hybrid CFRP/Ti6Al4V stacks, the drill edges underwent intense flank/crater wear and serious coating peeling even after drilling quite a few number of holes (15 holes). Therefore, it could be deduced that in current drilling cases, the benefits of TiAlN coating on improving the machinability of the hybrid CFRP/Ti stack would be minor. With regard to the torque component (T), it is greatly influenced by drill point angle and helix angle since these two geometrical angles primarily affect the proportion of torque in the nominal force generation. As such, drill B with high point and helix angles was observed to promote lower torque magnitudes especially for Ti phase drilling as shown in Fig.6.9.

For resected Ti chip type, both drill A and drill B were found to produce the similar chip morphology especially from a macro-scale observation as depicted in Figs.6.14 and 6.15. However, one point should be emphasized that from the aspect of chip ejection, twist drill with a high helix angle often facilitates the chip evacuation due to the increased rake angle contributing to chip breakage. As such, the drill B was found to promote easier chip ejection as compared to drill A throughout the drilling trials. With respect to the machined surface quality (surface roughness, hole diameter and roundness error), the differences between drill A and drill B were not so pronounced. However, for drilling-induced subsurface damage, drill A was found to globally outperform drill B in terms of delamination formation and burr width extent, which indicates a more significant influence of tool geometrical feature on CFRP/Ti drilling than tool material composition. For delamination damage, it is believed by many researchers [77-79] that thrust force is a key contributor responsible for its formation, *i.e.*, a higher thrust force often leads to a larger

delamination extent. In such circumstance, drill A with short chisel edge feature was confirmed to induce lower delamination damage (Ref. Fig.6.30) due to the lower thrust force generation as elaborated earlier. Furthermore, the short chisel edge length for drill A also facilitates the drill centering and improves the chip separation nearby the drill tip, thus decreasing the exit burr formation as shown in Fig.6.34. The reduced chisel edge plays clearly herein an important role in drill centering. By contrast, drill B with long chisel edge characteristics promotes high thrust force, and hence induces higher extents of delamination damage and burr width (Ref. Fig.6.34) even though the TiAlN coating may more or less bring some improvements on the harsh cutting conditions of hybrid CFRP/Ti drilling.

Therefore, through the above analyses, it can be deduced that when drilling hybrid CFRP/Ti stacks, tool geometrical feature plays a more significant role in affecting the final drilling responses than tool material composition. This means improving drill geometrical characteristics (chisel edge length, rake angle, point angle, helix angle, *etc*.) should be a more effective way to improve the machinability of the bi-material system. The experimental results also give the ideas to conclude some rules of the functional design of special drill bits when drilling hybrid CFRP/Ti stacks as summarized below. For decreasing thrust force, short or zero chisel edge length is preferred for a drill bit in order to minimize the drilling-induced delamination and strengthen the drill centering. For heat transfer, a high clearance angle often reduces frictional forces and hence heat generation. To decrease the temperature accumulation as well as wear at the outer cutting edges, the use of a double point angle in multifaceted drill design will be a possible means. Besides, for facilitating Ti chip ejection, *i.e*., reducing its influences on the secondary damage of the drilled composite holes, the geometrical design with high point angle and high helix angle should be adopted. Furthermore, with the recent advances in tooling technology, various types of specialized drill geometrical designs including K-land design [119], two-stage point design [44], and double cone design [129, 212] have been successfully applied in drilling hybrid composite stacks, and have been demonstrated to achieve improved hole quality and increased tool life as compared to conventionally designed twist drills. Nevertheless, there is no functional drilling tool for drilling CFRP/Ti material in existence. A new design of special drill bits for CFRP/Ti stacks as function of cutting sequence strategy could be suggested. The so-called Multifaceted Drill (MFD) with functional design can indeed be conceived. The functional design of such MFD aims at:

- Speeding up heat transfer and chip ejection: Since the thermal conductivities of both CFRP and Ti are very low, the point angle must be relatively larger to reduce the temperature of the periphery and to facilitate the chip ejection.
- Reducing drilling forces: An arc cutting edge in the middle of the cutting lip may increase the rake angle with a reduced chisel edge length to decrease the thrust force.
- Improving drill centering: The outer cutting edges of MFD must be short enough so that the tips of the outer cutting edges can touch the surface of the workpiece for centering.

6.9 Conclusions

This chapter has presented a thorough experimental study on drilling hybrid CFRP/Ti stacks by

implementing different cutting sequence strategies ($^{\text{CFRP} \rightarrow \text{Ti}}_{\text{Ti} \rightarrow \text{CFRP}}$). The effectiveness of different cutting sequence strategies ($^{\text{CFRP} \rightarrow \text{Ti}}_{\text{Ti} \rightarrow \text{CFRP}}$) and different tool geometries/materials in CFRP/Ti drilling has been systematically investigated, and their results are compared correspondingly. The experimental work has highlighted the vital roles of cutting sequence strategies and tool geometries/materials in affecting the final CFRP/Ti drilling responses. Based on the experimental investigations, the key conclusions can be drawn as follows.

- Drilling hybrid CFRP/Ti stacks in either CFRP → Ti sequence or Ti → CFRP sequence basically involves five cutting stages with respect to the characteristics of tool-work interaction. The most challenging cutting stage is usually the interface drilling due to the existence of the multi-tool-work interaction, in which coupled chip separation modes and severe transitions of mechanical/physical responses predominate. Besides, the conventionally used concepts for standard CFRP machining and single Ti alloy machining are inappropriate for stacked CFRP/Ti interface drilling. This will lead the manufacturing community to develop a new concept of the machinability of the interface zone. In interface drilling, a particular attention should be paid to the careful control of the coupling effects in chip separation, the instability of the tool-work interaction, as well as the tool wear and cutting-induced damage.

- The machinability classification of CFRP/Ti drilling can be made according to the on-site features of tool-work interactions governing the chip removal process. For CFRP → Ti cutting sequence, the cutting durations of $t \in [0, t_2]$ (stage *a* - *c*), $t \in [t_2, t_3]$ (stage *c* - *d*), and $t \in [t_3, t_5]$ (stage *d* - *f*) usually signify the machinability of pure CFRP phase drilling, stacked CFRP/Ti interface drilling and pure Ti phase drilling, respectively.

- The force analysis shows that the uncoated drill A promotes lower drilling forces than the TiAlN-coated drill B under the same cutting sequence and cutting parameters because of its small chisel edge length and low point angle. The findings probably indicate that the tool geometrical features (*e.g.*, chisel edge length, point angle and helix angle) exhibit more significant effects on drilling force generation than tool material composition when drilling hybrid CFRP/Ti stacks. In addition, both cutting speed and feed rate are found to have a significantly positive impact on the force magnitudes, regardless of the used drill bits or cutting sequences.

- Studies on specific drilling energy consumption (E_k) show that the E_k is primarily influenced by the feed rate rather than cutting speed. Additionally, the drill B in the Ti → CFRP drilling is found to promote less E_k consumption than that of drill A and drill B in the CFRP → Ti cutting sequence, indicating the decreased cutting energy consumption and improved machinability of the stacked composites.

- When drilling hybrid CFRP/Ti stacks, both long to short "ribbon" and "spiral" Ti chip types are produced with respect to different drill bits and cutting parameters. High feed rate usually results in the short segmented Ti chips and thus facilitates the improvement of chip breakability. By contrast, the effect of cutting speed on resected Ti chip type is insignificant.

- Hole quality including machined surface roughness and hole size accuracy is found to be

greatly affected by the implemented drilling sequences and cutting parameters. For surface roughness inspection, the feed rate is a key factor that greatly influences the drilled hole surface finish while the impact of cutting speed is obscure and insignificant. Moreover, for all tested trials, the arithmetic mean roughness (R_a) values of drilled Ti phase holes are found to be totally controlled below the criterion value of R_a = 1.6 μm, whereas for machined CFRP holes, the R_a values are partly achieved below the criterion value of R_a = 3.2 μm greatly dependent on the used cutting parameters. For hole diameter and roundness error, both cutting speed and feed rate have pronounced effects on the measured values. The Ti → CFRP cutting sequence is found to generate lower surface roughness values and more consistent CFRP/Ti hole diameters in contrast with the CFRP → Ti drilling due to the avoided severe abrasions on the drilled CFRP holes from Ti chip evacuation.

- Hole damage analysis shows that the CFRP → Ti drilling promotes lower delamination extent than Ti → CFRP drilling under the identical cutting conditions owing to the supporting role of bottom Ti alloy in increasing the stiffness of the exit CFRP hole layer. Besides, the feed rate is confirmed to play a vital role in affecting the drilling-induced delamination. Furthermore, from the aspect of minimizing the burr defects, the Ti → CFRP drilling commonly produces a lower defect extent when high feed rates are applied as compared to the CFRP → Ti drilling.

- Hole topography/morphology analyses reveal that the key damage modes of drilled CFRP surfaces are fiber/matrix crack, delamination and splintering while for drilled Ti surface they are re-deposited chip materials and feed marks. The CFRP → Ti drilling facilitates the improvement of the drilled hole wall surface quality due to the avoided problematic Ti chip evacuation. Further, the uncoated drill A is confirmed to promote better hole wall surface with a lower extent of subsurface damage formation as compared to the TiAlN-coated drill B.

- In general, the uncoated drill A yields a better tool performance than the TiAlN-coated drill B in terms of various drilling responses (*e.g.*, force generation, induced hole damage extent) when performed under the identical cutting conditions. The findings probably suggest that when drilling hybrid CFRP/Ti stacks, the selection of optimal geometrical features should be a more effective method to improve the machinability of the bi-material system than the choice of superior tool materials. The TiAlN coating has very negligible influences on the drilled hole quality mainly due to the occurrence of severe chipping failure or coating peeling even after drilling quite a few number of CFRP/Ti holes [42], which makes the drill edges lose effective coating protection for producing high hole quality.

- Drill geometrical features including chisel edge length, point angle, and helix angle are confirmed to play a more vital role in affecting CFRP/Ti drilling responses than tool material composition. The chisel edge length in a drill bit accounts for the area of extrusion deformation action (aka "negative rake angle cutting") in chip separation and contributes mainly to the drilling forces. For point angle and helix angle, they often determine the drill main cutting edge length, tool edge sharpness and the proportion of thrust force in the nominal force generation in drilling. As such, drill B in present research cases with longer chisel edge length, larger point angle and helix angle is found to promote higher thrust force

magnitudes and larger extents of delamination damage as compared to drill A.

- The key mechanisms governing the influences of different cutting sequence strategies on CFRP/Ti drilling output primarily depend on which stacked phase acts as a supporting role in increasing the stiffness of the exit top phase for minimizing the exit damage extent and also the absence/existence of the problematic Ti chip evacuation on the brittle CFRP hole wall surface. According to the present studies, the key effects of different cutting sequence strategies on various CFRP/Ti drilling responses can be summarized in Table 6.2, in which the symbol "↑" indicates the improvement or acceleration, "↓" signifies the deterioration or reduction, and "—" denotes the insignificant or minor effects. Through the acquired results, it can be concluded that both two cutting sequences ($^{\text{CFRP} \rightarrow \text{Ti}}_{\text{Ti} \rightarrow \text{CFRP}}$) have a significant effect on the final CFRP/Ti drilling responses. For Ti → CFRP drilling, the strategy is found to benefit the improvement of the drilled CFRP hole quality (*e.g.*, producing more consistent hole diameters and much better surface finish) and favor the decreased Ti burr extents, while the CFRP → Ti drilling facilitates only the reduced delamination extents throughout the experimental studies. In general, the Ti → CFRP configuration seems to be a more reasonable strategy for one-shot drilling of hybrid CFRP/Ti stacks especially under the utilized cutting conditions in the present work. However, this drilling strategy will inevitably give rise to an increased exit CFRP delamination extent. And this will lead the machinists to develop a particular process for CFRP/Ti drilling such as adding a supporting plate beneath the bottom CFRP phase in order to avoid the induced exit delamination damage.

- Finally, through the experimental results and theoretical analyses, a suggested functional design of MFD for drilling CFRP/Ti stacks is discussed and offered. In the future, the use of specialized drill bits will become an increasing trend in the industrial sectors in order to effectively improve the machinability of the multi-phase materials.

Table 6.2
Comparative influences of two different cutting sequences on CFRP/Ti drilling responses.

Drilling sequence	Drilling forces	Chip type	Hole quality		Hole damage	
			Surface roughness	Diameter error	Delamination	Burr width
CFRP → Ti	↑	—	↑	↑	↓	↑
Ti → CFRP	↓	—	↓	↓	↑	↓

Note: "↑" indicates the improvement or acceleration, "↓" signifies the deterioration or reduction, and "—" denotes the insignificant or minor effects.

Chapter VII

Key conclusions and perspectives

7.1 Key conclusions

The Ph.D. thesis has been dedicated to the investigations of the fundamental cutting mechanisms controlling hybrid CFRP/Ti stack machining via both numerical and experimental methodologies. To this aim, the numerical work was preliminarily performed to shed light on some implicit cutting physics dominating the bi-material machining when subjected to different cutting sequence strategies. The basic machining configurations of the CFRP/Ti stacks consisting of orthogonal cutting, combined interface machining and hole drilling were precisely addressed *versus* different cutting conditions and cutting sequence strategies. The key machining responses including chip separation mode, force generation, machined surface quality, induced subsurface damage and tool wear mechanism were carefully studied. A particular focus is made on the material removal mechanisms and cutting strategies of hybrid CFRP/Ti stacks. As compared to the existing studies in the open literate, the key originality and novelty of present research work can be summarized as follows.

- The Ph.D. work is among the earliest to develop the FE models to simulate the dynamic chip separation process of hybrid CFRP/Ti stack cutting and to address the key mechanisms and physical phenomena dominating the bi-material machining.
- The Ph.D. work reveals the activated mechanisms governing the interface machining, and subsequent interface delamination formation. Moreover, the influences of different cutting sequence strategies on hybrid CFRP/Ti machining are also clearly clarified via both numerical and experimental investigations.
- The current research provides a combined numerical and experimental method for an enhanced CFRP/Ti cutting comprehension. Several recommendations in terms of cutting sequence selection and tool geometrical design for real industrial machining of the bi-material stack are offered.

According to the systematic researches performed in this thesis, the following key conclusions can be drawn.

- Machining hybrid CFRP/Ti stacks is very challenging in chip removal process due to the varying properties of each stacked constituent and the predominance of multi-tool-work interaction. The chip separation modes controlling the CFRP/Ti cutting comprise both elastic-plastic deformation and brittle fracture. The changeable chip removal modes often result in the severe transfer of force/heat responses exerted on the interface zone. The numerical studies have revealed the activated mechanisms controlling the delamination damage formation concerning the CFRP/Ti interface. FE analyses show that the initiation and evolution of interface delamination primarily take place at the cutting period of AIZ, in which the interface damage formation involves a series of detaching and tearing variation. The key mechanisms governing the interface damage formation can be attributed to the coupled effects of fracture modes I and II exerted on the bi-material interface region, which consequently results in the “V shape”-like notch damage.
- Moreover, the FE analyses also reveal that the CFRP → Ti cutting sequence commonly

facilitates the chip breakage of the hybrid composite stack and promotes smoother surface morphology than that generated in Ti → CFRP cutting. Parametric studies have highlighted the significant effect of feed rate on the cutting force generation, and the crucial role of fiber orientation in affecting the composite-phase damage and interface delamination when cutting hybrid CFRP/Ti stacks. Besides, it is also confirmed that the multi-tool-work friction coefficient (μ) plays a crucial role in affecting the various frictional responses via its thermal and mechanical influences when machining hybrid CFRP/Ti stacks. The numerical results further suggest that the use of effective cutting fluid or superior tool material that can improve the multi-tool-work frictional behavior, *i.e.*, reducing μ, should be a direct way to achieve high-quality machining of hybrid CFRP/Ti stacks.

- Experimental work concerning orthogonal cutting and combined CFRP/Ti machining shows that the feed rate and fiber orientation are the two key factors greatly influencing the force generation and machined surface quality. The key damage modes of the trimmed Ti phase are found to be the deformation of feed marks and re-deposited chip materials while for the machined CFRP surface they are fiber pullout, resin loss, and surface cavity. The Ti → CFRP cutting promotes severe cracking damage and "V shape"-like notch delamination at the interface region. In contrast, the CFRP → Ti cutting generates much better surface finish that its counterpart one. The dominated wear mechanisms for PCD tools in orthogonal cutting CFRP/Ti are found to be crater wear, adhesion wear, and flank wear while the tool failure modes are micro chipping and edge fracture due to the sudden force variation resulting from CFRP/Ti interface machining and also the PCD's inherent brittleness.

- With respect to hole drilling, it is found that the feed rate has a pivotal role in affecting the drilling force development and resected Ti chip morphology. Hole quality including machined surface roughness and hole size accuracy is greatly influenced by the implemented drilling sequences and cutting parameters. The Ti → CFRP cutting sequence is found to generate lower surface roughness and more consistent CFRP/Ti hole diameters as compared to the CFRP → Ti drilling due to the avoided severe abrasions from Ti chip evacuation. Besides, hole damage analysis shows that the CFRP → Ti drilling commonly promotes lower delamination extent than Ti → CFRP drilling due to the supporting role of the bottom Ti alloy in increasing the stiffness of the exit CFRP hole layer when drilling CFRP/Ti stacks. By contrast, for minimizing the burr defect formation, the Ti → CFRP cutting sequence as well as the high cutting speed should be adopted in the hybrid stack drilling.

- Further, the uncoated twist drill is demonstrated to yield better tool performance than the superior TiAlN-coated twist drill in terms of various drilling responses (*e.g.*, force generation, induced hole damage extent) when performed under the identical cutting conditions. The acquired results probably indicate that when drilling hybrid CFRP/Ti stacks, the tool geometrical features exhibit more significant influences on CFRP/Ti drilling operation than tool material composition. To ensure high-quality drilling of the bi-material, the selection of optimal geometrical features should be considered as a primary choice in real production.

- In both orthogonal cutting and hole drilling, the entire CFRP/Ti machining operation can be physically categorized into three cutting stages according to the on-site features of tool-work

interaction: (*i*) pure CFRP-phase cutting, (*ii*) interface machining, and (*iii*) pure Ti-phase cutting. Among them, the interface machining, in reality, reflects the real machinability of the stacked CFRP/Ti material ($M_{\mathrm{CFRP/Ti}}$), in which the multi-tool-work interaction predominate. Besides, since the interface machining involves coupled chip separation modes and interrelated cutting responses, to fundamentally improve the bi-material machinability, a careful parameter/tool selection should be made regarding the interface cutting zone.

- The cutting sequence strategy is confirmed to have a significant effect on the final CFRP/Ti responses in either orthogonal cutting configuration (OCC) or hole drilling. In OCC, the CFRP → Ti cutting is demonstrated to favor the improvement of the trimmed surface quality as compared to its counterpart one (Ti → CFRP cutting). However, for hole drilling, the two cutting sequence strategies ($\substack{\mathrm{CFRP} \rightarrow \mathrm{Ti} \\ \mathrm{Ti} \rightarrow \mathrm{CFRP}}$) are found to have their own advantages and disadvantages. For instance, the Ti → CFRP drilling promotes higher quality of hole surface (*e.g.*, more consistent hole diameter and much better surface finish) with lower Ti burr formation, while the CFRP → Ti cutting strategy reduces only the induced delamination extents. The activated mechanisms controlling the different cutting sequences' influences can be attributed to the disparate effects of the problematic Ti chip adhesion on the material removal process. This is because in orthogonal cutting, the produced Ti chips can only cause chip adhesion on tool rake face without any scratching effect on the trimmed CFRP surface, while in drilling the resected Ti chips can cause both chip adhesion and severe abrasion damage on the drilled CFRP surface during their evacuation. Besides, for drilling operations, the Ti → CFRP configuration is found to be a more reasonable strategy for one-shot drilling of hybrid CFRP/Ti stacks from a global viewpoint. However, a particular process such as adding a supporting plate beneath the bottom CFRP phase should be developed during drilling in order to minimize the induced exit delamination damage.

- Furthermore, the experimental studies also give us some new ideas on functional tool design. When drilling hybrid CFRP/Ti stacks, it is needed to use a large point angle to speed up the heat transfer and chip evacuation. Besides, an arc cutting edge design and short outer cutting edges can usually reduce drilling forces and improve drill centering. This will lead the machinists to design a multifaceted drill bit for hybrid CFRP/Ti drilling.

7.2 Future perspectives

The key objective of the present study has been achieved. However, high-quality machining of CFRP/Ti stacks is usually a comprehensive and interrelated manufacturing operation, dependent on many internal-external factors like tool-work configuration, cutting parameters, cutting environment as well as the used machine tool. To completely improve the machinability of the bi-material system, there still remains a lot of work to be undertaken in the future. Based on the already-performed researches, the following suggestions/recommendations can be provided for future work on hybrid CFRP/Ti stacks machining through both numerical and experimental aspects.

- The numerical studies presented in this thesis were focused only on the analyses of orthogonal cutting process. The developed FE models have ignored some complex details of

the multi-tool-work interaction presented in real machining (*e.g.*, drilling or milling). To study the in-depth cutting mechanisms and also to reflect accurately the real manufacturing operation, more sophisticated models by considering rigorously the physical details of the multi-tool-work interaction (*e.g.*, tool behavior, tool wear) are critically demanded to be established in the further research work. Besides, some systematic work regarding the numerical modeling of 3D hole drilling of hybrid CFRP/Ti stacks is needed to be performed in the future.

- In addition, the experimental work in this thesis was solely performed under the dry cutting conditions. In the future, some systematic work regarding the applications of different lubrication/cooling methods in hybrid CFRP/Ti stack machining is also urgently demanded. Furthermore, since the cutting parameters and tool geometrical features have been demonstrated to play a crucial role in affecting the final CFRP/Ti cutting responses, in the future, great efforts should be made on the cutting parameter optimization and tool geometrical design in order to provide a superior tool-work configuration for high quality finishing of hybrid CFRP/Ti stacks.

Annexe A : Résumé de thèse

Étude numerique et experimentale de l'usinage des materiaux hybrides titane-composites

Chapitre I : Étude Bibliographique

Dans l'industrie de l'aérospatial moderne, les composites hybrides (FRP/Ti) ont été largement utilisés dans les assemblages mécaniques avancés d'avions en raison de leurs très hautes propriétés mécaniques et fonctions structurelles. Cependant, l'usinage des hybrides FRP/Ti reste toujours une tâche difficile en raison des propriétés très éloignées de chaque constituant et de leur mauvaise usinabilité. Pour améliorer cette dernière, de nombreux travaux de recherche ont été entrepris au cours des dernières années couvrant une variété de sujets, comprenant l'utilisation d'outils en matériaux de qualité supérieure et avec des géométries optimales ou même bien en se plaçant dans des environnements de coupe favorables pour la coupe des matériaux hybrides FRP/Ti.

Afin de faire un état de l'art de l'avancement de la recherche actuelle en ce qui concerne l'usinage des hybrides FRP/Ti, le premier chapitre a été consacré à une étude bibliographique rigoureuse des recheches les plus importantes dans l'usinage des matériaux hybrides FRP/Ti. Les multiples aspects, liés à la coupe des composites hybrids, ont été soigneusement abordés. Plusieurs stratégies et approches consacrées à l'usinage des FRP/Ti ont également été étudiées en détails. En outre, l'approche numérique de la coupe des matériaux hybrides FRP/Ti est également passée en revue.

Il resort que la recheche dans le domaine d'usinage des matériaux hybrides FRP/Ti a montré plusieurs progrés. Celle-ci a conduit, par des études de nature exclusivement expérimentale, à l'amélioration de l'usinabilité des matériaux hybrides FRP/Ti . Les conclusions clés sur les connaissances actuelles ainsi que les perspectives pour de futurs travaux sur ce sujet peuvent être déclinées ainsi :

- Les natures disparates des matériaux hybrides FRP/Ti ont inévitablement entraîné des discontinuités locales à l'interface ainsi que la non-conformité de couplage outil de travail/pièce régissant l'usinage de la pile. Les discontinuités à l'interface rendent les conditions de coupe beaucoup plus sévères et les mécanismes contrôlant le processus d'enlèvement de matière plus complexes. La rupture fragile régissant la formation des copeaux FRP et les différents types de ruptures de fibre par rapport à l'orientation de celles-ci sont les principales sources contribuant à la formation de l'endommagement au niveau du troue lors du perçage. Les copeaux chauds produits dans la phase de titane lors du perçage et les arêtes vives qu'ils possèdent provoquent toujours une forte abrasion et de l'érosion sur les trous FRP usinés. En outre, par rapport à l'usinage pur de l'une ou l'autre chacune des deux phases FRP et titane, la découpe de l'interface peut être considérée comme l'opération la plus difficile en raison des multi-interactions outil/matériau x et du transfert de sévères réponses mécaniques/physiques. Actuellement, le comportement de coupe régissant la coupe de l'interface FRP/Ti est encore peu étudié en profondeur, et ces travaux devraient aborder en détails pour répondre à cette question.

- Les endommagements induits par perçage de FRP/Ti comprennent à la fois les imperfections dues aux polymères et les défauts des métaux. Parmi ceux-ci, les endommagements à l'interface sont généralement les plus sévères. Le délaminage et les bavures sont considérés comme les principaux problèmes de la production réelle étant donné que ces deux types

d'endommagement conduisant souvent à des mauvaises tolérances pour l'assemblage et des rejets élevés des composants usinés.

- Les mécanismes d'usure de l'outil régissant le perçage de FRP/Ti sont généralement le couplage et l'interaction des deux modes d'usure composite et métallique. Malgré les différents dypes d'usures entre différents matériaux d'outil, l'usure par abrasion, l'arrondissement des bords, l'usure des flancs et l'usure d'adhérence sont généralement les motifs prédominant qui régissent la progression de l'usure des outils d'un point de vue global.

- Des solutions potentielles au perçage de haute qualité de FRP/Ti ont été discutées en détails en fonction des paramètres de coupe, des outils de coupe et de l'environnement de coupe. Cependant, le perçage de haute qualité est une opération de fabrication complète et interactive, dépendante de nombreux facteurs externes comme le matériau et la géométrie de l'outil, les paramètres de perçage, l'environnement, ainsi que les propriétés de la pièce et la machine utilisée. Pour obtenir de bons résultats, une expertise profonde et une expérience riche basées sur les questions mentionnées sont nécessaires pour proposer une configuration d'outil/facteurs extérieurs supérieure pour la coupe des matériaux hybrides FRP/Ti.

- En ce qui concerne les études numériques, la majorité des travaux antérieurs se sont entièrement concentrés sur la modélisation de coupe d'un composite standard (par exemple, CFRP ou GFRP) ou bien d'une phase métallique unique (par exemple, un alliage Ti). À ce jour, seuls de rares travaux de recherche sur la modélisation de la coupe composite hybride ont été publiés dans la littérature. Néanmoins, les connaissances et les compétences accumulées devraient fournir une aide suffisante pour les futurs travaux sur la simulation numérique de l'usinage des matériaux hybrides FRP/Ti.

En plus, les axes de recherche pertinents qui ont été significativement peu étudiés sont résumés ci-après.

- Dans l'état actuel de la recherche, presque tous les travaux existants dans la littérature traitant l'usinage des matériaux hybrides FRP/Ti sont uniquement expérimentaux, ce qui présente un coût élevé et beaucoup de temps. En revanche, l'approche numérique devrait être un outil alternatif qui peut considérablement aider à optimiser les recherches sur les mécanismes de la coupe de ce matériau multi-phases. Cependant, les études pertinentes concernant la modélisation numérique et l'analyse EF de coupe des matériaux hybrides FRP/Ti ont été à peine publiées. À l'avenir, des efforts devraient être faits sur cet axe de recherche prometteur. Et une recherche combinée à la fois la simulation numérique et l'expérimentation est également critique pour assurer une meilleure compréhension de la coupe des matériaux hybrides FRP/Ti.

- En outre, la coupe de l'interface, comme l'a souligné jusqu'à présent dans ce chapitre, joue habituellement un rôle clé dans la formation des endommagements finaux à l'interface FRP / Ti. Cependant, les recherches pertinentes concernant ce sujet sont rarement publiées dans la littérature. En outre, la plupart des études ignorent l'investigation de l'influence des différentes séquences de coupe ($^{\mathrm{FRP} \rightarrow \mathrm{Ti}}_{\mathrm{Ti} \rightarrow \mathrm{FRP}}$) sur le processus d'usinage hybride. Les principales

différences entre les deux stratégies de séquences de coupe ($^{FRP \rightarrow Ti}_{Ti \rightarrow FRP}$) mentionnées ainsi que leurs influences sur l'usinage des matériaux hybrides FRP/Ti ne sont toujours pas bien étudiées.

- Finalement, il est bien connu que les multi-interactions outil/matériaux représentent la source clé de divers phénomènes mécaniques/physiques induits dans la coupe des matériaux hybrides FRP/Ti. De nombreuses méthodes capables d'améliorer le comportement en frottement des multi-interactions outil/matériau (par exemple, l'utilisation de paramètres de coupe optimaux, d'outils de coupe de qualité supérieure et d'environnements de coupe favorables) ont confirmés l'amélioration, de manière significative, de l'usinabilité de l'alliance-composite/métal comme largement publié dans la littérature. Cependant, les mécanismes activés qui dominent les influences des multi-interactions outil/matériau sur l'usinage des matériaux hybrides FRP/Ti font encore grandement défaut dans ces études.

Chapitre II : Modèles EF multi-physiques pour modéliser la coupe des matériaux hybrides CFRP/Ti

Le deuxième chapitre est consacré à la description détaillée des modèles d'éléments finis établis pour modéliser la coupe des matériaux hybrides CFRP/Ti. Afin d'étudier les mécanismes fondamentaux contrôlant l'usinage de l'empilage CFRP/Ti, la configuration de coupe orthogonale simplifiée a été adoptée. Le modèle établi comprend quatre phases principales : la phase de l'outil, la phase du titane, la phase de l'interface et la phase du CFRP. Différentes lois de comportement avec des critères de rupturs ont été mis en œuvre dans le code Abaqus/Explicit (version 6.11) pour construire le comportement de l'usinage des matériaux composites hybrides. Les détails constitutifs des modèles numériques développés peuvent se résumer comme suit :

- La phase du titane a été supposée isotrope avec un comportement élastoplastique pendant le processus de coupe. Les critères Johnson-Cook et l'approche de Hiierborg basée sur l'énergie de rupture ont été utilisés pour reproduire l'échec local de la phase métallique.
- La phase du CFRP a été modélisée comme un matériau homogène équivalent en considérant également le comportement anisotrope dû à l'orientation de ses fibres (θ). Les critères d'endommagement de Hashin tenant compte de quatre types basiques d'échecs fibre/matrice ont été adoptés pour répliquer la rupture de la couche composite et la séparation des copeaux qui en découle.
- L'interface CFRP/Ti décrit physiquement comme un constituant intermédiaire a été modélisée en utilisant le concept de zone cohésive. La séparation des matériaux au sein de la zone cohésive a été contrôlée par des critères de traction-séparation. L'interface utilisée dans le modèle composite hybride vise à servir de contrôle technique pour la gestion des contacts « Ti-CFRP » et une très faible épaisseur (environ 5 μm) a été définie pour minimiser sa influence sur les autres réponses lors de l'usinage des matériaux hybrides CFRP/Ti.
- Deux configurations de modèles multi-physiques pour la modélisation de coupe des

matériaux hybrides CFRP/Ti ont été établies. Les modèles EF proposés prennent également en compte les influences des stratégies différentes de séquencement de la coupe ($^{\text{CFRP} \rightarrow \text{Ti}}_{\text{Ti} \rightarrow \text{CFRP}}$) pour la simulation numérique.

Les objectifs principaux de ces études numériques peuvent être résumés ainsi : (*i*) révéler les mécanismes clés qui contrôlent la découpe de l'interface et la formation de l'endommagement à l'interface, (*ii*) préciser les influences des différentes stratégies du séquencement de la coupe sur l'usinage des matériaux hybrides CFRP/Ti, et (*iii*) étudier les effets paramétriques et les réponses de frottement régissant l'opération de coupe hybride.

Chapitre III : Les détails expérimentaux de coupe des CFRP/Ti

Le troisième chapitre vise à élaborer les détails du dispositif expérimental, ainsi que la démarche expérimentale appliquée et les moyens de mesure utilisées pour l'usinage mécanique des hybrides CFRP / Ti. Les études expérimentales sont principalement composées de trois parties: la coupe orthogonale (en tenant compte des différentes stratégies de séquencement de la coupe), l'usinage de CFRP/Ti combiné et le perçage de trous. La structure principale de ce chapitre a été organisée comme suit :

Configurations de coupe et propriétés de la pièce

Au cours des études expérimentales, chaque pièce de composite empilé comprend un alliage recuit de Ti6AI4V (355HV) et un stratifié de T300/914 CFRP. Trois configurations d'échantillons CFRP/Ti fournies par VN Composites en France ont été adoptées pour les études sur la coupe orthogonale, l'usinage de CFRP/Ti combiné, et l'opération de perçage, respectivement.

Pour la coupe orthogonale et l'usinage de bi-matériaux combinés, le stratifié composite est fabriqué en carbone/époxy préimprégné unidirectionnels (UD) T300/914 (60% de la fraction volumique de fibres) avec trois différentes orientations de fibres de $\theta = 0°$, 45° et 90° en utilisant la main technique mise en place et composé de moulage en feuille. Pour les cas de perçage, l'échantillon est composé d'un alliage recuit de Ti6Al4V et d'un stratifié avec différentes orientations de T300/914 CFRP (60% de fraction volumique de fibres) soumis à la séquence d'empilement $[45°/-45°/0°/90°]_s$. Chaque couche empilée était 4 mm d'épaisseur. Ces couches ont ensuite été collées ensemble au moyen d'un film adhésif (3M Scotch - WeldTM 7240 FR B/A avec une température de durcissement d'environ 121°C) pour produire une dimension totale de 254 mm (longueur) × 34.5 mm (largeur) × 8 mm (épaisseur).

Détails des outils coupants

Afin de finaliser les études expérimentales, deux configurations d'outils de coupe normés par ISO (les plaquettes de coupe et forets), fournies par Sandvik Coromant, ont été utilisées. Pour les essais de coupe orthogonale, le diamant polycristallin de qualité supérieure (PCD) pressenti inserts (spécification ISO : TCMW16T304FLP CD10) a été choisi. L'insert PCD a une longueur de coupe effective de 7.4 mm avec des géométries définies par l'angle de coupe (α = 0°) et l'angle de

dépouille (γ = 7°).

En outre, pour l'usinage de CFRP/Ti combiné, 4 autres types d'outils revêtus, avec des dimensions géométriques identiques mais différentes qualités de revêtement, ont été utilisés. Tous ces outils ont les mêmes angles (un angle de coupe α = 0° et un angle de dépouille γ = 7°) et ils sont tous constitués du même substrat de carbure de tungstène (WC/Co). Pour les meilleures classifications et comparaisons expérimentales, les 4 types d'outils ont été désignés comme les outils A, B, C et D pour les études expérimentales. Notez que les outils A, B, C et D étaient tous les outils réalisés par MTCVD (Medium Température Chemical Vapor Deposition) et revêtus avec un revêtement multicouche de composition identique ($TiN+Al_2O_3+TiCN$), mais de qualités différentes . Les outils A et C ont été fabriqués avec une qualité de revêtement dégradée et fine, respectivement, tandis que les outils B et D ont été fabriqués avec une qualité de revêtement assez grossière.

Pour les essais de perçage, deux types de forets standards (spécification ISO : 452.1-0635-044A0-CM H10F et R846-0635-50-A1A 1220) avec un diamètre identique de 6.35 mm, fournis par Sandvik Coromant, en France, ont été utilisés pour le perçage de trous. Le premier foret, désigné par foret A, était un outil solide non revêtu de carbure de tungsten avec deux arêtes de coupe principales, un bord de ciseau de 0.11 mm en longueur, un angle d'hélice de 20° et un angle de point de 135°. En revanche, le deuxième foret, désigné par foret B, était un foret revêtus de TiAlN fabriqué avec deux flûtes, un bord de ciseau de 0.22 mm en longueur, un angle d'hélice de 27.2° et un angle de pointe de 140°. Le revêtement en TiAlN peut généralement fournir une résistance supérieure à l'usure et une dureté élevée homogène pour résister aux conditions élevées d'efforts et de températures présentes dans le perçage difficile de multi-matériaux.

Moyens de mesure et techniques expérimentales

Le travail expérimental comprend les mesures sur place et leur analyses en post-traitement. Le système de mesure sur place vise à mesurer les signatures de génération des efforts et de capturer le processus dynamique de séparation des copeaux régissant l'usinage des matériaux hybrides CFRP/Ti. En revanche, le post-traitement des analyses vise à étudier la qualité de la pièce usinée, les endommagements de la subsurface induites par la coupe, la morphologie de la surface usinée de l'outil, et le type des copeaux réséqués.

- Le système de mesure sur place : un dynamomètre piézoélectrique Kistler (le type 9255B pour la coupe orthogonale et l'usinage de CFRP/Ti combiné, et le type 9271A pour le perçage de trous), relié à un amplificateur de charge multicanal (le type 5017B1310 pour la coupe orthogonale et la coupe bi-matière combinée, et le type 5019A130 pour le perçage de trous) a été utilisé pour surveiller les signaux de effort pendant la coupe CFRP/Ti. En outre, un dispositif à couplage de charge (DCC) (le modèle de SA5 FASTCAM) a été également utilisé pour capturer les modes de séparation des copeaux régissant l'usinage des matériaux hybrides CFRP/Ti.

- Les analyses en post-traitement comprennent les études de la qualité de surface CFRP/Ti usinée (l'étendue des endommagements dans la subsurface, la morphologie de la pièce, l'intégrité de la surface, les caractéristiques géométriques de trous), les inspections de l'usure de l'outil (la morphologie de l'usure de la surface de l'outil, le mécanisme d'usure de l'outil et et le mode d'échec de l'outil), les examens des copeaux réséqués (la morphologie

géométrique des copeaux et le type de copeau). Le matériel suivant a été utilisé : microscope Nikon SMZ-2T , interféromètre à lumière blanche Veeco (Wyko 3300NT, Veeco WykoR, Mannheim, Allemagne), profilomètre Hommel Vague , CMM Mitutoyo BHN506 et SEM type JSM-5510LV.

Essais de coupe mise en oeuvre

Pour étudier la physique de la coupe des matériaux hybrides CFRP/Ti, la coupe orthogonale, l'usinage de CFRP/Ti combiné et l'opération de perçage, ont toutes été réalisés. Puisque la coupe de CFRP et la coupe du titane nécessitent des intervalles de paramètres de coupes optimaux différents, les paramètres de coupe utilisés ont été adoptés sur la base d'une sélection de compromis paramétrique.

Coupe orthogonale et usinage de CFRP/Ti combiné

La coupe orthogonale et l'usinage de CFRP/Ti combiné ont tous été effectués sur un shaper modèle de machine GSP - EL 136 avec une puissance maximale 5222 W, une course maximale de 650 mm et une vitesse maximale de 100 m / min. Pour l'opération de coupe orthogonale, les types de pièces 1, 2 et 3 avec les trois orientations de fibres de 0°, 45° et 90° et les inserts basculés en PCD ont été utilisés. Pour l'usinage de CFRP/Ti combiné, les types de pièces 4, 5 et 6 avec des orientations de fibres de 0°, 45° et 90° et les outils A, B, C et D ont été adoptés. Tous les essais de coupe ont été réalisés sous les conditions de coupe à sec. En outre, au cours du processus de coupe de bord, un dynamomètre Kistler (type 9255B) et une caméra CCD (modèle de SA5 FASTCAM) ont été utilisés pour mesurer respectivement les efforts et enregistrer le processus dynamique de séparation des copeaux.

Montage expérimental pour le perçage sandwich

Les essais de perçage ont été réalisés sous une grande vitesse, cinq axes CNC centre d'usinage DMU 60 monoBLOCK sous la condition de coupe à sec. Le type de pièce 7 fabriqué avec des dimensions de 254 mm × 34.5 mm × 8 mm a été adopté pour les essais de perçage. Le foret non couché (H10F) et le foret revêtu PVD (A1A) ont été utilisés pour finaliser ces opérations. En outre, un dynamomètre piézoélectrique Kistler (type 9271A) a été également utilisé pour mesurer les efforts de perçage.

Chapitre IV : Les résultats numériques et l'analyse EF

Ce chapitre présente les études EF approfondies des principaux mécanismes et des phénomènes physiques qui régissent l'usinage des matériaux hybrides CFRP/Ti. Plusieurs mécanismes physiques de coupe implicites manquant généralement dans les études, tels que (*i*) les mécanismes de contrôle de la coupe de l'interface et après la formation de l'endommagement, (*ii*) l'influence de la séquence de coupe, et (*iii*) les réponses en frottement contrôlant l'usinage des matériaux hybrides CFRP/Ti,

ont été clairement abordées dans nos études numériques. Les principales conclusions de ce chapitre peuvent être résumées ainsi :

- Les natures disparates de chaque constituant empilé font que le procédé de coupe présente trois étapes distincte : la coupe de la phase Ti, la coupe de l'interface et la coupe de la phase CFRP. Les modes de séparation des copeaux lors de la coupe bi-matière comprennent à la fois de la déformation élastique-plastique et de la rupture fragile. Les mécanismes modifiables d'élimination des copeaux aboutissent généralement à des conditions extrêmement difficiles qui dominent alors la coupe de l'interface. La fluctuation sévère des forces a été observée comme la caractéristique clé qui régit la coupe des matériaux hybrides CFRP/Ti. L'adhésion sérieuse des copeaux sur la surface de l'outil a été montrée comme étant le facteur important qui contribue à l'augmentation spectaculaire des efforts de coupe lors de l'usinage ultérieur de la phase CFRP.

- Les résultats numériques ont mis en évidence l'apparition de délaminage grave à l'interface CFRP/Ti. Les analyses EF ont révélées que l'initiation et l'évolution du délaminage à l'interface avaient principalement lieu lors de la coupe AIZ. La formation de dégâts à l'interface CFRP/Ti a impliquée une série de variation dans le détachement et la déchirure gouvernant le temps de coupe AIZ. Les principaux mécanismes régissant l'endommagement à l'interface pourraient être attribués aux effets couplés des modes de rupture I et II découlant des charges mécaniques uniques exercées sur la région de l'interface bi-matière. La caractéristique morphologique clé du délaminage de l'interface était une encoche « en V » sur la limite de contact « Ti-CFRP ».

- La coupe de l'interface a confirmée le rôle important de la vitesse de coupe et du débit d'alimentation en affectant la durée de coupe AIZ. Les variables d'entrées (v_c et f) ont présenté des effets marqués sur l'étendue du délaminage à l'interface par la manière de leurs influences sur l'AIZ. Pour minimiser la formation de graves endommagements à l'interface, une combinaison paramétrique de la vitesse élevée de coupe et du débit faible d'alimentation devrait être fortement préférée.

- L'opération de coupe CFRP/Ti complète peut être physiquement divisée en trois zones avec un point de vue des influences interdépendantes découlant de chaque phase d'usinage : (*i*) la coupe de la phase Ti pure, (*ii*) la coupe de la AIZ, et (*iii*) la coupe de la phase CFRP pure. Parmi eux, la coupe de la AIZ reflète en réalité la véritable usinabilité du CFRP/Ti couplé ($M_{\mathrm{CFRP/Ti}}$) ; elle peut être considérée comme la zone la plus difficile à usiner en raison de l'apparition d'influences de coupes interdépendantes et de l'existence de la zone la plus faible de l'interface. Dans ce cas, afin d'améliorer fondamentalement l'usinabilité des matériaux hybrides CFRP/Ti, une attention particulière devra être apportée à l'étude en profondeur des mécanismes et à l'optimisation des paramètres de coupe dans la zone AIZ. À l'avenir, des études plus systématiques doivent être effectuées pour répondre précisément aux questions susmentionnées.

- Il a été confirmé que la séquence de coupe CFRP → Ti favorisait la rupture des copeaux du système bi-matière. Le phénomène de l'adhésion des copeaux fonctionne comme un facteur majeur de l'influence de la séquence de coupe sur l'usinage hybride et composite. La séquence de coupe CFRP → Ti était plus adaptée pour l'usinage de haute qualité des

matériaux hybrides CFRP/Ti que la séquence de coupe Ti → CFRP. Pour améliorer l'usinabilité des matériaux hybrides CFRP/Ti, une séquence de coupe CFRP → Ti devrait d'être choisie de préférence dans la production réelle pour minimiser la formation des endommagements induits et garantir une meilleure qualité de la surface usinée.

- Les études paramétriques ont mis en évidence l'effet significatif de la vitesse d'avance sur les efforts de coupe, et le rôle crucial de l'orientation des fibres sur les dégâts dans la phase composite et le délaminage dans l'interface lors de la coupe des matériaux hybrides CFRP/Ti. L'impact de la vitesse de coupe sur les efforts de coupe est faible et précisément négatif en raison des effets adoucissants de hausse de la température de coupe sur le matériau lorsque v_c est élevée. Pour minimiser la génération des efforts de coupe et l'étendue des graves endommagements induits, un débit faible d'alimentation, une vitesse élevée de coupe et une configuration petite θ devraient être fortement recommandés lors de l'usinage des matériaux hybrides CFRP/Ti.

- Le coefficient de frottement multi-interactions outil/matériaux (μ) a joué un rôle crucial sur les différentes réponses en frottement lors de la coupe des hybrides CFRP/Ti principalement par ses influences thermiques et mécaniques. Cependant, pour une réponse spécifique d'usinage, l'effet du coefficient de frottement réel dépendait de manière significative sur un des deux facteurs (thermique ou mécanique) prédomine le processus concerné. Dans un tel cas, différents mécanismes ont été observés dans les études numériques. Pour réduire la consommation d'énergie, l'influence du μ dépendait principalement de la concurrence entre le ramollissement thermique et l'amélioration de la résistance de coupe régissant le processus de séparation des copeaux lorsque μ était élevé. Une valeur de seuil μ a ensuite prédite aux environs de 0.3, au-delà duquel l'impact du μ sur la consommation d'énergie spécifique de coupe est négatif en raison de l'adoucissement thermique accru sur l'amélioration de la résistance de coupe lorsque μ augmente. En outre, le μ présentait également un effet positif et significatif sur la formation induite des endommagements sous la surface (endommagements dans la phase composite et délaminage à l'interface) en raison des chargements thermomécaniques exercés sur la surface usinée lorsque μ était élevée. En ce qui concerne la contrainte résiduelle induite de la partie Ti usinée, le facteur prédominant à partir des influences du μ est des effets thermiques qui ont contribués à l'amélioration des contraintes de traction tandis que la réduction des contraintes de compression.

- Les études numériques ont finalement soulignées que l'amélioration du comportement du frottement multi-interactions outil/matériaux (la réduction de μ) serait une solution directe et bénéfique à l'usinage de haute qualité d'hybride CFRP/Ti. Dans ce but, plusieurs applications qui sont capables de réduire μ, tout comme l'utilisation du liquide de coupe efficace et un matériau d'outil supérieur, peuvent être adoptées dans la fabrication réelle du matériau sandwich. En outre, afin d'améliorer la qualité de la surface usinée ainsi que le choix d'une vitesse élevée de coupe, d'un débit faible d'alimentation et d'une petite orientation des fibres doivent être utilisés lors de la coupe des matériaux hybrides CFRP/Ti.

Chapitre V : Étude des mécanismes de coupe orthogonale des

matériaux hybrides CFRP/Ti

Les mécanismes de coupe fondamentaux des matériaux hybrides CFRP/Ti sont étudiés globalement dans ce chapitre lorsqu'ils sont soumis à une configuration de coupe orthogonale. Les différentes stratégies de séquencement de la coupe et l'usinage des matériaux combinés ont été soigneusement réalisés en utilisant des outils en PCD supérieurs et divers outils carbure revêtus. Les réponses de coupe clés incluant le processus de séparation des copeaux, les efforts de coupe, la qualité de la surface usinée, la performance de l'outil et le mécanisme d'usure de l'outil ont été précisément abordés. Basé sur les résultats expérimentaux obtenus, les conclusions suivantes peuvent être tirées.

- Grâce à l'inspection du mode de séparation des copeaux, les mécanismes de rupture fragile et de déformation plastique ont été identifiés comme dirigeant les opérations de coupe orthogonale des matériaux hybrides CFRP/Ti. Les copeaux réséqués de CFRP et de Ti se sont avérés respectivement essentielles aux natures « poudreuse » et « continue ». D'ailleurs, l'adhérence forte des copeaux de titane a également été trouvée lors de la séquence Ti → CFRP ; elle est la cause principale de la fissuration importante et du délaminage en encoche « en V » induit à l'interface. Le phénomène détecté corrèle également avec l'observation numérique lors de la modélisation de la coupe de l'interface CFRP/Ti soumise à la séquence de coupe identique. La coupe de CFRP/Ti combiné implique généralement les modes couplés de rupture fragile et de déformation plastique, et elle conduit à la formation de copeaux « poudreux » et « continus ». Le phénomène, dans une certaine mesure, induira inévitablement une répartition inégale des contraintes/températures sur les principales arêtes de coupe de l'outil, et il entraînera l'instabilité de l'interaction outil-matériau.

- L'analyse du signal des efforts a montré respectivement les cinq et trois étapes de coupe impliquées dans la coupe orthogonale et l'usinage de CFRP/Ti combiné. En outre, il a été montré que l'orientation des fibres (θ) avait des effets marqués sur les efforts de coupe de la phase CFRP tandis que sa influence sur ceux de la phase Ti étaient mineurs et négligeables. En outre, la vitesse de coupe (v_c) a été identifiée comme ayant un impact positif sur la génération des efforts CFRP/Ti à basse vitesse, alors qu'à grande vitesse, son impact a été négatif. Par contraste, la vitesse d'avance (f) avait un impact positif significatif à la fois les efforts de coupe et sur les efforts de poussée lors de la coupe orthogonale des matériaux hybrides CFRP/Ti. Lors de l'usinage de CFRP/Ti combiné, les effets paramétriques similaires ont été observés, et il a été montré que l'outil A avec la qualité de revêtement dégradée favorisait la génération des efforts les plus faibles par rapport à ses homologues.

- Les études sur la qualité de surface ont mis en évidence que les principaux endommagements de surface CFRP/Ti apparaissent principalement dans la phase CFRP et à l'interface. Il a été confirmé que l'orientation des fibres (θ) possède un rôle important sur la qualité de surface CFRP/Ti usinée. Les principaux modes d'endommagement de la phase Ti sont la déformation des marques d'avance et les copeaux redéposés tandis que les imperfections majeures ayant lieu sur la surface CFRP usinée se sont révélées être des arrachements des fibres, des pertes de résine et de la formation de cavités en surface. En outre, lorsque la séquence de coupe Ti → CFRP est utilisée, une différence importante a été observée à la

région de l'interface, dans laquelle l'apparition de fractures ductiles rapides ont été détectées. Concernant la surface usinée dans la coupe de l'interface combinée, la zone de l'interface intacte sans endommagements graves ni fissuration a été produite en raison de la non-ingérence de chaque usinage des phases empilées.

- La vitesse d'avance (f) et l'orientation des fibres (θ) sont avérées significativement positif sur la rugosité de la surface finale, indépendamment des stratégies de séquencement de la coupe utilisées. La séquence de coupe Ti → CFRP induit une rugosité de surface beaucoup plus élevée qu'avec la séquence de coupe CFRP → Ti, en raison de l'importante adhésion des copeaux de Ti sur qui substitue les bords outil pour une séparation de phase CFRP. En opposition, la rugosité de la surface usinée dans la séquence de coupe Ti → CFRP offre des amplitudes inférieures en raison des bords d'outils non-usés qui viennent couper la phase métallique. En outre, l'analyse de microdureté a également confirmée l'existence du ramollissement thermique dû à la vitesse de coupe élevée (v_c) et d'un écrouissage dû à la diminution de vitesse d'avance (f) sur la surface usinée de phase Ti.
- La performance de l'outil et les analyses d'usure ont révélé que l'outil PCD subit souvent une usure en cratère, mais une usure mineure de flanc, lors de la coupe orthogonale d'hybride CFRP/Ti. La première peut être principalement attribuée à la coupe de la phase Ti tandis que la seconde peut être attribuée à sa résistance à l'usure extrêmement élevée au cours du processus d'enlèvement de copeaux. En outre, le mode de défaillance de l'outil pour les outils de PCD a été identifié comme des éclats sur les bords en raison de la brusque variation des efforts résultant non seulement de la coupe à l'interface CFRP/Ti mais aussi de sa fragilité inhérente. L'échec de l'outil et la progression de l'usure des outils ont été confirmés comme ayant des influences néfastes sur la qualité de surface de CFRP/Ti usinée et les efforts de coupe. Afin d'assurer une excellente qualité de surface usinée, l'utilisation d'un outil fraîchement aiguisé et un contrôle rigoureux de l'usure de l'outil devraient être sérieusement mis en place lors de la coupe des matériaux hybrides CFRP/Ti.

Chapitre VI : Étude du perçage des matériaux hybrides CFRP/Ti

Par rapport aux études précédentes sur le perçage des matériaux hybrides CFRP/Ti, ce chapitre vise à contribuer et à clarifier les aspects suivants : (*i*) la fonction d'interaction outil-matériau et la classification de l'usinabilité régissant le perçage CFRP/Ti, (*ii*) les différentes influences des séquences de coupe ($^{\text{CFRP} \rightarrow \text{Ti}}_{\text{Ti} \rightarrow \text{CFRP}}$) sur les réponses du perçage, et (*iii*) les effets des différentes caractéristiques géométriques et matériaux des outils sur les performances du perçage CFRP/Ti. Dans ce but, les essais de perçage comparatifs des matériaux CFRP/Ti ont été réalisés en adoptant différents matériaux/géométries d'outils et stratégies de séquencement du perçage. Les réponses fondamentales d'usinage, comme la génération de effort, la qualité du trou usiné (par exemple, la rugosité de surface, le diamètre du trou, l'erreur de rotondité, la morphologie de la paroi du trou) et la formation d'endommagement par le perçage (par exemple, la formation de délaminage et de bavures) ont été précisément traités par rapport aux conditions de coupes utilisées. Les principales conclusions suivantes ont été obtenues au cours des études de perçage.

- Le perçage des matériaux hybrides CFRP/Ti utilisant la séquence CFRP → Ti ou la séquence Ti → CFRP consiste essentiellement à cinq étapes de coupe vis-à-vis des caractéristiques de l'interaction outil-matériau. Le perçage de l'interface est généralement l'étape la plus difficile en raison de l'existence de multi-interactions outil/matériaux, où les modes couplées de séparation des copeaux et la transition sévère des réponses mécaniques/physiques prédominant

- La classification de l'usinabilité du perçage CFRP/Ti peut être effectuée selon les caractéristiques dans la zone d'interaction outil-matériau qui régissent le processus de séparation des copeaux. Pour la séquence de coupe CFRP →Ti, les durées de coupe $t \in [0, t_2]$ (étape *a* - *c*), $t \in [t_2, t_3]$ (étape *c* - *d*) et $t \in [t_3, t_5]$ (étape *d* - *f*) signifient habituellement l'usinabilité en perçage de la phase pure CFRP, de l'interface CFRP/Ti empilé et de la phase Ti, respectivement.

- L'analyse des efforts a montrée que le foret A sans revêtement communément générait des efforts inférieurs à ceux du foret B revêtu en TiAlN, lorsqu'ils sont utilisés avec la même séquence de coupe et les mêmes paramètres, en raison de son petit ciseau longueur d'arête de coupe impliqués. Cette constatation a indiquée que les caractéristiques géométriques de l'outil (par exemple, la longueur du bord burin, l'angle de pointe et l'angle d'hélice) exercent des effets plus importants sur la génération des efforts de perçage que les caractéristiques matériaux de l'outil lors du perçage des matériaux hybrides CFRP/Ti. En outre, la vitesse de coupe et la vitesse d'avance sont toutes deux à l'origine d'un impact positif et significatif sur l'amplitude des forces, quels que soient les outils ou les séquences de coupe utilisés.

- Les études sur la consommation d'énergie spécifique du perçage (E_k) ont montré qu'elle a été principalement influencée par la vitesse d'avance plutôt que la vitesse de coupe. De plus, le foret B dans le perçage Ti → CFRP a tendance à moins augmenter la consommation d'énergie spécifique E_k que forets A et B dans la séquence de coupe CFRP → Ti. Ceci qui indique une réduction de la consommation d'énergie et une meilleure usinabilité du matériau composite empilé.

- Lors du perçage hybride CFRP/Ti, les deux types de copeaux en « ruban » et en « spirale » ont été obtenus par différents outils et paramètres de coupe. La vitesse d'avance possède un rôle central affectant la morphologie des copeaux réséqués de telle sorte qu'une vitesse accrue d'avance conduit généralement à des copeaux segmentées, et elle améliore donc la sécabilité des copeaux. En revanche, l'effet de la vitesse de coupe est négligeable sur le type de copeaux.

- La qualité des trous, c'est-à-dire la rugosité de la surface et la taille du trou, a montré qu'elle était remarquablement affectée par la séquence de perçage mise en œuvre ainsi que les paramètres de coupe. La vitesse d'avance était généralement un facteur clé qui a largement influencé la finition de surface de trou tandis que l'impact de la vitesse de coupe n'était pas significatif. En outre, pour tous les essais testés, la rugosité moyenne arithmétique (R_a) des trous de phase Ti a toujours été eu une mesure en dessous de la valeur de R_a = 1.6 µm, tandis que pour les trous de CFRP usinés, les valeurs de R_a était partiellement en dessous de la valeur de R_a = 3.2 µm et était fortement dépendante des paramètres de coupe utilisées. Pour le diamètre du trou et la rondeur, à la fois la vitesse de coupe et l'avance en perçage avaient

des effets prononcés sur les valeurs mesurées. En outre, la séquence de coupe Ti → CFRP générait une rugosité de surface plus faible et des diamètres de trous CFRP/Ti consistants par rapport au perçage CFRP → Ti en raison des abrasions graves évitées lors de l'évacuation des copeaux de Ti.

- L'analyse de l'endommagement des trous a montré que le perçage CFRP → Ti induit généralement moins de délaminage que le perçage Ti → CFRP sous les conditions de coupe identiques, en raison du rôle de support de l'alliage de Ti qui augmente la rigidité de la couche de CFRP en sortie des trous lors du perçage des matériaux hybrides CFRP/Ti. En outre, la vitesse d'avance jouait un rôle prédominant dans la formation du délaminage induit par le perçage. Par ailleurs, dans le but de minimiser la formation de défauts de bavure, le perçage Ti → CFRP produit couramment une étendue plus faible de défauts si une vitesse élevée a été utilisée par rapport au perçage CFRP → Ti.

- Les analyses des topographies/morphologies des trous ont révélé que les modes d'endommagement de surface principaux dans le CFRP étaient les fissures fibre / matrice, le délaminage et l'écaillage tandis que pour le Ti. Il s'agissait de copeaux re-déposés et de marques d'avance. La séquence de perçage CFRP → Ti a facilité l'amélioration de la qualité de surface de la paroi du trou percé en raison de la problématique de l'évacuation des copeaux de Ti évitée. En outre, le foret A sans revêtement favorisait une meilleure surface de la paroi du trou avec moins d'endommagement de la sub-surface par rapport au foret revêtu de TiAlN.

- En général, le foret A sans revêtement a montré une meilleure performance que le foret B revêtu de TiAlN sur diverses réponses de perçage (par exemple, la génération des efforts, la consommation E_k, l'étendue de l'endommagement du trou) lorsqu'il est effectué dans des conditions de coupe identiques. Cela suggère probablement que lors du perçage des matériaux hybrides CFRP/Ti, la sélection des caractéristiques géométriques optimales devrait être plus efficace que le choix du matériau de l'outil pour améliorer l'usinabilité du système bi-matière.

- Toutes les deux séquences de coupe ($^{\text{CFRP} \rightarrow \text{Ti}}_{\text{Ti} \rightarrow \text{CFRP}}$) possèdent des effets significatifs sur les réponses du perçage d'empilage CFRP/Ti, tel que résumé dans le Tableau 1. La séquence de perçage Ti → CFRP améliore la qualité de perçage de trou de CFRP (par exemple, le diamètre consistent du trou et la bonne qualité de sa surface), la mesure Ti Burr diminué, mais engendre une formation de délaminage plus importante. En revanche, la séquence de perçage CFRP → Ti a facilité la réduction de la formation du délaminage au cours de l'intégralité des essais. Étant donné que les deux séquences de coupe ont leurs propres avantages et inconvénients, le choix de la stratégie de perçage devrait être subordonné aux préoccupations qui doivent être prises en fonction des besoins particuliers des processus et de leur importance relative.

Tableau 1 :
Influences comparées des deux stratégies de séquencement de coupe sur des réponses du perçage d'empilage CFRP/Ti.

Séquence de perçage	Efforts de perçage	Type des copeaux	Qualité du trou		Endommagement du trou	
			Rugosité de surface	Diamètre du trou	Délaminage	Largeur de bavure
CFRP → Ti	↑	—	↑	↑	↓	↑
Ti → CFRP	↓	—	↓	↓	↑	↓

Remarques : « ↑ » indique une amélioration ou une acceleration, « ↓ » signifie une réduction ou une deterioration, et « — » désigne des effets insignifiants ou mineurs.

Chapitre VII : Conclusions générales et perspectives

Conclusions générales

Cette thèse a été consacrée aux études des mécanismes de coupe qui contrôlent d'usinage des matériaux hybrides CFRP/Ti via des méthodes numériques et expérimentales. Dans ce but, le travail numérique a été effectué préalablement pour faire la lumière sur certaines physiques de coupe implicites qui dominent l'usinage bi-matière lorsqu'elle est soumise à stratégies différentes de séquencement de coupe. Les configurations de base de l'usinage des matériaux hybrides CFRP/Ti consistant en coupe orthogonale, l'usinage de l'interface combinée et le perçage de trous ont été précisément traités par rapport à des conditions et stratégies de coupe différentes. Les réponses d'usinage clés, comprenant les modes de séparation des copeaux, la génération des efforts, la qualité des surfaces usinées, les endommagements induits dans la sub-surface et les mécanismes d'usure de l'outil ont été soigneusement étudiées. Une attention particulière a été apportée sur les mécanismes d'enlèvement de matière et des stratégies de coupe des matériaux hybrides CFRP/Ti. Par rapport aux études existantes dans la littérature, l'originalité et la nouveauté de ce travail de recherche peuvent être résumées ainsi :

- Le travail de doctorat a été parmi les premières recherches qui mettent au point les modèles FE pour simuler le processus dynamique de coupe des matériaux hybrides CFRP/Ti et révéler les mécanismes clés et les phénomènes physiques qui dominent l'usinage bi-matière.
- Ce travail a révélé les mécanismes activés régissant l'usinage de l'interface et la formation induite de délaminage dans cette zone. De plus, les influences des stratégies différentes de séquencement de coupe sur l'usinage des matériaux hybrides CFRP/Ti ont été clairement précisées par les études numériques et expérimentales.
- La recherche actuelle a fourni une méthode numérique et expérimentale combinée pour une meilleure compréhension de la coupe des matériaux hybrides CFRP/Ti. Plusieurs recommandations en termes de choix de séquencement de coupe et de géométrie/matériau d'outil pour l'usinage industriel des matériaux hybrides CFRP/Ti ont été proposées.

Selon les recherches systématiques effectuées dans cette thèse, les principales conclusions suivantes peuvent être tirées.

- L'usinage des matériaux hybrides CFRP/Ti est un grand défi en ce qui concerne le processus d'évacuation des copeaux en raison de l'usinabilité variable de chaque matériau empilé et la prédominance des multi-interactions outil/matériaux. Les modes de séparation des copeaux contrôlant la coupe des matériaux hybrides CFRP/Ti comprennent à la fois les déformations

élastoplastiques et la rupture fragile. Les modes d'enlèvement des copeaux variables ont souvent entraîné un transfert sévère des réponses en efforts/chaleur exercé sur la zone de l'interface. Les études numériques ont révélé les mécanismes activés contrôlant la formation de lésions de délaminage à l'interface CFRP/Ti. Les analyses EF ont montrées que l'initiation et l'évolution du délaminage à l'interface ont principalement eu lieu lors de la coupe de AIZ, dans laquelle l'endommagement de l'interface est impliqué dans une série de détachements et de déchirures. Les principaux mécanismes qui régissent la formation des dégâts à l'interface pourraient être soigneusement reliés aux effets couplés des modes de rupture I et II exercés sur la région de l'interface bi-matière, qui par conséquent conduit à la « forme en V » comme un endommagement cran.

- Par ailleurs, les analyses EF ont également révélé que la séquence de coupe CFRP → Ti facilite la rupture des copeaux et promeut des morphologies de surface plus lisse que celles générées dans la coupe Ti → CFRP. Des études paramétriques ont mis en évidence l'effet significatif de la vitesse d'avance sur la génération des efforts de coupe, et le rôle crucial de l'orientation des fibres sur l'endommagement de la phase composite et le délaminage à l'interface lors de la coupe des matériaux hybrides CFRP/Ti. En outre, il a également été confirmé que le coefficient de frottement des multi-interactions outil/matériaux (μ) a joué un rôle crucial sur les différentes réponses en frottement par ses influences thermiques et mécaniques lors de l'usinage des matériaux hybrides CFRP/Ti. Les résultats numériques ont en outre suggéré que l'utilisation d'un meilleur liquide de coupe ou d'un outil dans un matériau supérieur peut améliorer le comportement en frottement des multi-interactions outil/matériaux, à savoir réduire μ, et sont donc un moyen direct pour obtenir un usinage de haute qualité des matériaux hybrides CFRP/Ti.

- Les travaux expérimentaux concernant la coupe orthogonale et l'usinage de CFRP/Ti combiné ont montré que la vitesse d'avance et l'orientation des fibres sont les principaux facteurs qui ont considérablement influencé la génération des efforts et la qualité de la surface usinée. Les modes principaux d'endommagement de la phase titane se sont révélés être la déformation des marques d'avance et la redéposition des copeaux tandis que pour la surface usinée CFRP. Il s'agissait de retraits de fibres, de pertes de résine et de formations de cavités sur la surface. La coupe Ti → CFRP a induit de sérieux endommagement de fissuration et de délaminage « en V » dans la région de l'interface. En revanche, la coupe CFRP → Ti a suscité un meilleur état de surface que la coupe Ti → CFRP. Les mécanismes d'usure dominent les outils PCD lors de la coupe orthogonale des matériaux hybrides CFRP/Ti se sont révélés comme l'usure en cratère, l'usure par adhérence et l'usure des flancs tandis que les modes de défaillance de l'outil ont été le micro-écaillage et la fissuration des bords dus à la variation soudaine des efforts résultant de l'usinage de l'interface CFRP/Ti et de la fragilité inhérente du matériau PCD.

- En ce qui concerne le perçage de trous, il a été constaté que la vitesse d'avance avait un rôle central sur le développement des efforts de perçage et sur la morphologie des copeaux. La qualité du trou, c'est-à-dire la rugosité de la surface usinée et la précision de la taille du trou, a été fortement influencée par les séquences de coupe mises en œuvre ainsi que les paramètres de process. La séquence de coupe Ti → CFRP montrait qu'elle générait une

rugosité de surface plus faible et des diamètres de trous plus consistants par rapport à la coupe CFRP → Ti en raison des abrasions graves évités par l'évacuation des copeaux de titane. Par ailleurs, l'analyse de l'endommagement des trous a montré que le perçage CFRP → Ti engendre moins de délaminage que le perçage Ti → CFRP en raison du rôle de soutien du support en alliage de titane qui augmente également la rigidité de la couche de sortie du trou de la phase CFRP pendant le perçage d'empilage CFRP/Ti. En revanche, afin de minimiser la formation de bavures, la séquence de coupe Ti → CFRP ainsi qu'une vitesse élevée de coupe devraient être adoptées dans le perçage des matériaux hybrides CFRP/Ti.

- En outre, le foret sans revêtement permet d'obtenir les meilleures performances que le foret avec un revêtement de TiAlN sur diverses réponses de perçage (par exemple, la génération des efforts, l'étendue de l'endommagement du trou) quand ils ont été effectués dans les mêmes conditions de coupe. Les résultats acquis indiquent que lors du perçage des matériaux hybrides CFRP/Ti, les caractéristiques géométriques de l'outil présentaient une influence plus forte que la composition du matériau de l'outil. Pour assurer un perçage de haute qualité de la bi-matière, le choix des caractéristiques géométriques optimales devrait être considéré comme un facteur majeur en production réelle.

- Dans la coupe orthogonale et le perçage de trous, selon les caractéristiques des interactions outil/matière suivant la zone, l'ensemble de l'opération d'usinage des matériaux hybrides CFRP/Ti peut être décomposé physiquement en trois étapes de coupe : (*i*) la coupe pure de la phase CFRP, (*ii*) l'usinage de l'interface, et (*iii*) la coupe pure de la phase titane. Parmi celles-ci, l'usinage de l'interface, en réalité, reflète la véritable usinabilité du matériau empilé CFRP/Ti ($M_{\mathrm{CFRP/Ti}}$), où les multi-interactions outil/matériaux sont présentées. En outre, étant donné que l'usinage de l'interface comprend des modes couplés de séparation de copeaux et des réponses de coupe liées, une sélection soigneuse des paramètres et de l'outil doit être focalisée sur la zone de coupe de l'interface afin d'améliorer l'usinabilité fondamentale de la bi-matière.

- La stratégie de séquencement de la coupe possède des effets significatifs sur les réponses de coupe des matériaux hybrides CFRP/Ti pour la coupe orthogonale et le perçage de trous. Dans la coupe orthogonale, la coupe CFRP → Ti a montré une forte tendance à favoriser une meilleure qualité de surface contrairement à la coupe Ti → CFRP. Cependant, pour le perçage de trous, les deux stratégies de séquencement de la coupe ($^{\mathrm{CFRP} \rightarrow \mathrm{Ti}}_{\mathrm{Ti} \rightarrow \mathrm{CFRP}}$) ont montré que toutes les deux avaient des avantages et des inconvénients. Par exemple, le perçage de Ti → CFRP a généré une meilleure qualité de surface du trou (par exemple, un diamètre de trou consistant et une bonne qualité de surface) avec une formation faible de bavures de Ti alors que le perçage de Ti → CFRP réduit seulement l'étendue du délaminage induit par l'usinage. Les mécanismes activés contrôlant les influences des différentes séquences de coupe pourraient être attribués aux effets disparates de l'adhérence des copeaux de Ti sur le processus d'enlèvement de matière. En effet, dans la coupe orthogonale, les copeaux de titane ne peuvent provoquer que l'adhérence sur l'arrête de l'outil de coupe, n'engendrant ainsi par de rayure sur la surface du CFRP, tandis que dans le processus de perçage. Les copeaux de titane réséqués pourraient provoquer l'adhérence du copeau et de l'endommagement par abrasion sur la surface du CFRP au cours de leur évacuation. Par conséquent, pour le perçage de trou, le choix de la stratégie de séquencement de la coupe doit

être dépendante des critères à prendre en compte pour un besoin particulier du processus et leur importance relative.

Perspectives

Le objectif principal de cette étude a été finalisé. Cependant, l'usinage de haute qualité des matériaux hybrides CFRP/Ti est habituellement une opération de fabrication complète et interdépendante, dépendant de nombreux facteurs internes et externes. Par example, la configuration de l'outil de travail, des paramètres de coupe, de l'environnement de coupe ainsi que de la machine-outil utilisée. Pour améliorer complètement l'usinabilité du système bi-matière, il reste encore beaucoup de travail nécessaire à entreprendre à l'avenir. Basé sur les recherches déjà effectuées, les suggestions/recommandations suivantes peuvent être fournies pour les futurs travaux sur l'usinage des matériaux hybrides CFRP/Ti à travers les deux aspects numériques et expérimentaux.

- Les études numériques présentées dans cette thèse ont porté uniquement sur les analyses des processus de coupe orthogonale. Les modèles EF développés ont ignoré certains détails complexes des multi-interactions outil/matériaux présentées dans l'usinage réel (par exemple, le perçage ou le fraisage). Pour étudier les mécanismes de coupe en profondeur et ainsi refléter le fonctionnement réel de la fabrication, des modèles plus sophistiqués prenant en compte rigoureusement les détails physiques des multi-interactions outil/matériaux (par exemple, le comportement de l'outil, l'usure des outils) devraient être mis en place dans les futurs travaux de recherche.

- En outre, le travail expérimental effectué dans cette thèse a été réalisé uniquement sous les conditions de coupe à sec. A l'avenir, un travail systématique en ce qui concerne les applications des différentes méthodes de lubrification/refroidissement dans l'usinage des matériaux hybrides CFRP/Ti est également exigé de toute urgence. En outre, étant donné que les paramètres de coupe et les caractéristiques géométriques des outils possèdent un rôle crucial sur les réponses finales de la coupe des matériaux hybrides CFRP/Ti, des efforts doivent être déployés sur l'optimisation des paramètres de coupe et de la conception géométrique de l'outil afin de fournir une configuration supérieure d'outil de travail pour une meilleure qualité de finition de l'usinage des matériaux hybrides CFRP/Ti.

Appendix B: Publication list and scientific presentation

JCR Refereed Journal Articles

1. **Jinyang Xu**, Mohamed El Mansori. Experimental study on drilling mechanisms and strategies of hybrid CFRP/Ti stacks. ***Composite Structures*** 2016; page 1-22, doi: 10.1016/j.compstruct.2016.07.025.
2. **Jinyang Xu**, Ali Mkaddem, Mohamed El Mansori. Recent advances in drilling hybrid FRP/Ti composite: a state-of-the-art review. ***Composite Structures*** 2016; 135: 316-338.
3. **Jinyang Xu**, Mohamed El Mansori. Cutting modeling of hybrid CFRP/Ti composite with induced damage analysis. ***Materials*** 2016; 9 (1): 1-22.
4. **Jinyang Xu**, Mohamed El Mansori. Numerical studies of frictional responses when cutting hybrid CFRP/Ti composite. ***International Journal of Advanced Manufacturing Technology*** 2016; Page 1-19, doi: 10.1007/s00170-016-8512-9.
5. **Jinyang Xu**, Mohamed El Mansori. Numerical modeling of stacked composite CFRP/Ti machining under different cutting sequence strategies. ***International Journal of Precision Engineering and Manufacturing*** 2016; 17 (1): 99-107.
6. **Jinyang Xu**, Mohamed El Mansori. Cutting modeling using cohesive zone concept of titanium/CFRP composite stacks. ***International Journal of Precision Engineering and Manufacturing*** 2015; 16 (10): 2091-2100.

Refereed International Conference Proceedings

1. **Jinyang Xu**, Mohamed El Mansori. Experimental studies on the cutting characteristics of hybrid CFRP/Ti composite. ***Procedia Manufacturing*** 2016; Page 1-12. (Accepted)
2. **Jinyang Xu**, Mohamed El Mansori, Julien Voisin. Numerical modeling and FE analysis of CFRP/Ti stack orthogonal cutting. ***Procedia CIRP*** 2016; 46 (1): 67-70.
3. **Jinyang Xu**, Mohamed El Mansori. An experimental investigation on orthogonal cutting of hybrid CFRP/Ti stacks. ***AIP Conference Proceedings*** 2016; Page 1-7. (Accepted)
4. **Jinyang Xu**, Mohamed El Mansori. Orthogonal cutting modeling of hybrid CFRP/Ti toward specific cutting energy and induced damage analyses. ***AIP Conference Proceedings*** 2016; Page 1-6. (Accepted)
5. **Jinyang Xu**, Mohamed El Mansori. Finite element analysis when orthogonal cutting of hybrid composite CFRP/Ti. ***IOP Conf Ser Mater Sci Eng*** 2015; 87 (1): 012059.

International Conference Oral Presentations

1. **Jinyang Xu**, Mohamed El Mansori. Experimental studies on the cutting characteristics of hybrid CFRP/Ti composite. ***The 44th North American Manufacturing Research Conference***, Virginia, USA, June 27 - July 1, 2016.

2. **Jinyang Xu**, Mohamed El Mansori, Julien Voisin. Numerical modeling and FE analysis of CFRP/Ti stack orthogonal cutting. ***The 7th CIRP Conference on High Performance Cutting***, Chemnitz, Germany, May 31 - June 2, 2016.

3. **Jinyang Xu**, Mohamed El Mansori. An experimental investigation on orthogonal cutting of hybrid CFRP/Ti stacks. ***ESAFORM 2016***, Nantes, France, April 27 - 29, 2016.

4. **Jinyang Xu**, Mohamed El Mansori. Orthogonal cutting modeling of hybrid CFRP/Ti toward specific cutting energy and induced damage analyses. ***ESAFORM 2016***, Nantes, France, April 27 - 29, 2016.

5. **Jinyang Xu**, Mohamed El Mansori. Numerical modeling of hybrid composite (CFRP/Ti) cutting under different cutting-sequence strategies. ***2015 International Symposium on Green Manufacturing and Applications (ISGMA 2015)***, Qingdao, China, June 23 - 27, 2015. **(Winner of Best Paper Award)**

6. **Jinyang Xu**, Mohamed El Mansori. Finite element analysis when orthogonal cutting of hybrid composite CFRP/Ti. ***2015 Global Conference on Polymer and Composite Materials (PCM 2015)***, Beijing, China, May 16 - 19, 2015.

References

[1] J. Xu, A. Mkaddem and M. El Mansori. Recent advances in drilling hybrid FRP/Ti composite: a state-of-the-art review. *Composite Structures* 2016; **135**: 316-338.

[2] M. Ramulu, T. Branson and D. Kim. A study on the drilling of composite and titanium stacks. *Composite Structures* 2001; **54** (1): 67-77.

[3] E. Brinksmeier, S. Fangmann and R. Rentsch. Drilling of composites and resulting surface integrity. *CIRP Annals - Manufacturing Technology* 2011; **60** (1): 57-60.

[4] J. Xu and M. El Mansori. Cutting modeling using cohesive zone concept of titanium/CFRP composite stacks. *International Journal of Precision Engineering and Manufacturing* 2015; **16** (10): 2091-2100.

[5] W. D. Brewer, R. K. Bird and T. A. Wallace. Titanium alloys and processing for high speed aircraft. *Materials Science and Engineering: A* 1998; **243** (1-2): 299-304.

[6] E. O. Ezugwu and Z. M. Wang. Titanium alloys and their machinability - a review. *Journal of Materials Processing Technology* 1997; **68** (3): 262-274.

[7] E. A. Rahim and H. Sasahara. A study of the effect of palm oil as MQL lubricant on high speed drilling of titanium alloys. *Tribology International* 2011; **44** (3): 309-317.

[8] K. H. Park, A. Beal, D. Kim, P. Kwon and J. Lantrip. A comparative study of carbide tools in drilling of CFRP and CFRP-Ti stacks. *Journal of Manufacturing Science and Engineering-Transactions of the ASME* 2014; **136** (1): 014501.

[9] J. P. Davim. Machining of metal matrix composites. London: Springer London, 2012.

[10] B. Denkena, D. Boehnke and J. H. Dege. Helical milling of CFRP–titanium layer compounds. *CIRP Journal of Manufacturing Science and Technology* 2008; **1** (2): 64-69.

[11] P. P. Camanho and F. L. Matthews. Stress analysis and strength prediction of mechanically fastened joints in FRP: a review. *Composites Part A: Applied Science and Manufacturing* 1997; **28** (6): 529-547.

[12] P. P. Camanho, A. Fink, A. Obst and S. Pimenta. Hybrid titanium-CFRP laminates for high-performance bolted joints. *Composites Part A: Applied Science and Manufacturing* 2009; **40** (12): 1826-1837.

[13] B. Kolesnikov, L. Herbeck and A. Fink. CFRP/titanium hybrid material for improving composite bolted joints. *Composite Structures* 2008; **83** (4): 368-380.

[14] A. Vijayaraghavan and D. A. Dornfeld. Challenges in modeling machining of multilayer materials. *In: Proc 8th CIRP Workshop on Modeling of Machining Operations*. Chemnitz, Germany, 2005, p. 17-24.

[15] E. Brinksmeier and R. Janssen. Drilling of multi-layer composite materials consisting of carbon fiber reinforced plastics (CFRP), titanium and aluminum alloys. *CIRP Annals - Manufacturing Technology* 2002; **51** (1): 87-90.

[16] D. Kim and M. Ramulu. Study on the drilling of titanium/graphite hybrid composites. *Journal of Engineering Materials and Technology - Transactions of the ASME* 2007; **129** (3): 390-396.

[17] J. Xu, Q. An, X. Cai and M. Chen. Drilling machinability evaluation on new developed high-strength T800S/250F CFRP laminates. *International Journal of Precision Engineering and Manufacturing* 2013; **14** (10): 1687-1696.

[18] Q. An, J. Xu, X. Cai and M. Chen. Experimental investigation on drilling force and hole quality when drilling of T800S/250F CFRP laminate. *Advanced Materials Research* 2013; **797**: 155-160.

[19] J. Xu, Q. An and M. Chen. A comparative evaluation of polycrystalline diamond drills in drilling high-strength T800S/250F CFRP. *Composite Structures* 2014; **117**: 71-82.

[20] Z. Liu, Q. An, J. Xu, M. Chen and S. Han. Wear performance of (nc-AlTiN)/(a-Si_3N_4) coating and (nc-AlCrN)/(a-Si_3N_4) coating in high-speed machining of titanium alloys under dry and minimum quantity lubrication (MQL) conditions. *Wear* 2013; **305** (1-2): 249-259.

[21] Z. Liu, J. Xu, S. Han and M. Chen. A coupling method of response surfaces (CRSM) for cutting parameters optimization in machining titanium alloy under minimum quantity lubrication (MQL) condition. *International Journal of Precision Engineering and Manufacturing* 2013; **14** (5): 693-702.

[22] J. Xu, Z. Liu, Q. An and M. Chen. Wear mechanism of high-speed turning Ti-6Al-4V with TiAlN and AlTiN coated tools in dry and MQL conditions. *Advanced Materials Research* 2012; **497**: 30-34.

[23] W. C. Chen. Some experimental investigations in the drilling of carbon fiber-reinforced plastic (CFRP) composite laminates. *International Journal of Machine Tools and Manufacture* 1997; **37** (8): 1097-1108.

[24] A. Faraz, D. Biermann and K. Weinert. Cutting edge rounding: an innovative tool wear criterion in drilling CFRP composite laminates. *International Journal of Machine Tools and Manufacture* 2009; **49** (15): 1185-1196.

[25] S. C. Lin and I. K. Chen. Drilling carbon fiber-reinforced composite material at high speed. *Wear* 1996; **194** (1-2): 156-162.

[26] S. Rawat and H. Attia. Wear mechanisms and tool life management of WC-Co drills during dry high speed drilling of woven carbon fibre composites. *Wear* 2009; **267** (5-8): 1022-1030.

[27] S. Sharif and E. A. Rahim. Performance of coated- and uncoated-carbide tools when drilling titanium alloy-Ti-6Al4V. *Journal of Materials Processing Technology* 2007; **185** (1-3): 72-76.

[28] P. F. Zhang, N. J. Churi, Z. J. Pei and C. Treadwell. Mechanical drilling processes for titanium alloys: a literature review. *Machining Science and Technology* 2008; **12** (4): 417-444.

[29] C. Soutis. Fibre reinforced composites in aircraft construction. *Progress In Aerospace Sciences* 2005; **41** (2): 143-151.

[30] J. P. Davim, P. Reis and C. C. António. Experimental study of drilling glass fiber reinforced plastics (GFRP) manufactured by hand lay-up. *Composites Science and Technology* 2004; **64** (2): 289-297.

[31] T. Sinmazçelik, E. Avcu, M. Ö. Bora and O. Çoban. A review: fbre metal laminates, background, bonding types and applied test methods. *Materials & Design* 2011; **32** (7): 3671-3685.

[32] D. Gay, S. V. Hoa and S. W. Tsai. Composite Materials: Design and Applications. New York: CRC Press, 2003.

[33] D. Liu, Y. Tang and W. L. Cong. A review of mechanical drilling for composite laminates. *Composite Structures* 2012; **94** (4): 1265-1279.

[34] S. C. Lee, S. T. Jeong, J. N. Park, S. J. Kim and G. J. Cho. Study on drilling characteristics and mechanical properties of CFRP composites. *Acta Mechanica Solida Sinica* 2008; **21** (4): 364-368.

[35] X. Yang and C. R. Liu. Machining titanium and its alloys. *Machining Science and Technology* 1999; **3** (1): 107-139.

[36] A. K. M. Nurul Amin, A. F. Ismail and M. K. Nor Khairusshima. Effectiveness of uncoated WC–Co and PCD inserts in end milling of titanium alloy—Ti–6Al–4V. *Journal of Materials Processing Technology* 2007; **192**: 147-158.

[37] E. O. Ezugwu, J. Bonney, R. B. Da Silva and O. Cakir. Surface integrity of finished turned Ti–6Al–4V alloy with PCD tools using conventional and high pressure coolant supplies. *International Journal of Machine Tools and Manufacture* 2007; **47** (6): 884-891.

[38] A. Beal, D. Kim, K. H. Park and P. Kwon. A comparative study of carbide tools in drilling of CFRP and CFRP-Ti stacks. *In: The ASME 2011 International Manufacturing Science and Engineering Conference* 2011, p. 145-152.

[39] R. Carvajal, P. L. Gonzalez-R and S. Lozano. Research study of factors affecting difference between hole diameters in hybrid metal-composite drilling. *Proceedings of the Institution of Mechanical Engineers, Part B: Journal of Engineering Manufacture* 2011; **225** (7): 991-1000.

[40] J. Fujiwara, R. Nagaura, K. Kuroda and T. Tashiro. Drilling of CFRP/Ti6Al4V stack board. *In: Proc 16th International Conference on Mechatronics Technology*. Tianjin, China, 2012, 16-19 October, p. 285-289.

[41] E. Ghassemieh. Performance and wear of coated carbide drill in machining of carbon fibre reinforced composite/titanium stack. *International Journal of Materials and Product Technology* 2012; **43** (1-4): 165-183.

[42] O. Isbilir and E. Ghassemieh. Comparative study of tool life and hole quality in drilling of CFRP/titanium stack using coated carbide drill. *Machining Science and Technology* 2013; **17** (3): 380-409.

[43] D. Kim and M. Ramulu. Drilling process optimization for graphite/bismaleimide–titanium alloy stacks. *Composite Structures* 2004; **63** (1): 101-114.

[44] C. L. Kuo, S. L. Soo, D. K. Aspinwall, S. Bradley, W. Thomas, R. M'Saoubi, et al. Tool wear and hole quality when single-shot drilling of metallic-composite stacks with diamond-coated tools. *Proceedings of the Institution of Mechanical Engineers, Part B: Journal of Engineering Manufacture* 2014; **228** (10): 1314-1322.

[45] K. H. Park, A. Beal, D. Kim, P. Kwon and J. Lantrip. Tool wear in drilling of composite/titanium stacks using carbide and polycrystalline diamond tools. *Wear* 2011; **271** (11-12): 2826-2835.

[46] K. H. Park, P. Kwon and D. Kim. Wear characteristic on BAM coated carbide tool in drilling of composite/titanium stack. *International Journal of Precision Engineering and Manufacturing* 2012; **13** (7): 1073-1076.

[47] A. Poutord, F. Rossi, G. Poulachon, R. M'Saoubi and G. Abrivard. Local approach of wear in drilling Ti6Al4V/CFRP for stack modelling. *Procedia CIRP* 2013; **8**: 316-321.

[48] M. SenthilKumar, A. Prabukarthi and V. Krishnaraj. Study on tool wear and chip formation during drilling carbon fiber reinforced polymer (CFRP)/titanium alloy (Ti6Al4V) stacks. *Procedia Engineering* 2013; **64**: 582-592.

[49] I. S. Shyha, S. L. Soo, D. K. Aspinwall, S. Bradley, R. Perry, P. Harden, et al. Hole quality assessment following drilling of metallic-composite stacks. *International Journal of Machine Tools and Manufacture* 2011; **51** (7-8): 569-578.

[50] T. Tashiro, J. Fujiwara and K. Inada. Drilling of CFRP/Ti-6Al-4V stacks. *Advanced Materials Research* 2011; **325**: 369-374.

[51] X. Wang, P. Y. Kwon, C. Sturtevant, D. Kim and J. Lantrip. Comparative tool wear study based on drilling experiments on CFRP/Ti stack and its individual layers. *Wear* 2014; **317** (1-2): 265-276.

[52] P. S. Sreejith, R. Krishnamurthy, S. K. Malhotra and K. Narayanasamy. Evaluation of PCD tool performance during machining of carbon/phenolic ablative composites. *Journal of Materials*

Processing Technology 2000; **104** (1): 53-58.

[53] H. Hocheng and H. Y. Puw. On drilling characteristics of fiber-reinforced thermoset and thermoplastics. *International Journal of Machine Tools and Manufacture* 1992; **32** (4): 583-592.

[54] D. Kim, M. Ramulu and X. Doan. Influence of consolidation process on the drilling performance and machinability of PIXA-M and PEEK thermoplastic composites. *Journal of Thermoplastic Composite Materials* 2005; **18** (3): 195-217.

[55] D. Arola and M. Ramulu. Orthogonal cutting of fiber-reinforced composites: a finite element analysis. *International Journal of Mechanical Sciences* 1997; **39** (5): 597-613.

[56] D. Arola, M. Ramulu and D. H. Wang. Chip formation in orthogonal trimming of graphite/epoxy composite. *Composites Part A: Applied Science and Manufacturing* 1996; **27** (2): 121-133.

[57] A. Ben Soussia, A. Mkaddem and M. El Mansori. Rigorous treatment of dry cutting of FRP - interface consumption concept: a review. *International Journal of Mechanical Sciences* 2014; **83**: 1-29.

[58] D. Che, I. Saxena, P. Han, P. Guo and K. F. Ehmann. Machining of carbon fiber reinforced plastics/polymers: a literature review. *Journal of Manufacturing Science and Engineering-Transactions of the ASME* 2014; **136** (3): 034001.

[59] T. Kaneeda. CFRP Cutting mechanism. *In: Proc 16th North American Manufacturing Research Conference*. Illinois, USA, 1991, 24-27 May 1988, p. 216-221.

[60] A. Koplev, A. Lystrup and T. Vorm. The cutting process, chips, and cutting forces in machining CFRP. *Composites* 1983; **14** (4): 371-376.

[61] Y. Turki, M. Habak, R. Velasco, Z. Aboura, K. Khellil and P. Vantomme. Experimental investigation of drilling damage and stitching effects on the mechanical behavior of carbon/epoxy composites. *International Journal of Machine Tools and Manufacture* 2014; **87**: 61-72.

[62] D. H. Wang, M. Ramulu and D. Arola. Orthogonal cutting mechanisms of graphite/epoxy composite. Part II: multi-directional laminate. *International Journal of Machine Tools and Manufacture* 1995; **35** (12): 1639-1648.

[63] D. H. Wang, M. Ramulu and D. Arola. Orthogonal cutting mechanisms of graphite/epoxy composite. Part I: unidirectional laminate. *International Journal of Machine Tools and Manufacture* 1995; **35** (12): 1623-1638.

[64] W. Hintze, D. Hartmann and C. Schütte. Occurrence and propagation of delamination during the machining of carbon fibre reinforced plastics (CFRPs) - an experimental study. *Composites Science and Technology* 2011; **71** (15): 1719-1726.

[65] E. D. Eneyew and M. Ramulu. Experimental study of surface quality and damage when drilling unidirectional CFRP composites. *Journal of Materials Research and Technology* 2014; **3** (4): 354-362.

[66] V. Krishnaraj, R. Zitoune and F. Collombet. Comprehensive review on drilling of multimaterials stacks. *Journal of Machining and Forming Technologies* 2010; **2** (3-4): 1-32.

[67] K. H. Park, P. Y. Kwon, G. Castro, D. Kim and J. Lantrip. Preliminary study on tool wear in drilling of composite/titanium stacks with carbide and PCD tools. *Trans North Am Manuf Res Inst SME* 2010; **38**: 283-290.

[68] H. Barish. Quality drills contribute to successful titanium tooling. *Cutting Tool Engineering* 1988; **40**: 38-42.

[69] V. N. Gaitonde, S. R. Karnik, J. C. C. Rubio, A. E. Correia, A. M. Abrao and J. P. Davim. A study

aimed at minimizing delamination during drilling of CFRP composites. *Journal of Composite Materials* 2011; **45** (22): 2359-2368.

[70] F. Lachaud, R. Piquet, F. Collombet and L. Surcin. Drilling of composite structures. *Composite Structures* 2001; **52** (3-4): 511-516.

[71] C. K. H. Dharan and M. S. Won. Machining parameters for an intelligent machining system for composite laminates. *International Journal of Machine Tools and Manufacture* 2000; **40** (3): 415-426.

[72] B. Latha, V. S. Senthilkumar and K. Palanikumar. Modeling and optimization of process parameters for delamination in drilling glass fiber reinforced plastic (GFRP) composites. *Machining Science and Technology* 2011; **15** (2): 172-191.

[73] Z. Qi, K. Zhang, Y. Li, S. Liu and H. Cheng. Critical thrust force predicting modeling for delamination-free drilling of metal-FRP stacks. *Composite Structures* 2014; **107**: 604-609.

[74] E. Capello. Workpiece damping and its effect on delamination damage in drilling thin composite laminates. *Journal of Materials Processing Technology* 2004; **148** (2): 186-195.

[75] U. A. Khashaba. Delamination in drilling GFR-thermoset composites. *Composite Structures* 2004; **63** (3-4): 313-327.

[76] K. Palanikumar, S. Prakash and K. Shanmugam. Evaluation of delamination in drilling GFRP composites. *Materials and Manufacturing Processes* 2008; **23** (8): 858-864.

[77] H. Hocheng and C. C. Tsao. The path towards delamination-free drilling of composite materials. *Journal of Materials Processing Technology* 2005; **167** (2-3): 251-264.

[78] C. C. Tsao and H. Hocheng. Effect of tool wear on delamination in drilling composite materials. *International Journal of Mechanical Sciences* 2007; **49** (8): 983-988.

[79] C. C. Tsao and H. Hocheng. Taguchi analysis of delamination associated with various drill bits in drilling of composite material. *International Journal of Machine Tools and Manufacture* 2004; **44** (10): 1085-1090.

[80] A. Langella, L. Nele and A. Maio. A torque and thrust prediction model for drilling of composite materials. *Composites Part A: Applied Science and Manufacturing* 2005; **36** (1): 83-93.

[81] J. P. Davim and P. Reis. Drilling carbon fiber reinforced plastics manufactured by autoclave-experimental and statistical study. *Materials & Design* 2003; **24** (5): 315-324.

[82] L. M. P. Durão, M. F. S. F. de Moura and A. T. Marques. Numerical prediction of delamination onset in carbon/epoxy composites drilling. *Engineering Fracture Mechanics* 2008; **75** (9): 2767-2778.

[83] U. A. Khashaba, I. A. El-Sonbaty, A. I. Selmy and A. A. Megahed. Machinability analysis in drilling woven GFR/epoxy composites: part I – effect of machining parameters. *Composites Part A: Applied Science and Manufacturing* 2010; **41** (3): 391-400.

[84] U. A. Khashaba, I. A. El-Sonbaty, A. I. Selmy and A. A. Megahed. Machinability analysis in drilling woven GFR/epoxy composites: part II - effect of drill wear. *Composites Part A: Applied Science and Manufacturing* 2010; **41** (9): 1130-1137.

[85] C. C. Tsao. Experimental study of drilling composite materials with step-core drill. *Materials & Design* 2008; **29** (9): 1740-1744.

[86] J. P. Davim and P. Reis. Study of delamination in drilling carbon fiber reinforced plastics (CFRP) using design experiments. *Composite Structures* 2003; **59** (4): 481-487.

[87] M. Mehta, T. J. Reinhart and A. H. Soni. Effect of fastener hole drilling anomalies on structural integrity of PMR-15/Gr composite laminates. *In: Machining Composite Materials Symposium, ASM*

Materials Week. 1992, p. 113-126.

[88] J. P. Davim, J. C. Rubio and A. M. Abrao. A novel approach based on digital image analysis to evaluate the delamination factor after drilling composite laminates. *Composites Science and Technology* 2007; **67** (9): 1939-1945.

[89] D. A. Dornfeld, J. S. Kim, H. Dechow, J. Hewson and L. J. Chen. Drilling burr formation in titanium alloy, Ti-6AI-4V. *CIRP Annals - Manufacturing Technology* 1999; **48** (1): 73-76.

[90] A. Ginting and M. Nouari. Surface integrity of dry machined titanium alloys. *International Journal of Machine Tools and Manufacture* 2009; **49** (3-4): 325-332.

[91] A. L. Mantle and D. K. Aspinwall. Surface integrity and fatigue life of turned gamma titanium aluminide. *Journal of Materials Processing Technology* 1997; **72** (3): 413-420.

[92] J. C. Aurich and D. Dornfeld. Burrs - analysis, control and removal. Berlin, Heidelberg: Springer Berlin Heidelberg, 2010.

[93] S. L. Ko and J. K. Lee. Analysis of burr formation in drilling with a new-concept drill. *Journal of Materials Processing Technology* 2001; **113** (1-3): 392-398.

[94] S. L. Ko, J. E. Chang and G. E. Yang. Burr minimizing scheme in drilling. *Journal of Materials Processing Technology* 2003; **140** (1-3): 237-242.

[95] D. Kim, C. Sturtevant and M. Ramulu. Usage of PCD tool in drilling of titanium/graphite hybrid composite laminate. *International Journal of Machining and Machinability of Materials* 2013; **13** (2-3): 276-288.

[96] R. Neugebauer, U. Ben-Hanan, S. Ihlenfeldt, M. Wabner and A. Stoll. Acoustic emission as a tool for identifying drill position in fiber-reinforced plastic and aluminum stacks. *International Journal of Machine Tools and Manufacture* 2012; **57**: 20-26.

[97] K. E. Kohkonen and N. Potdar. Composite machining. Hand book of Composites, Chapman and Hall. Peters ST ed1998, p. 596-609.

[98] R. Komanduri. Machining of fiber-reinforced composites. *Machining Science and Technology* 1997; **1** (1): 113-152.

[99] K. K. Wika, A. R. C. Sharman, D. Goulbourne and K. Ridgway. Impact of number of flutes and helix angle on tool performance and hole quality in drilling composite/titanium stacks. SAE 2011 AeroTech Congress and Exhibition. Toulouse2011.

[100] V. N. Gaitonde, S. R. Karnik, J. C. Rubio, A. E. Correia, A. M. Abrão and J. P. Davim. Analysis of parametric influence on delamination in high-speed drilling of carbon fiber reinforced plastic composites. *Journal of Materials Processing Technology* 2008; **203** (1-3): 431-438.

[101] S. R. Karnik, V. N. Gaitonde, J. C. C. Rubio, A. E. Correia, A. M. Abrão and J. P. Davim. Delamination analysis in high speed drilling of carbon fiber reinforced plastics (CFRP) using artificial neural network model. *Materials & Design* 2008; **29** (9): 1768-1776.

[102] S. Rawat and H. Attia. Characterization of the dry high speed drilling process of woven composites using machinability maps approach. *CIRP Annals - Manufacturing Technology* 2009; **58** (1): 105-108.

[103] D. Kim and M. Ramulu. Machinability of titanium/graphite hybrid composites in drilling. *Trans North Am Manuf Res Inst SME* 2005; **33**: 445-452.

[104] J. Ahmad. Machining of polymer composites. Boston, MA: Springer US, 2009.

[105] A. Mkaddem, A. Ben Soussia and M. El Mansori. Wear resistance of CVD and PVD multilayer coatings when dry cutting fiber reinforced polymers (FRP). *Wear* 2013; **302** (1-2): 946-954.

[106] K. S. Kim, D. G. Lee, Y. K. Kwak and S. Namgung. Machinability of carbon fiber-epoxy composite materials in turning. *Journal of Materials Processing Technology* 1992; **32** (3): 553-570.

[107] W. König and P. Graß. Quality definition and assessment in drilling of fibre reinforced thermosets. *CIRP Annals - Manufacturing Technology* 1989; **38** (1): 119-124.

[108] K. Sakuma and M. Seto. Tool wear in cutting glass-fiber-reinforced plastics: the relation between fiber orientation and tool wear. *Bulletin of the JSME* 1983; **26** (218): 1420-1427.

[109] G. Santhanakrishnan, R. Krishnamurthy and S. K. Malhotra. Machinability characteristics of fibre reinforced plastics composites. *Journal of Mechanical Working Technology* 1988; **17**: 195-204.

[110] G. Santhanakrishnan, R. Krishnamurthy and S. K. Malhotra. Investigation into the machining of carbon-fibre-reinforced plastics with cemented carbides. *Journal of Materials Processing Technology* 1992; **30** (3): 263-275.

[111] J. Lantrip. New tools needed. *Cutting Tool Engineering* 2008; **60**: 72-84.

[112] J. Fujiwara, R. Nagaura and T. Tashiro. Drilling of CFRP/Ti6Al4V stack board. *International Journal of Automation Technology* 2013; **7**: 426-432.

[113] I. S. Jawahir and C. A. van Luttervelt. Recent developments in chip control research and applications. *CIRP Annals - Manufacturing Technology* 1993; **42** (2): 659-693.

[114] A. Ben Soussia, A. Mkaddem and M. El Mansori. Effect of coating type on dry cutting of glass/epoxy composite. *Surface & Coatings Technology* 2013; **215**: 413-420.

[115] J. R. Ferreira, N. L. Coppini and G. W. A. Miranda. Machining optimisation in carbon fibre reinforced composite materials. *Journal of Materials Processing Technology* 1999; **92-93**: 135-140.

[116] E. Uhlmann, U. Lachmund and M. Brücher. Wear behavior of HFCVD-diamond coated carbide and ceramic tools. *Surface & Coatings Technology* 2000; **131** (1-3): 395-399.

[117] Q. An, X. Cai, J. Xu and M. Chen. Experimental investigation on drilling of high strength T800S/250F CFRP with twist and dagger drill bits. *International Journal of Abrasive Technology* 2014; **6** (3): 183-196.

[118] T. J. Grilo, R. M. F. Paulo, C. R. M. Silva and J. P. Davim. Experimental delamination analyses of CFRPs using different drill geometries. *Composites Part B: Engineering* 2013; **45** (1): 1344-1350.

[119] R. Garrick. Drilling advanced aircraft structures with PCD (poly-crystalline diamond) drills. *In: AeroTech congress & exhibition*. Los Angeles, CA, USA, 2007, 18-20 September, p. 1-9.

[120] L. M. P. Durão, D. J. S. Gonçalves, J. M. R. S. Tavares, V. H. C. de Albuquerque, A. Aguiar Vieira and A. Torres Marques. Drilling tool geometry evaluation for reinforced composite laminates. *Composite Structures* 2010; **92** (7): 1545-1550.

[121] M. Fernandes and C. Cook. Drilling of carbon composites using a one shot drill bit. Part I: five stage representation of drilling and factors affecting maximum force and torque. *International Journal of Machine Tools and Manufacture* 2006; **46** (1): 70-75.

[122] H. Hocheng and C. C. Tsao. Effects of special drill bits on drilling-induced delamination of composite materials. *International Journal of Machine Tools and Manufacture* 2006; **46** (12-13): 1403-1416.

[123] H. Hocheng and C. C. Tsao. Comprehensive analysis of delamination in drilling of composite materials with various drill bits. *Journal of Materials Processing Technology* 2003; **140** (1-3): 335-339.

[124] D. Iliescu, D. Gehin, M. E. Gutierrez and F. Girot. Modeling and tool wear in drilling of CFRP. *International Journal of Machine Tools and Manufacture* 2010; **50** (2): 204-213.

[125] M. B. Lazar and P. Xirouchakis. Experimental analysis of drilling fiber reinforced composites. *International Journal of Machine Tools and Manufacture* 2011; **51** (12): 937-946.

[126] C. Murphy, G. Byrne and M. Gilchrist. The performance of coated tungsten carbide drills when machining carbon fibre-reinforced epoxy composite materials. *Proceedings of the Institution of Mechanical Engineers, Part B: Journal of Engineering Manufacture* 2002; **216** (2): 143-152.

[127] R. Piquet, B. Ferret, F. Lachaud and P. Swider. Experimental analysis of drilling damage in thin carbon/epoxy plate using special drills. *Composites Part A: Applied Science and Manufacturing* 2000; **31** (10): 1107-1115.

[128] C. C. Tsao. Prediction of thrust force of step drill in drilling composite material by Taguchi method and radial basis function network. *International Journal of Advanced Manufacturing Technology* 2006; **36** (1-2): 11-18.

[129] R. Zitoune, M. El Mansori and V. Krishnaraj. Tribo-functional design of double cone drill implications in tool wear during drilling of copper mesh/CFRP/woven ply. *Wear* 2013; **302** (1-2): 1560-1567.

[130] C. Santiuste, X. Soldani and M. H. Miguélez. Machining FEM model of long fiber composites for aeronautical components. *Composite Structures* 2010; **92** (3): 691-698.

[131] C. Santiuste, H. Miguélez and X. Soldani. Out-of-plane failure mechanisms in LFRP composite cutting. *Composite Structures* 2011; **93** (11): 2706-2713.

[132] G. V. G. Rao, P. Mahajan and N. Bhatnagar. Micro-mechanical modeling of machining of FRP composites – Cutting force analysis. *Composites Science and Technology* 2007; **67** (3-4): 579-593.

[133] K. a. Calzada, S. G. Kapoor, R. E. DeVor, J. Samuel and A. K. Srivastava. Modeling and interpretation of fiber orientation-based failure mechanisms in machining of carbon fiber-reinforced polymer composites. *Journal of Manufacturing Processes* 2012; **14** (2): 141-149.

[134] A. Mkaddem, I. Demirci and M. El Mansori. A micro-macro combined approach using FEM for modelling of machining of FRP composites: cutting forces analysis. *Composites Science and Technology* 2008; **68** (15-16): 3123-3127.

[135] A. Mkaddem and M. El Mansori. Finite element analysis when machining UGF-reinforced PMCs plates: chip formation, crack propagation and induced-damage. *Materials & Design* 2009; **30** (8): 3295-3302.

[136] M. V. Ramesh, K. N. Seetharamu, N. Ganesan and M. S. Sivakumar. Analysis of machining of FRPs using FEM. *International Journal of Machine Tools and Manufacture* 1998; **38** (12): 1531-1549.

[137] M. Mahdi and L. Zhang. A finite element model for the orthogonal cutting of fiber-reinforced composite materials. *Journal of Materials Processing Technology* 2001; **113** (1-3): 373-377.

[138] N. Bhatnagar, D. Nayak, I. Singh, H. Chouhan and P. Mahajan. Determination of machining-induced damage characteristics of fiber reinforced plastic composite laminates. *Materials and Manufacturing Processes* 2004; **19** (6): 1009-1023.

[139] G. V. G. Rao, P. Mahajan and N. Bhatnagar. Three-dimensional macro-mechanical finite element model for machining of unidirectional-fiber reinforced polymer composites. *Materials Science and Engineering: A* 2008; **498** (1-2): 142-149.

[140] D. Nayak, N. Bhatnagar and P. Mahajan. Machining studies of UD-FRP composites part 2: finite element analysis. *Machining Science and Technology* 2005; **9** (4): 503-528.

[141] L. Lasri, M. Nouari and M. El Mansori. Modelling of chip separation in machining unidirectional FRP composites by stiffness degradation concept. *Composites Science and Technology* 2009; **69** (5):

684-692.

[142] G. R. Johnson and W. H. Cook. Fracture characteristics of three metals subjected to various strains, strain rates, temperatures and pressures. *Engineering Fracture Mechanics* 1985; **21** (1): 31-48.

[143] G. R. Johnson and W. H. Cook. A constitutive model and data for metals subjected to large strains, high strain rates and high temperatures. *In: Proc of the 7th International Symposium on Ballistics*. 1983, 1983, p. 541-547.

[144] F. J. Zerilli and R. W. Armstrong. Dislocation - mechanics - based constitutive relations for material dynamics calculations. *Journal of Applied Physics* 1987; **61** (5): 1816-1825.

[145] P. Follansbee and U. Kocks. A constitutive description of the deformation of copper based on the use of the mechanical threshold stress as an internal state variable. *Acta Metallurgica* 1988; **36** (1): 81-93.

[146] D. J. Bammann, M. L. Chiesa and G. C. Johnson. Modeling large deformation and failure in manufacturing processes. *In: Tatsumi T., Wannabe E., Kambe T., editors.* Theoretical and Applied Mechanics. Amsterdam: Elsevier; 1996, p. 359-376.

[147] T. Obikawa and E. Usui. Computational machining of titanium alloy - finite element modeling and a few results. *Journal of Manufacturing Science and Engineering-Transactions of the ASME* 1996; **118** (2): 208-215.

[148] S.-H. Rhim and S.-I. Oh. Prediction of serrated chip formation in metal cutting process with new flow stress model for AISI 1045 steel. *Journal of Materials Processing Technology* 2006; **171** (3): 417-422.

[149] L. Li and N. He. A FEA study on mechanisms of saw-tooth chip deformation in high speed cutting of Ti–6–Al–4V alloy. *In: Fifth International Conference on High Speed Machining (HSM), Metz, France*. 2006, p. 14-16.

[150] M. Barge, H. Hamdi, J. Rech and J.-M. Bergheau. Numerical modelling of orthogonal cutting: influence of numerical parameters. *Journal of Materials Processing Technology* 2005; **164**: 1148-1153.

[151] O. Pantalé, J.-L. Bacaria, O. Dalverny, R. Rakotomalala and S. Caperaa. 2D and 3D numerical models of metal cutting with damage effects. *Computer Methods In Applied Mechanics and Engineering* 2004; **193** (39): 4383-4399.

[152] Y. Guo and D. W. Yen. A FEM study on mechanisms of discontinuous chip formation in hard machining. *Journal of Materials Processing Technology* 2004; **155**: 1350-1356.

[153] J. Hua and R. Shivpuri. Prediction of chip morphology and segmentation during the machining of titanium alloys. *Journal of Materials Processing Technology* 2004; **150** (1-2): 124-133.

[154] E. Ceretti, M. Lucchi and T. Altan. FEM simulation of orthogonal cutting: serrated chip formation. *Journal of Materials Processing Technology* 1999; **95** (1-3): 17-26.

[155] Y. Xi, M. Bermingham, G. Wang and M. Dargusch. Finite element modeling of cutting force and chip formation during thermally assisted machining of Ti6Al4V alloy. *Journal of Manufacturing Science and Engineering-Transactions of the ASME* 2013; **135** (6): 061014.

[156] G. Chen, C. Ren, X. Yang, X. Jin and T. Guo. Finite element simulation of high-speed machining of titanium alloy (Ti-6Al-4V) based on ductile failure model. *International Journal of Advanced Manufacturing Technology* 2011; **56** (9-12): 1027-1038.

[157] D. Umbrello. Finite element simulation of conventional and high speed machining of Ti6Al4V alloy. *Journal of Materials Processing Technology* 2008; **196** (1-3): 79-87.

[158] M. Calamaz, D. Coupard and F. Girot. A new material model for 2D numerical simulation of serrated chip formation when machining titanium alloy Ti-6Al-4V. *International Journal of Machine Tools and Manufacture* 2008; **48** (3-4): 275-288.

[159] M. Sima and T. Özel. Modified material constitutive models for serrated chip formation simulations and experimental validation in machining of titanium alloy Ti-6Al-4V. *International Journal of Machine Tools and Manufacture* 2010; **50** (11): 943-960.

[160] R. Liu, S. Melkote, R. Pucha, J. Morehouse, X. Man and T. Marusich. An enhanced constitutive material model for machining of Ti-6Al-4V alloy. *Journal of Materials Processing Technology* 2013; **213** (12): 2238-2246.

[161] M. Cotterell and G. Byrne. Dynamics of chip formation during orthogonal cutting of titanium alloy Ti-6Al-4V. *CIRP Annals - Manufacturing Technology* 2008; **57** (1): 93-96.

[162] P. Castany, F. Pettinari-Sturmel, J. Crestou, J. Douin and A. Coujou. Experimental study of dislocation mobility in a Ti-6Al-4V alloy. *Acta Materialia* 2007; **55** (18): 6284-6291.

[163] C. Bonnet. Compréhension des mécanismes de coupe lors du perçage à sec de l'empilage Ti6Al4V/Composite fibre de carbone. France: **Arts et Métiers ParisTech [Ph.D. dissertation]**, 2010.

[164] L. Lasri. Modélisation macromécanique et micromécanique de l'usinage des composites à matrice polymère et fibres longues. France: **Arts et Métiers ParisTech [Ph.D. dissertation]**, 2009.

[165] J. Xu and M. El Mansori. Cutting modeling of hybrid CFRP/Ti composite with induced damage analysis. *Materials* 2016; **9** (1): 1-22.

[166] L. Lasri, M. Nouari and M. El Mansori. Wear resistance and induced cutting damage of aeronautical FRP components obtained by machining. *Wear* 2011; **271** (9-10): 2542-2548.

[167] H. Hocheng, H. Y. Puw and Y. Huang. Preliminary study on milling of unidirectional carbon fibre-reinforced plastics. *Composites Manufacturing* 1993; **4** (2): 103-108.

[168] D. Arola, M. B. Sultan and M. Ramulu. Finite element modeling of edge trimming fiber reinforced plastics. *Journal of Manufacturing Science and Engineering-Transactions of the ASME* 2002; **124** (1): 32-41.

[169] J. Xu and M. El Mansori. Numerical modeling of stacked composite CFRP/Ti machining under different cutting sequence strategies. *International Journal of Precision Engineering and Manufacturing* 2016; **17** (1): 99-107.

[170] J. Xu and M. El Mansori. Numerical studies of frictional responses when cutting hybrid CFRP/Ti composite. *International Journal of Advanced Manufacturing Technology* 2016. http://dx.doi.org/10.1007/s00170-016-8512-9

[171] N. N. Zorev. Inter-relationship between shear processes occurring along tool face and shear plane in metal cutting. *International Research in Production Engineering* 1963; **49**: 42-49.

[172] S. Hibbit K. Abaqus/Explicit Theory and User Manuals 2006.

[173] Y. Karpat. A modified material model for the finite element simulation of machining titanium alloy Ti-6Al-4V. *Machining Science and Technology* 2010; **14** (3): 390-410.

[174] D. Iliescu. Approches experimentale et numerique de l'usinage a sec des composites carbone-epoxy. France: **Arts et Métiers ParisTech [Ph.D. dissertation]**, 2008.

[175] D. Iliescu, D. Gehin, I. Iordanoff, F. Girot and M. E. Gutiérrez. A discrete element method for the simulation of CFRP cutting. *Composites Science and Technology* 2010; **70** (1): 73-80.

[176] F. Aymerich, F. Dore and P. Priolo. Prediction of impact-induced delamination in cross-ply

composite laminates using cohesive interface elements. *Composites Science and Technology* 2008; **68** (12): 2383-2390.

[177] E. Savani, A. Pirondi, F. Carta1, A. C. Nogueira and E. Hombergsmeier. Modeling delamination of Ti-CFRP interfaces. *In: 15th European Conference on Composite Materials*. Venice, Italy, 2012, 24-28 June, p. 1-8.

[178] H. M. Jensen. Mixed mode interface fracture criteria. *Acta Materialia* 1990; **38** (12): 2637-2644.

[179] D. Lesuer. Experimental investigation of material models for Ti-6Al-4V and 2024-T3. Livermore: University of California, Lawrence Livermore National Laboratory; 1999, p. 1-36.

[180] A. Hillerborg, M. Modeer and P. E. Petersson. Analysis of crack formation and crack growth in concrete by means of fracture mechanics and finite elements. *Cement and Concrete Research* 1976; **6** (6): 773-781.

[181] J. William and D. Callister. Materials science and engineering: an introduction. New York: Wiley, 1994.

[182] http://www.matweb.com.

[183] H. Pwu and H. Hocheng. Chip formation model of cutting fiber-reinforced plastics perpendicular to fiber axis. *Journal of Manufacturing Science and Engineering-Transactions of the ASME* 1998; **120** (1): 192-196.

[184] X. M. Wang and L. C. Zhang. An experimental investigation into the orthogonal cutting of unidirectional fibre reinforced plastics. *International Journal of Machine Tools and Manufacture* 2003; **43** (10): 1015-1022.

[185] Z. Hashin. Failure criteria for unidirectional fiber composites. *Journal of Applied Mechanics - Transactions of the ASME* 1980; **47** (2): 329-334.

[186] Z. Hashin and A. Rotem. A fatigue failure criterion for fiber reinforced materials. *Journal of Composite Materials* 1973; **7** (4): 448-464.

[187] P. P. Camanho and C. G. Dávila. Mixed-mode decohesion finite elements for the simulation of delamination in composite materials. *NASA-Technical paper* 2002; **211737** (1): 1-37.

[188] J. C. Fish and S. W. Lee. Delamination of tapered composite structures. *Engineering Fracture Mechanics* 1989; **34** (1): 43-54.

[189] J. Hou, N. Petrinic, C. Ruiz and S. Hallett. Prediction of impact damage in composite plates. *Composites Science and Technology* 2000; **60** (2): 273-281.

[190] M. L. Benzeggagh and M. Kenane. Measurement of mixed-mode delamination fracture toughness of unidirectional glass/epoxy composites with mixed-mode bending apparatus. *Composites Science and Technology* 1996; **56** (4): 439-449.

[191] I. Lapczyk and J. A. Hurtado. Progressive damage modeling in fiber-reinforced materials. *Composites Part A: Applied Science and Manufacturing* 2007; **38** (11): 2333-2341.

[192] A. Gente, H. W. Hoffmeister and C. J. Evans. Chip formation in machining Ti6A14V at extremely high cutting speeds. *CIRP Annals - Manufacturing Technology* 2001; **50** (1): 49-52.

[193] A. G. Evans, B. Dalgleish, M. He and J. Hutchinson. On crack path selection and the interface fracture energy in bimaterial systems. *Acta Materialia* 1989; **37** (12): 3249-3254.

[194] Z. H. Jin and C. T. Sun. Cohesive zone modeling of interface fracture in elastic bi-materials. *Engineering Fracture Mechanics* 2005; **72** (12): 1805-1817.

[195] M. Rahman, S. Ramakrishna, J. Prakash and D. Tan. Machinability study of carbon fiber reinforced composite. *Journal of Materials Processing Technology* 1999; **89-90**: 292-297.

[196] X. Wang and L. Zhang. An experimental investigation into the orthogonal cutting of unidirectional fibre reinforced plastics. *International Journal of Machine Tools and Manufacture* 2003; **43** (10): 1015-1022.

[197] A. E. Bayoumi and J. Q. Xie. Some metallurgical aspects of chip formation in cutting Ti-6wt.% Al-4wt.% V alloy. *Materials Science and Engineering: A* 1995; **190** (1): 173-180.

[198] J. Barry, G. Byrne and D. Lennon. Observations on chip formation and acoustic emission in machining Ti-6Al-4V alloy. *International Journal of Machine Tools and Manufacture* 2001; **41** (7): 1055-1070.

[199] D. Iliescu, D. Gehin, M. Nouari and F. Girot. Damage modes of the aeronautic multidirectional carbon/epoxy composite T300/914 in machining. *International Journal of Materials and Product Technology* 2008; **32** (2-3): 118-135.

[200] M. C. Shaw. Metal cutting principles. New York: Oxford University Press, 2005.

[201] J. Xu, M. El Mansori and J. Voisin. Numerical modeling and FE analysis of CFRP/Ti stack orthogonal cutting. *Procedia CIRP* 2016; **46** (1): 67-70.

[202] K. Liu and S. N. Melkote. Material strengthening mechanisms and their contribution to size effect in micro-cutting. *Journal of Manufacturing Science and Engineering-Transactions of the ASME* 2006; **128** (3): 730-738.

[203] A. Meena and M. El Mansori. Specific cutting force, tool wear and chip morphology characteristics during dry drilling of austempered ductile iron (ADI). *International Journal of Advanced Manufacturing Technology* 2013; **69** (9-12): 2833-2841.

[204] Q. An, W. Ming, X. Cai and M. Chen. Study on the cutting mechanics characteristics of high-strength UD-CFRP laminates based on orthogonal cutting method. *Composite Structures* 2015; **131**: 374-383.

[205] L. Chen, T. El-Wardany and W. Harris. Modelling the effects of flank wear land and chip formation on residual stresses. *CIRP Annals - Manufacturing Technology* 2004; **53** (1): 95-98.

[206] L. Zhou, J. Shimizu, A. Muroya and H. Eda. Material removal mechanism beyond plastic wave propagation rate. *Precision Engineering* 2003; **27** (2): 109-116.

[207] C.-S. Chang, J.-E. Ho, C.-H. Chan and B.-C. Hwang. Prediction of cutting temperature in turning carbon fiber reinforced plastics composites with worn tools. *Journal of Applied Sciences* 2011; **11** (22): 3698-3707.

[208] J. Xu and M. El Mansori. Experimental study on drilling mechanisms and strategies of hybrid CFRP/Ti stacks. *Composite Structures* 2016. http://dx.doi.org/10.1016/j.compstruct.2016.07.025

[209] R. Zitoune, V. Krishnaraj and F. Collombet. Study of drilling of composite material and aluminium stack. *Composite Structures* 2010; **92** (5): 1246-1255.

[210] J. Davim, P. Sreejith, R. Gomes and C. Peixoto. Experimental studies on drilling of aluminium (AA1050) under dry, minimum quantity of lubricant, and flood-lubricated conditions. *Proceedings of the Institution of Mechanical Engineers, Part B: Journal of Engineering Manufacture* 2006; **220** (10): 1605-1611.

[211] O. A. Pawar, Y. S. Gaikhe, A. Tewari, R. Sundaram and S. S. Joshi. Analysis of hole quality in drilling GLARE fiber metal laminates. *Composite Structures* 2015; **123**: 350-365.

[212] R. Zitoune, V. Krishnaraj, F. Collombet and S. Le Roux. Experimental and numerical analysis on drilling of carbon fibre reinforced plastic and aluminium stacks. *Composite Structures* 2016; **146**: 148-158.

ÉTUDE NUMERIQUE ET EXPERIMENTALE DE L'USINAGE DES MATERIAUX HYBRIDES TITANE-COMPOSITES

RESUME : Dans l'industrie aérospatiale, l'utilisation des matériaux hybrides CFRP/Ti montre une tendance à la hausse en raison de leurs propriétés mécaniques/physiques améliorées ainsi que des fonctions structurelles plus flexibles. En dépit de leurs nombreuses applications, l'usinage CFRP/Ti en perçage en une seule passe reste le principal défi scientifique et technologique de l'assemblage multi-matériaux. Par rapport au coût de production élevé et le temps des recherches basées sur des approches exclusivement expérimentales de l'usinage multi-matériaux, cette étude a pour objectif d'amener une meilleure compréhension de la coupe CFRP/Ti à travers une approche physique hybride qui fait dialoguer les méthodes numériques et expérimentales. Un modèle EF utilisant le concept de zone cohésive a été développé pour étudier l'usinabilité anisotrope de pièces structurales CFRP/Ti à des fins d'assemblage. L'approche numérique explicite, par des études préliminaires, les mécanismes de coupe clés qui contrôlent l'usinage CFRP/Ti. Par la suite, l'approche expérimentale a été conduite sous différentes conditions d'usinage en configuration de coupe orthogonale et de perçage. Une attention spéciale a été consacrée aux effets des stratégies des séquences de coupe CFRP/Ti sur la formation des endommagements d'interface induits. Ces études expérimentales et numériques ont permit (*i*) d'expliciter les mécanismes physiques activés qui contrôlent la coupe à l'interface ainsi que les endommagements induits par celle-ci, (*ii*) de préciser les effets des différentes stratégies d'assemblage multi-matériaux sur l'usinage CFRP/Ti, (*iii*) de définir la classification d'usinabilité CFRP/Ti, et (*iv*) d'analyser enfin les effets paramétriques géométrie/matériau d'outil régissant l'opération d'usinage CFRP/Ti.

Mots clés : composite hybride CFRP/Ti, analyse EF, usinage expérimentale, coupe orthogonale, perçage, stratégie d'usinage, endommagements en usinage multi-matériaux.

NUMERICAL AND EXPERIMENTAL STUDY OF MACHINING TITANIUM-COMPOSITE STACKS

ABSTRACT : In modern aerospace industry, the use of hybrid CFRP/Ti stacks has experienced an increasing trend because of their enhanced mechanical/physical properties and flexible structural functions. In spite of their widespread applications, machining hybrid CFRP/Ti stacks in one shot time still consists of the main scientific and technological challenge in multi-material fastening. Compared to the high cost of pure experimental investigations on the multi-material machining, this study aims to provide an improved CFRP/Ti cutting comprehension via both numerical and experimental methodologies. To this aim, an FE model by using the cohesive zone concept was established to construct the anisotropic machinability of the bi-material system. The numerical work aims to provide preliminary inspections of the key cutting mechanisms dominating the hybrid CFRP/Ti stack machining. Afterward, some systematic experimental work including orthogonal cutting and hole drilling was carefully performed *versus* different input cutting conditions. A special attention was made on the examination of different cutting sequences strategies on CFRP/Ti cutting responses and induced interface damage formation. The combined numerical-experimental studies provide the key findings aiming to (*i*) reveal the activated mechanisms controlling interface cutting and subsequent interface damage formation, (*ii*) clarify the influences of different cutting-sequence strategies on hybrid CFRP/Ti stack machining, (*iii*) outline the machinability classification of hybrid CFRP/Ti stacks, and (*iv*) analyze finally the parametric effects of material/tool geometry on cutting hybrid CFRP/Ti stacks.

Keywords : hybrid CFRP/Ti stack, FE analysis, experimental machining, orthogonal cutting, drilling, cutting-sequence strategy, damage in cutting multi-phase materials.

ARTS ET MÉTIERS ParisTech

ParisTech INSTITUT DES SCIENCES ET TECHNOLOGIES PARIS INSTITUTE OF TECHNOLOGY